

INFORMATION TO USERS

This manuscript has been reproduced from the microfilm master. UMI films the text directly from the original or copy submitted. Thus, some thesis and dissertation copies are in typewriter face, while others may be from any type of computer printer.

The quality of this reproduction is dependent upon the quality of the copy submitted. Broken or indistinct print, colored or poor quality illustrations and photographs, print bleedthrough, substandard margins, and improper alignment can adversely affect reproduction.

In the unlikely event that the author did not send UMI a complete manuscript and there are missing pages, these will be noted. Also, if unauthorized copyright material had to be removed, a note will indicate the deletion.

Oversize materials (e.g., maps, drawings, charts) are reproduced by sectioning the original, beginning at the upper left-hand corner and continuing from left to right in equal sections with small overlaps.

Photographs included in the original manuscript have been reproduced xerographically in this copy. Higher quality 6" x 9" black and white photographic prints are available for any photographs or illustrations appearing in this copy for an additional charge. Contact UMI directly to order.

**Bell & Howell Information and Learning
300 North Zeeb Road, Ann Arbor, MI 48106-1346 USA
800-521-0600**

UMI[®]

**The Pennsylvania State University
The Graduate School
College of Earth and Mineral Sciences**

NITROGEN IN PLASMAS AND STEEL WELD METAL

**A Thesis in
Materials Science and Engineering
By
Todd A. Palmer**

© 1999 Todd A. Palmer

**Submitted in Partial Fulfillment
of the Requirements
for the Degree of**

Doctor of Philosophy

December 1999

UMI Number: 9961285

UMI[®]

UMI Microform 9961285

Copyright 2000 by Bell & Howell Information and Learning Company.

**All rights reserved. This microform edition is protected against
unauthorized copying under Title 17, United States Code.**

Bell & Howell Information and Learning Company

300 North Zeeb Road

P.O. Box 1346

Ann Arbor, MI 48106-1346

We approve the thesis of Todd A. Palmer.

Date of Signature



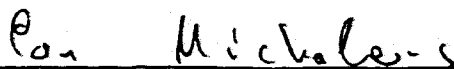
10/21/99

Tarasankar DebRoy
Professor of Materials Science and Engineering
Thesis Adviser
Chair of Committee



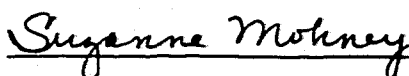
Oct. 25, 1999

Russell Messier
Professor of Engineering Science and Mechanics



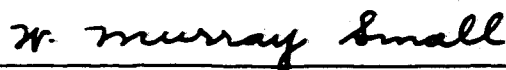
10/25/99

Pan Michaleris
Assistant Professor of Mechanical Engineering



10/25/99

Suzanne Mohnney
Assistant Professor of Materials Science and Engineering



10/21/99

W. Murray Small
Associate Professor of Metallurgy



October 25 '99

K. Osseo-Asare
Professor of Metallurgy
Chair, Metals Science and Engineering Options

ABSTRACT

The observation of nitrogen concentrations, well above those predicted by Sieverts' Law, during the arc welding of iron and steel is well established. Several models, based on the role of monatomic nitrogen and a competition between nitrogen absorption and desorption, are currently available. This work represents the first comprehensive effort to combine knowledge of the plasma phase, the plasma-metal interaction, and the transport of nitrogen in the weldment in a single model to determine the nitrogen concentration in iron during gas tungsten arc (GTA) welding.

The development of this model is based, in part, on a comprehensive analysis of the species density distribution in a typical GTA welding arc. A detailed calculation methodology has been developed and used here to determine the densities of various species as a function of electron temperature for both pure gases and a number of gas mixtures. According to these calculations, ionized species dominate at temperatures commonly found close to the electrode, while neutral monatomic and diatomic nitrogen are the primary species near the metal surface.

This calculation methodology can also shed light on physical processes occurring in more complex gas mixtures. For example, oxygen additions to inert gas-nitrogen mixtures further enhance the resulting nitrogen concentration in the weld metal and affect the species density distribution in the plasma phase. Using this calculation scheme, definitive proof is provided for an increase in the monatomic nitrogen partial pressure with the presence of NO in the plasma phase at temperatures below 6000K. These results are further validated by emission spectroscopy of glow discharge plasmas containing these same gas mixtures.

The calculated species densities can then be applied to determine the monatomic nitrogen partial pressure above the weld pool. Using these values at electron temperatures characteristic of the region adjacent to the weld pool surface, the resulting nitrogen concentration on the weld pool surface is calculated with knowledge of the weld pool surface temperatures, determined from the heat transfer and fluid flow characteristics of the weld pool. Once absorbed, nitrogen is then transported to the weld pool interior by convection

and diffusion. A quasi-steady-state three-dimensional mathematical model is developed to numerically solve the equations of conservation of energy, nitrogen concentration, and momentum during the GTA welding of pure iron and determine the resulting nitrogen concentration in the weld pool.

With the presence of turbulence in the weld pool also considered, the model produces realistic nitrogen concentrations in the weld metal. It is shown that the desorption of the dissolved nitrogen via bubble formation in the nitrogen supersaturated weld pool plays an important role in determining the resulting nitrogen concentration. When nitrogen supersaturation levels in the liquid metal are in the range of 50 to 75% greater than the equilibrium nitrogen solubility at one atmosphere of diatomic nitrogen at the weld pool surface, the calculated nitrogen concentrations are equivalent to the experimental observations.

In addition to the development of this model, it has been observed that changes in welding parameters also produce significant changes in the weld pool appearance and microstructure. For example, weld pools produced at a higher travel speed with nitrogen additions to the shielding gas exhibit no porosity while weld pools formed at the lower travel speed exhibit significant porosity. The predominant weld pool microstructures are also significantly different in each case. Therefore, a connection between the nitrogen concentration in the weld metal, the resulting microstructure, and the presence or absence of porosity is indicated.

TABLE OF CONTENTS

LIST OF FIGURES.....	x
LIST OF TABLES.....	xxvii
ACKNOWLEDGMENTS.....	xxxii
Chapter 1. INTRODUCTION.....	1
1.1 NITROGEN DISSOLUTION DURING ARC WELDING.....	1
1.2 CURRENT UNDERSTANDING OF THE NITROGEN DISSOLUTION REACTION.....	7
1.2.1 Plasma-Metal Interactions.....	7
1.2.2 Existing Models.....	10
1.3 CALCULATION OF ATOMIC NITROGEN PARTIAL PRESSURE IN THE PLASMA.....	13
1.4 MATHEMATICAL MODELING OF THE WELDING PROCESS.....	16
1.5 OBJECTIVE AND MOTIVATION FOR RESEARCH.....	17
REFERENCES.....	20
Chapter 2. BACKGROUND AND LITERATURE REVIEW.....	24
2.1 NITROGEN SOLUBILITY IN CONVENTIONAL MATERIALS PROCESSING.....	24
2.1.1 Dissolved Gases in Metals.....	24
2.1.2 Iron-Nitrogen System.....	25
2.1.3 Nitrogen Absorption Reaction.....	28
2.1.4 Effect of Alloying Elements on Nitrogen Absorption.....	31
2.2 NITROGEN DISSOLUTION IN PLASMA - METAL SYSTEMS.....	35
2.2.1 Observation of Enhanced Nitrogen Concentrations during Arc Melting.....	35
2.2.1.1 Species Present in the Plasma Phase.....	37
2.2.1.2 Predominant Mechanisms Responsible for Enhanced Nitrogen Concentration.....	41
2.2.1.3 Use of Glow Discharges to Model Arcs.....	44

2.2.1.4	Effect of Changes in Arc Parameters on Nitrogen Concentration.....	47
2.2.2	Role of Alloying Element Additions on Resulting Nitrogen Concentration.....	52
2.2.3	Role of Surface Active Elements on Nitrogen Concentration.....	58
2.2.4	Role of Convection.....	63
2.2.5	Steady-State Nature of Nitrogen Dissolution Process.....	70
2.2.6	Time-Dependent Nature of the Nitrogen Dissolution Process.....	73
2.2.6.1	Rate Of Nitrogen Absorption and Desorption Reactions at Equilibrium.....	73
2.2.6.2	Effect of Surface Active Element Additions on the Reaction Rate.....	75
2.2.6.3	Rate of Nitrogen Absorption and Desorption During Arc Melting.....	77
2.3	NITROGEN DISSOLUTION DURING THE WELDING OF IRON AND STEELS.....	85
2.3.1	Role of Arc Welding Process in Affecting Nitrogen Dissolution Reaction.....	85
2.3.2	GTA Welding of Iron and Plain Carbon Steels.....	85
2.3.2.1	Structure of Arc Column in GTA Welding.....	85
2.3.2.2	Nitrogen Concentrations in GTA Weld Pool.....	87
2.3.2.3	Role of Alloying Elements in Nitrogen Dissolution During GTA Welding.....	91
2.3.3	GMA Welding of Iron and Plain Carbon Steels.....	94
2.3.4	Formation of Porosity in the Weld Pool.....	103
2.3.5	Role of Oxygen and Hydrogen Additions on Nitrogen Dissolution.....	108
2.4	PROPOSED MECHANISMS FOR ENHANCED NITROGEN DISSOLUTION.....	115
2.4.1	Interaction Between Plasma Phase and Weld Pool.....	115
2.4.2	Development of Two Temperature Model.....	119
2.4.3	Validation of Two-Temperature Model.....	121

2.5 OVERVIEW.....	125
REFERENCES.....	129
Chapter 3. THERMODYNAMIC CALCULATION OF SPECIES DENSITIES IN THE PLASMA PHASE.....	139
3.1 INTRODUCTION.....	139
3.2 CURRENT STATUS OF SPECIES DENSITY CALCULATIONS IN NITROGEN-CONTAINING PLASMAS.....	140
3.3 CALCULATION METHODOLOGY.....	142
3.4 RESULTS AND DISCUSSION.....	151
3.4.1 Species Densities in Plasmas Formed From a Single Source Feed Gas.....	151
3.4.2 Species Densities in Plasmas Formed From a Source Gas Containing a Monatomic and a Diatomic Gas Mixture.....	157
3.4.3 Species Densities in Plasmas Formed From Nitrogen- Oxygen Gas Mixtures.....	165
3.4.4 Use of Species Densities in Calculation of Nitrogen Concentrations.....	179
3.4.5 Emission Spectroscopy Of Glow Discharges.....	184
3.5 SUMMARY AND CONCLUSIONS.....	198
REFERENCES.....	203
Chapter 4. NITROGEN DISSOLUTION DURING THE GTA WELDING OF PURE IRON.....	206
4.1 BACKGROUND.....	206
4.2 EXPERIMENTAL PROCEDURE.....	207
4.2.1 GTA Welding of Pure Iron Samples.....	207
4.2.2 Measurement of Nitrogen Concentration in Weld Metal.....	212
4.3 RESULTS AND DISCUSSION.....	221
4.3.1 Nitrogen Concentration in the Weld Metal.....	221
4.3.2 Weld Pool Appearance.....	226
4.3.3 Porosity in Weld Pool.....	231

4.3.3.1 Radiography of Weld Metal.....	233
4.3.3.2 Density Measurements.....	238
4.3.4 Weld Metal Microstructure.....	240
4.3.5 Microhardness Distribution Across the Weld Pool.....	255
4.3.6 X-Ray Analysis of Weld Metal.....	262
4.3.6 Effect of Microstructure on Nitrogen Solubility.....	271
4.4 OVERVIEW.....	276
REFERENCES.....	280
Chapter 5. MATHEMATICAL MODELING OF NITROGEN DISSOLUTION IN GTA WELDING.....	284
5.1 BACKGROUND.....	284
5.2 MATHEMATICAL FORMULATION.....	285
5.2.1 Governing Equations.....	285
5.2.1.1 Momentum Equation in Moving Coordinate System (ζ , y , z).....	287
5.2.1.2 Energy Equation.....	289
5.2.1.3 Conservation of Nitrogen Equations.....	291
5.2.1.4 Effects of Turbulence in the Weld Pool.....	294
5.2.2 Solution Procedure.....	295
5.2.3 Grid Generation.....	297
5.2.4 Boundary Conditions.....	300
5.2.4.1 Momentum Equations.....	302
5.2.4.2 Energy Equation.....	303
5.2.4.3 Conservation of Nitrogen Concentration.....	304
5.3 RESULTS OF MODELING CALCULATIONS.....	308
5.3.1 Temperature and Velocity Calculations.....	308
5.3.2 Electron Temperature and Monatomic Nitrogen Partial Pressure Calculations.....	310
5.3.3 Nitrogen Surface Concentrations.....	327
5.3.4 Nitrogen Transport Mechanism.....	333

5.3.5 Nitrogen Concentration Distribution in the Weld Pool Interior.....	336
5.3.5.1 Role of Electron Temperature Distribution.....	336
5.3.5.2 Level of Nitrogen Supersaturation in the Weld Pool.....	353
5.3.5.3 Effect Of Changes In The Level of Turbulence in the Weld Pool	362
5.4 OVERVIEW.....	369
REFERENCES.....	374
 Chapter 6. SUMMARY AND CONCLUSIONS.....	 379
6.1 CURRENT STATE OF THE ART.....	379
6.1.1 Nitrogen in the Plasma Phase.....	380
6.1.2 Nitrogen in the Weld Metal.....	381
6.2 FUTURE WORK.....	383
 Appendix A. CALCULATION OF PARTITION FUNCTIONS.....	 385
A.1 PARTITION FUNCTIONS OF ATOMIC SPECIES.....	385
A.2 PARTITION FUNCTIONS OF MOLECULAR SPECIES.....	385
REFERENCES.....	402
 Appendix B. THERMODYNAMIC BASIS FOR DISSOCIATION REACTION CALCULATIONS.....	 403
REFERENCES.....	407
 Appendix C. SUMMARY OF X-RAY ANALYSIS OF WELD SAMPLES.....	 408
REFERENCES.....	426

LIST OF FIGURES

Figure		Page
1.1	Computed equilibrium solubility of nitrogen in iron exposed to diatomic nitrogen (a) as a function of temperature and partial pressure of diatomic nitrogen, (b) as a function of partial pressure of diatomic nitrogen at three temperatures, and (c) as a function of temperature at three partial pressures of diatomic nitrogen. ³	3
1.2	Nitrogen concentration in an arc melted iron sample plotted as a function of the square root of the nitrogen partial pressure. ⁴	5
1.3	Relation between the nitrogen content of the weld metal and the nitrogen partial pressure (P_{N_2}) for an Ar- N_2 shielding gas mixture at a welding current of 250 A, an arc length of 10 mm, and a travel speed of 1.67 mm/sec. ¹⁷	6
1.4	Computed equilibrium solubility of nitrogen in iron exposed to monatomic nitrogen (a) as a function of temperature and partial pressure of monatomic nitrogen, (b) as a function of partial pressure of monatomic nitrogen at three temperatures, and (c) as a function of temperature at three partial pressures of monatomic nitrogen. ³	9
1.5	Plot of effective dissociation temperature vs. percent nitrogen dissociated ²⁵ for the experimental conditions of Bandopadhyay <i>et al.</i> ²⁰	12
1.6	Schematic diagram of the arc column structure in GTA welding operations.	14
2.1	Iron Nitrogen Phase Diagram. ⁷	26
2.2(a)	The solubility of nitrogen in iron over a wide temperature range for both solid and liquid iron phases at 1 atm. ¹²	29
2.2(b)	The solubility of nitrogen in iron as a function of the square root of P_{N_2} at 1600°C. ¹⁵	32
2.3	The effect of alloying element additions on the nitrogen solubility in liquid iron at a nitrogen pressure of 1 atm. and	

	a temperature of 1600° C. ¹⁵	34
2.4	Nitrogen concentrations observed in iron samples during arc melting in several nitrogen containing atmospheres. ²⁸	36
2.5	Degree of dissociation (α_d) of several gases as a function of temperature. ⁴⁰	39
2.6	Experimental nitrogen solubility plotted as a function of the nitrogen partial pressure for iron samples at a temperature of 1300 C exposed to glow discharges composed of various He-N ₂ gas mixtures at a total pressure of 1.316×10^{-3} atm. ⁵⁹ The range of observed nitrogen concentrations is shown.	46
2.7	Relationship between the nitrogen saturation level in an iron sample as a function of the arc current for various nitrogen gas additions to the atmosphere. ³⁰	48
2.8	Relationship between the nitrogen concentration in the sample and changes in the arc length. ³⁰	50
2.9	Schematic diagrams of (a) the influence of torch polarity on the behavior of nitrogen ions at the melt surface and (b) the effect of arc polarity on arc jet momentum at the surface of the steel melt. ⁶⁰	51
2.10	Relation between the nitrogen concentration in arc melted (a) Fe-Cr and (b) Fe-Ni alloys and the nitrogen partial pressure for an arc current of 150 A in an Ar-N ₂ atmosphere at a total pressure of 1.0 atm. ⁶¹	53
2.11	The measured nitrogen concentration in arc-melted (a) Fe-Cr alloys, (b) Fe-Mo alloys, and (c) Fe-V alloys in N ₂ atmospheres at a pressure of 1.0 atm. ⁶⁴	54
2.12(a)	Relationship between the nitrogen concentration and the arc current in an Fe-Cr alloy. ⁶¹	56
2.12(b)	Relationship between the nitrogen concentration and the arc current in an Fe-Ni alloy. ⁶¹	56
2.13	The effect of alloying element additions, including Ni, Co, Ta, and Si, to pure iron on the nitrogen content in Ar-3% N ₂ gas mixtures at atmospheric pressure. ⁶²	57

2.14	Nitrogen concentration in various iron-oxygen alloys arc melted at various nitrogen partial pressures. ⁶⁷	59
2.15	Nitrogen saturation concentration in iron samples as a function of the oxygen concentration in the sample arc melted in pure nitrogen at atmospheric pressure. ⁶⁹	60
2.16	Surface coverage isotherms on high-purity liquid iron. ⁷⁹	62
2.17	The behavior of the nitrogen absorption reaction in binary Fe-X alloys during arc melting. ⁶² The alloys are categorized into several types, including (a) Type I, (b) Type II, (c) Type III, and (d) Type IV. ⁶²	65
2.18	Computed temperature and velocity fields for (a) pure iron and (b) an Fe-0.003 wt.% O alloy. ⁷²	67
2.19	Surface tension of iron-oxygen alloys plotted as a function of temperature and oxygen concentration. ⁷²	68
2.20	(a) Schematic model of steady-state process believed to be responsible for the nitrogen concentrations observed in liquid iron during arc melting. ⁶⁸ (b) Schematic model of nitrogen dissolution and evolution during the arc melting of an Fe-O sample. ⁶⁷	71
2.21	Relation between the nitrogen content in arc melted iron samples and the melting time at a number of nitrogen partial pressures. ³²	78
2.22(a)	Relation between the nitrogen concentration in arc melted Fe-Cr and alloys and melting time for an arc current of 150 A in a pure nitrogen atmosphere at a pressure of 1 atm. ⁶¹	80
2.22(b)	Relation between the nitrogen concentration in arc melted Fe-Ni and alloys and melting time for an arc current of 150 A in a pure nitrogen atmosphere at a pressure of 1 atm. ⁶¹	80
2.23	Weight percent nitrogen as a function of time for an Ar-5%N ₂ plasma. ³¹	81
2.24	Nitrogen concentration as a function of arc time for four samples with different oxygen concentrations. ⁶⁹	83

2.25	Schematic representation of the gas tungsten welding arc including the non-consumable electrode and the weld pool. ⁵⁰	86
2.26	Relation between the nitrogen content of the weld metal and the nitrogen partial pressure (P_{N_2}) under (a) Ar-N ₂ and (b) He-N ₂ atmospheres at a welding current of 250 A, an arc length of 10 mm, and a travel speed of 1.67 mm/sec. ¹⁰⁷	88
2.27	Relation between the nitrogen concentration in a weld metal and the nitrogen pressure (P_{N_2}) for a pure N ₂ atmosphere, a welding current of 250 A, an arc length of 10 mm, and a travel speed of 1.67 mm/sec. ¹⁰⁷	90
2.28	Relation between the nitrogen concentration and nitrogen partial pressure (P_{N_2}) in Ar-N ₂ gas mixtures for (a) Fe-Cr and (b) Fe-Ni alloys during GTA welding at a travel speed of 3.33 mm/sec and at atmospheric pressure. ⁶⁵	91
2.29	Relationship between the nitrogen concentration in the weld metal and the arc current for several (a) Fe-Cr and (b) Fe-Ni alloys at a travel speed of 3.33 mm/sec and at atmospheric pressure. ⁶⁵	93
2.30	Schematic representation of a GMA welding arc including the consumable electrode and the weld pool. ⁵⁰	95
2.31	Relationship between the nitrogen concentration in the weld metal during the GMA welding of a mild steel in an Ar-N ₂ shielding gas environment at atmospheric pressure with a welding current of 260 A, a welding voltage of 24 V, and a travel speed of 20 cm/min. ¹¹⁰	96
2.32	Relationship between the nitrogen content in the weld metal during the GMA welding of a mild steel in a nitrogen atmosphere and the total pressure in the welding chamber for a welding current of 260 A, an arc voltage of 24 V, and a travel speed of 20 cm/min. ¹¹⁰	98
2.33	Relationship between the nitrogen concentration in the weld metal and the nitrogen partial pressure (P_{N_2}) during the GMA welding of iron samples at total pressures much greater than atmospheric pressure. ¹¹⁴	99
2.34	Relationship between the nitrogen concentration in the weld metal as a function of the nitrogen content in a CO ₂ carrier gas for both	

	(1) a positive electrode and (2) a negative electrode. ¹¹¹	101
2.35	Comparison among the nitrogen absorption curves during CO ₂ welding for different metal transfer modes and the equilibrium nitrogen concentrations at 1600 and 2200°C. ¹¹³	102
2.36	Schematic diagram of the change in nitrogen content during the welding process. ¹¹¹	105
2.37	Effect of weld pool convection on weld porosity: (a) convection pattern favoring trapping of gas bubbles; (b) convection pattern favoring removal of gas bubbles. ⁴⁹	107
2.38	Schematic diagram showing a model for the ejection of a spattering particle from liquid iron during arc melting. ⁶⁸	109
2.39	Relationship between the nitrogen concentration and the nitrogen partial pressure (P_{N_2}) for several oxygen containing shielding gas mixtures during the GMA welding of iron samples. ¹¹⁰	111
2.40	Relation between the nitrogen concentration in the weld metal and the nitrogen partial pressure for nitrogen-hydrogen gas mixtures at a welding current of 250 A, arc lengths of 6 and 10 mm, and a travel speed of 1.67 mm/sec. ¹⁰⁷	113
2.41	Schematic representation of the nitrogen content of a weld metal under a moving welding arc in an atmosphere containing nitrogen. ¹¹¹	116
2.42	(a) Plot of effective dissociation temperature vs. percent nitrogen dissociated ⁴⁷ for the experimental conditions of Bandopadhyay <i>et al.</i> ⁴⁵ (b) Plot of solubility vs. effective dissociation temperature ⁴⁷ for the experimental conditions of Ouden and Griebing. ³⁰	121
2.43	Comparison of the experimental nitrogen concentrations (ppm) and the effective dissociation temperatures over the range of experimental conditions. ⁵¹	122
2.44	Computed values for (a) temperature ¹²⁸ and (b) nitrogen concentration across the radius of the weld pool for T_{MAX} values of 2500 K and 2200 K and diatomic nitrogen partial pressure of 0.6 atm. ⁵¹	124
2.45	Comparison between the experimental nitrogen concentrations observed during the GTA welding of pure iron ¹⁰⁷ and computed	

	nitrogen concentration predictions. ⁵¹	126
3.1	Comparison of the computed values for the extent of dissociation between N ₂ , O ₂ , and NO as a function of temperature. In this graph, a value of 0 for the degree of dissociation describes no dissociation occurring, while a value of 1 describes complete dissociation.	149
3.2	Plots of the computed species density for the inert gases (a) argon and (b) helium as a function of temperature.	152
3.3	Plot of computed species densities for nitrogen species at 1 atm. total pressure as a function of temperature.	153
3.4	Plot of computed species densities for oxygen species at 1 atm. total pressure as a function of temperature.	154
3.5	Schematic diagram of the spectroscopically measured temperatures in a 100% Ar arc, with an arc current of 150 A, and a 30° vertex angle for the electrode tip. ²²	159
3.6	Temperature distribution in the arc column under GTA welding conditions for an arc current of 100 A. The temperatures in the arc column were calculated using electrostatic probes. ²¹	160
3.7	Temperature profile for a 100 A argon arc. ²⁶	161
3.8	Temperature profile for a 200 A argon arc. ²⁶	162
3.9	Plots of computed species densities for two component systems, (a) Ar-5%N ₂ and (b) He-5%N ₂ as a function of temperature.	163
3.10	Plots of computed species densities for two component systems, (a) Ar-5%O ₂ and (b) He-5%O ₂ as a function of temperature.	164
3.11	Comparison of computed total electron densities for pure gases.	166
3.12	Comparison of computed total electron densities for argon-diatom gas mixtures.	167
3.13	Comparison of computed total electron densities for helium-diatom gas mixtures.	168
3.14	Plot of the computed species densities for a three component system consisting of Ar-8%N ₂ -2%O ₂ , as a function of temperature	

	assuming no interaction.	169
3.15	Plot of the computed species densities for a three component system consisting of He-8%N ₂ -2%O ₂ , as a function of temperature assuming no interaction.	170
3.16	Plot of the computed species densities for a three component system consisting of Ar-8%N ₂ -2%O ₂ , as a function of temperature with interaction between nitrogen and oxygen.	172
3.17	Plot of the computed species densities for a three component system consisting of He-8%N ₂ -2%O ₂ , as a function of temperature with interaction between nitrogen and oxygen.	173
3.18	Comparison of the computed number density of monatomic nitrogen for Ar - 8%N ₂ and Ar - 8%N ₂ - 2%O ₂ plasmas.	174
3.19	Comparison of the computed number density of monatomic nitrogen for He - 8%N ₂ and He - 8%N ₂ -2%O ₂ plasmas.	175
3.20	Comparison between the computed monatomic nitrogen partial pressures at temperatures characteristic of the plasma phase and on the weld pool surface for a pure nitrogen plasma at atmospheric pressure.	180
3.21	Nitrogen solubility in pure iron in contact with an Ar - 1% N ₂ plasma determined as a function of the arc temperature and the sample temperature, characteristic of the weld pool surface.	182
3.22	(a) The nitrogen solubility is plotted as a function of the arc temperature for several sample temperatures. (b) The nitrogen solubility is plotted as a function of the sample temperature for several arc temperatures.	183
3.23	Comparison between the calculated nitrogen concentrations in argon – nitrogen plasma phases both with and without oxygen additions.	186
3.24	Schematic diagram of the experimental setup used to produce the glow discharges used to analyze several gas mixtures.	187
3.25	Boltzmann plot for an Ar – 8% N ₂ – 2% O ₂ glow discharge plasma at a total pressure of 1.5 Torr with a measured electron temperature of 2968 K.	195

3.26	Boltzmann plot for a He-8% N ₂ -2% O ₂ glow discharge plasma at a total pressure of 1.5 Torr with a measured electron temperature of 5475 K.	196
3.27	Boltzmann plot for an Ar - 8% N ₂ - 2% O ₂ glow discharge plasma at a total pressure of 1.5 Torr with a measured electron temperature of 5885 K.	197
3.28	(a) Emission spectra for a low temperature Ar-8%N ₂ -2%O ₂ glow discharge plasma and (b) the portion of the spectra with the NO peaks highlighted.	199
3.29	(a) Emission spectra for a low temperature He-8%N ₂ -2%O ₂ glow discharge plasma and (b) the portion of the spectra with the NO peaks highlighted.	200
3.30	(a) Emission spectra for a high temperature Ar-8%N ₂ -2%O ₂ glow discharge plasma and (b) the portion of the spectra with the N and O peaks highlighted.	201
4.1	Schematic diagram of experimental chamber used for controlled GTA welding experiments.	211
4.2	Schematic representation of location of samples along weld line removed for nitrogen concentration analysis.	214
4.3	Schematic diagram of weld metal samples analyzed for the residual nitrogen concentration.	215
4.4	Schematic drawing of the weld pool cross section.	218
4.5	Plot of the experimentally measured nitrogen concentration in the weldment as a function of the inlet nitrogen partial pressure at a travel speed of 0.847 cm/sec.	222
4.6	Plot of the nitrogen concentrations (ppm) in each of the samples taken from the weld lines made for each of the inlet nitrogen partial pressures at a travel speed of 0.847 cm/sec.	223
4.7	Plot of the experimentally measured nitrogen concentration in the weldment as a function of the inlet nitrogen partial pressure at a	

	travel speed of 0.423 cm/sec.	224
4.8	Plot of the nitrogen concentrations (ppm) in each of the samples taken from the weld lines made for each of the inlet nitrogen partial pressures at a travel speed of 0.423 cm/sec.	225
4.9	Comparison of the nitrogen concentrations from each welding condition plotted as a function of inlet nitrogen partial pressure.	227
4.10	Comparison of Cross Sections for a travel speed of 0.847 cm/sec: (a) Pure Ar; (b) 5% N ₂ ; (c) 10% N ₂ ; (d) 15% N ₂ ; (e) 20% N ₂	228
4.11	Comparison of Cross Sections for a travel speed of 0.423 cm/sec: (a) Pure Ar; (b) 5% N ₂ ; (c) 10% N ₂ ; (d) 15% N ₂ ; (e) 20% N ₂	229
4.12	Comparison of appearance of weld line for each welding condition, demonstrating the role of changes in the travel speed on the appearance of the weld line. (a&f) Pure Ar; (b&g) 5% N ₂ ; (c&h) 10% N ₂ ; (d&i) 15% N ₂ ; (e&j) 20% N ₂	232
4.13	Radiographs of the base metal and section of weld line for a travel speed of 0.847 cm/sec with (a) pure Ar shielding gas, (b) 5% N ₂ , (c) 10% N ₂ , (d) 15% N ₂ , and (e) 20% N ₂	236
4.14	Radiographs of section of weld line for a travel speed of 0.423 cm/sec with (a) pure Ar shielding gas, (b) 5% N ₂ , (c) 10% N ₂ , (d) 15% N ₂ , and (e) 20% N ₂	237
4.15	Typical base metal microstructure.	241
4.16	Typical fusion zone microstructure for a travel speed of 0.847 cm/sec.	243
4.17	Typical fusion zone microstructure for a travel speed of 0.423 cm/sec.	244
4.18	Examples of typical fusion zone microstructures with a 5% N ₂ addition to the shielding gas for a travel speed of 0.847 cm/sec.	245
4.19	Examples of typical fusion zone microstructures with a 10% N ₂ addition to the shielding gas at a travel speed of 0.847 cm/sec.	246
4.20	Examples of typical fusion zone microstructures with a 15% N ₂ addition to the shielding gas and a travel speed of 0.847 cm/sec.	247

4.21	Examples of typical fusion zone microstructures with a 20% N ₂ addition to the shielding gas at a travel speed of 0.847 cm/sec.	248
4.22	Examples of typical fusion zone microstructures with a 5% N ₂ addition to the shielding gas at a travel speed of 0.423 cm/sec.	249
4.23	Examples of typical fusion zone microstructures with a 5% N ₂ addition to the shielding gas at a travel speed of 0.423 cm/sec.	251
4.24	Examples of typical fusion zone microstructures with a 10% N ₂ addition to the shielding gas at a travel speed of 0.423 cm/sec.	252
4.25	Examples of typical fusion zone microstructures with a 15% N ₂ addition to the shielding gas at a travel speed of 0.423 cm/sec.	253
4.26	Examples of typical fusion zone microstructures with a 20% N ₂ addition to the shielding gas and a travel speed of 0.423 cm/sec.	254
4.27	Microhardness measurements taken across both the (a) width and (b) depth of the weldment with a pure Ar shielding gas for a travel speed of 0.847 cm/sec.	258
4.28	Microhardness measurements taken across both the (a) width and (b) depth of the weldment with a pure Ar shielding gas for a travel speed of 0.423 cm/sec.	259
4.29	Microhardness measurements taken across both the (a) width and (b) depth of the weldment with a 5% N ₂ addition to the shielding gas for a travel speed of 0.847 cm/sec.	260
4.30	Microhardness measurements taken across both the (a) width and (b) depth of the weldment with a 10% N ₂ addition to the shielding gas for a travel speed of 0.847 cm/sec.	261
4.31	Microhardness measurements taken across both the (a) width and (b) depth of the weldment with a 5% N ₂ addition to the shielding gas for a travel speed of 0.423 cm/sec.	263
4.32	Microhardness measurements taken across both the (a) width and (b) depth of the weldment with a 10% N ₂ addition to the shielding gas for a travel speed of 0.423 cm/sec.	264
4.33	Comparison between average microhardness measurements	

	for each welding condition across the (a) width and (b) depth of the weldment.	265
4.34	Comparison between maximum microhardness measurements for each welding condition across the (a) width and (b) depth of the weldment.	266
4.35	Change in the nitrogen solubility with the presence of nitride phases in α -Fe.	275
4.36	Summary of experimental nitrogen concentrations observed during the GTA welding of pure iron. ³	278
5.1	Schematic diagram of welding process with coordinate system attached to the heat source.	286
5.2	Summary of enthalpy-temperature relationship used in the calculations for heat transfer and fluid flow.	290
5.3	Schematic diagram of grid scheme used in these calculations.	299
5.4	Summary of boundary conditions used in the mathematical model for solution of heat transfer and fluid flow in the weldment.	301
5.5	Summary of boundary conditions used in the mathematical model for solution of nitrogen concentration distribution in the weldment.	305
5.6	Three-dimensional diagram showing modeling results for both temperature and fluid flow fields in the weld pool for a travel speed of 0.847 cm/sec.	312
5.7	Three-dimensional diagram showing modeling results for both temperature and fluid flow fields in the weld pool for a travel speed of 0.423 cm/sec.	313
5.8	Comparison of calculated temperature and velocity fields along the cross section of the weld line with the corresponding experimental weld pool cross sections for a travel speed of (a) 0.847 cm/sec and (b) 0.423 cm/sec.	314
5.9	Schematic diagram showing the structure of the dark region between the equilibrium plasma phase in the arc column and the weld pool surface. ⁵³	316

5.10	Graph showing dramatic changes in monatomic nitrogen partial pressures with rather small changes in the electron temperature. The electron temperature range shown in this figure matches those temperatures similar to those found in the anode boundary layer.	317
5.11	Electron temperature distributions for differences in electron temperature of 250 K between the center of the heat source and the edge of the weld pool for maximum electron temperatures of (a)3500 K, (b) 3250 K, (c) 3000 K, and (d) 2750 K for a travel speed of 0.847 cm/sec.	320
5.12	Electron temperature distributions for differences in electron temperature of 250 K between the center of the heat source and the edge of the weld pool for maximum electron temperatures of (a)3500 K, (b) 3250 K, (c) 3000 K, and (d) 2750 K for a travel speed of 0.423 cm/sec.	321
5.13	Monatomic nitrogen partial pressure distribution calculations based on the electron temperature distributions used above with a difference of 250 K between the center of the heat source and the edge of the weld pool for maximum electron temperatures of (a)3500 K, (b) 3250 K, (c) 3000 K, and (d) 3000 K for a travel speed of 0.847 cm/sec with a 10% N ₂ addition to the shielding gas.	323
5.14	Monatomic nitrogen partial pressure distribution calculations based on the electron temperature distributions used above with a difference of 250 K between the center of the heat source and the edge of the weld pool for maximum electron temperatures of (a)3500 K, (b) 3250 K, (c) 3000 K, and (d) 2750 K for a travel speed of 0.423 cm/sec with a 10% N ₂ addition to the shielding gas.	324
5.15	Monatomic nitrogen partial pressure distribution calculations for an electron temperature distribution between 3250 and 3000 K with nitrogen additions to the shielding gas of (a) 5%, (b) 10%, (c) 15%, and (d) 20% for a travel speed of 0.847 cm/sec.	325
5.16	Monatomic nitrogen partial pressure distribution calculations for an electron temperature distribution between 3250 and 3000 K with nitrogen additions to the shielding gas of (a) 5%, (b) 10%, (c) 15%, and (d) 20% for a travel speed of 0.423 cm/sec.	326
5.17	Temperature profiles on the weld pool surface for a travel speed of (a) 0.847 cm/sec and (b) 0.423 cm/sec.	328

5.18	Calculated thermal cycle on the weld pool surface at the weld centerline for a travel speed of (a) 0.847 cm/sec and (b) 0.423 cm/sec.	329
5.19	Nitrogen concentration distributions calculated based on the monatomic nitrogen partial pressure and electron temperature distributions across the weld pool surface with a difference of 250 K between the center of the heat source and the edge of the weld pool for maximum electron temperatures of (a) 3500 K, (b) 3250 K, (c) 3000 K, and (d) 2750 K for a travel speed of 0.847 cm/sec with a 10% N ₂ addition to the shielding gas.	331
5.20	Nitrogen concentration distributions calculated based on the monatomic nitrogen partial pressure and electron temperature distributions across the weld pool surface with a difference of 250 K between the center of the heat source and the edge of the weld pool for maximum electron temperatures of (a) 3500 K, (b) 3250 K, (c) 3000 K, and (d) 2750 K for a travel speed of 0.423 cm/sec with a 10% N ₂ addition to the shielding gas.	332
5.21	Nitrogen concentration distributions calculated based on an electron temperature distribution between 2750 and 2500 K above the weld pool surface and nitrogen additions of (a) 5% N ₂ , (b) 10% N ₂ , (c) 15% N ₂ , and (d) 20% N ₂ to the shielding gas at a travel speed of 0.847 cm/sec.	334
5.22	Nitrogen concentration distributions calculated based on an electron temperature distribution between 2750 and 2500 K above the weld pool surface and nitrogen additions of (a) 5% N ₂ , (b) 10% N ₂ , (c) 15% N ₂ , and (d) 20% N ₂ to the shielding gas at a travel speed of 0.423 cm/sec.	335
5.23	Three dimensional plot of nitrogen concentrations in the weld pool at several times for a travel speed of 0.847 cm/sec. Electron temperatures between 3250 and 3000 K for a 10% N ₂ addition to the shielding gas are assumed.	338
5.24	Three dimensional plot of nitrogen concentrations in the weld pool at several times for a travel speed of 0.423 cm/sec. Electron temperatures between 3250 and 3000 K for a 10% N ₂ addition to the shielding gas are assumed.	339
5.25	Nitrogen concentration distribution in the weld pool over a range	

	of times for electron temperatures assumed to range from 3250 to 3000 K for a travel speed of 0.847 cm/sec with a 10% N ₂ addition to the shielding gas. (a) 0 sec., (b) 0.25 sec., (c) 0.50 sec., (d) 1.0 sec.	341
5.26	Nitrogen concentration distribution in the weld pool over a range of times for electron temperatures assumed to range from 2750 to 2500 K for a travel speed of 0.847 cm/sec with a 10% N ₂ addition to the shielding gas. (a) 0 sec., (b) 0.25 sec., (c) 0.50 sec., (d) 1.0 sec.	342
5.27	Nitrogen concentration distribution in the weld pool over a range of times for electron temperatures assumed to range from 3250 to 3000 K for a travel speed of 0.423 cm/sec with a 10% N ₂ addition to the shielding gas. (a) 0 sec., (b) 0.25 sec., (c) 0.50 sec., (d) 1.0 sec., (e) 2.0 sec.	343
5.28	Nitrogen concentration distribution in the weld pool over a range of times for electron temperatures assumed to range from 2750 to 2500 K for a travel speed of 0.423 cm/sec with a 10% N ₂ addition to the shielding gas. (a) 0 sec., (b) 0.25 sec., (c) 0.50 sec., (d) 1.0 sec., (e) 2.0 sec.	344
5.29	Nitrogen concentration distributions in the weld pool for electron temperature distributions across the weld pool ranging between (a) 3500 and 3250 K, (b) 3250 and 3000 K, (c) 3000 and 2750 K, and (d) 2750 and 2500 K, with a 10% N ₂ addition to the shielding gas.	345
5.30	Nitrogen concentration distributions in the weld pool for electron temperature distributions across the weld pool ranging between (a) 3500 and 3250 K, (b) 3250 and 3000 K, (c) 3000 and 2750 K, and (d) 2750 and 2500 K, with a 10% N ₂ addition to the shielding gas.	346
5.31	Nitrogen concentration distributions in the weld pool for an electron temperature distribution across the weld pool surface between 2750 and 2500 K for (a) 5% N ₂ , (b) 10% N ₂ , (c) 15% N ₂ , and (d) 20% N ₂ additions to the shielding gas.	348
5.32	Nitrogen concentration distributions in the weld pool for an electron temperature distribution across the weld pool surface between 2750 and 2500 K for (a) 5% N ₂ , (b) 10% N ₂ , (c) 15% N ₂ , and (d) 20% N ₂ additions to the shielding gas.	349
5.33	Comparison between experimental and modeled nitrogen concentrations in the weld pool for both high and low assumed electron temperatures above the weld pool for a travel speed of 0.847 cm/sec.	351

5.34	Comparison between experimental and modeled nitrogen concentrations in the weld pool for both high and low assumed electron temperatures above the weld pool for a travel speed of 0.423 cm/sec.	352
5.35	Calculated nitrogen concentrations on the weld pool surface (expressed in ppm) at a travel speed of 0.847 cm/sec and a 10% N ₂ addition to the shielding gas at an electron temperature distribution between 3250 and 3000 K for enhancements in the nitrogen supersaturation of (a) 1.25, (b) 1.50, (c) 1.75, (d) 2.00.	355
5.36	Calculated nitrogen concentrations on the weld pool surface (expressed in ppm) at a travel speed of 0.423 cm/sec and a 10% N ₂ addition to the shielding gas at an electron temperature distribution between 3250 and 3000 K for enhancements in the nitrogen supersaturation of (a) 1.25, (b) 1.50, (c) 1.75, and (d) 2.00.	356
5.37	Calculated nitrogen concentration distributions in the weld pool interior (expressed in ppm) at a travel speed of 0.847 cm/sec and a 10% N ₂ addition to the shielding gas for enhancements in the level of nitrogen supersaturation of (a) 1.25, (b) 1.50, (c) 1.75, and (d) 2.00.	357
5.38	Calculated nitrogen concentration distributions in the weld pool interior (expressed in ppm) at a travel speed of 0.423 cm/sec and a 10% N ₂ addition to the shielding gas for enhancements in the level of nitrogen supersaturation of (a) 1.25, (b) 1.50, (c) 1.75, and (d) 2.00.	358
5.39	Comparison between experimental and calculated nitrogen concentrations over a range of nitrogen additions to the shielding gas at several levels of nitrogen supersaturation for a travel speed of 0.847 cm/sec and an electron temperature range between 3250 and 3000 K.	360
5.40	Comparison between experimental and calculated nitrogen concentrations over a range of nitrogen additions to the shielding gas at several levels of nitrogen supersaturation for a travel speed of 0.423 cm/sec and an electron temperature range between 3250 and 3000 K.	361
5.41	Summary of final nitrogen concentration distributions for several mass transport enhancement factors for a travel speed of 0.847 cm/sec and a 10% N ₂ addition to the shielding gas	

	for electron temperatures ranging from 3250 to 3000 K. (a) 1, (b) 10, (c) 30 and (d) 50. A nitrogen supersaturation level of 50% is assumed.	363
5.42	Summary of final nitrogen concentration distributions for several mass transport enhancement factors for a travel speed of 0.423 cm/sec and a 10% N ₂ addition to the shielding gas for electron temperatures ranging from 3250 to 3000 K. (a) 1, (b) 10, (c) 30, and (d) 50. A nitrogen supersaturation level of 50% is assumed.	364
5.43	Summary of calculated nitrogen concentrations for a number of enhancement factors for a travel speed of 0.847 cm/sec and 5% and 20% N ₂ additions to the shielding gas and an electron temperature distribution above the weld pool ranging from 3250 to 3000 K and a 50% nitrogen supersaturation level.	367
5.44	Summary of calculated nitrogen concentrations for a number of enhancement factors for a travel speed of 0.423 cm/sec and 5% and 20% N ₂ additions to the shielding gas and an electron temperature distribution above the weld pool ranging from 3250 to 3000 K and a 50% nitrogen supersaturation level.	368
5.45	Comparison between experimental nitrogen concentrations and modeled results for several mass transport enhancement factors at electron temperatures between 3250 and 3000 K for a travel speed of 0.847 cm/sec and nitrogen supersaturation levels of (a) 50% and (b) 75% greater than the nitrogen equilibrium concentration.	370
5.46	Comparison between experimental nitrogen concentrations and modeled results for several mass transport enhancement factors at electron temperatures between 3250 and 3000 K for a travel speed of 0.423 cm/sec and nitrogen supersaturation levels of (a) 50% and (b) 75% greater than the nitrogen equilibrium concentration.	371
A.1	Plot of computed partition functions vs. temperature for argon and helium species in the plasma phase.	399
A.2	Plot of computed partition functions vs. temperature for molecular oxygen and nitrogen species in the plasma phase.	400
A.3	Plot of computed partition functions vs. temperature for atomic oxygen and nitrogen species in the plasma phase.	401

B1	Comparison of the computed equilibrium constants for the dissociation of N_2 , O_2 , and NO expressed by reactions (5), (12), and (28) plotted as a function of temperature.	406
----	---	-----

LIST OF TABLES

Table	Page
2.1 Summary of iron nitride phases present in the iron-nitrogen system.	27
2.2 Free energy relationships for nitrogen solubility calculations in pure iron.	30
2.3 Summary of interaction parameters on the nitrogen solubility in iron for common alloying elements calculated during the heating of liquid iron and during arc melting.	33
2.4 Comparison of several important features of plasmas formed during common welding processes.	45
2.5 Summary of alloying elements in several categories and their relationship with the presence of surface active elements in liquid iron. ⁶³	64
3.1 Summary of species considered in the species density calculations for oxygen, nitrogen, argon, and helium.	145
3.2 Comparison between calculated and literature values for calculation of species densities in nitrogen over a range of temperatures.	155
3.3 Comparison between calculated and literature values for calculation of species densities in oxygen over a range of temperatures.	156
3.4 Summary of welding conditions used to calculate temperature distributions in the arc column.	158
3.5 Summary of free energy values for the formation of NO. ³⁰	177
3.6 Comparison between calculated species densities (m^{-3}) in two and three component gas mixtures.	178
3.7 Comparison between calculated nitrogen concentrations in iron with and without the addition of oxygen to an argon-nitrogen plasma.	185

3.8	Summary of experimental conditions used for the analysis of glow discharges containing argon-nitrogen-oxygen and helium-nitrogen-oxygen gas mixtures.	189
3.9	Summary of experimental parameters used by spectrometer in spectroscopic analysis of glow discharges.....	190
3.10	Summary of argon peaks used in the determination of electron temperature for argon-nitrogen-oxygen plasmas. ³⁴	193
3.11	Summary of helium peaks used in the determination of electron temperature for argon-nitrogen-oxygen plasmas. ^{33,34}	194
4.1	Chemical composition and interaction parameters for the alloying elements in base plate. ⁷⁻¹¹	208
4.2	Experimental welding parameters considered in this study.	213
4.3	Summary of raw experimental residual nitrogen concentrations measured in each of the samples.	216
4.4	Summary of measured weld pool dimensions.	219
4.5	Summary of converted residual nitrogen concentrations.	220
4.6	Summary of the parameters used in the radiographic examination of the weld metal samples.	234
4.7	Summary of x-ray radiographic analysis of iron samples.	235
4.8	Summary of weights of samples and resulting porosity calculations.	239
4.9	Summary of Vickers' hardness measurements across the width of the weldment for the three welding conditions. Load is 200 gm for all conditions.	256
4.10	Summary of Vickers' hardness measurements across the depth of the weldment for the three welding conditions. Load is 200 gm for all conditions.	257
4.11	Summary of lattice parameters for prominent phases in the iron-nitrogen system.	268
4.12	Summary of values of free energies of formation at 298 K	

	for iron nitride phases.	273
4.13	Experimental Welding Parameters in Kuwana and Kokawa study. ²	277
5.1	Summary of nitrogen diffusion constants in α , γ , δ , and liquid iron phases. ³³⁻³⁴	293
5.2	Summary of the thermophysical properties used in the calculations described here. ^{33,37-39}	298
5.3	Summary of free energies used in nitrogen absorption reactions. ⁴¹⁻⁴⁵	307
5.4	Summary of welding parameters output data from these calculations.	309
5.5	Comparison between modeled and experimental weld pool dimensions.	311
5.6	Summary of electron temperature and monatomic nitrogen partial pressure (P_N) distributions.	319
5.7.	Summary of calculated cooling rates based on the thermal cycles from each set of welding parameters.	330
5.8	Summary of Peclet number calculations for each set of welding parameters.	337
5.9	Comparison between experimental and computed nitrogen concentrations in the fusion zone. Calculations are performed with both high and low assumed electron temperatures above the weld pool and an enhancement factor of 20.	350
5.10	Summary of calculated nitrogen concentrations for several levels of nitrogen supersaturation with an electron temperature distribution between 3250 and 3000 K.	359
5.11	Summary of mass transport enhancement factors used in the calculation of the nitrogen concentration distribution in the weld metal for an electron temperature distribution ranging from 3250 to 3000 K and a nitrogen supersaturation of 50%.	365
5.12	Summary of mass transport enhancement factors used in the calculation of the nitrogen concentration distribution in the weld metal for an electron temperature distribution ranging from 3250 to 3000 K and a nitrogen supersaturation of 75%.	366

A1	Summary of important constants.	386
A2	Summary of Electronic energy levels ⁴ for nitrogen atoms (N).	387
A3	Summary of Electronic energy levels ⁴ for singly charged monatomic nitrogen ions (N ⁺).	388
A4	Summary of Electronic energy levels ⁴ for oxygen atoms (O).	389
A5	Summary of Electronic energy levels ⁴ for singly charged monatomic oxygen ions (O ⁺).	390
A6	Summary of Electronic energy levels ⁴ for doubly charged monatomic oxygen ions (O ⁺⁺).	391
A7	Summary of spectroscopically determined values ⁵ used in calculation of partition functions for nitrogen molecule, N ₂	393
A8	Summary of spectroscopically determined values ⁵ used in calculation of partition functions for nitrogen molecular ion, N ₂ ⁺	394
A9	Summary of spectroscopically determined values ⁵ used in calculation of partition functions for oxygen molecule, O ₂	395
A10	Summary of spectroscopically determined values ⁵ used in calculation of partition functions for oxygen molecular ion, O ₂ ⁺	396
B1	Summary of ionization and dissociation energies for several species of interest.	405
C.1	Summary of d-spacing and 2θ values for ferrite(α-Fe) in the iron system. ¹	409
C.2	Summary of d-spacing and 2θ values for nitrogen austenite (γ-Fe) in the iron-nitrogen system. ²	410
C.3	Summary of d-spacing and 2θ values for nitrogen martensite (α'-Fe) in the iron-nitrogen system. ²	411
C.4	Summary of d-spacing and 2θ values for nitrogen Fe ₄ N. ³	412
C.5	Summary of d-spacing and 2θ values for nitrogen Fe ₈ N. ⁴	413

C.6	Summary of d-spacing and 2θ values for nitrogen Fe_2N . ⁵	414
C.7	Summary of d-spacing and 2θ values for nitrogen Fe_3N . ²	415
C.8	Summary of peaks observed in the base metal.	416
C.9	Summary of peaks observed with pure Ar additions to the shielding gas for all welding conditions.	417
C.10	Summary of peaks observed for several N_2 additions to the shielding gas for a welding speed of 0.847 cm/sec and a 5% N_2 addition to the shielding gas.	418
C.11	Summary of peaks observed for several N_2 additions to the shielding gas for a welding speed of 0.847 cm/sec and a 10% N_2 addition to the shielding gas.	419
C.12	Summary of peaks observed for several N_2 additions to the shielding gas for a welding speed of 0.847 cm/sec and a 15% N_2 addition to the shielding gas.	420
C.13	Summary of peaks observed for several N_2 additions to the shielding gas for a welding speed of 0.847 cm/sec and a 20% N_2 addition to the shielding gas.	421
C.14	Summary of peaks observed for several N_2 additions to the shielding gas for a welding speed of 0.423 cm/sec and a 5% N_2 addition to the shielding gas.	422
C.15	Summary of peaks observed for several N_2 additions to the shielding gas for a welding speed of 0.423 cm/sec and a 10% N_2 addition to the shielding gas.	423
C.16	Summary of peaks observed for several N_2 additions to the shielding gas for a welding speed of 0.423 cm/sec and a 15% N_2 addition to the shielding gas.	424
C.17	Summary of peaks observed for several N_2 additions to the shielding gas for a welding speed of 0.423 cm/sec and a 20% N_2 addition to the shielding gas.	425

ACKNOWLEDGMENTS

This work has been supported by the United States Department of Energy, Office of Basic Energy Sciences, Division of Materials Science, under Grant No. DEFG02-84ER45158. I would also like to acknowledge the financial support provided by the American Welding Society Foundation and the Navy Joining Center in the form of an AWS Graduate Research Fellowship. Radiographic analysis of the weld samples has been provided by Mr. Joe Blackburn at the Carderock Division of the Naval Surface Warfare Center in Carderock, MD.

Chapter 1

INTRODUCTION

1.1 NITROGEN DISSOLUTION DURING ARC WELDING

A wide range of fusion welding processes is utilized in an equally wide range of manufacturing processes. These welding processes vary primarily in the choice of the power source, which can range from advanced lasers or electron beams to arcs. Methods for producing arcs can vary from non-consumable tungsten electrodes used in gas-tungsten arc (GTA) welding processes to consumable metal electrodes used in gas-metal arc (GMA) welding processes. Given the high temperatures prevalent in these various welding processes, the liquid metal must be shielded from the surrounding atmosphere. Shielding may be achieved by means of a flux, an external gas supply, a combination of the two, or from the evacuation of the atmosphere. The means of shielding the weld pool depends on the welding process to be used.

During GTA welding processes, which are of primary interest here, shielding is achieved using an inert shielding gas, such as argon or helium. A plasma phase is formed by the interaction between the inert shielding gas and the electromagnetic radiation produced by the arc. At times, weld metal shielding may be inadequate, and diatomic gases present in the surrounding atmosphere, such as hydrogen, nitrogen, and oxygen, may impinge upon the shielding gas stream and dissolve into the weld metal. The impingement of nitrogen gas from the surrounding atmosphere or its purposeful addition into an inert shielding gas produces enhanced levels of nitrogen in iron and steel. At the high temperatures characteristic of welding, the rapid absorption of gases such as oxygen and nitrogen is possible. For example, oxygen and nitrogen contents as high as 0.7 and 0.2 wt.%, respectively, have been obtained in steel welds during arc welding.¹ These concentration levels are far greater than those present in the base metal and indicate the importance of the dissolution of these species into the metal from the gas phase. In this case, the dissolution of nitrogen into iron and steels is considered.

Typically, the nitrogen concentration in solution in iron is calculated using Sieverts' Law, which is based on Equation (1.1) for the iron-nitrogen system. The equilibrium nitrogen concentration in iron at a constant temperature is proportional to the square root of the partial pressure of diatomic nitrogen² and is shown in Equation (1.2):



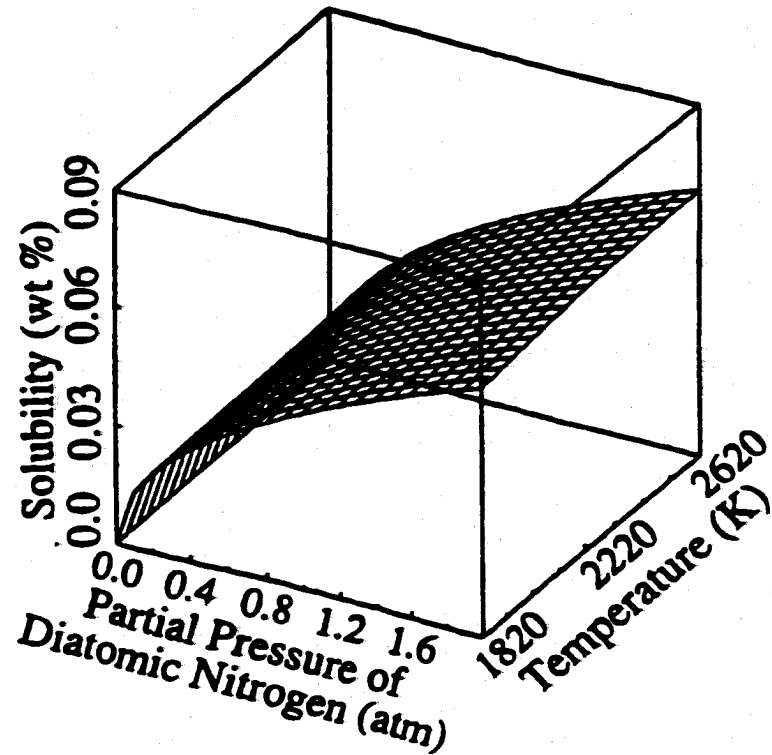
$$\underline{N}(\text{wt.}\%) = K_{\text{eq}} \sqrt{P_{N_2}} = \sqrt{P_{N_2}} e^{-\frac{\Delta G_1^\circ}{RT}} \quad (1.2)$$

where ΔG_1° is the standard free energy for the reaction in Equation (1.1), \underline{N} (wt.%) is the nitrogen concentration in solution at equilibrium with the diatomic nitrogen gas, K_{eq} is the equilibrium constant for this reaction, P_{N_2} is the partial pressure of N_2 , and T is the temperature of iron. The computed equilibrium concentration of nitrogen in liquid iron is shown in Figures 1.1(a-c)³ and is based on the following free energy relationship^{4,5} for the reaction in Equation (1.1) for a temperature range between 1820 and 2620 K:

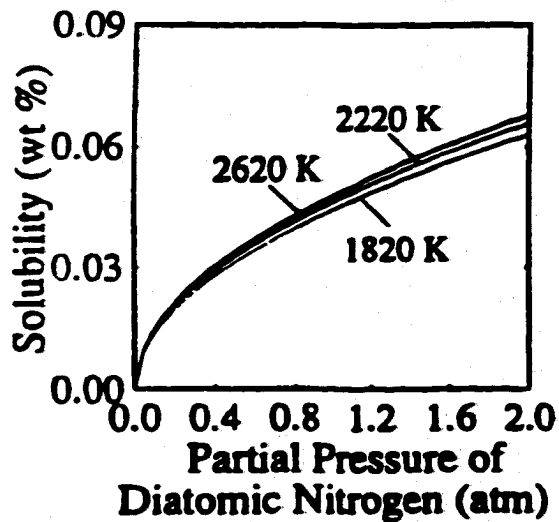
$$\Delta G_1^\circ = 860.0 + 5.71T \quad (\text{cal/mol}) \quad (1.3)$$

In these figures, the relationship between the nitrogen concentration in liquid iron, the temperature, and the partial pressure of diatomic nitrogen are highlighted. For example, at a given temperature, the equilibrium nitrogen concentration increases linearly with an increase in the nitrogen partial pressure. At a given nitrogen partial pressure, the equilibrium nitrogen concentration also increases with a rising temperature. This behavior is specific to liquid iron and changes with the iron phase being analyzed.

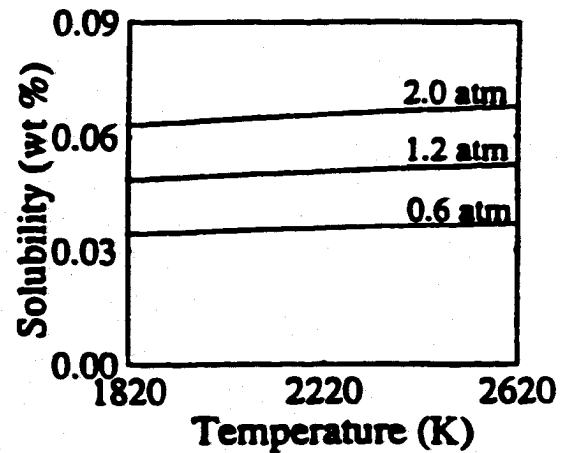
However, such conditions are not always present in materials processing operations. For example, arc melting is a common practice in the processing of iron and steel. Dur-



(a)



(b)



(c)

Figure 1.1(a-c). Computed equilibrium solubility of nitrogen in iron exposed to diatomic nitrogen (a) as a function of temperature and partial pressure of diatomic nitrogen, (b) as a function of partial pressure of diatomic nitrogen at three temperatures, and (c) as a function of temperature at three partial pressures of diatomic nitrogen.³

ing arc melting, there is a plasma phase present above the liquid iron, which significantly alters nitrogen absorption from the surrounding environment into liquid iron and steel.⁴⁻¹¹ Typically, nitrogen concentrations are observed to be far in excess of the equilibrium values calculated using Sieverts' Law. Figure 1.2 compares a series of experimental nitrogen concentration in small arc melted iron samples with Sieverts' Law calculations for a range of nitrogen partial pressures.⁴ Nitrogen concentrations in these samples are considerably larger than those based on equilibrium calculations and display a different behavior as a function of the nitrogen partial pressure. As the nitrogen partial pressure is further increased, the nitrogen concentration plateaus at a level equivalent to the nitrogen solubility in pure iron at 1 atm using Sieverts' Law calculations.

Nitrogen concentrations far in excess of Sieverts' Law calculations are also typically observed during arc welding operations with nitrogen present in the shielding gas.¹²⁻¹⁸ One study of this phenomenon by Kuwana and Kokawa¹⁷ involves the GTA welding of pure iron samples with controlled nitrogen additions to an argon shielding gas. Figure 1.3 shows the relationship between the nitrogen partial pressure in the shielding gas and the measured nitrogen concentration in the weld metal along with Sieverts' Law calculations for three temperatures in liquid iron.¹⁷ The nitrogen concentrations in the weld metal are significantly higher than the Sieverts' Law calculations. These nitrogen concentrations increase rapidly at very low nitrogen partial pressures until reaching a plateau, corresponding to approximately 0.06 wt.% [N], at a nitrogen partial pressure of approximately 0.005 MPa. This behavior is nearly identical to that observed in the arc melting operations. This agreement in results shows that there are common mechanisms in the fusion welding conditions contributing to these large nitrogen concentrations in the weld pool. Therefore, the mechanisms of the enhanced nitrogen dissolution and the reasons and conditions for the observed nitrogen solubility are of interest.

Even though weld metal nitrogen concentrations far in excess of Sieverts' Law calculations have been a long-standing problem, the mechanisms for the nitrogen dissolution reaction are not well understood. This study will concentrate on nitrogen dissolution during the GTA welding of pure iron. GTA is studied here because it provides a much simpler case for understanding nitrogen dissolution than other welding operations. Dur-

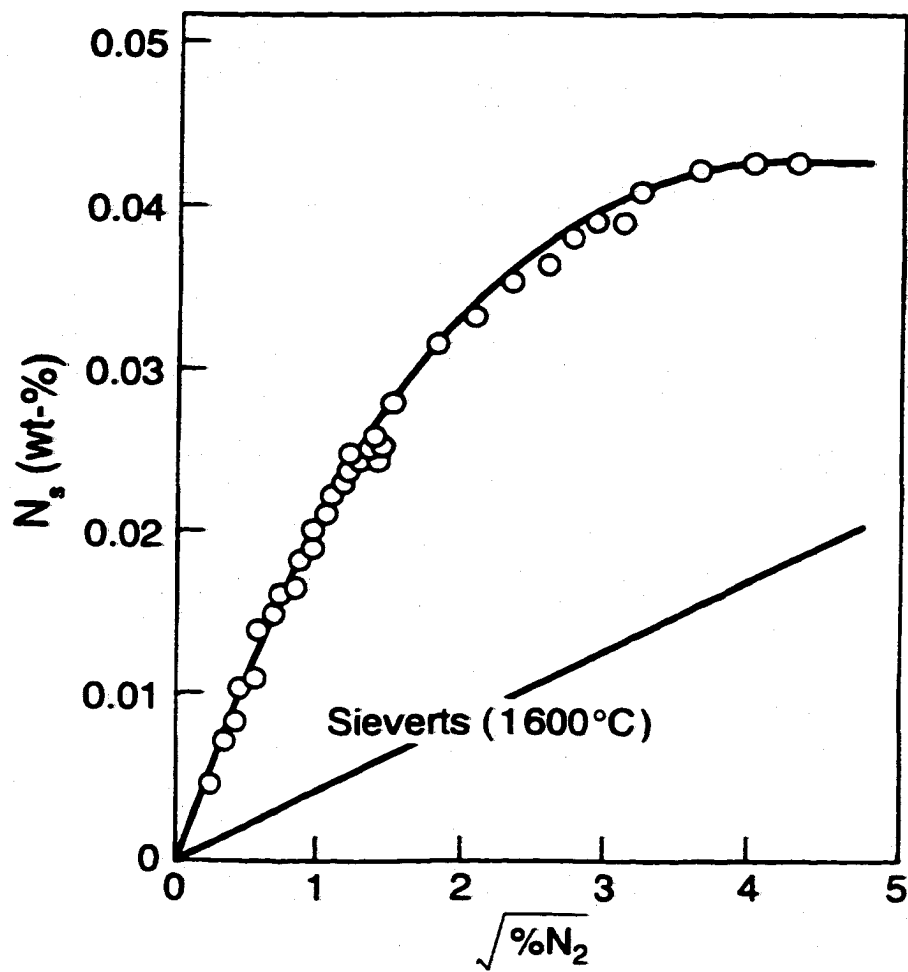


Figure 1.2. Nitrogen concentration in an arc melted iron sample plotted as a function of the square root of the nitrogen partial pressure.⁶

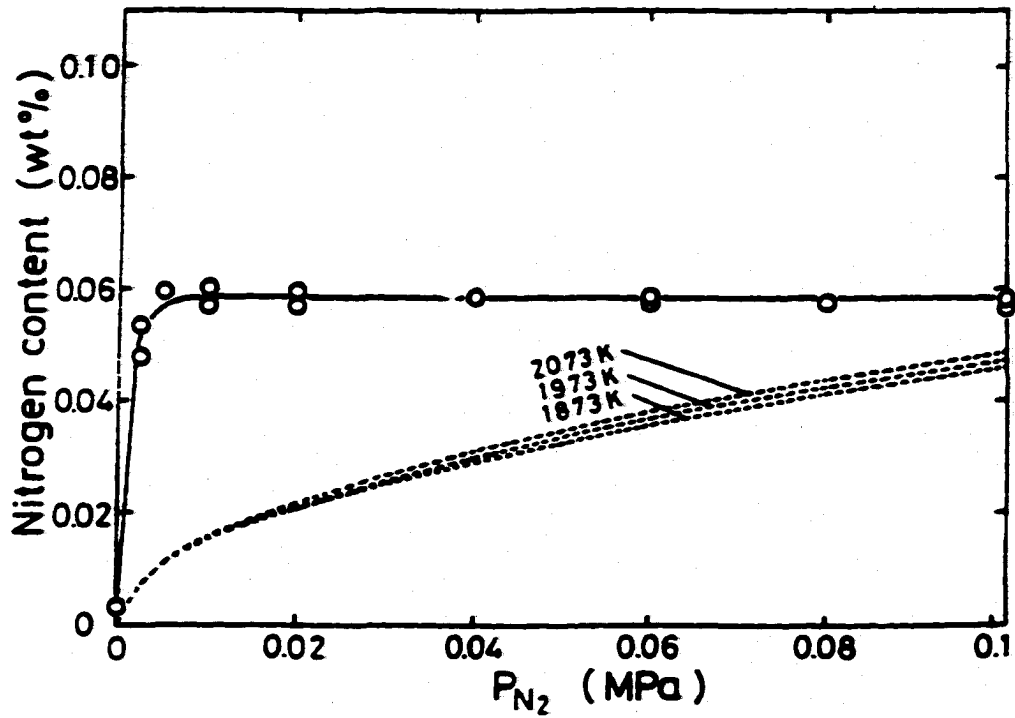


Figure 1.3. Relation between the nitrogen content of the weld metal and the nitrogen partial pressure (P_{N_2}) for an Ar- N_2 shielding gas mixture at a welding current of 250 A, an arc length of 10 mm, and a travel speed of 1.67 mm/sec.¹⁷

ing GTA welding, nitrogen is introduced into the weldment only through an interaction between the plasma phase in the arc column and the weld pool surface. Therefore, the study of this welding process allows for only the plasma-metal reactions occurring at the weld pool surface to be considered. Characteristics of this plasma phase and the current understanding of this process are discussed in the following sections.

1.2 CURRENT UNDERSTANDING OF THE NITROGEN DISSOLUTION REACTION

1.2.2 Plasma - Metal Interactions

During GTA welding, a plasma phase resides above the weld pool as the result of an interaction between the shielding gas and electromagnetic radiation. This plasma phase consists of electrons, ions, excited atoms, and molecules, and can collectively be both electrically conducting and neutral.¹⁹ When a diatomic gas is transformed to a plasma phase, it may dissociate, ionize, or become electrically or vibrationally excited. The transformation of diatomic molecules to excited neutral atoms and ions in the gas phase involves inelastic collisions between these diatomic molecules and electrons.²⁰ Plasma properties such as the electron density and energy affect the formation of these various species from the diatomic molecules. Atomic and excited gases and electrons present in the gas phase introduce several special features to the system, of which three are of special interest in welding. These features include: the extent of dissociation of a diatomic gas in the welding environment; the effect of temperature on the species concentration in the weld metal for different gases; and the concentration of dissolved species in the weld pool retained by the weld metal after cooling.

Plasma-metal interactions have been studied in the arc melting of iron and steel. The general plasma/metal reactions, which occur in simple arc melting operations, are also present in fusion welding operations. Based upon observations, there are primarily two mechanisms available to explain the enhanced levels of diatomic gas present in the metal. In the first model, Lakomskii and Torkhov⁸ have postulated that the reaction between excited nitrogen molecules, N_2^* , which possess a higher energy of internal degrees of freedom, and the liquid metal is responsible for the enhanced concentrations of nitrogen in

iron. The retention of a sufficient amount of vibrational energy in excited nitrogen molecules enhances the breaking of interatomic bonds when the nitrogen is adsorbed on the surface of the liquid iron. An additional excitation energy thus lowers the energy required for dissociation of the nitrogen molecules on the iron surface, thus increasing the equilibrium constant of the absorption of nitrogen, K^* , and the equilibrium concentration of nitrogen in solution.

A second reaction has been suggested to be responsible for the enhanced levels of nitrogen in the iron weld metal.⁹ Among the number of activated states present in the arc column, monatomic nitrogen, $N(g)$, is primarily absorbed at the surface of the liquid iron under the arc column. Equation (1.4) shows the reaction described by this model, and Equation (1.5) shows the relationship used to calculate the nitrogen concentration in the liquid metal:



$$\underline{N}(\text{wt}\%) = P_N e^{\frac{\Delta G_4^\circ}{RT}} \quad (1.5)$$

where P_N is the partial pressure of monatomic nitrogen, ΔG_4° is the standard free energy for the reaction in Equation (1.4), \underline{N} (wt.%) is the nitrogen concentration in solution at equilibrium with the diatomic nitrogen gas, K_{eq} is the equilibrium constant for this reaction, and T is the temperature of liquid iron. The standard free energy for the reaction shown in Equation (1.4) is defined by the following relation:^{4,5}

$$\Delta G_4^\circ = -85736 + 21.405T \quad (\text{cal/mol}) \quad (1.6)$$

The computed equilibrium solubility of monatomic nitrogen gas in liquid iron is shown in Figures 1.4(a-c).³ As a result, the iron-monatomic nitrogen equilibrium system displays much different behavior than the iron-diatomic nitrogen system. The equilibrium solubility of nitrogen in iron exposed to monatomic nitrogen increases in a linear

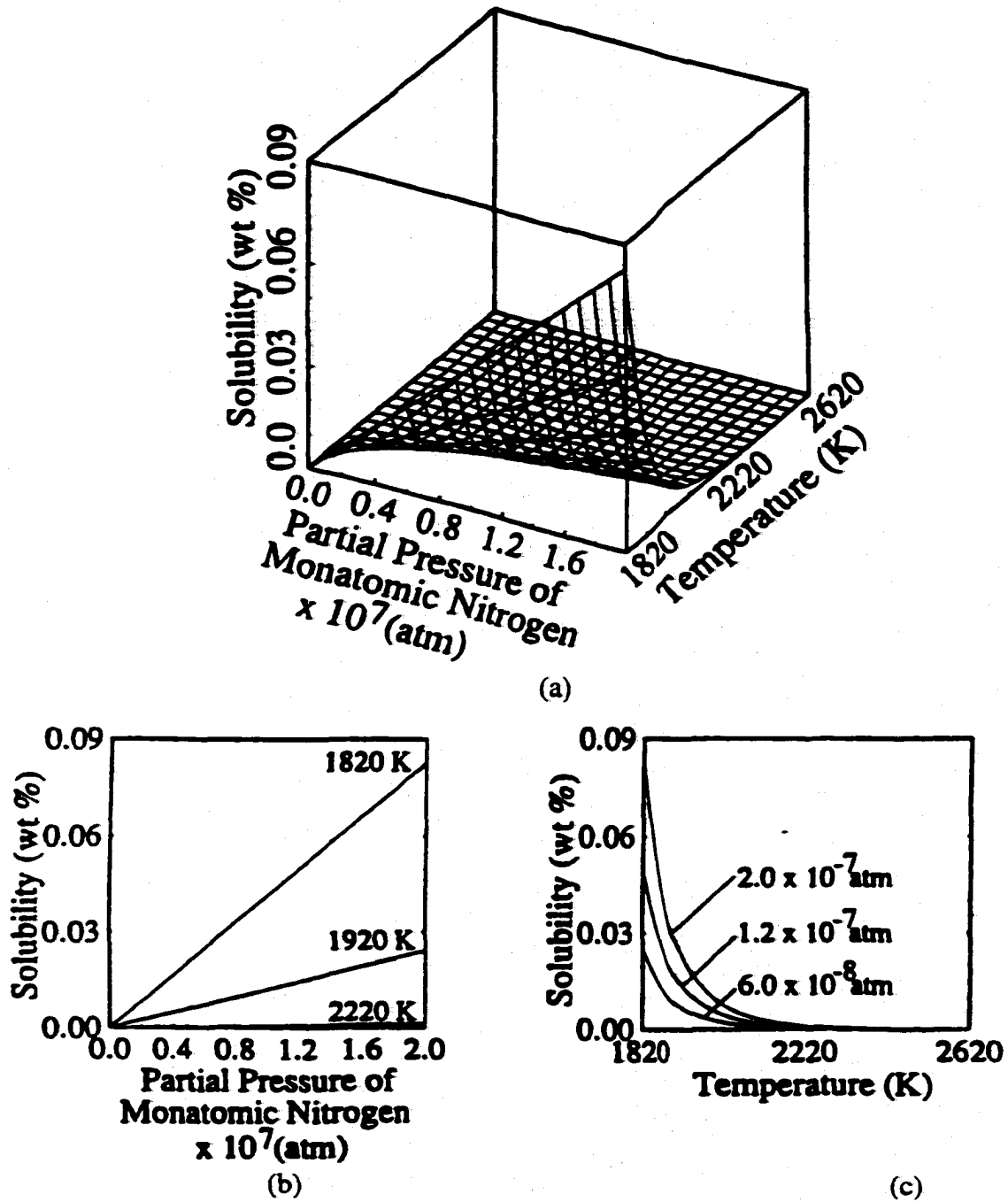


Figure 1.4(a-c). Computed equilibrium solubility of nitrogen in iron exposed to monatomic nitrogen (a) as a function of temperature and partial pressure of monatomic nitrogen, (b) as a function of partial pressure of monatomic nitrogen at three temperatures, and (c) as a function of temperature at three partial pressures of monatomic nitrogen.³

manner with respect to increasing monatomic nitrogen partial pressure, as shown in Figure 1.4(b). On the other hand, it decreases significantly in a non-linear manner with temperature over the defined range of temperatures, as shown in Figure 1.4(c). Since the monatomic nitrogen solubility increases rather sharply with decreasing temperature below 1575 K, small changes in temperature can cause large changes in the ensuing equilibrium nitrogen concentration. When compared, this variation in temperature plays a much greater role than that of pressure in determining the extent of nitrogen solubility in iron exposed to monatomic nitrogen gas.

1.2.2 Existing Models

Several authors have proposed that the total amount of nitrogen present in the liquid metal is the balance of two independent processes.^{6,21-24} Nitrogen is first absorbed through the interface between the arc and the liquid metal. Once a saturation level is reached at the metal surface, nitrogen is then expelled from the surface of the liquid metal outside the arc column. Nitrogen desorption occurs via bubble formation at the surface and other heterogeneous nucleation sites in the liquid melt. These bubbles are filled with nitrogen gas, which has been rejected from the liquid iron. Outside the arc column, the nitrogen in solution in the iron is in equilibrium with diatomic nitrogen rather than monatomic nitrogen, which dominates the arc column.

Other researchers have concentrated on the role of the plasma phase in producing these enhanced nitrogen concentrations. Gedeon and Eagar²⁵ have developed a basic model for further understanding the dissolution of monatomic species during welding. This model is based on the assumption that the diatomic gas dissociates into monatomic gas at a temperature higher than that at the sample surface. The monatomic species is then transported to the liquid metal surface where it is absorbed into the liquid metal at the temperature of the liquid surface. Mundra and DebRoy³ have developed a model based on this same premise. They have also attempted to define the monatomic nitrogen partial pressure responsible for the nitrogen concentrations observed in the weld metal.

In the plasma phase, the extent of dissociation of diatomic nitrogen depends on factors such as the nature of the power source, the energy dissipated, the overall system ge-

ometry, and the nature of the diatomic gas. The thermal dissociation of diatomic nitrogen is defined in Equation (1.7), and its standard free energy value is defined in Equation (1.8).



$$\Delta G^\circ = 86596 - 15.659T \quad (\text{cal/mol}) \quad (1.8)$$

Figure 1.5 defines the relationship between the percentage dissociation of diatomic nitrogen species into monatomic species, based on the experimental work of Bandopadhyay *et al.*,²⁰ showing that the dissociation of diatomic nitrogen increases with increasing temperature. A hypothetical temperature, T_d , is defined. This temperature is equal to the temperature at which the equilibrium thermal dissociation of diatomic nitrogen produces the partial pressure of monatomic nitrogen in the plasma.

Since the dissociation occurs at T_d and nitrogen absorption occurs at T_s , the equilibrium nitrogen concentration in iron can be defined by the following relationship:³

$$\underline{\text{N}}(\text{wt}\%) = \sqrt{P_{\text{N}_2}^{\text{in}}} e^{-\frac{1}{R} \left(\frac{\Delta G_d^\circ}{T_d} + \frac{\Delta G_s^\circ}{T_s} \right)} \quad (1.9)$$

where $P_{\text{N}_2}^{\text{in}}$ is the inlet nitrogen pressure (atm), ΔG_d° is the standard free energy for the nitrogen dissociation reaction, and ΔG_s° is the standard free energy for the absorption of monatomic nitrogen in liquid iron. The hypothetical dissociation temperature, T_d , is higher than the temperature of the sample, T_s , and is a measure of the partial pressure of the atomic nitrogen in the plasma. These hypothetical dissociation temperatures fall in a range of 100 to 300°C above the sample temperature for all of the systems analyzed.

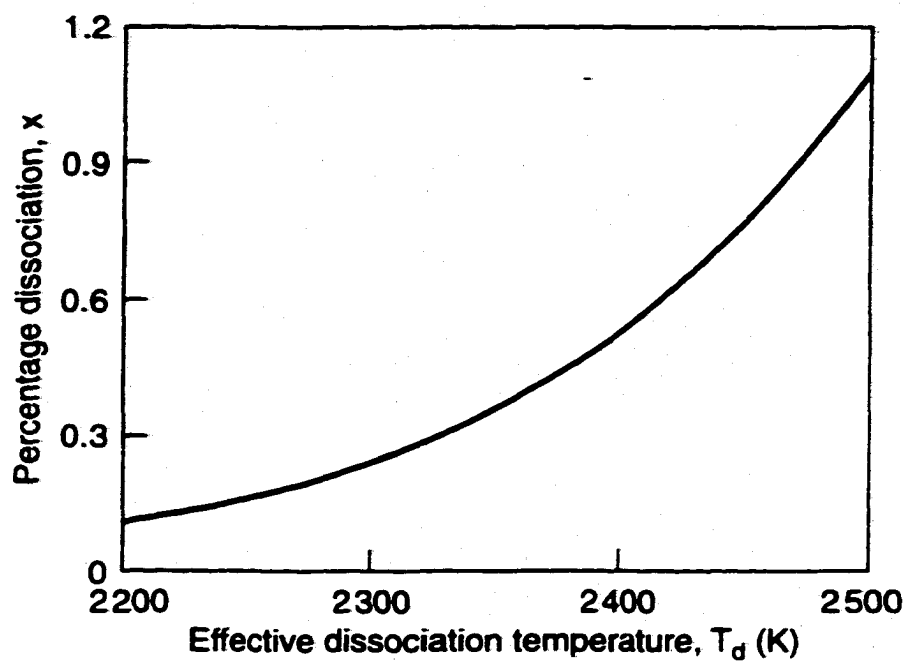


Figure 1.5. Plot of effective dissociation temperature vs. percent nitrogen dissociated²⁵ for the experimental conditions of Bandopadhyay *et al.*²⁰

Each of these methodologies provides a semi-quantitative explanation of the nitrogen dissolution reaction in plasma-metal systems. The two-temperature model provides an order of magnitude level agreement between the calculated and experimental nitrogen concentrations. On the other hand, it relies on an assumption of the effective dissociation temperature and does not provide an *a priori* capability for predicting the nitrogen concentration. Unfortunately, the characteristics of the plasma phase, as well as the interaction between the plasma phase and the liquid metal, are not yet fully understood. No quantitative means for predicting these enhanced nitrogen concentrations in the liquid metal has been developed. It is thus desired to develop a model with the capability of predicting the nitrogen concentration in the weld metal with only knowledge of the experimental parameters. In order to accomplish this task, more detailed knowledge of the plasma phase and the transport of nitrogen within the weld metal must be integrated. Each of these components is further discussed in the subsequent sections.

1.3 CALCULATION OF ATOMIC NITROGEN PARTIAL PRESSURE IN THE PLASMA

The arc present above the weld pool during GTA welding processes is produced by the interaction between the electrode and the shielding gas over the area between the electrode and the weld metal surface. Based on the potential distribution across the arc length,²⁶ the arc is divided into five parts: the cathode spot, the cathode fall region, the arc column, the anode fall region, and the anode spot,²⁷ as shown in Figure 1.6. Characteristics of the plasma phase in the arc column vary across these various regions. Only the arc column is in local thermodynamic equilibrium (LTE), which is defined, in this case, by a condition when the electron temperature is identical to the heavy particle temperature. The regions adjacent to the electrode and the weld pool surface, which are defined by the cathode and anode fall regions, respectively, display significant voltage drops and exhibit substantial deviations from LTE conditions.^{26,28}

Temperatures in the arc column can vary many thousands of degrees between the electrode and the work piece.²⁹⁻³⁴ The highest temperatures are observed in the vicinity of the electrode, in some cases approaching 20000 K, while lower temperatures are ob-

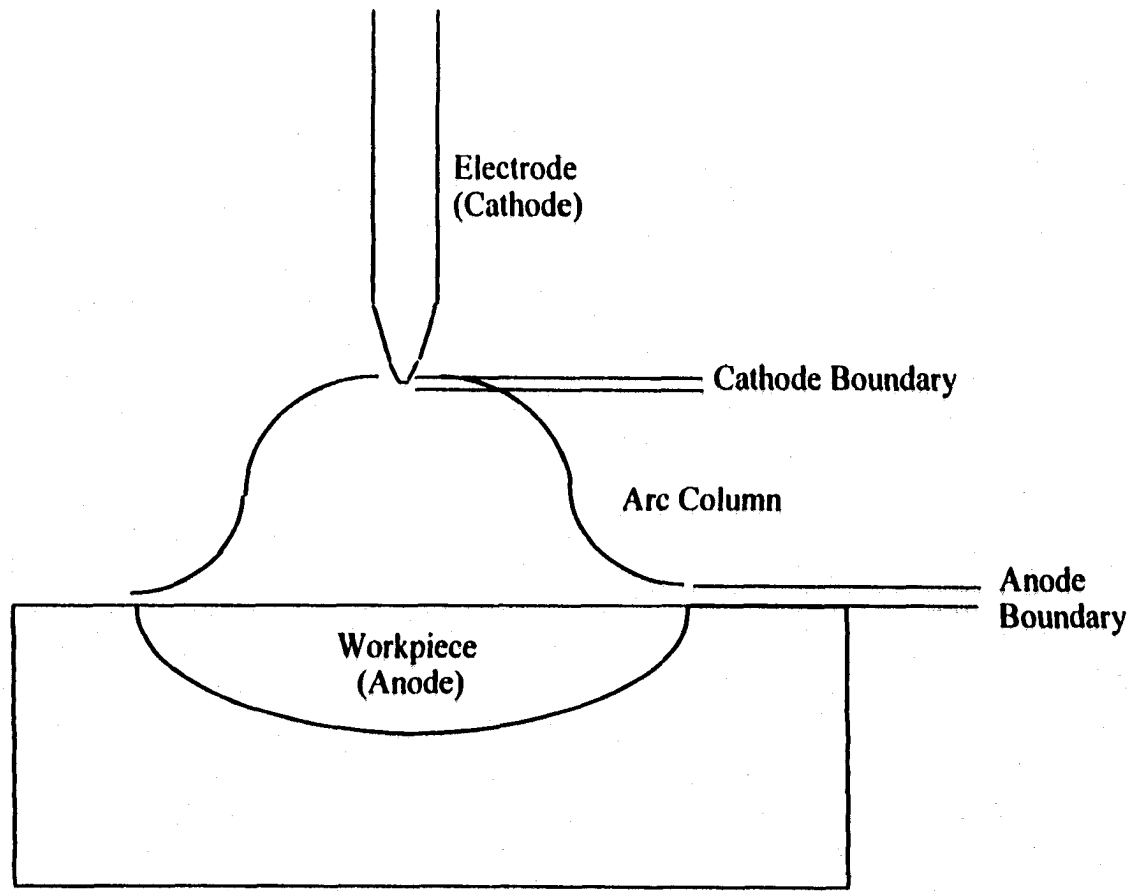


Figure 1.6. Schematic diagram of the arc column structure in GTA welding operations.

served as the work piece is approached. Even more significant temperature gradients exist in the boundary region adjacent to either the electrode or the weld pool surface. In the region adjacent to the weld pool surface, the temperatures approach those found on the weld metal surface.

Once the temperatures in the plasma phase are known, the distribution of various species in the plasma phase can be determined. Knowledge of the concentration of various species within the plasma phase is the key to a quantitative understanding of the enhanced dissolution of nitrogen in the weld metal. Theoretical studies of the number densities of various species in inert gaseous, pure nitrogen and oxygen plasmas at atmospheric pressures have been performed.³⁵⁻³⁸ In these studies, ionization and dissociation reactions have been primarily considered to calculate the number density of species in the plasma phase. These calculations provide a database of species densities over a range of temperatures.

The calculation of species densities in the plasma phase has not been extended to temperatures approaching those on the weld pool surface. In addition, the calculation of the number densities for these various species has been limited to pure gases. Monatomic nitrogen number densities at temperatures adjacent to the weld pool surface must be determined for inert gas-nitrogen mixtures. The number densities of various gaseous species calculated can then be integrated into the calculation of the nitrogen concentration on the weld pool surface. In addition to inert gas-nitrogen mixtures, even more complex gas mixtures are commonly found in the plasma phase in the arc column.

Nitrogen mixed with oxygen and hydrogen is much more likely than pure nitrogen to enter the arc column above the weld metal during arc welding processes. The role played by the second diatomic gas additions in the shielding gas stream in affecting the amount of nitrogen absorbed by the weld metal must be considered. Oxygen and hydrogen additions to a nitrogen-containing shielding gas have been shown to have a rather significant effect on the resulting nitrogen concentration in the weld pool. These gas additions have significant effects on the resulting nitrogen concentration in the weld metal, and, in particular, the addition of a small amount of oxygen to the shielding gas increases the nitrogen concentration in the weld metal.^{11,12,39-41} This increase in nitrogen concentration in

the presence of oxygen has been explained by the formation of FeO on the surface of the solidifying metal and by the presence of NO in the plasma. However, there is currently no unified theory to understand the effect of oxygen in the gas phase on nitrogen solubility. The role of oxygen on the enhanced nitrogen dissolution reaction is also investigated using these calculations.

1.4 MATHEMATICAL MODELING OF THE WELDING PROCESS

Heat transfer and fluid flow processes contribute significantly to the development of weld metal properties.^{42,43} Calculations of these heat transfer and fluid flow processes are commonly used to determine the resulting weld pool size and shape and thermal cycles at different locations in the weldment. These calculations have proven to be a reliable method for predicting weld pool characteristics in a number of different welding processes.⁴²⁻⁴⁵ The welding process can significantly alter the heat transfer and fluid flow characteristics in the weld pool. For example, the driving forces for fluid flow in the weld pool during gas-metal arc (GMA) and gas tungsten arc (GTA) welding operations and even laser welding are different. In the GTA welding process, for example, fluid flow is driven by the surface tension gradient on the weld pool surface, or Marangoni convection, as well as the electromagnetic force field. The contributions of electromagnetic and buoyancy forces to fluid flow in the GTA weld pool are much less.

Arc welding processes are also dominated by a large number of complex physical processes, which are driven in large part by heat transfer and fluid flow in the weld pool. Similar mathematical modeling techniques have been applied to analyze these processes. Examples include the prediction of weld metal microstructures for various C-Mn steels during GMA and SMA welding^{46,47} and the calculation of the growth and dissolution of oxide inclusions during the arc welding of low alloy steels.^{48,49}

Nitrogen dissolution into the weld pool is intimately tied to a number of these same physical processes. Nitrogen dissolution into the weld metal is typically characterized by a competition between the absorption of monatomic nitrogen at the weld pool surface and the desorption of diatomic nitrogen gas from the solidified weld metal outside the arc column.²⁰⁻²³ Existing models provide a qualitative basis for understanding the nitrogen

absorption reaction and the principal role of the plasma phase in this reaction. Since fluid flow and heat transfer processes significantly impact on the properties of the weld metal surface and interior, there should be a similar effect on the nitrogen dissolution reaction during GTA welding. During GTA welding, gaseous species are introduced into the weldment only through an interaction between the plasma phase in the arc column and the weld pool surface.

Therefore, the dissolution of nitrogen from an inert shielding gas during the GTA welding of iron can also be better understood through the calculation of heat transfer and fluid flow in the weld pool. A mathematical model, which combines these calculations with others for the plasma phase above the weld pool and monatomic nitrogen absorption on the weld pool surface, has been developed. The validity of this model has also been tested by comparing the modeling results with previously discussed experimental results from a series of (GTA) welding experiments.

1.5 OBJECTIVE AND MOTIVATION FOR RESEARCH

Previous models of the nitrogen dissolution reaction provide a good qualitative understanding of the nitrogen dissolution process. These models primarily take into account the role of the plasma in supplying monatomic nitrogen to the weld pool surface. In fact, the two-temperature model provides predictions of nitrogen concentrations in the weld metal within an order of magnitude level accuracy. On the other hand, these existing models do not take into account the role which fluid flow processes in the weld pool play on the distribution of nitrogen in the weldment.

The welding process is complex, with a large number of physical processes occurring simultaneously in and around the weld pool. There are three primary areas of interest in the arc welding process, including the plasma phase in the arc column above the weld pool, the interface between the plasma phase and the weld pool, and the weld metal. A number of important physical and chemical processes occur in each of these areas, which interact with each of the other processes, and thus affect the nature of the welding process. For example, reactions in the plasma phase produce monatomic nitrogen, which is then absorbed on the liquid metal surface. Once absorbed at the liquid metal surface, ni-

nitrogen is transported to the interior regions of the molten metal. Nitrogen concentration levels can rapidly reach saturation at the molten metal surface. Once the saturation level in the melt is reached, the metal can no longer hold this amount of nitrogen in solution. It must, therefore, be expelled, resulting in a phenomenon similar to boiling occurring near the surface of the melt.

A quantitative methodology to accurately determine the nitrogen concentration in the weldment during the GTA welding of iron and steels is lacking. In order to determine the nitrogen concentration in the weldment, knowledge of the plasma phase above the weld pool, the absorption of nitrogen on the weld pool surface, and the transport of nitrogen throughout the weldment is integrated. Detailed calculations of the monatomic nitrogen partial pressures in the plasma phase present above the weld pool are coupled with the absorption of monatomic nitrogen on the weld pool surface. The resulting nitrogen concentration on the surface will then be integrated with heat transfer and fluid flow calculations in order to determine the distribution of nitrogen in the weld pool and the nitrogen concentration in the weldment. Finally, the computed nitrogen concentrations are compared with the corresponding experimentally determined values.

There are several primary objectives to be accomplished here in order to develop a quantitative model for the calculation of the nitrogen concentration in the iron during GTA welding processes. Nitrogen containing shielding gases and nitrogen-oxygen gas mixtures are studied, and a comprehensive model for accurately determining the residual nitrogen concentration in a steel weldment is developed. The primary objectives of this research project are listed here:

- (a) To calculate the number densities of the inert gases, nitrogen, and oxygen present in the plasma phase in the arc column for temperatures characteristically found during GTA welding operations.
- (b) To examine the role of oxygen additions on the nitrogen dissolution reaction and develop a model to describe the further enhancements in the residual nitrogen concentration in the presence of oxygen.

- (c) To integrate heat transfer and fluid flow calculations with the plasma phase calculations to determine the distribution of nitrogen species within the weldment during GTA welding operations.
- (d) To investigate the effects of changes in welding parameters on the nitrogen dissolution reaction and the residual nitrogen concentration.
- (e) To investigate the effects of nitrogen present in the weld metal on the presence of porosity and the microstructure of the weld pool, and how these characteristics may affect the nitrogen concentration.

References

- ¹ S. Kou, Welding Metallurgy, John Wiley and Sons, New York, 1987, pp. 61-63.
- ² R. D. Pehlke, Unit Processes in Extractive Metallurgy, Elsevier, New York, (1979), 141-145.
- ³ K. Mundra and T. DebRoy, "A General Model for Partitioning of Gases between a Metal and its Plasma Environment", *Metall. and Mat. Trans.*, 1995, 26B, 149-157.
- ⁴ J.F. Elliott and M. Gleiser, Thermochemistry for Steelmaking I, Addison-Wesley Publishing Co., Reading, MA, 1963, 75.
- ⁵ H.E. McGannon, ed., The Making, Shaping and Treating of Steel, 9th edition, United States Steel Corporation, 1971, 330-331.
- ⁶ G. den Ouden and O. Griebing, "Nitrogen Absorption during Arc Welding", in Recent Trends in Welding Science and Technology, ed. S.A. David and J.M. Vitek, (ASM International, Materials Park, OH), 1990, 431-435.
- ⁷ F.S. Death and D.A. Haid, "Method for Adding Nitrogen to Molten Metals", U.S. Patent No. 3,257,197, 1966.
- ⁸ V.I. Lakomskii and G.F. Torkhov, "Absorption of Nitrogen from a Plasma by Liquid Metal", *Soviet Physics-Doklady*, 1969, 13(11), 1159-1161.
- ⁹ J.D. Katz and T.B. King, "The Kinetics of Nitrogen Absorption and Desorption from a Plasma Arc by Molten Iron", *Met. Trans. B*, 1989, 20B, 175-185.
- ¹⁰ T. Kuwana and H. Kokawa, "The Nitrogen Absorption of Arc-Melted Iron and Stainless Steel", *Trans. Jap. Weld. Soc.*, 1988, 19(2), 12-19.
- ¹¹ P.D. Blake and M.F. Jordan, "Nitrogen Absorption during the Arc Melting of Iron", *J. Iron Steel Inst.*, 1971, 209(3), 197-200.
- ¹² C.J. Allum, "Nitrogen Absorption from Welding Arcs", *Bulletin of Welding Research Council*, 369, Dec. 1991-2, 68-84.
- ¹³ P.D. Blake, "Oxygen and Nitrogen in Weld Metal", *Weld. Res. Int.*, 9(1), 1979, 23-56.
- ¹⁴ T.A. Palmer, K. Mundra, and T. DebRoy, "Nitrogen Dissolution in the Weld Metal – Current Status and Research Opportunities", in Mathematical Modelling of Weld Phenomena 3, ed. by H. Cerjak, (The Institute of Materials, London), 1997, 3-40.

- ¹⁵ T. Kuwana, "The Oxygen and Nitrogen Absorption of Iron Weld Metal During Arc Welding", in Advanced Joining Technologies. Proceedings of the International Institute of Welding Congress on Joining Research, ed. T.H. North, (Chapman and Hall, New York), 1990, 117-128.
- ¹⁶ T. Kuwana, H. Kokawa, and M. Saotome, "Quantitative Prediction of Nitrogen Absorption by Steel during Gas Tungsten Arc Welding", in Mathematical Modelling of Weld Phenomena 3, ed. by H. Cerjak, (The Institute of Materials, London), 1997, 64-81.
- ¹⁷ T. Kuwana and H. Kokawa, "The Nitrogen Absorption of Iron Weld Metal during Gas Tungsten Arc Welding", *Trans. Jap. Weld. Soc.*, 1986, 17(1), 20-26.
- ¹⁸ T. Kuwana, H. Kokawa, and K. Naitoh, "Effects of Chromium and Nickel on Nitrogen Absorption of Iron Weld Metal during Gas Tungsten Arc Welding", *Trans. Jap. Weld. Soc.*, 1990, 21(2), 85-91.
- ¹⁹ F.S. Chen, Introduction to Plasma Physics and Controlled Fusion, Volume 1: Plasma Physics, (Plenum Press, New York), 1984, 3-7.
- ²⁰ A. Bandopadhyay, A. Banerjee, and T. DebRoy, "Nitrogen Activity Determination in Plasmas", *Metall. Trans. B*, 1992, 23B, 207-214.
- ²¹ M. Uda and S. Ohno, "Spattering Phenomenon for Iron-Nitrogen System during Arc Melting", *Trans. Nat. Res. Inst. Metals*, 1978, 20(6), 358-365.
- ²² K. Takeda and Y. Nakamura, "Behavior of Nitrogen in Plasma Arc Melting", *Trans. ISIJ*, 1978, 18, 641-647.
- ²³ S. Ohno and M. Uda, "Effects of Hydrogen and Nitrogen on Blowhole Formation in Pure Nickel at Arc Welding and Non-Arc Melting", *Trans. Nat. Res. Inst. Metals*, 1981, 23(4), 243-248.
- ²⁴ M. Uda and T. Wada, "Solubility of Nitrogen in Arc-Melted and Levitation-Melted Iron and Iron Alloys", *Trans. Nat. Res. Inst. Metals*, 1968, 10(2), 21-33.
- ²⁵ S.A. Gedeon and T.W. Eagar, "Thermochemical Analysis of Hydrogen Absorption in Welding", *Weld. J.*, 1990, 69, 264s-271s.
- ²⁶ A.E. Guile, "The Electric Arc", in The Physics of Welding, ed. by J.F. Lancaster, (Pergamon Press, Oxford), 109-133.
- ²⁷ P.G. Jönsson, J. Szekely, R.T.C. Choo, and T.P. Quinn, "Mathematical Models of Transport Phenomena Associated with Arc-Welding Process: A Survey", *Modelling Simul. Mater. Sci. Eng.*, 1994, 2, 995-1016.

- ²⁸ H.A. Dinulescu and E. Pfender, "Analysis of the Anode Boundary Layer of High Intensity Arcs", *J. Appl. Phys.*, 1980, 51(6), 3149-3157.
- ²⁹ J.F. Key, J.W. Chan, and M.E. McIlwain, "Process Variable Influence on Arc Temperature Distribution", *Weld. J.*, 62(7), 1983, 179s-184s.
- ³⁰ A.E.F. Gick, M.B.C. Quigley, and P.H. Richards, "The Use of Electrostatic Probes to Measure the Temperature Profiles of Welding Arcs", *J. Phys. D: Appl. Phys.*, 6, 1973, 1941-1949.
- ³¹ J. Wendelstorf, I. Decker, H. Wohlfahrt, and G. Simon, "TIG and Plasma Arc Modeling: A Survey", in *Mathematical Modelling of Weld Phenomena 3*, ed. by H. Cerjak, (The Institute of Materials, London, 1997), pp. 848-897.
- ³² R.T.C. Choo, J. Szekely, and R.C. Westhoff, "On the Calculation of the Free Surface Temperature of Gas-Tungsten-Arc Weld Pools from First Principles: Part I. Modeling the Welding Arc", *Met. Trans. B*, 23B, 1992, 357-369.
- ³³ G.N. Haddad and A.J.D. Farmer, "Temperature Measurements in Gas Tungsten Arcs". *Weld. J.*, 1985, 64(12), 399s-342s.
- ³⁴ A.J.D. Farmer and G.N. Haddad, "Temperature Determinations in a Free-Burning Arc: I. Experimental Techniques and Results in Argon", *J. Phys. D: Appl. Phys.*, 1984, 17, 1189-1196.
- ³⁵ K.S. Drellishak, C.F. Knopp, and A.B. Cambel, "Partition Functions and Thermodynamic Properties of Argon Plasma", *Phys. of Fluids*, 1963, 6(9), 1280-1288.
- ³⁶ K.S. Drellishak, D.P. Aeschliman, and A.B. Cambel, "Partition Functions and Thermodynamic Properties of Nitrogen and Oxygen Plasmas", *Phys. of Fluids*, 1965, 8(9), 1590-1600.
- ³⁷ J.D. Fast, "The Dissociation of Nitrogen in the Welding Arc", *Philips Res. Rep.*, 1947, 2, 382-398.
- ³⁸ G.J. Dunn and T.W. Eagar, "Metal Vapors in Gas Tungsten Arcs: Part II. Theoretical Calculations of Transport Properties", *Met. Trans. A*, 1986, 17A, 1865-1871.
- ³⁹ T. Kobayashi, T. Kuwana, and Y. Kikuchi, "Arc Atmosphere and Nitrogen Content of Weld Metal", *Welding in the World*, 5(2), 1967, 58-73.
- ⁴⁰ I.K. Pokhodnya and A.P. Pal'tsevich, "The Part Played by Oxygen in the Absorption of Nitrogen by Metal During Arc Welding", *Avt. Svarka*, 1971, 25(2), 8-11.

- ⁴¹ H. Thier and R. Killing, "Absorption of Oxygen and Nitrogen during Welding - Spatial Sequence of the Reactions", *Welding and Casting*, 1991, 2, 5-8.
- ⁴² S.A. David and T. DebRoy, "Current Issues and Problems in Welding Science", *Science*, 1992, 257, 497-502.
- ⁴³ T. DebRoy and S.A. David, "Physical Processes in Fusion Welding", *Reviews of Modern Physics*, 1995, 67(1), 85-112.
- ⁴⁴ S. Kou and Y.H. Wang, "Computer Simulation of Convection in Moving Arc Weld Pools", *Met. Trans. A*, 1986, 17A, 2271-2277.
- ⁴⁵ C. Chan, J. Mazumder, and M.M. Chen, "A Two-Dimensional Transient Model for Convection in Laser Melted Pool", *Metall. Trans. A*, 1984, 15A, 2175-2184.
- ⁴⁶ K. Mundra, T. DebRoy, S.S. Babu, and S.A. David, "Weld Metal Microstructure Calculations from Fundamentals of Transport Phenomena in the Arc Welding of Low-Alloy Steels", *Weld. J.*, 1997, 76(4), 163-s - 171-s.
- ⁴⁷ Z. Yang and T. DebRoy, "Weld Metal Microstructure Prediction from Fundamentals of Transport Phenomena and Phase Transformation Theory", *Sci. Tech. Weld. Joining*, 1997, 2(2), 53-58.
- ⁴⁸ T. Hong, W. Pitscheneder, and T. DebRoy, "Quantitative Modelling of Motion, Temperature Gradients, and Growth of Inclusions in Weld Pool", *Sci. Tech. Weld. Joining*, 1998, 3(1), 33-41.
- ⁴⁹ W. Pitscheneder, M. Gruböck, K. Mundra, T. DebRoy, and R. Ebner, "Numerical and Experimental Investigations of Conduction-Mode Laser Weld Pools", in Mathematical Modelling of Weld Phenomena 3, ed. by H. Cerjak, London, The Institute of Materials, 1997, 41-63.

Chapter 2

BACKGROUND AND LITERATURE REVIEW

2.1 NITROGEN SOLUBILITY IN CONVENTIONAL MATERIALS PROCESSING

2.1.1 Dissolved Gases in Metals

The ability to control the amount of dissolved gas in a liquid metal is very important in determining its final product quality. During processing, diatomic species, such as N_2 , O_2 , and H_2 , and more complex species, such as CO_2 , CO , H_2O , and SO_2 , are often present above a liquid metal. Various elements from these species, such as C, H, S, and O, can be easily dissolved in the metal, leading to higher gaseous concentrations in the solidified metal.¹⁻⁴ Nitrogen, oxygen, and hydrogen present in the solidified metal at these elevated levels may cause changes in the final properties of iron and plain carbon steels. For example, the presence of nitrogen in steels increases their hardness and machinability but decreases ductility and toughness.¹ On the other hand, nitrogen can improve the toughness and strength in aluminum-killed steels by forming aluminum nitride particles, which, in turn, controls the grain size of the steel.¹

These properties thus depend, in part, on the gaseous concentration in the liquid and solid iron. At these gaseous concentrations, porosity and inclusions in the solidified metal become a concern. The presence of gas-induced porosity in the solidified metal is caused by a large difference in the gas solubility between the liquid and solid states. Once these gases are in the metal, their removal is made difficult by the inability of removing relatively large volumes of gas at both the solidification front and in the solidified metal. Inclusions and second phase particles in the solidified iron or steel are the result of excess nitrogen or oxygen reacting with alloying elements, such as Al or Ti, in either the liquid or solid iron to form secondary particles.

2.1.2 Iron-Nitrogen System

The iron-nitrogen system⁵ shown in Figure 2.1 is of greatest interest here. In many ways, the iron-nitrogen system is similar to iron-carbon. Aside from the same general shape of each phase diagram, many of the phases commonly found in iron-carbon alloys, i.e. austenite and ferrite, are also found in the iron-nitrogen phases. One major difference between the phase diagrams is the temperature at which the eutectoid transformation occurs in the iron nitrogen system. The eutectoid reaction equates to the commonly known pearlite reaction ($\gamma \rightarrow \alpha + \text{Fe}_3\text{C}$) in Fe-C and a similar reaction in Fe-N ($\gamma \rightarrow \alpha + \text{Fe}_4\text{N}$). In Fe-C, the eutectoid reaction occurs at approximately 727°C, while the reaction is depressed to approximately 590°C for Fe-N.

There are additional nitride phases present in the Fe-N system at nitrogen concentrations well in excess of the concentration range for the Fe_4N (γ') nitride phase.⁶⁻⁸ Several phases and their respective equilibrium concentration ranges are listed in Table 2.1. The formation of these various nitride phases in the Fe-N system requires rather significant amounts of nitrogen in solution in order to remain stable. Such levels are difficult to achieve in bulk. Therefore, these phases tend to be observed on the surface of the metal, and are formed only as the result of a solid phase reaction.

The formation of a martensitic phase has also been reported during the quenching of iron powder or thin iron wire in ammonia-hydrogen gas mixtures.⁹⁻¹¹ The iron-nitrogen martensite is very similar in both structure and appearance to that observed in the iron-carbon system.⁹ Using electron microscopy, low-nitrogen martensite (~0.3 wt.% N) appears as a lath shaped crystal with a length large in comparison to its width and thickness. Above 0.5 wt.% N, the crystals become generally wider and often show twins, suggesting that the martensite crystals at these nitrogen levels are mainly internally - twinned plates.⁹

Nitrogen concentrations in pure iron can range from 0 to 2.7 wt.% N. Iron samples containing up to 0.7 wt.% N have been observed to be fully martensitic when quenched from an austenitizing temperature to 20°C. As the nitrogen concentration is further increased, the alloys contain progressively more retained austenite. Fe-N alloys, though,

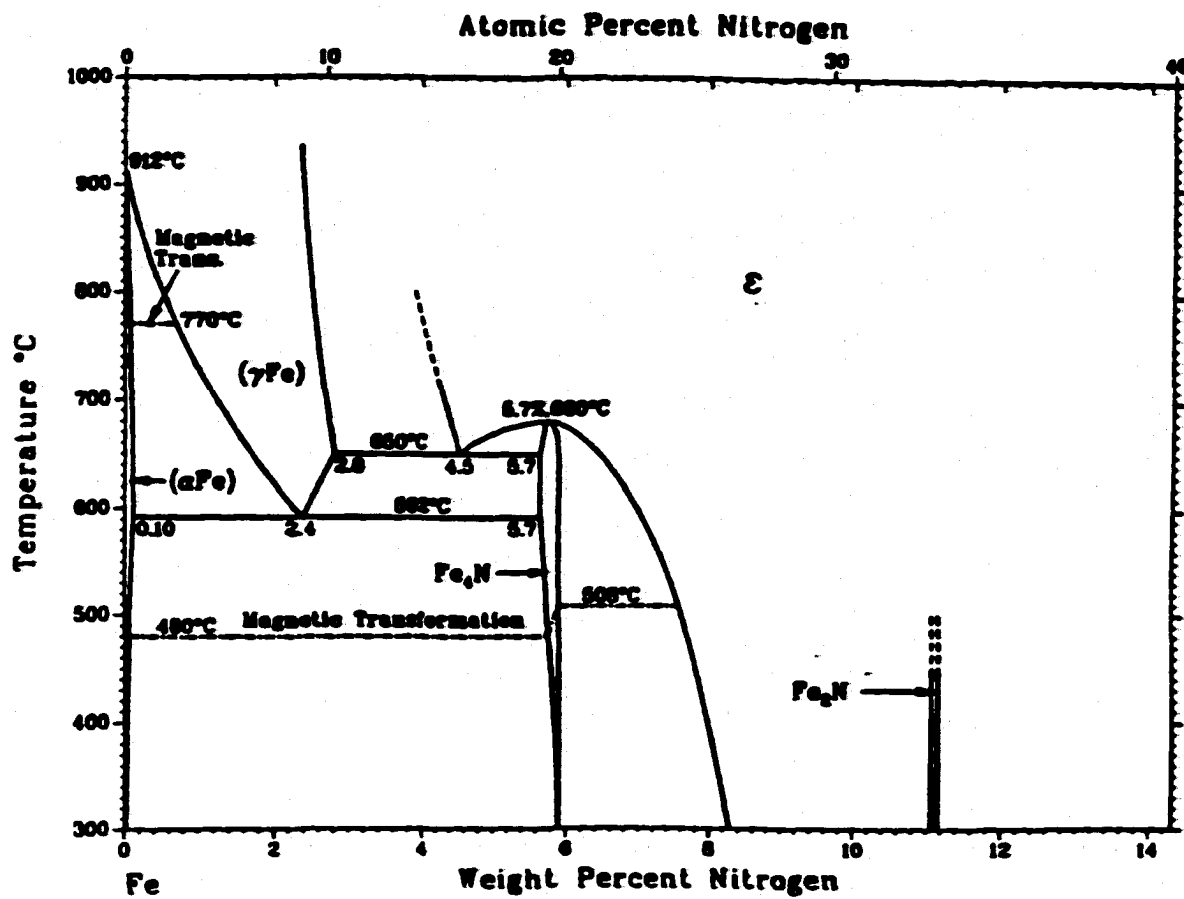


Figure 2.1. Iron Nitrogen Phase Diagram.⁷

Table 2.1. Summary of iron nitride phases present in the iron-nitrogen system.

<u>Iron Nitride</u> <u>Phase</u>	<u>Crystal Structure</u>	<u>Nitrogen Concentration</u> <u>(wt.%)</u>	<u>Reference</u>
Fe ₄ N (γ)	BCC	5.77 – 5.88	9
Fe ₈ N (α'')	Tetragonal	5.77 – 5.88	9
Fe ₁₆ N ₂ (α'')	Tetragonal	5.77 – 5.88	7
Fe ₂ N (ξ)	Orthorhombic	11.1 – 11.3	6
Fe ₃ N (ϵ)	Hexagonal	< 11.0	6

cannot be re-austenitized in a vacuum or in an inert atmosphere. During the re-austenitizing heat treatment, nitrogen is desorbed from the alloy into the surrounding environment, leaving an alloy devoid of nitrogen and with altered physical properties.¹⁰⁻¹²

2.1.3 Nitrogen Absorption Reaction

Absorption of nitrogen in liquid iron is an important consideration in the processing of iron and steel. For example, during processing, large quantities of superheated molten steel come in contact with the surrounding atmosphere. In this vein, a great deal of work has been devoted to understand the thermodynamics and kinetics of the absorption of nitrogen in liquid iron.¹²⁻¹⁵ Pehlke and Elliott,¹⁵ for example, have examined this phenomenon and developed a mathematical formulation describing its thermodynamic behavior. The equilibrium nitrogen concentration in iron ($\frac{1}{2} N_2(g) \rightarrow \underline{N}(\text{wt.}\%)$) at a constant temperature is given by Sieverts' Law and is proportional to the square root of the partial pressure of diatomic nitrogen:¹²

$$\underline{N}(\text{wt.}\%) = K_{\text{eq}}^d \sqrt{P_{N_2}} = \sqrt{P_{N_2}} e^{-\frac{\Delta G^\circ}{RT}} \quad (2.1)$$

where ΔG° is the standard free energy for the overall solution reaction, $\underline{N}(\text{wt.}\%)$ is the nitrogen concentration in solution at equilibrium with the diatomic nitrogen gas, K_{eq}^d is the equilibrium constant for nitrogen absorption reaction, P_{N_2} is the partial pressure of N_2 , and T is the temperature of liquid iron. Based on the above calculation scheme, a linear relationship between the square root of the nitrogen partial pressure and the resulting nitrogen concentration in the liquid iron at 1600°C is shown in Figure 2.2(a).¹² The free energy relationships used to calculate these nitrogen concentrations are shown in Table 2.2.

The solubility of nitrogen in iron has also been studied using similar Sieverts' Law calculations over a large temperature range, containing both solid and liquid iron

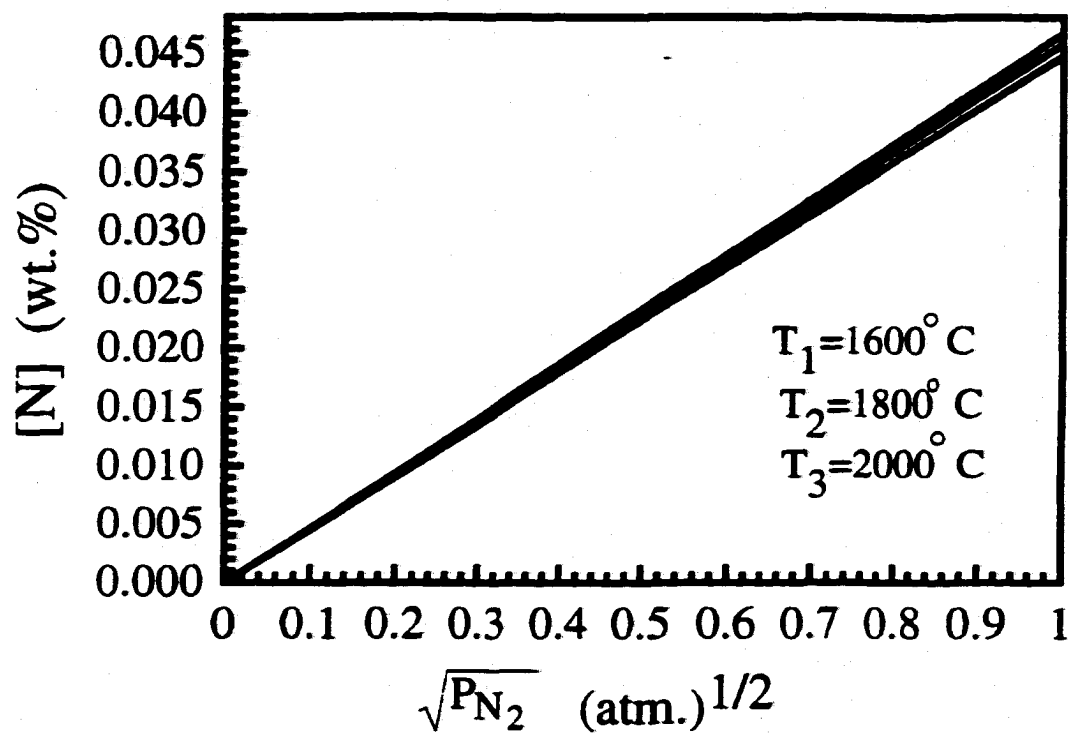


Figure 2.2(a). The solubility of nitrogen in iron as a function of the square root of P_{N_2} at 1600°C.¹²

Table 2.2. Free energy relationships for nitrogen solubility calculations in pure iron.

Reaction	Free Energy-Temperature Relationship (cal/mol)	Temperature Range (K)	Reference
$\frac{1}{2}\text{N}_2(\text{g}) \rightarrow \text{N}(\text{g})$	$86,596.0 - 15.659 T$	273 - 1811	13
$\frac{1}{2}\text{N}_2(\text{g}) \rightarrow \text{N}(\text{wt.}\%)$			
Liquid Fe	$860.0 + 5.71 T$	>1811	13,15
δ -Fe	$7200 + 4.62 T$	1663 - 1810	13,16
γ -Fe	$-2060 + 8.94 T$	1185 - 1662	13,17
α -Fe	$7200 + 4.62 T$	273 - 1184	13,16
$\text{N}(\text{g}) \rightarrow \text{N}(\text{wt.}\%)$			
Liquid Fe	$-85,736 + 21.405 T$	>1811	13-15
δ -Fe	$-79396 + 20.28 T$	1663 - 1810	13,16
γ -Fe	$-84536 + 24.599 T$	1185 - 1662	13,17
α -Fe	$-79396 + 20.28 T$	273 - 1184	13,16

phases.¹²⁻¹⁷ Figure 2.2(b)¹⁴ shows the calculated nitrogen solubility across this temperature range at a nitrogen partial pressure of 1 atm. In this figure, there is a rather significant difference in the nitrogen solubility between both liquid and solid iron and between the various solid iron phases.

2.1.4 Effect of Alloying Elements on Nitrogen Absorption

Additions of dilute solute elements in iron cause a number of interactions between each solute and the nitrogen present in solution.¹⁸⁻²⁷ Thus, these interactions affect the nitrogen solubility in ternary and multi-component iron alloys. The effect of the individual alloying elements on the resulting nitrogen solubility can be determined based on the calculation of their interaction coefficients, $\epsilon_N^{(j)}$, which are defined in terms of the activity coefficient of nitrogen (f_N):

$$\epsilon_N^{(j)} = \left(\frac{\partial \ln f_N}{\partial X_j} \right)_{\%X_j \rightarrow 0} \quad (2.2)$$

where X_j is the mole fraction of the alloying element, j . Table 2.3 lists the values for the interaction coefficients of common alloying elements present in liquid iron at 1600 C. These interaction coefficients are then used to determine the influence of these common alloying elements on the activity coefficient of nitrogen and the resulting nitrogen solubility in the alloy. The effect of these various alloying elements on the nitrogen activity coefficient in liquid iron is determined using a Taylor's series expansion of $\ln f_N$ which is given by the following relationship:

$$\ln f_N(\%N, \%2, \%3, \dots) = \epsilon_N^{(N)} (\%N) + \epsilon_N^{(2)} (\%2) + \epsilon_N^{(3)} (\%3) + \dots \quad (2.3)$$

Figure 2.3 shows the effect of several dilute alloy element additions on the nitrogen solubility in liquid iron.¹⁵ Some of these alloying elements, for example, Cr, V, and Nb, significantly increase the nitrogen solubility with rather small additions to the melt. On

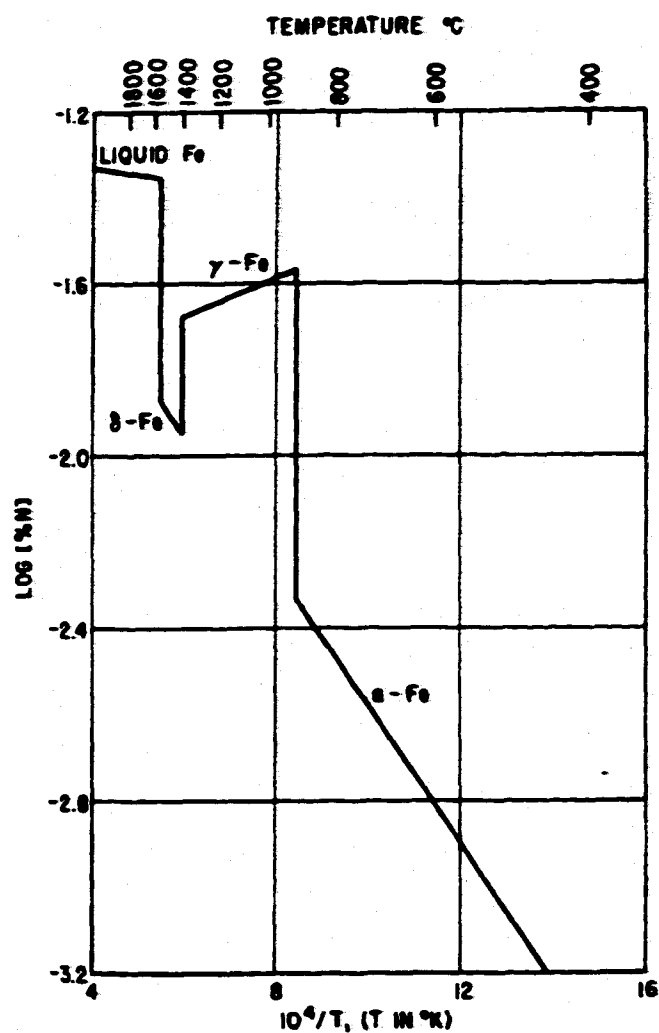


Figure 2.2(b). The solubility of nitrogen in iron over a wide temperature range for both solid and liquid iron phases at 1 atm.¹⁵

Table 2.3. Summary of interaction parameters on the nitrogen solubility in iron for common alloying elements calculated during the heating of liquid iron and during arc melting.

<u>Alloying Element</u>	<u>Interaction Parameter (Heating of Melt)</u>	<u>References</u>	<u>Interaction Parameter (Arc Melting)</u>	<u>References</u>
Al	0.0025 to 0.0060	15,27,62		
C	0.1250 to 0.2500	15,25-27,62		
Cr	-0.040 to -0.057	15,27,62	-0.028 to -0.044	64,65
Mn	-0.0200	15,27,62		
Mo	-0.0040 to -0.025	15,25-27,62	-0.0051	64
Ni	0.007 to 0.011	15,25-27,62	0.003	65
O	0.05 or -0.014	14,63		
S	0.0130	25,26,62		
Si	0.047	15		
Ti	-0.6300	27, 62		
V	-0.10	27,62	-0.062	64

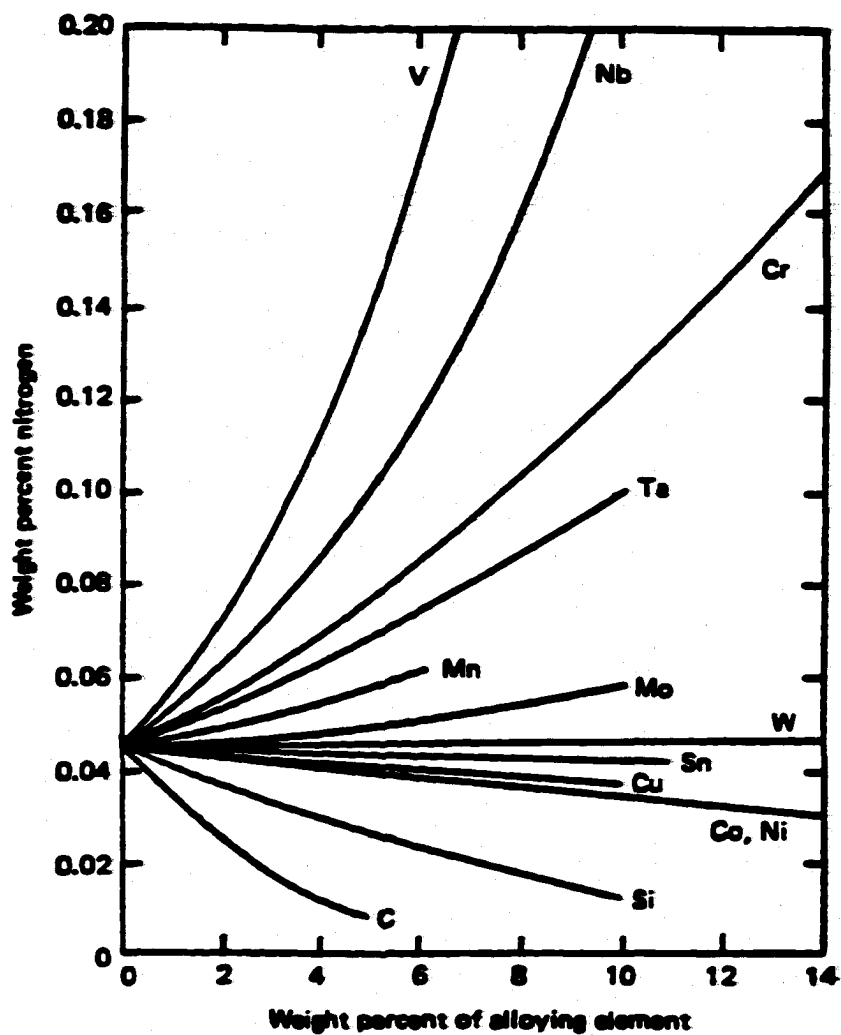


Figure 2.3. The effect of alloying element additions on the nitrogen solubility in liquid iron at a nitrogen pressure of 1 atm. and a temperature of 1600° C.¹⁵

the other hand, several other alloying elements, such as C and Si, significantly decrease the nitrogen solubility in liquid iron. The roles which these alloying elements play are important in understanding the significantly different nitrogen concentrations observed in low alloy steels and stainless steels, even though a Sieverts' Law type behavior is followed.

2.2 NITROGEN DISSOLUTION IN PLASMA – METAL SYSTEMS

2.2.1 Observation of Enhanced Nitrogen Concentrations During Arc Melting

Sieverts' Law based calculations of the nitrogen concentration in liquid iron are based on a metal-diatomic gas system. However, such conditions are not always present in materials processing operations. For example, arc melting is a common practice in the processing of plain carbon and other steels. During arc melting, there is a plasma phase present above the liquid iron. With a plasma phase present above the liquid metal, the metal-diatomic gas equilibrium defined by Sieverts' Law is not present. Under these conditions, nitrogen concentrations much greater than Sieverts' Law calculations are observed in the liquid iron.²⁸⁻³⁵ For example, oxygen and nitrogen contents as high as 0.7 and 0.2 wt.%, respectively, have been observed in liquid steel exposed to a nitrogen containing arc.³⁶

Several researchers²⁸⁻³⁵ have thus investigated the role which the presence of a plasma phase above the liquid metal plays on the absorption of nitrogen from the surrounding environment into liquid iron and steel. Death and Haid²⁸ investigated the dissolution of nitrogen in arc melted iron by adding predetermined amounts of nitrogen to an argon atmosphere in an electric arc furnace. Very high nitrogen concentrations in the liquid iron bath, not attainable using conventional gas-metal reactions, were achieved in this case. Lakomskii and Torkhov²⁹ performed similar arc melting experiments on carbonyl iron samples in several argon-nitrogen atmospheres. Nitrogen levels in the iron samples were far in excess of calculated values for equilibrium conditions. In Figure 2.4,²⁹ the nitrogen content in the metal is proportional to the square root of nitrogen partial pressure at low gas pressures. At higher nitrogen partial pressures (P_{N_2}), the nitrogen concentration in

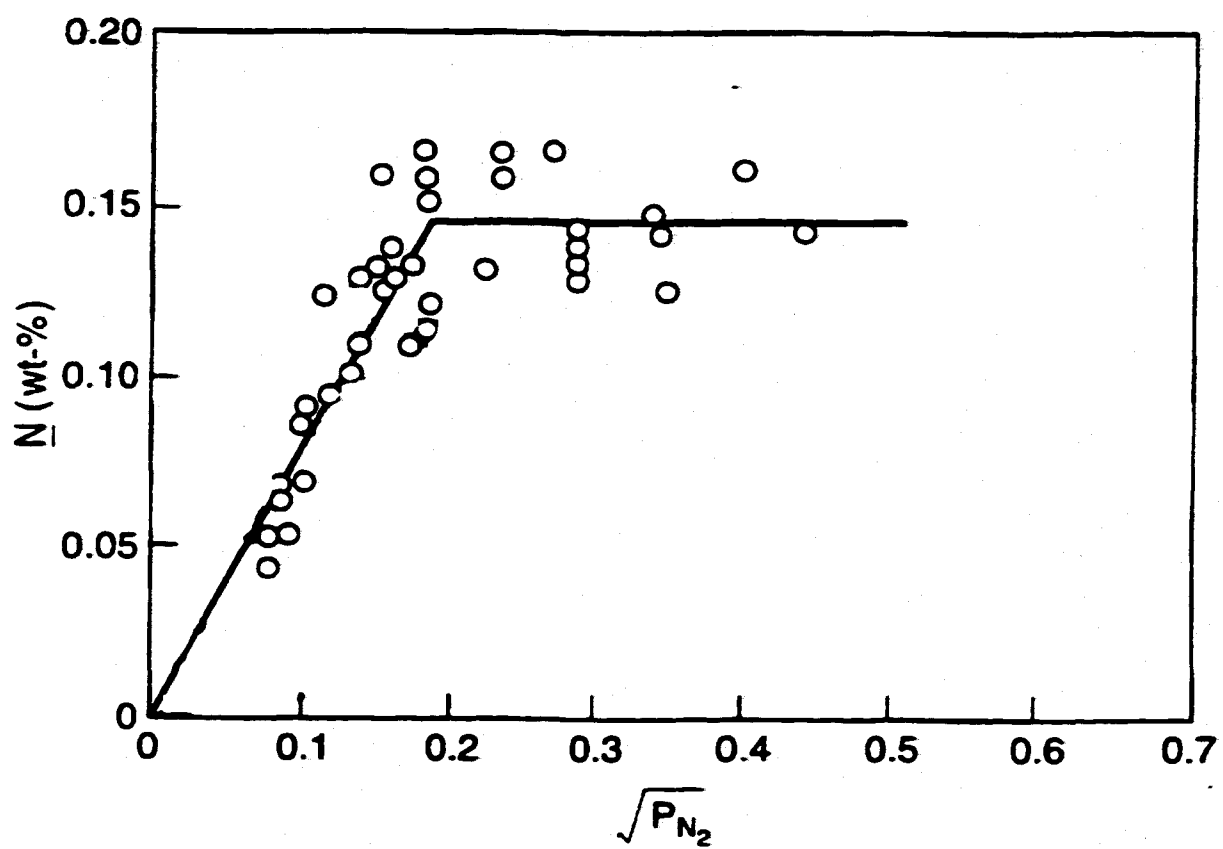


Figure 2.4. Nitrogen concentrations observed in iron samples during arc melting in several nitrogen containing atmospheres.²⁸

the metal remains constant, which corresponds to the saturation of nitrogen in the iron. Above this level, nitrogen begins to bubble from the metal.

Unlike previous researchers,²⁸⁻³³ who analyzed nitrogen absorption into large molten iron baths, Ouden and Griebeling³⁰ studied the nitrogen absorption in small iron buttons in a small arc-melting chamber. The nitrogen concentrations in the small arc melted samples were also considerably larger than those based on equilibrium calculations. In Figure 1.2, the nitrogen concentrations in the iron samples are compared with Sieverts' Law calculations as a function of the square root of nitrogen partial pressure in the shielding gas. The linear behavior previously noted²⁹ at low nitrogen partial pressures is not observed here. However, the nitrogen concentration plateaus at higher nitrogen partial pressures. The level of this nitrogen concentration plateau is equivalent to the nitrogen solubility in pure iron at 1 atm using Sieverts' Law calculations.

One difference between most high temperature materials processing operations and those described in this section is the presence of a plasma phase above the liquid iron. This gaseous plasma phase is formed as the arc interacts with the surrounding atmosphere. The original equilibrium conditions, therefore, no longer exist in the plasma-metal system during the arc melting of iron and steel. As a result, Sieverts' Law calculations cannot be used to determine the nitrogen concentration during the arc melting of iron and steel. Unfortunately, the characteristics of the plasma phase, as well as the interaction between the plasma phase and the liquid metal, are not yet fully understood. No quantitative means for predicting these enhanced nitrogen concentrations in the liquid metal has been developed. On the other hand, several studies analyzing the plasma phase above the metal and several others, which describe proposed mechanisms for the enhanced nitrogen absorption in plasma-metal systems are available.

2.2.1.1 Species Present in the Plasma Phase

Within a plasma phase, there are electrons, ions, excited atoms, and molecules.³⁷⁻³⁹ When a diatomic gas, such as nitrogen, oxygen, or hydrogen, is transformed into a plasma phase, it may dissociate, ionize, or become electrically or vibrationally excited. Ouden⁴⁰ investigated the forms in which nitrogen may exist in the plasma phase present

in the arc. Nitrogen enters the arc from the surrounding atmosphere in its molecular form, N_2 . Once the nitrogen molecules enter the arc column, the high temperatures prevalent in the arc column cause the molecules to be dissociated into atoms or ionized.

Fast⁴¹ has investigated the dissociation of diatomic nitrogen gas in the plasma phase in an arc column and has determined the number densities for both nitrogen molecules and atoms over a range of temperatures. In this analysis, ideal gas law behavior is assumed to prevail in the plasma phase. A simplified measure of the role of temperature in the plasma phase on the nitrogen dissociation reaction is expressed by the degree of dissociation, α_d . It is defined as the fraction of molecules which is dissociated into atoms, and is shown in the following two relations:⁴¹

$$\alpha_d = \sqrt{\frac{K_p}{K_p + 4p}} \quad (2.4)$$

$$K_p = \frac{(P_N)^2}{P_{N_2}} = C \frac{4n^2\alpha_d^2}{n(1-\alpha_d)} = P \frac{4\alpha_d^2}{1-\alpha_d^2} \quad (2.5)$$

where p is the total pressure, K_p is the reaction constant for the dissociation reaction ($N_2(g) \rightarrow 2N(g)$), which is calculated from fundamental spectroscopic data, n is the number of moles of diatomic gas to be dissociated, and C is a constant. The dissociation behavior for nitrogen and several other diatomic gases, including O_2 , H_2 , and CO_2 , is shown as a function of temperature in Figure 2.5.⁴⁰

The dissociation behavior for each diatomic gas shown here is similar. For example, each curve displays a steep transition between no dissociation and complete dissociation, indicating that a small change in the arc temperature can give rise to a considerable change in the degree of dissociation.⁴⁰⁻⁴¹ Near complete dissociation of the diatomic nitrogen species occurs between temperatures from approximately 6000 K to 10000 K, which are common in the arc column. In this temperature range, CO_2 , H_2 , and O_2 com-

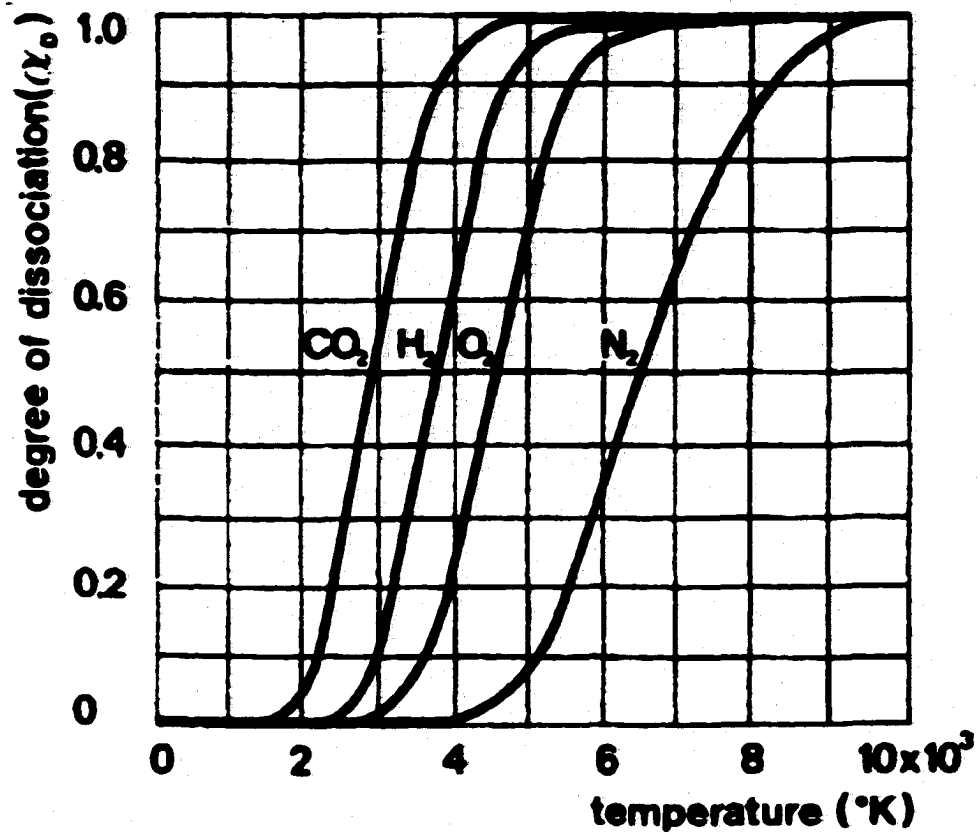


Figure 2.5. Degree of dissociation (α_d) of several gases as a function of temperature.⁴⁰

pletely dissociate at much lower temperatures than N_2 . Therefore, only the dissociated forms of these various molecules are present at temperatures prevalent in the arc column.

At even higher temperatures, nitrogen atoms and molecules can also be ionized. The number density of the various ionized species and the electron density in the plasma phase can be calculated using the Saha-Eggert relationship.⁴²⁻⁴⁴

$$\frac{n_i n_e}{n_{i-1}} = \frac{2(2\pi m_e kT)^{3/2}}{h^3} \frac{Q_i}{Q_{i-1}} e^{-(\epsilon_i - \epsilon_{i-1})/kT} \quad (2.6)$$

where n_i , n_e , and n_{i-1} are the number densities (m^{-3}) of the ions, electrons, and ground state atoms or molecules, respectively, m_e is the mass of an electron, h is Planck's constant, k is Boltzmann constant, T is the temperature, Q_i and Q_{i-1} are the partition functions for the ions and atoms or molecules, respectively, and ϵ_i and ϵ_{i-1} are the ground state energies of the ions and their respective ground state atoms or molecules.

The degree of ionization of either a molecular or atomic species can be determined in much the same way as the degree of dissociation of a diatomic molecule. It is defined below using a modified version of the Saha Equation:⁴⁰

$$\frac{\alpha_i^2}{1-\alpha_i} = 3.0 \times 10^{-7} \left(\frac{T^{5/2}}{p} \right) \exp \left[-\frac{E_i}{kT} \right] \quad (2.7)$$

where p is the gas pressure (atm.), T is the temperature (K), α_i is the degree of ionization, E_i is the ionization energy, and k is the Boltzmann constant. As shown in this relationship, the arc temperature and the system pressure determine the degree of ionization.

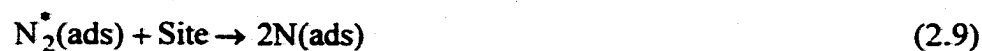
Several other investigators⁴¹⁻⁴⁴ have combined these calculations and attempted to compute the number densities of various species in a plasma phase over a range of temperatures. Dunn and Eagar,⁴² for example, investigated inert gaseous plasmas, and Drellichak *et al.*,⁴¹⁻⁴⁴ examined both inert gaseous and pure nitrogen and oxygen plasmas at atmospheric pressures. They assumed that a number of different species are present in the plasma, depending on the gases from which the plasma phase was formed. Plasma

properties, such as the electron density and energy, affect the formation of various atomic, ionic, and excited neutral species in the plasma phase. These studies provide a database for the distribution of species over a range of temperatures prevalent in the plasma phase. On the other hand, these calculations have not been extended to temperatures approaching those on the weld pool surface nor have they been used to calculate the nitrogen concentration in liquid iron during arc melting or welding.

2.2.1.2 Predominant Mechanisms Responsible for Enhanced Nitrogen Concentration

The presence of these various atomic and excited species and electrons in the plasma phase is responsible for the enhanced nitrogen concentrations observed in arc melted iron and steel. Researchers^{29,31} have attributed these results to one of two species present in the plasma phase above the weld pool. Lakomskii and Torkhov²⁹ first postulated that the excited nitrogen molecule, N_2^* , is the primary species responsible for the enhanced nitrogen concentrations observed in the liquid metal. A N_2^* species has a higher energy of internal degrees of freedom than a N_2 species. It results from various collision processes and other effects commonly associated with the plasma phase.

The nitrogen dissolution reaction involving N_2^* is represented by the following set of reactions:



Lakomskii and Torkhov²⁹ based their hypothesis on the observation of a linear relationship between the square root of the nitrogen partial pressure and the nitrogen concentration in the metal at low nitrogen partial pressures. These results are shown in Figure 2.4 and resemble a Sieverts' Law type relationship, providing a role for diatomic nitrogen

in the nitrogen dissolution process. In this model, the retention of additional energy in the nitrogen molecules enhances nitrogen dissociation at the moment when the nitrogen is adsorbed on the surface of the liquid iron.²⁹ The equilibrium constant for the absorption of nitrogen, K^* , is thus increased, along with the equilibrium concentration of nitrogen in solution.

Katz and King³¹ have presented a second mechanism, which is responsible for the enhanced absorption of nitrogen in the metal. They refute the arguments of Lakomskii and Torkhov²⁹ supporting a diatomic species and propose that monatomic nitrogen is the dominant species in this reaction. The mechanism involving monatomic nitrogen is described through the following set of reactions:



The formation of monatomic nitrogen in the plasma phase has been previously studied and proposed to involve inelastic collisions of the diatomic molecules with electrons.⁴⁵⁻⁴⁶ The first step in the dissociation process involves the formation of N_2^+ as a precursor to the formation of nitrogen atoms, which involves the collision of fast electrons, e_f^- , with diatomic nitrogen molecules. The N_2^+ species can also be formed by a Penning ionization mechanism in which metastable He atoms, He^* , collide with N_2 molecules as shown below.



The collisions of N_2^+ with electrons can lead to excited nitrogen atoms of 2D and 2P states by the following relationships:



The presence of monatomic nitrogen in the plasma phase begs the question of its effect on the nitrogen concentration in the liquid metal. Table 2.2 lists the free energy relationships for the dissociation of diatomic nitrogen and the absorption of the resulting monatomic nitrogen species in liquid iron. Based on these relationships, the equilibrium solubility of monatomic nitrogen gas in liquid iron is shown in Figures 1.4(a-c).⁴⁷ Its behavior is significantly different than that observed when the liquid iron is exposed to diatomic nitrogen. For example, the nitrogen concentration in liquid iron due to monatomic nitrogen decreases significantly as the temperature increases, as shown in Figure 1.4(c). Since the monatomic nitrogen solubility increases sharply with decreasing temperature below 1575 K, small changes in temperature can cause large changes in the ensuing equilibrium nitrogen concentration.

Foremost among the many unique characteristics of this system is the rather potent nature of a small amount of monatomic nitrogen. In order to attain a specific nitrogen concentration, the necessary equilibrium partial pressure of monatomic nitrogen is about a million times lower than that of diatomic nitrogen. Let us consider an equilibrium system at 2000 K and 1 atm. total pressure. Based on the nitrogen dissociation reaction shown in Table 2.2, an equilibrium system of nitrogen gas at 1 atm. contains 9.1×10^{-7} atm. of $N(g)$. The equilibrium nitrogen solubility in liquid iron due to the diatomic nitrogen species is 0.045 wt.% \underline{N} and that due to monatomic nitrogen is also 0.045 wt.% \underline{N} .

2.2.1.3 Use of Glow Discharges to Model Arcs

Plasma-metal interactions, which dominate the nitrogen absorption reaction during arc melting, are rather complex and only further complicated by the nature of the arc column. In particular, the arc is a non-isothermal heat source, characterized by rather large temperature gradients within the plasma phase. The temperature distribution primarily influences the nature of the species present above the liquid metal surface. The liquid metal surface is also characterized by significant temperature gradients, further complicating the absorption reaction.

In order to analyze the fundamental nature of the plasma-metal interaction, these complicating factors in the arc plasma must be mitigated. Glow discharge plasmas have been used in the past to model the reactions occurring in the arc column.⁴⁸⁻⁵⁰ A comparison between the major features for several common plasmas and those found in glow discharge plasmas is shown in Table 2.4. For example, the same species are present in each of these plasmas, and, specifically, monatomic nitrogen is present in both arcs and glow discharges. Most importantly, though, the absence of temperature gradients on the metal surface and the very small temperature gradients within the glow discharge are very much desired.

Glow discharges have also been used to model the enhanced nitrogen dissolution reaction in iron. Small iron samples have been exposed to low pressure helium-nitrogen glow discharges at a temperature of 1300°C for a period of time sufficient to ensure nitrogen saturation of the sample.⁵¹ Unlike the arc melting experiments discussed above, the iron samples in these experiments are still in the solid state (γ -Fe) when exposed to the glow discharge plasma. Figure 2.6 shows the relationship between the observed nitrogen concentrations and the nitrogen partial pressure.⁵⁹ Even with these samples being in the solid state, the observed nitrogen concentrations are significantly higher than the Sieverts' Law calculations predicted at these nitrogen partial pressures. Thus, no matter what the state of the metal in contact with the plasma, the interaction of the iron sample with a nitrogen containing plasma results in enhanced nitrogen concentrations over those without a plasma phase present.

Table 2.4. Comparison of several important features of plasmas formed during common welding processes.

Feature	Electric Arc	Laser/ Electron Beam	Glow Discharge Plasma
Species in the Gas Phase	Electrons, Ions (N_2^+ , N^+), Excited Neutral Atoms and Molecules (N^* , N_2^*), and Monoatomic and Diatomic Species (N , N_2)	Electrons, Ions (N_2^+ , N^+), Excited Neutral Atoms and Molecules (N^* , N_2^*), and Monoatomic and Diatomic Species (N , N_2)	Electrons, Ions (N_2^+ , N^+), Excited Neutral Atoms and Molecules (N^* , N_2^*), and Monoatomic and Diatomic Species (N , N_2)
Typical Electron Energy (K)	6000 - 16000 (Ref. 55)	3400 - 17000 (Refs. 52 and 58)	4000 - 13500 (Ref. 51 and 54)
Typical Electron Density (m^{-3})	10^{21} - 10^{23} (Ref. 53)	10^{20} - 10^{23} (Refs. 56 and 57)	10^{13} - 10^{20} (Ref. 51 and 53)
Temperature Gradient on Metal Surface	Present, Strong	Present, Strong	Absent
Energy Density During Welding	Medium	High	Low

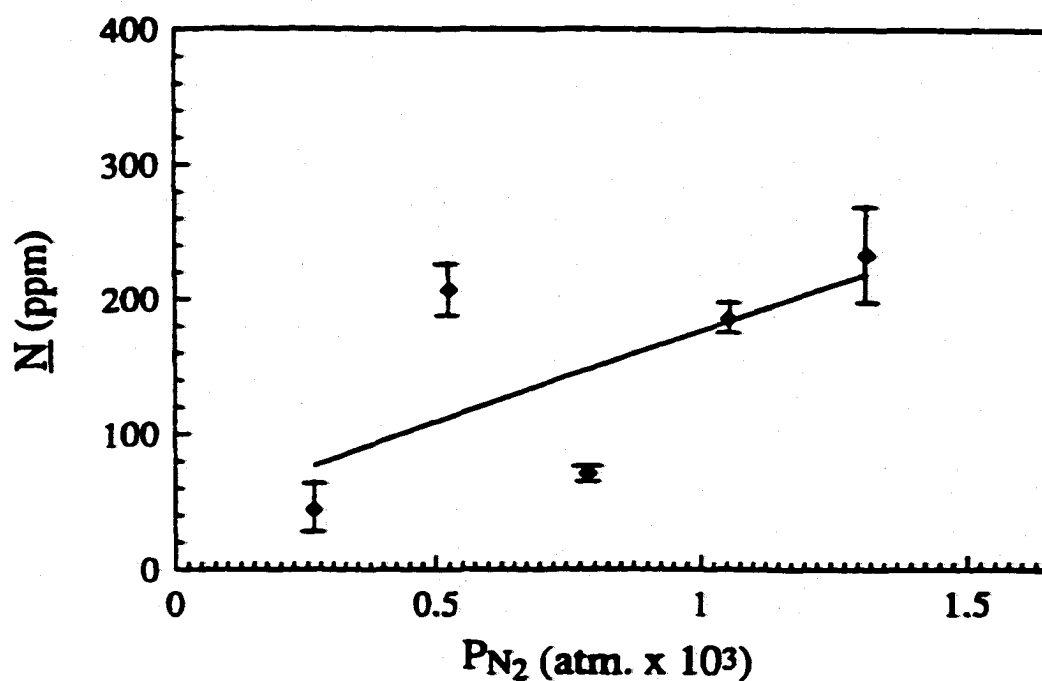


Figure 2.6. Experimental nitrogen solubility plotted as a function of the nitrogen partial pressure for iron samples at a temperature of 1300 C exposed to glow discharges composed of various He-N₂ gas mixtures at a total pressure of 1.316×10^{-3} atm.⁵⁹ The range of observed nitrogen concentrations is shown.

2.2.1.4 Effect of Changes in Arc Parameters on Nitrogen Concentration

It is well established that the resulting nitrogen concentration in iron exposed to a nitrogen-containing plasma phase cannot be fully explained using equilibrium calculations. Changes in the melting parameters primarily affect the energy transfer from the electrode to the metal surface, and change the temperature distribution both within the plasma phase in the arc column and within the iron sample. These changes, in turn, affect the mechanisms controlling the nitrogen dissolution reaction in a plasma-metal system.

Several researchers³⁰⁻³⁵ have investigated the effect of such changes on the enhanced nitrogen concentration in liquid iron and steel samples. Ouden and Griebing,³⁰ for example, arc melted a number of iron samples at various arc currents and nitrogen partial pressures. Their results³⁰ are shown in Figure 2.7 for several small nitrogen additions to the melting environment, ranging from 0.1% to 4% N₂. At arc currents below approximately 60 A, the nitrogen saturation value decreases with a rising current. Above an arc current of 60 A, the nitrogen saturation value rises with increasing arc current above 60 A. Based on these results, they³⁰ observed that the amount of nitrogen entering the molten metal and the interfacial area between the arc column and the liquid metal increase with the arc current. These effects at the molten metal surface are believed to be due to an increase in the arc temperature, which equates to an increase in the degree of dissociation of diatomic nitrogen in the arc column, and an increase in the arc volume. Kuwana and Kokawa³² observed an increase in the temperature of the molten metal as the arc current was increased from 100 to 200 A. On the other hand, they did not observe a concomitant change in the nitrogen concentration over this same arc current range.

In Figure 2.7, the nitrogen concentrations are far below the nitrogen solubility in iron predicted by Sieverts' Law at 1 atm., except for a nitrogen addition of 4%, at which point the nitrogen concentration in the liquid metal reaches the saturation level.²⁸ They investigated only two levels of nitrogen additions, 10% and 100% and observed nitrogen concentrations in both cases near the level of nitrogen solubility at 1 atm. The absence of any significant change in the nitrogen concentration may be due to the amount of nitrogen added to the melting environment. Since the levels of nitrogen present in the weld

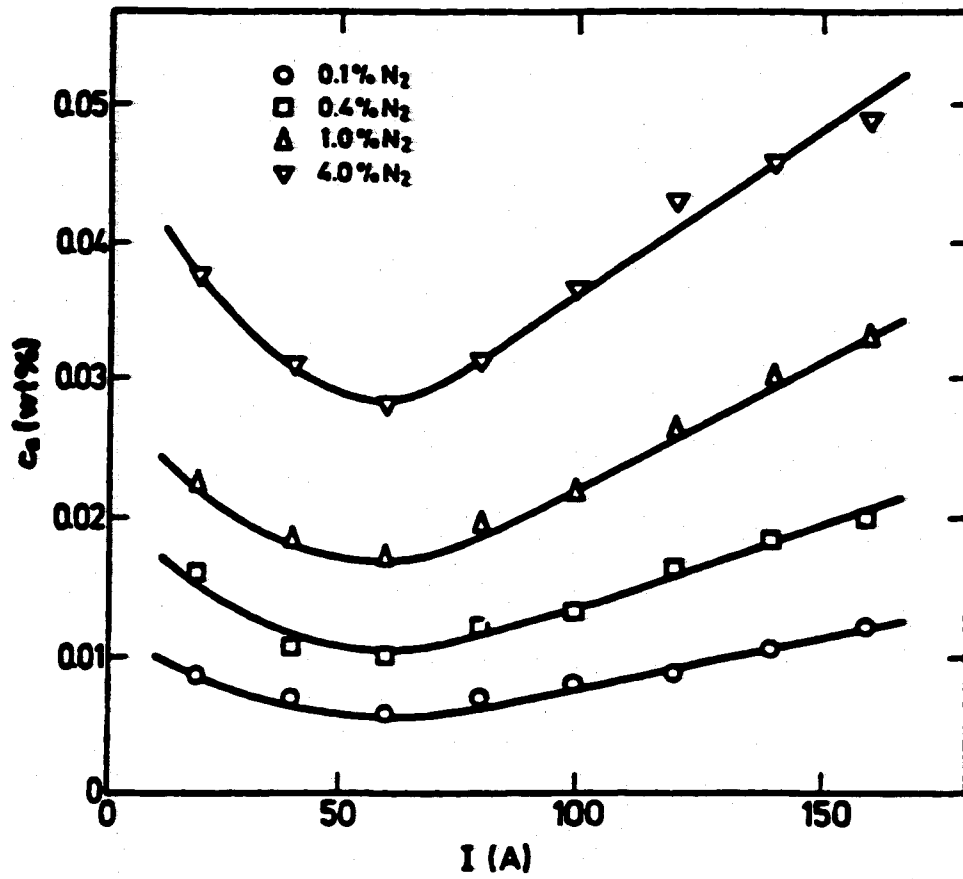


Figure 2.7. Relationship between the nitrogen saturation level in an iron sample as a function of the arc current for various nitrogen gas additions to the atmosphere.³⁰

metal were near saturation, no further increases in the nitrogen concentration could be attained with further changes in the arc characteristics.

In addition to the arc current, changes in the arc voltage, which can be equated with the arc length, also affect the energy transfer from the arc column to the metal surface. Ouden and Griebing,³⁰ for example, analyzed the effect of increasing the arc length, the distance between the tungsten electrode and the metal surface, on the resulting nitrogen concentration. Figure 2.8 shows the effect³⁰ of increasing the arc length on the nitrogen saturation value in the metal sample for a melting environment containing 0.1% N₂. For arc lengths less than 3 mm, the nitrogen saturation value in the metal sample increases with arc length. Above approximately 3 mm, though, the nitrogen saturation value reaches a plateau at about 0.02 wt.% N, which is far below the nitrogen saturation level for atmospheric diatomic nitrogen.

The properties of the arc column in contact with a liquid metal can also be affected by changes in the arc polarity.³⁵ For example, the researchers above used what is considered a straight polarity case, with the tungsten electrode serving as the cathode with a negative charge and the liquid metal serving as the anode with a positive charge. On the other hand, Neuschutz *et al.*⁵⁷ attempted to select the optimum current mode and torch polarity to minimize unwanted nitrogen pick-up in the liquid metal. In several experiments, the polarity of the plasma torch was operated in three different configurations: DC cathodic, AC, and DC anodic. Nitrogen concentrations varied with changes in the arc configurations, with the lowest nitrogen levels in DC cathodic conditions and the highest in DC anodic conditions.

Figures 2.9(a&b)⁶⁰ show the influence of torch polarity on the behavior of nitrogen ions present in the arc column and the effect of arc polarity on the arc jet momentum, respectively. Based on their experimental observations, the authors concluded that the choice of the arc polarity affects the nitrogen pick-up by creating a stirring effect. In their explanation, the impact of the arc agitates the melt, thereby enhancing the mass transport in the melt, and raising the rate of nitrogen pick-up. On the other hand, the melt is more strongly agitated when the torch acts as the cathode rather than as the anode.

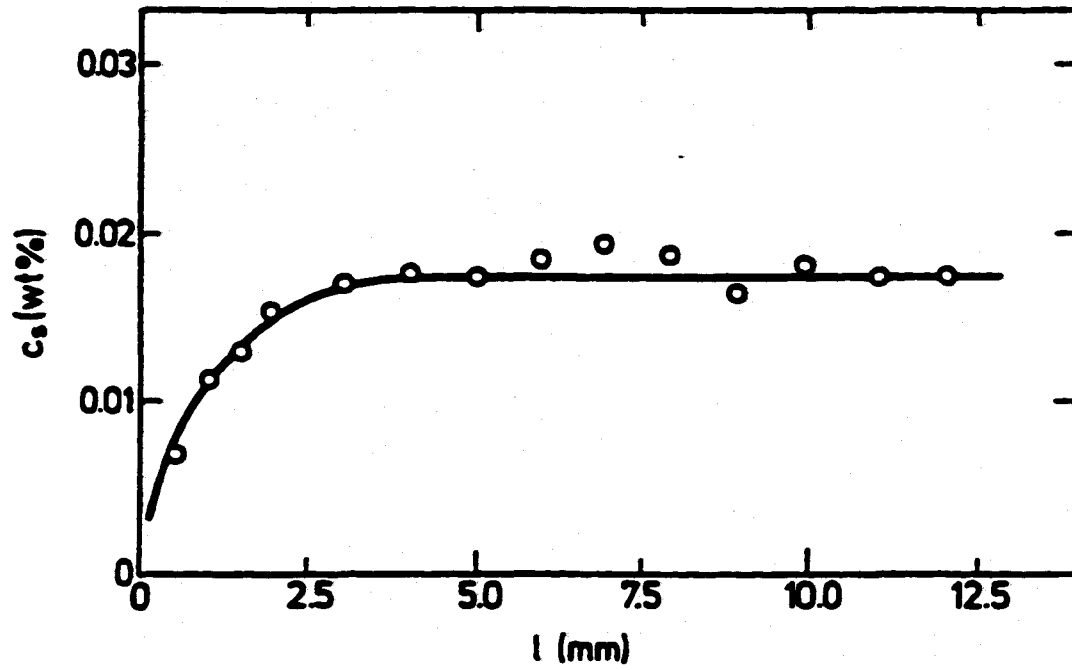


Figure 2.8. Relationship between the nitrogen concentration in the sample and changes in the arc length (l).³⁰

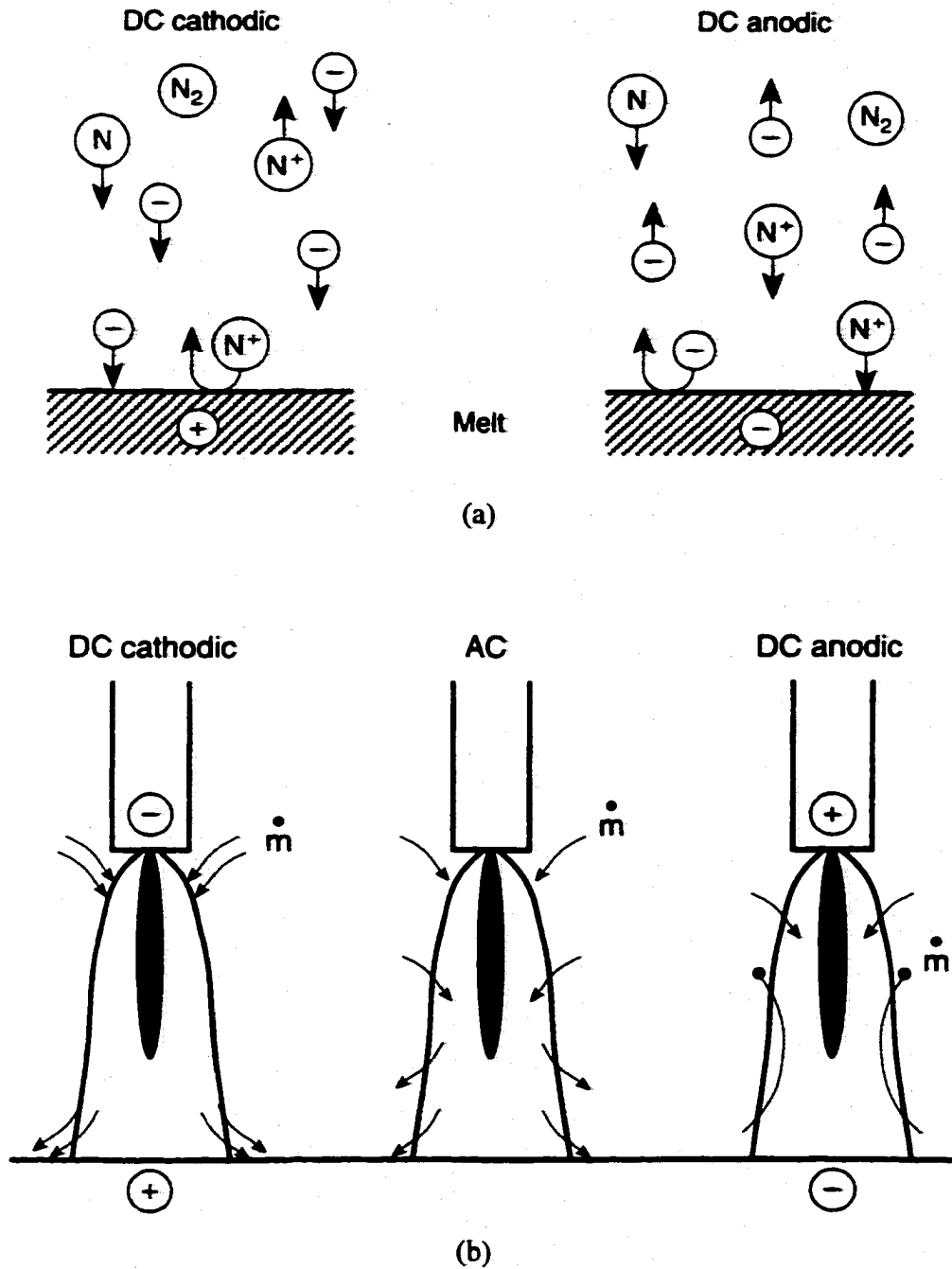


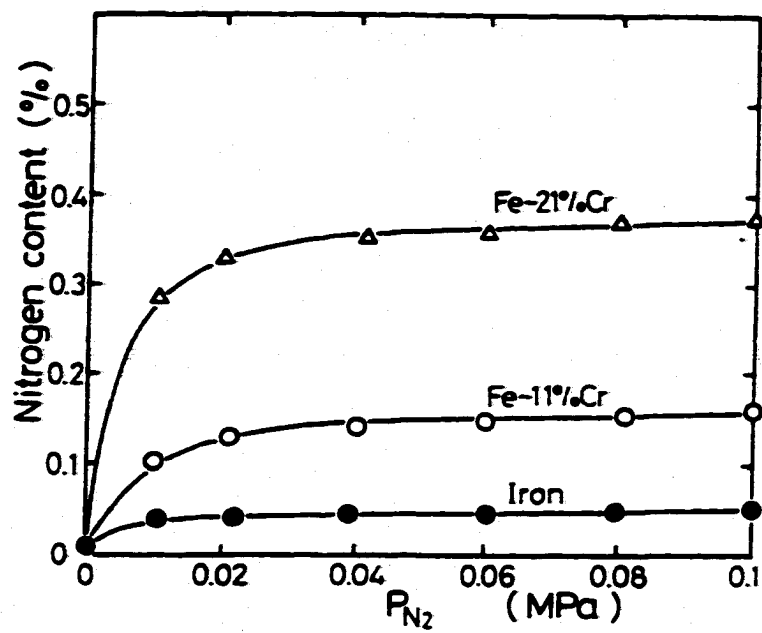
Figure 2.9(a&b). Schematic diagrams of (a) the influence of torch polarity on the behavior of nitrogen ions at the melt surface and (b) the effect of arc polarity on arc jet momentum at the surface of the steel melt.⁶⁰

In addition to the effect on the agitation in the melt, the authors⁶⁰ also describe a pumping effect, in which the plasma arc enhances the transfer of nitrogen from the gas phase to the melt. For example, when the torch acts as the anode, N^+ ions contribute to the nitrogen pick-up and increase the steady-state nitrogen concentration. When the arc acts as the cathode, the effect of N^+ ions is reversed and they do not contribute to the nitrogen pick-up. In the AC operating mode, the arc was more diffuse and provided a weaker flow impact than the two DC conditions and did not influence the nitrogen concentration values in the melt.⁶⁰

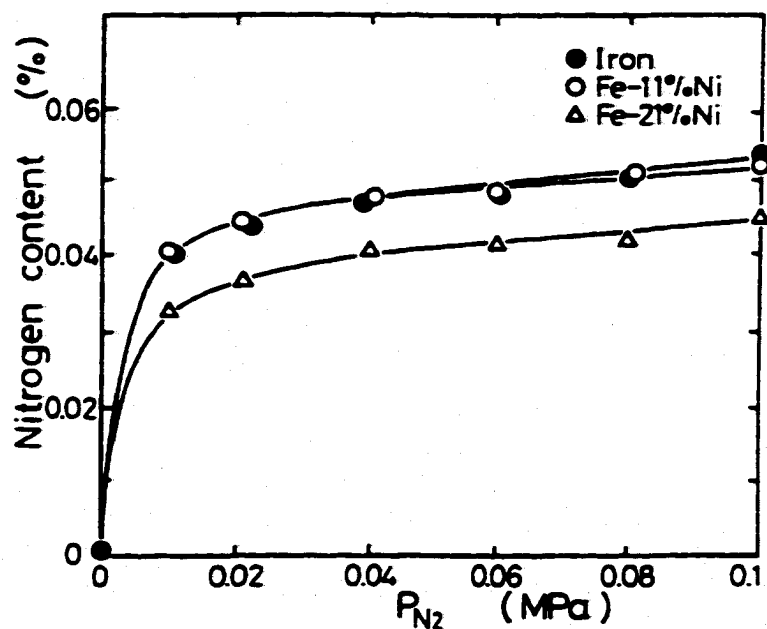
2.2.2 Role of Alloying Element Additions on Resulting Nitrogen Concentration:

Changes in the arc parameters affect the nitrogen concentration in the arc-melted samples. In addition, changes in the base metal chemistry can also provoke changes in the enhanced nitrogen dissolution process by significantly affecting the equilibrium nitrogen concentration in iron. For example, the addition of V, Nb, Ta, Ti, Cr, Mn, or Al to iron increase the nitrogen solubility, while the addition of Ni, Co, Si, and C decrease the nitrogen solubility.¹⁸⁻²⁷ Several researchers have studied the effect of these additions on the nitrogen concentration during arc-melting.^{35,37-39} Kuwana *et al.*,⁶¹ as shown in Figures 2.10(a&b), have investigated the effect of chromium (4 to 32 wt.%) and nickel (3 to 30 wt.%) additions to iron during arc melting in a nitrogen containing environment. They have observed an increase in the nitrogen concentration with the addition of Cr and a decrease with the addition of Ni. As shown in Table 2.3, the apparent interaction parameters of Cr and Ni on the nitrogen absorption reaction during the arc melting of iron closely correspond to the interaction parameters calculated under equilibrium calculations. In general, though, the nitrogen concentration in the liquid iron, whether it contains chromium or nickel alloying additions, exceeds Sieverts' Law calculations and behaves much like that in pure iron.

Uda and Wada⁶⁴ have also investigated the effect of alloying element additions on the nitrogen concentration during the arc melting of iron. Figures 2.11(a-c)⁶⁴ display the behavior of the nitrogen concentration as a function of the amount of Cr, Mo, and V additions to pure iron at two nitrogen pressures. Both Cr and V additions in Figures 2.11(a)

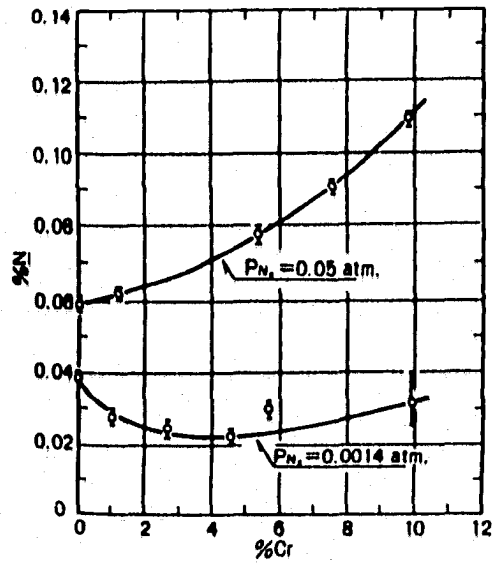


(a)

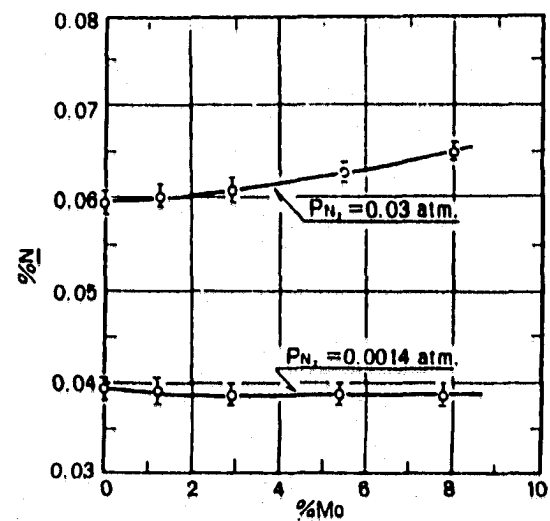


(b)

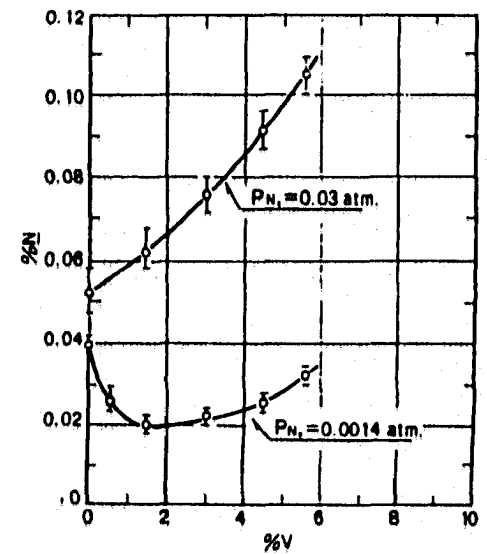
Figure 2.10(a&b). Relation between the nitrogen concentration in arc melted (a) Fe-Cr and (b) Fe-Ni alloys and the nitrogen partial pressure for an arc current of 150 A in a Ar-N₂ atmosphere at a total pressure of 1.0 atm.⁶¹



(a)



(b)



(c)

Figure 2.11(a-c). The measured nitrogen concentration in arc-melted (a) Fe-Cr alloys, (b) Fe-Mo alloys, and (c) Fe-V alloys in N_2 atmospheres at a pressure of 1.0 atm.⁶⁴

and 2.11(c) affect the nitrogen concentration in a similar fashion. On the other hand, the addition of Mo, in Figure 2.11(b), has little to no effect on the nitrogen concentration for either nitrogen partial pressure. The apparent interaction parameters for Cr, Mo, and V for both arc-melting conditions are also included in Table 2.3. In each case, the interaction parameters for the arc melting conditions are higher than those calculated for equilibrium conditions. Any potential effects of these alloying additions are related to the high affinity these alloying elements may have for nitrogen.

Only Kuwana *et al.*⁶¹ have studied the effect of changes in the melting parameters on the nitrogen concentration in iron alloys. Their results are shown in Figure 2.12(a&b)⁶¹ for a number of Fe-Cr and Fe-Ni alloys. In each case, the nitrogen content with low alloy element additions increases slightly with arc current. On the other hand, the nitrogen content in Fe-Cr alloys with about 5 to 8wt.% Cr additions decreases with an increase in the arc current and with higher additions of Cr. The nitrogen content in the Fe-Ni alloys, though, continues to increase with an increase in the arc current for all the alloys studied. Such a difference in behavior appears to be the result of changes in the liquid metal properties rather than those of the arc or the nitrogen dissolution reaction. A more in-depth study of the remaining Cr and Ni in each liquid metal, to account for the vaporization of the alloying elements with the increase in temperature accompanying the increase in the arc current, would be beneficial.

Changes in the nitrogen concentration during the arc melting of Fe-Ta, Fe-Ni, Fe-Co, and Fe-Si alloys have been studied by Uda and Ohno.⁶² Figure 2.13 shows the nitrogen concentrations in these alloys, which have been arc melted in an Ar-3% N₂ environment. In all cases, the effect of these alloying element additions on the nitrogen concentration differs from that observed under non-arc melting conditions. Uda and Ohno⁶² have assumed that the anomalous nitrogen concentrations are dependant upon both the physical state of the molten alloy surface under the arc and the mutual reaction between the deoxidizing power and the nitrogen affinity of the alloying elements.

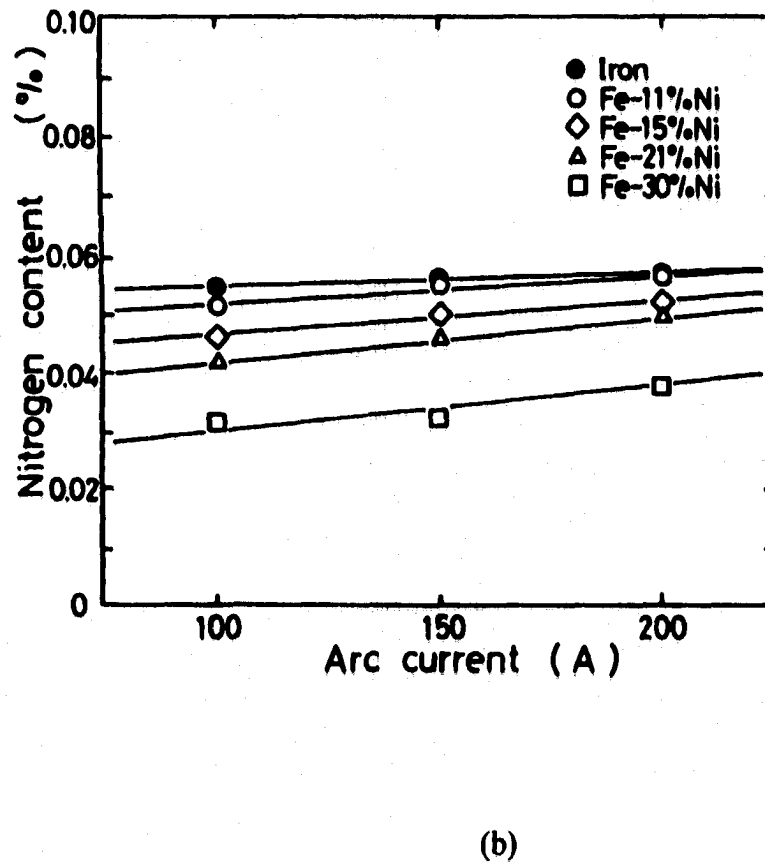
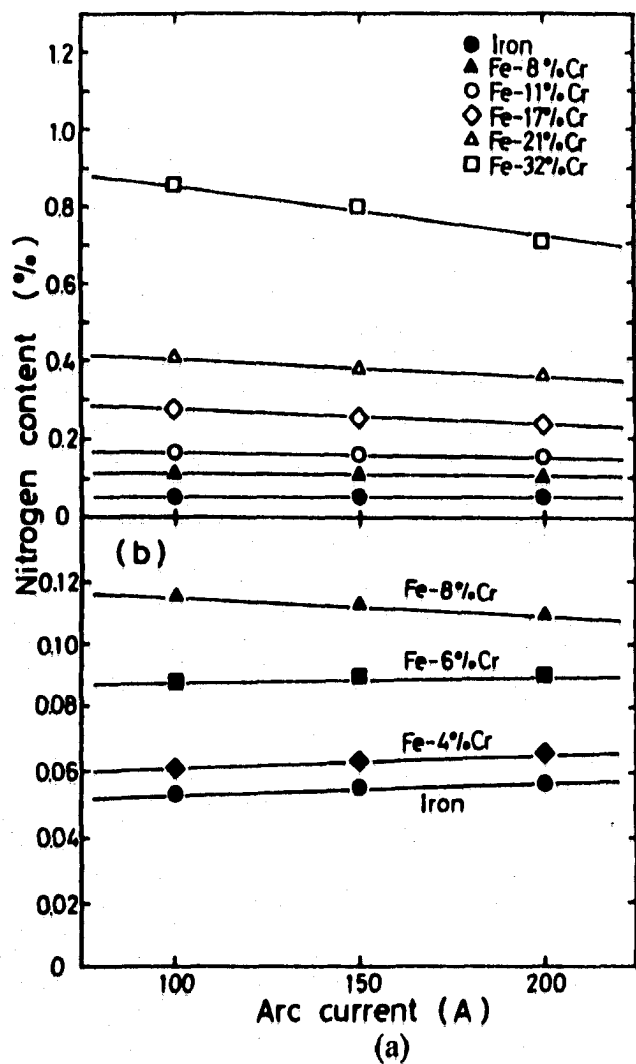


Figure 2.12(a&b). Relationship between the nitrogen concentration and the arc current in (a) Fe-Cr and (b) Fe-Ni alloys.⁶¹

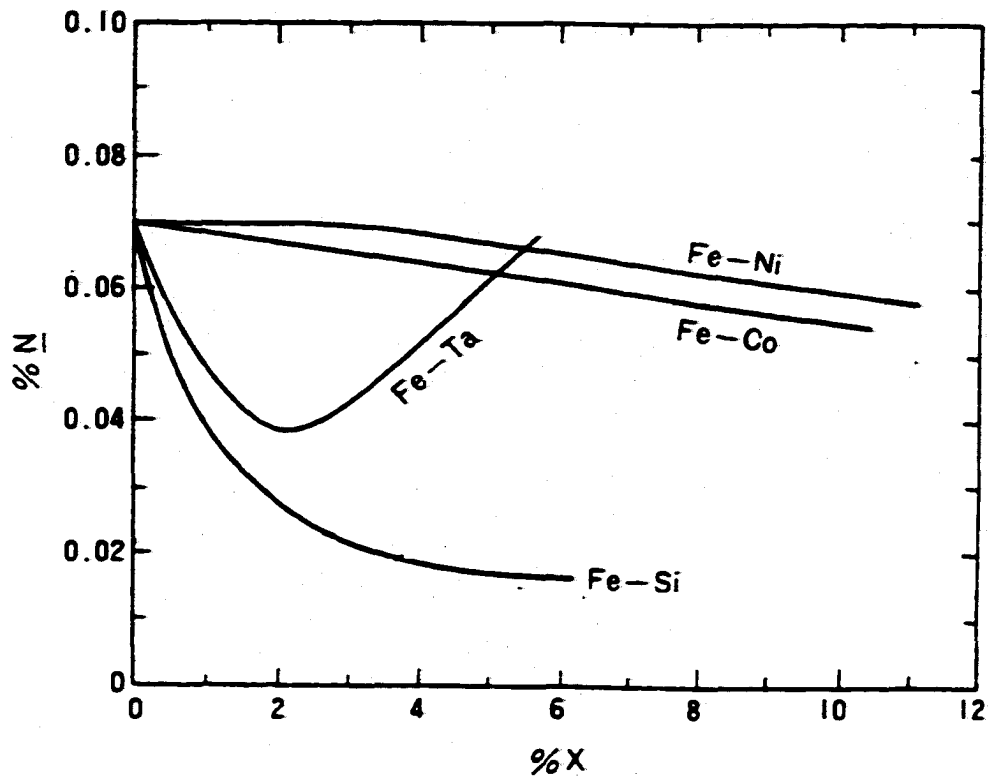


Figure 2.13. The effect of alloying element additions, including Ni, Co, Ta, and Si, to pure iron on the nitrogen content in Ar-3% N₂ gas mixtures at atmospheric pressure.⁶²

2.2.3 Role of Surface Active Elements on Nitrogen Concentration

Surface active elements, including oxygen and sulfur, display effects different from alloying elements discussed previously. In particular, these elements affect the surface tension of iron. The effect of the presence of these elements in solution in liquid iron on the resulting nitrogen concentration has been investigated under non-arc melting conditions.⁶⁶⁻⁶⁸ Much like these substitutional alloying elements, surface active elements, such as oxygen and sulfur, affect the resulting nitrogen concentration in iron, and their interaction parameters are also shown in Table 2.4. Unfortunately, the effect of these alloying elements on the nitrogen concentration is mixed, with different researchers reporting contradictory results, especially for oxygen.

The liquid metal surface, though, plays a more important role during arc melting. Even though their effect during non-arc melting is mixed, surface active elements are expected to display a much more prominent effect on the nitrogen concentration during arc melting. Uda and Ohno⁶⁶⁻⁶⁷ have investigated the effects of sulfur, oxygen, and selenium on the nitrogen concentration in iron during arc melting in N₂-Ar gas mixtures. The effect of these oxygen additions on the nitrogen solubility⁶⁷ is shown in Figure 2.14. Nitrogen concentrations markedly increase to levels far above those previously observed in pure iron exposed to a nitrogen-containing arc. For example, an Fe-O alloy with 2200 ppm of oxygen displays a nitrogen concentration near 1000 ppm, which is nearly double that expected for a pure iron sample. The equilibrium nitrogen concentration increases with rising oxygen concentrations in the liquid metal. This increase in the nitrogen saturation level is most rapid between 200 and 400 ppm [O]. Similar results have been reported by Hoojijmans and Ouden,⁶⁹ as shown in Figure 2.15. In this figure, the nitrogen saturation level in the liquid metal, represented by a plateau in the nitrogen concentration behavior, increases to nearly 900 ppm [N] with oxygen concentrations in the base metal approaching 800 ppm [O].

The effect of these alloying element additions on the properties of the melt surface has also been examined. Belton⁷⁰⁻⁷¹ has described the extent of surface coverage of the liquid metal with the addition of surface active elements using the following relationship.

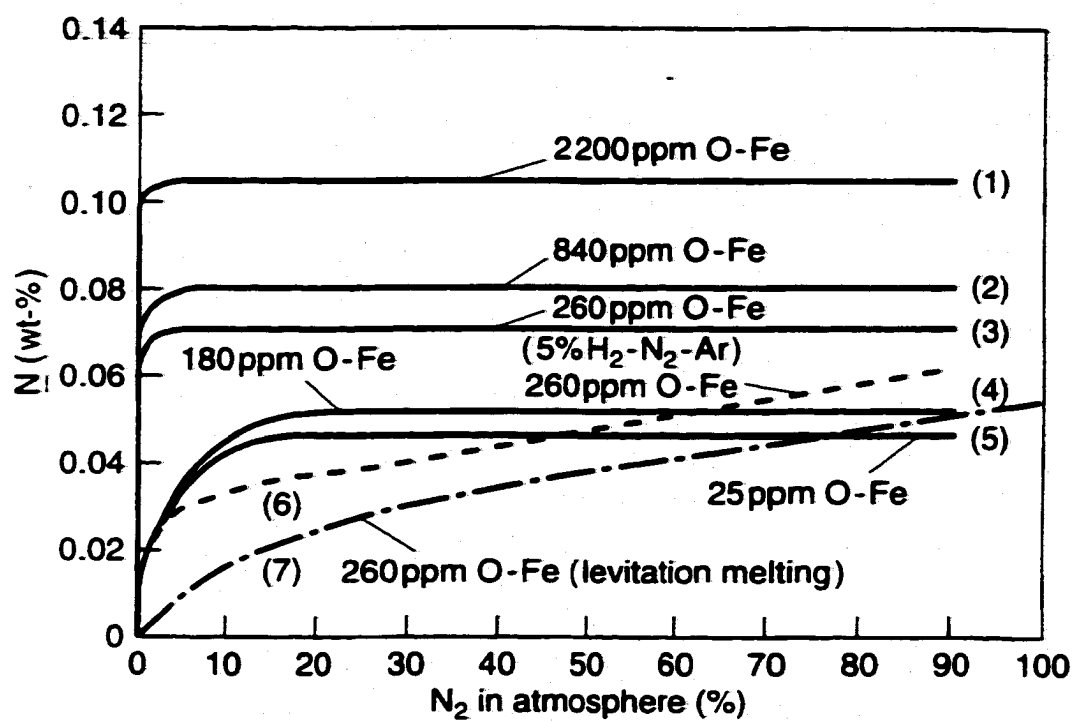


Figure 2.14. Nitrogen concentration in various iron-oxygen alloys arc melted at various nitrogen partial pressures.⁶⁷

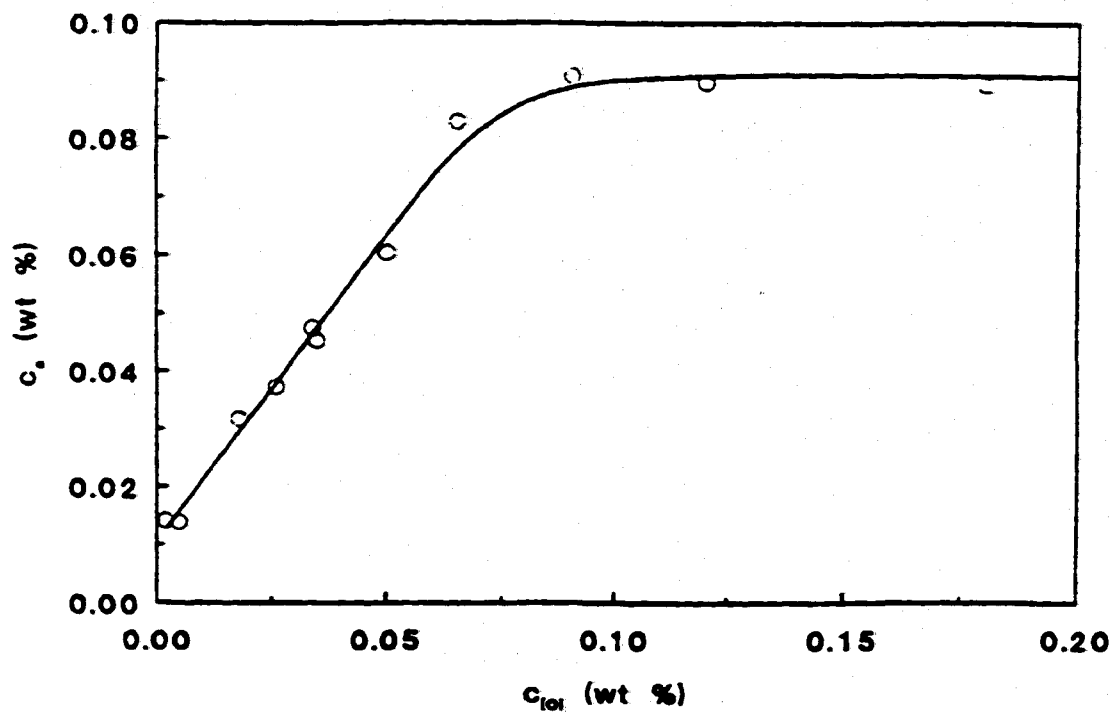


Figure 2.15. Nitrogen saturation concentration in iron samples as a function of the oxygen concentration in the sample arc melted in pure nitrogen at atmospheric pressure.⁶⁹

$$\frac{\theta}{1-\theta} = K_a a_s \quad (2.19)$$

where a_s is the activity of the solute, expressed in wt.%, K_a is the adsorption coefficient (wt.%⁻¹), and θ is the fraction coverage by the solute. In this relationship, the Gibbs adsorption isotherm, which relates changes in surface tension to changes in solute activity, and the Langmuir isotherm, which relates activity to surface coverage, are combined.

Figure 2.16 shows a relationship between the fractional surface coverage on high purity liquid iron and the solute concentration⁷⁰ for Se, S, and O. It becomes clear that even a small addition of any of these solutes causes an appreciable coverage of the liquid metal surface. For example, only 100 ppm O present in the liquid metal can cause coverage over 50% of the surface.⁷⁰ Nearly complete coverage of the liquid metal surface is observed with the addition of these elements at solute concentrations approaching 1000 ppm. These results correspond well with the nitrogen concentration behavior discussed above. Even though these results are only approximations and are prone to rather significant error, they point to the role which the presence of surface active elements play on the absorption and desorption of nitrogen in the liquid melt. This relationship will be addressed in a later section.

Up to this point, discussions of the effect of surface active element additions on the nitrogen dissolution reaction has been limited to that in pure iron. Several researchers^{62,66} have investigated the effect of substitutional alloying elements on the behavior of surface active element additions. For example, Sinha and Gupta⁶⁶ have investigated the effect of oxygen and sulfur additions on the nitrogen concentration during the arc melting of Fe-Cr-Ni alloys in atmospheric nitrogen environments. Their results are significantly different from previous results dealing with pure iron.⁶⁷⁻⁶⁹ Instead of increasing with the addition of surface active elements, the nitrogen saturation values decrease with the addition of each of these surface active elements to the liquid iron alloy. On the other hand, the nitrogen concentrations, ranging between 0.24 and 0.16 wt.% N, are significantly higher than those reported in pure iron. Sinha and Gupta⁶⁶ attributed these nitrogen concentra-

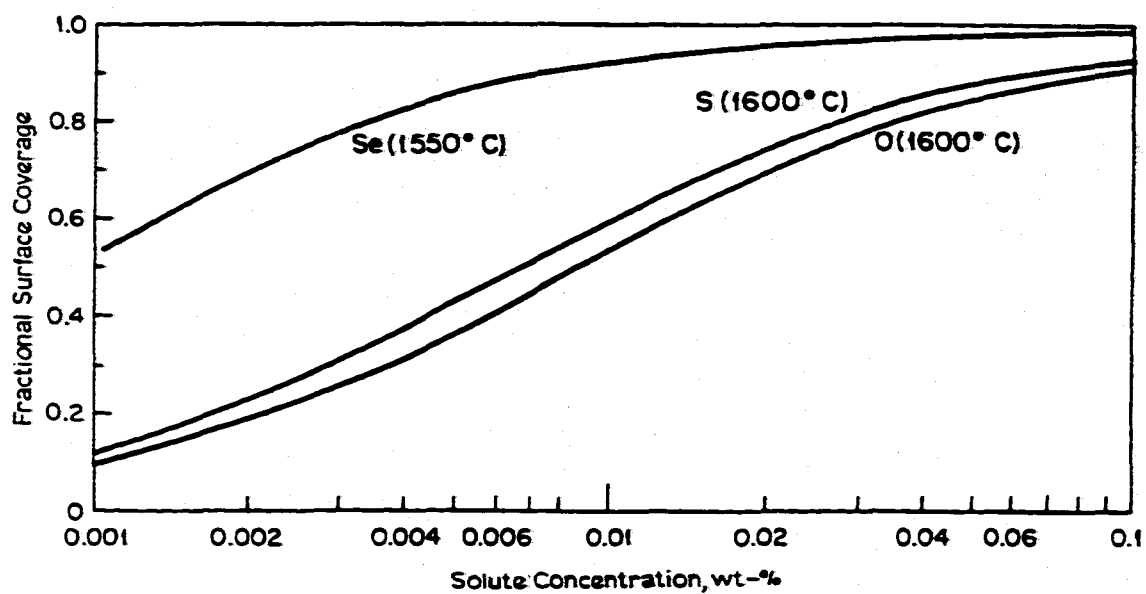


Figure 2.16. Surface coverage isotherms on high-purity liquid iron.⁷⁹

tions in the alloys and the change in the behavior of the nitrogen concentrations with S and O additions to differences in the experimental conditions.

Uda and Ohno⁶² have investigated the effect of the interaction between surface active element additions and a number of other substitutional alloying element additions on the resulting nitrogen concentration. They⁶² have attributed these dissolved nitrogen concentrations to the physical properties of the surface of the molten metal alloy. With the addition of surface active elements, the amount of dissolved nitrogen in the liquid metal during arc melting is, thus, the result of the mutual reaction between the deoxidizing power of the alloying element and the nitrogen affinity of this same alloying element. Table 2.5 shows four categories of alloy elements commonly added to iron. A summary of the behavior common to these four categories of alloying elements is shown⁶² in Figure 2.17(a-d). In each figure, curve I illustrates the effect of the alloying element on the nitrogen concentration when the oxygen content is held constant. Curve III illustrates the nitrogen content as a function of the oxygen content in the alloy, and curve II represents the nitrogen content in arc melted iron from the mutual reaction between curves I and III.

Each alloying element category displays a different nitrogen concentration behavior. With the addition of the first category alloying elements, the nitrogen concentrations in the metal during arc melting initially decrease and then increase with further amounts of alloying elements. In the second group, the nitrogen content in the metal initially decreases dramatically with the addition of these alloying elements, but the nitrogen content levels out with increasing amounts of alloying elements in the liquid metal. With the third group, the nitrogen content does not significantly change for any amount of alloying element added to the iron. Small alloying element additions from the fourth group cause the nitrogen content to decrease dramatically and then remain constant as the amount of this alloying element in the iron alloy increases.

2.2.4 Role of Convection

During arc melting, fluid flow and heat transfer in the liquid metal have been proven to have significant effects on the final properties of the metal.^{48-49,72-74} The flow of liquid metal is affected by the spatial variation in surface tension at the metal surface, electr-

Table 2.5. Summary of alloying elements in several categories and their relationship with the presence of surface active elements in liquid iron.⁶⁶

Category I	V, Nb, Ta, Ti, Cr, and Mn	- Increase the nitrogen solubility - Decrease oxygen content in iron
Category II	Si and C	- Decrease the nitrogen solubility - Decrease the oxygen content
Category III	Ni, Co, Mo, Cu, W, and Sn	- Little effect on nitrogen solubility - Little effect on oxygen content
Category IV	Al	- Little effect on nitrogen solubility - Decrease the oxygen content

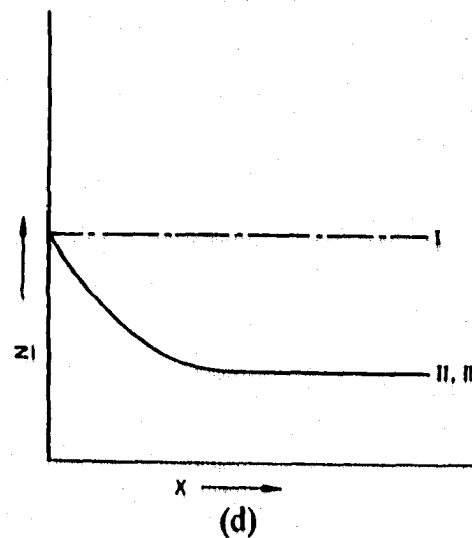
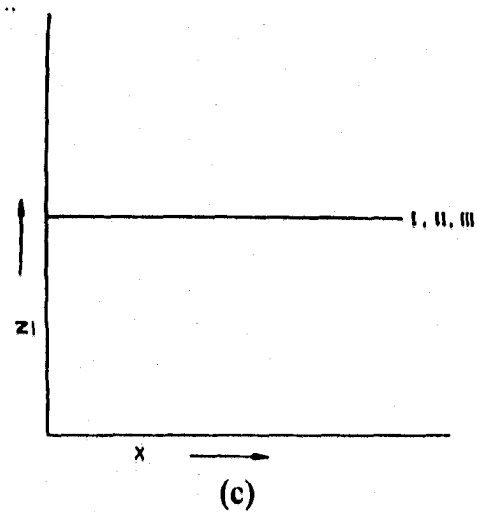
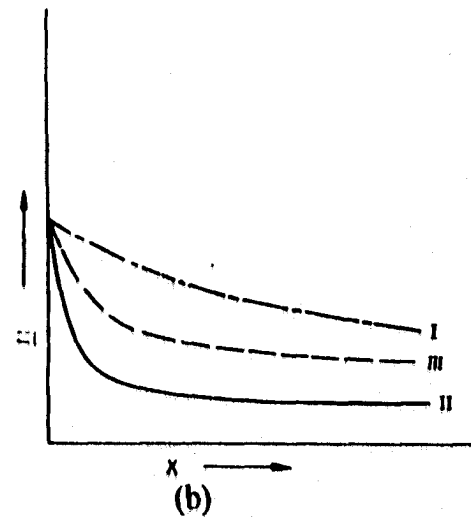
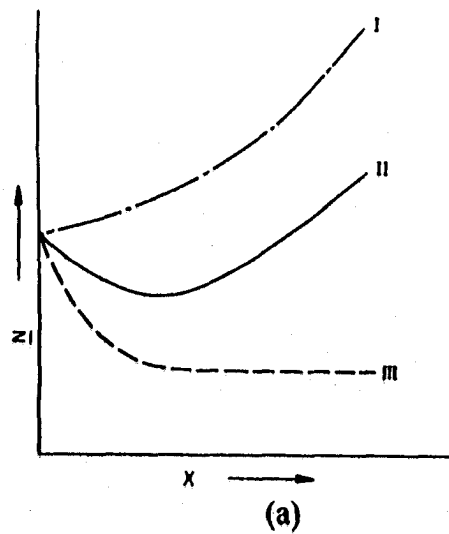


Figure 2.17(a-d). The behavior of the nitrogen absorption reaction in binary Fe-X alloys during arc melting.⁶² The alloys are categorized into several types, including (a) Category I, (b) Category II, (c) Category III, and (d) Category IV.

magnetic forces, and the buoyancy force, which is the smallest and has little impact on the resulting fluid flow.

Of these three driving forces for fluid flow, the spatial variations in surface tension have received a great deal of attention. These spatial variations in surface tension are the result of significant temperature or concentration gradients at the liquid metal surface and are commonly referred to as a Marangoni stress, which is defined below.⁷⁵

$$\tau = \frac{dy}{dT} \frac{dT}{dx} + \frac{dy}{dC} \frac{dC}{dx} \quad (2.20)$$

where τ is the Marangoni stress due to the temperature and concentration gradients, γ is the interfacial tension, T is the temperature, and y is the distance along the surface from the axis of the heat source. In many situations, the spatial variation of concentration is negligible, and the first term on the right hand side of Equation 2.20 describes the Marangoni stress.

For pure metals, $\frac{dy}{dT}$ is negative, resulting in a radially outward flow of liquid metal from the center of the weld pool surface to the liquid-metal interface, as shown in Figure 2.18(a). The effect of oxygen additions on the calculated surface tension in pure Fe is shown⁷² in Figure 2.19, in which the surface tension for a given concentration of oxygen can significantly vary over a given temperature range. This effect can become even more pronounced at higher oxygen concentrations, leading to changes in $\frac{dy}{dT}$ from a positive value at low temperatures to a negative value as the temperature is increased. These changes in the surface tension with the presence of surface active elements, such as oxygen and sulfur, result in a reversal in the direction of fluid flow in the metal pool,⁷²⁻⁷⁴ as shown⁷² in Figure 2.18(b). Positive gradients are observed in the presence of surface active elements, which produce fluid flow fields opposite in direction to those for pure metals, thus significantly changing the fluid flow fields and the general shape of the liquid metal pool.

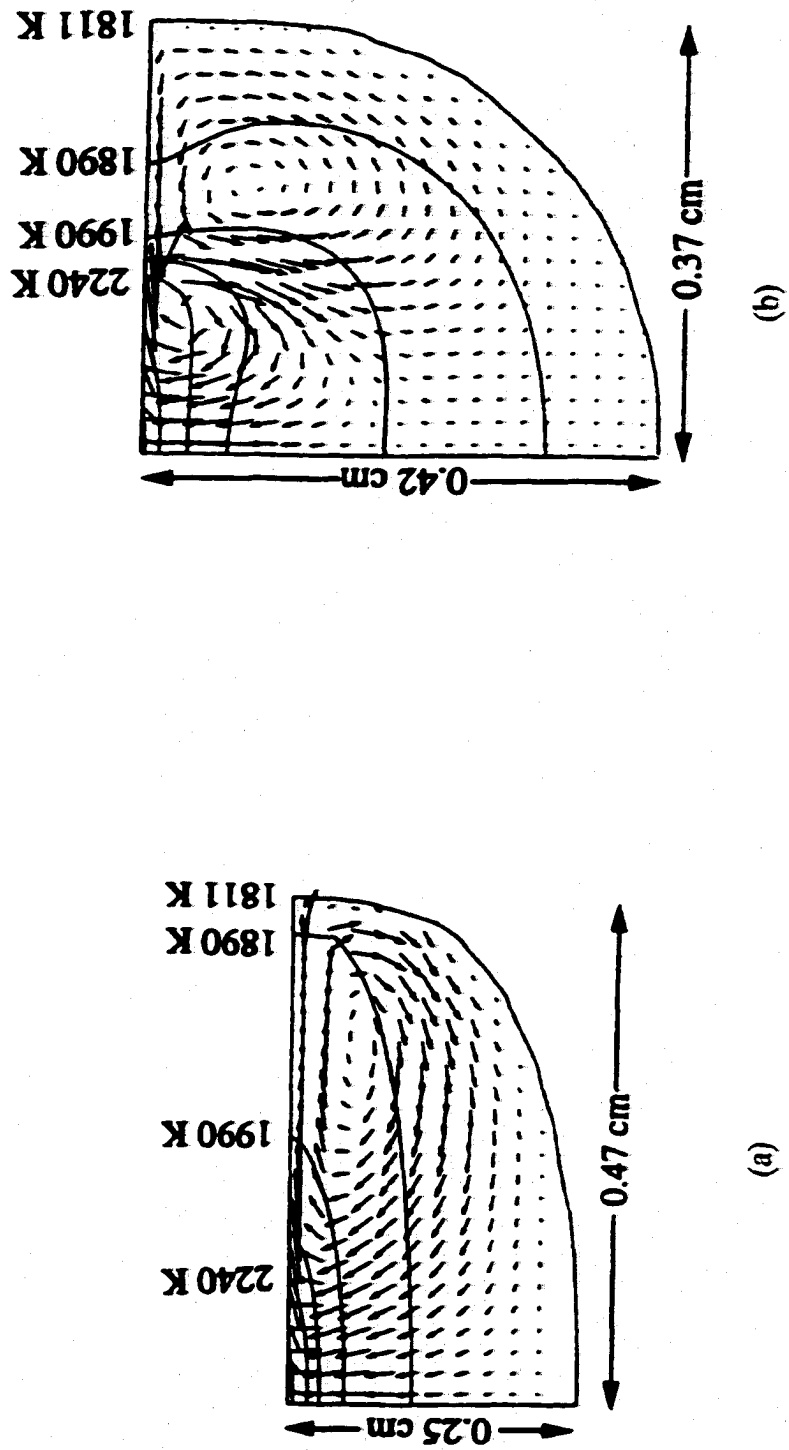


Figure 2.18(a&b). Computed temperature and velocity fields for (a) pure iron and (b) an Fe-0.003 wt.% O alloy.⁷²

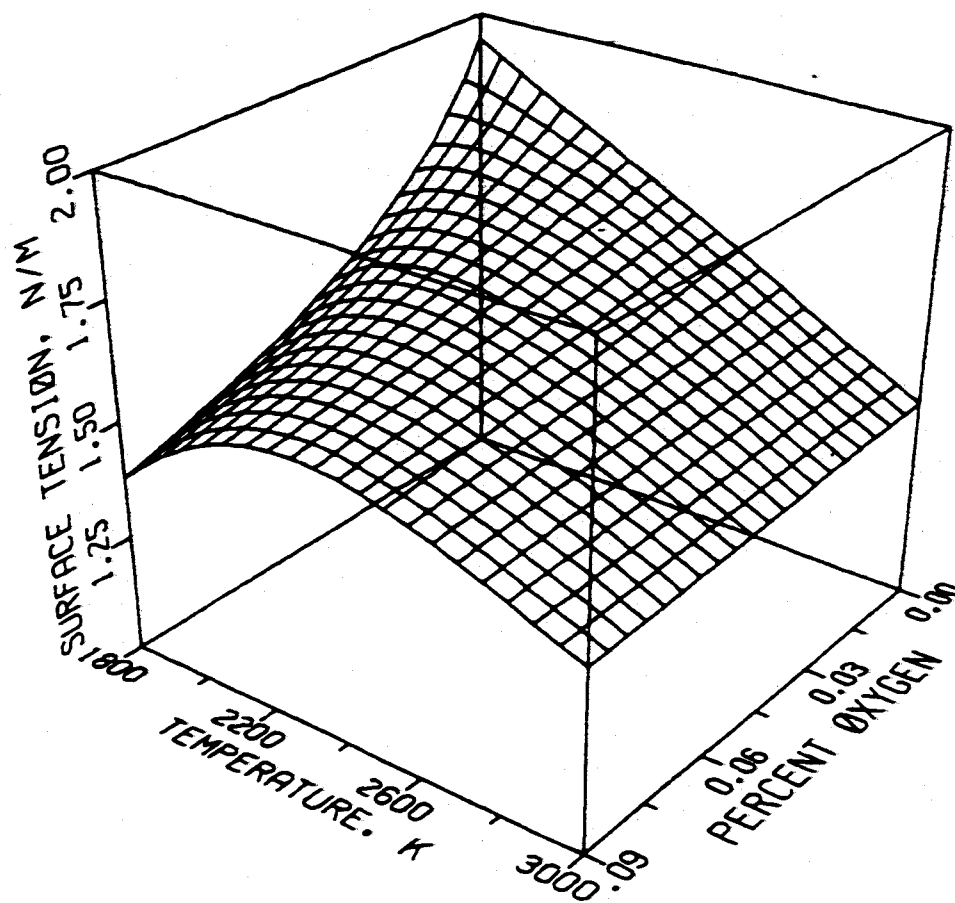


Figure 2.19. Surface tension of iron-oxygen alloys plotted as a function of temperature and oxygen concentration.⁷²

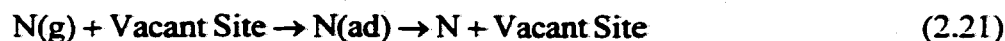
Previous researchers have pointed out that Marangoni convection, induced by either a surface or an interfacial tension gradient, may also promote mass transfer across the surface/interface and enhance reaction rates.^{31,72,73} Katz and King³¹ have recognized the importance of the Marangoni and electromagnetically driven flows on the dissolution of nitrogen and the rapid absorption of nitrogen into arc melted iron in nitrogen containing atmospheres. Four major factors, which control nitrogen transfer into molten iron during arc melting, have been cited. These factors include electromagnetic stirring, natural convection, momentum transfer from the impinging plasma jet, and surface tension driven flow between regions of the melt surface with different potentials of surface active elements. The effect of surface active elements on the surface tension-driven flow dominates the mass transfer in the melt. On the other hand, the effect of the flow patterns on the resulting nitrogen concentration has been largely ignored. Therefore, the role played by fluid flow and Marangoni convection on the resulting nitrogen concentration in the liquid metal should be studied further.

Nitrogen in solution in iron has also been observed to have an effect on the surface tension of pure liquid iron.^{76,77} Its effect on the surface tension is rather small, though, and is much less than that of O, S, and Se. In iron-nitrogen systems, this gradient, $\frac{d\gamma}{dT}$, tends to be negative, resulting in a radially outward flow of liquid metal from the center of the liquid melt towards the liquid-metal interface during welding.

The effect of nitrogen concentration gradients on the Marangoni convection in liquid iron has been analyzed by Hirashima *et al.*⁷⁶ They performed nitrogen absorption measurements by blowing nitrogen gas through a lance over the free surface of liquid iron under resistance heating. In these experiments, the absorption measurements indicated that the mass transfer coefficient of nitrogen in liquid iron due to Marangoni convection ($k'_m = 1.5 \times 10^{-4}$ m/sec) is slightly less than that due to induction stirring ($k'_m = 2.1 \times 10^{-4}$ to 1.5×10^{-4} m/sec). Both the surface tension of liquid iron and the resulting fluid flow fields are affected by the presence of nitrogen in solution. This effect is not as significant as that for traditionally identified surface active elements. Nevertheless, the effect of nitrogen on the flow patterns in the liquid iron should be considered.

2.2.5 Steady-State Nature of Nitrogen Dissolution Process

Based on the observations of significantly enhanced nitrogen concentrations in iron samples during arc melting,^{28-35,57} several models have been developed. There is a consensus among these various models that the observed nitrogen concentrations in the liquid iron are the result of a type of steady-state mechanism involving both the absorption and desorption of nitrogen from the arc-melted iron sample. The basis for this steady-state mechanism is shown⁶⁸ in Figure 2.20(a), where nitrogen is absorbed from the area in the arc column. Among the number of activated states present in the arc column, monatomic nitrogen is primarily absorbed at the surface of the liquid iron under the arc column. Based on this mechanism, Takeda and Nakamura⁷⁸ have developed a general reaction mechanism to describe the resulting nitrogen concentration in liquid iron. A part of this mechanism includes the nitrogen absorption reaction in liquid iron in the area defined by the arc spot described by the following relation:



If monatomic nitrogen is the primary species absorbed on the liquid iron surface, its amount in the arc column needs to be determined. Uda and Wada,⁶⁴ who assumed that atomic nitrogen is dissolved in the liquid metal, have developed a rather rudimentary statistical thermodynamic treatment of the nitrogen-iron system. In their model, they define a ratio between the solubility of nitrogen in the liquid metal and the number of nitrogen atoms in the arc atmosphere and in non-arc atmospheres. This relationship is shown below:

$$\frac{x_N}{x'_N} = \frac{\eta_B^{(G)}(T_P)}{\eta_N^{(G)}(T_m)} \quad (2.22)$$

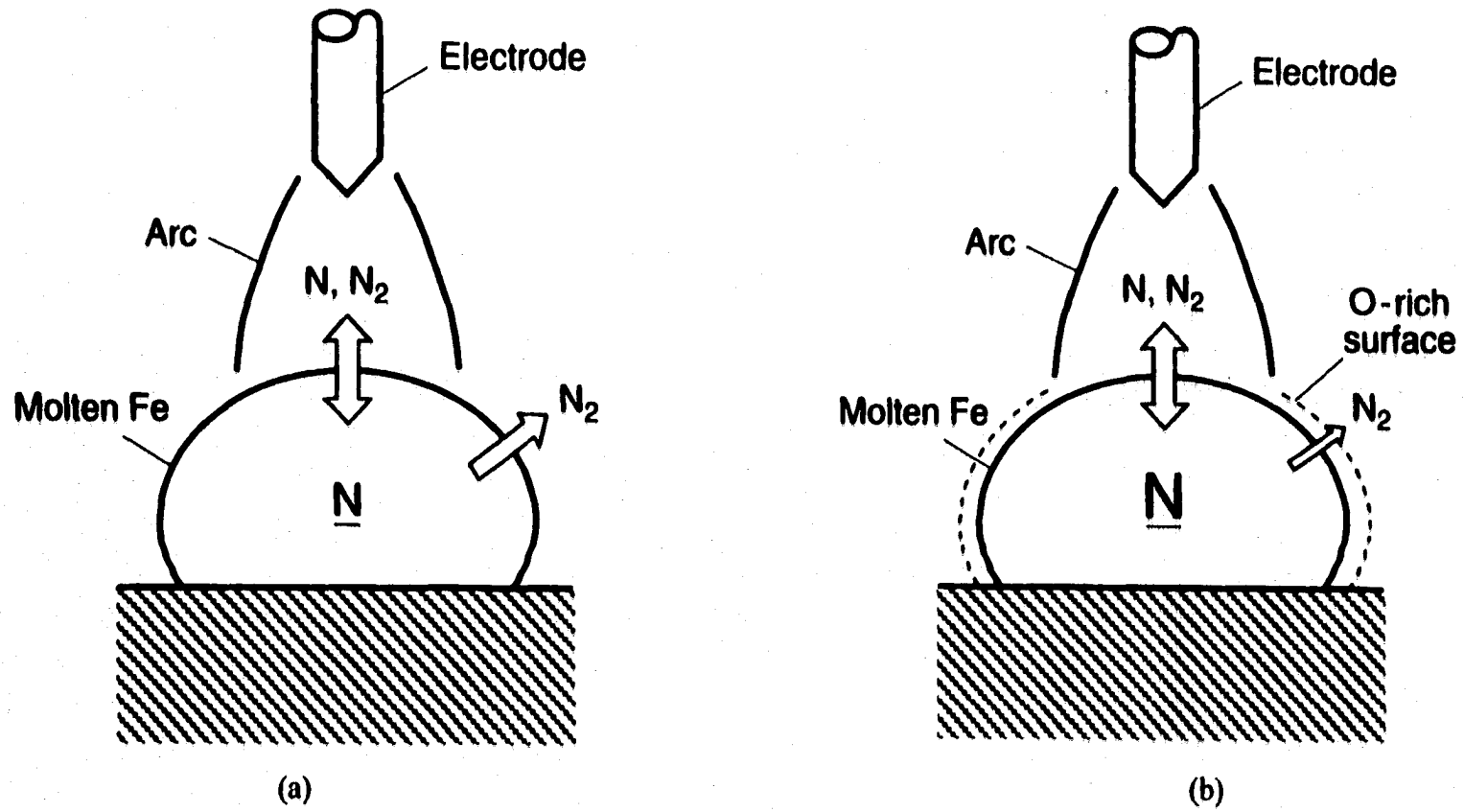
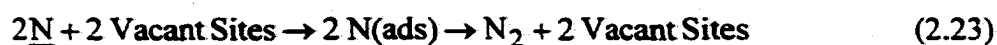


Figure 2.20(a&b). (a) Schematic model of steady-state process believed to be responsible for the nitrogen concentrations observed in liquid iron during arc melting.⁶⁸ (b) Schematic model of nitrogen dissolution and evolution during the arc melting of an Fe-O sample.⁶⁷

where x_N and x'_N are the atom fraction of nitrogen in the liquid iron for arc and non-arc melting conditions, respectively, $\eta_B^{(G)}(T_p)$ and $\eta_N^{(G)}(T_m)$ are the number of nitrogen atoms in the gas phase in arc-melting and non-arc-melting conditions, respectively. Using this relationship, the authors determined that the temperature at which the equilibrium nitrogen dissociation constant would have the value corresponding to the number of atoms required to meet the nitrogen concentration in the metal would be approximately 3000 K. This temperature is much lower than those normally believed to exist in the arc column, usually on the order of 5000 to 10000 K.

On the other hand, the reactions described above occur at the liquid metal surface. Once absorbed at the liquid metal surface, nitrogen is transported by fluid flow to the interior regions of the molten metal. Nitrogen concentration levels can rapidly reach saturation, which corresponds to the nitrogen solubility at 1 atm. total pressure, at the molten metal surface. Once the saturation level in the melt is reached, the metal can no longer hold this amount of nitrogen in solution. It must, therefore, be expelled, resulting in a phenomenon similar to boiling occurring near the surface of the melt, which is referred to as 'spattering' or 'splattering.'

The authors have thus postulated that the total amount of nitrogen present in the liquid metal is the balance of two independent processes. Nitrogen is first absorbed through the interface between the arc and the liquid metal. Once a saturation level is reached at the metal surface, nitrogen is then expelled from the surface of the liquid metal outside the arc column. Nitrogen desorption occurs via bubble formation at the surface and other heterogeneous nucleation sites in the liquid melt. These bubbles are filled with nitrogen gas, which has been rejected from the liquid iron. Outside the arc column, the nitrogen in solution in the iron is in equilibrium with diatomic nitrogen rather than monatomic nitrogen, which dominates the arc column. Based on this assumption, nitrogen is desorbed from the metal surface in the area outside the arc spot as shown below.⁷⁸



The evolution of nitrogen is affected by the characteristics of the surface in the region outside the arc column. As discussed previously, the presence of surface active elements in the liquid iron significantly alters the nature of the liquid metal surface.⁶⁷⁻⁶⁹ Figure 2.20(b) schematically shows the modified steady-state model taking into account the presence of oxygen concentrations in the liquid metal.⁶⁸ In the region underneath the arc column, monatomic nitrogen is absorbed by the liquid metal. An oxygen rich film forms on the surface of the droplet outside the arc column. This oxide film does not allow nitrogen to easily evolve from the melt, and the nitrogen concentration within the liquid metal increases. It is thus apparent that if oxygen or sulfur covers a part of the surface, nitrogen does not evolve from the surface as easily as in the absence of these surface active elements.

2.2.6 Time-Dependent Nature of the Nitrogen Dissolution Process

2.2.6.1 Rate Of Nitrogen Absorption and Desorption Reactions at Equilibrium

Nitrogen absorption and desorption in iron and steels under conditions typical of ironmaking and steelmaking operations have been studied over the past several decades.⁷⁹⁻⁸⁹ The absorption of nitrogen into liquid iron is believed to follow four major steps. Nitrogen molecules are first transferred through the gas phase to the vicinity of the gas/liquid interface. Adsorption or dissociation of nitrogen molecules then occurs, followed by the transfer of nitrogen atoms through the interfacial region. The adsorbed nitrogen is then transferred from the surface into the bulk melt.⁹⁰ Based on this reaction mechanism, three rate-limiting processes have been identified, including mass transfer in the gaseous phase, a chemical reaction at the interface, and mass transfer in the liquid phase.

The order of the nitrogen absorption reaction into the liquid iron melt obeys a first order rate law, such as that shown in the following equation:⁷⁹

$$R = \frac{dC}{dt} = k_1 \frac{A}{V} (C_e - C) \quad (2.24)$$

where k_1 is the first-order rate constant for absorption (cm/sec), A is the exposed surface area (cm²), V is the melt volume (cm³), C_e is the equilibrium nitrogen concentration for the specified nitrogen pressure (mol cm⁻³), and C (mol cm⁻³) is the nitrogen concentration in the melt at time, t . Rate constants for the absorption of nitrogen range from 19 to 35×10^{-3} cm-sec⁻¹.

Since most studies on the nitrogen absorption reaction have been performed in inductively stirred melts, the circulation of liquid metal is thus enhanced.^{79-81,88} Flow conditions in the melt are primary contributors to the liquid phase mass transfer mechanism. Liquid-phase mass transfer is the rate-limiting step in the nitrogen absorption reaction.

Nitrogen can also be removed from the liquid iron through a desorption reaction. The mechanism for nitrogen desorption from liquid iron is the same as that for nitrogen absorption, only with the steps reversed in order.⁷⁹ On the other hand, the rate-limiting step in the nitrogen desorption reaction in an inert atmosphere is not simple but based on a sequential mixed-control model, involving both interfacial reactions and gas-phase mass transfer. This change in the rate-limiting step makes nitrogen desorption a second order reaction. The second order rate constant governing this reaction is shown in the following relation:⁷⁹

$$R = \frac{dC}{dt} = k_{2rv} \frac{A}{V} (C_e^2 - C^2) \quad (2.25)$$

where k_{2rv} is the second order rate constant (cm⁴ mol⁻¹ s⁻¹) when the rate of the reaction increases inversely with the volume of the system. Rate constants for the nitrogen desorption reaction range from 62 to 693 cm⁴ mol⁻¹ sec⁻¹.

Changes in the experimental conditions have also been shown to have an impact upon both the nitrogen absorption and desorption reaction rates in a liquid iron melt. Both absorption and desorption rates, for example, are shown to increase with the temperature of the melt, while the absorption rate has also been shown to increase with the nitrogen partial pressure above the liquid melt. The addition of Cr and Mn⁸⁰⁻⁸³ has no effect on the rate limiting steps in the reaction, but the nitrogen absorption and desorption rates are

connected with their rate of vaporization.⁸² Specifically, the nitrogen desorption rate decreases as the local temperature drops at the gas-liquid interface, due to the latent heat of vaporization and the decrease in the number of available surface sites taken up by vaporizing metal atoms.⁸² Other researchers have observed that carbon dissolved in the liquid iron increases the rate of nitrogen desorption by affecting the nitrogen activity.⁸⁴ Other researchers⁸⁷ have observed that Al, Cb, and Si have little to no effect on the rate of nitrogen absorption or desorption, except when these elements serve as deoxidizers.

The nitrogen absorption and desorption reactions differ in solid iron phases.⁸⁶ Since there is no fluid flow in the solid phase, the rate-limiting step in these reactions involves the interfacial chemical reaction between the nitrogen gas and the iron surface or the diffusion of nitrogen into the iron. The interfacial chemical reaction is dominated by the condition in which the amount of nitrogen in the atmosphere above the metal is significantly higher than the amount of nitrogen absorbed. The interfacial chemical reaction can be considered to proceed by two consecutive steps. First, a chemisorption reaction characterized by the dissociation of nitrogen at the surface occurs and is followed by the transport of the nitrogen atoms from the occupied surface sites to the solid metal interior.



The solid iron surface is essentially saturated with nitrogen at short times. It can thus be assumed that the interfacial chemical reaction reaches equilibrium in a short period. Therefore, the rate controlling process for the desorption of nitrogen must be the diffusion of nitrogen into the solid iron.

2.2.6.2 Effect of Surface Active Element Additions on the Reaction Rate

The addition of surface active elements to the melt decreases the rate of both nitrogen absorption and desorption reactions.^{79-81,83,87,89} At low oxygen and sulfur levels, the ab-

sorption reaction is first order and the desorption reaction is second order, which are the same as those observed in iron samples without these elemental additions. There is little change in the measured rate constant with the addition of these solutes at low levels. On the other hand, reaction rates decrease with further increases in the surface-active element concentration since oxygen and sulfur atoms occupy surface sites normally available for nitrogen absorption.^{79-81,89} The absorption reaction becomes second order and the chemical reaction rate at the interface the rate-limiting step with these increased concentrations of surface active elements. Even further increases in the oxygen or sulfur concentration causes the reaction rate to become constant. At this point, the liquid-phase mass transfer mechanism once again limits the rate of the reaction.⁷⁹

At intermediate levels of these surface-active elements, the nitrogen absorption and desorption reactions can best be described by a mixed-control model. These models have been developed to take into account the role of multiple controlling mechanisms. For example, both the interfacial chemical reaction rate and the mass transfer rate affect the overall reaction rate for the nitrogen desorption reaction. The reaction rate is primarily determined by the surface coverage caused by the addition of these surface active elements to the liquid metal.

$$R = (1 - \theta)R_{bs} + \theta R_s \quad (2.28)$$

where R is the observed reaction rate, θ is the fraction of surface coverage due to the oxygen and sulfur additions, R_{bs} is the rate of reaction through the bare surface, and R_s is the rate of reaction through covered sites. The reaction is thus also controlled by the mass transfer rate in liquid iron.

Two types of mixed-control models have been developed to explain the absorption and desorption of nitrogen from iron melts. The first of these models is the parallel reactions model,⁷⁹⁻⁸¹ which assumes that the desorption process can follow one of two paths, and that the overall rate of the reaction is the sum of the rates of the individual reactions. The second mixed mode model is the sequential reaction model, which is based on the

assumptions that these steady state reactions occur in series. This second model is described by the following relationship:

$$R = \frac{dC}{dt} = k_{2rv} \frac{A}{V} (C_e^2 - C_i^2) = k_1 \frac{A}{V} (C_i - C) \quad (2.29)$$

where C_i is the nitrogen concentration at the interface, k_1 is the first order rate constant, and k_{2rv} is the rate constant for the nitrogen desorption reaction when the rate of reaction increases inversely with the volume of the system. The use of this mixed control model between the gas-phase mass transfer and the interfacial chemical reaction appears to be applicable, for the most part, to the nitrogen desorption reaction in an inert atmosphere.⁹¹

2.2.6.3 Rate of Nitrogen Absorption and Desorption During Arc Melting

Several researchers³¹⁻³³ have examined the kinetics of the nitrogen absorption and desorption reactions during the arc melting of iron and steels. These researchers have generally found that the presence of an arc above liquid iron significantly enhances the rate of the nitrogen absorption reaction. For example, Kuwana and Kokawa³² and Blake and Jordan³³ observed a rapid increase in the nitrogen concentration with melting time. The observed nitrogen concentrations reach a saturation value within approximately 30 to 50 seconds. This behavior is shown in Figure 2.21 for a number of nitrogen partial pressures in Ar-N₂ gas mixtures.³⁰ As the nitrogen partial pressure in the atmosphere is increased, a shorter time is required to reach a saturation value, especially at higher nitrogen partial pressures, and a higher nitrogen saturation value is observed.

Changes in the arc melting parameters, such as arc current or gas flow rate in the chamber have been examined,^{32,33} but conflicting results are observed by different researchers. For example, Kuwana and Kokawa³² observed little effect on the rate of nitrogen absorption in the liquid metal with changes in the arc current, sample weight, or gas flow rate in the chamber. On the other hand, Blake and Jordan³³ observed an increase in the nitrogen concentration with an increase in arc current at times on the order of 30 to 40 seconds, at which point nitrogen saturation levels were reached. The amount of nitrogen

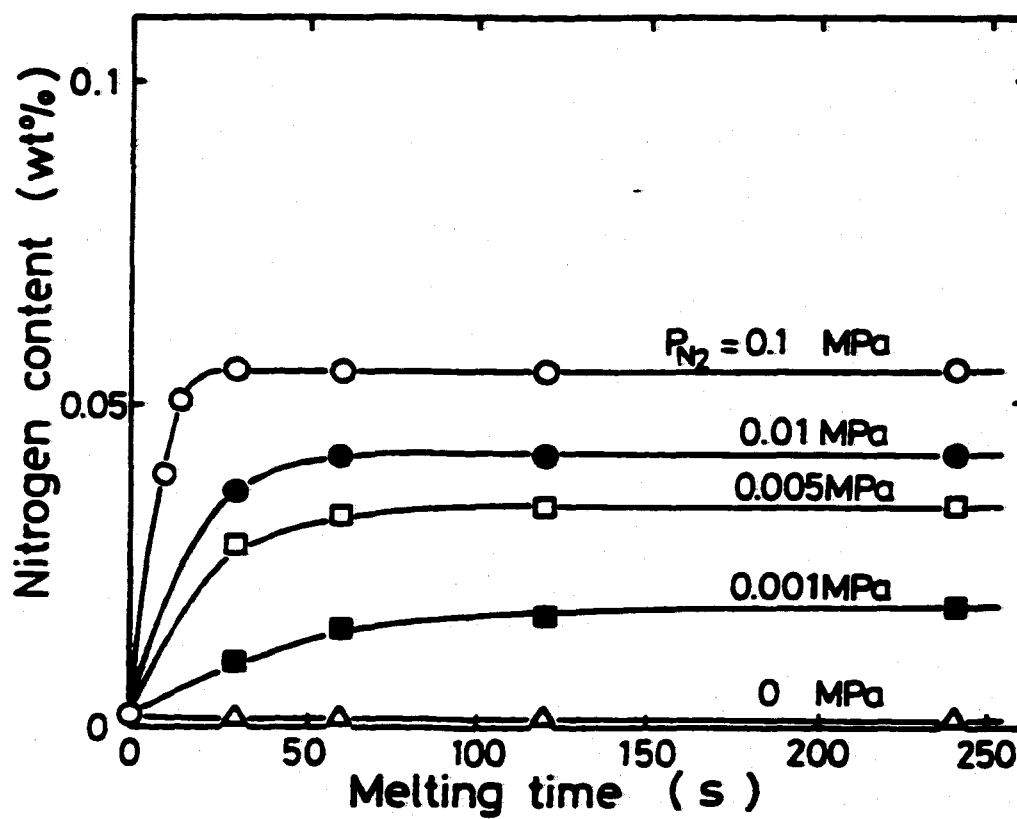


Figure 2.21. Relation between the nitrogen content in arc melted iron samples and the melting time at a number of nitrogen partial pressures.³²

entering the metal surface as a function of time also rises with an increase in arc current over a range from 100 to 300 A.

The effect of Cr and Ni additions to liquid iron on the rate of nitrogen absorption is shown in Figure 2.22(a&b).⁶¹ There is little to no difference in the rate of increase in the nitrogen concentration with time for each level of alloying element addition. Each alloy system reaches a saturation value at approximately the same time. The only real difference between the nitrogen concentrations observed for each of these alloys is a result of the effect of the alloying element additions on the nitrogen saturation level. As expected, the nitrogen concentration in liquid iron increases with additions of Cr to the liquid metal and decreases with the additions of Ni.

Katz and King³¹ further investigated the kinetics of both nitrogen absorption and desorption during the arc melting of iron in a much more systematic fashion. Figure 2.23 shows a typical plot of the nitrogen concentration in the liquid iron as a function of time. The experimental results show three regions relating to the absorption of nitrogen, a steady-state plateau relating to the saturation of nitrogen, and, finally, a region of desorption, which occurs in a pure Ar environment. Their analysis is based on the nitrogen concentration being the result of a steady state reaction with monatomic nitrogen as the dominant species. In their model, nitrogen absorption occurs only in the area of the melt where the arc plasma impinges on the melt surface, and desorption occurs outside the area covered by the arc plasma.

The absorption process is composed of a sequence of steps similar to that observed in non-arc melting conditions. During arc melting, this complex process is primarily influenced by electromagnetic stirring, natural convection, momentum transfer from the impinging plasma jet, and surface tension-driven flow. In general, the higher the atomic nitrogen content in the plasma, the larger the rate of absorption. Based on these results, the nitrogen absorption reaction is first order with respect to atomic nitrogen. Mass transfer in the melt is the rate-limiting step in the nitrogen absorption, and the nitrogen absorption reaction rate is defined below.

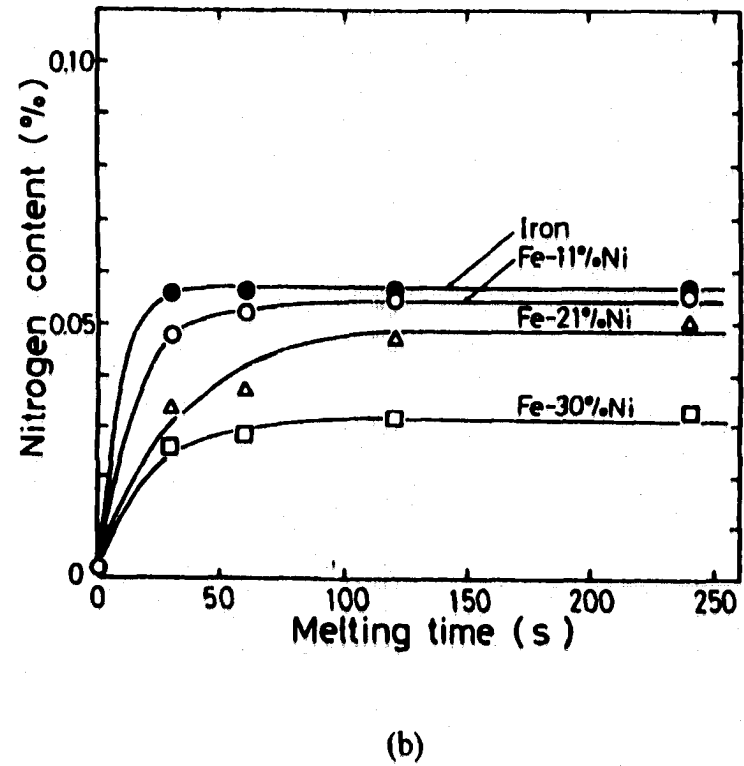
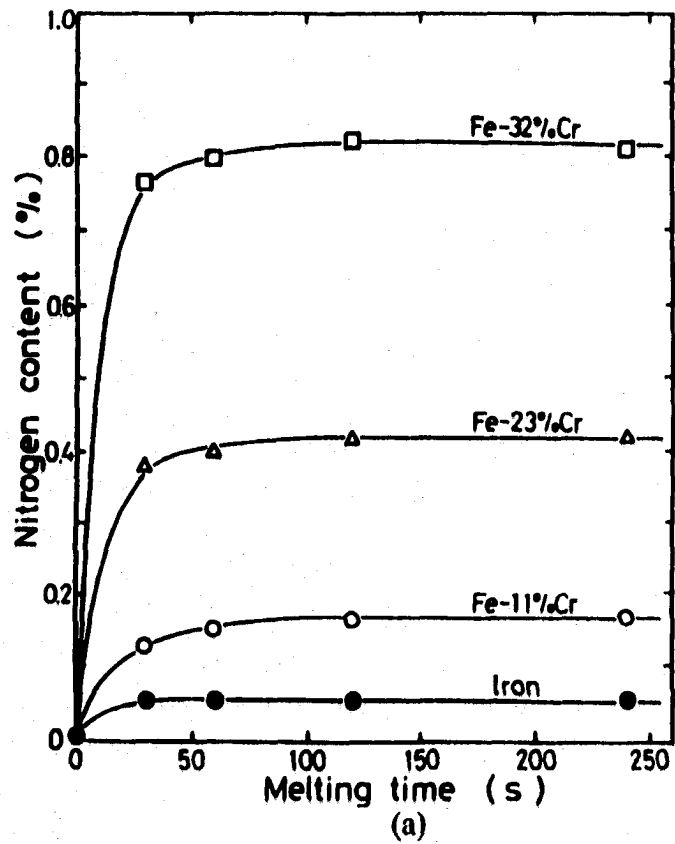


Figure 2.22(a&b). Relation between the nitrogen concentration in arc melted (a) Fe-Cr and (b) Fe-Ni alloys and melting time for an arc current of 150 A in a pure nitrogen atmosphere at a pressure of 1 atm.⁶¹

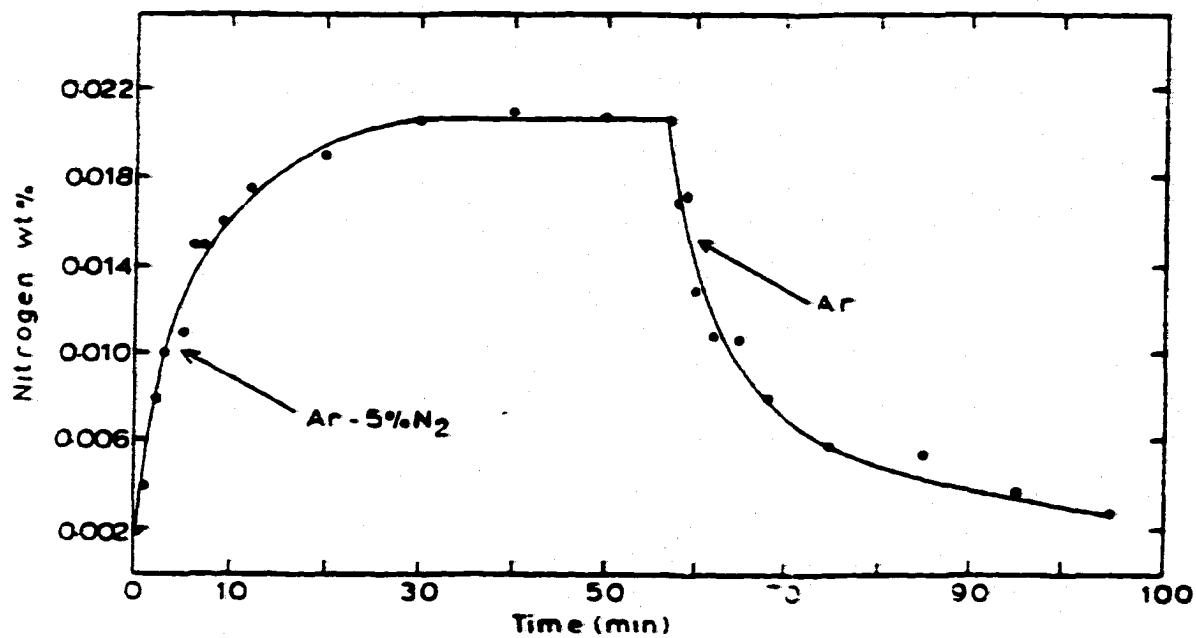


Figure 2.23. Weight percent nitrogen as a function of time for an Ar-5%N₂ plasma.³¹

$$\left\{ \frac{d[N(\text{pct})]}{dt} \right\}_{t=0} = k_F [N_f(\text{pct})] \quad (2.30)$$

where $[N_f(\text{pct})]$ is the nitrogen content of a melt in equilibrium with the atomic nitrogen potential of the plasma arc and k_F is the forward rate constant for the nitrogen absorption reaction. Nitrogen desorption from a pure iron surface is governed by many of the same mechanisms and is also a first order reaction. With this agreement, the mass transport in the melt also appears to be the rate-limiting step in the nitrogen desorption reaction.

Surface-active elements in liquid iron significantly affect the nitrogen absorption and desorption reactions during the arc melting of iron and steels. Hooijmans and Ouden⁶⁹ investigated the effect of several oxygen concentrations in the liquid iron on the rate of nitrogen absorption in an Ar-0.4%N₂ melting environment. In Figure 2.24, the nitrogen concentration rose rapidly at short times and leveled off at longer times when the nitrogen saturation value was reached for each oxygen concentration analyzed. The level of nitrogen saturation increased with an increase in the oxygen concentration in the base metal. On the other hand, the addition of increasing levels of oxygen does not seem to affect the kinetics of the nitrogen absorption reaction to any extent, since the individual saturation levels are reached at approximately the same time.

On the other hand, the effect of oxygen, in particular, on the absorption rate in the region under the arc column is negligibly small. Under the arc column, the liquid metal is vigorously stirred and the liquid metal at the surface is continually replenished. Therefore, oxygen which may occupy surface sites at one instant are quickly transported away from the surface, thus allowing the surface sites to be available for nitrogen absorption. Surface active elements, which are present in the area outside the arc column, halt nitrogen desorption by decreasing the frequency of this bubble formation.

Nitrogen desorption outside the arc column is sensitive to the availability of surface sites and thus easily affected by the presence of surface active elements. These elements occupy vacant locations on the liquid metal surface, where the nitrogen desorption reaction would normally occur. The reaction rate is thus limited by the association of two absorbed nitrogen atoms on the liquid metal surface outside the arc column. The extent

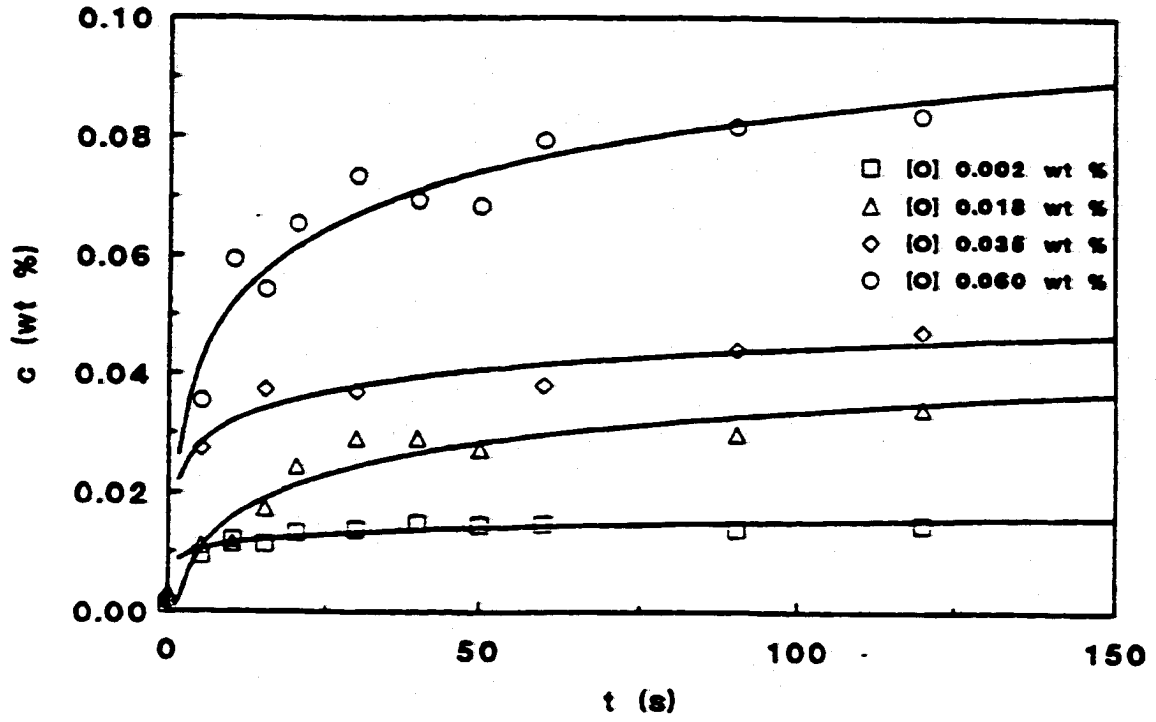


Figure 2.24. Nitrogen concentration as a function of arc time for four samples with different oxygen concentrations.⁶⁹

of surface coverage of the surface active elements and its effect on the reaction rate are defined below.⁸⁹

$$1 - \theta_T = \frac{1}{(1 + K_O^{ads}(\text{wt.\%O}) + K_S^{ads}(\text{wt.\%S}))} \quad (2.31)$$

$$k^{app} = k^{bs}(1 - \theta_T)^2 \quad (2.32)$$

where K_O^{ads} and K_S^{ads} are the rate constant for the adsorption of oxygen and sulfur, respectively, k^{app} is the apparent rate constant, and k^{bs} is the apparent rate constant on the bare melt surface. Therefore, when surface active elements are present in any amount, the desorption reaction becomes a second order reaction. The following relation shows the rate change of nitrogen desorption with the presence of an appreciable amount of surface active elements in the liquid metal:

$$-\left(\frac{d[N(\text{pct})]}{dt}\right)_{t=0} = k^{app}[N_i(\text{pct})]^2 - k^{app}p_{N_2} \quad (2.33)$$

They also recognized that the steady-state nitrogen content is the net effect of both the absorption and desorption of nitrogen from the melt, and it is not a simple function of the surface coverage, even though the surface-active elements played an important role. Based on the proposed steady-state nature of the process and the computed reaction orders for both the nitrogen absorption and desorption reactions, the following relation has been developed.³¹

$$\left(\frac{d[N(\text{pct})]}{dt}\right)_{t=0} - k_F[N_{ss}(\text{pct})] = k_B \left[N_e(\text{pct})^2 - [N_{ss}(\text{pct})]^2 \right] \quad (2.34)$$

where $N_{ss}(\text{pct})$ is the steady-state nitrogen concentration, $N_e(\text{pct})$ is the equilibrium nitrogen concentration in the liquid metal, k_F is the forward rate constant, and k_B is the backward rate constant.

2.3 NITROGEN DISSOLUTION DURING THE WELDING OF IRON AND STEELS

2.3.1 Role of Arc Welding Process in Affecting Nitrogen Dissolution Reaction

The nitrogen concentrations in arc melted iron are the result of the interaction between a nitrogen-containing plasma phase and liquid iron. In both arc melting and arc welding operations, a plasma phase exists above the liquid metal. Several reviews are available⁸²⁻⁹⁸ on the enhanced nitrogen concentrations in the weld metal during the arc welding of iron and steels. Nitrogen in the weld metal can originate from welding consumables, such as a filler wire or as a flux, which are common in both gas-metal arc (GMA) and submerged metal arc (SMA) welding operations.⁹⁷ Otherwise, nitrogen in the weld metal can originate from the interaction between the surrounding atmosphere, which is 80% nitrogen, and the plasma phase above the weld pool. The impingement of the surrounding atmosphere into the arc column can be due, in part, to insufficient shielding of the weld metal.

The mechanism for nitrogen absorption into the weld metal varies significantly in each case. For example, if nitrogen originates primarily from the welding consumable, the resulting nitrogen in the weld pool is simply transported from the consumable to the weld pool. If the nitrogen in the weld pool originates from the atmosphere, the plasma-metal reaction dominates. This reaction is nearly identical in nature to that discussed above for the arc melting of iron and other ferrous materials. Therefore, it can be assumed that common mechanisms exist between these various processes which contribute to the large nitrogen concentrations observed.

2.3.2 GTA Welding of Iron and Plain Carbon Steels

2.3.2.1 Structure of Arc Column in GTA Welding

The GTA welding process, shown in Figure 2.25, consists of a non-consumable tungsten electrode, which acts as the cathode, and the weld pool, which acts as the anode.⁶⁰

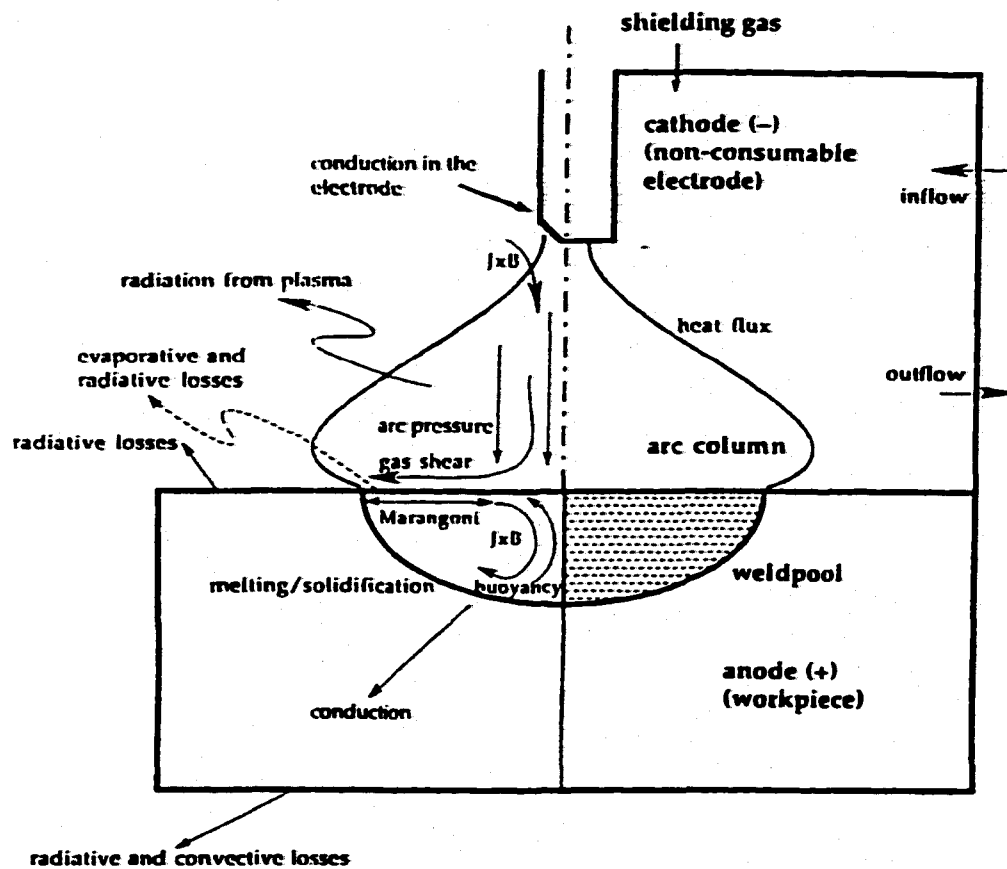


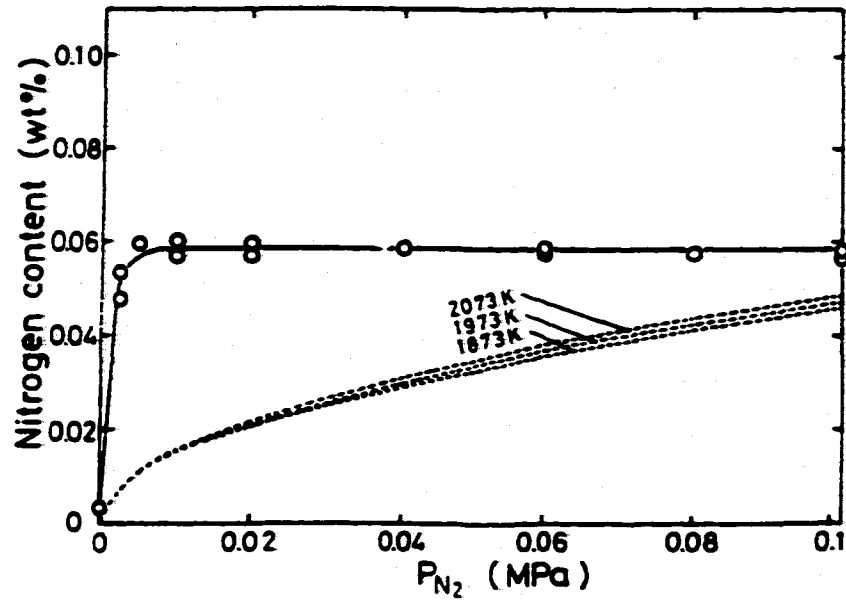
Figure 2.25. Schematic representation of the gas tungsten welding arc including the non-consumable electrode and the weld pool.⁵⁰

Energy is transported from the electrode to the workpiece via conductive heat transfer in the electrode, ohmic heating in the electrode, radiative exchange between the electrode and the arc, and the distributions of heat flux and current density at the surface of the electrode tip.^{60,99} Electrons, emitted from a cathode spot and transferred to the anode spot, provide the main components of the heat and current fluxes that enter the workpiece.^{60,99}

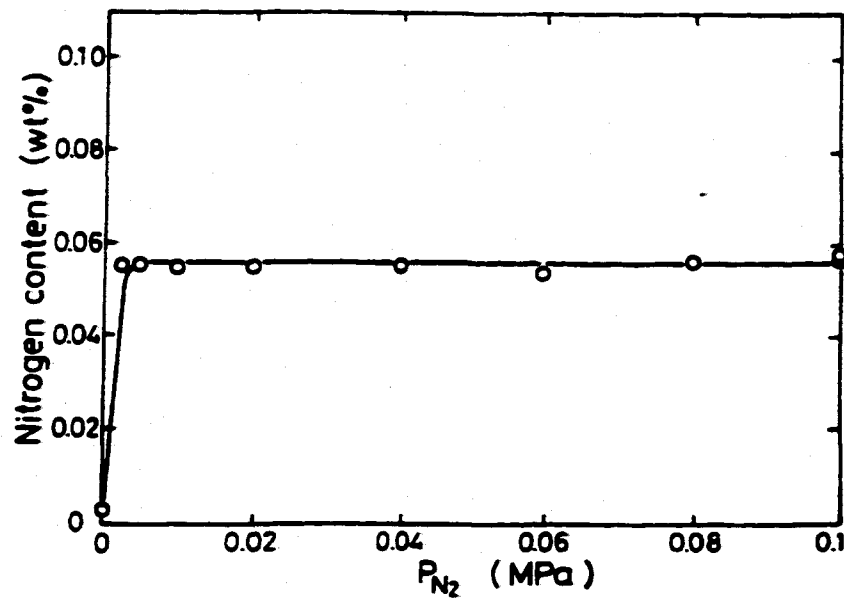
The GTA welding arc is produced by the interaction between the electrode and the shielding gas residing in the area between the electrode and the weld metal surface. Based on the potential distribution across the arc length,⁹¹ the arc is divided into five parts: the cathode spot, the cathode fall region, the arc column, the anode fall region, and the anode spot.⁹¹ Only the arc column is in local thermodynamic equilibrium (LTE), in which the electron temperature is identical to the heavy particle temperature. Temperatures in the arc column can vary many thousands of degrees between the electrode and the work piece.¹⁰⁰⁻¹⁰⁵ The highest temperatures are observed in the vicinity of the electrode, in some cases approaching 20000 K, while lower temperatures are observed as the work piece is approached. The cathode and anode fall regions display significant voltage drops, making the analysis of these regions difficult.^{91,106} Unlike the arc column, there are substantial deviations from LTE conditions, with the temperatures of the heavy species approaching the temperature of the molten metal. On the other hand, the electron temperature remains sufficiently high to ensure the required electrical conductivity across this boundary to allow electron transfer to the anode to occur.

2.3.2.2 Nitrogen Concentrations in GTA Weld Pool

Nitrogen concentrations in iron and steel during GTA welding are much higher than Sieverts' Law calculations.^{92-99,107-109} Kuwana and Kokawa¹⁰⁷ have studied the nitrogen dissolution reaction during the GTA welding of pure iron samples with controlled additions of nitrogen to argon and helium shielding gases. Figure 2.26(a&b)¹⁰⁷ shows the relationship between the nitrogen partial pressure in Ar and He shielding gas, respectively, and the measured nitrogen concentration in the weld metal. Sieverts' Law calculations for three temperatures in liquid iron and the nitrogen partial pressures are also shown in



(a)



(b)

Figure 2.26(a&b). Relation between the nitrogen content of the weld metal and the nitrogen partial pressure (P_{N_2}) under (a) Ar- N_2 and (b) He- N_2 atmospheres at a welding current of 250 A, an arc length of 10 mm, and a travel speed of 1.67 mm/sec.¹⁰⁷

Figure 2.26(a). In both cases, the nitrogen content in the weld metal is significantly higher than the Sieverts' Law calculations shown in Figure 2.26(a) and rapidly increases at very low nitrogen partial pressures. Above approximately 0.005 MPa, the nitrogen concentration reaches a plateau, corresponding to approximately 0.06 wt.% \underline{N} , which is a little higher than the equilibrium solubility at the measured temperature of the weld molten pool. A larger amount of nitrogen is thus absorbed into the molten weld pool than that evolved during the cooling process. Based on this result, the authors¹⁰⁷ suggested that the weld metal cooling rate significantly influences the nitrogen content in the weld metal, especially for nitrogen welding atmospheres of 0.1 MPa.

The effect of changes in the total pressure from 0.1 to 1 atm with a pure nitrogen shielding gas on the resulting nitrogen concentration during GTA welding is shown¹⁰⁷ in Figure 2.27. At low values of P_{N_2} , the nitrogen concentrations in the weld metal rapidly increase at a pressure of 0.005 MPa to a nitrogen concentration, 0.26 wt.%, which is far above the equilibrium solubility of nitrogen in iron at 0.1 MPa. As the pressure is further increased, the nitrogen concentrations rapidly fall to levels much closer to the equilibrium nitrogen solubility. The authors provide no explanation for this behavior, but it can be attributed, at least in part, to an increased monatomic nitrogen partial pressure at these low total pressures. Little is known of the effect of this low pressure on the arc behavior and the interaction between the plasma phase and the liquid metal.

The nitrogen concentration in the weld metal was also dependent upon the choice of welding conditions. An increase in the welding current from 50 to 300 A at a constant travel speed and arc length causes a decrease in the nitrogen content in the weld metal for a nitrogen shielding gas at atmospheric pressure. On the other hand, the nitrogen content shows little to no dependence on the arc length, arc voltage, and travel speed at atmospheric pressure with a nitrogen shielding gas. An increase in the travel speed, up to approximately 1.67 mm/sec, causes the nitrogen content in the weld metal to also increase from a level of approximately 0.04 wt.%. At travel speeds above approximately 1.67 mm/sec, the nitrogen concentration remains constant at approximately 0.06 wt.% \underline{N} . During these experiments, the weld penetration area of the welds decreased dramatically

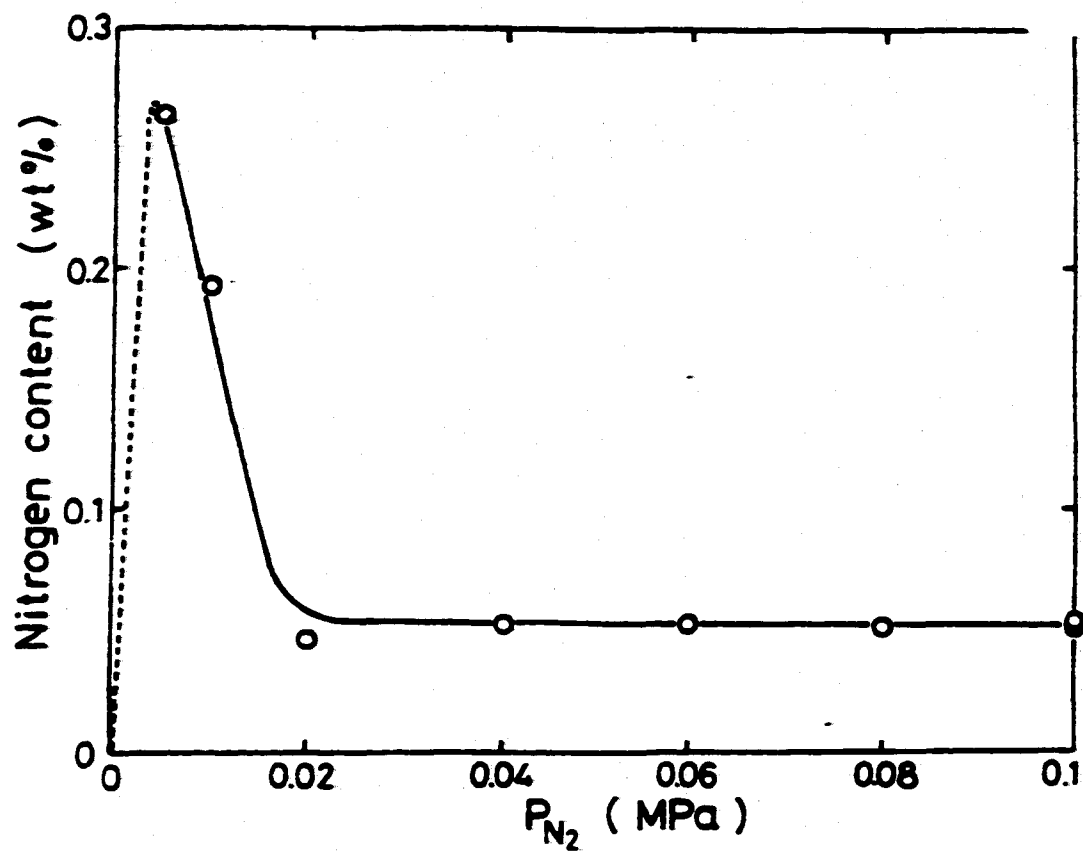


Figure 2.27. Relation between the nitrogen concentration in a weld metal and the nitrogen pressure (P_{N_2}) for a pure N_2 atmosphere, a welding current of 250 A, an arc length of 10 mm, and a travel speed of 1.67 mm/sec.¹⁰⁷

with an increase in travel speed. The nitrogen content of the weld metal is thus believed to decrease with an increase in the penetration area.

2.3.2.3 Role of Alloying Elements in Nitrogen Dissolution During GTA Welding

The effect of chromium and nickel, respectively, on the resulting nitrogen concentration during the GTA welding of iron is shown in Figure 2.28(a&b).⁶⁵ The addition of Cr and Ni have different effects on the magnitude of the nitrogen concentration in the weld metal. For example, the chromium additions increase the nitrogen concentration, while nickel additions decrease the nitrogen concentration. -For each alloy addition, though, the nitrogen concentration markedly increases at nitrogen partial pressures lower than 0.01 MPa, after which it becomes constant. Based on these results, the effects of Cr and Ni additions on the nitrogen concentration during arc welding are very close to those observed during arc melting and under equilibrium conditions.

The effect of changes in the arc current on the resulting nitrogen concentration with each alloying element addition is shown in Figure 2.29(a&b).⁶⁵ In addition to the nitrogen concentrations, temperatures within the weld pool were also measured. These temperatures show little to no dependence on the welding current, which runs contradictory to previous observations in arc-melting experiments. Nitrogen concentrations in the weld metal decrease with an increase in the welding current as Cr is added to the base metal. With increasing chromium contents, the tendency for the nitrogen concentration in the weld metal to further decrease becomes more pronounced. On the other hand, the nitrogen content remains constant in the Fe-Ni alloys even with an increase in the welding current.

These alloy additions to the iron base metal closely resemble the compositions of common stainless steels. Stainless steels have significant industrial relevance, and the role which nitrogen plays on their resulting properties is of significant interest. Several researchers have also investigated the effect of nitrogen additions to the shielding gas during the GTA welding of stainless steels on the resulting nitrogen concentration in the weld metal.^{97,108-109} On the other hand, the majority of the work reported in the literature deals primarily with the effect of nitrogen additions on the resulting properties and mi-

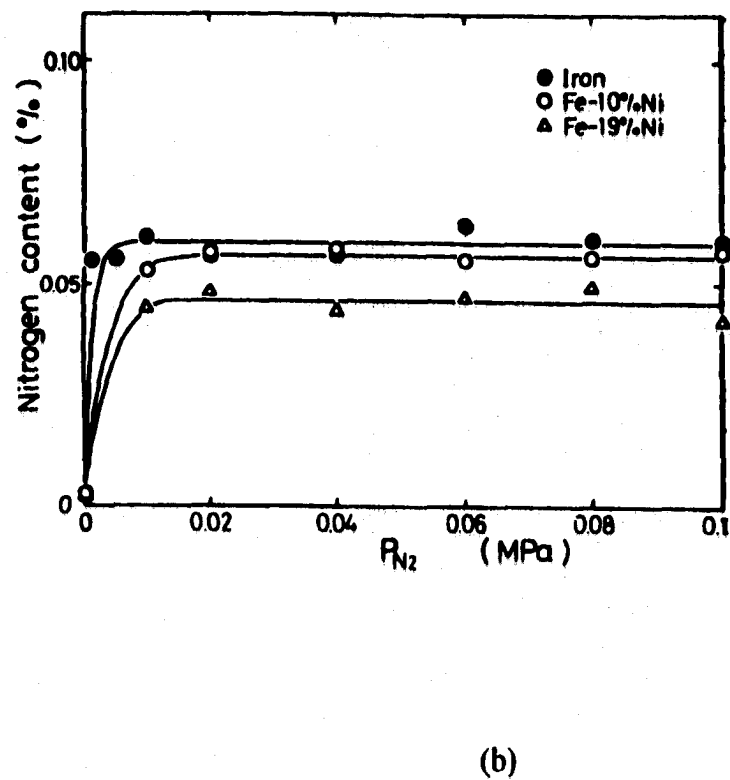
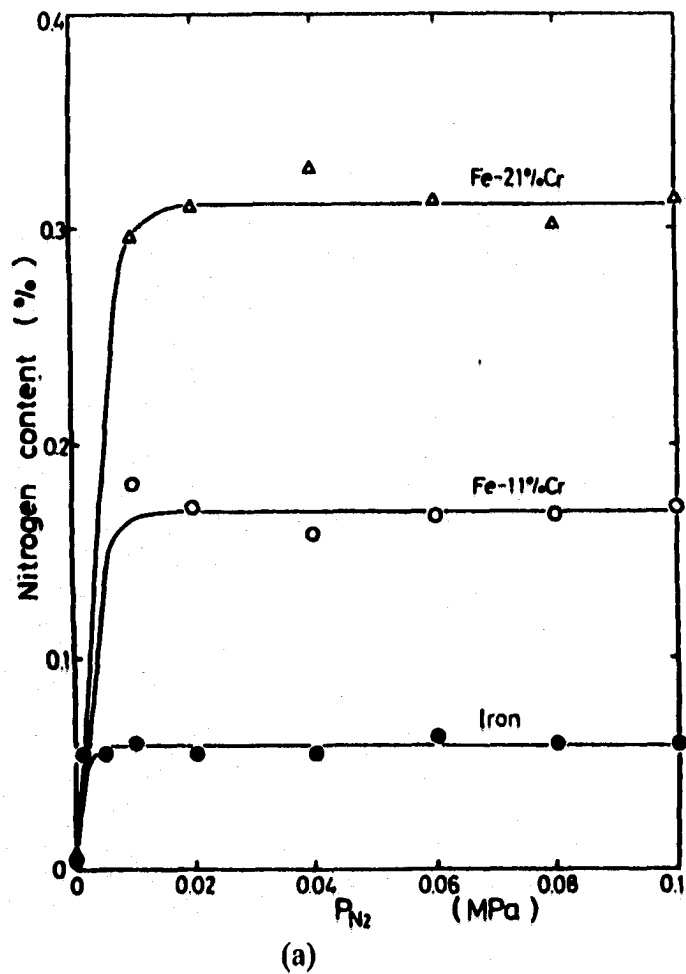
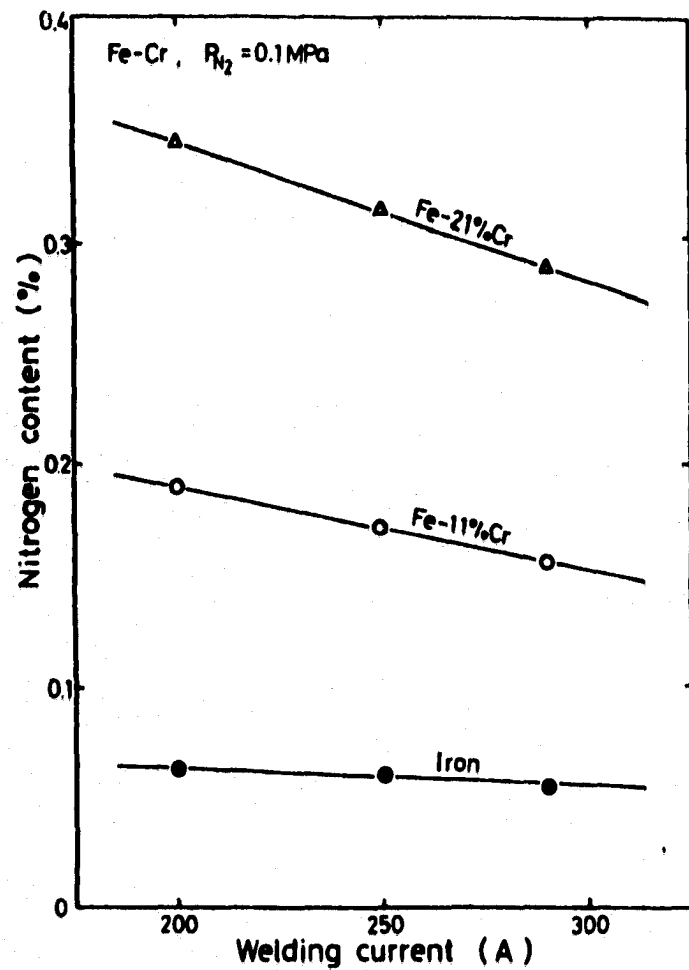
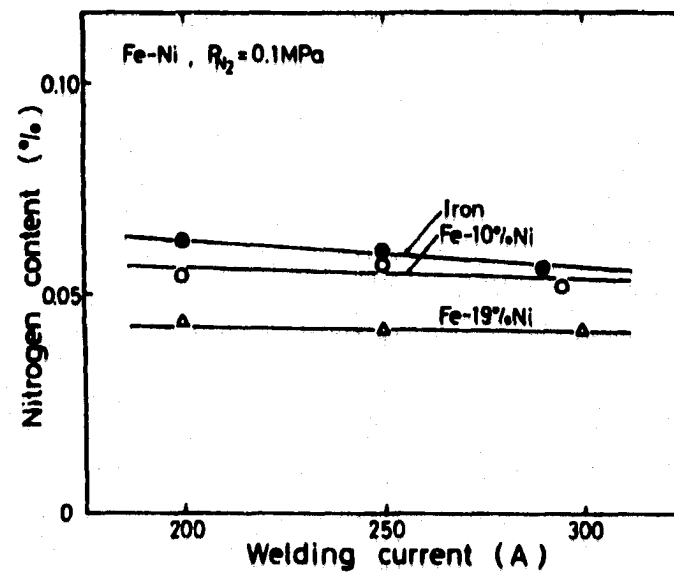


Figure 2.28(a&b). Relation between the nitrogen concentration and nitrogen partial pressure (P_{N_2}) in Ar- N_2 gas mixtures for (a) Fe-Cr and (b) Fe-Ni alloys during GTA welding at a travel speed of 3.33 mm/sec and at atmospheric pressure.⁶⁵



(a)



(b)

Figure 2.29(a&b). Relationship between the nitrogen concentration in the weld metal and the arc current for several (a) Fe-Cr and (b) Fe-Ni alloys at a travel speed of 3.33 mm/sec and at atmospheric pressure.⁶⁵

microstructure of the stainless steel, primarily in austenitic stainless steels.⁹⁷ The small amount of work performed on the nitrogen dissolution mechanism in stainless steels,^{96,98,108,109} though, sheds no further light on other mechanisms which may be responsible for the enhanced nitrogen concentration observed during the welding of these alloys. Rather, the results are similar to those reported for high concentrations of Cr additions in binary Fe-Cr alloys.

2.3.3 GMA Welding of Iron and Plain Carbon Steels

The GMA welding process shown in Figure 2.30 is fundamentally different from GTA welding.⁶⁰ GMA welding begins with the melting of the electrode and is followed by the growth and detachment of the metal droplet from the electrode and the transfer of the molten metal droplet to the workpiece, where it solidifies.⁹⁰ In this process, the anode is a consumable electrode, which acts as filler material in the welded joint, and the work piece serves as the cathode. The GMA welding arc also differs from the GTA welding arc,⁶⁰ but many of the same transport processes prevalent in GTA welding are also main contributors to the transport of energy here. These additional components in the GMA welding process lead to several additional transport processes, including the transient melting of the electrode, the interaction of the arc with the continuously deformed free surface of the electrode, and the losses of heat and mass due to vaporization. The electron transfer in this process is also more complex, since the anode spots are mobile and the solid electrode and liquid melt attached to its tip continually change shape.

Differences in the GTA and GMA welding processes also lead to differences in the nature of the nitrogen dissolution reaction. Based on these differences, several researchers¹¹⁰⁻¹¹⁴ have studied the nitrogen dissolution reaction in iron and plain carbon steels during GMA welding. Kobayashi *et al.*¹¹⁰ have performed controlled GMA welding experiments on mild steel samples using a low C electrode wire similar in chemistry to the base metal. They analyzed the effect of various nitrogen additions to an argon shielding gas on the resulting nitrogen concentration in the weld metal. In Figure 2.31, nitrogen concentrations in the weld metal increase considerably¹¹⁰ for nitrogen partial pressures below 0.15 atm., above which they remain constant at approximately 0.048 wt.% N.

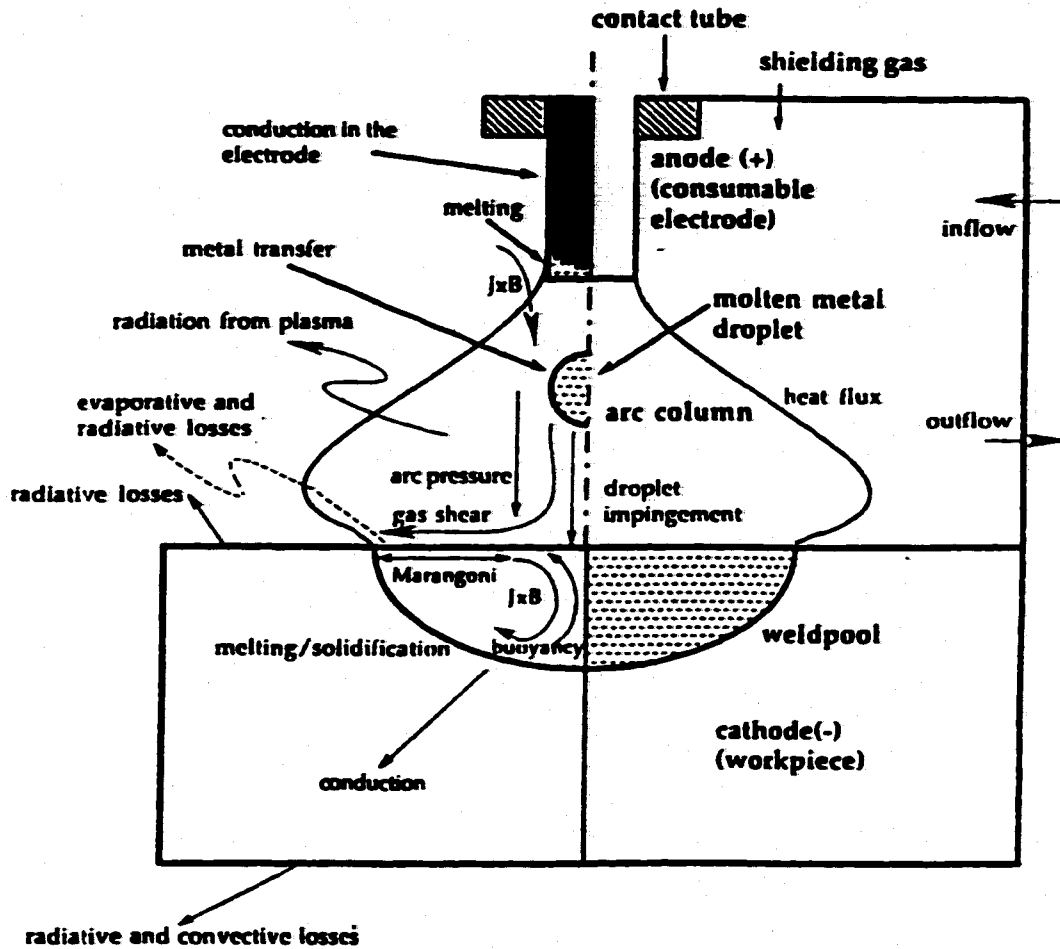


Figure 2.30. Schematic representation of a GMA welding arc including the consumable electrode and the weld pool.⁵⁰

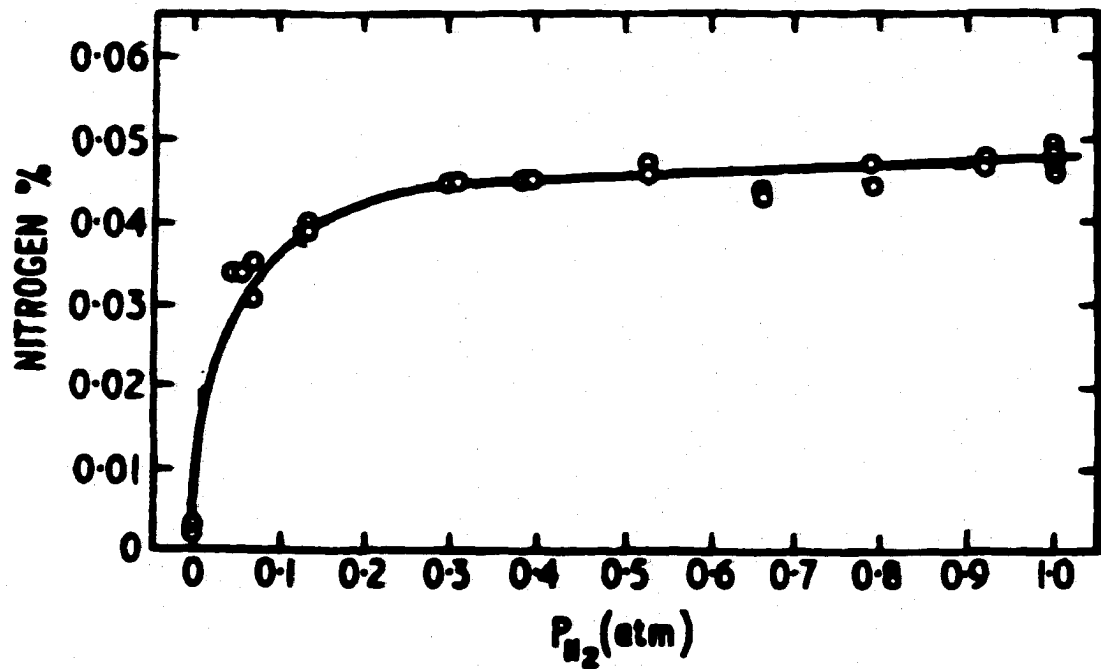


Figure 2.31. Relationship between the nitrogen concentration in the weld metal during the GMA welding of a mild steel in an Ar-N₂ shielding gas environment at atmospheric pressure with a welding current of 260 A, a welding voltage of 24 V, and a travel speed of 20 cm/min.¹¹⁰

These results are almost identical to those for GTA welding, especially in terms of the general behavior of the nitrogen content over the range of nitrogen partial pressures.

The effect of changes in the total pressure on the resulting nitrogen concentration in the weld metal in pure nitrogen atmospheres at pressures is shown¹¹⁰ in Figure 2.32. Here, the nitrogen concentration increases rapidly to approximately 0.055 wt.% N at a pressure of only 0.065 atm. This increase in nitrogen concentration is not observed at the same nitrogen partial pressure in Ar-N₂ shielding gases at atmospheric pressure. As the pressure increases further, the nitrogen concentration decreases significantly to a more acceptable level of approximately 0.034 wt.% at a pressure of 0.13 atm. Above this pressure, the nitrogen content in the weld metal increases linearly, ending at a nitrogen concentration of 0.048 wt.% N at a pressure of 1 atm. This behavior is nearly identical to that observed by Kuwana and Kokawa⁶⁵ over this same pressure range in GTA welding.

The authors¹¹⁰ also investigated the role of changes in the arc current and arc voltage on the nitrogen concentration in the weld metal. Like previous investigations, the nitrogen content decreases with an increase in the arc current. This reduction in the amount of nitrogen absorbed by the weld metal may be in part due to the enhanced transfer rate of molten metal drops, which occurs with an increase in the welding current. Nitrogen contents, though, were unaffected by any changes in the arc voltage, matching those observed in the GTA welding of iron and steels. On the other hand, Verhagen *et al.*¹¹¹ observed an increase in the nitrogen concentration in the weld metal with increasing welding voltage during the GMA welding of a ferritic base metal containing Mn, Si, and C using both solid and flux cored electrode wires.

The effect of hyperbaric atmospheres on the nitrogen concentration in high purity iron during GMA welding has also been studied.¹¹⁴ In these experiments, the authors used electrode wire identical in composition to the base metal in order to avoid any change in chemistry affecting the nitrogen concentration. Figure 2.33 displays¹¹⁴ the relationship between the nitrogen concentration and the nitrogen partial pressure at pressures up to 30 atm. At nitrogen partial pressures greater than 1 atm., the nitrogen concentrations continue to increase until a plateau double this concentration (1000 ppm) is reached at pressures above 20 atm. Little to no difference is observed between the nitro-

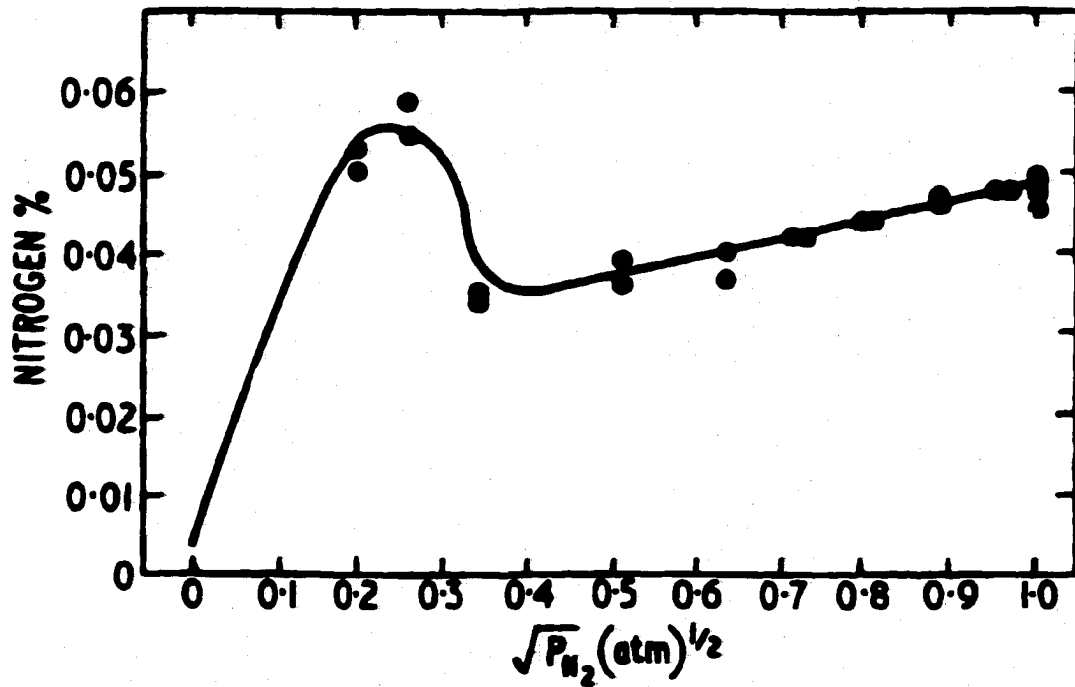


Figure 2.32. Relationship between the nitrogen content in the weld metal during the GMA welding of a mild steel in a nitrogen atmosphere and the total pressure in the welding chamber for a welding current of 260 A, an arc voltage of 24 V, and a travel speed of 20 cm/min.¹¹⁰

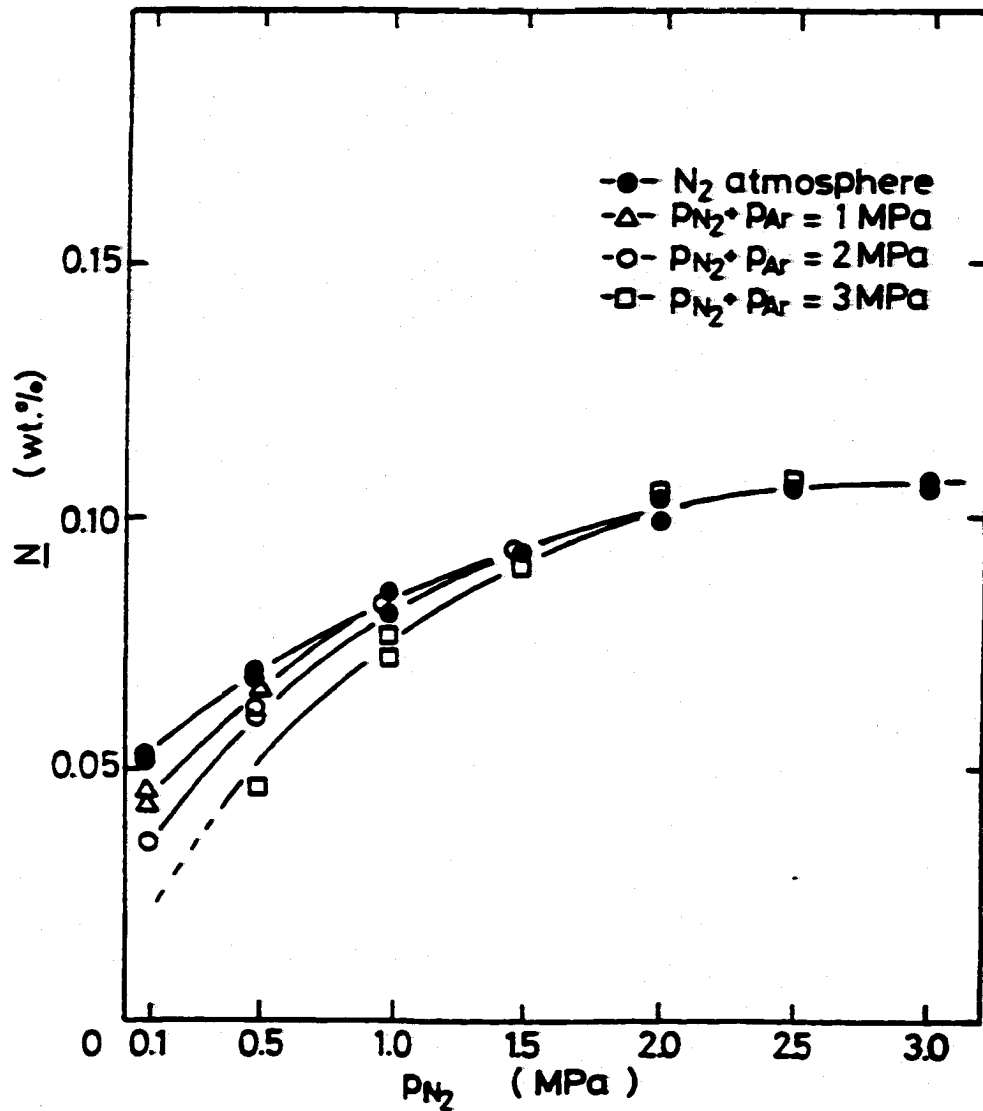


Figure 2.33. Relationship between the nitrogen concentration in the weld metal and the nitrogen partial pressure (P_{N_2}) during the GMA welding of iron samples at total pressures much greater than atmospheric pressure.¹¹⁴

gen concentrations reported for the different nitrogen partial pressures measured under different total pressures and shielding gas conditions. With these results, the authors suggested that the reaction time in the welding process was too short to allow for equilibrium values of nitrogen concentration in the weld metal to be reached under high pressure.

During GMA welding, the electrode polarity can also be reversed, resulting in rather significant changes in the nitrogen concentration. Nitrogen concentrations are nearly twice as large with a positively charged electrode as with a negatively charged one, as shown¹¹¹ in Figure 2.34. These results indicate a role for nitrogen ions (N^+) in the arc column in the enhanced nitrogen dissolution reaction. Since the number of nitrogen ions in the arc column are extremely low, their effect on the nitrogen concentration is insignificant. In contrast to these results, an analysis of the droplets present at the end of the welding wire shows the nitrogen absorption into the wire is much greater with the electrode negatively charged than with it positively charged. Therefore, the nitrogen absorption reaction must occur at both the metal droplet at the electrode and at the weld pool surface. On the other hand, little is known of which process and location dominates the nitrogen absorption reaction.

There are three primary metal transfer mechanisms in GMA welding, including the short circuiting transfer, globular transfer, and spray transfer. The choice of metal transfer mechanisms from the electrode to the workpiece is determined by the choice of electrode polarity, arc current, voltage, and even shielding gas mixtures.⁹⁰ Miller and Salter¹¹² and O'Brien and Jordan¹¹¹ have studied the effect of nitrogen additions to the shielding gas for both short-circuiting and spray transfer type arcs for mild steels with a CO_2 carrier gas. In both cases, the nitrogen concentration is much lower for the spray-type arc than for the short circuiting arc. Short circuiting transfer produces nitrogen concentrations nearly double to those observed for the spray transfer¹¹³ mode in Figure 2.35. As the nitrogen in the shielding gas approaches 100%, the weld metal nitrogen concentration drops significantly to that observed during spray transfer with a pure nitrogen shielding gas. This difference in nitrogen concentration is believed to be due to the freezing rate of the weld pool and the differences in the heat input. The faster freezing

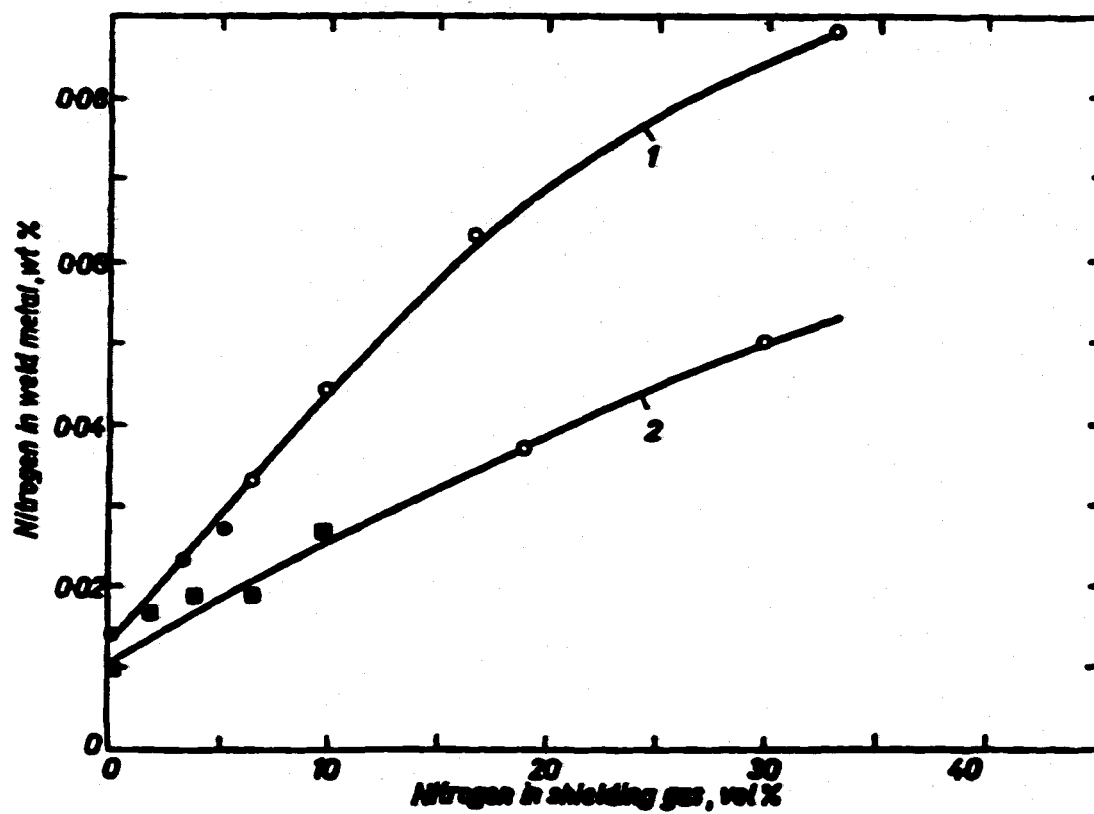


Figure 2.34. Relationship between the nitrogen concentration in the weld metal as a function of the nitrogen content in a CO₂ carrier gas for both (1) a positive electrode and (2) a negative electrode.¹¹¹

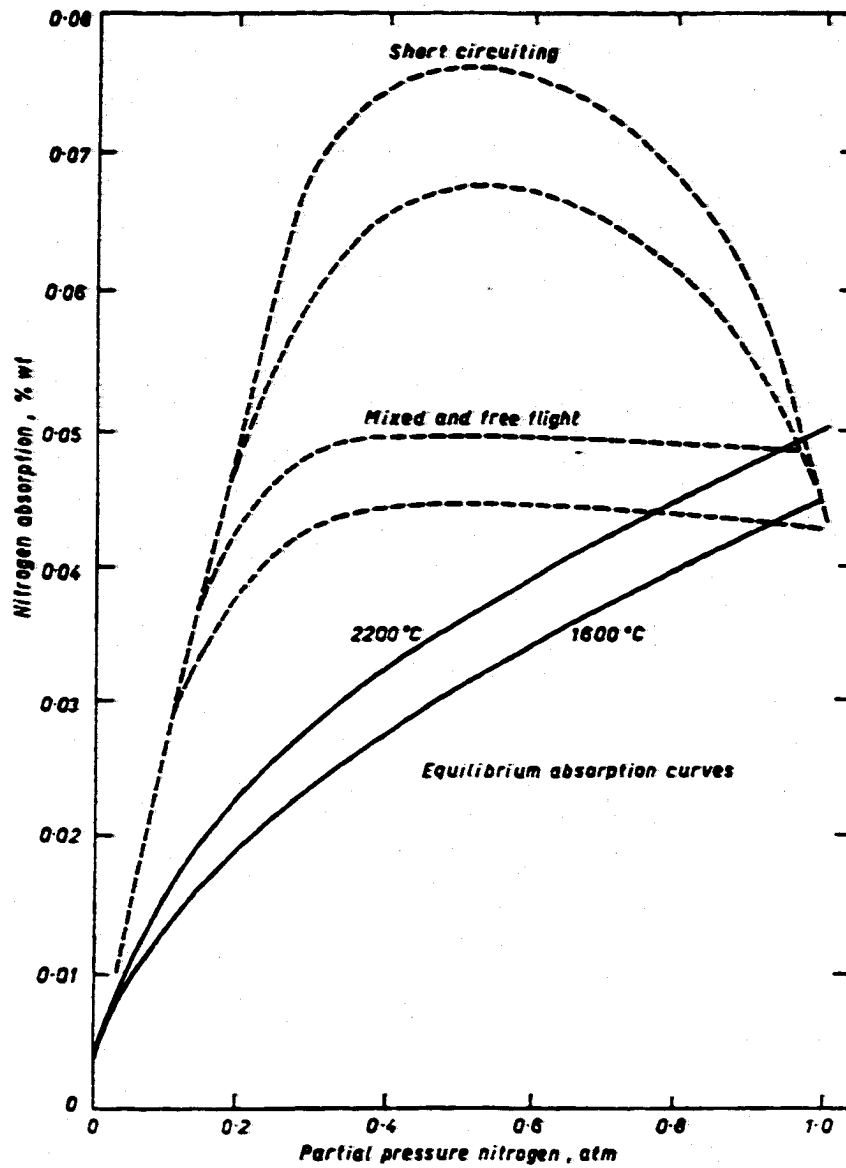


Figure 2.35. Comparison among the nitrogen absorption curves during CO₂ welding for different metal transfer modes and the equilibrium nitrogen concentrations at 1600 and 2200°C.¹¹³

rate of the short-circuiting arc weld allows less time for gas desorption and may cause more bubbles to be trapped before they rise to the surface of the weld pool.

A relationship has been shown to exist between the welding speed (v), the bead area (a), and the amount of gas absorbed per unit volume of weld metal.¹¹² For decreasing values of the product (va), the gas absorbed per unit volume of weld metal increases. Therefore, a small weld bead and low welding speed result in higher amounts of nitrogen absorbed per unit volume of weld metal. Based on this supposed relationship, the authors¹¹² also examined the role changes in the weld speed for each of these arc types would play on the resulting nitrogen concentrations in the weld metal. For the short circuiting arc, an increase in the welding speed decreased both the volume of the weld metal and the amount of nitrogen retained in the weld metal. This increase in the welding speed also reduced the observed weld metal porosity.

2.3.4 Formation of Porosity in the Weld Pool

Porosity in the weld metal has been studied in a number of materials systems.^{115,116-122} In terms of size, shape, and location, porosity can be described as either interdendritic porosity or bulk pores.¹²² Interdendritic porosity is characterized by the trapping of gas bubbles between dendrite arms in the solidification substructure. Furthermore, when pores can stay near or nucleate inside the dendritic solidification region, they can also originate or stay near other heterogeneous sites. Bulk pores, which originate from the supersaturation of gases in the weld metal, are much larger in size and are generally divided into two categories. When the cavities observed exceed 1 mm in diameter, they are considered blowholes, and when the cavity is less than 1 mm, they are simply gas pores.¹²²

Nitrogen solubility is much greater in liquid iron than in solid iron. Porosity is formed in the weld metal when nitrogen is present in amounts greater than their solubility limit when the metal solidifies. The thermodynamic limits for the maximum concentration of nitrogen in liquid iron are established by the formation of nitride compounds or by the nucleation of gas bubbles. In the Fe-N system, the thermodynamic solubility limit is determined by the nitrogen solubility in liquid iron, which is approximately 450 ppm at

1873 K and 1 atm. N_2 , and the pressure at which the reaction occurs.⁴⁷ If the concentration of nitrogen in solution in the weld metal exceeds this limit, nitrogen gas is desorbed from the liquid metal, either as diatomic or monatomic nitrogen. This evolution of nitrogen is supported by the formation of blowholes and pits in the weld metal. The weld metal nitrogen concentration is thus primarily controlled by the evolution of nitrogen during the cooling of the weld metal. Nitrogen desorption from the weld metal is thus the driving force for the formation of porosity, blowholes, and spatter in the weldment.

Porosity can form in the solidified metal by either the rejection of dissolved gas at the advancing solid/liquid interface or, when gas contamination levels are high, by the nucleation of bubbles ahead of the solid/liquid interface. Figure 2.36 shows¹¹¹ several absorption curves describing how nitrogen may be trapped in the solid metal by the passing solidification front. In situation I, no pores are formed because the nitrogen concentration in the liquid remains below the nitrogen solubility value. On the other hand, situation II arises when the nitrogen concentration in the liquid metal exceeds the nitrogen saturation value in front of the solid-liquid interface. N_2 gas bubbles are formed at nucleation sites along the solid-liquid interface, and additional nitrogen from the solid phase diffuses across the interface, leading to the formation of a porous weld. In Situation III, a maximum nitrogen concentration is reached, and the nitrogen concentration in the weld metal decreases. At this point, the nitrogen content in the weld metal is so high that gas bubbles form in the free liquid, and a great deal of nitrogen evolves from the liquid before it meets the solidification front.

During the GTA welding of iron and steels, porosity in the weld metal is generally observed with the addition of a sufficient amount of nitrogen to the shielding gas.^{65,107} Kuwana and Kokawa,¹⁰⁷ for example, have observed no blowholes or pits in the weld metal for nitrogen pressures lower than 0.01 MPa during the GTA welding of pure iron. In cases when only argon is used as the shielding gas, no porosity of any kind is observed. As the nitrogen addition to the shielding gas increases, the number of blowholes increase. Miller and Salter¹¹² also observed porosity in the weld metal during GMA welding of mild steels in a CO_2 carrier gas for both short-circuiting and spray transfer type arcs. In both cases, no apparent deterioration in the weld metal properties is ob-

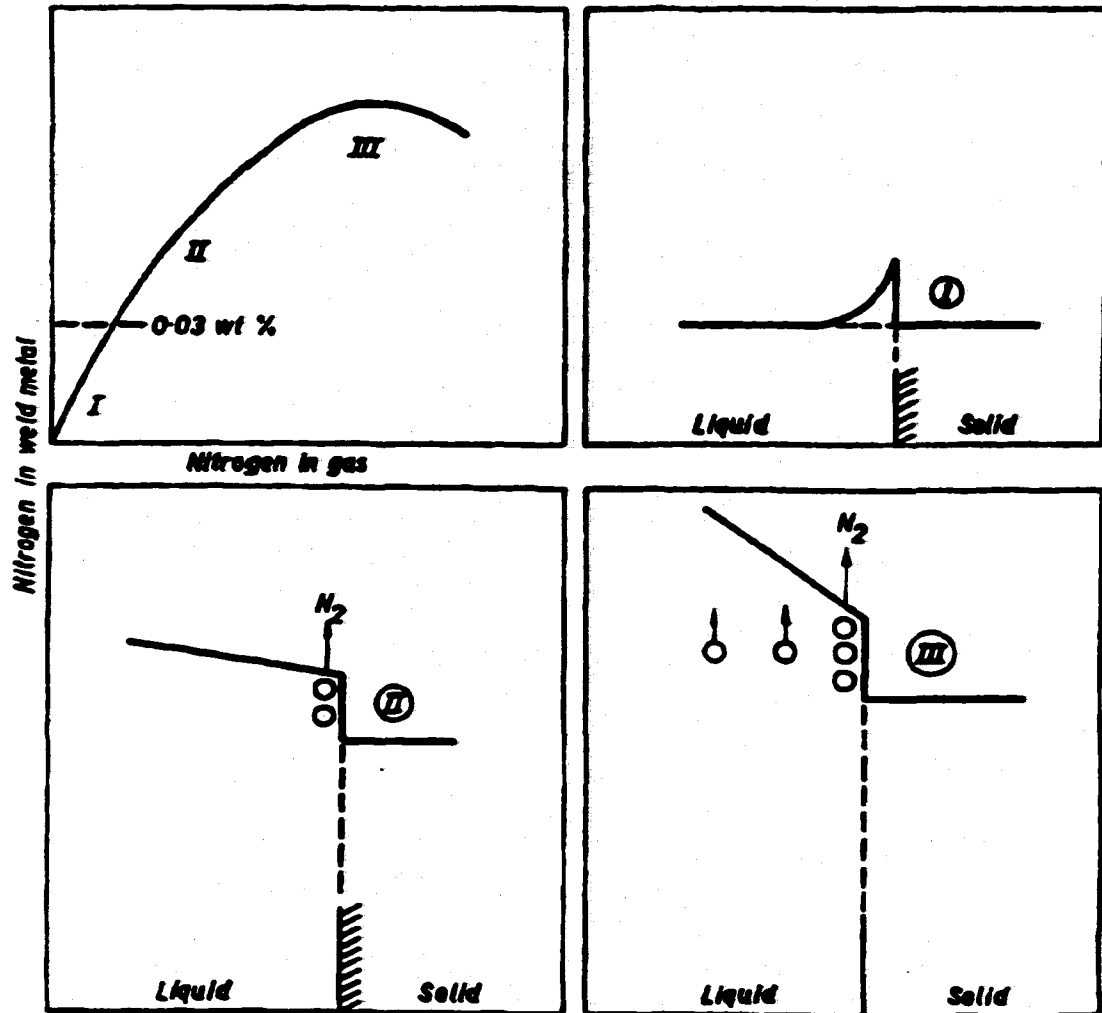


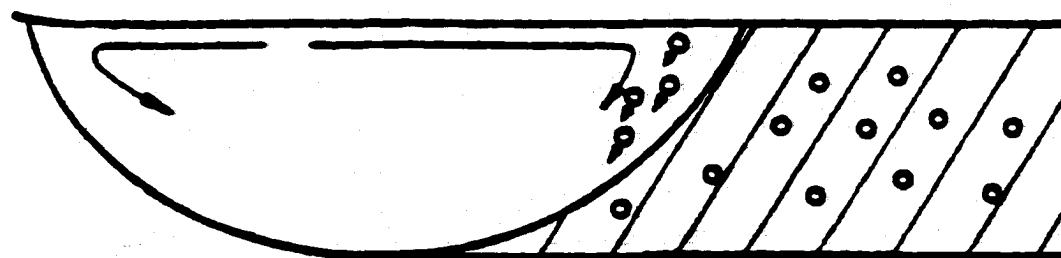
Figure 2.36. Schematic diagram of the change in nitrogen content during the welding process.¹¹¹

served up to nitrogen concentrations of 0.02 wt.%. Above this nitrogen concentration, weld metal porosity is observed. Metallographic examination of the weld pools for a short-circuiting arc and nitrogen additions of 3, 5, and 15% show scattered nitride needles within the ferrite grains and at the grain boundaries. The appearance of nitrogen in this form in the weld metal has not been extensively studied and has rarely been noted.³⁶

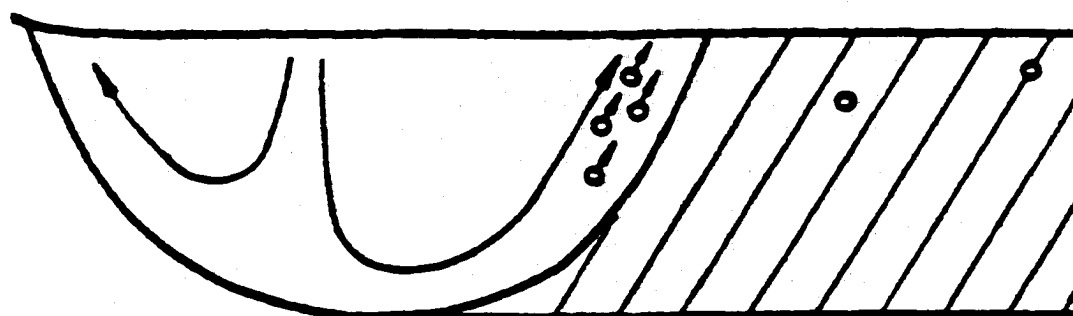
Changes in welding conditions also affected both the formation and the characteristics of the porosity present in the weld metal. For example, the pore size increases with increasing welding current. However, changes in the arc length have no effect. Once again, blowholes and pits were detected in all of the weld metals, and the number of blowholes and pits seemed to increase with travel speed. On the other hand, the number of these blowholes and other forms of porosity were rather small in alloys with higher amounts of chromium.⁶⁵ Therefore, the presence of blowholes and porosity can be related to the nitrogen solubility in the alloy.

An examination of the effect of weld pool convection patterns on the formation of gas porosity in the weld pool has been performed by Kou and Wang.⁴⁹ Convection conditions in the absence and presence of surface active elements, respectively, are shown in Figure 2.37(a&b).⁴⁹ In Figure 2.37(a), the convection patterns produce a downward sweeping action, trapping the gas bubbles within the fusion zone as the solidification front advances. The convection pattern is reversed in Figure 2.37(b),⁴⁹ creating an upward sweeping action, which has the reverse effect on the motion of the gas bubbles in the weld pool. Rather than being trapped within the fusion zone, the gas bubbles are brought to the free surface and thus allowed to escape.

The formation of blowholes in the weld metal and the forcible ejection of liquid metal from the weld pool in the form of spatter can also result from the liquid metal being supersaturated with nitrogen. Ohno and Uda¹²³ have studied the formation of blowholes caused by enhanced nitrogen dissolution during the arc welding of nickel. Given the much lower nitrogen solubility in nickel (18 ppm at 2000 K), the formation of porosity occurs at low nitrogen partial pressures in the shielding gas, as low as 0.025% N₂. The pores and blowholes in all of the samples are generally spherical in shape, and the size of the pores increases as the nitrogen addition to the shielding gas is increased.¹²³ Many of



(a)



(b)

Figure 2.37(a&b). Effect of weld pool convection on weld porosity: (a) convection pattern favoring trapping of gas bubbles; (b) convection pattern favoring removal of gas bubbles.⁴⁹

the same conclusions can be made as to the mechanisms of blowhole formation in the Fe-N system.

Weld metal spattering has a distinct relationship with the nitrogen concentration in the weld pool. Uda and Ohno⁶⁸ observed that at low residual nitrogen concentrations in the weld metal, spattering does not seem to occur. On the other hand, spattering is observed as the nitrogen concentration reaches its characteristic plateau. A proposed mechanism for spattering has been developed by Uda and Ohno⁶⁸ and is shown in Figure 2.38. The driving force for the ejection of a spattered particle is initiated from inside the liquid iron near the periphery of the arc spot area. This bubble has a high internal pressure, calculated to be greater than two atmospheres. It grows quickly toward the surface, where there is the least resistance for the movement of the bubble. A columnar projection is produced on the surface of the melt by the growing bubble, a portion of which is thrown from the weld pool, resulting in a spattered particle.

2.3.5 Role of Oxygen and Hydrogen Mixtures on Nitrogen Dissolution

Air containing additional amounts of oxygen and hydrogen is much more likely than pure nitrogen to enter the arc column above the weld metal during arc welding processes. The role played by the second diatomic gas additions in the shielding gas stream, in affecting the amount of nitrogen absorbed by the weld metal, must be considered. The presence of oxygen in the welding arc can also be the result of a purposeful addition to the shielding gas stream. Pure Ar and He are commonly used as the shielding gas during the GMA welding of nonferrous metals. However, when these pure gases are used to shield ferrous alloys during GMA welding, an erratic arc is produced. Therefore, additions of 1 to 5% O₂ or 3 to 25% CO₂ to the shielding gas, produce a noticeable improvement in arc stability. The optimum amount of oxygen or CO₂ to be added is a function of the work surface condition, the joint geometry, the welding position, and the base metal composition.⁹⁰

Several researchers^{78,92,93,107,110-113,124-125} have studied the effects of oxygen and hydrogen additions to a nitrogen-containing shielding gas on the resulting nitrogen concentration in the weld pool. These gas additions have significant effects on the resulting ni-

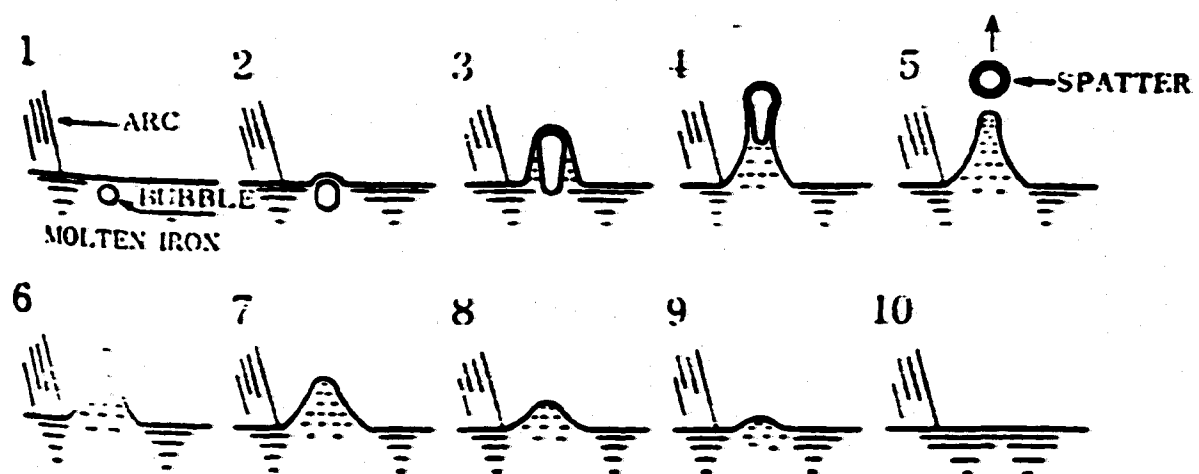


Figure 2.38. Schematic diagram showing a model for the ejection of a spattering particle from liquid iron during arc melting.⁶⁸

nitrogen concentration in the weld metal, and, in particular, the addition of a small amount of oxygen to the shielding gas increases the nitrogen concentration in the weld metal.^{60,92,93,110,115} Kobayashi *et al.*¹¹⁰ and Verhagen *et al.*¹¹¹ have performed a series of GMA welding experiments with several multiple component shielding gas atmospheres containing air, oxygen, and carbon-dioxide. Nitrogen concentrations in the weld metal for several of these shielding gas mixtures are shown⁹² in Figure 2.39. In each case, the nitrogen concentration reaches a maximum value significantly higher than the nitrogen saturation value at atmospheric pressure. The shape of the curve depends on the carrier gas used.¹¹¹⁻¹¹³

It is obvious that the nitrogen concentration in the weld metal is significantly enhanced with oxygen or CO₂ present in the shielding gas. The authors¹¹¹ point to the possibility that the presence of oxygen in the shielding gas allows the weld metal to accommodate more nitrogen or that the nucleation of N₂ bubbles is hindered. In addition to these effects, the presence of oxygen in the shielding gas can lead to the formation of an oxygen-rich surface layer, which may retard the passage of nitrogen being desorbed from the weld metal. Since the pick-up of nitrogen from the arc atmosphere is not affected by the addition of oxygen, the loss from the liquid metal must be decreased in order to achieve the nitrogen concentrations observed.

Pokhodnya *et al.*¹²⁵ and others^{40,92,93,115,124} have hypothesized that the presence of NO in these plasma resulting from the interaction between nitrogen and oxygen is the main contributor to this enhancement. There is currently no unified theory to explain this behavior, but two mechanisms for the formation of NO in the plasma phase above the weld metal are shown below.



With the addition of CO₂ to the shielding gas, Blake⁹³ proposed that NO in the arc column is formed by the following reaction:

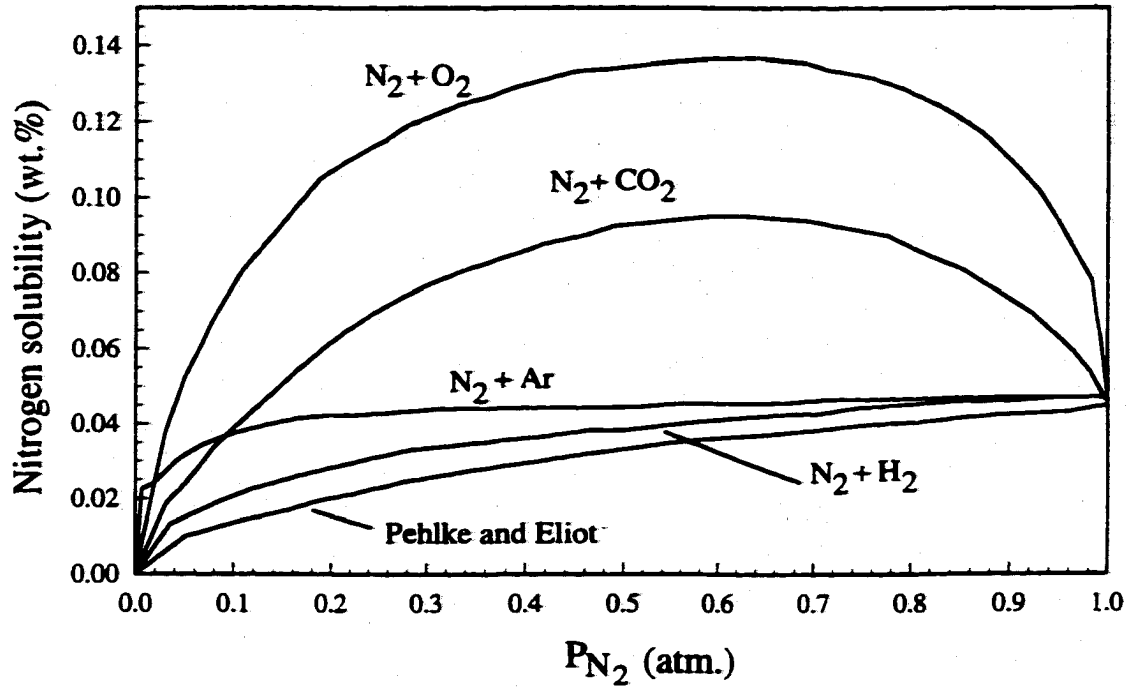


Figure 2.39. Relationship between the nitrogen concentration and the nitrogen partial pressure (P_{N_2}) for several oxygen containing shielding gas mixtures during the GMA welding of iron samples.¹¹⁰



At comparatively low temperatures (3500 to 4000 K) in the arc column, oxygen reacts with nitrogen to form NO. As NO is transported to the surface of either the metal droplets or the weld pool, it dissociates at the lower temperatures present there. The atomic gases are then rapidly dissolved into the iron. Based on this proposed reaction mechanism, it is believed that the lower dissociation temperature of NO leads to an increased amount of monatomic nitrogen (N) near the metal surface. Therefore, the addition of oxygen to the nitrogen-containing shielding gas may lead to higher than otherwise expected partial pressures of monatomic nitrogen near the metal surface, thus leading to higher nitrogen concentration in the weld metal.

Ouden⁴⁰ has suggested that the NO molecules present in the hotter arc column will diffuse to the cooler liquid surface, allowing the reaction shown below to occur. This reaction not only produces an increased partial pressure of monatomic nitrogen above the weld metal surface, but it also produces an iron oxide layer on the weld metal surface. As previously discussed, this oxide layer can inhibit the desorption of nitrogen gas from the solidifying weld metal, thus leading to an increased amount of nitrogen remaining in the weld metal.



On the other hand, hydrogen additions to the nitrogen-containing shielding gas have the opposite effect on the nitrogen concentration. Several authors^{78,92,93} have shown that hydrogen additions cause the nitrogen concentration in the weld metal to decrease to levels below that observed for solely nitrogen additions to the shielding gas. Kuwana and Kokawa⁹³ performed a series of GTA welding experiments on pure iron samples at atmospheric pressure with shielding gases containing both nitrogen and hydrogen. In general, the nitrogen concentrations in the weld metal, shown in Figure 2.40, are lower than

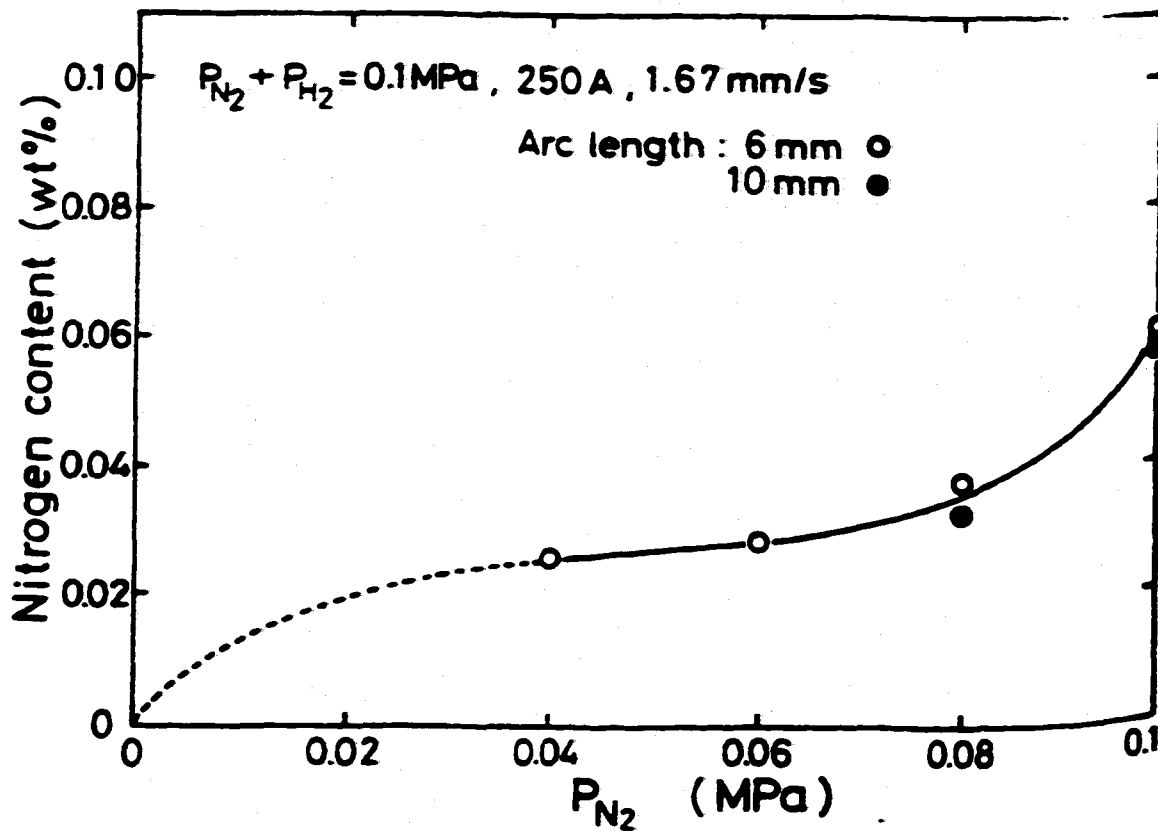
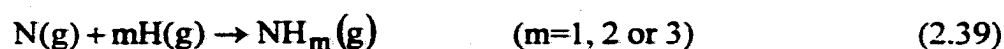


Figure 2.40. Relation between the nitrogen concentration in the weld metal and the nitrogen partial pressure for nitrogen-hydrogen gas mixtures at a welding current of 250 A, arc lengths of 6 and 10 mm, and a travel speed of 1.67 mm/sec.¹⁰⁷

those observed for shielding gases containing only nitrogen.⁹³ Rather than remaining constant at higher nitrogen partial pressures, though, the nitrogen concentrations in the weld metal slowly increase as the nitrogen partial pressure is increased. This increase in the nitrogen concentration is due in part to the influence of a second dissociation reaction, that of H₂. This reaction in the arc column is believed to lead to better thermal efficiency in the arc, thus leading to a larger penetration area and a slower cooling rate. A decreased cooling rate thus leads to a larger amount of nitrogen evolution from the weld metal, which results in lower residual nitrogen concentrations.

Takeda and Nakamura⁷⁸ have attributed this reduction in the nitrogen concentration to the conversion of the dissociated nitrogen in the arc column to a hydrogen-nitride species. They have divided the welding process into a several areas, including the high temperature zone of the plasma arc, the thermal boundary layer of the plasma arc adjacent to the surface of the melt, the surface of the melt, and the bulk of the melt. In the high temperature region of the plasma arc, temperatures reach levels above 6000 K, allowing for nitrogen and hydrogen to be completely dissociated. Within the thermal boundary layer, the temperature drops to that of the liquid iron surface, which has been reported to be between 2000 and 2600 K. In the thermal boundary layer, NH_m, N, and H are in equilibrium, and the rates for recombination are neglected. Therefore, the following reaction occurs with both nitrogen and hydrogen present in the shielding gas:



Based on this framework, the authors⁷⁸ have developed a semi-quantitative analysis for determining the nitrogen concentration in the weld metal as shown below:

$$\frac{[\%N]}{[\%N]_{so}} = \left[\frac{1}{1+K_m(2P_{H_2}^\circ)^m} + \left(\frac{k'_{am}}{k'_a} \right) \frac{K_m(2P_{H_2}^\circ)^m}{1+K_m(2P_{H_2}^\circ)^m} \right]^{1/2} \quad (2.40)$$

where K_m denotes the equilibrium constant for the reaction, $NH_m \rightarrow N + mH$, $P_{H_2}^\circ$ and $P_{N_2}^\circ$ are the apparent partial pressures of hydrogen and nitrogen, respectively, $[\%N]$ is the nitrogen solubility, $[\%N]_{SO}$ is the nitrogen solubility at $P_H = 0$, k'_{am} is the apparent rate constant of nitrogen absorption from NH_m (where $m=1, 2, \text{ or } 3$), and k'_a is the apparent rate constant for nitrogen absorption.

2.4 PROPOSED MECHANISMS FOR ENHANCED NITROGEN DISSOLUTION

2.4.1 Interaction Between Plasma Phase and Weld Pool

Nitrogen concentrations typically exceed those calculated by Sieverts' Law during arc melting and arc welding operations.^{31-33,40,46} A general agreement in the observed results suggests a common mechanism for nitrogen dissolution in both arc melting and arc welding operations. This mechanism is not well understood due to the range and complexity of the related arc and weld pool phenomena. A number of researchers have thus attempted to develop both qualitative and semi-quantitative models for the nitrogen dissolution reaction.^{29-33,40,45,47,64,67,68,111,126,127} These models are similar to the steady-state models developed for arc melted conditions.^{28-35,60} Ouden and Griebeling,³⁰ for example, proposed that the nitrogen is adsorbed into the weld pool directly under the arc and is then desorbed at the weld periphery. The amount of nitrogen leaving the liquid metal will increase with increasing nitrogen concentration, and a steady state will be reached when the amount of nitrogen entering the weld pool per unit time equals the amount of nitrogen leaving the weld pool per unit time.

Verhagen *et al.*¹¹¹ developed a model to explain the resulting nitrogen concentration and the formation of porosity in the weld metal. The model, shown¹¹¹ in Figure 2.41, is based on the arc temperature, the degree of dissociation, the condition of the liquid material, and the weld metal cooling rate. The presence of nitrogen atoms in the arc column is a primary contributor in explaining the supersaturation of nitrogen in the weld metal. As the heat source moves past a specific point along the weld line, the weld metal at this location passes through a sequence of events. First, the weld metal is heated and subsequently begins to melt (1). After melting, the liquid metal in contact with the arc heats

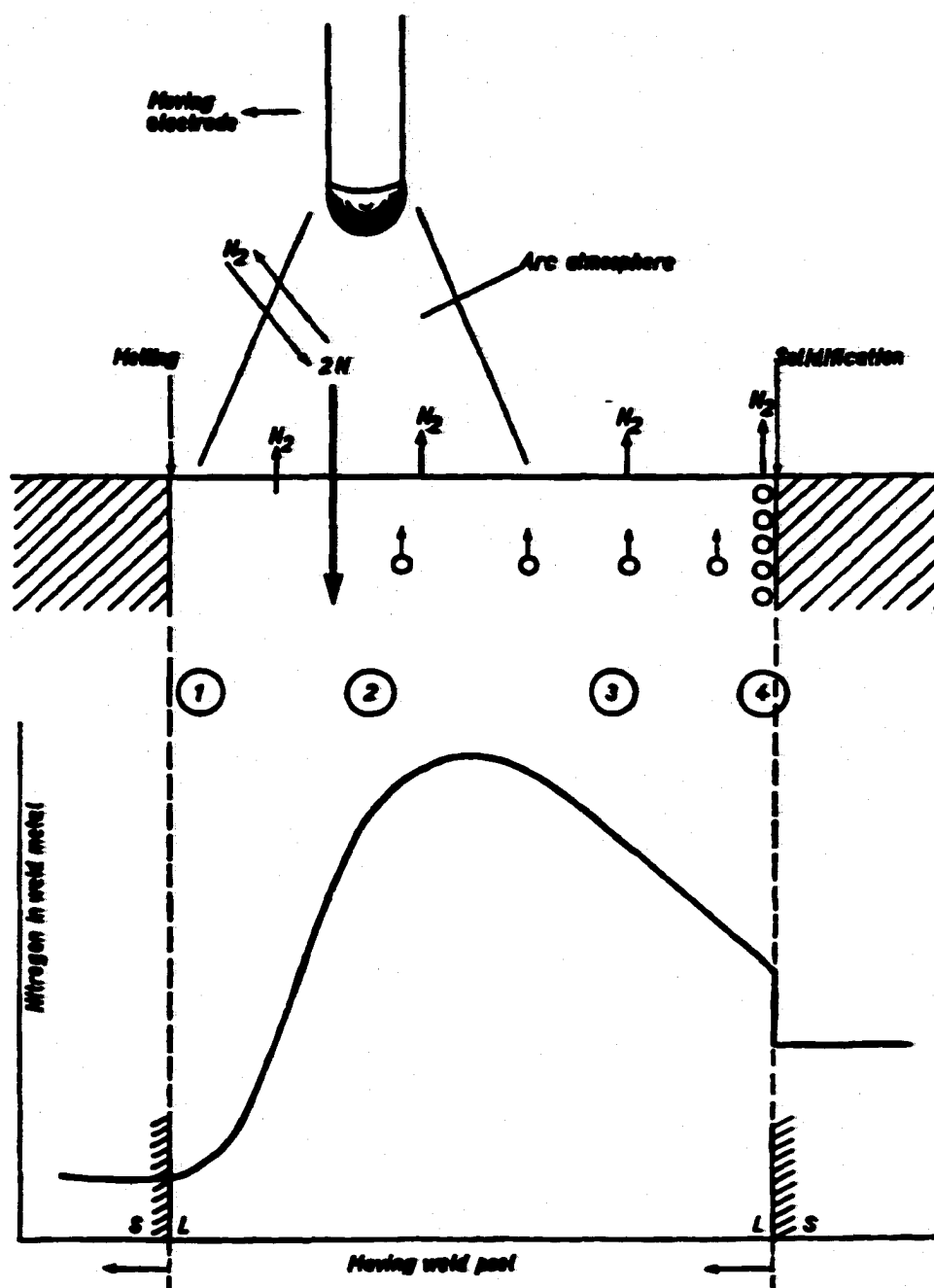


Figure 2.41. Schematic representation of the nitrogen content of a weld metal under a moving welding arc in an atmosphere containing nitrogen.¹¹¹

up, (2), and once the arc passes, the liquid metal in contact with the shielding gas cools, (3), and finally solidifies, (4). Nitrogen enters the weld metal predominantly in stage (2) through the melt surface layer, from where it is further transported throughout the liquid metal by diffusion and convection. If the nitrogen concentration exceeds the nitrogen saturation value in the interior of the weld metal, N_2 gas bubbles with a pressure slightly exceeding one atmosphere may be formed. The availability of suitable nucleation sites, such as oxide particles, will determine the nitrogen concentration at which the evolution of N_2 bubbles will actually occur.

As the arc moves, the liquid metal left behind comes in contact with the shielding gas outside the arc column, where the gaseous phase contains molecular nitrogen and a negligible amount of N atoms. At this point, the absorption of diatomic nitrogen will also occur, and the nitrogen concentration in the weld metal depends on whether the current nitrogen concentration is higher or lower than what would be in equilibrium with the amount of nitrogen molecules present in the shielding gas. If the weld metal exposure to the arc atmosphere has been sufficient, the nitrogen concentration will diminish in this stage. Whether equilibrium is reached before solidification sets in depends on the available reaction time and rate.

Upon solidification, nitrogen diffusion between liquid and solid iron becomes prominent. The nitrogen solubility in solid iron is lower than in the liquid metal at the melting temperature, 0.015 wt.% and 0.045 wt.%, respectively. Nitrogen concentrations much greater than 0.015 wt.% are commonly observed in the weld metals. Therefore, it is apparent that the loss of nitrogen from the solid to the gas phase is rather small and is due, in part, to the rapid slowing down of nitrogen diffusion in the bulk solid as the temperature drops. When the solid phase is formed, N atoms will diffuse across the interface to liquid iron. If the solidification front moves into the liquid, it is not possible for these atoms to become uniformly distributed in the liquid, resulting in a higher nitrogen concentration in front of the moving interface.

Cross *et al.*¹²⁶ have proposed a similar model in which the nitrogen concentration in the weld pool is driven by two simultaneous equilibrium conditions. The first of these conditions occurs beneath the arc, where the weld pool will attempt to approach its equi-

librium solubility (C_{E2}) with the monatomic nitrogen. A second equilibrium solubility (C_{E1}) exists at the periphery of the weld pool with diatomic nitrogen. After a period of time, a balance between nitrogen adsorption in the arc column and nitrogen desorption at the periphery will be achieved and a steady-state condition will prevail. It is then assumed that the rate of change of nitrogen concentration (dC/dt) in the weld pool is proportional to this deviation from equilibrium. The following relationship describes this condition:

$$\frac{dC}{dt} = k_1 A_1 (C_{E1} - C) + k_2 A_2 (C_{E2} - C) \quad (2.41)$$

where A_1 and A_2 are the surface areas of the weld pool periphery and that directly under the arc, respectively, and k_1 and k_2 represent the corresponding rate constants. By integrating Equation (2.41), the following relationship is derived:

$$C = C_s + (C_0 - C_s) e^{-[k_1 A_1 + k_2 A_2]t} \quad (2.42)$$

where C_0 is the initial concentration of the base metal and C_s is the steady-state concentration. This model is difficult to apply on a practical level. The application requires the values of parameters, k_1 , k_2 , A_1 , and A_2 , which are not generally available. In addition, the model is based on an assumption of a constant temperature across the weld pool surface, which is commonly characterized by steep temperature gradients.

It has also been suggested⁴⁰ that ionic nitrogen is the dominant species responsible for the high nitrogen contents in the weld metal. These ions are transported under the influence of the electric field towards the cathode or work piece, where dissolution would take place. Ouden⁴⁰ has developed a modified form of Sieverts' Law to take into account the deviations occurring due to the lack of equilibrium and to describe the nitrogen concentrations observed during welding. The following relationship has thus been developed:

$$C_N = K_1 \sqrt{P_{N_2}} + K_2 P_N + K_3 P_{N^+} + \dots \quad (2.43)$$

where P_{N_2} , P_N , P_{N^+} represent the partial pressures of diatomic nitrogen, monatomic nitrogen, and monatomic nitrogen ions, respectively, and K_1 , K_2 , and K_3 are the proportionality constants for the absorption of this species into the weld metal. The difference in absorption at the cathode and anode is due to differences in the temperature, reaction time, and reaction surface. On the other hand, other calculations have shown that the contribution of nitrogen ions to the total arc current is so small that it can be neglected.

2.4.2 Development of Two Temperature Model

The models discussed in the previous section provide a framework for understanding the nitrogen dissolution reaction during arc welding. On the other hand, they are rather incomplete and do not provide a means for determining the nitrogen concentration in the weld pool. In a related study, Gedeon and Eagar¹²⁷ examined the absorption of hydrogen during the GMA welding of low alloy steels. Based on their results, they have developed a model based on the dissociation of diatomic hydrogen in the arc column at a temperature higher than that directly above the weld pool surface and the absorption of the resulting monatomic species in the weld pool. The amount of atomic nitrogen in the plasma phase is higher than that obtained solely from the consideration of thermal equilibrium between these two species at the system temperature and pressure.

Mundra and DebRoy⁴⁷ have utilized this theoretical concept to develop a semi-quantitative model to calculate the nitrogen concentration in the weld pool. Their model is based on the premise that if the actual concentration of the atomic nitrogen were known, its concentration in iron could be estimated by considering equilibrium between the atomic nitrogen and the metal. In the plasma, the extent of dissociation of diatomic nitrogen depends on factors such as the nature of the power source, the energy dissipated, the overall system geometry, and the nature of the diatomic gas. To take these various mechanisms into account, a hypothetical dissociation temperature, T_d , is defined. At this temperature, the thermal dissociation of N_2 produces a partial pressure of atomic nitrogen

gas equal to that in the plasma phase. Figure 2.42(a) defines the relationship⁴⁷ between the percentage dissociation of diatomic nitrogen species and the effective dissociation temperature.⁴⁵ In this figure, it is shown that the dissociation of diatomic nitrogen increases with increasing temperature.

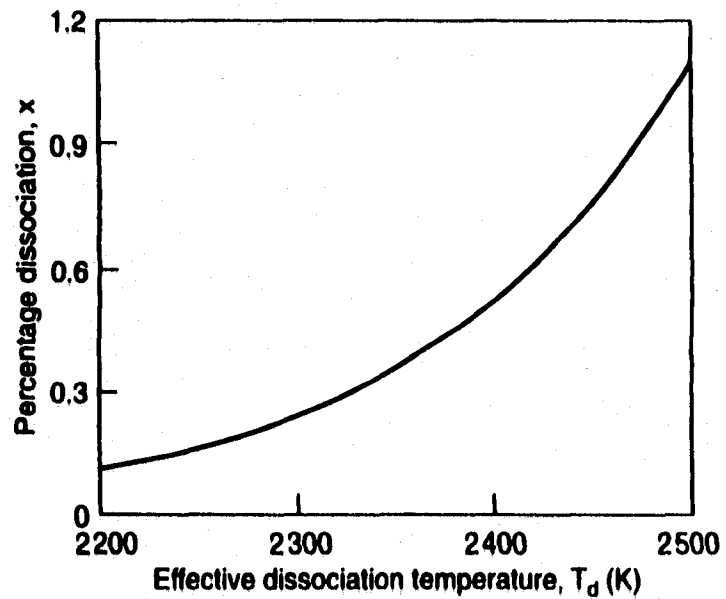
Combining the dissociation of $N_2(g)$ at T_d and the dissolution of $N(g)$ in liquid iron at T_s , the equilibrium nitrogen concentration in iron can be defined by the following relationship. Since the extent of dissociation of diatomic nitrogen is considered to be rather low under typical welding conditions, P_{N_2} can be assumed to be equal to the partial pressure of N_2 in the inlet gas, $P_{N_2}^{\text{in}}$.

$$\underline{N}(\text{wt}\%) = \sqrt{P_{N_2}^{\text{in}}} e^{-\frac{1}{R} \left(\frac{\Delta G^\circ|_{T_d}}{T_d} + \frac{\Delta G^\circ|_{T_s}}{T_s} \right)} \quad (2.44)$$

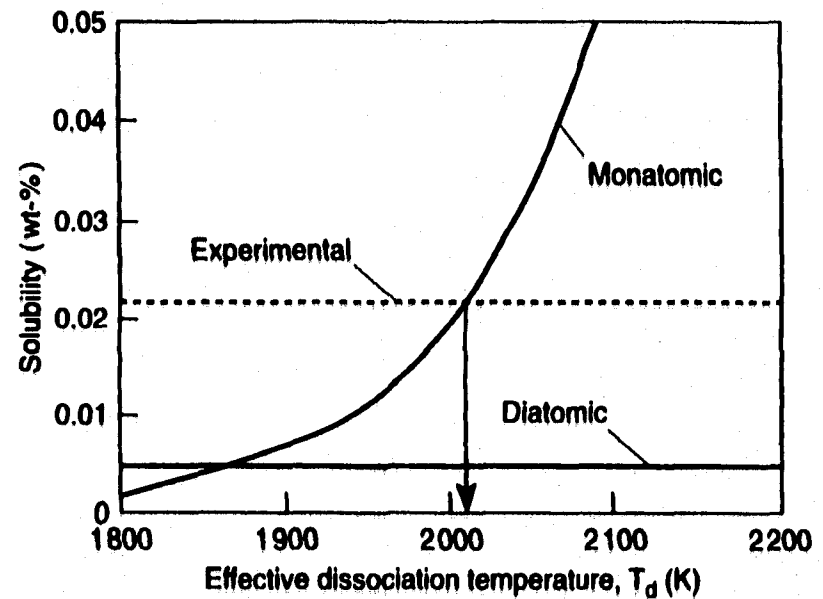
The nitrogen concentration in the iron weld pool is explained by assuming that the atomic nitrogen partial pressure in the plasma can be effectively modeled by a hypothetical thermal dissociation of diatomic nitrogen, at a temperature of dissociation, T_d . Figure 2.42(b)⁴⁷ shows the effective dissociation temperature based on the experimental solubility and the theoretical monatomic nitrogen solubility from the experimental work of Ouden and Griebing.³⁰ In this figure, the effective dissociation temperature is higher than the sample temperature, thus providing a higher partial pressure of monatomic nitrogen species than that possible through thermal dissociation processes alone. The exact difference between the surface temperature and the dissociation temperature is unknown.

2.4.3 Validation of Two-Temperature Model

When this model is applied to several sets of data, the calculated dissociation temperatures fall in a range of 100 to 300 C above the sample temperature.⁶³ An example of these results is plotted⁵¹ in Figure 2.43. In this figure, the calculated dissociation temperatures for the nitrogen concentrations in solid iron samples exposed to glow discharge



(a)



(b)

Figure 2.42(a&b). (a) Plot of effective dissociation temperature vs. percent nitrogen dissociated⁴⁷ for the experimental conditions of Bandopadhyay *et al.*⁴⁵ (b) Plot of solubility vs. effective dissociation temperature⁴⁷ for the experimental conditions of Ouden and Griebing.³⁰

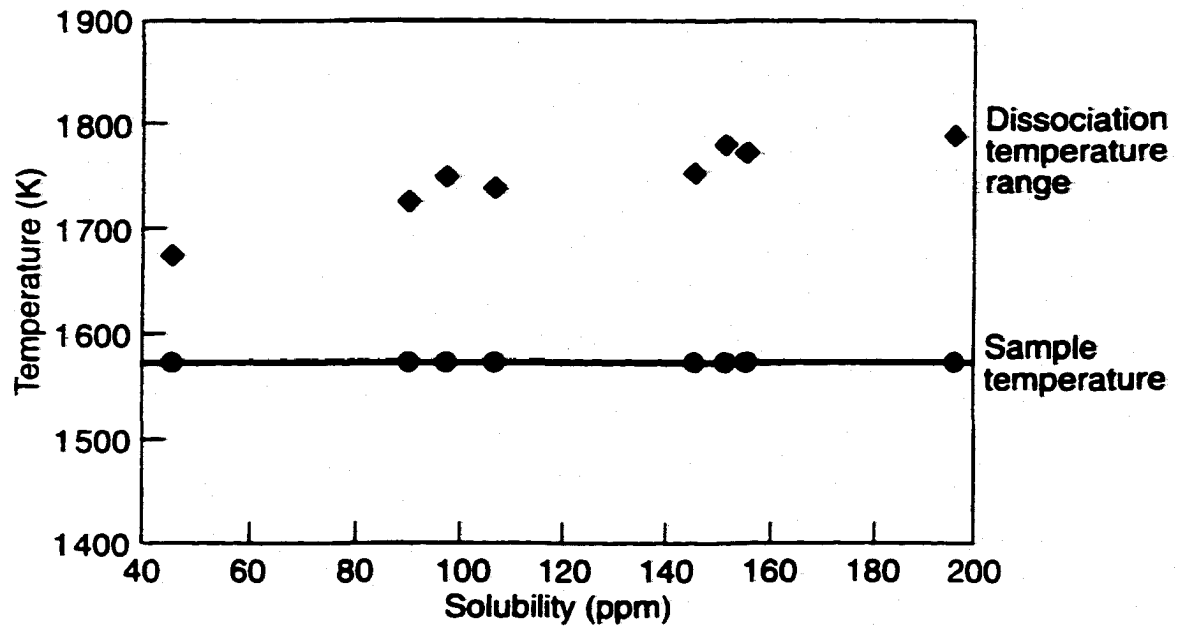


Figure 2.43. Comparison of the experimental nitrogen concentrations (ppm) and the effective dissociation temperatures over the range of experimental conditions.⁵¹

plasmas are plotted as a function of experimental nitrogen concentrations. The calculated dissociation temperatures for the experimental concentrations are approximately 100 to 215 C higher than the sample temperature.⁵¹ It can thus be assumed that if experimental data are not available, a rough estimate of the nitrogen concentration may be obtained by assuming a hypothetical dissociation temperature about 100 to 200 K higher than the sample temperature.

These results have arisen from the application of the two-temperature model to isothermal conditions. On the other hand, weld pool surface temperatures show significant spatial variations. Since this temperature distribution is not known, a simplifying assumption of the temperature distribution on the surface of the weld pool has been made.¹²⁸ Figure 2.44(a) shows temperature profiles for two assumed values of maximum temperature on the weld pool surface, T_{MAX} . In this figure, r^* is the dimensionless distance from the axis of the arc to the liquid/metal interface defined by the radial distance from the center of the molten pool. The calculated equilibrium nitrogen concentrations on the weld pool surface are shown in Figure 2.44(b). The nitrogen concentrations are higher at the outer edge of the weld pool, which has also been observed in the case of hydrogen dissolution.

Since the liquid metal in the weld pool undergoes vigorous recirculation,^{72,73} the nitrogen from the surface is readily transported to the interior of the weld pool. This vigorous recirculation of material thoroughly mixes the nitrogen absorbed at the weld pool surface throughout the weld pool interior. It is thus assumed that the overall nitrogen concentration of the weld metal, $(wt.\%N)_{AV}$ is determined by an average concentration of nitrogen on the weld pool surface:

$$(wt.\%N)_{AV} = \frac{1}{\pi r_0^2} \int_0^{r_0} 2\pi r [wt.\%N] dr = \int_0^1 2r^* [wt.\%N] dr^* \quad (2.45)$$

where $[wt.\%N]$ is the local value of nitrogen concentration at any location on the weld pool surface.

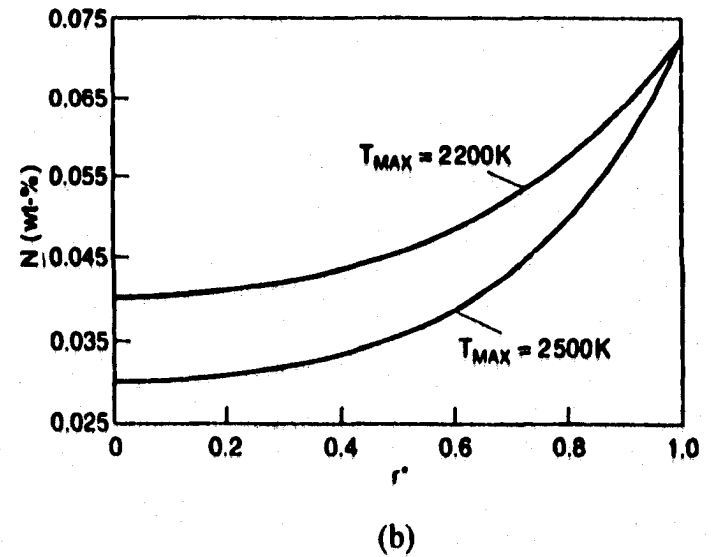
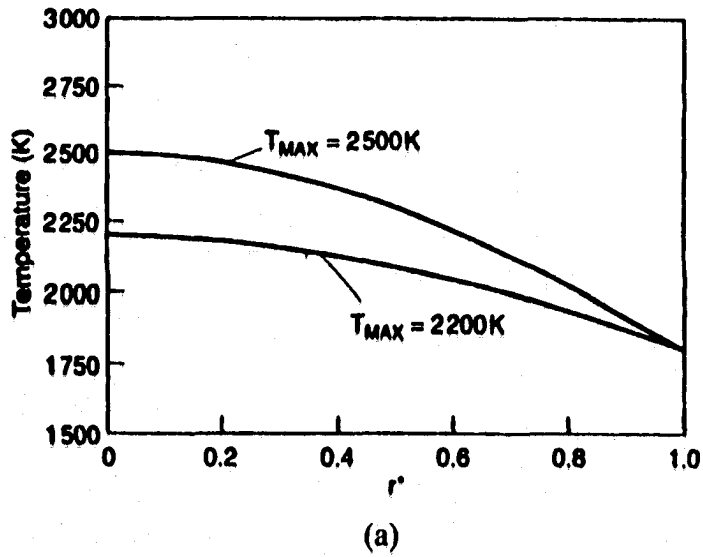


Figure 2.44(a&b). Computed values for (a) temperature¹²⁸ and (b) nitrogen concentration across the radius of the weld pool for T_{MAX} values of 2500 and 2200 K and a diatomic nitrogen partial pressure of 0.6 atm.⁵¹

In view of the continuous movement of the arc with respect to the workpiece, the plasma continually mixes with the surrounding gas, and the mixing tends to reduce the concentration of atomic nitrogen in the plasma. Therefore, a relatively small difference between the dissociation temperature and the surface temperature of the weld pool is appropriate. A difference of 125 C between the dissociation temperature and the surface temperature is assumed, and nitrogen concentrations¹⁰⁷ in the weld pool, as a function of p_{N_2} , are shown⁵¹ in Figure 2.45 for two values of T_{MAX} . The calculations show that a fair agreement between the computed results and the experimental data. An improved agreement between the experimental data and the predicted values can be obtained by selecting a temperature difference of about 100 C between the surface temperatures and the dissociation temperatures.

2.5 OVERVIEW

Nitrogen concentrations significantly larger than Sieverts' Law calculations are commonly found when an iron or steel sample comes into contact with a nitrogen containing plasma. These plasmas are usually formed above liquid iron or steel during arc melting and arc welding operations. The relationship between the nitrogen concentration and the amount of nitrogen added to the shielding gas is similar in all cases. For example, the nitrogen concentration rises sharply with increases in the nitrogen partial pressures until it reaches a maximum level equivalent to the nitrogen concentration calculated by Sieverts' Law at a nitrogen partial pressure of 1 atm. Monatomic nitrogen present in the plasma phase is responsible for these high nitrogen concentration levels.

The study of the nitrogen dissolution reaction during the arc melting and welding of iron and steels has concentrated on the effects of changes in experimental conditions on the final nitrogen concentration. These various experimental conditions include changes in the arc current, arc voltage, travel speed, the base metal chemistry, and nitrogen addition to the shielding gas. Changes in the arc current, arc voltage, and arc length have little to no effect on the nitrogen concentration in the weld pool. Even variations in the

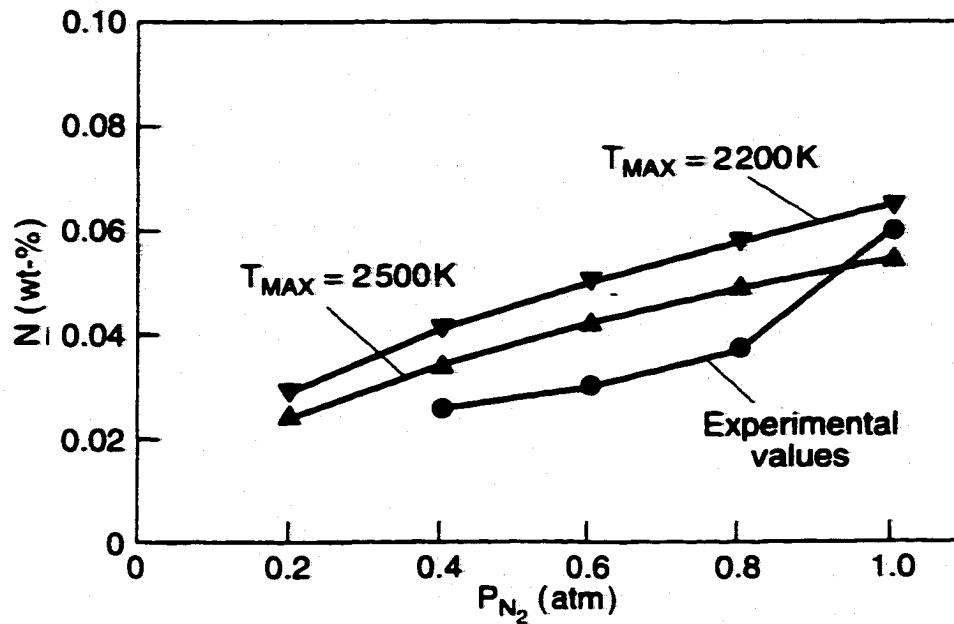


Figure 2.45. Comparison between the experimental nitrogen concentrations observed during the GTA welding of pure iron¹⁰⁷ and computed nitrogen concentration predictions.⁵¹

nitrogen addition to the shielding gas produce little to no change in the nitrogen concentrations observed in the weld pool.

In arc welding, the high temperatures present within the arc are responsible for accelerating the nitrogen absorption reaction. On the other hand, the nitrogen absorption reaction is not always completed, since the arc may travel quickly within a short period of time, allowing the weld metal to quickly solidify. The travelling arc complicates the situation, since the nitrogen is absorbed in the portion of the weld pool exposed to the arc and simultaneously escapes into the atmosphere from the solidifying metal behind the arc column. These facts can explain the differences between the nitrogen content of the weld metal and the equilibrium solubility and the arc melting of the same metal.

On the other hand, changes in the base metal chemistry affect the nitrogen concentration observed in the metal during arc melting and arc welding operations. The effects of alloying element additions, such as chromium and nickel, are identical to those observed in the absence of an arc or plasma phase in contact with the base metal. For example, the addition of chromium increases the final nitrogen concentration to levels above that observed in pure iron, and the addition of nickel decreases the final nitrogen concentration. Surface active elements, such as oxygen and sulfur, present in the liquid metal also have significant effects on the nitrogen concentration in the metal. The addition of these elements significantly increases the magnitude of the nitrogen concentration in the liquid metal. In all these cases, though, a behavior similar to that described above is observed with the addition of these alloying element to the base metal.

Several researchers have developed models based on the assumption that the nitrogen concentration observed in the liquid metal is the result of a competitive process between nitrogen absorption in the arc column and nitrogen desorption in the region outside the arc column. With surface active elements present in the weld metal, a reaction layer is formed on the surface of the solidifying metal and does not allow the nitrogen to desorb. Thus, the nitrogen concentration in the liquid metal is further enhanced. This model also takes into account the saturation of the liquid metal with nitrogen, which is defined as the maximum amount of nitrogen which the liquid metal can hold with a nitrogen partial pressure equivalent to the total pressure of the atmosphere above the liquid metal.

Others have concentrated on the role of the plasma phase in the nitrogen dissolution reaction. The plasma phase acts as a source of enhanced amounts of monatomic nitrogen for the nitrogen absorption reaction on the weld metal surface. This amount of monatomic nitrogen is difficult to determine, but has been estimated by assuming that the nitrogen dissociation reaction takes place at an effective dissociation temperature higher than that found on the liquid metal surface. Effective temperatures in the range of 100 to 300°C higher than the surface temperature provide good approximations and give calculated nitrogen concentrations close to the experimental results.

Further complexities are also found with the addition of nitrogen to the shielding gas. For example, the formation of porosity in the weld metal is the result of excessive gas absorption in the liquid metal. On the other hand, the correlation between the nitrogen dissolution reaction and porosity formation is not well understood. Additions of small amounts of oxygen and hydrogen to nitrogen-containing shielding gases also have noticeable effects on the resulting nitrogen concentration in liquid iron. Like porosity formation, there is little understanding of the physical processes controlling these reactions. Even though qualitative models exist to explain these phenomena, more work is required to provide a greater qualitative and quantitative understanding.

This review has provided a summary of the existing knowledge of the nitrogen dissolution reaction in iron and steel during arc melting and welding processes. In general, previous researchers have examined the effects of nitrogen additions to the shielding gas and changes in the process parameters on the resulting nitrogen concentration in the base metal. Different welding processes and base metal chemistries have been lumped together without examining the different mechanisms responsible for these observed nitrogen concentrations. Rigorous quantitative analyses of the plasma phase and of the transport properties in the weld pool have also not been performed. Therefore, there is little understanding of the interaction between the plasma phase, the nitrogen absorption reaction, and the transport of nitrogen in the weld pool. A comprehensive model, which takes into account the unique properties of each of these components, thus needs to be developed.

REFERENCES

- ¹ Metals Handbook, Vol. 1, 9th ed., (ASM International, Materials Park, OH), 1978, 116.
- ² Metals Handbook, Vol. 1, 9th ed., (ASM International, Materials Park, OH), 1978, 556.
- ³ J.J. Moore, Chemical Metallurgy, 2nd ed., (Butterworth-Heinemann, Oxford), 1990.
- ⁴ M.C. Flemings, Solidification Processing, (McGraw-Hill, New York), 1974, 203-210.
- ⁵ Binary Alloy Phase Diagrams, 2nd ed., ed. by T.B. Massalski, H. Okamoto, P.R. Subramanian, and L. Kacprzak, (ASM International, Materials Park, OH), 1990, 1728-1730.
- ⁶ K.H. Jack, "Binary and Ternary Interstitial Alloys I. The Iron-Nitrogen System: The Structures of Fe_4N and Fe_2N ", *Proc. Roy. Soc. A*, 1948, 195, 34-40.
- ⁷ K.H. Jack, "The Occurrence and the Crystal Structure of α'' - Iron Nitride; A New Type of Interstitial Alloy Formed During the Tempering of Nitrogen-Martensite", *Proc. Roy. Soc. A*, 1951, 208, 216-224.
- ⁸ K.H. Jack, "The Iron-Nitrogen System: The Crystal Structures of ϵ -Phase Iron Nitrides", *Acta Cryst.*, 1952, 5, 404-411.
- ⁹ K.H. Jack, "The Iron-Nitrogen System: The Preparation and the Crystal Structure of Nitrogen-Austenite (γ) and Nitrogen-Martensite (α')", *Proc. Roy. Soc. A*, 1951, 208, 200-215.
- ¹⁰ T. Bell and W.S. Owen, "Martensite in Iron-Nitrogen Alloys", *J. Iron Steel Inst.*, 1967, 205(4), 428-434.
- ¹¹ T. Bell and W.S. Owen, "The Thermodynamics of the Martensite Transformation in Iron-Carbon and Iron-Nitrogen", *Trans. Met. Soc. AIME*, 1967, 239, 1940-1949.
- ¹² R. D. Pehlke, Unit Processes in Extractive Metallurgy, Elsevier, New York. (1979), 141-145.
- ¹³ F. Elliott and M. Gleiser, Thermochemistry for Steelmaking I, Addison-Wesley Publishing Co., Reading, MA, 1963, 75.
- ¹⁴ H.E. McGannon, ed., The Making, Shaping and Treating of Steel, 9th edition, United States Steel Corporation, 1971, 330-331.
- ¹⁵ R.D. Pehlke and J.F. Elliott, "Solubility of Nitrogen in Liquid Iron Alloys. 1. Thermodynamics", *Trans. AIME*, 1960, 218, 1088-1101.

- ¹⁶ J.D. Fast and M.B. Verrijp, "Solubility of Nitrogen in Alpha-Iron", *J. Iron Steel Inst.*, 1955, 180, 337-343.
- ¹⁷ R.B. McLellan and K. Alex, "The Thermodynamics of Nitrogen Austenite", *Scripta Met.*, 1970, 4, 967-970.
- ¹⁸ N.S. Corney and E.T. Turkdogan, "The Effect of Alloying Elements on the Solubility of Nitrogen in Iron. Part I: The Solubility of Nitrogen in Pure Iron and in 2.83% Silicon Iron", *J. Iron Steel Inst.*, 1955, 180, 344-348.
- ¹⁹ H. Wada and R.D. Pehlke, "Solubility of Nitrogen in Liquid Fe-Cr-Ni Alloys Containing Manganese and Molybdenum", *Met. Trans. B*, 1977, 8B, 675-682.
- ²⁰ H. Wada and R.D. Pehlke, "Nitrogen Solution and Titanium Nitride Precipitation in Liquid Fe-Cr-Ni Alloys", *Met. Trans. B*, 1977, 8B, 443-450.
- ²¹ J.C. Humbert and J.F. Elliott, "The Solubility of Nitrogen in Liquid Fe-Cr-Ni Alloys", *Trans. AIME*, 1960, 218, 1076-1088.
- ²² D.S. Shahapurkar and W.M. Small, "Effect of Titanium on the Nitrogen Solubility in Complex Liquid Fe-Cr-Ni Alloys: Part I", *Met. Trans. B*, 1987, 18B, 225-230.
- ²³ D.S. Shahapurkar and W.M. Small, "Effect of Titanium on the Nitrogen Solubility in Complex Liquid Fe-Cr-Ni Alloys: Part II", *Met. Trans. B*, 1987, 18B, 231-235.
- ²⁴ W.M. Small and R.D. Pehlke, "The Effect of Alloying Elements on the Solubility of Nitrogen in Liquid Iron-Chromium-Nickel Alloys", *Trans. Metall. Soc. AIME*, 1968, 242, 2501-2505.
- ²⁵ H. Schenck, M. Froberg, and H. Graf, "Investigation of the Influence of the Equilibria of Nitrogen with Liquid Iron Solutions by the Addition of Further Elements, I", *Arch. Eisenhüttenw.*, 1958, 29, 673.
- ²⁶ H. Schenck, M. Froberg, and H. Graf, "Investigation of the Influence of the Equilibria of Nitrogen with Liquid Iron Solutions by the Addition of Further Elements, II", *Arch. Eisenhüttenw.*, 1959, 30, 533.
- ²⁷ S. Maekawa and Y. Nakagawa, "Solubility of Nitrogen in Liquid Iron and Iron Alloys", *Tetsu-to-Hagane, J. Iron Steel Inst.*, 1959, 45, 255.
- ²⁸ F.S. Death and D.A. Haid, "Method for Adding Nitrogen to Molten Metals", U.S. Patent No. 3,257,197, 1966.

- ²⁹ V.I. Lakomskii and G.F. Torkhov, "Absorption of Nitrogen from a Plasma by Liquid Metal", *Soviet Physics-Doklady*, 1969, 13(11), 1159-1161.
- ³⁰ G. den Ouden and O. Griebing, "Nitrogen Absorption during Arc Welding", in Recent Trends in Welding Science and Technology, ed. S.A. David and J.M. Vitek, (ASM International, Materials Park, OH), 1990, 431-435.
- ³¹ J.D. Katz and T.B. King, "The Kinetics of Nitrogen Absorption and Desorption from a Plasma Arc by Molten Iron", *Met. Trans. B*, 1989, 20B, 175-185.
- ³² T. Kuwana and H. Kokawa, "The Nitrogen Absorption of Arc-Melted Iron and Stainless Steel", *Trans. Jap. Weld. Soc.*, 1988, 19(2), 12-19.
- ³³ P.D. Blake and M.F. Jordan, "Nitrogen Absorption during the Arc Melting of Iron", *J. Iron Steel Inst.*, 1971, 209(3), 197-200.
- ³⁴ S. Tochowicz, J. Siwka, and J. Jowza, "Alloying Steel with Nitrogen from Gas Phase in High-Pressure Plasma Reactor", *Steel Research*, 1993, 64(3), 165-170.
- ³⁵ T. El Gammel, B. Yostos, and F.N. El Sabbahy, "Nitrogen Pick-up of Steels through a Plasma Process", *Steel Research*, 1992, 63(6), 234-241.
- ³⁶ S. Kou, Welding Metallurgy, John Wiley and Sons, New York, 1987, 61-63.
- ³⁷ M.A. Uman, Introduction to Plasma Physics, (McGraw-Hill Book Company, New York), 1964, 1-7.
- ³⁸ F.F. Chen, Introduction to Plasma Physics and Controlled Fusion, Volume 1: Plasma Physics, (Plenum Press, New York), 1984, 3-7.
- ³⁹ A.B. Cambel, Plasma Physics and Magnetofluidmechanics, (McGraw-Hill Book Company, New York), 1963.
- ⁴⁰ G. den Ouden, "The Role of Nitrogen in Electric Arc Welding", *Philips Weld. Reporter*, 13(1), 1977, 1-6.
- ⁴¹ J.D. Fast, "The Dissociation of Nitrogen in the Welding Arc", *Philips Res. Rep.*, 1947, 2, 382-398.
- ⁴² G.J. Dunn and T.W. Eagar, "Metal Vapors in Gas Tungsten Arcs: Part II. Theoretical Calculations of Transport Properties", *Met. Trans. A*, 1986, 17A, 1865-1871.
- ⁴³ K.S. Drellishak, C.F. Knopp, and A.B. Cambel, "Partition Functions and Thermodynamic Properties of Argon Plasma", *Phys. of Fluids*, 1963, 6(9), 1280-1288.

- ⁴⁴ K.S. Drellishak, D.P. Aeschliman, and A.B. Cambel, "Partition Functions and Thermodynamic Properties of Nitrogen and Oxygen Plasmas", *Phys. of Fluids*, 1965, 8(9), 1590-1600.
- ⁴⁵ A. Bandopadhyay, A. Banerjee, and T. DebRoy, "Nitrogen Activity Determination in Plasmas", *Metall. Trans. B*, 1992, 23B, 207-214.
- ⁴⁶ S.K. Mitra, "Active Nitrogen", *Phys. Rev.*, 1953, 90, 516-22.
- ⁴⁷ K. Mundra and T. DebRoy, "A General Model for Partitioning of Gases between a Metal and Its Plasma Environment", *Metall. and Mater. Trans. B*, 1995, 26B, 149-157.
- ⁴⁸ J. Szekely, Fluid Flow Phenomena in Metals Processing, (Academic Press, New York), 1979.
- ⁴⁹ S. Kou and Y.H. Wang, "Weld Pool Convection and Its Effect", *Weld. J.*, 1986, 65(3), 63s-70s.
- ⁵⁰ P.G. Jönsson, J. Szekely, R.T.C. Choo, and T.P. Quinn, "Mathematical Models of Transport Phenomena Associated with Arc-Welding Process: A Survey", *Modelling Simul. Mater. Sci. Eng.*, 1994, 2, 995-1016.
- ⁵¹ T.A. Palmer and T. DebRoy, "Physical Modeling of Nitrogen Partition between the Weld Metal and Its Plasma Environment", *Weld J.*, 1996, 75(7), 197s-207s.
- ⁵² H.C. Peebles and R.L. Williamson, "The Role of the Metal Vapor Plume in Pulsed Nd:YAG Laser Welding on Aluminum 1100", Proceedings of LAMP '87, 1987, 19-24.
- ⁵³ R.F. Bunshah, J.M. Blocher, Jr., *et al.*, Deposition Technologies for Films and Coatings: Developments and Applications, Noyes Publications, Park Ridge, NJ, 1982, 41.
- ⁵⁴ A. Banerjee and T. DebRoy, "Optical Emission Investigation of the Plasma Enhanced Chemical Vapor Deposition of Silicon Oxide Films", *J. Vac. Sci. Technol. A*, 10(6), 1992, 3395-3400.
- ⁵⁵ J.F. Key, M.E. McIlwain, and L. Isaacson, Sixth International Conference on Gas Discharges and Their Applications, Pub. No. 189, Part 2 (New York, NY, Institution of Electrical Engineers, 1980), 235-236.
- ⁵⁶ R.K. Holbert, Jr., T.M. Mustaleski, Jr., and L.D. Frye, "Laser Beam Welding of Stainless Steel Sheet", *Welding Journal*, 1987, 77(8), 21-25.

- ⁵⁷ J.A. McKay *et al.*, "Pulsed-CO₂-Laser Interaction with Aluminum in Air: Thermal Response and Plasma Characteristics", *J. Appl. Phys.*, 1979, 50(5), 3231-3240.
- ⁵⁸ T.J. Rockstroh and J. Mazumder, "Spectroscopic Studies of Plasma during CW Laser Materials Interaction", *J. Appl. Phys.*, 1987, 61(3), 917-923.
- ⁵⁹ T.A. Palmer, "Physical Modeling of the Nitrogen Partition between the Weld Metal and its Plasma Environment", Masters Thesis, The Pennsylvania State University, 1995.
- ⁶⁰ D. Neuschutz, Y. Zhai, and A. Hauck, "Nitrogen Transfer into Plasma Heated Steel Melts as a Function of Arc Polarity", *Steel Research*, 1994, 65(6), 219-224.
- ⁶¹ T. Kuwana, H. Kokawa, and N. Muramatsu, "Effects of Chromium and Nickel on Nitrogen Absorption of Arc-Melted Iron", *Trans. Jap. Weld Soc.*, 1989, 20(1), 10-16.
- ⁶² M. Uda and S. Ohno, "Nitrogen Absorption in Liquid Fe-Ta, Fe-Ni, Fe-Co, and Fe-Si Alloys During Arc Melting", *Trans. Nat. Res. Inst. Metals*, 1975, 17(2), 15-22.
- ⁶³ H. Wada, K. Gunji, and T. Wada, "Solubility of Nitrogen and Interaction with Oxygen in Liquid Iron", *Trans. ISIJ*, 1968, 8, 323-328.
- ⁶⁴ M. Uda and T. Wada, "Solubility of Nitrogen in Arc-Melted and Levitation-Melted Iron and Iron Alloys", *Trans. Nat. Res. Inst. Metals*, 1968, 10(2), 21-33.
- ⁶⁵ T. Kuwana, H. Kokawa, and K. Naitoh, "Effects of Chromium and Nickel on Nitrogen Absorption of Iron Weld Metal during Gas Tungsten Arc Welding", *Trans. Jap. Weld. Soc.*, 1990, 21(2), 85-91.
- ⁶⁶ O.P. Sinha and R.C. Gupta, "Fe-Cr Melt Nitrogenation when Exposed to Nitrogen Plasma", *ISIJ International*, 1993, 33(5), 567-576.
- ⁶⁷ M. Uda and S. Ohno, "Effect of Surface Active Elements on Nitrogen Content of Iron under Arc Melting", *Trans. Nat. Res. Inst. Met.*, 1973, 15(1), 20-28.
- ⁶⁸ M. Uda and S. Ohno, "Spattering Phenomenon for Iron-Nitrogen System during Arc Melting", *Trans. Nat. Res. Inst. Metals*, 1978, 20(6), 358-365.
- ⁶⁹ J.W. Hooijmans and G. den Ouden, "The Influence of Oxygen on Nitrogen Absorption during Arc Melting of Iron", *Weld. J.*, 1992, 71(10), 377s-380s.
- ⁷⁰ G.R. Belton, "Langmuir Adsorption, the Gibbs Adsorption Isotherm, and Interfacial Kinetics in Liquid Metal Systems", *Met. Trans. B*, 1976, 7B, 35-42.

- ⁷¹ G.R. Belton and R.A. Belton, "On the Rate of Desulfurization of Liquid Iron by Hydrogen", *Trans. ISIJ*, 1980, 20(2), 87-91.
- ⁷² T. DebRoy and S.A. David, "Physical Processes in Fusion Welding", *Reviews of Modern Physics*, 1995, 67(1), 85-112.
- ⁷³ S.A. David and T. DebRoy, "Current Issues and Problems in Welding Science", *Science*, 1992, 257, 497-502.
- ⁷⁴ W. Pitscheneder, T. DebRoy, K. Mundra, and R. Ebner, "Role of Sulfur and Processing Variables on the Temporal Evolution of Weld Pool Geometry during Multikilowatt Laser Beam Welding of Steels", *Weld. J.*, 1996, 75(3), 71s-80s.
- ⁷⁵ S.A. David and T. DebRoy, "Current Issues and Problems in Welding Science", *Science*, 1992, 257, 497-502.
- ⁷⁶ N. Hirashima, R.T.C. Choo, J.M. Toguri, and K. Mukai, "The Effect of Surface Movements on Nitrogen Mass Transfer in Liquid Iron", *Metall. and Mater. Trans. B*, 1995, 26B, 971-980.
- ⁷⁷ F.D. Richardson, Physical Chemistry of Melts in Metallurgy, Volume 2. (Academic Press, London), 1974, 426-434.
- ⁷⁸ K. Takeda and Y. Nakamura, "Behavior of Nitrogen in Plasma Arc Melting", *Trans. ISIJ*, 1978, 18, 641-647.
- ⁷⁹ T.P. Battle and R.D. Pehlke, "Kinetics of Nitrogen Absorption/Desorption by Liquid Iron and Iron Alloys", *Ironmaking and Steelmaking*, 1986, 13(4), 176-189.
- ⁸⁰ Y.K. Rao and H.G. Lee, "Rate of Nitrogen Absorption in Molten Iron: Part 1. Experimental", *Ironmaking and Steelmaking*, 1985, 12(5), 209-220.
- ⁸¹ Y.K. Rao and H.G. Lee, "Rate of Nitrogen Absorption in Molten Iron: Part 2. Mathematical Model", *Ironmaking and Steelmaking*, 1985, 12(5), 221-232.
- ⁸² T. Choh, T. Moritani, and M. Iouye, "Kinetics of Nitrogen Desorption of Liquid Iron, Liquid Fe-Mn, and Fe-Cu alloys Under Reduced Pressures", *Trans. ISIJ*, 1979, 19(4), 221-230.
- ⁸³ K. Ito, K. Amano, and H. Sakao, "Kinetic Study on Nitrogen Absorption and Desorption of Molten Iron", *Trans. ISIJ*, 1988, 28(1), 41-48.

- ⁸⁴ S. Ban-Ya, F. Ishii, Y. Iguchi, and T. Nagasaka, "Rate of Nitrogen Desorption from Liquid Iron-Carbon and Iron-Chromium Alloys with Argon", *Met. Trans. B*, 1988, 19B, 233-242.
- ⁸⁵ M. Inouye and T. Choh, "Some Considerations on the Nitrogen Transfer across Gas-Liquid Iron Interface", *Trans. ISIJ*, 1972, 12, 189-196.
- ⁸⁶ P. Grieveson and E.T. Turkdogan, "Kinetics of Reaction of Gaseous Nitrogen with Iron, Part II: Kinetics of Nitrogen Solution in Alpha and Delta Iron", *Trans. Met. Soc. AIME*, 1964, 230, 1604-1609.
- ⁸⁷ R.D. Pehlke and J.F. Elliott, "Solubility of Nitrogen in Liquid Iron Alloys II. Kinetics", *Trans. Met. Soc. AIME*, 1963, 227, 844-855.
- ⁸⁸ O.P. Sinha and R.C. Gupta, "Nitrogen Absorption Rate under Plasma Arc Compared to Resistance and Induction Melting", *ISIJ International*, 1994, 34(3), 295-297.
- ⁸⁹ L.A. Greenberg and A. McLean, "Nitrogen Pick Up in Low Sulphur Steel", *Ironmaking and Steelmaking*, 1982, 9(2), 58-63.
- ⁹⁰ Welding Handbook, Volume 2, Welding Processes, 8th Edition, R.L. O'Brien, (American Welding Society, Miami, FL), 1991, 109.
- ⁹¹ A.E. Guile, "The Electric Arc", in The Physics of Welding, ed. by J.F. Lancaster. (Pergamon Press, Oxford), 1984, 109-133.
- ⁹² C.J. Allum, "Nitrogen Absorption from Welding Arcs", *Bulletin of Welding Research Council*, 369, Dec. 1991-2, 68-84.
- ⁹³ P.D. Blake, "Oxygen and Nitrogen in Weld Metal", *Weld. Res. Int.*, 9(1), 1979, 23-56.
- ⁹⁴ A. Banerjee, C. Onneby, T. DebRoy, and M. Small, "Nitrogen Dissolution in the Weld Pool", in International Trends in Welding Science and Technology, ed. S.A. David and J.M. Vitek, (ASM International, Materials Park, OH), 1993, 39-44.
- ⁹⁵ T.A. Palmer, K. Mundra, and T. DebRoy, "Nitrogen Dissolution in the Weld Metal – Current Status and Research Opportunities", in Mathematical Modelling of Weld Phenomena 3, ed. by H. Cerjak, (The Institute of Materials, London), 1997, 3-40.
- ⁹⁶ T. Kuwana, "The Oxygen and Nitrogen Absorption of Iron Weld Metal During Arc Welding", in Advanced Joining Technologies, Proceedings of the International Institute of Welding Congress on Joining Research, ed. T.H. North, (Chapman and Hall, New York), 1990, 117-128.

- ⁹⁷ R. Menon and D.J. Kotecki, "Literature Review-Nitrogen in Stainless Steel Weld Metal", WRC Bulletin 369, 142-161.
- ⁹⁸ T. Kuwana, H. Kokawa, and M. Saotome, "Quantitative Prediction of Nitrogen Absorption by Steel during Gas Tungsten Arc Welding", in Mathematical Modelling of Weld Phenomena 3, ed. by H. Cerjak, (The Institute of Materials, London), 1997, 64-81.
- ⁹⁹ J.F. Lancaster, "The Physics of Fusion Welding. Part 1: The Electric Arc in Welding", *IEEE Proceedings*, 1987, 135B(5), 233-254.
- ¹⁰⁰ J.F. Key, J.W. Chan, and M.E. McIlwain, "Process Variable Influence on Arc Temperature Distribution", *Weld. J.*, 62(7), 1983, 179s-184s.
- ¹⁰¹ A.E.F. Gick, M.B.C. Quigley, and P.H. Richards, "The Use of Electrostatic Probes to Measure the Temperature Profiles of Welding Arcs", *J. Phys. D: Appl. Phys.*, 6, 1973, 1941-1949.
- ¹⁰² J. Wendelstorf, I. Decker, H. Wohlfahrt, and G. Simon, "TIG and Plasma Arc Modelling: A Survey", in Mathematical Modelling of Weld Phenomena 3, ed. by H. Cerjak, (The Institute of Materials, London, 1997), pp. 848-897.
- ¹⁰³ R.T.C. Choo, J. Szekely, and R.C. Westhoff, "On the Calculation of the Free Surface Temperature of Gas-Tungsten-Arc Weld Pools from First Principles: Part I. Modeling the Welding Arc", *Met. Trans. B*, 23B, 1992, 357-369.
- ¹⁰⁴ G.N. Haddad and A.J.D. Farmer, "Temperature Measurements in Gas Tungsten Arcs", *Weld. J.*, 1985, 64(12), 399s-342s.
- ¹⁰⁵ A.J.D. Farmer and G.N. Haddad, "Temperature Determinations in a Free-Burning Arc: I. Experimental Techniques and Results in Argon", *J. Phys. D: Appl. Phys.*, 1984, 17, 1189-1196.
- ¹⁰⁶ H.A. Dinulescu and E. Pfender, "Analysis of the Anode Boundary Layer of High Intensity Arcs", *J. Appl. Phys.*, 1980, 51(6), 3149-3157.
- ¹⁰⁷ T. Kuwana and H. Kokawa, "The Nitrogen Absorption of Iron Weld Metal during Gas Tungsten Arc Welding", *Trans. Jap. Weld. Soc.*, 1986, 17(1), 20-26.
- ¹⁰⁸ T. Kuwana, H. Kokawa, and K. Naitoh, "The Nitrogen Absorption of Stainless Steel Weld Metal during Gas Tungsten Arc Welding", *Trans. Jap. Weld. Soc.*, 1986, 17(2), 15-21.
- ¹⁰⁹ S. Hertzman, R. Jargelius Pettersson, R. Blom, E. Kivineva, and J. Eriksson, "Influence of Shielding Gas Composition and Welding Parameters on the N-Content and Cor-

- rosion Properties of Welds in N-Alloyed Stainless Steel Grades”, *ISIJ Int.*, 1996, 36(7), 968-976.
- ¹¹⁰ T. Kobayashi, T. Kuwana, and Y. Kikuchi, “Arc Atmosphere and Nitrogen Content of Weld Metal”, *Welding in the World*, 5(2), 1967, 58-73.
- ¹¹¹ J.G. Verhagen, G. den Ouden, A. Liefkens, and G.W. Tichelaar, “Nitrogen Absorption by Ferritic Weld Metal During Arc Welding”, *Metal Construction and British Welding Journal*, 1970, 2, 135-143.
- ¹¹² N.A. Miller and G.R. Salter, “Effects of Nitrogen in CO₂ Welding”, *British Welding Journal*, 1964, 11, 18-27.
- ¹¹³ J.E. O’Brien and M.F. Jordan, “Nitrogen Absorption and Porosity in CO₂ Arc Welding of Mild Steel”, *Metal Construction and British Welding Journal*, 1971, 3, 299-303.
- ¹¹⁴ T. Kuwana, H. Kokawa, and S. Matsuzaki, “Nitrogen Absorption of Iron Weld Metal in Pressurized Welding Atmospheres”, *Trans. Jap. Weld. Soc.*, 1987, 18(1), 12-18.
- ¹¹⁵ V.I. Galinich and V.V. Podgaetskii, “The Effects of Nitrogen on Weld Porosity When Welding Steel Under Argon or CO₂ Shielding”, *Avt. Svarka*, 1961, 16(2), 18-27.
- ¹¹⁶ R.A. Woods, “Porosity and Hydrogen Absorption in Aluminum Welds”, *Weld. J.*, 1974, 53(3), 97s-108s.
- ¹¹⁷ R.P. Martukanitz and P.R. Michnuk, “Sources of Porosity in Gas Metal Arc Welding of Aluminum”, *Aluminium*, 1982, 58(5), 276-279.
- ¹¹⁸ J. Littleton, J. Lammas, and M.F. Jordan, “Nitrogen Porosity in Gas Shielded Arc Welding of Copper”, *Weld J.*, 1974, 53(12), 561s-565s.
- ¹¹⁹ T. Kuwana, H. Kokawa, and A. Honda, “Effects of Nitrogen and Titanium on Porosity and Microstructure in Ar-N₂ Gas Metal Arc Welded Copper”, *Trans. Jap. Weld. Soc.*, 1987, 18(2), 159-166.
- ¹²⁰ K.N. Kapranov and G.G. Utlinskii, “Porosity in Welding Copper in Nitrogen Plasma”, *Welding Int.*, 1991, 5(9), 735-737.
- ¹²¹ V.N. Lipodaev, *et al.*, “Porosity of Joints in the Welding of High-Alloy Austenitic Nitrogen-Bearing Steels”, *Avt. Svarka*, 1975, No. 8, 12-15.
- ¹²² J.E. Ramirez, B. Han, and S. Liu, “Effect of Welding Variables and Solidification Substructure on Weld Metal Porosity”, *Metall. And Mater. Trans. A*, 1994, 25A, 2285-2294.

- ¹²³ S. Ohno and M. Uda, "Effects of Hydrogen and Nitrogen on Blowhole Formation in Pure Nickel at Arc Welding and Non-Arc Melting", *Trans. Nat. Res. Inst. Metals*, 1981, 23(4), 243-248.
- ¹²⁴ H. Thier and R. Killing, "Absorption of Oxygen and Nitrogen during Welding - Spatial Sequence of the Reactions", *Welding and Casting*, 1991, 2, 5-8.
- ¹²⁵ I.K. Pokhodnya and A.P. Pal'tsevich, "The Part Played by Oxygen in the Absorption of Nitrogen by Metal During Arc Welding", *Avt. Svarka*, 1971, 25(2), 8-11.
- ¹²⁶ C.E. Cross, H. Hoffmeister, and G. Huisman, "Nitrogen Control in Hyperbaric Welding of Duplex Stainless Steel", *Welding in the World*, 1997, 39(3), 154-161.
- ¹²⁷ S.A. Gedeon and T.W. Eagar, "Thermochemical Analysis of Hydrogen Absorption in Welding", *Weld. J.*, 1990, 69, 264s-271s.
- ¹²⁸ P.A.A. Khan, "Mass Transfer During Laser Welding of High Manganese Stainless Steels, Ph.D. Thesis, The Pennsylvania State University, 1987, 72-74.

Chapter 3

THERMODYNAMIC CALCULATION OF SPECIES DENSITIES IN THE PLASMA PHASE

3.1 INTRODUCTION

The presence of a plasma phase is a common feature in a wide range of materials processing operations, including thin film deposition via sputtering or chemical vapor deposition (CVD) and plasma nitriding processes. This plasma phase contains excited species not normally observed in typical gas-metal systems. These excited species take part in the reactions and, in many cases, significantly enhance the rate or efficiency of these reactions. Knowledge of the number densities of these activated species can provide needed insight into the dominant reaction processes. For example, knowledge of the monatomic nitrogen partial pressure in the reactive sputtering or CVD processing of a TiN thin film can lead to the development of operating parameters which make the process more efficient.

During arc welding, the plasma phase in the arc column interacts with the liquid metal in the weld pool. With nitrogen present in the plasma phase, concentrations of this element in an iron weld pool are significantly enhanced, and monatomic nitrogen species in the plasma phase above the weld pool surface are considered responsible. As discussed in the previous chapters, researchers have recognized the important role of monatomic nitrogen and incorporated it into their models.¹⁻⁴ On the other hand, the inclusion of the monatomic nitrogen partial pressure in these models has been rather qualitative in nature or the result of a simplification of the nitrogen dissociation reaction. In order to accurately calculate the nitrogen concentration in the weld pool, the actual monatomic nitrogen partial pressure in the plasma phase must be known. A quantitative study of the species density of monatomic nitrogen and other species present in the plasma phase formed from either pure gases or gas mixtures has not, till now, been integrated into a study of the nitrogen dissolution reaction.

3.2 CURRENT STATUS OF SPECIES DENSITY CALCULATIONS IN NITROGEN-CONTAINING PLASMAS

Enhanced concentrations of hydrogen and other diatomic gases in the weld metal are based on the dominant role of monatomic gaseous species in the plasma phase.¹⁻⁶ If the concentration of the monatomic species in the gas phase near the weld pool is known, the species concentration can then be estimated by considering equilibrium between the monatomic gas and metal. Dissociation of diatomic nitrogen into monatomic nitrogen species in the welding arc has been well established.^{5,7} The resulting concentration of atomic nitrogen in the plasma is higher than what would be obtained solely from consideration of thermal equilibrium between these two species at the temperature and pressure prevailing at the metal surface. Rather, the amount of monatomic nitrogen in the plasma phase depends on the nature of the power source, the energy dissipated, the overall system geometry, and the nature of the diatomic gas.³ It is very difficult to quantify many of these factors which determine the species concentrations in the welding arc, thus creating many problems in calculating the residual nitrogen concentration in the weld metal.

Taking these difficulties into account, Gedeon and Eagar² have developed a model, which considers both the dissociation and absorption reactions. The dissociation of the diatomic gas is governed by the temperature of the plasma phase adjacent to the weld pool surface, while the absorption reaction is governed by the surface temperature of the weld pool. Based on this model, several available plasma-metal systems have been analyzed, and the enhanced nitrogen solubility in the weld metal is explained by a super-equilibrium concentration of monatomic species above the weld metal.³

Uda and Wada⁸ also recognized the complexity of the interaction between the plasma phase and the weld metal. They divided the absorption reaction into three areas: the bulk plasma area, a boundary layer adjacent to the weld metal, and the weld metal itself. Within this boundary layer, the temperature is considered to be nearly equal to the melting point of the molten metal. The experimentally observed nitrogen concentrations under arc melting conditions correspond to a partial pressure of atomic nitrogen obtained by

equilibrium thermal dissociation of diatomic nitrogen at about 3000 K. This temperature is much lower than the temperatures in the arc column.

It has been well known that the presence of a small amount of oxygen enhances the nitrogen concentration in the weld metal.⁹⁻¹⁴ This behavior is illustrated earlier in Figure 2.41, which also includes a comparison with equilibrium nitrogen concentrations.¹⁵ Several authors¹²⁻¹³ have hypothesized that the presence of NO in the plasma, which is the result of the interaction between nitrogen and oxygen, is the main contributor to this enhancement. Currently there is no unified theory to explain this behavior. Furthermore, there is no experimental evidence available for the presence of NO. Detailed calculation of species concentrations in an Ar-N₂-O₂ system, considering possible reaction between the nitrogen and oxygen, can provide a definitive understanding of this behavior.

A number of researchers have investigated the characteristics of the plasma phase in the arc column.^{12,14,16-21} Theoretical studies of the number densities of various species in a plasma phase include those performed by Dunn and Eagar,¹⁹ who investigated inert gaseous plasmas, and by Drellishak *et al.*,²⁰⁻²¹ who investigated both inert gaseous and pure nitrogen and oxygen plasmas at atmospheric pressures. Dunn and Eagar¹⁸⁻¹⁹ have calculated the electron densities and the resulting transport properties of argon and helium plasmas with small additions of metal vapors. In order to calculate these transport properties, only ionization reactions need to be considered, given the dominant role of the electron density in determining the electrical and thermal conductivities. They therefore have calculated species and electron densities in the plasma phase using the Saha-Eggert relationship and the ideal gas law. Fast⁷ has investigated the dissociation of nitrogen in the welding arc based on thermodynamic calculations and ignoring the role of ionization reactions. Number density calculations for both nitrogen molecules and atoms over a range of temperatures have been determined from fundamental spectroscopic data. These studies provided a data base for the distribution of species in a plasma over a range of temperatures but have not been extended to temperatures approaching those on the weld pool surface. A rigorous quantitative analysis of the plasma phase to determine the concentration of various nitrogen-bearing species has not been performed.

The number densities of various gaseous species calculated here have been used to understand nitrogen dissolution in the weld pool. In order to provide a complete picture of the species present in the welding arc plasma, both dissociation and ionization reactions have been considered. The species densities for nitrogen, oxygen, argon, and helium plasmas have been calculated for both pure gases and mixtures. In addition, the role of oxygen on the enhanced nitrogen dissolution reaction is also investigated using these calculations. Finally, the nitrogen absorption reaction during arc welding is examined by considering the interaction between the plasma phase and the weld pool surface during GTA welding. Experimental verification of these calculations is achieved through the use of emission spectroscopic analysis of glow discharge plasmas.

3.2 CALCULATION METHODOLOGY

In order to calculate the number densities of species present in the plasma phase, ionization and dissociation reactions for both diatomic and monatomic species must be considered simultaneously. Furthermore, the balance of charge throughout the system and the conservation of mass must be considered. The ionization reactions of interest for a pure nitrogen plasma are as follows:

$$N_2 = N_2^+ + e^- \quad (3.1)$$

$$N = N^+ + e^- \quad (3.2)$$

Assuming local thermodynamic equilibrium, the relation between the various species densities can be expressed from the Saha-Eggert relation¹⁹⁻²¹ as follows:

$$\frac{n_e n_{N_2^+}}{n_{N_2}} = \frac{2(2\pi m_e kT)^{3/2}}{h^3} \frac{Z_{N_2^+}}{Z_{N_2}} e^{-(\epsilon_{N_2})/kT} \quad (3.3)$$

$$\frac{n_e n_{N^+}}{n_N} = \frac{2(2\pi m_e kT)^{3/2}}{h^3} \frac{Z_{N^+}}{Z_N} e^{-(\epsilon_N)/kT} \quad (3.4)$$

where n_e is the electron density, and n_{N_2} , $n_{N_2^+}$, n_N , and n_{N^+} are the number densities for each of the respective nitrogen species, m_e is the rest mass of an electron, k is the Boltzmann Constant, T is the electron temperature, h is Planck's Constant, Z_{N_2} , $Z_{N_2^+}$, Z_N , and Z_{N^+} are the partition functions for the respective nitrogen species, and ϵ_{N_2} and ϵ_N are the ground state energies for the nitrogen molecule and atom, respectively. The partition functions^{7,19-20} for a number of pure species are calculated in Appendix A.

The dissociation reaction of diatomic nitrogen is shown in Equation (3.5). Its equilibrium constant, K , is simplified in Equations (3.6) to (3.8), with the final relation to be used shown in Equation (3.8).



$$K_5 = \frac{p_N^2}{p_{N_2}} = \frac{(P_{tot})^2 (X_N)^2}{P_{tot} X_{N_2}} = P_{tot} \frac{(X_N)^2}{X_{N_2}} \quad (3.6)$$

$$K_5 = P_{tot} \frac{\left(\frac{n_N}{N_A}\right)^2}{\frac{n_{N_2}}{N_A}} = P_{tot} \frac{(n_N)^2}{n_{N_2}} \left(\frac{1}{N_A}\right) \quad (3.7)$$

$$K_5 = \frac{(n_N)^2}{n_{N_2}} \left(\frac{RT}{N_A}\right) \quad (3.8)$$

where P_{tot} is the total system pressure(atm), p_N is the partial pressure of monatomic nitrogen, p_{N_2} is the partial pressure of diatomic nitrogen, X_N and X_{N_2} are the mole fractions of N and N_2 , respectively, n_N and n_{N_2} are the number densities (m^{-3}) for N and N_2 , re-

spectively, R is the gas constant, and N_A is Avogadro's number, which is defined by the following relationship.

$$N_A \frac{P_{\text{tot}}}{RT} = \sum n \quad (3.9)$$

At temperatures commonly used for conventional materials processing, the standard free energy values are available and the value of K can be easily calculated. On the other hand, accurate thermodynamic data are not readily available for the high temperatures commonly found in the welding plasma. A recourse is to calculate the necessary data and the procedure used here is presented in Appendix B.

In the case of pure nitrogen plasma, there are five species concentrations, i.e., of n_{N_2} , $n_{N_2^+}$, n_N , n_{N^+} , and n_e to be determined. Thus, in addition to Equations (3.3), (3.4), and (3.8), two more equations must be developed, one based on the principle of quasineutrality in the plasma phase and the other based on the conservation of mass:

$$n_e = n_{N_2^+} + n_{N^+} \quad (3.10)$$

$$N_A \left(\frac{P}{RT} \right) = n_{N_2} + 2n_{N_2^+} + n_N + 2n_{N^+} \quad (3.11)$$

where P is the total pressure. Since the total number of species present in the plasma phase is based on the ideal gas law, a decrease in the number density of particles with an increase in temperature should be expected. Equations (3.3), (3.4), (3.8), and (3.10) through (3.11) can be solved simultaneously to obtain values of n_{N_2} , $n_{N_2^+}$, n_N , n_{N^+} , and n_e . To obtain the species densities over the range of temperatures commonly found in the welding arc, the system of equations must be solved simultaneously for each individual temperature.

Table 3.1. Summary of species considered in the species density calculations for oxygen, nitrogen, argon, and helium.

<u>Input Gas</u>	<u>Species Considered</u>
Argon	Ar, Ar ⁺ , Ar ⁺⁺
Helium	He, He ⁺
Nitrogen	N ₂ , N ₂ ⁺ , N, N ⁺
Oxygen	O ₂ , O ₂ ⁺ , O, O ⁺ , O ⁺⁺

When the plasma contains other gases, such as oxygen, additional species densities need to be considered. Table 3.1 lists the species of interest for each of the pure gases analyzed. For pure oxygen, the species densities to be determined include n_{O_2} , $n_{O_2^+}$, n_O , n_{O^+} , $n_{O^{++}}$, and n_e . These are obtained from the solution of the following system of six equations:

$$\frac{n_e n_{O_2^+}}{n_{O_2}} = \frac{2(2\pi m_e kT)^{3/2}}{h^3} \frac{Z_{O_2^+}}{Z_{O_2}} e^{-(\epsilon_{O_2})/kT} \quad (3.12)$$

$$\frac{n_e n_{O^+}}{n_O} = \frac{2(2\pi m_e kT)^{3/2}}{h^3} \frac{Z_{O^+}}{Z_O} e^{-(\epsilon_O)/kT} \quad (3.13)$$

$$\frac{n_e n_{O^{++}}}{n_{O^+}} = \frac{2(2\pi m_e kT)^{3/2}}{h^3} \frac{Z_{O^{++}}}{Z_{O^+}} e^{-(\epsilon_{O^+})/kT} \quad (3.14)$$

$$K_{12} = \frac{p_{O_2}^2}{p_{O_2}} = \frac{(n_O)^2}{n_{O_2}} \left(\frac{RT}{N_A} \right) \quad (3.15)$$

$$n_e = n_{O_2^+} + n_{O^+} + n_{O^{++}} \quad (3.16)$$

$$N_A \left(\frac{P}{RT} \right) = n_{O_2} + 2n_{O_2^+} + n_O + 2n_{O^+} + 3n_{O^{++}} \quad (3.17)$$

For pure monatomic inert gases such as argon and helium, no dissociation reaction needs to be considered. The argon species densities, i.e. n_{Ar} , n_{Ar^+} , $n_{Ar^{++}}$, and n_e , can be determined by the solution of the following system of equations.

$$\frac{n_e n_{\text{Ar}^+}}{n_{\text{Ar}}} = \frac{2(2\pi m_e kT)^{3/2}}{h^3} \frac{Z_{\text{Ar}^+}}{Z_{\text{Ar}}} e^{-(\epsilon_{\text{Ar}})/kT} \quad (3.18)$$

$$\frac{n_e n_{\text{Ar}^{++}}}{n_{\text{Ar}^+}} = \frac{2(2\pi m_e kT)^{3/2}}{h^3} \frac{Z_{\text{Ar}^{++}}}{Z_{\text{Ar}^+}} e^{-(\epsilon_{\text{Ar}^+})/kT} \quad (3.19)$$

$$n_e = n_{\text{Ar}^+} + 2n_{\text{Ar}^{++}} \quad (3.20)$$

$$N_A \left(\frac{P}{RT} \right) = n_{\text{Ar}} + 2n_{\text{Ar}^+} + 3n_{\text{Ar}^{++}} \quad (3.21)$$

This same methodology is used to calculate the species densities for helium, but only three species densities need to be solved, i.e., n_{He} , n_{He^+} , and n_e , since just a single ionization level needs to be considered. The following three equations are thus solved in order to determine the number densities of these species.

$$\frac{n_e n_{\text{He}^+}}{n_{\text{He}}} = \frac{2(2\pi m_e kT)^{3/2}}{h^3} \frac{Z_{\text{He}^+}}{Z_{\text{He}}} e^{-(\epsilon_{\text{He}})/kT} \quad (3.22)$$

$$n_e = n_{\text{He}^+} \quad (3.23)$$

$$N_A \left(\frac{P}{RT} \right) = n_{\text{He}} + 2n_{\text{He}^+} \quad (3.24)$$

When considering binary, ternary, or higher-order gas mixtures, the particle densities of the individual species can be calculated by considering a system of equations involving both the ionization and dissociation reactions and the overall charge and mass balances. For example, the species densities in an Ar-N₂-O₂ gas mixture at 1 atm. total pressure can be determined by solving a system of equations which takes into account the re-

actions for argon (Equations (3.18) and (3.19)), nitrogen (Equations (3.3), (3.4), and (3.8)), oxygen (Equations (3.12) through (3.15)), and the overall charge and mass balances in Equations (3.25) through (3.28).

$$n_e = X_{Ar}(n_{Ar^+} + 2n_{Ar^{++}}) + X_{N_2}(n_{N_2^+} + n_{N^+}) + X_{O_2}(n_{O_2^+} + n_{O^+} + 2n_{O^{++}}) \quad (3.25)$$

$$X_{Ar} \left(N_A \left(\frac{P}{RT} \right) \right) = n_{Ar} + 2n_{Ar^+} + 3n_{Ar^{++}} \quad (3.26)$$

$$X_{N_2} \left(N_A \left(\frac{P}{RT} \right) \right) = n_{N_2} + n_{N_2^+} + n_N + n_{N^+} \quad (3.27)$$

$$X_{O_2} \left(N_A \left(\frac{P}{RT} \right) \right) = n_{O_2} + 2n_{O_2^+} + n_O + 2n_{O^+} + 3n_{O^{++}} \quad (3.28)$$

where X_{Ar} , X_{N_2} , and X_{O_2} are the mole fractions of argon, nitrogen, and oxygen, respectively, in the feed gas into the welding arc. Both pure gases and binary and ternary gas mixtures have been analyzed using this methodology at total pressures of 1 atm. and a broad temperature range indicative of the temperatures in the welding arc.

The above calculation scheme does not take into account the formation of any intermediate species, such as NO, in the plasma phase. Several authors^{12,14} have hypothesized the presence of NO in plasmas containing nitrogen and oxygen, and several others^{10,12-14} have reported a further increase in the nitrogen solubility in the weld metal with oxygen present in the plasma phase, for which the presence of NO is considered responsible. Once the NO species is formed in the plasma phase, it also undergoes dissociation and ionization reactions, as shown in Equations (3.29) and (3.32). When compared with the extent of dissociation of pure N_2 and O_2 , NO is intermediate between the two. (See Figure 3.1.)

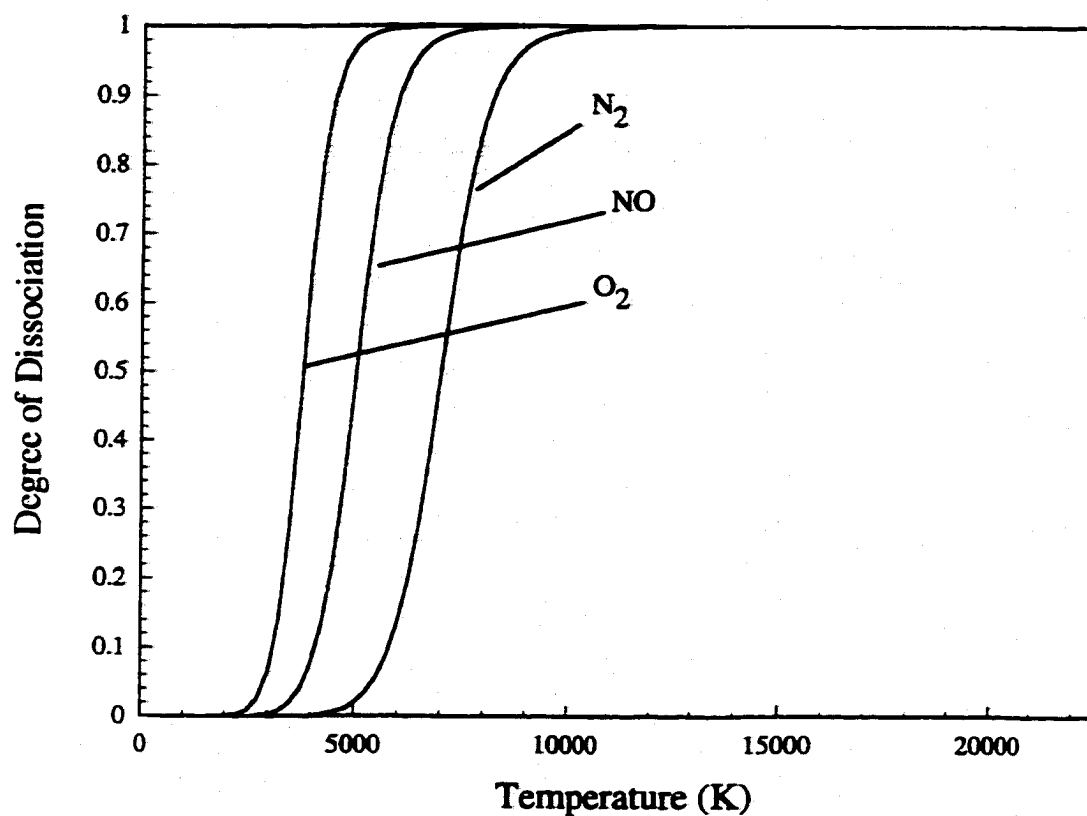


Figure 3.1. Comparison of the computed values for the extent of dissociation between N₂, O₂, and NO as a function of temperature. In this graph, a value of 0 for the degree of dissociation describes no dissociation occurring, while a value of 1 describes complete dissociation.



$$K_{29} = \frac{p_{\text{NPO}}}{p_{\text{NO}}} = \frac{n_{\text{N}}n_{\text{O}}}{n_{\text{NO}}} \left(\frac{RT}{N_A} \right) \quad (3.30)$$



$$\frac{n_e n_{\text{NO}^+}}{n_{\text{NO}}} = \frac{2(2\pi m_e kT)^{3/2} Z_{\text{NO}^+}}{h^3 Z_{\text{NO}}} e^{-(\epsilon_{\text{NO}})/kT} \quad (3.32)$$

In order to calculate the various species considering the interaction between nitrogen and oxygen, all of the reactions for the dissociation and ionization of nitrogen, oxygen, and NO must be solved along with the ionization reactions for either argon or helium. For the case of an Ar-8% N₂-2% O₂ system, the individual species densities can be determined by solving a system of equations which takes into account reactions for argon (Equations (3.18) and (3.19)), nitrogen (Equations (3.3), (3.4), and (3.8)), oxygen (Equations (3.12) through (3.15)), NO (Equations (3.30) and (3.32)), and the overall charge balance in Equation (3.33) and mass balances in Equations (3.25), (3.34), and (3.35).

$$n_e = X_{\text{Ar}}(n_{\text{Ar}^+} + 2n_{\text{Ar}^{++}}) + X_{\text{N}_2}(n_{\text{N}_2^+} + n_{\text{N}^+} + n_{\text{NO}^+}) + X_{\text{O}_2}(n_{\text{O}_2^+} + n_{\text{O}^+} + 2n_{\text{O}^{++}}) \quad (3.33)$$

$$X_{\text{N}_2} \left(N_A \left(\frac{P}{RT} \right) \right) = n_{\text{N}_2} + 2n_{\text{N}_2^+} + n_{\text{N}} + 2n_{\text{N}^+} + n_{\text{NO}} + 2n_{\text{NO}^+} \quad (3.34)$$

$$X_{\text{O}_2} \left(N_A \left(\frac{P}{RT} \right) \right) = n_{\text{O}_2} + 2n_{\text{O}_2^+} + n_{\text{O}} + 2n_{\text{O}^+} + 3n_{\text{O}^{++}} + n_{\text{NO}} + 2n_{\text{NO}^+} \quad (3.35)$$

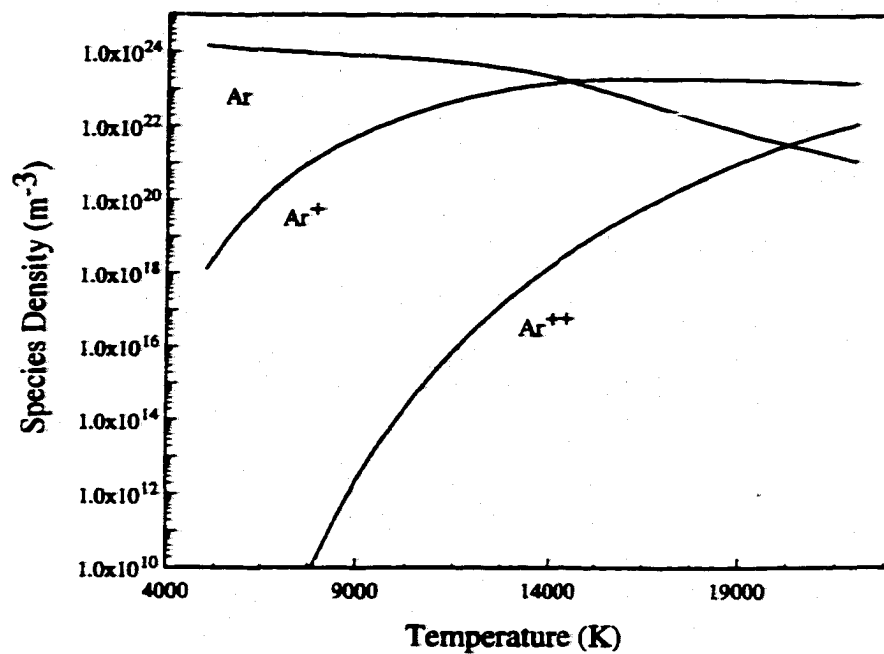
3.4 RESULTS AND DISCUSSION

3.4.1 Species Densities in Plasmas from a Single Source Feed Gas

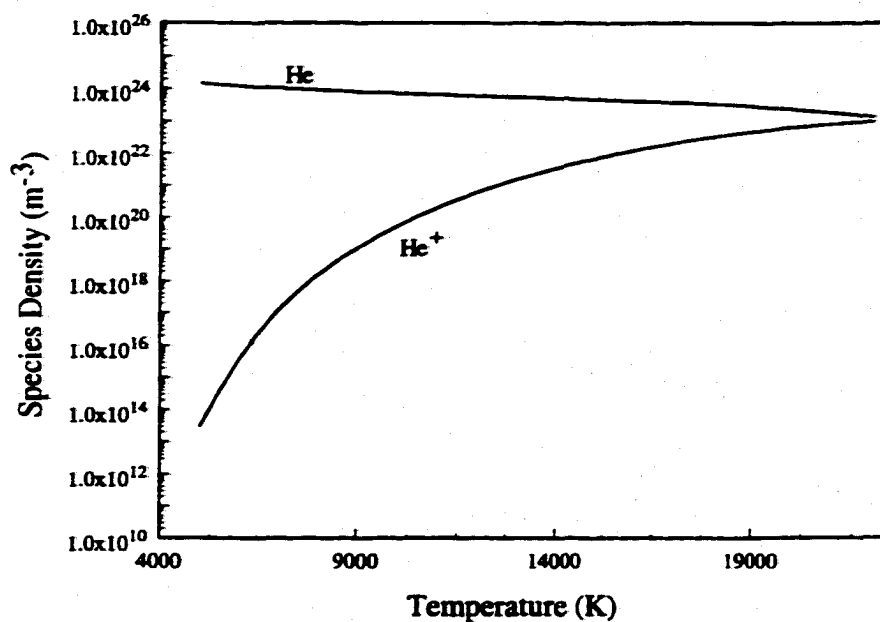
Figures 3.2(a&b) show the species density distributions for argon and helium, respectively, in the temperature range from 4000 to 20000K. Since helium is much more difficult to ionize than argon, only the first ionization level of helium, He^+ , is considered, while both Ar^+ and Ar^{++} are considered for argon. Differences in the ionization behavior between argon and helium are consistent with their specific ionization potentials. Very little ionization occurs at temperatures below 8000K for argon and 14000K for helium. At higher temperatures, the concentration of the singly charged species increases. In pure argon plasmas, the singly charged argon ions dominate above 14000K. On the other hand, the number density of the helium ions does not exceed that of the helium atoms for temperatures below 22000K. These results agree with reported values.^{19,21} Thus, the calculation scheme provides accurate predictions.

Computed number densities of various nitrogen species are shown in Figure 3.3 over a temperature range from approximately 2000 to 22000K. At temperatures below 6000 K, the extent of dissociation and ionization is low and diatomic nitrogen dominates. In this temperature range, ionized species play no role and are not considered. Above approximately 7000 K, monatomic nitrogen is the dominant species, and N^+ dominates as the temperature is increased above 14000 K. Oxygen, on the other hand, dissociates and ionizes much more easily than nitrogen, as shown in Figure 3.4. Much like nitrogen, O_2 and O dominate at temperatures below 5000 K, and O^+ dominates at temperatures greater than approximately 14000 K.

For each species analyzed here, the calculated results are compared with previous results available in the literature,¹⁹ as shown in Tables 3.2 and 3.3 for nitrogen and oxygen, respectively. The calculated results for nitrogen compare fairly well with those previously available in the literature. On the other hand, previous examinations^{17,20} of oxygen have been limited to species densities above 10^{20} m^{-3} . In many instances, there are rather significant differences between the calculated and literature values, but similar trends are observed between the values for each of the species analyzed. In the calculations performed here, additional energy states for the ionized species have been considered, and a



(a)



(b)

Figure 3.2(a&b). Plots of the computed species density for the inert gases (a) argon and (b) helium as a function of temperature.

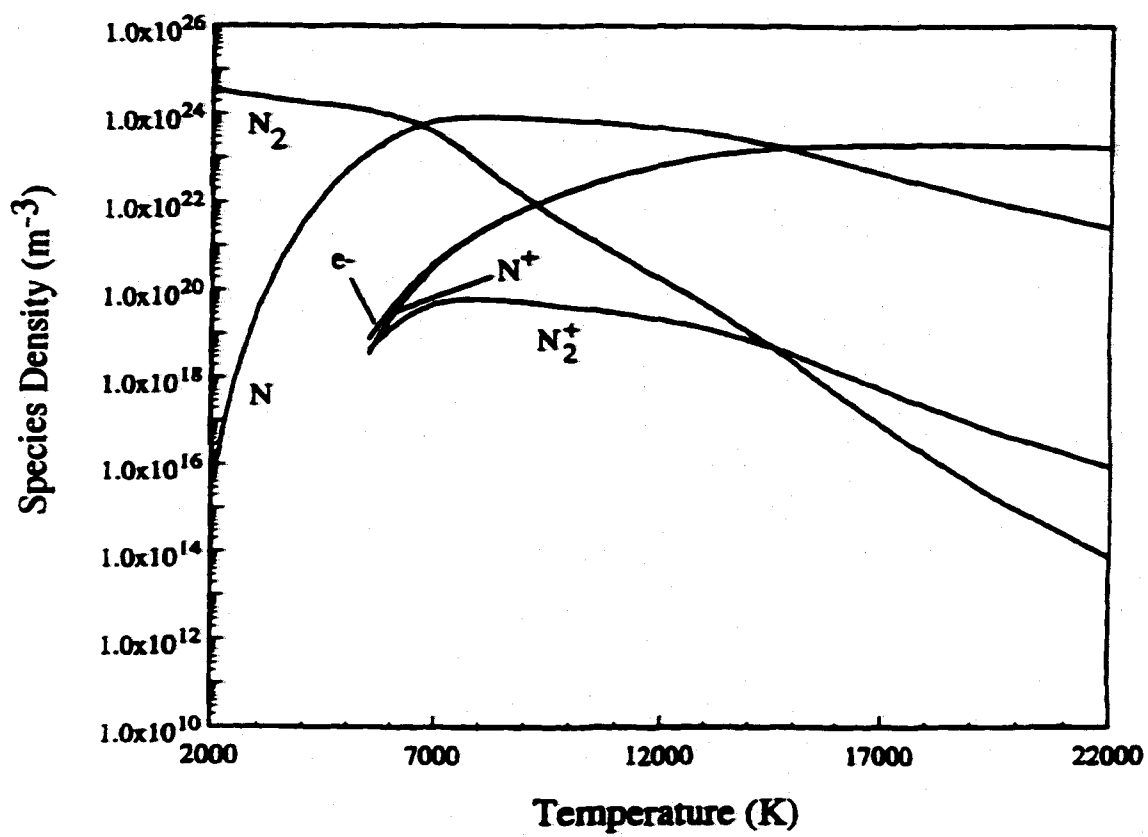


Figure 3.3. Plot of computed species densities for nitrogen species at 1 atm. total pressure as a function of temperature.

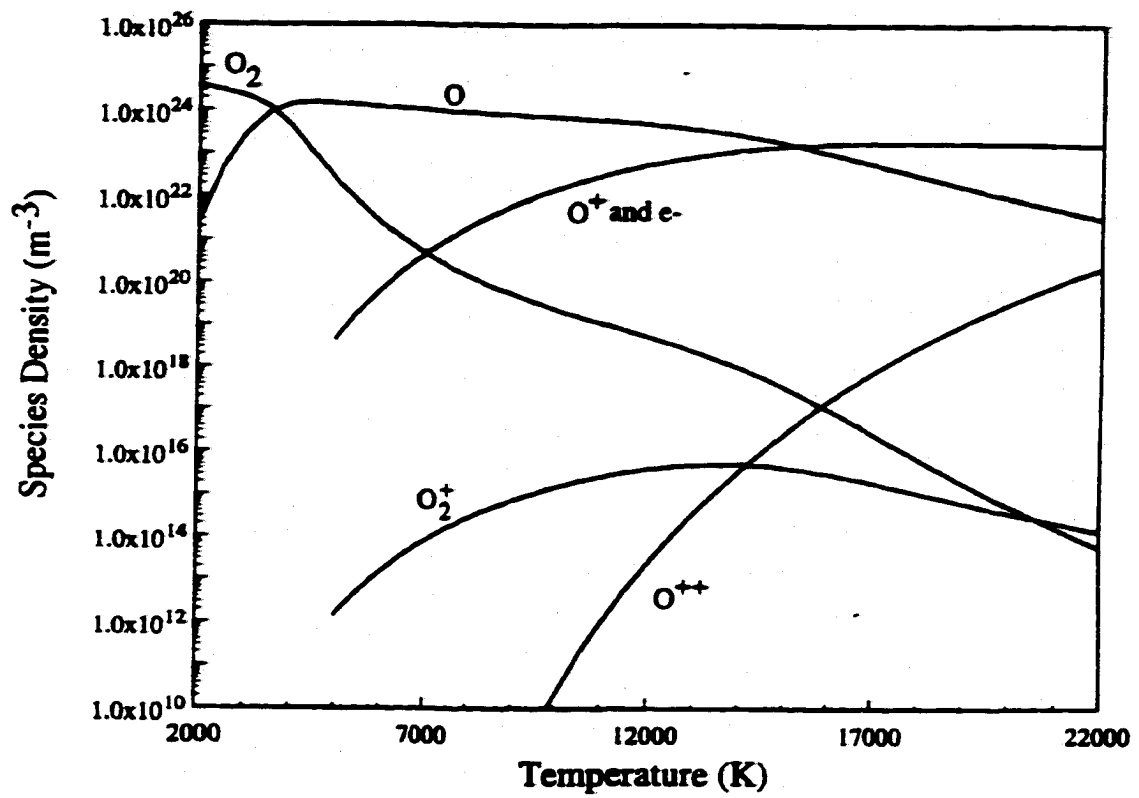


Figure 3.4. Plot of computed species densities for oxygen species at 1 atm. total pressure as a function of temperature.

Table 3.2. Comparison between calculated and literature values for calculation of species densities (m^{-3}) in nitrogen over a range of temperatures.²⁰

		Temperature (K)			
		5000	10000	15000	20000
N_2	Calculated	1.42×10^{24}	2.77×10^{21}	2.38×10^{18}	9.07×10^{14}
	Literature	1.42×10^{24}	3.37×10^{21}	2.62×10^{18}	9.34×10^{14}
N_2^+	Calculated	1.99×10^{18}	4.12×10^{19}	3.50×10^{18}	3.93×10^{16}
	Literature	9.88×10^{17}	3.54×10^{19}	3.45×10^{18}	3.26×10^{16}
N	Calculated	5.24×10^{22}	6.95×10^{23}	1.47×10^{23}	7.23×10^{21}
	Literature	4.77×10^{22}	5.91×10^{23}	1.51×10^{23}	1.47×10^{22}
N^+	Calculated	1.55×10^{17}	1.79×10^{22}	1.71×10^{23}	1.80×10^{23}
	Literature	3.07×10^{17}	3.76×10^{22}	1.69×10^{23}	1.76×10^{23}
e^-	Calculated	2.14×10^{18}	1.80×10^{22}	1.71×10^{23}	1.80×10^{23}
	Literature	1.30×10^{18}	3.77×10^{22}	1.69×10^{23}	1.76×10^{23}

Table 3.3. Comparison between calculated and literature values for calculation of species densities in oxygen over a range of temperatures.²⁰

		Temperature (K)			
		5000	10000	15000	20000
O_2	Calculated	2.37×10^{22}	2.36×10^{19}	3.48×10^{17}	5.72×10^{13}
	Literature	1.44×10^{20}	---	---	---
O_2^+	Calculated	1.41×10^{12}	1.50×10^{13}	4.57×10^{13}	3.86×10^{13}
	Literature	---	---	---	---
O	Calculated	1.44×10^{24}	7.04×10^{23}	1.82×10^{23}	9.71×10^{21}
	Literature	1.39×10^{24}	5.18×10^{23}	8.02×10^{21}	5.40×10^{20}
O^-	Calculated	4.65×10^{18}	1.50×10^{22}	1.54×10^{23}	1.79×10^{23}
	Literature	2.82×10^{19}	1.45×10^{23}	2.75×10^{23}	2.18×10^{23}
e^-	Calculated	4.65×10^{18}	1.50×10^{22}	1.54×10^{23}	1.79×10^{23}
	Literature	6.75×10^9	1.29×10^{23}	2.75×10^{23}	2.26×10^{23}

more rigorous calculation scheme adopted here. When taken together, both of these considerations lead to higher accuracy.

In order to apply these calculations to welding conditions, temperatures in the arc column must be known. These temperatures can vary depending on the welding conditions.²²⁻²⁹ Several examples are shown in Figures 3.5 to 3.8, with the respective experimental conditions summarized in Table 3.4. High temperatures are seen close to the electrode and decrease as the workpiece is approached in all cases. For the temperature distributions shown in Figures 3.5 and 3.6, monatomic nitrogen (N) dominates throughout the arc column. Although the two temperature distributions are different, the temperatures are sufficiently high for significant dissociation of the diatomic nitrogen. In Figures 3.7 and 3.8, the temperatures at locations much closer to the electrode are on the level of 21000 K and ionic nitrogen (N^+) dominates. Throughout the remainder of the plasma phase in the arc column, the temperatures are high enough for significant dissociation of the diatomic nitrogen to occur and for monatomic nitrogen (N) to dominate. Therefore, ionized species tend to dominate at locations closer to the electrode, and neutral species are dominant as the workpiece is approached.

3.4.2 Species Densities in Plasmas Formed From a Source Gas Containing a Monatomic and a Diatomic Gas Mixture

Pure nitrogen and oxygen arcs are not normally observed in welding applications. On the other hand, only small amounts of these gases are added, whether purposely or not, to the welding arc. Therefore, calculations have been performed for inert gas plasmas with the addition of diatomic gases. Figures 3.9(a&b) show the species distributions for argon - nitrogen and helium - nitrogen mixtures. In each case, argon and helium species dominate across the range of temperatures considered. The choice of shielding gas affects the extent of ionization at high temperatures. Similar calculated results for argon-oxygen and helium-oxygen mixtures are presented in Figures 3.10(a&b), and the same behavior as that seen in Figures 3.9(a&b) is observed.

Knowledge of the electron density is necessary in order to calculate plasma transport properties, especially the electrical conductivity, important in the analysis of the welding

Table 3.4. Summary of welding conditions used to calculate temperature distributions in the arc column.

<u>Number</u>	<u>Study</u>	<u>Arc Current (A)</u>	<u>Arc Voltage (V)</u>	<u>Arc Length (mm)</u>	<u>Shielding Gas</u>	<u>Electrode Diameter (mm)</u>
a	Key, <i>et al.</i> ²²	150	varied	2.0	Ar	2.38
b	Gick, <i>et al.</i> ²¹	100	16	8	Ar	1.5
c	Haddad and Farmer ²⁶	100	varied	5	Ar	3.2
d	Haddad and Farmer ²⁶	200	varied	5	Ar	3.2

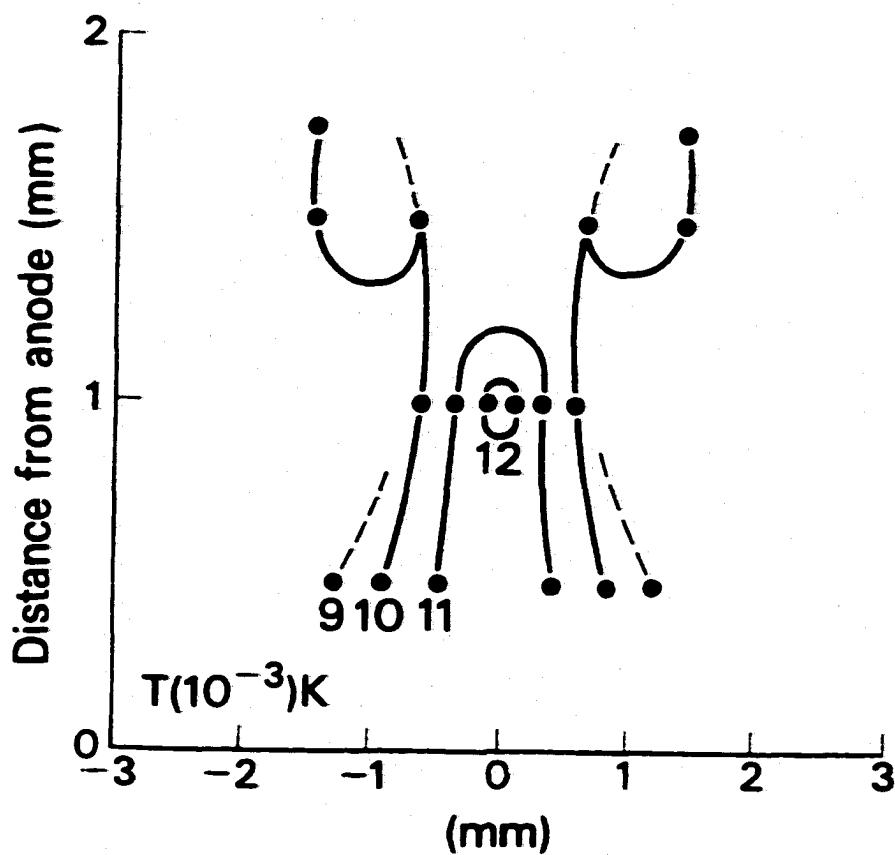


Figure 3.5. Schematic diagram of the spectroscopically measured temperatures in a 100% Ar arc, with an arc current of 150 A, and a 30° vertex angle for the electrode tip.²²

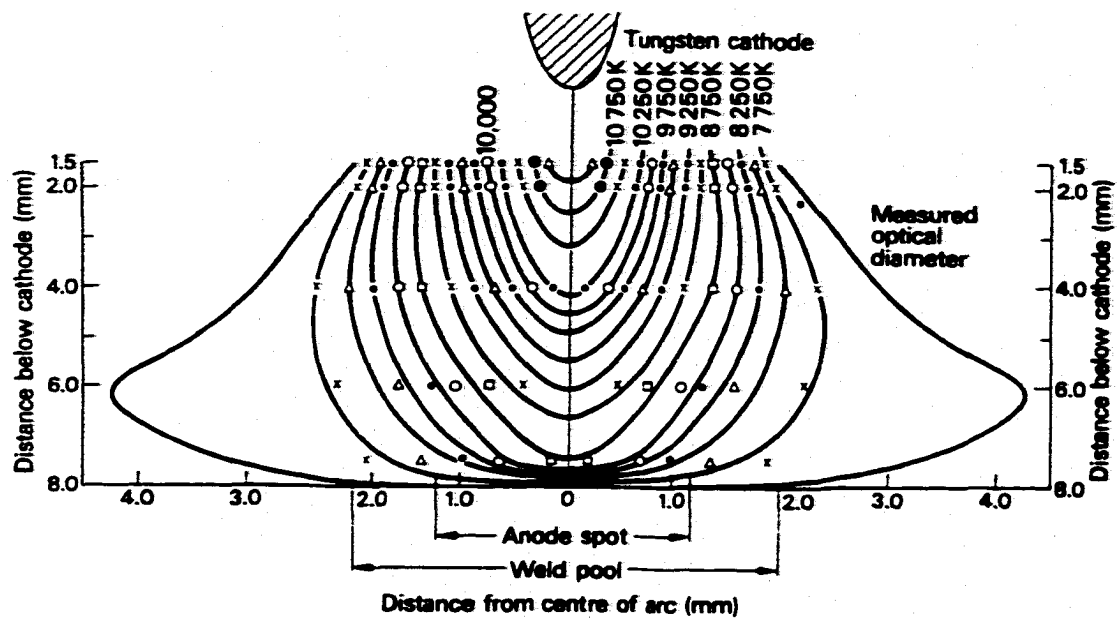


Figure 3.6. Temperature distribution in the arc column under GTA welding conditions for an arc current of 100 A. The temperatures in the arc column were calculated using electrostatic probes.²¹

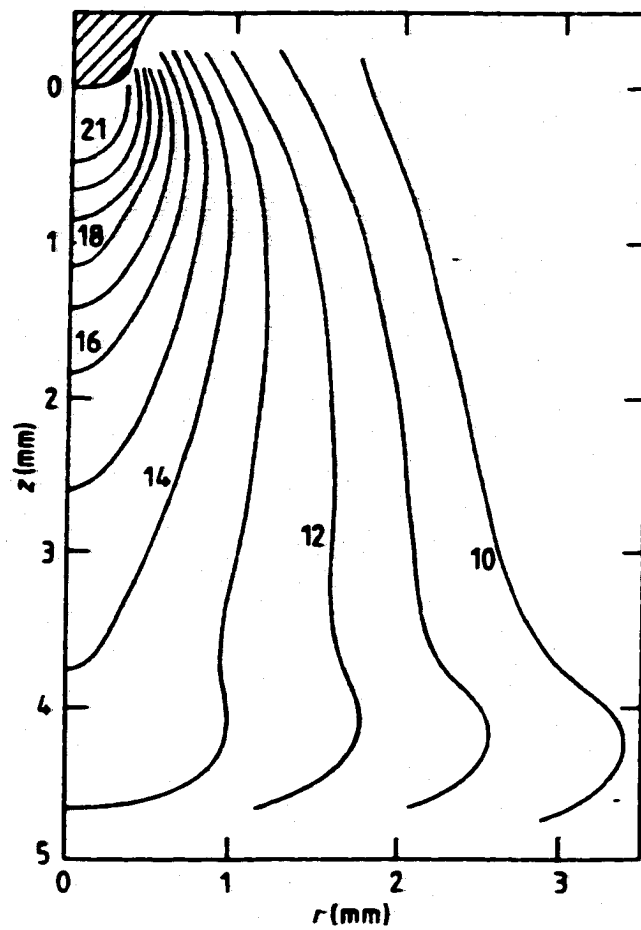


Figure 3.7. Temperature profile for a 100 A argon arc.²⁶

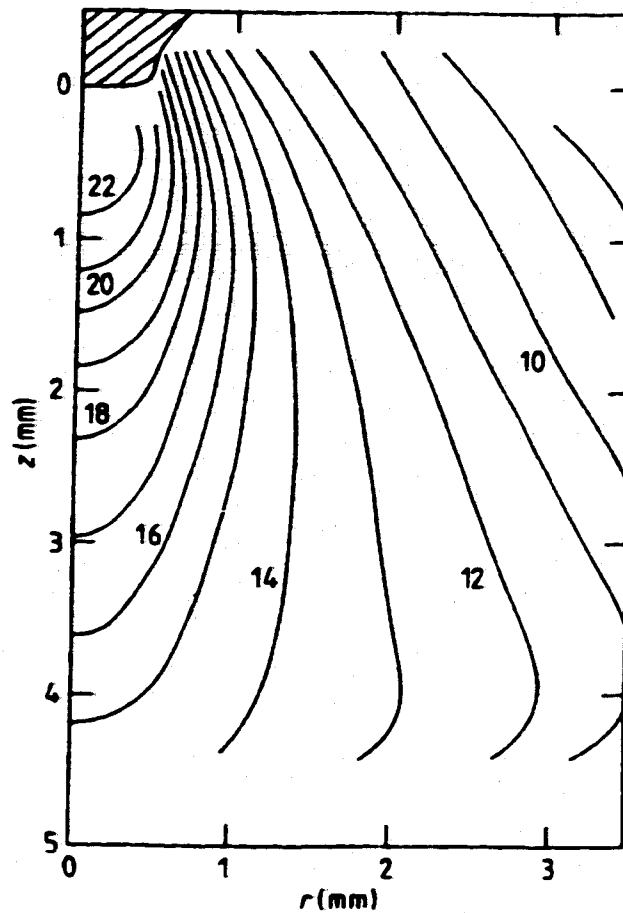
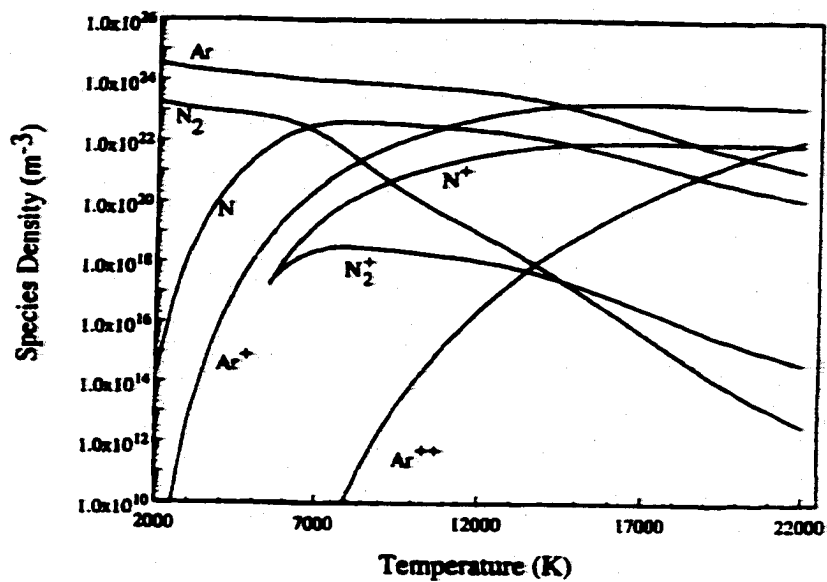
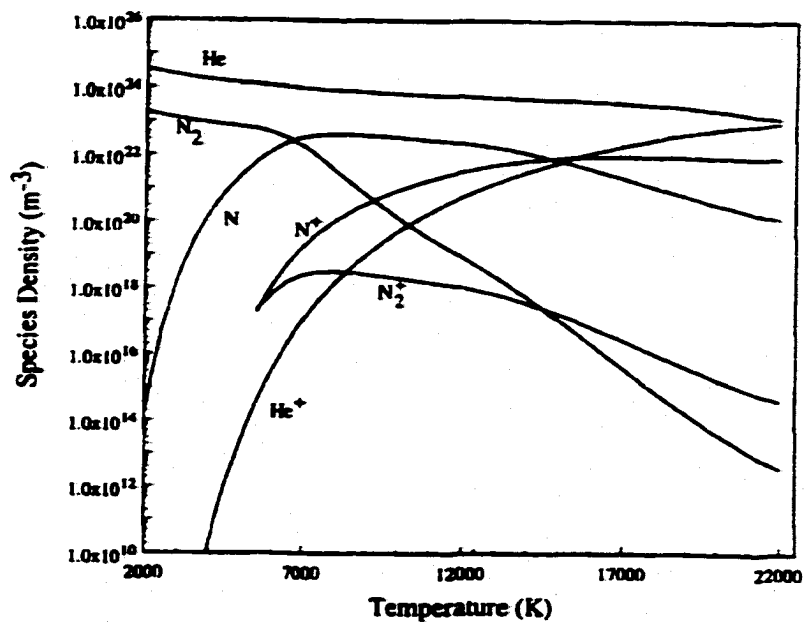


Figure 3.8. Temperature profile for a 200 A argon arc.²⁶

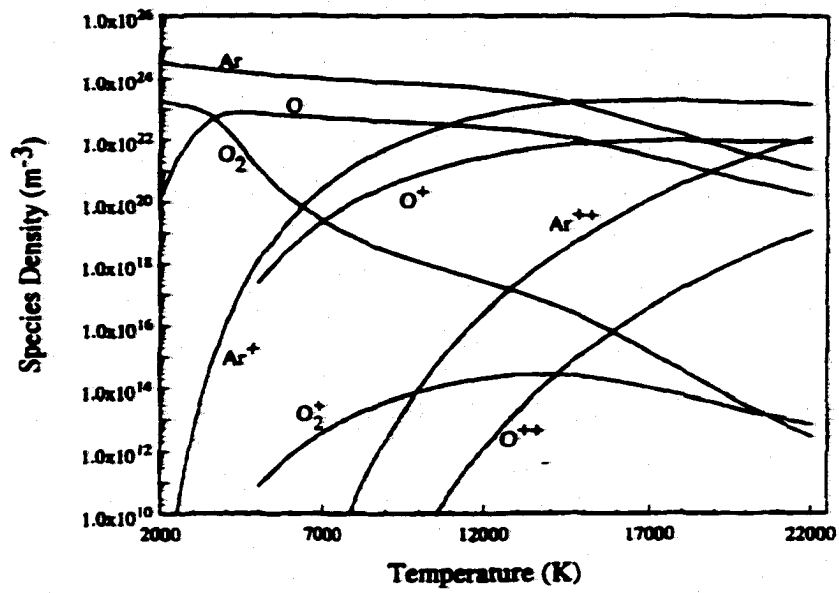


(a)

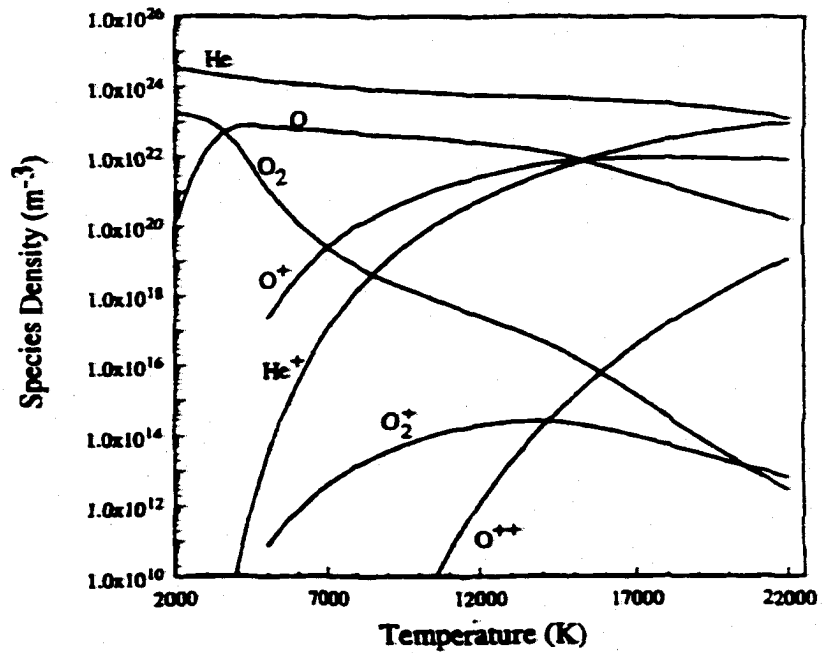


(b)

Figure 3.9(a&b). Plots of computed species densities for two component systems, (a) Ar-5%N₂ and (b) He-5%N₂ as a function of temperature.



(a)



(b)

Figure 3.10(a&b). Plots of computed species densities for two component systems, (a) Ar-5%O₂ and (b) He-5%O₂ as a function of temperature.

arc. Dunn and Eagar¹⁹ investigated the role of metal vapor additions to the GTA welding arc on the electrical and thermal conductivity. They found that small additions of these metals have no significant effect on the transport properties of the arc. In this work, the effects of diatomic gas additions on the electron density of pure inert gaseous plasmas have been examined.

Figures 3.11 to 3.13 show the calculated electron densities for pure gases, for argon-diatom gas mixtures, and for helium-diatom gas mixtures, respectively. The calculated results in Figure 3.11 show that pure argon, nitrogen, and oxygen are roughly equivalent in their capacity to donate electrons to the plasma phase over the entire temperature range investigated. This effect is further illustrated in Figure 3.12, where it is shown that additions of nitrogen and oxygen to argon plasmas have little effect on the overall electron density for the argon based gas mixtures. On the other hand, there are fairly sizable differences between the electron densities of argon and helium gases over the same temperature range in Figure 3.11, given the much higher ionization energy for helium. In the case of the helium-diatom gas mixtures in Figure 3.13, the additions of oxygen and nitrogen increase the overall electron density above that for the pure helium gas.

3.4.3 Species Densities in Plasmas Formed From Nitrogen-Oxygen Gas Mixtures

Enhancement of the nitrogen concentration in the weld metal with the addition of nitrogen and oxygen-bearing gases to the arc is well documented in the literature.^{10,12-14} Detailed calculations of the species densities, considering the interaction between nitrogen and oxygen, can provide a definitive scientific basis for this behavior. Figures 3.14 and 3.15 display the species density distributions for argon-nitrogen-oxygen and helium-nitrogen-oxygen mixtures, respectively, in which no interaction between the nitrogen and oxygen species is considered. At temperatures below 6000K, apart from the inert gaseous species, diatomic nitrogen is present in appreciable concentrations. As this temperature is exceeded, monatomic nitrogen and oxygen concentrations increase significantly. In the argon-nitrogen-oxygen plasmas, singly charged argon ions dominate above 14000 K, while in the helium-oxygen-nitrogen plasma, helium atoms dominate up to 17000 K.

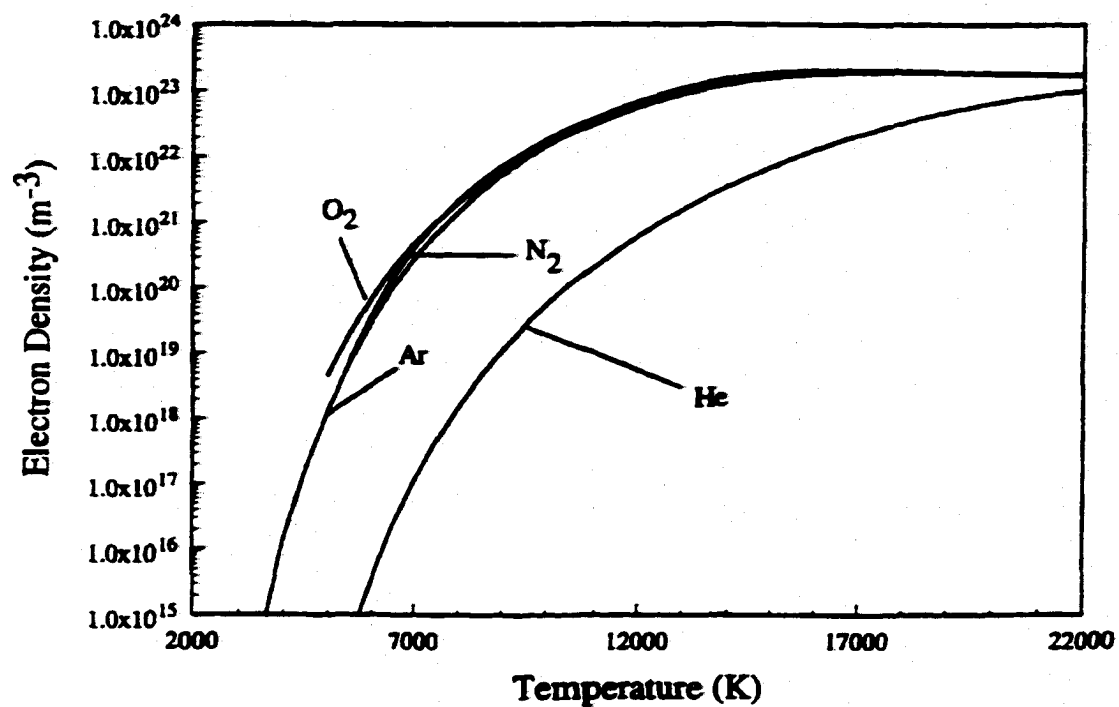


Figure 3.11. Comparison of computed total electron densities for pure gases.

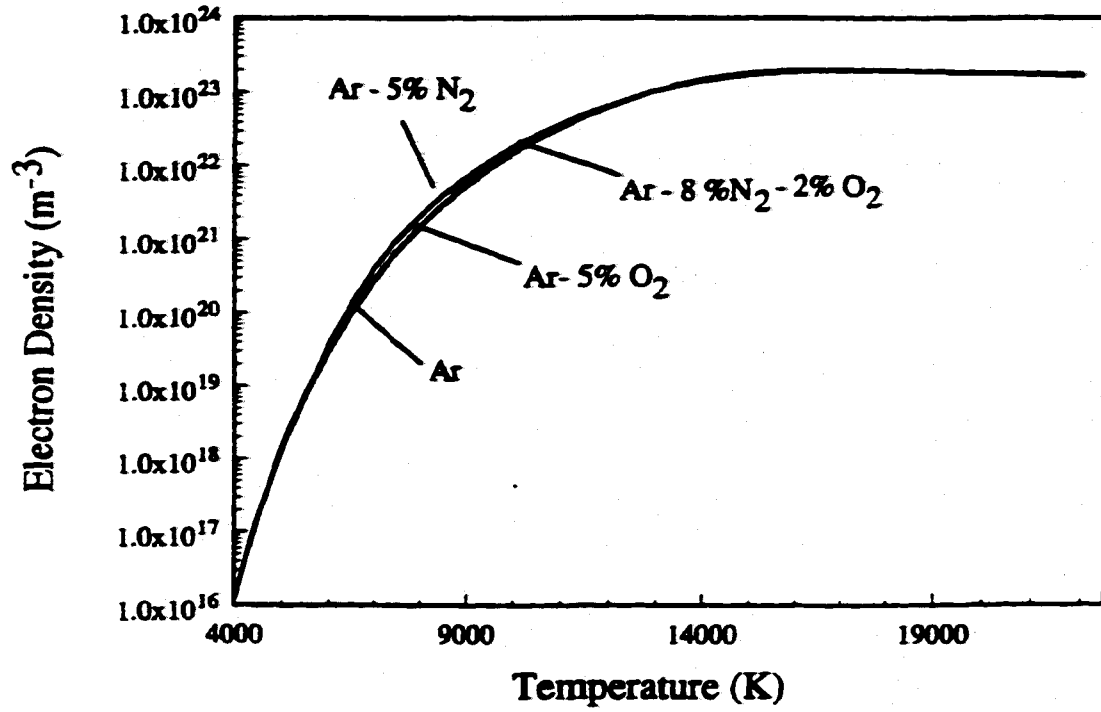


Figure 3.12. Comparison of computed total electron densities for argon-diatom gas mixtures.

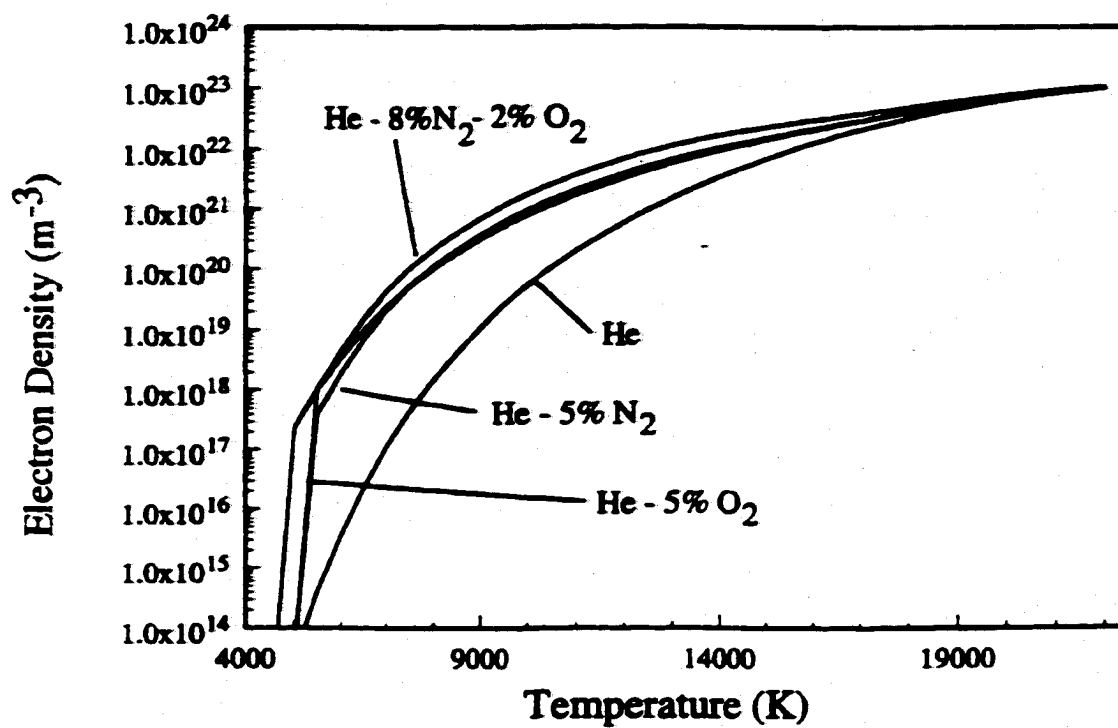


Figure 3.13. Comparison of computed total electron densities for helium-diatomic gas mixtures.

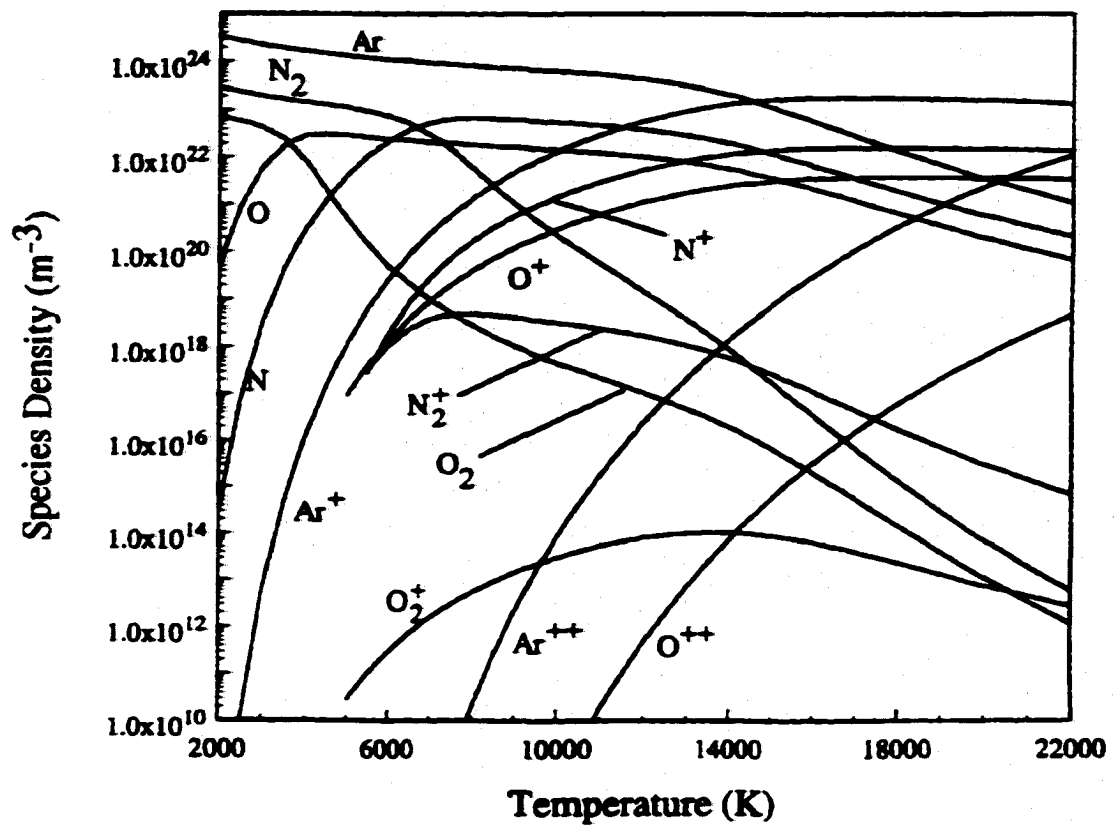


Figure 3.14. Plot of the computed species densities for a three component system consisting of Ar-8% N_2 -2% O_2 as a function of temperature assuming no interaction.

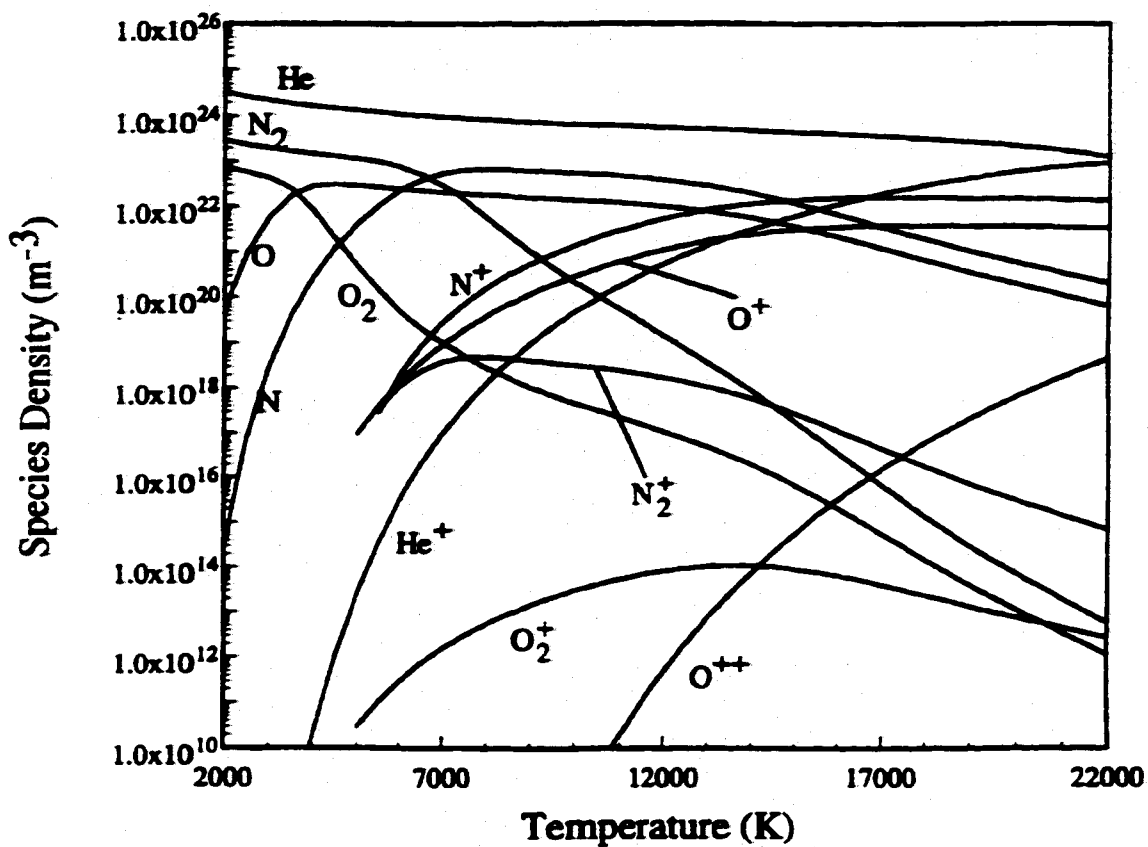


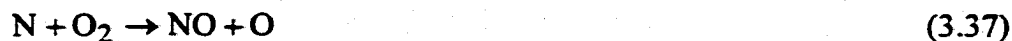
Figure 3.15. Plot of the computed species densities for a three component system consisting of He-8%N₂-2%O₂ as a function of temperature assuming no interaction.

above which the concentration of He^+ increases significantly and almost equals the concentration of He at about 22000 K.

Results of calculations, taking into account the formation of NO and its dissociation and ionization in Ar-8% N_2 -2% O_2 and He-8% N_2 -2% O_2 , are shown in Figures 3.16 and 3.17. The NO species distribution in both cases closely follows that of the N_2 species over the entire temperature range considered, and the ionization of NO is so insignificant that the NO^+ species densities do not fall in the range of the plots. Species present in the plasma phase display much the same trends here as for cases assuming no interaction. On the other hand, there are significant changes in the number densities for both O_2 and O at temperatures below 6000 K. As the temperature is increased above 6000 K, the species density distributions for both O_2 and O are the same as those for the calculations assuming no interaction, i.e. ignoring the formation of species containing both nitrogen and oxygen. There is no noticeable difference in appearance between the calculated species densities for helium or argon based gas mixtures shown in Figures 3.16 and 3.17.

Most importantly, these calculations show that the formation of NO increases the number density of monatomic nitrogen in the plasma. In Figures 3.18 and 3.19, the monatomic nitrogen number density in both Ar-8% N_2 -2% O_2 and He-8% N_2 -2% O_2 plasmas, respectively, exceeds the monatomic nitrogen number density for Ar-8% N_2 and He-8% N_2 plasmas, respectively, at temperatures less than approximately 8000 K. There is little difference between the monatomic nitrogen species densities calculated here in argon and helium gas mixtures over this temperature range.

A physical mechanism explaining the increase in the monatomic nitrogen species density with the addition of oxygen to the feed gas mixture is not currently available. As discussed in Chapter 2, several researchers^{10,12,14} have proposed two reaction mechanisms, in particular, to explain the formation of NO in these gas mixtures and are shown below:



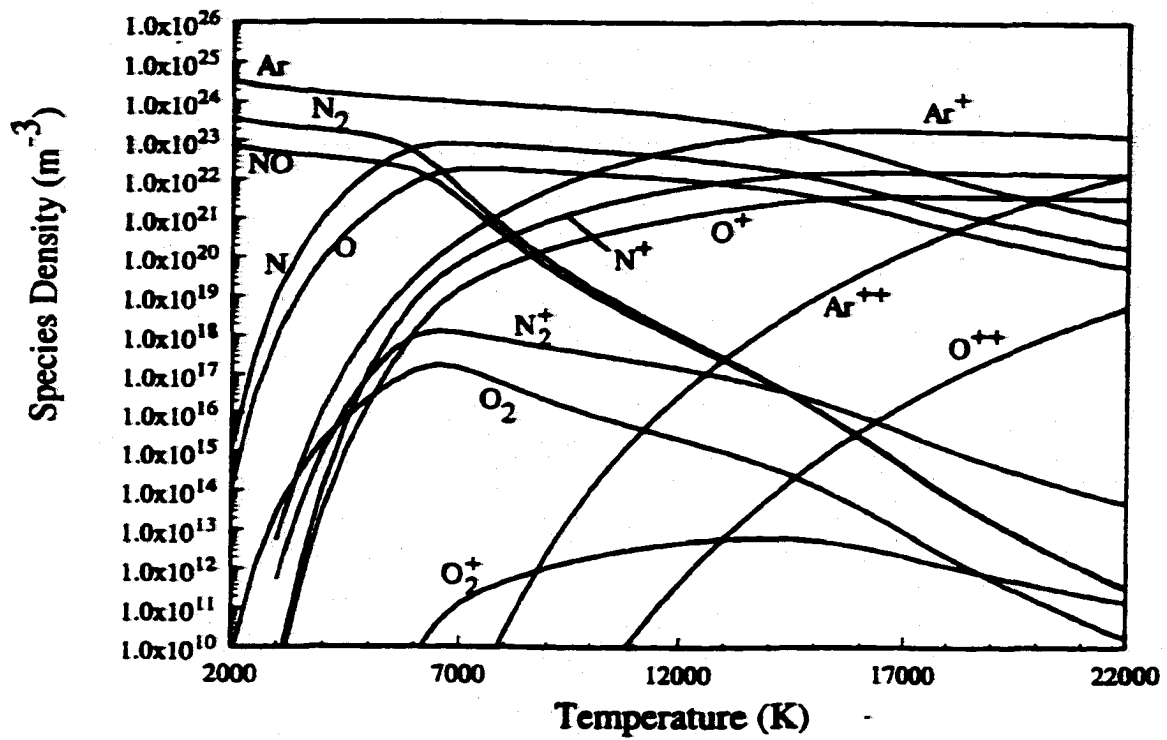


Figure 3.16. Plot of the computed species densities for a three component system consisting of Ar-8%N₂-2%O₂ as a function of temperature with interaction between nitrogen and oxygen.

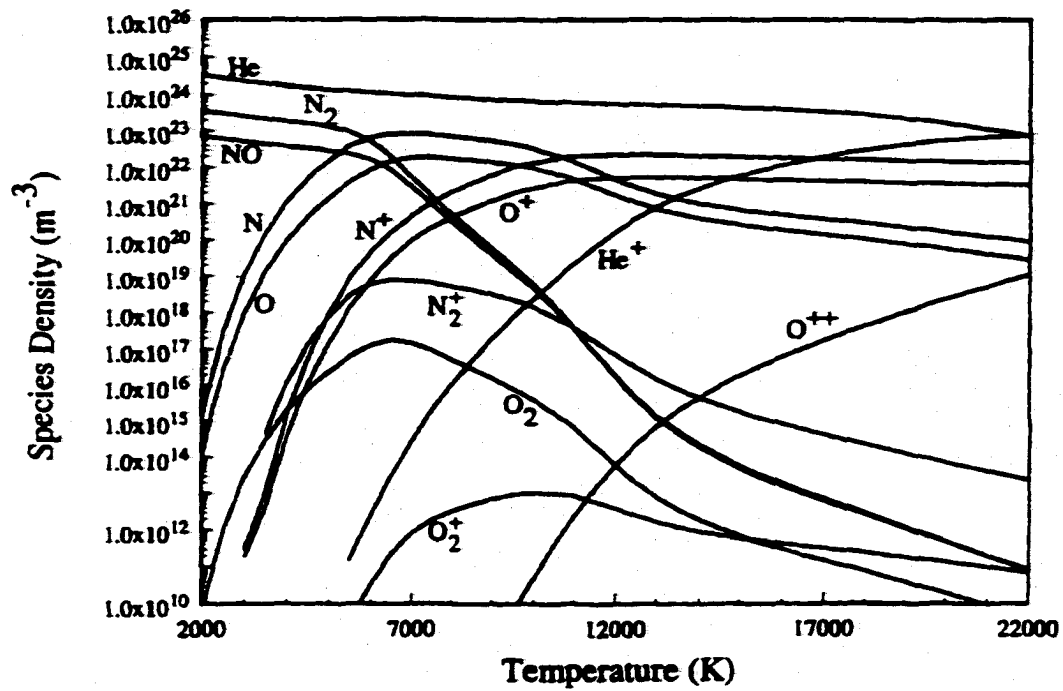


Figure 3.17. Plot of the computed species densities for a three component system consisting of He-8% N_2 -2% O_2 as a function of temperature with interaction between nitrogen and oxygen.

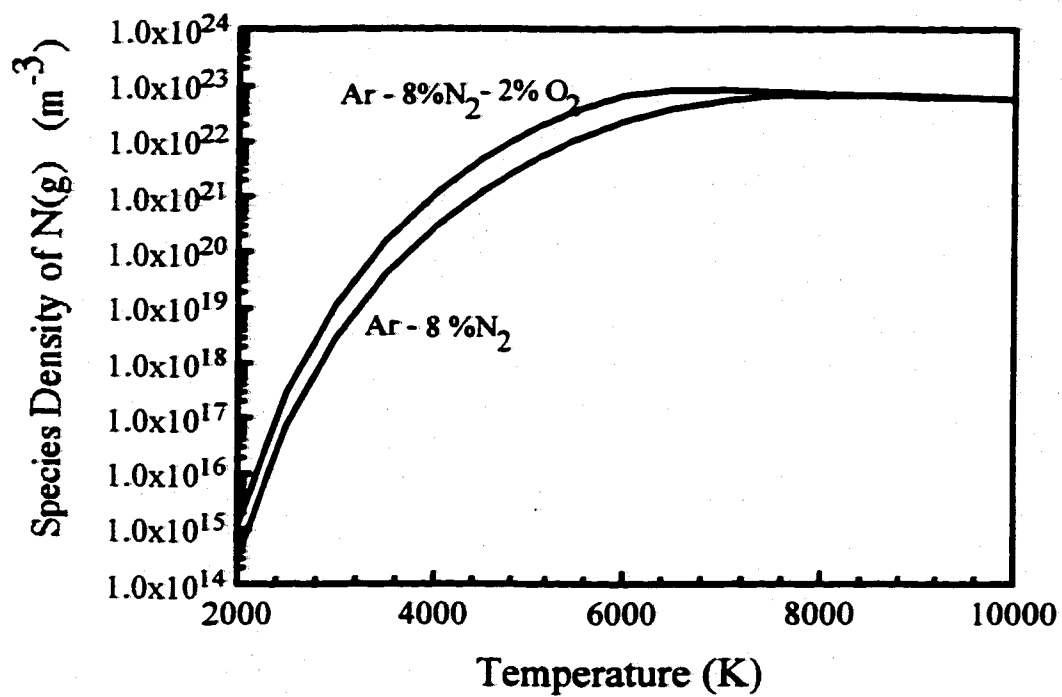


Figure 3.18. Comparison of the computed number density of monatomic nitrogen for Ar - 8%N₂ and Ar - 8%N₂ - 2%O₂ plasmas.

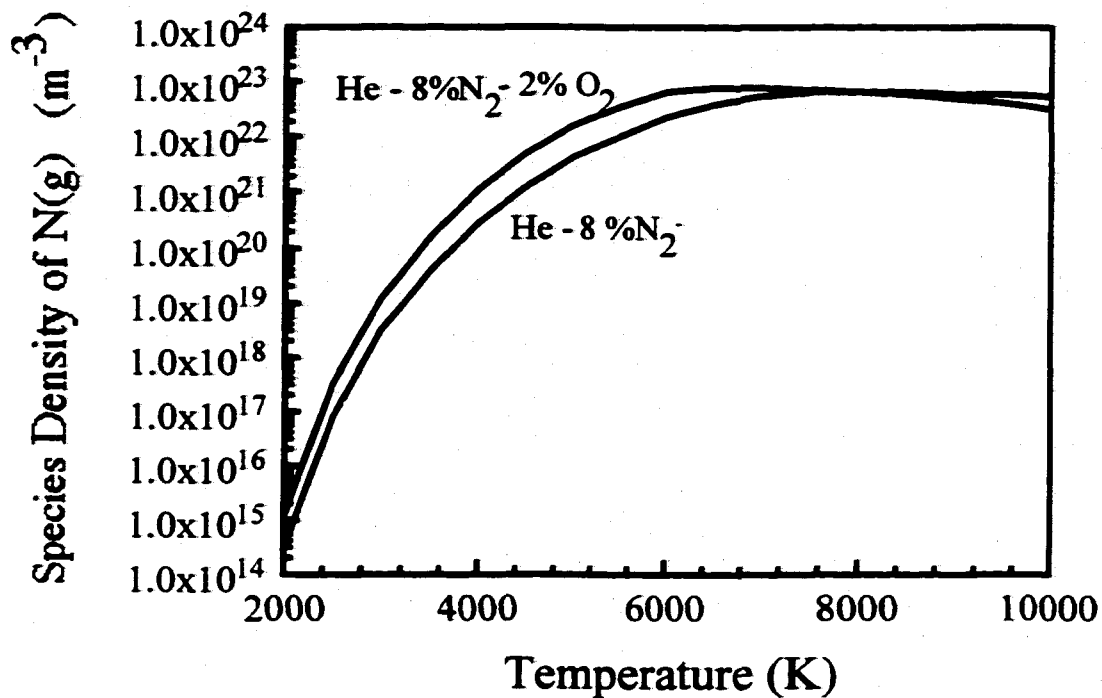


Figure 3.19. Comparison of the computed number density of monatomic nitrogen for He - 8%N₂ and He - 8%N₂ - 2%O₂ plasmas.

There is one significant difference between these two reactions. Equation (3.36) produces N(g) and consumes O(g), while Equation(3.37) consumes N(g) and produces O(g). Table 3.5 lists the standard free energies of formation for the species present in these reactions and the standard free energy for each reaction.³⁰ When compared, it is shown that Equation (3.36) has a positive free energy change, and Equation (3.37) a negative value at temperatures between 2000 and 3000 K. With a negative free energy change, Equation (3.37) is expected to proceed and lead to the formation of NO. This reaction mechanism is also, in part, supported by a significant decrease in the calculated O₂ species density. On the other hand, the fact that N(g) is consumed in Equation (3.37) is detrimental to the formation of a higher N(g) species density in the plasma phase.

An additional reaction, shown in Equation (3.38) has also been considered here to describe a reaction mechanism for the formation of NO. This reaction also displays a negative free energy change, which would also allow it to proceed under these conditions.



The effect of oxygen additions to the feed gas on the resulting species densities of various species is also an important consideration in determining the dominant reaction mechanisms. Table 3.6 compares the calculated species densities in plasmas with two and three component feed gas mixtures. In the nitrogen-oxygen mixtures, the species densities of oxygen species, specifically O₂ and O are lower than in the corresponding argon-oxygen mixtures over the temperature range of interest. From these comparisons, it is apparent that oxygen species are consumed in the formation of NO, and subsequently N in the plasma phase.

These oxygen additions to the inert gas - nitrogen mixtures also have an effect on the temperature at which the complete dissociation of nitrogen occurs and monatomic nitrogen dominates other nitrogen-bearing species in the plasma. For example, with oxygen present, the monatomic nitrogen number density exceeds that of diatomic nitrogen at a

Table 3.5. Summary of free energy values for the formation of NO.³⁰

	ΔG_f° (kJ/mol)		
	2000 K	2500 K	3000 K
N(g)	346.339	312.77	278.946
O(g)	121.552	88.012	54.327
NO(g)	65.060	58.72	52.439
N ₂ (g)	0	0	0
O ₂ (g)	0	0	0
O + N ₂ → NO + N	289.85	283.48	277.058
N + O ₂ → NO + O	-159.73	-166.04	-172.18
$\frac{1}{2}$ N ₂ + O → NO	-56.49	-29.29	-1.89

Table 3.6. Comparison between calculated species densities (m^{-3}) in two and three component gas mixtures.

	2000 K		2500 K		3000 K	
	Ar-8%N ₂ -2%O ₂	Ar-8%N ₂ Ar-2%O ₂	Ar-8%N ₂ -2%O ₂	Ar-8%N ₂ Ar-2%O ₂	Ar-8%N ₂ -2%O ₂	Ar-8%N ₂ Ar-2%O ₂
N ₂	3.670x10 ²³	2.936x10 ²³ ----	2.936x10 ²³	2.352x10 ²³ ----	2.447x10 ²³	1.96x10 ²³ ----
N	1.131x10 ¹⁵	2.8621x10 ¹⁴ ----	2.945x10 ¹⁷	7.450x10 ¹⁶ ----	1.173x10 ¹⁹	2.967x10 ¹⁸ ----
O ₂	5.216x10 ⁹	---- 7.335x10 ²²	9.171x10 ¹¹	---- 5.780x10 ²²	2.793x10 ¹³	---- 4.323x10 ²²
O	1.008x10 ¹⁴	---- 5.345x10 ¹⁹	2.597x10 ¹⁶	---- 9.221x10 ²⁰	1.026x10 ¹⁸	---- 5.707x10 ²¹
NO	7.341x10 ²²	---- ----	5.872x10 ²²	---- ----	4.894x10 ²²	---- ----

temperature of less than 6000 K, as compared to 7000 K with no oxygen. This temperature equates to the temperature for complete dissociation of NO shown in Figure 3.1. This decrease in the temperature for complete dissociation accentuates the importance of the dissociation of NO in increasing the number density of monatomic nitrogen in the plasma phase at lower temperatures. A higher number density of monatomic nitrogen with the addition of oxygen to the plasma phase may be, in part, responsible for the higher nitrogen concentrations observed in the weld metal in Figure 2.41.

3.4.4 Use of Species Densities in Calculation of Nitrogen Concentrations

A rather significant difference arises between the monatomic nitrogen partial pressures at temperatures characteristic of the arc column and those on the weld pool surface. Figure 3.20 shows the relationship between the monatomic nitrogen partial pressure in these two temperature ranges for a pure nitrogen plasma at atmospheric pressure. In this figure, the monatomic nitrogen partial pressures on the surface are shown for only a single temperature, 2250 K, which is indicative of the higher range of temperatures to be found there. The monatomic nitrogen partial pressures in the plasma are significantly higher than those prevailing at the weld pool surface. For example, at a surface temperature of 2250 K, the atomic nitrogen partial pressure in equilibrium with diatomic nitrogen is 2.42×10^{-8} atm., whereas the atomic nitrogen partial pressure in a nitrogen plasma at 2500 K is 3.17×10^{-7} atm. Over the temperature range shown in Figure 3.20, which is indicative of the temperatures close to the weld pool surface, the monatomic nitrogen partial pressure can vary up to six orders of magnitude in a small distance.

Based on these calculated monatomic nitrogen partial pressures, the resulting equilibrium nitrogen concentration in the weld metal is then calculated. The following equilibrium relationships are used to calculate the absorption of monatomic nitrogen into iron.



$$\text{N(wt.\%)} = P_{\text{N}} e^{-\frac{\Delta G^\circ}{RT}} \quad (3.40)$$

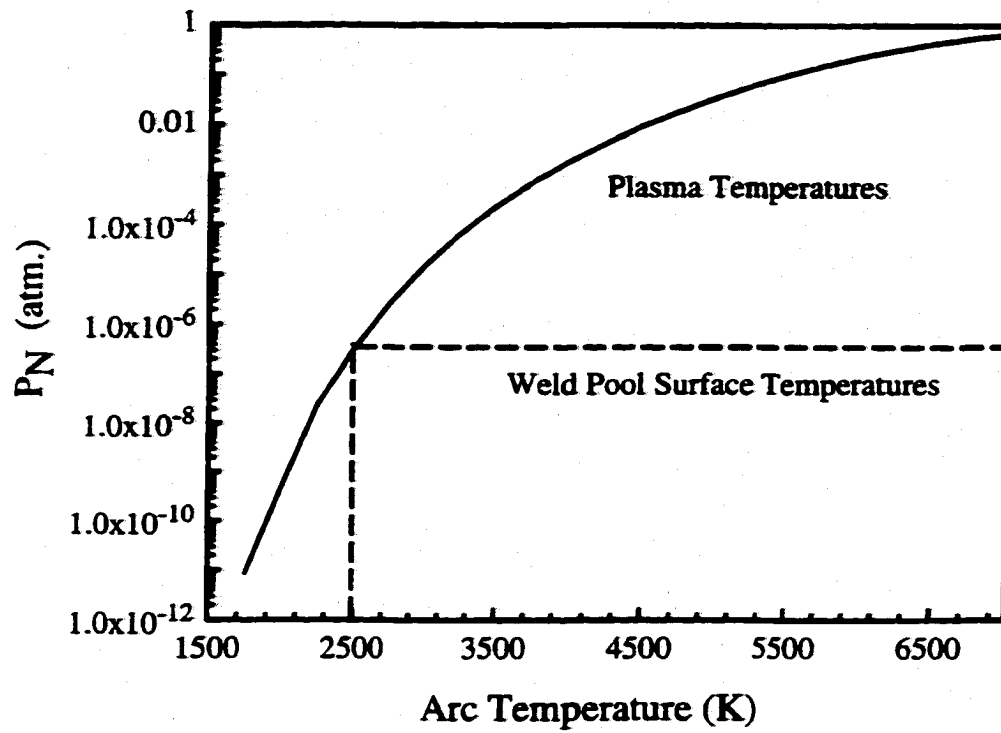


Figure 3.20. Comparison between the computed monatomic nitrogen partial pressures at temperatures characteristic of the plasma phase and on the weld pool surface for a pure nitrogen plasma at atmospheric pressure.

where P_N is the monatomic nitrogen partial pressure (atm.) and the relationship for the standard free energy for the reaction shown in Equation (3.39) is listed in Table 2.2.

Figure 3.21 shows the computed equilibrium nitrogen concentration in pure iron as a function of arc and sample temperatures for an Ar-1% N_2 gas mixture. In this figure, the nitrogen dissociation reaction is expressed in terms of the arc temperature, whereas the nitrogen absorption reaction is expressed in terms of the sample temperature. Even at this low level of nitrogen gas input, the monatomic nitrogen partial pressure is significant enough to cause nitrogen saturation in the sample at relatively low arc temperatures. For example, as shown in both Figures 3.21 and 3.22(a), the nitrogen solubility increases rapidly with increasing arc temperature until at an arc temperature of 5000 K, liquid iron is saturated with nitrogen at all sample temperatures.

This level of nitrogen saturation is controlled by the solubility of diatomic nitrogen in iron at one atmosphere pressure at the temperature on the weld pool surface.³ Nitrogen saturation in the weld metal can lead to the formation of gas bubbles and pin holes during the solidification of weld metals and arc melted iron, thus degrading the properties of the weld.³ It can also be inferred that arc temperatures at levels approaching 100 to 200°C above the sample temperature provide sufficient monatomic nitrogen to the metal surface to significantly increase the nitrogen concentration, very similar to the assumptions made in previous models.

As predicted by equilibrium calculations, monatomic nitrogen species possess a higher solubility, and the nitrogen saturation limit is reached at fairly low arc temperatures. For example, at 1850 K an iron sample theoretically reaches the nitrogen saturation limit at an arc temperature approximately 1000 K lower than for a sample at 2400 K, as shown in Figure 3.22(a). The sample temperature and nitrogen solubility are compared for various arc temperatures in Figure 3.22(b), in which the range of sample temperatures at which nitrogen saturation is reached rapidly increases as the arc temperature is increased. At these temperatures, the diatomic nitrogen species is significantly dissociated into the monatomic species and the partial pressure of monatomic nitrogen reaches exceptionally high levels, on the order of approximately 0.001 atm for an Ar-1% N_2 gas mixture.

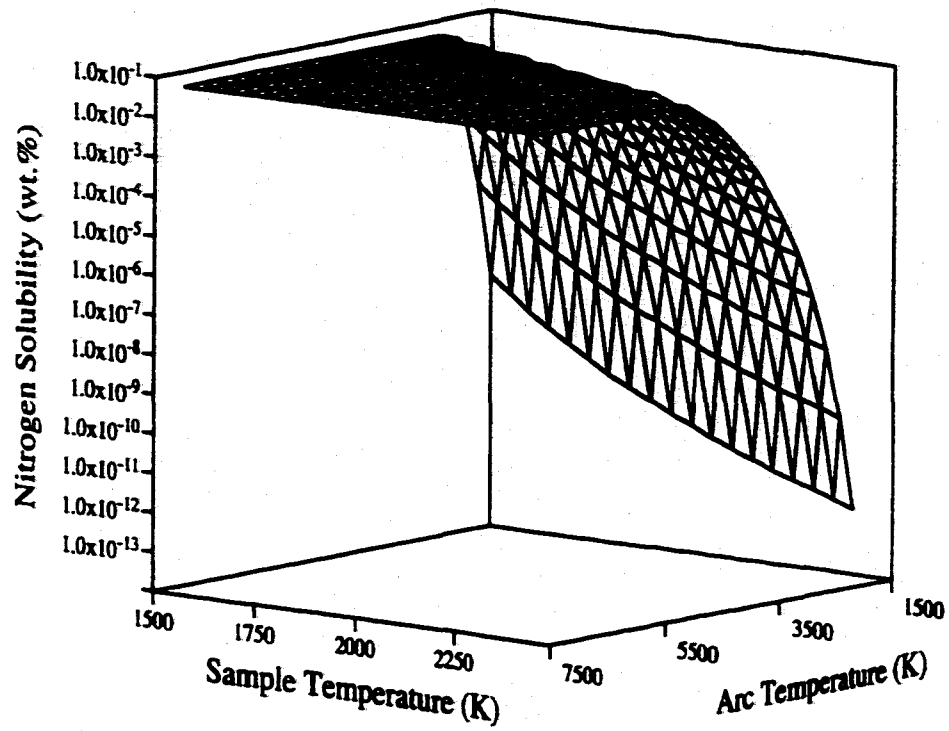
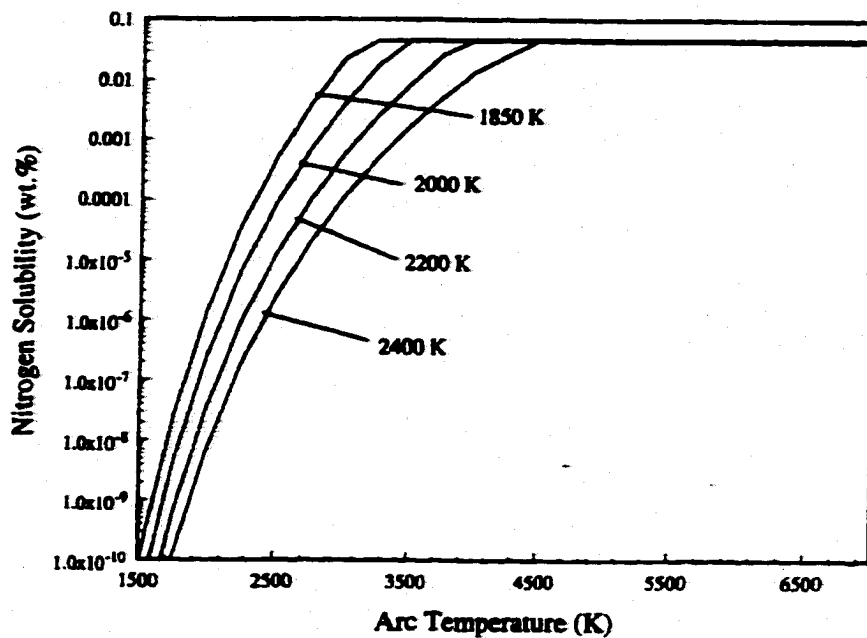
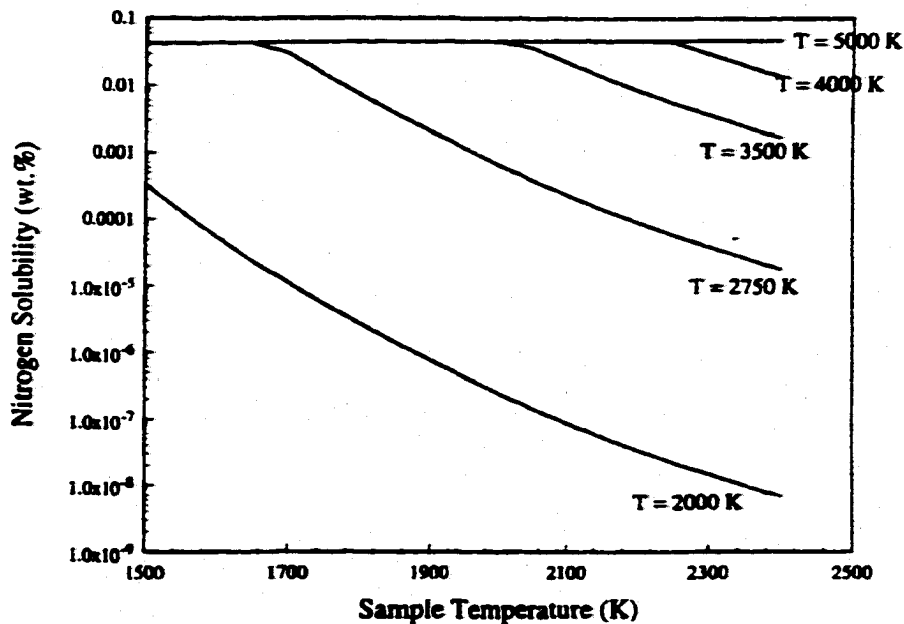


Figure 3.21. Nitrogen solubility in pure iron in contact with an Ar-1% N₂ plasma determined as a function of the arc temperature and the sample temperature, characteristic of the weld pool surface.



(a)



(b)

Figure 3.22(a&b). (a) The nitrogen solubility is plotted as a function of the arc temperature for several sample temperatures. (b) The nitrogen solubility is plotted as a function of the sample temperature for several arc temperatures.

The effect of oxygen additions to nitrogen-containing shielding gases on the resulting nitrogen concentration in liquid iron has also been examined. Table 3.7 and Figure 3.23 compare the calculated nitrogen concentrations in liquid iron for Ar - 8% N₂ and Ar - 8% N₂ - 2% O₂ gas mixtures at several electron and sample temperatures. As shown in Figures 3.18 and 3.19, the addition of oxygen to the plasma phase significantly enhances the nitrogen concentration in liquid iron. The most prominent effect of the oxygen additions to the plasma phase on the calculated nitrogen concentrations occurs in the lower electron temperature ranges. For example, at an electron temperature of 3000 K, the addition of oxygen to the plasma causes a factor of 4 or 5 increase in the nitrogen concentration in the liquid iron. At higher electron temperatures, the liquid iron reaches saturation with both gas mixtures. Once again, there is little to no difference in the effect of argon or helium as the inert gas addition on the resulting behavior of the nitrogen species.

3.4.5 Emission Spectroscopy Of Glow Discharges

The suitability of glow discharges to model several important features of welding plasmas has been previously addressed,^{4,5} and an experimental setup used in these previous studies and described in the literature⁴ has been utilized here to analyze glow discharges composed of nitrogen and oxygen mixtures. A schematic diagram of this experimental set-up is shown in Figure 3.24. This system can be divided into three main parts: the rf generator, the reaction chamber, and the emission spectroscopy equipment. A Westinghouse Model 7.5K80 industrial radio frequency (rf) generator capable of generating 10 kW continuous power output at a frequency of 450 kHz was utilized to create inductively coupled rf plasmas of the feed gases. The rf energy was applied through a copper coil wound around the reaction chamber, composed of GE 214 quartz with an outer diameter of 50 mm and an inner diameter of 46 mm.

Gaseous atmospheres in the reaction chamber are created by introducing ultra high purity (99.99% pure) helium and nitrogen into the reaction chamber. Precise control of the individual gases was achieved through the use of MKS Type 1259C flow controllers, and the conditions in the chamber are controlled by a MKS Multi-Gas Controller Model

Table 3.7. Comparison between calculated nitrogen concentrations in iron with and without the addition of oxygen to an argon-nitrogen plasma.

Electron Temperature (K)	T = 1873 K		T = 1973 K		T = 2073 K		T = 2173 K	
	[N] (ppm) (8% N₂)	[N] (ppm) (8%N₂- 2%O₂)	[N] (ppm) (8% N₂)	[N] (ppm) (8%N₂- 2%O₂)	[N] (ppm) (8% N₂)	[N] (ppm) (8%N₂- 2%O₂)	[N] (ppm) (8% N₂)	[N] (ppm) (8%N₂- 2%O₂)
2000	0.2	0.7	0.1	0.2	0.02	0.07	0.007	0.03
2500	53.8	212.7	16.8	66.2	5.8	23.0	2.2	8.8
3000	448.4	448.4	453.6	453.6	278.6	458.5	106.9	422.5
3500	448.4	448.4	453.6	453.6	458.5	458.5	462.9	462.9
4000	448.4	448.4	453.6	453.6	458.5	458.5	462.9	462.9
4500	448.4	448.4	453.6	453.6	458.5	458.5	462.9	462.9
5000	448.4	448.4	453.6	453.6	458.5	458.5	462.9	462.9

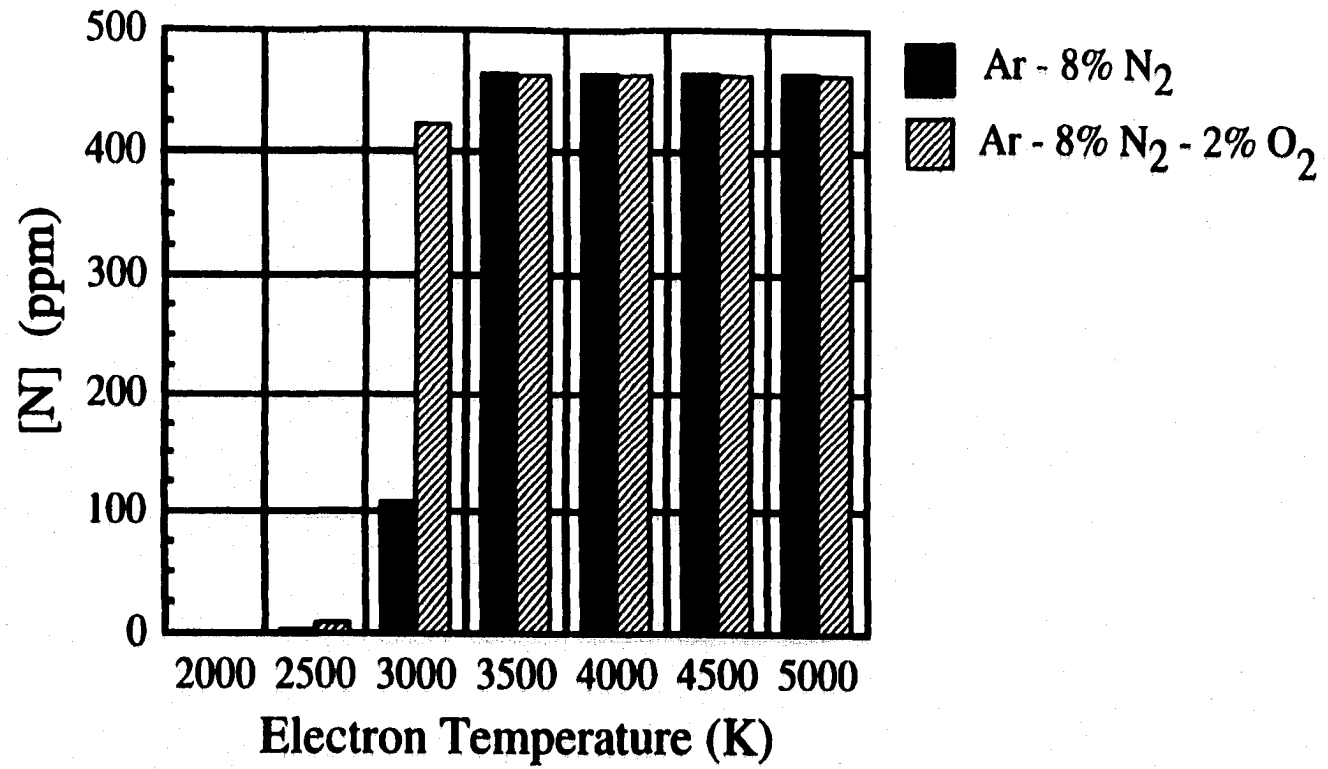


Figure 3.23. Comparison between the calculated nitrogen concentrations in for argon – nitrogen plasma phases both with and without oxygen additions.

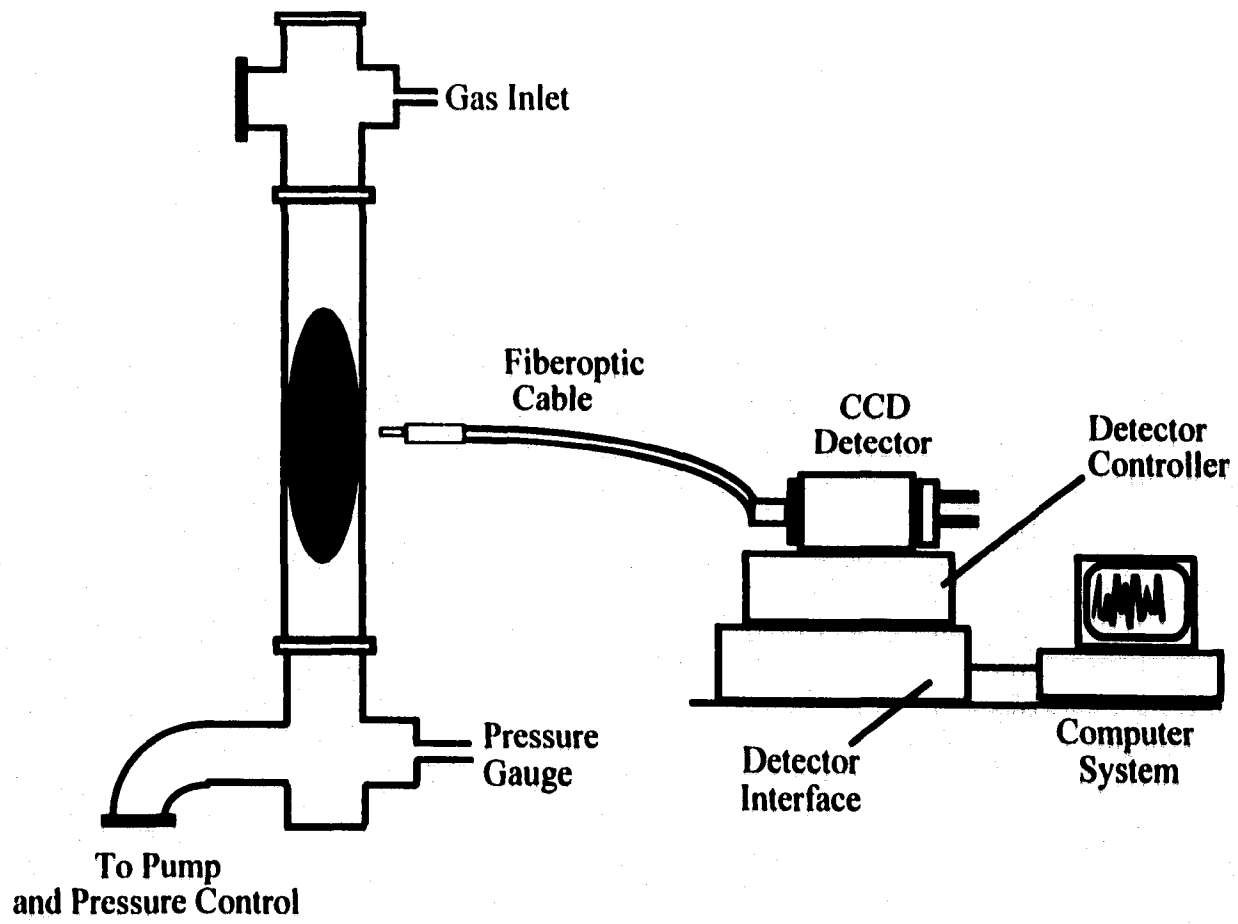


Figure 3.24. Schematic diagram of the experimental setup used to produce the glow discharges used to analyze several gas mixtures.

147. Total pressures for the experiments are maintained by a Leroy Somer mechanical roughing pump controlled by a MKS electronic throttling valve with a maximum pressure of 10 Torr and a MKS Type 252 Exhaust valve controller. A summary of the experimental conditions used here is given in Table 3.8.

Spectroscopic data are gathered from the glow discharge plasma generated in the experimental chamber using an EG&G Princeton Applied Research Corporation (PARC) model 1235 Digital Triple Grating Spectrograph connected to a Model 1430-P Peltier cooled Charge Coupled Device (CCD) Detector. The detector is under the control of an EG&G PARC Model 1430-1 Detector Controller, which is connected to an EG&G PARC Model 1461 Detector Interface. The detector is cooled by a NESLAB Instruments Coolflow CFT-25 Refrigerated Recirculator, using ethylene glycol as the cooling medium. This overall set-up is controlled by a Swan 386 personal computer using an optical multichannel analyzer applications software package (EG&G PARC OMA SPEC 2000). Throughout all of the spectroscopic analyses, a 1200 gratings/mm diffraction grating is used. Optical emissions from the plasmas are analyzed from the side of the setup using a fiber-optic cable connected to the CCD detector. The plasmas analyzed spectroscopically contains no sample. A summary of the settings used in this equipment for the analysis of these glow discharges is shown in Table 3.9.

There are a variety of methods for determining the electron temperature which are discussed in several sources.³¹⁻³³ Of these methods, the most relevant method for analyzing laboratory and welding plasmas is discussed below and can be determined from the spectral data of a plasma.³² This method relies on the assumptions of a Boltzmann population distribution and is derived as follows. First, the intensity of an atomic line, which represents the transition from an upper energy state to a lower energy state, is calculated.

$$I_{qp} = \frac{d}{4\pi} A_{qp} n_a q h\nu_{qp} \quad (3.41)$$

Table 3.8. Summary of experimental conditions used for the analysis of glow discharges containing argon-nitrogen-oxygen and helium-nitrogen-oxygen gas mixtures.

	Low Temperature		High Temperature
	Ar-8% N ₂ - 2% O ₂	He - 8%N ₂ - 2% O ₂	Ar-8% N ₂ - 2% O ₂
<i>RF Generator</i>			
Plate Current (A)	0.70	0.85	1.2
Grid Current (A)	0.145	0.195	0.045
<i>Reaction Chamber</i>			
Total Pressure (Torr)	1.5	1.5	1.5
Gas Flow Rates (SCCM)	100	100	100
Ar or He	90	90	90
N ₂	8	8	8
O ₂	2	2	2

Table 3.9. Summary of experimental parameters used by spectrometer in spectroscopic analysis of glow discharges.

	High Temperatures		Low Temperatures	
	Ar-8% N ₂ - 2% O ₂	He - 8%N ₂ - 2% O ₂	Ar-8% N ₂ - 2% O ₂	He - 8%N ₂ - 2% O ₂
(gratings/mm)	1200	---	1200	1200
Exposure Time (sec)	0.07	---	1.0	2.0
Data Scans	10	---	10	10

where I_{qp} is the absolute intensity, d is the plasma depth (cm), A_{qp} is the transition probability for the transition from the upper energy state, q , to the lower energy level (sec^{-1}), ν_{qp} is the frequency (sec^{-1}), and h is the Planck's constant (6.626176×10^{-34} J/sec). Local thermodynamic equilibrium (LTE) assumptions must be valid within the plasma domain in order to determine the electron temperature and density. When LTE conditions are valid, the density of atoms at a given energy level can be defined by the following relationship:

$$n_{aq} = n_a \frac{g_q}{Z} e^{-\frac{E_q}{kT}} \quad (3.42)$$

where n_{aq} is the density of atoms at level q (cm^{-3}), g_q is the degeneracy of the upper energy level, q , Z is the internal partition function, E_q is the energy of level q (cm^{-1}), and k is the Boltzmann constant (1.380662×10^{-23} J/K).

By inserting the term for the density of atoms, the equation for the absolute intensity of the spectral line is thus defined as follows:

$$I_{qp} = \frac{d}{4\pi} A_{qp} h \nu_{qp} n_a \frac{g_q e^{-\frac{E_q}{kT}}}{Z} \quad (3.43)$$

By taking the natural logarithm of Equation (3.43) and including a number of terms in a generic constant term, C , the final version of the equation for the Boltzmann's distribution of energy level populations is expressed in the following expression:

$$\ln\left(\frac{I}{gAv}\right) = \ln C - \left(\frac{E_q}{kT}\right) \quad (3.44)$$

where I is the integrated intensity, g is the degeneracy of the upper energy level q , A is the transition probability for the transition from state q to the lower-energy level, ν is the

frequency, E_q is the energy associated with the level q , k is the Boltzmann constant, T is the electron temperature, and C is a constant. A summary of the spectroscopically determined constants for argon and helium are shown in Tables 3.10 and 3.11, respectively.^{34,35}

There are basically two methods for determining the electron temperature of a plasma using the Boltzmann population method. The first method is the multi-line method in which a number of points computed from the same number of atomic peaks, and the second method relies on the same mathematical derivation, but only uses two points to perform the linear regression. The electron temperature is then obtained from a plot of the left hand side of Equation (3.44) versus E_q , in which the electron temperature is determined from the slope of the linear regression of the points calculated, which is $(-1/kT)$.

An attempt has been made to analyze glow discharges with both high and low electron temperature ranges in order to analyze the effect of temperature on the presence of NO species. Low electron temperatures are characterized by a diffuse plasma which fills the entire reaction chamber. On the other hand, high electron temperatures are characterized by a more concentrated glow discharge isolated in the center of the reaction chamber. Glow discharges composed of argon-nitrogen-oxygen and helium-nitrogen-oxygen mixtures have been examined. Boltzmann plots for each glow discharge are shown in Figures 3.25 to 3.27. In the argon based glow discharges, electron temperatures of 2968 K and 5885 K are measured. A helium-based glow discharge has also been analyzed. Unlike the argon-based glow discharges, the helium glow discharges do not display a significant difference in appearance with changes in the electron temperature. Without this difference, it is difficult to know if a low or high electron temperature glow discharge is being observed. In any case, a single helium glow discharge, which displays a measured electron temperature of approximately 5475 K, is presented here.

A systematic analysis of glow discharge plasmas using emission spectroscopy techniques can validate the existence of species present in the plasma phase. Plasmas with the same compositions as those used in previous calculations have been analyzed in order to determine the species present. Identification of these various species is based on data present in several standard references.³⁶⁻³⁷ Plots of the emission spectra for each of the

Table 3.10. Summary of argon peaks used in the determination of electron temperature for argon-nitrogen-oxygen plasmas.³⁴

Wavelength (nm)	ν (sec ⁻¹)	A_{qp} (sec ⁻¹)	g_k	E_q (cm ⁻¹)
394.90	25322.8	4.67×10^5	3	118460
404.44	24725.5	3.46×10^5	5	118469
415.86	24046.5	1.45×10^6	5	117184
420.07	23805.5	1.03×10^6	7	116943
425.94	23477.5	4.15×10^6	1	118871
427.22	23407.1	8.40×10^5	3	117151
430.01	23255.3	3.13×10^5	5	118407
433.36	23075.5	3.94×10^5	5	116999
434.52	23013.9	6.00×10^5	3	118469
667.73	14976.1	2.41×10^5	1	108723
675.28	14808.7	2.01×10^6	5	118907
687.13	14553.3	2.90×10^6	3	118651
693.77	14414.0	3.21×10^6	1	118512
696.54	14356.7	6.70×10^6	3	107496
703.03	14224.1	2.78×10^6	5	119683
706.72	14150.0	3.95×10^6	5	107290
714.70	13991.9	6.50×10^5	3	107132
727.29	13749.7	2.00×10^6	3	107496
737.21	13564.7	2.00×10^6	9	119024
738.40	13542.8	8.70×10^6	5	107290
750.39	13326.4	4.72×10^7	1	108723
751.46	13307.4	4.30×10^7	1	107054

Table 3.11. Summary of helium peaks used in the determination of electron temperature for argon-nitrogen-oxygen plasmas.^{33,34}

Wavelength (nm)	ν (sec ⁻¹)	A_{qp} (sec ⁻¹)	g_k	E_q (cm ⁻¹)
388.86	25715.9	9.48×10^6	9	185565
402.62	24851.1	1.17×10^7	15	193917
447.15	22363.9	2.51×10^7	15	191445
492.19	20317.2	2.02×10^7	5	191447
501.57	19937.5	1.34×10^7	3	186210
587.57	17019.2	7.06×10^7	15	186102
667.82	14974.2	6.38×10^7	5	186105
706.57	14153.9	1.54×10^7	3	183237
728.13	13733.7	1.81×10^7	1	184865

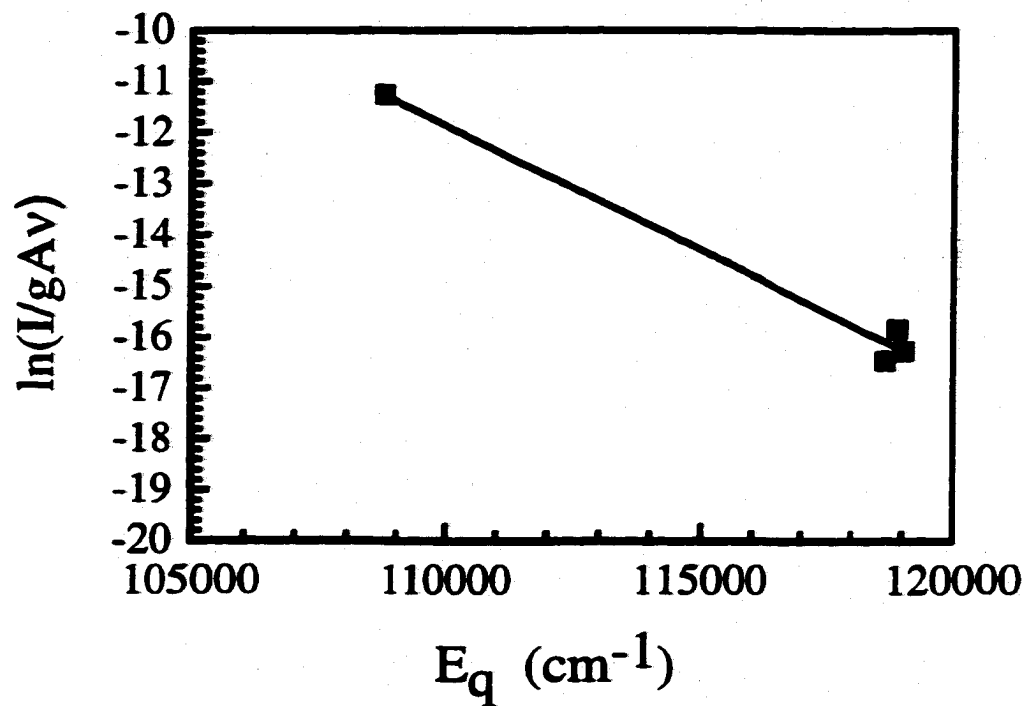


Figure 3.25. Boltzmann plot for an Ar – 8% N₂ – 2% O₂ glow discharge plasma at a total pressure of 1.5 Torr with a measured electron temperature of 2968 K.

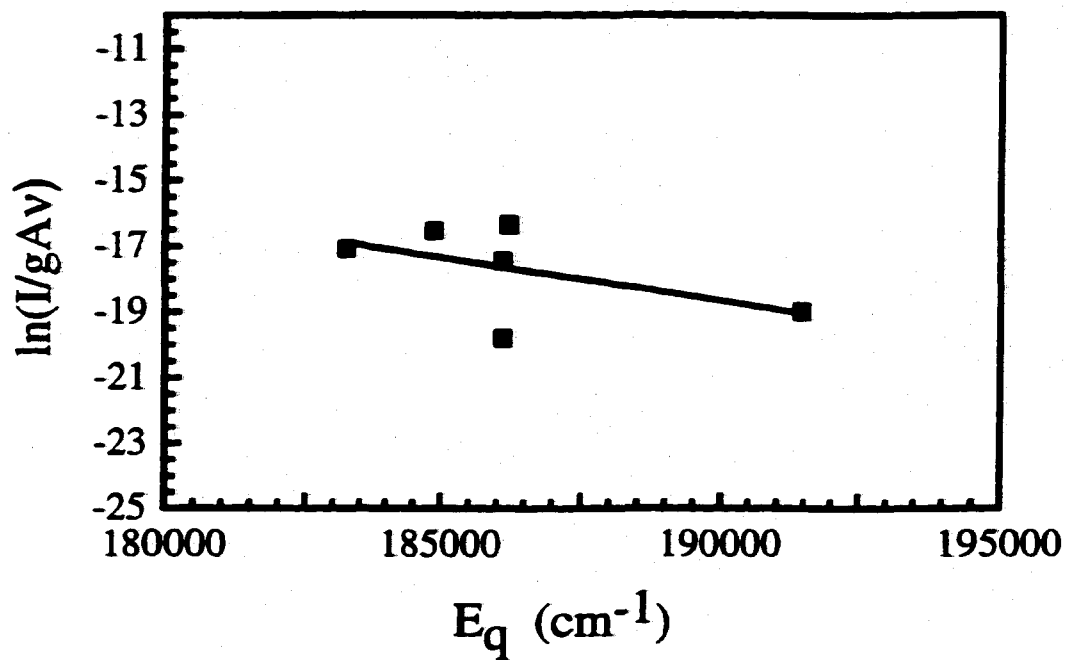


Figure 3.26. Boltzmann plot for a He-8% N₂-2% O₂ glow discharge plasma at a total pressure of 1.5 Torr with a measured electron temperature of 5475 K.

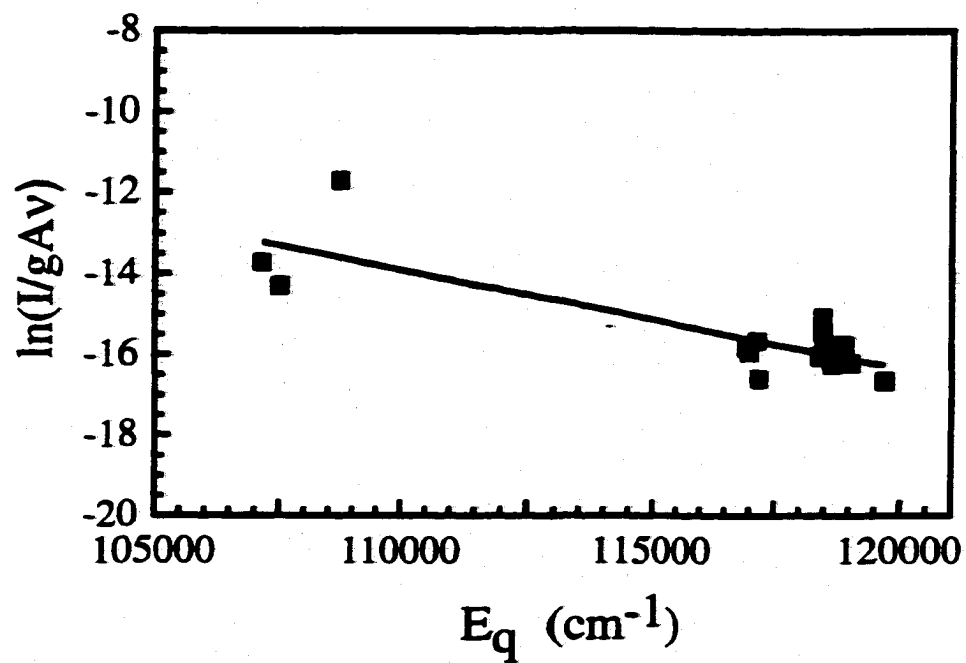


Figure 3.27. Boltzmann plot for an Ar – 8% N₂ – 2% O₂ glow discharge plasma at a total pressure of 1.5 Torr with a measured electron temperature of 5885 K.

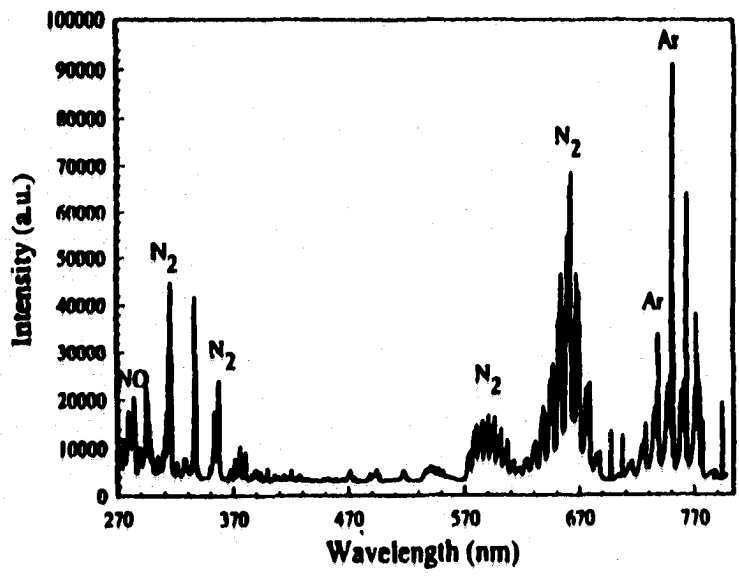
glow discharges analyzed here are shown in Figures 3.28 to 3.30. In the low temperature argon-nitrogen-oxygen spectra shown in Figure 3.28(a), there is a significant molecular nitrogen component to the spectra analyzed. NO peaks are also present in the spectra, indicating a reaction between the nitrogen and oxygen in the plasma phase. These peaks are highlighted in Figure 3.28(b).

When the electron temperature of the plasma is raised, the NO peaks begin to disappear. As shown in Figures 3.29(a&b), these NO peaks become less pronounced at an increased electron temperature for a helium-based glow discharge. Similar results are also observed in the case of argon glow discharges. As the temperature is further increased, the NO peaks disappear, and monatomic nitrogen and oxygen peaks become dominant. Figure 3.30(a) shows the spectra measured for an argon-based glow discharge at a higher temperature. Peaks for the monatomic nitrogen species are highlighted in Figure 3.30(b). Thus, the use of emission spectroscopy provides definitive proof for the presence of NO at low electron temperatures and validates the conclusions from the comprehensive calculations performed here.

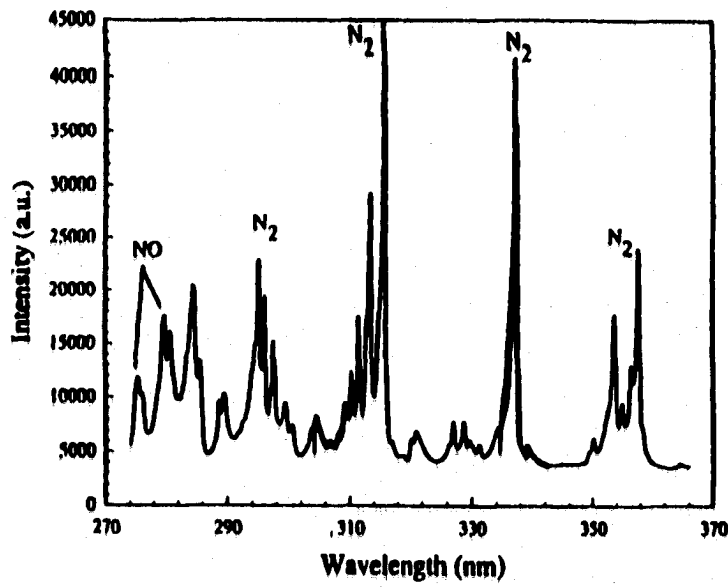
3.5 SUMMARY AND CONCLUSIONS

The nature and concentration of various nitrogen-bearing species in the welding arc during GTA welding operations have been determined based on detailed calculations of the partition functions for each nitrogen-bearing species. Number density calculations show that neutral monatomic and diatomic species dominate near the surface of the weld pool in GTA welding arcs. On the other hand, ionic and atomic species dominate away from the weld pool surface.

The monatomic nitrogen partial pressures in the plasma formed at temperatures higher than those at the weld pool surface cause dramatic increases in the amount of nitrogen absorbed in the weld metal. At plasma temperatures higher than 5000 K, the iron weld pool surface reaches nitrogen saturation at all temperatures. Therefore, the temp-



(a)



(b)

Figure 3.28(a&b). (a) Emission spectra for a low-temperature Ar-8%N₂-2%O₂ glow discharge plasma and (b) the portion of the spectra with the NO peaks highlighted.

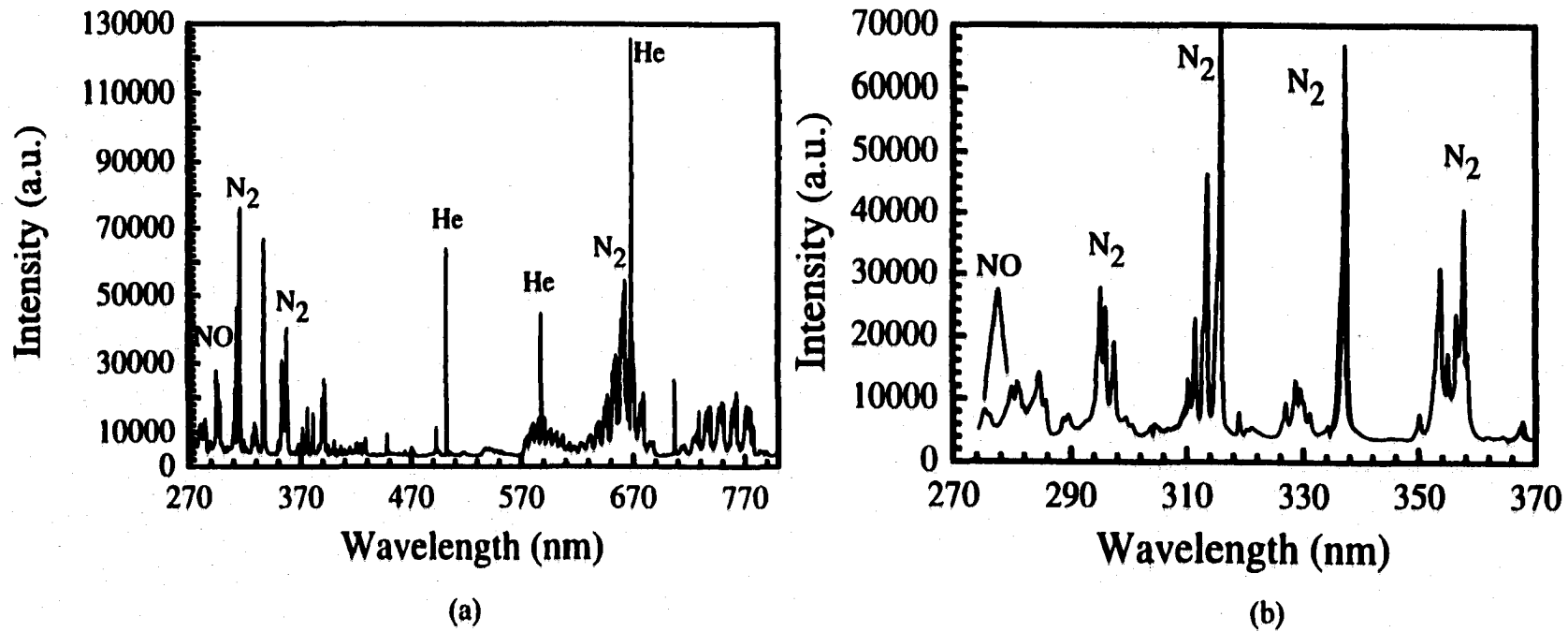
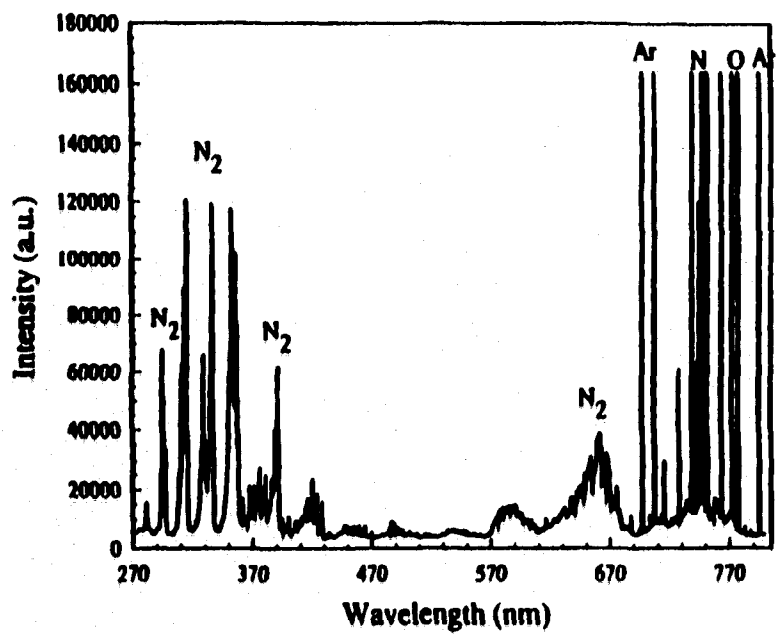
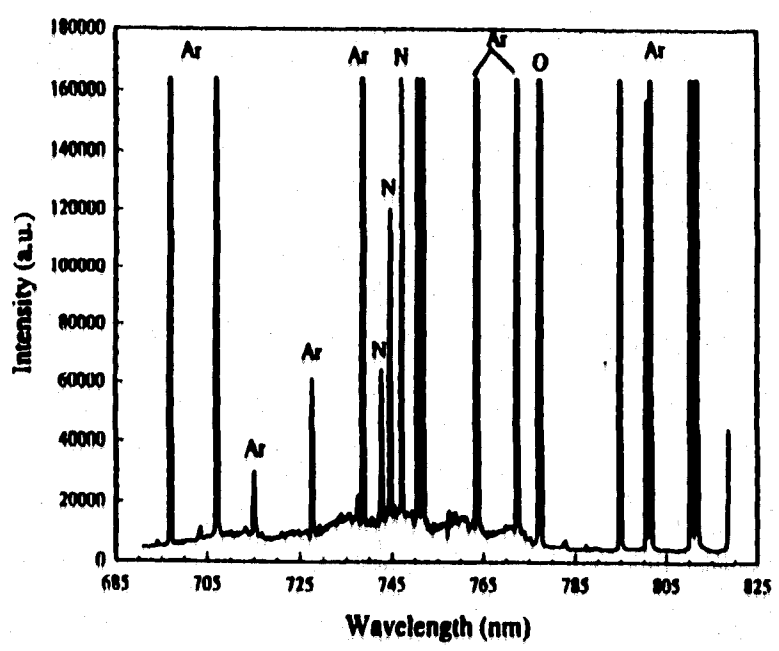


Figure 3.29(a&b). (a) Emission spectra for a low temperature He-8%N₂-2%O₂ glow discharge plasma and (b) the portion of the spectra with the NO peaks highlighted.



(a)



(b)

Figure 3.30(a&b). (a) Emission spectra for a high temperature Ar-8%N₂-2%O₂ glow discharge plasma and (b) the portion of the spectra with the N and O peaks highlighted.

erature difference between the plasma and the weld metal surface plays a significant role in the enhanced nitrogen dissolution process.

Additions of oxygen into a nitrogen-containing plasma, like the addition of air into the welding arc, affect the species density distribution of nitrogen species in the welding arc. Calculations show a significant increase in the number density of monatomic nitrogen gas when oxygen is added to the shielding gas in the welding arc. These calculations therefore provide a conclusive scientific basis to explain the experimentally observed enhancement in nitrogen concentrations with the addition of oxygen to the arc.

There are significant differences in the electron density between an argon and a helium plasma for electron temperatures below approximately 15000 K. This difference in electron density decreases progressively as the electron temperature increases. Additions of oxygen and nitrogen to pure argon have little effect on the electron density over the range of temperatures. On the other hand, when oxygen and nitrogen are added to pure helium, significant increases in the electron density are observed at temperatures below approximately 15000 K.

Emission spectroscopic studies of glow discharge plasmas containing the same gas compositions as those in the above calculations have also been performed. These studies provide evidence for the existence of NO species in the plasma phase at low temperatures and the important role of dissociation of diatomic species as the temperature is increased. As a whole, these emission spectroscopic studies reinforce the trends in species densities calculated here.

REFERENCES

- ¹ J.D. Katz and T.B. King, "The Kinetics of Nitrogen Absorption and Desorption from a Plasma Arc by Molten Iron", *Met. Trans. B*, 1989, 20B, 175-185.
- ² S.A. Gedeon and T.W. Eagar, "Thermochemical Analysis of Hydrogen Absorption in Welding", *Weld. J.*, 1990, 69, 264s-271s.
- ³ K. Mundra and T. DebRoy, "A General Model for Partitioning of Gases between a Metal and Its Plasma Environment", *Metall. and Mater. Trans. B*, 1995, 26B, 149-157.
- ⁴ T.A. Palmer and T. DebRoy, "Physical Modeling of Nitrogen Partition between the Weld Metal and Its Plasma Environment", *Weld. J.*, 1996, 75(7), 197s-207s.
- ⁵ A. Bandopadhyay, A. Banerjee, and T. DebRoy, "Nitrogen Activity Determination in Plasmas", *Metall. Trans. B*, 1992, 23B, 207-214.
- ⁶ T.A. Palmer, K. Mundra, and T. DebRoy, "Nitrogen Dissolution in the Weld Metal – Current Status and Research Opportunities", in Mathematical Modelling of Weld Phenomena 3, ed. by H. Cerjak, (The Institute of Materials, London), 1997, 3-40.
- ⁷ J.D. Fast, "The Dissociation of Nitrogen in the Welding Arc", *Philips Res. Rep.*, 1947, 2, 382-398.
- ⁸ M. Uda and T. Wada, "Solubility of Nitrogen in Arc-Melted and Levitation-Melted Iron and Iron Alloys", *Trans. Nat. Res. Inst. Metals*, 1968, 10(2), 21-33.
- ⁹ P.D. Blake, "Oxygen and Nitrogen in Weld Metal", *Weld. Res. Int.*, 9(1), 1979, 23-56.
- ¹⁰ T. Kobayashi, T. Kuwana, and Y. Kikuchi, "Arc Atmosphere and Nitrogen Content of Weld Metal", *Welding in the World*, 5(2), 1967, 58-73.
- ¹¹ J.W. Hooijmans and G. den Ouden, "The Influence of Oxygen on Nitrogen Absorption during Arc Melting of Iron", *Weld. J.*, 1992, 71(10), 377s-380s.
- ¹² C.J. Allum, "Nitrogen Absorption from Welding Arcs", *Bulletin of Welding Research Council*, 369, Dec. 1991-2, 68-84.
- ¹³ V.I. Galinich and V.V. Podgaetskii, "The Effects of Nitrogen on Weld Porosity When Welding Steel Under Argon or CO₂ Shielding", *Avt. Svarka*, 1961, 16(2), 18-27.
- ¹⁴ I.K. Pokhodnya and A.P. Pal'tsevich, "The Part Played by Oxygen in the Absorption of Nitrogen by Metal During Arc Welding", *Avt. Svarka*, 1971, 25(2), 8-11.

- ¹⁵ R.D. Pehlke and J.F. Elliott, "Solubility of Nitrogen in Liquid Iron Alloys. 1. Thermodynamics", *Trans. AIME*, 1960, 218, 1088-1101.
- ¹⁶ G. den Ouden, "The Role of Nitrogen in Electric Arc Welding", *Philips Weld. Reporter*, 13(1), 1977, 1-6.
- ¹⁷ H.M.J. Pflanz, Thesis, Techn. University, Eindhoven, 1967.
- ¹⁸ G.J. Dunn, C.D. Allemand, and T.W. Eagar, "Metal Vapors in Gas Tungsten Arcs. I. Spectroscopy and Monochromatic Photography", *Met. Trans. A*, 1986, 17A, 1851-1863.
- ¹⁹ G.J. Dunn and T.W. Eagar, "Metal Vapors in Gas Tungsten Arcs: Part II. Theoretical Calculations of Transport Properties", *Met. Trans. A*, 1986, 17A, 1865-1871.
- ²⁰ K.S. Drellishak, D.P. Aeschliman, and A.B. Cambel, "Partition Functions and Thermodynamic Properties of Nitrogen and Oxygen Plasmas", *Phys. of Fluids*, 1965, 8(9), 1590-1600.
- ²¹ K.S. Drellishak, C.F. Knopp, and A.B. Cambel, "Partition Functions and Thermodynamic Properties of Argon Plasma", *Phys. of Fluids*, 1963, 6(9), 1280-1288.
- ²² J.F. Key, J.W. Chan, and M.E. McIlwain, "Process Variable Influence on Arc Temperature Distribution", *Weld. J.*, 62(7), 1983, 179s-184s.
- ²³ A.E.F. Gick, M.B.C. Quigley, and P.H. Richards, "The Use of Electrostatic Probes to Measure the Temperature Profiles of Welding Arcs", *J. Phys. D: Appl. Phys.*, 6, 1973, 1941-1949.
- ²⁴ J. Wendelstorf, I. Decker, H. Wohlfahrt, and G. Simon, "TIG and Plasma Arc Modeling: A Survey", in Mathematical Modelling of Weld Phenomena 3, ed. by H. Cerjak, (The Institute of Materials, London, 1997), pp. 848-897.
- ²⁵ C.S. Wu, M. Ushio, and M. Tanaka, "Analysis of the TIG Welding Arc Behavior", *Comp. Mat. Sci.*, 1997, 7, 308-314.
- ²⁶ G.N. Haddad and A.J.D. Farmer, "Temperature Measurements in Gas Tungsten Arcs", *Weld. J.*, 1985, 64(12), 399s-342s.
- ²⁷ R.T.C. Choo, J. Szekely, and R.C. Westhoff, "On the Calculation of the Free Surface Temperature of Gas-Tungsten-Arc Weld Pools from First Principles: Part I. Modeling the Welding Arc", *Met. Trans. B*, 23B, 1992, 357-369.

- ²⁸ A.J.D. Farmer and G.N. Haddad, "Temperature Determinations in a Free-Burning Arc: I. Experimental Techniques and Results in Argon", *J. Phys. D: Appl. Phys.*, 1984, 17, 1189-1196.
- ²⁹ P.G. Jönsson, J. Szekely, R.T.C. Choo, and T.P. Quinn, "Mathematical Models of Transport Phenomena Associated with Arc-Welding Process: A Survey", *Modelling Simul. Mater. Sci. Eng.*, 1994, 2, 995-1016.
- ³⁰ M.W. Chase, Jr., C.A. Davies, J.R. Downey, Jr., D.J. Frurip, R.A. McDonald, and A.N. Syverud, JANAF Thermochemical Tables, 3rd Ed., (American Chemical Society and American Institute for Physics, Washington, DC), 1985.
- ³¹ F. Cabannes and J. Chapelle, "Spectroscopic Plasma Diagnostics", in Reactions Under Plasma Conditions, Volume 1, ed. by M. Venugopalan, (Wiley Interscience, New York), 1971, 367-469.
- ³² P.W.J.M. Boumans, Theory of Spectrochemical Excitation, (Plenum Press, New York), 1966, 79-88.
- ³³ H.R. Griem, Plasma Spectroscopy, (McGraw-Hill, New York), 1964.
- ³⁴ W.L. Wiese, M.W. Smith, and B.M. Glennon, Atomic Transition Probabilities: Volume I Hydrogen Through Neon, NSRDS-NBS 4, National Standard Reference Data Series, (National Bureau of Standards, Washington, DC), 1966.
- ³⁵ C.E. Moore, Atomic Energy Levels, NSRDS-NBS 35, Vols. 1-3; (National Bureau of Standards, Washington, DC, 1971).
- ³⁶ R.W.B. Pearse and A.G. Gaydon, The Identification of Molecular Spectra, 4th edn.; (Chapman and Hall, New York, 1976).
- ³⁷ G.R. Harrison, *et al.*: M.I.T. Wavelength Tables, (M.I.T. Press, Cambridge), 1982.

Chapter 4

NITROGEN DISSOLUTION DURING THE GTA WELDING OF PURE IRON

4.1 BACKGROUND

The presence of nitrogen concentrations in excess of Sieverts' Law calculations during the arc welding of iron and steel with nitrogen containing shielding gases is well established.¹⁻⁷ In general, these studies have primarily compiled the nitrogen concentrations in the weld metal resulting from a variety of welding conditions. As a result, a catalog of experimental results showing how changes in welding parameters and base metal composition affect the weld metal nitrogen concentration has been recorded. In all cases, the nitrogen concentration quickly rises at low nitrogen partial pressures in the gas phase and reaches a saturation value. Several models have been developed to explain these observations.¹⁻⁷ These models are primarily based on a steady-state mechanism involving the absorption of monatomic nitrogen in the portion of the weld pool under the arc column and desorption of nitrogen from the solidifying metal outside the arc.^{3,6,7} A comprehensive review of this previous work is included in Chapter 2.

Any analysis of the nitrogen dissolution reaction during welding is further complicated by differences between the various welding operations. For example, gas metal arc (GMA) and gas tungsten arc (GTA) welding operations display different mechanisms for the introduction of nitrogen and other diatomic gases into the weld pool. The primary difference between these two welding operations is the characteristics of the electrode or heat source. A non-consumable tungsten electrode is used during GTA welding operations. Therefore, only a single pathway for gaseous dissolution is created between the plasma phase and the weld pool surface. On the other hand, a consumable metal electrode is used in GMA welding. This type of electrode introduces a second pathway for nitrogen dissolution between the molten metal at the electrode tip and the plasma phase surrounding it. Multiple pathways for nitrogen dissolution introduce additional plasma-

metal interactions and more complexity than desired into the study of the nitrogen dissolution reaction. For the purposes of this study, a single pathway for nitrogen dissolution is therefore desired.

In order to further understand the fundamental nature of the nitrogen dissolution reaction, a series of controlled GTA welding experiments on pure iron samples has been performed. The goal of these experiments is to provide a basis for an increased understanding of the nitrogen dissolution reaction in iron during GTA welding. These experiments investigate the effects of changes in the nitrogen addition to the shielding gas and travel speed on the resulting nitrogen concentration in the weld pool. Nitrogen concentrations have been measured at several locations along the weld line. The effects of nitrogen in the weld metal on the weld pool characteristics, such as the formation of porosity in the weld metal and its resulting microstructure, have also been analyzed. Results will be used to develop and test a mathematical model to predict the nitrogen concentration in the weld pool.

4.2 EXPERIMENTAL PROCEDURE

4.2.1 GTA Welding of Pure Iron Samples

A series of autogenous, bead-on plate GTA welds have been made on pure iron samples in a controlled atmosphere chamber. The base plate used in these welding experiments, whose chemical composition is shown in Table 4.1, is part of a special heat produced at the LTV Technology Center. The chemical analysis of the base metal has been provided by Spectrochemical Laboratories, Inc., of Pittsburgh, PA. Individual coupons have been cut from this base plate with dimensions of 58 mm in width, 124 mm in length, and 7.3 mm in depth. Three weld lines, each 101.6 mm in length, have been placed on each coupon. Each weld line has a sufficient separation from the others on the coupon to avoid undesired interactions, such as re-heating of the weld lines and additional nitrogen dissolution from subsequent welding runs.

Nearly pure iron samples, with only trace levels of alloying elements, have been used in order to avoid the effects of additional alloying elements on the nitrogen solubility. On the other hand, even the presence of trace levels of many of the alloying elements present

Table 4.1. Chemical composition and interaction parameters for the alloying elements in the base plate.⁸⁻¹²

<u>Alloying Element</u> (i)	<u>Composition</u> (wt.%)	ϵ_N^i
Fe	99.7358	---
Al	0.031	0.002
C	0.0022	0.25
Cr	0.002	-0.045
Mn	0.20	-0.02
Mo	0.003	-0.011
[N]	0.002	----
Ni	0.006	0.010
[O]	0.002	0.05 -0.14
P	0.006	0.051
S	0.001	0.013
Si	0.009	0.047

in the base metal affects the nitrogen solubility. The effect of the alloying elements present in the base plate on the resulting nitrogen solubility is based on the calculation of the individual interaction coefficients, $\epsilon_N^{(j)}$. These expressions are defined in terms of the activity coefficient of nitrogen (f_N) in the following relation:⁸⁻¹²

$$\epsilon_N^{(j)} = \frac{\partial \ln f_N}{\partial X_j} \quad (4.1)$$

where j is the alloying element and X_j is the mole fraction of the alloying element. Table 4.1 also contains the values of the interaction coefficients for the alloying elements present in the base plate with nitrogen in iron.⁸⁻¹² This relationship and those that follow are based on a Henrian Law behavior for solutions, making the interaction parameters and activity coefficients valid only in relatively dilute solutions. Further, the interaction coefficients, once calculated, are used to determine the effect of these alloy additions on the activity coefficient of nitrogen in solution.

$$\ln f_N(X_N, X_2, X_3, \dots) = X_N \frac{\partial \ln f_N}{\partial X_N} + X_2 \frac{\partial \ln f_N}{\partial X_2} + X_3 \frac{\partial \ln f_N}{\partial X_3} + \dots \quad (4.2)$$

Combining the above two relations, the interaction coefficients can be calculated in the following relationships, based either on the mole fraction or weight fraction of alloying elements present in solution in iron.

$$\ln f_N(X_N, X_2, X_3, \dots) = X_N \epsilon_N^{(N)} + X_2 \epsilon_N^{(2)} + X_3 \epsilon_N^{(3)}, \dots \quad (4.3)$$

$$\ln f_N(\%N, \%2, \%3, \dots) = \epsilon_N^{(N)} (\%N) + \epsilon_N^{(2)} (\%2) + \epsilon_N^{(3)} (\%3), \dots \quad (4.4)$$

The calculated activity coefficient, f_N , for the base metal used in these welding experiments is not significantly different from that in pure iron. It is on the order of 0.997

for the base metal, as compared to a value of unity for a pure material. This modified activity coefficient for nitrogen in solution is now used to determine the nitrogen solubility in the base metal. The calculation of the nitrogen solubility in the base plate is based on Sieverts' Law, which is derived from the chemical reaction shown in Equation (4.5). The relations used here to calculate the equilibrium constant, K , and the nitrogen concentration are also shown in Equations (4.6) and (4.7).



$$K = \frac{a_{\text{N}}}{(P_{\text{N}_2})^{1/2}} = \frac{(\text{N}) \cdot f_{\text{N}}}{(P_{\text{N}_2})^{1/2}} = \exp\left(\frac{-\Delta G^\circ}{RT}\right) \quad (4.6)$$

$$[\text{N}](\text{wt.}\%) = \frac{(P_{\text{N}_2})^{1/2}}{f_{\text{N}}} \exp\left(\frac{-\Delta G^\circ}{RT}\right) \quad (4.7)$$

The nitrogen solubility in the base plate shows little to no difference with that calculated for pure iron. For example, at 1873 K and P_{N_2} of 1 atm., the nitrogen solubility in pure iron is 448 ppm. The base metal nitrogen solubility is only slightly higher (449.7 ppm).^{9,10,12} Therefore, the small amounts of alloying elements present in the base metal have a negligible effect on the nitrogen solubility at this temperature and 1 atm. pressure of N_2 .

The welding chamber used here is schematically shown in Figure 4.1. Within the chamber, the welding head and electrode are maintained stationary, and the sample is fastened to a computer-controlled stage which controls travel speed. The distance between the electrode tip and the workpiece, defined as the arc length, is maintained constant throughout the welding runs, and the electrode is manipulated in the vertical axis using a track system constructed using components available from Bug-O Systems.[®] A 2% thoriated tungsten non-consumable electrode with a diameter of 2.38 mm has been used. Power is supplied to the electrode using a PowCon[®] 300 power supply. Two sets

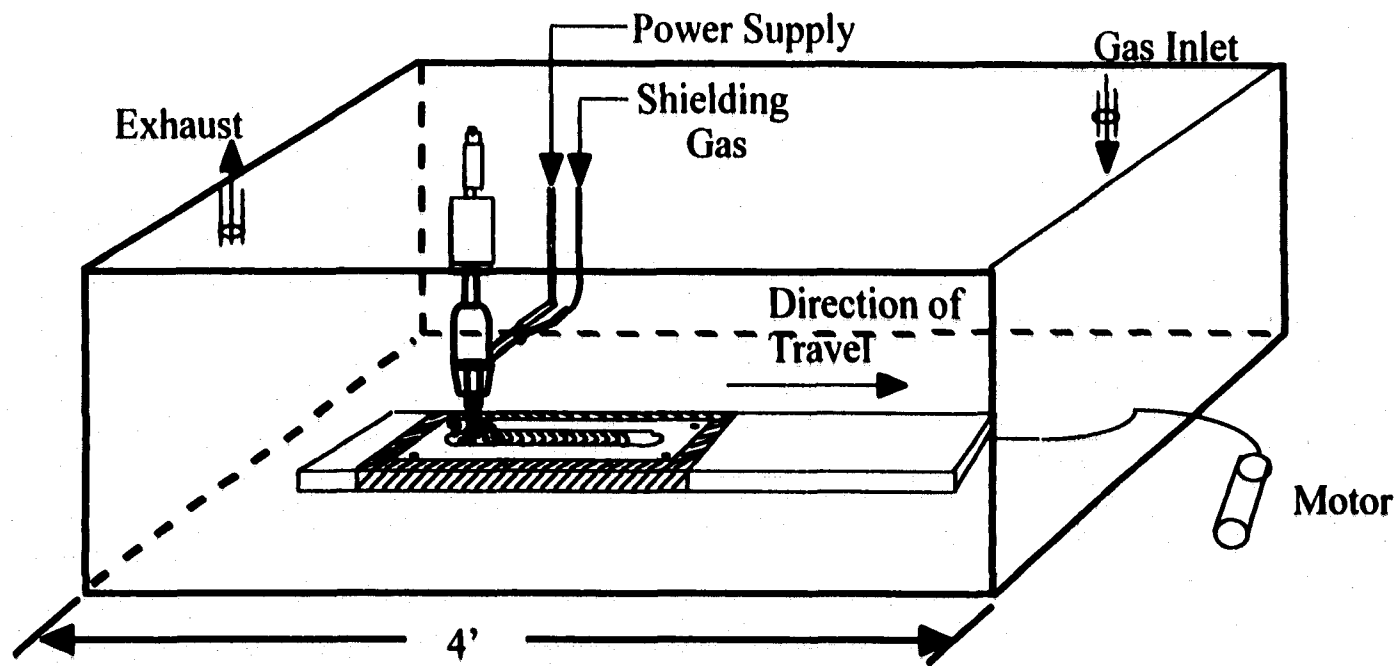


Figure 4.1. Schematic diagram of experimental chamber used for controlled GTA welding experiments.

of welding parameters have been studied here and are summarized in Table 4.2. In general, only the effect of a change in the travel speed on the resulting nitrogen concentration is studied.

Since environmental purity is very important in this study, several precautions have been taken to avoid contamination of the shielding gas and weld pool with the surrounding atmosphere. First, the chamber has been back-filled with argon to purge the system of unwanted environmental impurities. Throughout the duration of each welding run, a total pressure of 1 atm. has been maintained within the experimental chamber. Shielding of the weld pool is provided by the introduction of controlled argon-nitrogen gas mixtures onto the weld pool surface through the welding torch head. The nitrogen addition to the argon shielding gas acts as the nitrogen source for the study of the nitrogen dissolution reaction. Nitrogen additions ranging between 0 and 20% have been made to the argon shielding gas. In all cases, ultra high purity (UHP) argon and nitrogen gases are used. These gases contain extremely low quantities of impurities, thus increasing the controls on the experiments and decreasing any factors, which may unduly affect the nitrogen concentration results.

4.2.2 Measurement of Nitrogen Concentration in Weld Metal

The nitrogen concentration in the weld metal has been measured at several locations along the weld line. Figure 4.2 schematically shows the location of the samples removed from the weld line for analysis. All of these samples are 0.635 mm in thickness and located at 12.7, 38.1, 63.5, and 88.9 mm from the start point of each weld line. The majority of the remaining base metal is then removed along both the depth and width of each sample, as schematically shown in Figure 4.3. Therefore, each sample has a uniform depth of 3 mm and contains base metal surrounding the fusion zone. Nitrogen concentrations have been measured using conventional thermal conductivity methods by USX Engineering Consultants in Monroeville, PA. The results of this analysis are shown in Table 4.3.

The samples shown in Figure 4.3 contain base metal along with metal from the fusion zone. This extra material in each sample dilutes the resulting nitrogen concentration in

Table 4.2. Experimental Welding Parameters Considered in this study.

<u>Welding Parameters</u>	<u>Condition #1</u>	<u>Condition #2</u>
Arc Current (A)	150	150
Arc Length (mm)	3.175	3.175
Total Flow Rate (cfh)	70	70
Total Pressure (atm.)	1.0	1.0
Travel Speed (mm/sec)	8.46	4.23
Electrode Diameter (mm)	2.38	2.38
Ar-N ₂ Shielding Gas Mixture (Vol.%)	0 – 20%	0 – 20%

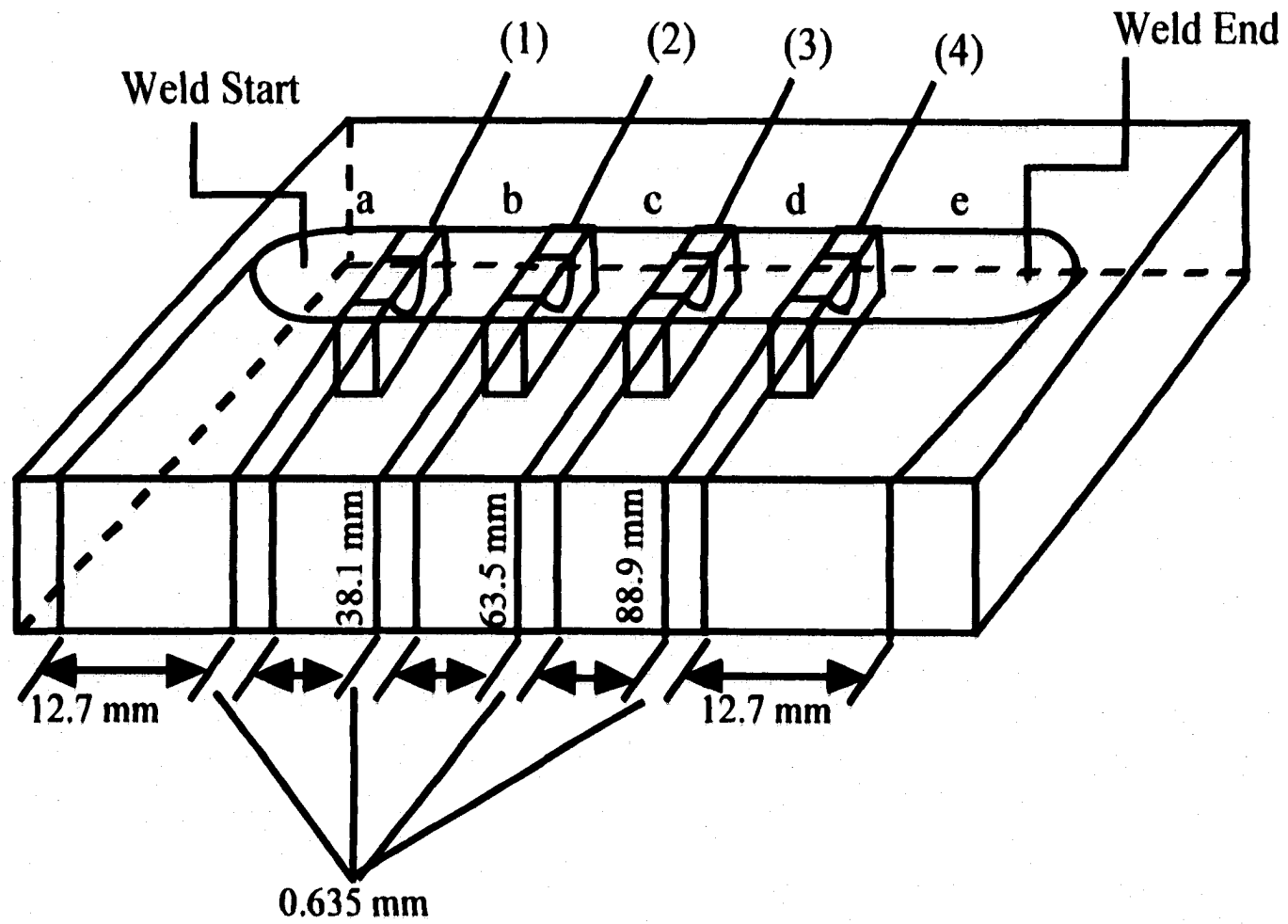


Figure 4.2. Schematic representation of location of samples along weld line removed for nitrogen concentration analysis.

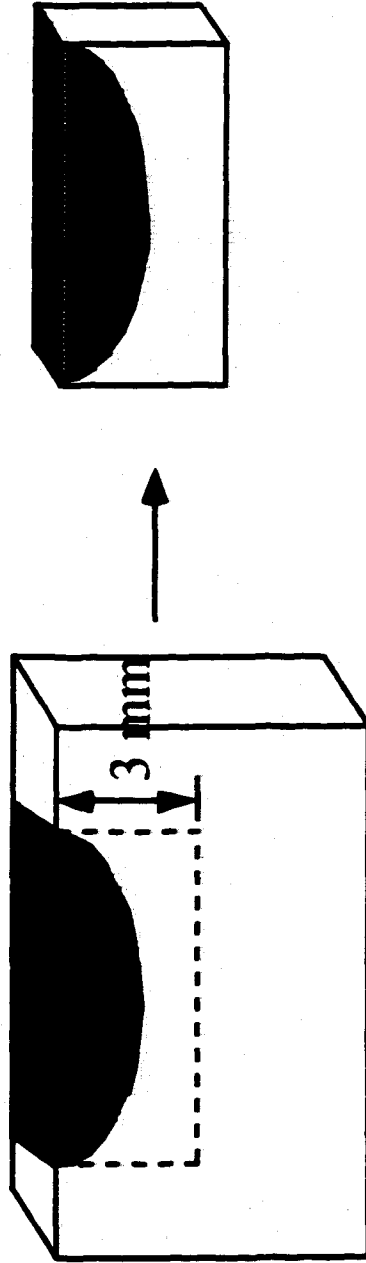


Figure 4.3. Schematic diagram of weld metal samples analyzed for the residual nitrogen concentration.

Table 4.3. Summary of raw experimental residual nitrogen concentrations measured in each of the samples.

NITROGEN CONCENTRATION (PPM)

<u>Welding Conditions</u>	<u>Sample 1</u>	<u>Sample 2</u>	<u>Sample 3</u>	<u>Sample 4</u>	<u>Average</u>
<i>Condition #1</i>					
Pure Ar	20	20	20	18	20 ± 1
Ar – 5% N ₂	108	149	159	147	141 ± 19
Ar – 10% N ₂	145	138	155	130	142 ± 9
Ar – 15% N ₂	126	146	133	150	139 ± 10
Ar – 20% N ₂	171	175	162	152	165 ± 9
<i>Condition #2</i>					
Pure Ar	---	---	---	---	---
Ar – 5% N ₂	122	216	223	133	173.5 ± 46
Ar – 10% N ₂	224	245	248	236	238 ± 9
Ar – 15% N ₂	263	325	256	257	275 ± 29
Ar – 20% N ₂	209	199	196	194	199.5 ± 6

the weld metal. In order to take into account the extra material included in the samples, the nitrogen concentrations are converted so that only the nitrogen present in the fusion zone is measured. The conversion is based on the following relationship:

$$C_{\text{Tot}}(V_{\text{Tot}}) = C_{\text{FZ}}(V_{\text{FZ}}) + C_{\text{BM}}(V_{\text{BM}}) \quad (4.8)$$

where C_{BM} is the concentration in the base metal, which is 20 ppm according to the chemical analysis of the base metal, C_{Tot} is the total concentration of the samples analyzed, C_{FZ} is the fusion zone concentration, V_{Tot} is the total volume of the material analyzed, V_{BM} is the volume of the base metal, and V_{FZ} is the volume of the fusion metal. In this relationship, all concentrations are expressed in terms of weight percent.

Measurements for the width and depth of the fusion zone and the columnar grains of each sample are required to determine the volume of the fusion zone (V_{FZ}). Upon examination, each weld pool cross section displays many of the same characteristics. A schematic diagram of the weld pool cross sections featuring these common regions and explanations of the measurement locations is shown in Figure 4.4. The columnar grain region shown in this figure can be equated to the heat-affected zone (HAZ) in a typical weldment. Since pure iron is being used in these experiments, only grain growth is expected in the HAZ. The measurements are listed in Table 4.4, along with the aspect ratio, which is the ratio between the measured width and depth and provides a general measure of the weld pool shape.

The concentration in the fusion zone, C_{FZ} , is defined by the following relationship:

$$C_{\text{FZ}} = \frac{C_{\text{Tot}}(V_{\text{Tot}}) - C_{\text{BM}}(V_{\text{BM}})}{V_{\text{FZ}}} \quad (4.9)$$

Table 4.5 lists the converted nitrogen concentrations in the fusion zone for each welding condition, along with the range of concentrations and the average concentration for each weld line. There is a significant difference between these converted nitrogen

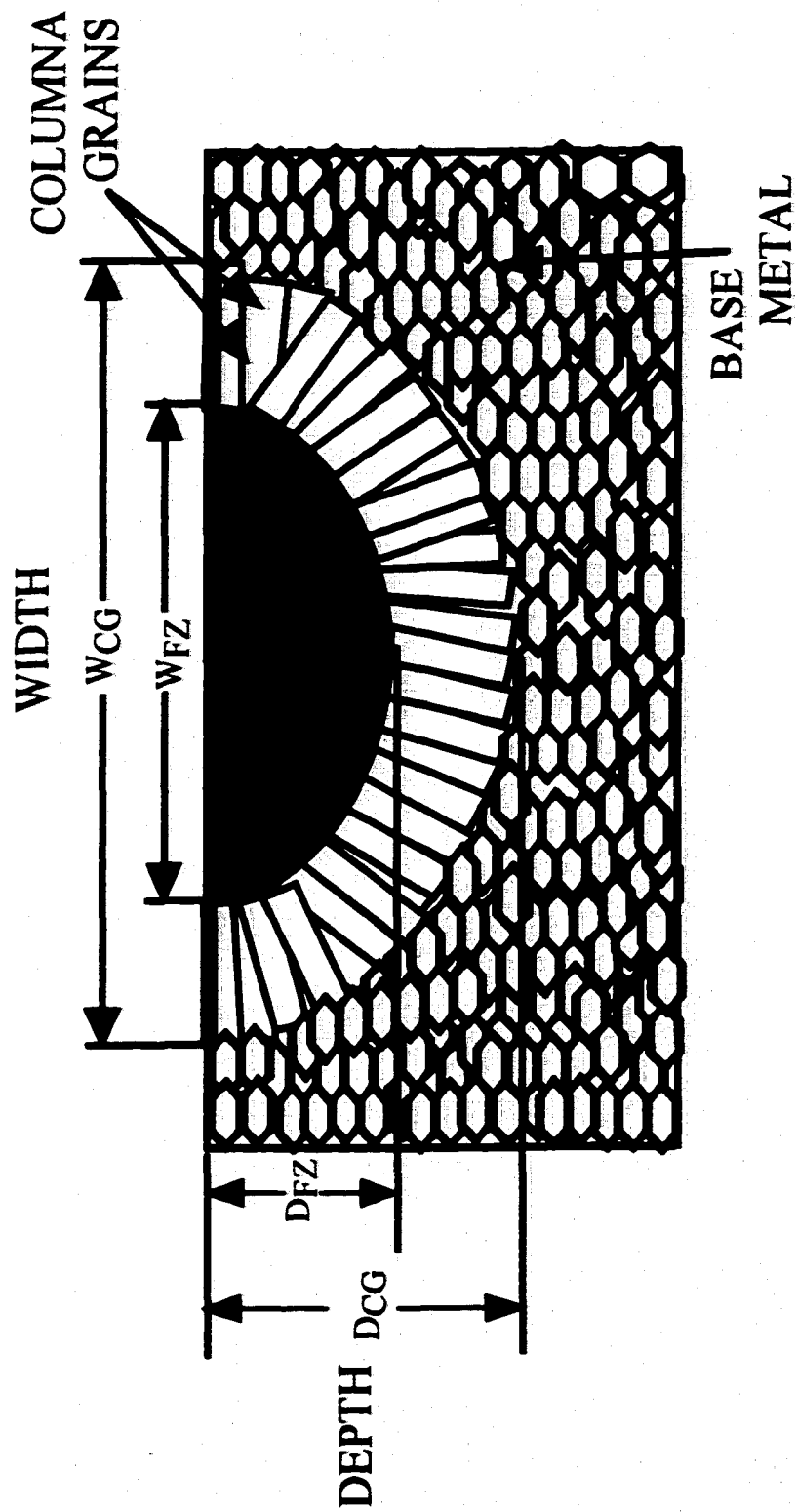


Figure 4.4. Schematic drawing of the weld pool cross section.

Table 4.4. Summary of measured weld pool dimensions.

<u>Welding Conditions</u>	<u>WELD POOL WIDTH</u> (mm)		<u>WELD POOL DEPTH</u> (mm)		<u>ASPECT RATIO</u> (Width-to-Depth)	
	<u>Fusion Zone</u> (W _{FZ})	<u>Columnar Grains</u> (W _{CG})	<u>Fusion Zone</u> (D _{FZ})	<u>Columnar Grains</u> (D _{CG})	<u>Fusion Zone</u> (W _{FZ} /D _{FZ})	<u>Columnar Grains</u> (W _{CG} /D _{CG})
<i>Condition #1</i>						
Pure Ar	4.5	8.0	1.0	2.0	4.5	4.0
Ar – 5% N ₂	5.1	7.0	1.0	2.0	5.1	3.5
Ar – 10% N ₂	6.5	8.5	0.75	2.0	8.7	4.2
Ar – 15% N ₂	5.5	7.5	0.75	2.0	7.3	3.8
Ar – 20% N ₂	6.0	8.0	0.75	2.25	8.0	3.6
<i>Condition #2</i>						
Pure Ar	5.25	9.5	1.5	3.0	3.5	3.2
Ar – 5% N ₂	7.5	10.0	1	3.5	7.5	2.9
Ar – 10% N ₂	7.75	10.0	1.1	3.0	7.0	3.3
Ar – 15% N ₂	6.5	10.0	1.1	3.0	5.9	3.3
Ar – 20% N ₂	8.0	10.5	1.0	3.5	8.0	3.2

Table 4.5. Summary of converted residual nitrogen concentrations.

NITROGEN CONCENTRATION (PPM)

<u>Welding Conditions</u>	<u>Sample 1</u>	<u>Sample 2</u>	<u>Sample 3</u>	<u>Sample 4</u>	<u>Average</u>
<i>0.847 cm/sec</i>					
Pure Ar	20	20	20	20	20 ± 0
Ar – 5% N ₂	284	407	437	401	382.25 ± 58
Ar – 10% N ₂	520	492	560	460	508 ± 37
Ar – 15% N ₂	444	524	472	540	495 ± 39
Ar – 20% N ₂	624	640	588	548	600 ± 35
<i>0.423 cm/sec</i>					
Pure Ar	20	20	20	20	20 ± 0
Ar – 5% N ₂	326	608	629	359	480.5 ± 139
Ar – 10% N ₂	576	634	642	609	615 ± 26
Ar – 15% N ₂	683	852	664	666	716 ± 79
Ar – 20% N ₂	587	557	548	542	558.5 ± 17

concentrations and the values listed in Table 4.3. The values shown in this table are used in the following discussion.

4.3 RESULTS AND DISCUSSION

4.3.1 Nitrogen Concentration in the Weld Metal

The nitrogen concentration measured in each sample has been examined for each welding condition. Figure 4.5 shows the concentrations measured at a travel speed of 0.847 cm/sec as a function of the inlet nitrogen partial pressure. Under these conditions, the average nitrogen concentration increases linearly with increasing inlet nitrogen partial pressure. Nitrogen concentrations vary between approximately 400 and 600 ppm [N] and exhibit a scatter of 90 to 150 ppm [N] for each inlet nitrogen partial pressure examined here. Figure 4.6 compares the nitrogen concentrations measured in each sample for each inlet nitrogen partial pressure. There is no discernible trend between the nitrogen concentration in each of the samples and its location along the length of the weld line. It is therefore assumed that the nitrogen concentration does not vary with its location along the weld line. Any variation in the nitrogen concentration is assumed to be the result of experimental variance.

A change in the choice of welding parameters creates a concomitant change in the nitrogen concentration in the fusion zone and its behavior as a function of the inlet nitrogen partial pressure. Figure 4.7 shows the nitrogen concentrations plotted as a function of the inlet nitrogen partial pressure at a travel speed of 0.423 cm/sec. The nitrogen concentration increases rapidly at low nitrogen partial pressures and reaches higher levels than observed at a higher travel speed. As the nitrogen partial pressure increases further, the nitrogen concentration begins to decrease. At a nitrogen partial pressure of 0.20 atm., the nitrogen concentration is the same as that observed at the higher travel speed. Once again, no general trend in the nitrogen concentration as a function of location along the weld line is observed. The nitrogen concentrations measured under this set of welding parameters are plotted for each nitrogen addition to the shielding gas in Figure 4.8. In this figure, the nitrogen concentrations display a much wider range of variation, from 45 to 303 ppm, than that observed for the more rapid travel speed.

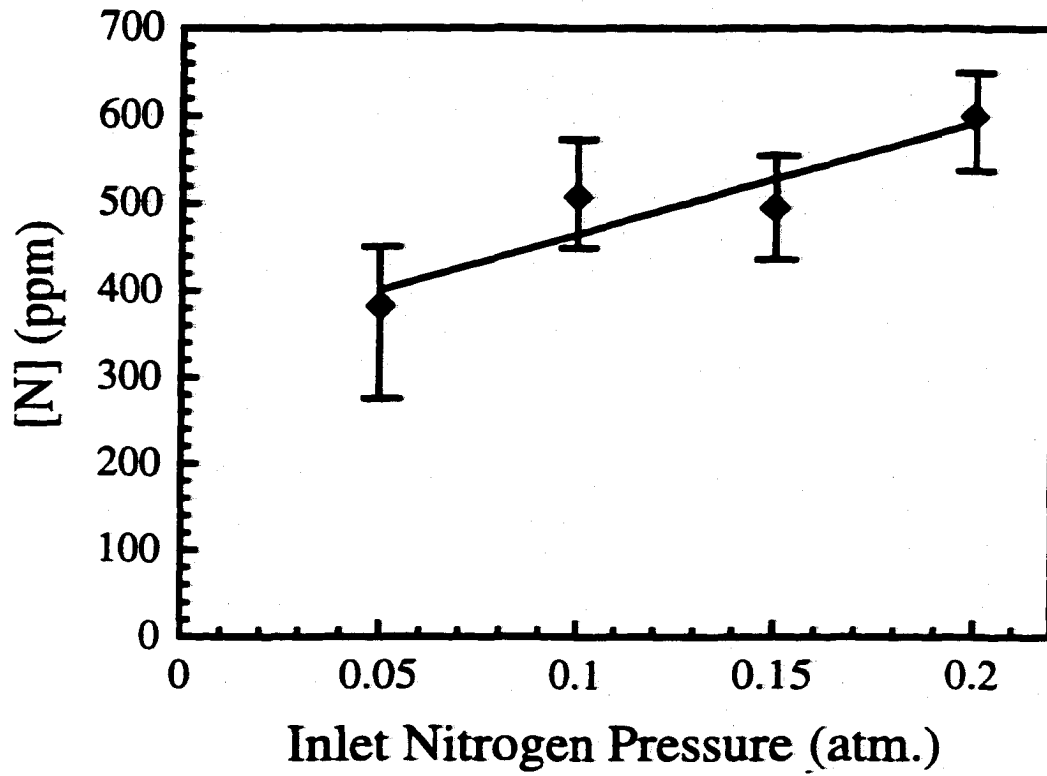


Figure 4.5. Plot of the experimentally measured nitrogen concentration in the weldment as a function of the inlet nitrogen partial pressure at a travel speed of 0.847 cm/sec.

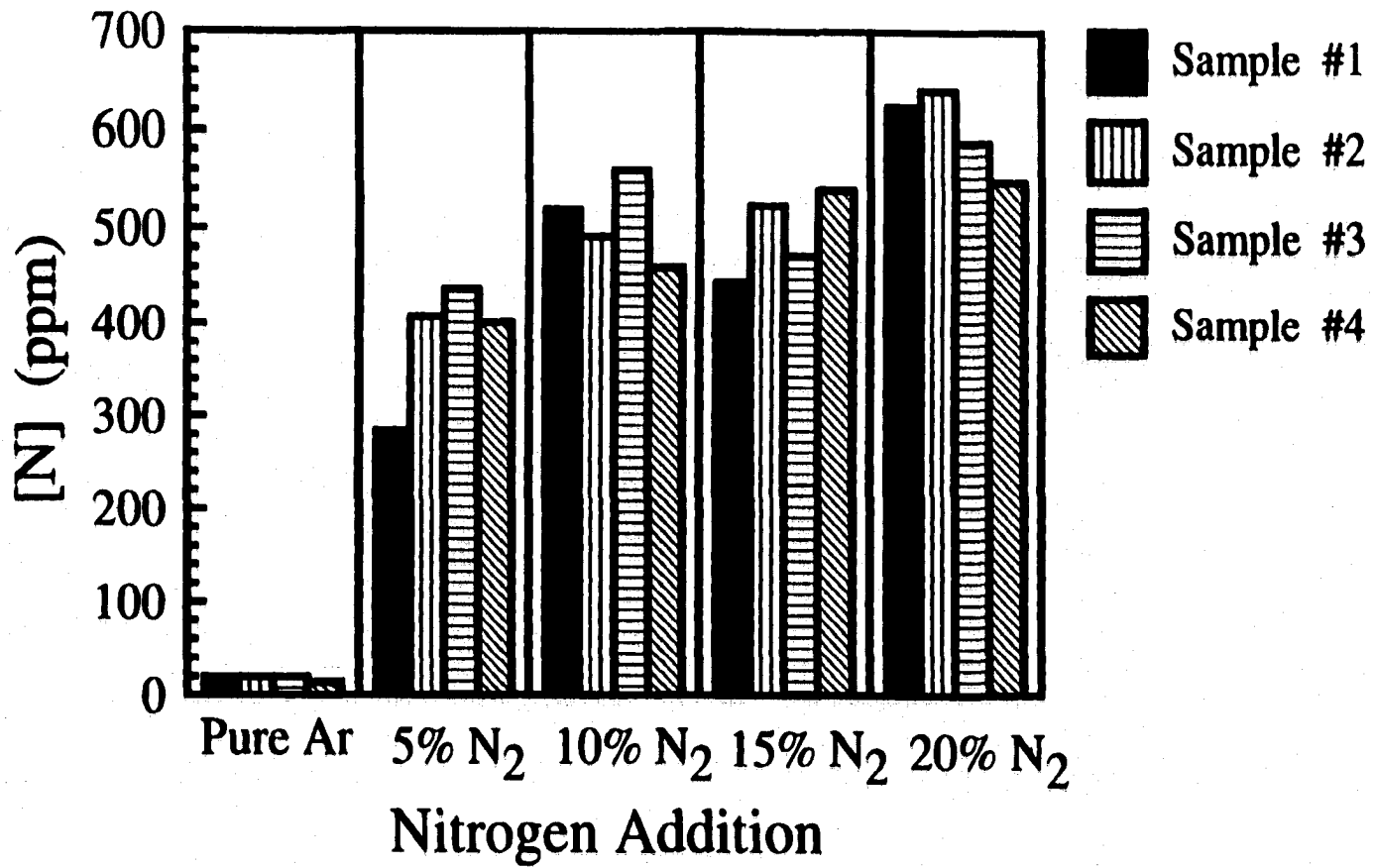


Figure 4.6. Plot of the nitrogen concentrations (ppm) in each of the samples taken from the weld lines made for each of the inlet nitrogen partial pressures at a travel speed of 0.847 cm/sec.

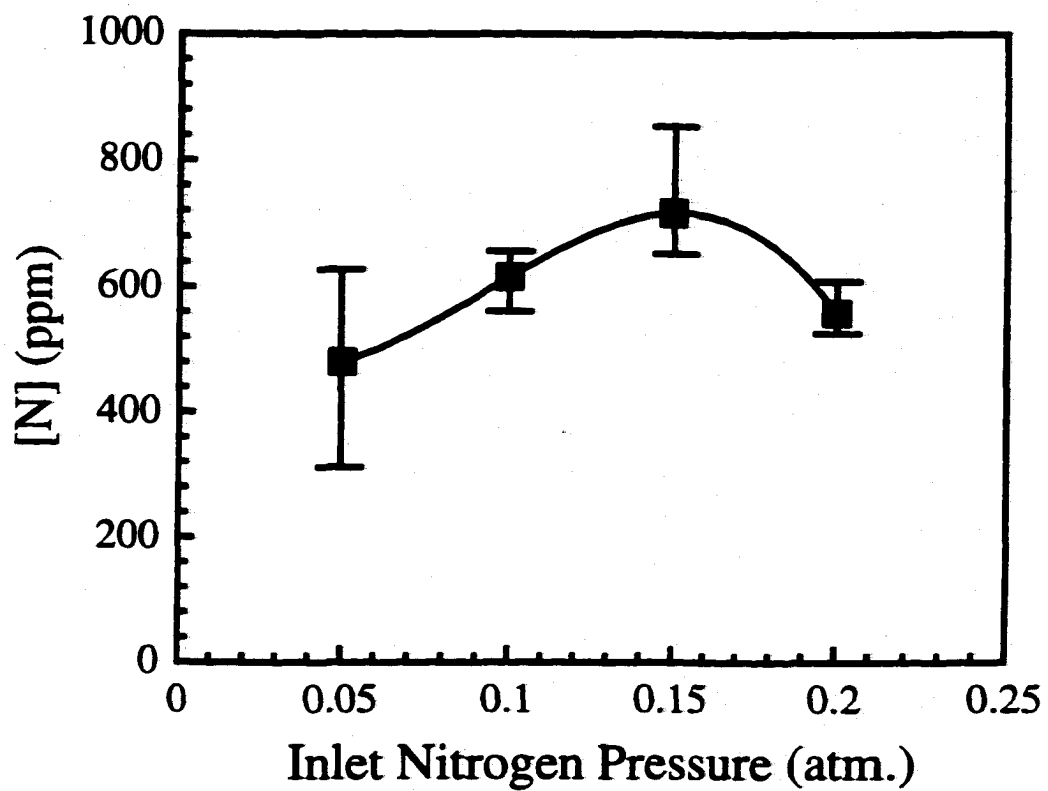


Figure 4.7. Plot of the experimentally measured nitrogen concentration in the weldment as a function of the inlet nitrogen partial pressure at a travel speed of 0.423 cm/sec.

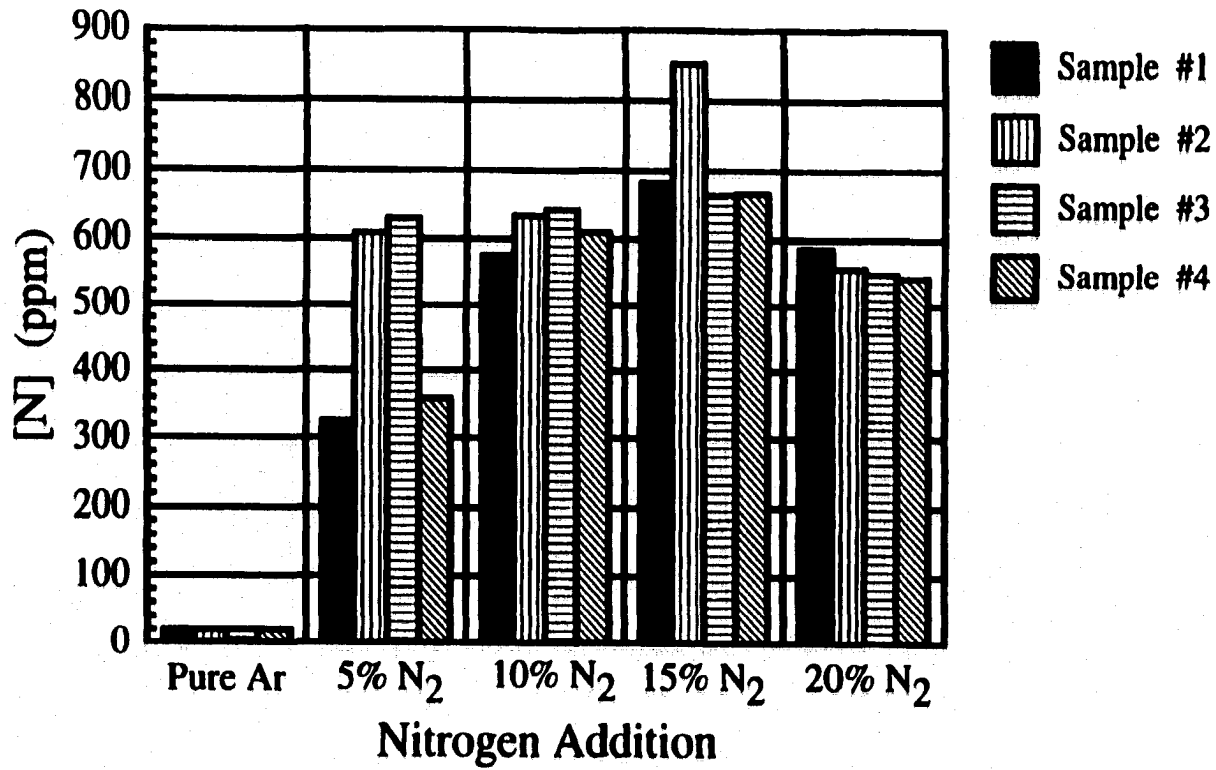


Figure 4.8. Plot of the nitrogen concentrations (ppm) in each of the samples taken from the weld lines made for each of the inlet nitrogen partial pressures at a travel speed of 0.847 cm/sec.

A comparison between the nitrogen concentrations observed for the two travel speeds is shown in Figure 4.9. At first glance, the decrease in travel speed seems to produce, on average, a higher nitrogen concentration, especially at low to intermediate nitrogen partial pressures. On the other hand, the range of nitrogen concentrations measured in both cases tends to overlap. It thus appears that the choice of welding parameters has little bearing on the resulting nitrogen concentration in the weld pool. Therefore, it would be more proper to view the nitrogen concentrations as falling in a range of values around 600 ppm [N], regardless of the choice of welding parameters.

Nothing new is learned about the nitrogen dissolution reaction by just simply examining the nitrogen concentration measured in the sample after welding. On the other hand, the weld pool displays a number of characteristics related to the addition of nitrogen to the shielding gas, ranging from the general appearance of the weld pool and the formation of porosity to microstructural characteristics of the fusion zone. By examining these various weld pool characteristics, a correlation between the observed nitrogen concentration and any one or more of the above weld pool characteristics can be determined.

4.3.2 Weld Pool Appearance

The effects of changes in the welding parameters and the addition of nitrogen to the shielding gas on the resulting weld pool appearance and properties have been examined. Changes in the weld pool appearance can come in the form of variations in the shape and dimensions of the weld pool cross section or in the formation of pores and blowholes in the weld pool. Each of these characteristics has been examined here, and the results are summarized and discussed below.

Weld pool cross sections for each set of welding parameters and nitrogen addition to the shielding gas have been taken from section (c) of each weld line and are shown in Figures 4.10(a-e) and 4.11(a-e). Each of these weld pool cross sections represents a snapshot of the weld line and may vary in appearance with other sections of the weld line. When the weld pool cross sections are compared, a common structure containing a prominent fusion zone, a region of columnar grain growth, and the base metal is observed.

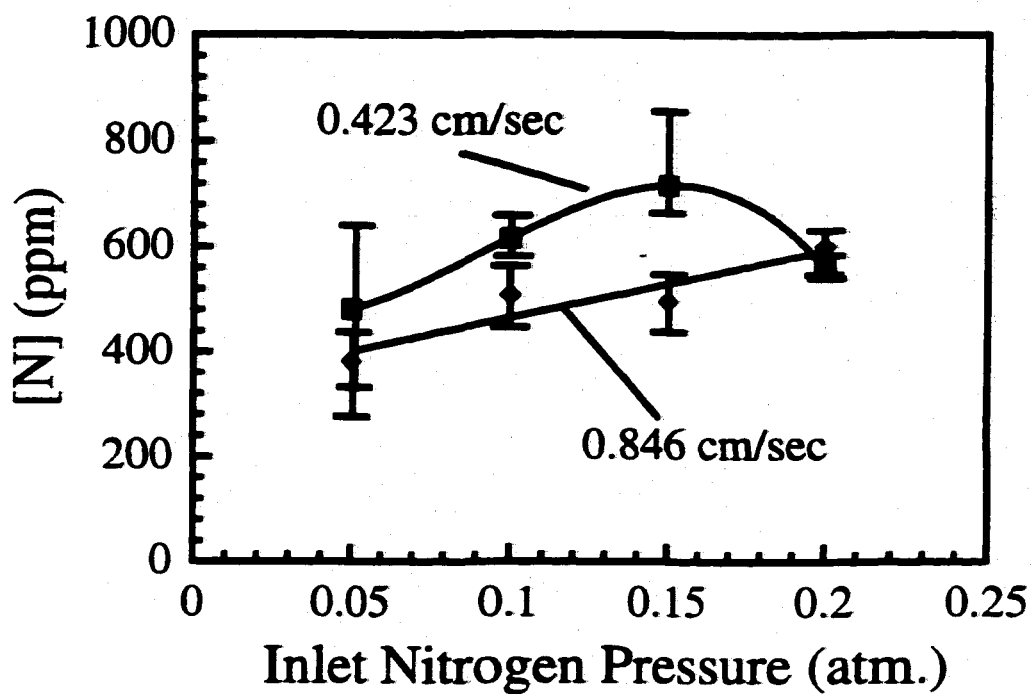


Figure 4.9. Comparison of the nitrogen concentrations from each welding condition plotted as a function of inlet nitrogen partial pressure.

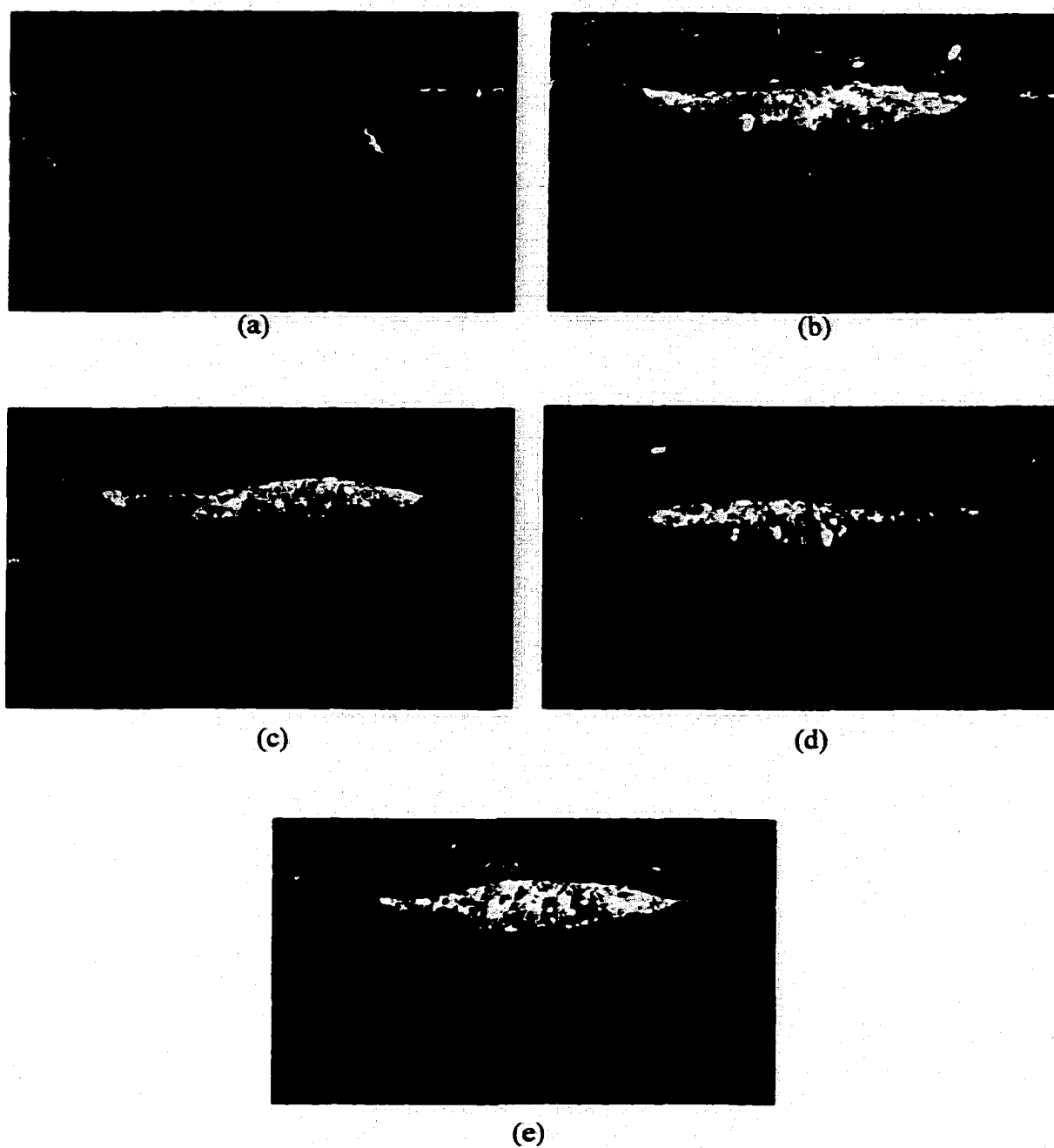


Figure 4.10(a-e). Comparison of Cross Sections for a travel speed of 0.847 cm/sec: (a) Pure Ar; (b) 5% N₂; (c) 10% N₂; (d) 15% N₂; (e) 20% N₂.

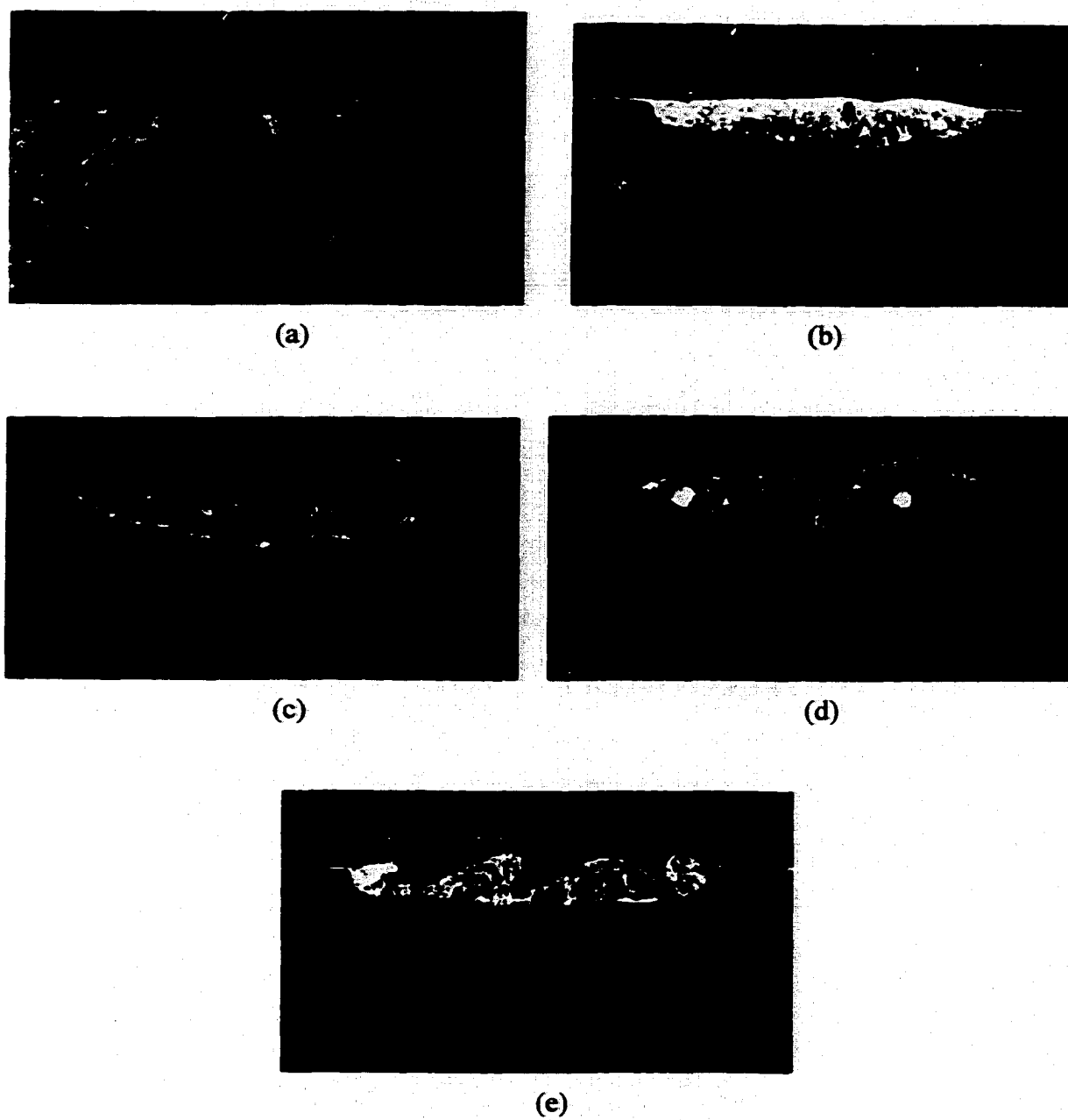


Figure 4.11(a-e). Comparison of Cross Sections for a travel speed of 0.423 cm/sec: (a) Pure Ar; (b) 5% N₂; (c) 10% N₂; (d) 15% N₂; (e) 20% N₂.

Several interesting features are apparent when comparing weld pool cross sections without nitrogen additions to the shielding gas. For example, the weld pool cross section at a travel speed of 0.847 cm/sec shows a visible fusion zone adjacent to the columnar grain region. On the other hand, the weld pool cross section formed with a pure Ar shielding gas at a travel speed of 0.423 cm/sec only an area of large grains with no distinct orientation surrounded by the oriented columnar grains. This change in appearance can be attributed to a change in the thermal cycles experienced by the weld pool as the travel speed is decreased. A less extreme thermal cycle is perhaps observed at the lower travel speed, which allows for grain growth to occur.

The appearance of the weld pool cross section is affected by the addition of nitrogen to the shielding gas. For example, the top surface of the weld pool profile, at a travel speed of 0.847 cm/sec, changes from a flat surface with a pure Ar shielding gas, as shown in Figures 4.10(a), to one with a wavy appearance, as shown in Figures 4.10(b-e). On the other hand, when the travel speed is reduced to 0.423 cm/sec, the weld pool cross section displays a wavy appearance along the surface and large internal pores, even at the lowest nitrogen additions to the shielding gas. At higher nitrogen additions, the profile along the weld pool surface becomes much more jagged, and it appears that there has been an ejection of metal from the weld pool. This effect may be caused by the spatter of metal saturated with nitrogen.¹³

Weld pool dimensions, which are listed in Table 4.4, are also dependent on the choice of welding speed. For example, the fusion zone and columnar grain depths noticeably increase with a decrease in the travel speed with a pure Ar shielding gas. The change in the fusion zone width is not as significant as the depth increase, and there is little to no change in the width of the columnar grains. When these measurements are considered together, the aspect ratio decreases, indicating a deeper weld pool. The addition of nitrogen to the shielding gas also affects the weld pool dimensions. In general, the addition of nitrogen causes a decrease in the fusion zone depth, while simultaneously increasing the fusion zone width, resulting in a significant increase in the aspect ratio. An increased aspect ratio relates to a slightly wider and shallower weld pool. Further increases in the

nitrogen addition to the shielding gas, though, do not further affect the weld pool dimensions.

4.3.3 Porosity in Weld Pool

Porosity is a common defect in the weld metal and has been studied in a number of materials systems.¹⁴⁻²⁰ It is generally recognized as the result of excessive gas absorption in the molten weld metal in GTA welding. Once the weld metal begins to solidify, the resulting porosity can be caused by either gas rejection at the advancing solid/liquid interface and by the nucleation of bubbles ahead of the solid/liquid interface. These bubbles are subsequently trapped as the solid/liquid interface passes them by, leaving them frozen within the weld pool.¹⁵ Therefore, the formation of porosity is prevalent in materials systems in which there is a significant difference between the gas solubility in the liquid and solid regions, such as the iron-nitrogen system. Some of the materials systems where porosity is observed include the iron-nitrogen system, the aluminum-hydrogen system, and the copper-nitrogen system.

There are several means for determining the presence of porosity in the weld metal. In this case, a visual inspection of the weld line, density measurements, and x-ray radiography have been performed. Figures 4.12(a-j) show the top surfaces of the weld lines for each welding condition and nitrogen addition to the shielding gas. At a travel speed of 0.847 cm/sec, the addition of nitrogen to the shielding gas does not produce any significant change in the weld line appearance, as shown in Figures 4.12(a-e). On the other hand, there is a significant change in the appearance of the weld line at a travel speed of 0.423 cm/sec with the addition of nitrogen to the shielding gas, as shown in Figures 4.12(f-j). Porosity and blowholes appear along the length of the weld line, accompanied by a rippling effect on the top surface. Increasing amounts of porosity are observed on the weld pool surface at this travel speed with increasing additions of nitrogen to the shielding gas.

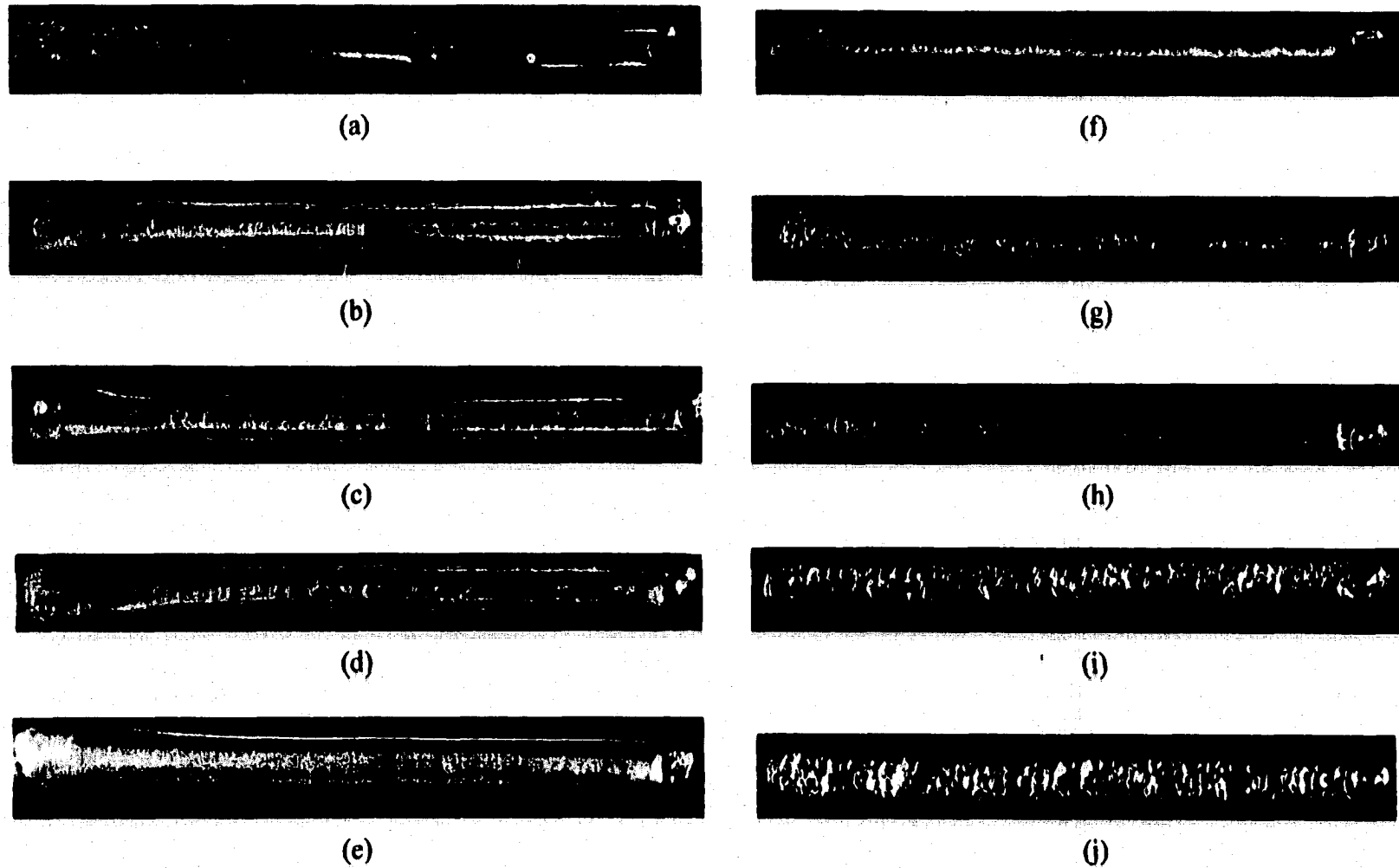


Figure 4.12(a-j). Comparison of appearance of weld line for each welding condition, demonstrating the role of changes in the travel speed on the appearance of the weld line. (a&f) Pure Ar; (b&g) 5% N₂; (c&h) 10% N₂; (d&i) 15% N₂; (e&j) 20% N₂. (a) to (e) are for a welding speed of 0.847 cm/sec and (f) to (j) are for at a welding speed of 0.423 cm/sec.

4.3.3.1 Radiography of Weld Metal

Radiographic inspection is a common non-destructive evaluation (NDE) technique for observing both surface and internal defects in fusion welds. Previous investigations have used this technique to observe porosity and other defects in the weld metal.^{13,21-24} These defects can range from gas pores, which are characterized by spherical, elongated, or "worm hole" shapes, and can appear in random, clustered, or linear patterns. In this case, radiographic techniques are used to examine the presence and location of gas porosity in each of the weld line samples.

Samples removed from the weld line at location (d), shown in Figure 4.2, have been analyzed using an x-ray radiography system at the Carderock Division of the Naval Surface Warfare Center in West Bethesda, MD. Each of the samples consists of the entire base plate thickness and is approximately 15 mm in length, representing a rather small section of the weld line. An analysis of only a small portion of the weld line for the nature and amount of porosity suffices since porosity is assumed to exist along the entire weld line. Table 4.6 lists the parameters used here. Porosity can thus be detected down to 2T indications, equating to 0.005 inch in diameter using AA film, and when M film is used, down to 1T indications, equating to 0.0025 inch in diameter.

Table 4.7 summarizes the results of the radiographic analysis of each sample, which are also shown in Figures 4.13(a-f) and 4.14(a-e). In general, the radiography analysis shows many of the same results as the visual observation discussed previously. For example, Figure 4.13(a-f) shows that there is no porosity observed in either the base metal or in samples welded at a travel speed of 0.847 cm/sec. Even with a 20% N₂ addition to the shielding gas, there is no porosity in the weld pool. On the other hand, a reduction in travel speed to 0.423 cm/sec, as shown in Figure 4.14(a-e), produces porosity in each of the weld samples. A slight amount of porosity is observed in the sample welded even with a pure Ar shielding gas and becomes more pronounced with the addition of nitrogen to the shielding gas. It is again apparent that the choice of welding parameters has an effect on the formation of porosity in the weld metal.

Table 4.6. Summary of the parameters used in the radiographic examination of the weld metal samples.

X-Ray Source Voltage	160 KV
X-Ray Source Current	9 mA
Exposure Time	6 minutes
Film Type	Kodak AA/M
Film Size	7" x 17"
Screen Type	Pb

Table 4.7. Summary of x-ray radiographic analysis of iron samples.

Experimental Conditions	Classification	Film Type
Base Metal	None	AA
<i>0.847 cm/sec</i>		
Pure Ar	None	AA
Ar-5% N ₂	None	AA
Ar-10% N ₂	None	AA
Ar-15% N ₂	None	AA
Ar-20% N ₂	None	AA
<i>0.423 cm/sec</i>		
Pure Ar	Some Light Indications	AA
Ar-5% N ₂	Gross Porosity	M
Ar-10% N ₂	Some Light Indications	AA
Ar-15% N ₂	Gross Porosity	AA
Ar-20% N ₂	Gross Porosity	AA

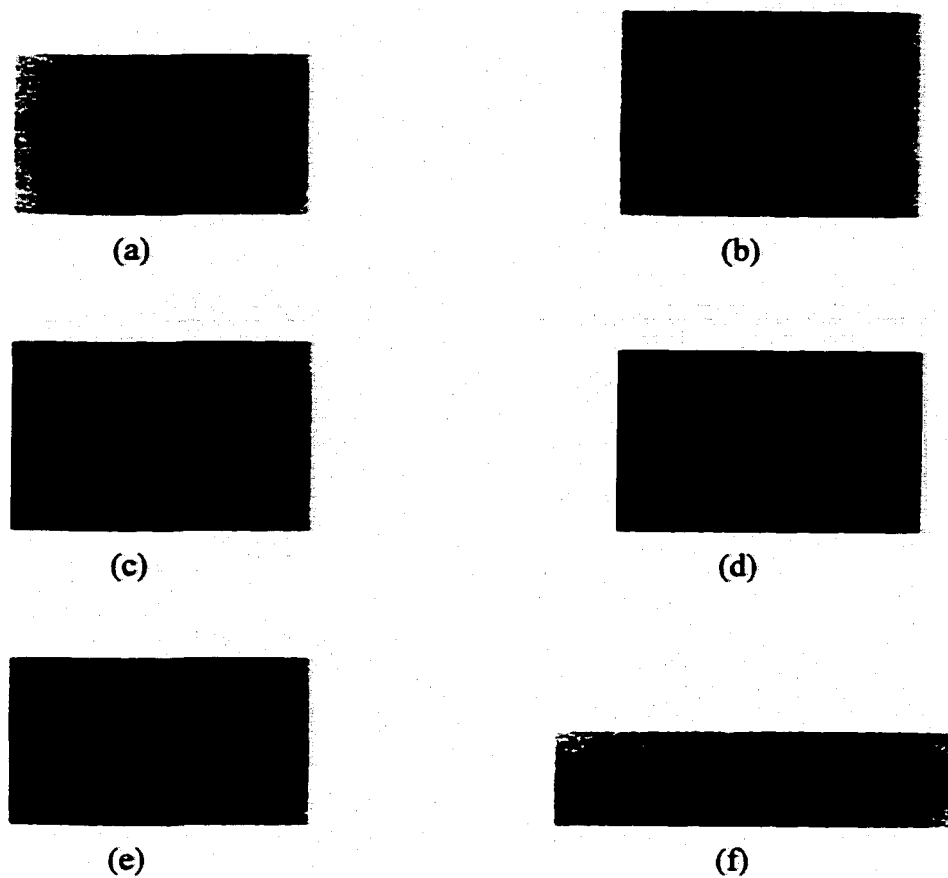


Figure 4.13(a-e). Radiographs of (a) the base metal and weld line sections for a travel speed of 0.847 cm/sec with (b) pure Ar shielding gas, (c) 5% N₂, (d) 10% N₂, (e) 15% N₂, and (f) 20% N₂.

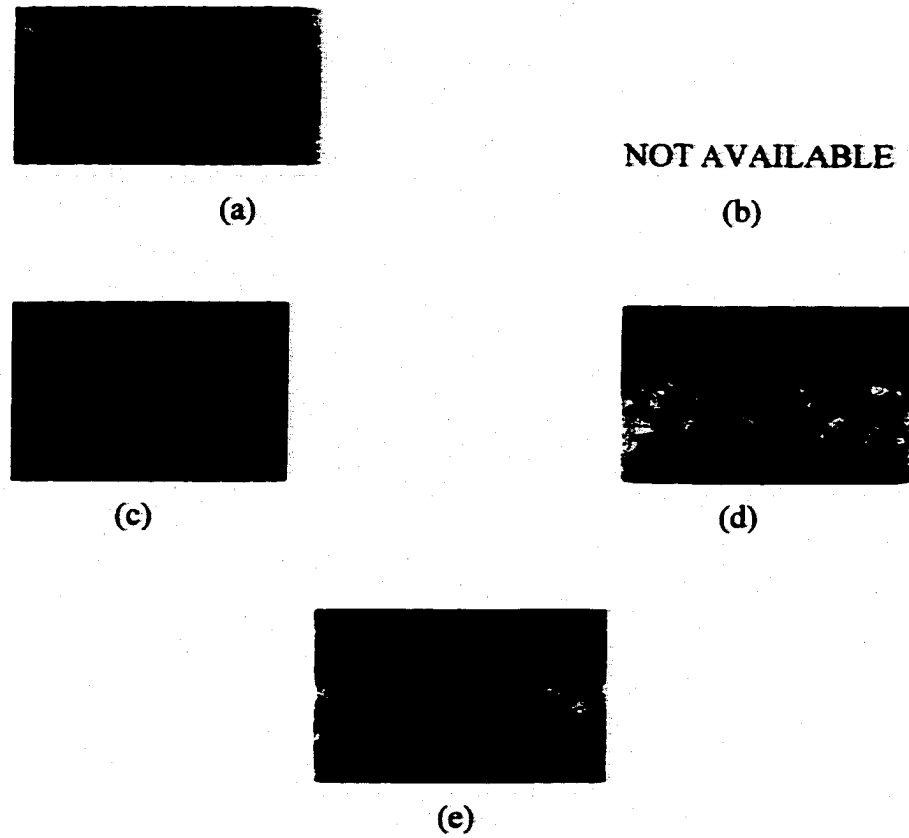


Figure 4.14(a-e). Radiographs of section of weld line for a travel speed of 0.423 cm/sec with (a) pure Ar shielding gas, (b) 5% N₂, (c) 10% N₂, (d) 15% N₂, and (e) 20% N₂.

4.3.3.2 Density Measurements

Both visual inspection and radiographic analysis has been used to characterize porosity formation in the weld metal for each of the welding conditions analyzed here. Calculation of the weld metal density can provide a general measure of the amounts of porosity and nitrogen present in solution as a function of the nitrogen addition to the shielding gas. Previous researchers^{15,16} have used density measurements to determine the amount of gas in solution in the weld pool and to relate the difference in density to the amounts of porosity and soluble gas in the sample. This technique is also used here.

Samples have been removed from location (b), as shown in Figure 4.2, on the weld line and prepared. This procedure leaves a majority of the sample as weld metal, significantly increasing the accuracy of the reported densities. The samples are then weighed in both air and water, and the results are shown in Table 4.8 for both welding conditions. In addition, the density of each sample has been calculated and compared with the density of the base metal and the fusion zone from the pure Ar weld as a ratio between the two values.

There is a difference between the measured densities in the samples with and without nitrogen additions for a single set of welding parameters. Changes in the choice of welding parameters also produce significant differences in the observed densities. For example, at a travel speed of 0.847 cm/sec, there is little difference between the measured densities of the samples with or without the addition of nitrogen to the shielding gas. When the travel speed is decreased to 0.423 cm/sec, nitrogen additions to the shielding gas cause significant density decreases. These lower densities in the weld pool samples point to the presence of porosity within the weld metal, which is visible on the top surface of the weld line.

Ratios between the weld metal samples and both the base metal and the weld metal sample welded with a pure Ar shielding gas provide an easily understandable measure of the amount of porosity in the weld metal. For example, ratios below 1.0 can translate into a certain amount of porosity in the weld metal. There is an unexpected difference, though, between the density ratios computed using the base metal and those using weld metal samples with a pure Ar shielding gas. The density of each weld metal sample with

Table 4.8. Summary of weights of samples and resulting porosity calculations.

<u>Welding Conditions</u>	<u>Volume of Sample (cm³)</u>	<u>Sample Weight (gm)</u>	<u>Sample Density (gm/cm³)</u>	<u>Density Ratio (Base Metal)</u>	<u>Density Ratio (Pure Ar Weld)</u>
In Air					
Base Metal	1.104	8.642	7.825	1.000	---
<i>0.847 cm/sec</i>					
Pure Ar	0.280	2.052	7.325	0.936	1.000
Ar - 5% N ₂	0.328	2.360	7.185	0.918	0.981
Ar - 10% N ₂	0.373	2.593	6.952	0.888	0.949
Ar - 15% N ₂	0.365	2.682	7.339	0.938	1.002
Ar - 20% N ₂	0.413	3.189	7.713	0.986	1.053
<i>0.423 cm/sec</i>					
Pure Ar	0.441	3.257	7.392	0.945	1.000
Ar - 5% N ₂	0.362	2.508	6.926	0.885	0.937
Ar - 10% N ₂	0.448	3.200	7.150	0.914	0.967
Ar - 15% N ₂	0.416	2.621	6.299	0.805	0.852
Ar - 20% N ₂	0.390	2.434	6.237	0.797	0.844

a pure Ar shielding gas is similar but less than that of the base metal. This smaller density produces a density ratio on the order of 0.94, for each welding condition. Since this value is less than unity, there is an indication of the presence of porosity in the weld metal not previously observed either visually or radiographically. Even though the density ratios display different values, each set of ratios indicates a similar trend. Therefore, only those density ratios, which use the weld sample for a pure Ar shielding gas as a baseline, are considered.

Variations between the density ratios using the density of the samples welded in pure Ar as a baseline are dependent on the choice of welding condition. At a travel speed of 0.847 cm/sec, there is no change in the value of the density ratio as more nitrogen is added to the shielding gas. In each case, the value of the density ratio is near unity, indicating that there is little to no porosity in the weld pool. On the other hand, when the travel speed is decreased to a value of 0.423 cm/sec, the density ratio decreases significantly with the addition of nitrogen to the shielding gas. The density ratios reach values of 0.84 for a 20% N₂ addition to the shielding gas. Both these conditions compare favorably with the visual observations for porosity in each of the weld lines.

4.3.4 Weld Metal Microstructure

In addition to the formation of porosity in the weld pool, changes in the predominant weld pool microstructures are observed with the addition of nitrogen to the shielding gas. An analysis of the microstructure can shed light on the effect of nitrogen on the weld pool properties and its distribution throughout the weldment. Gross microstructural changes in the weld metals are analyzed using optical microscopy techniques. Cross sections composed of section (c), as defined in Figure 4.2, of each weld line have been polished and etched with a 2% Nital solution. An Olympus® BXM60 light microscope with a Sony 3-chip CCD Camera and an attached video printing system has been used here to analyze these microstructures.

The base metal microstructure, shown in Figure 4.15, is composed of a homogenous equiaxed structure. Since the base metal is pure iron, no secondary phases, such as Fe₃C or pearlite, commonly found even in low C steels, are present. An analysis of the fusion

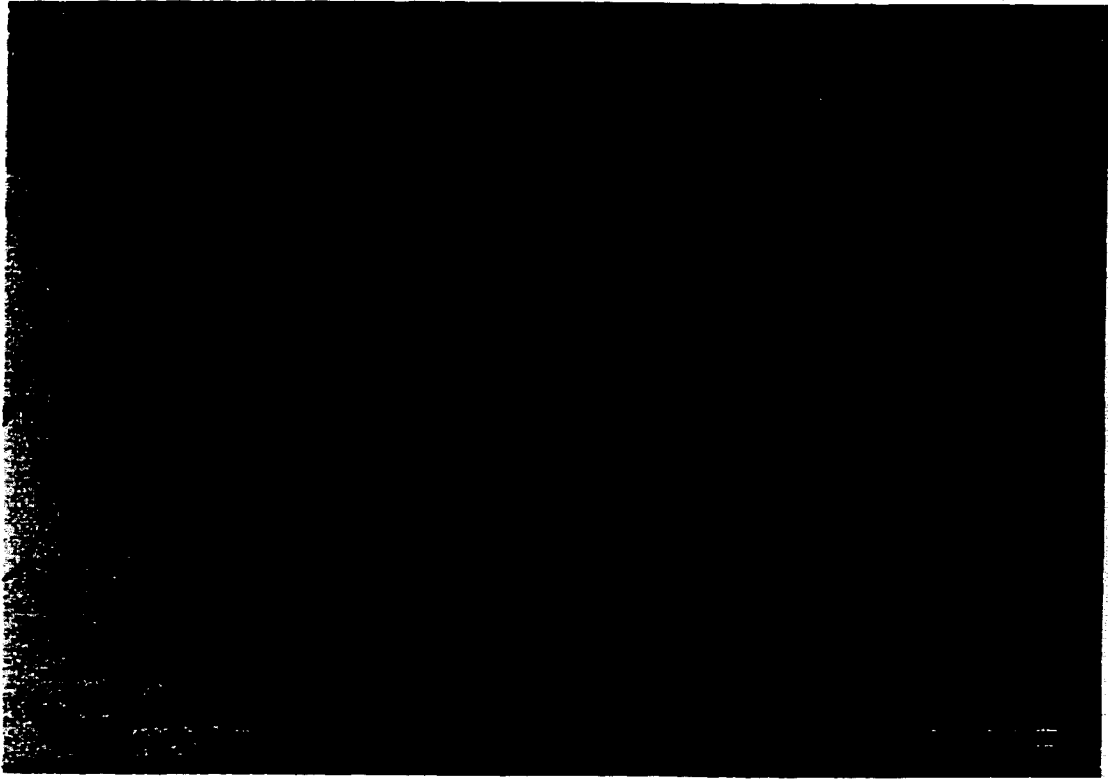


Figure 4.15. Typical base metal microstructure.

zone for each welding condition does not produce any significant change in the microstructural appearance. These fusion zones, which are shown in Figures 4.16 and 4.17 for each set of welding parameters, respectively, contain ferrite grains much larger than those in the base metal and contain no second phases.

Significant changes are observed, though, when nitrogen additions are made to the shielding gas. When nitrogen is present, the fusion zone microstructure no longer contains just large ferritic grains. Rather, the microstructure contains multiple phases and becomes non-homogenous across both the depth and width of the weld pool. Figure 4.18(a) shows a small area of the fusion zone microstructure for a 5% N₂ addition to the shielding gas. A number of different microstructures are present in this small region. For example, microstructural features, which resemble non-equilibrium structures common in steels, appear throughout the weld pool. A closer examination of some of these structures adjacent to a ferritic region in the fusion zone is shown in Figure 4.18(b). In this region, there appear to be small second phase precipitates, which appear in the darker regions. The appearance of these precipitates in well-defined lines indicates the product of an eutectoid reaction is present. Just such a reaction appears on the Fe-N phase diagram between the γ -Fe and the α - Fe - Fe₄N region, much like the pearlite reaction observed in Fe-C alloys.

As more nitrogen is added to the shielding gas, the fusion zone microstructure does not significantly change in appearance. The microstructures observed with a 5% N₂ addition to the shielding gas are also observed with a 10% N₂ addition, examples of which are shown in Figures 4.19(a&b). Typical fusion zone microstructures for even higher nitrogen additions to the shielding gas are shown in Figures 4.20(a&b) for a 15% N₂ addition and in Figures 4.21(a&b) for a 20% N₂ addition. In both cases, these microstructures display no unique characteristics not previously observed with lower nitrogen additions.

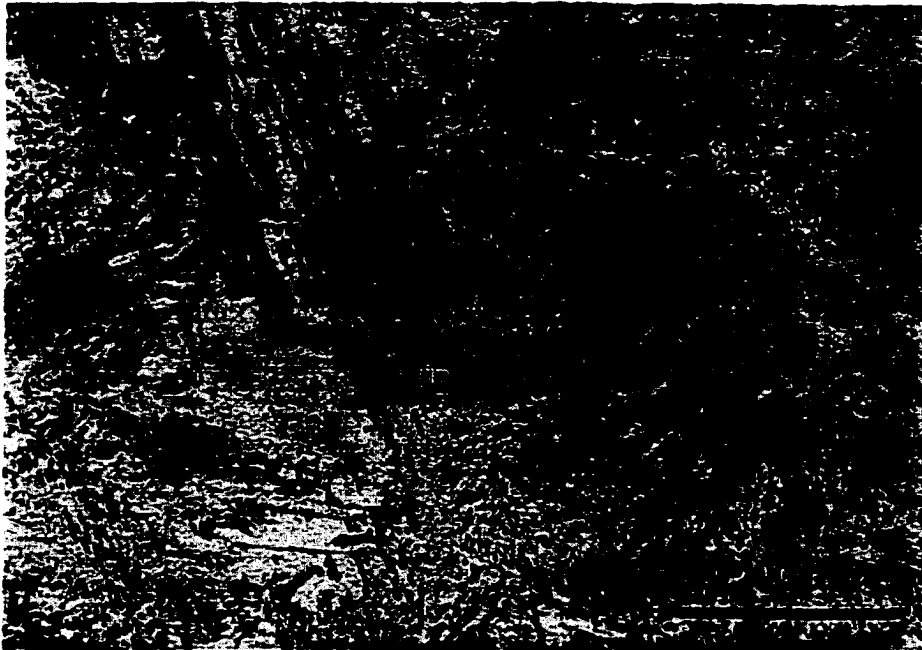
Fusion zone microstructures produced at a decreased travel speed have also been examined. Figure 4.22 shows a small portion of the fusion zone microstructure at this decreased travel speed with a 5% N₂ addition to the shielding gas. In this figure, there is little discernible difference between this microstructure and that observed at the more



Figure 4.16. Typical fusion zone microstructure for a travel speed of 0.847 cm/sec.



Figure 4.17. Typical fusion zone microstructure for at a travel speed of 0.423 cm/sec.

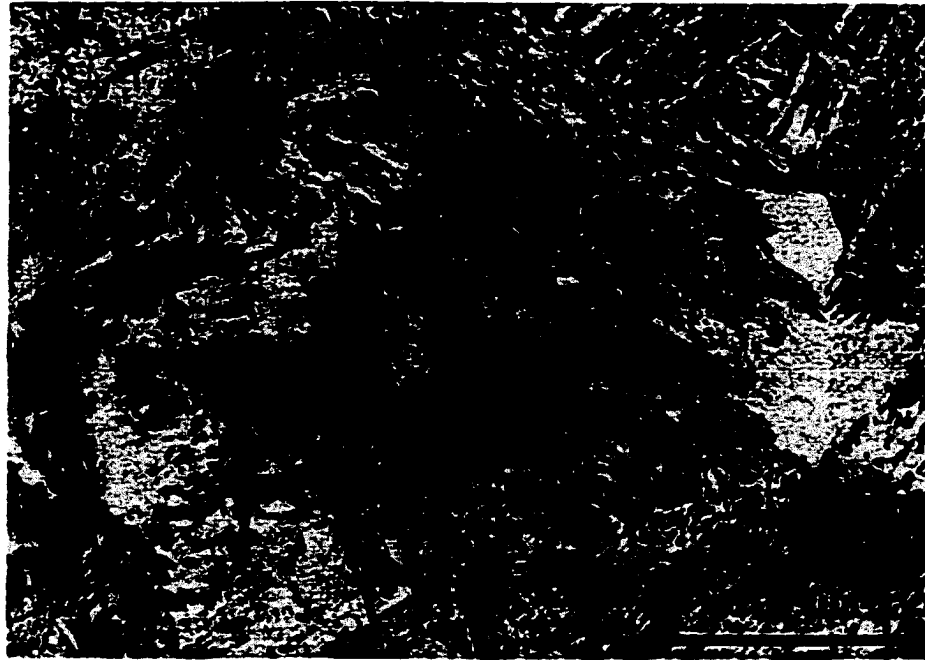


(a)

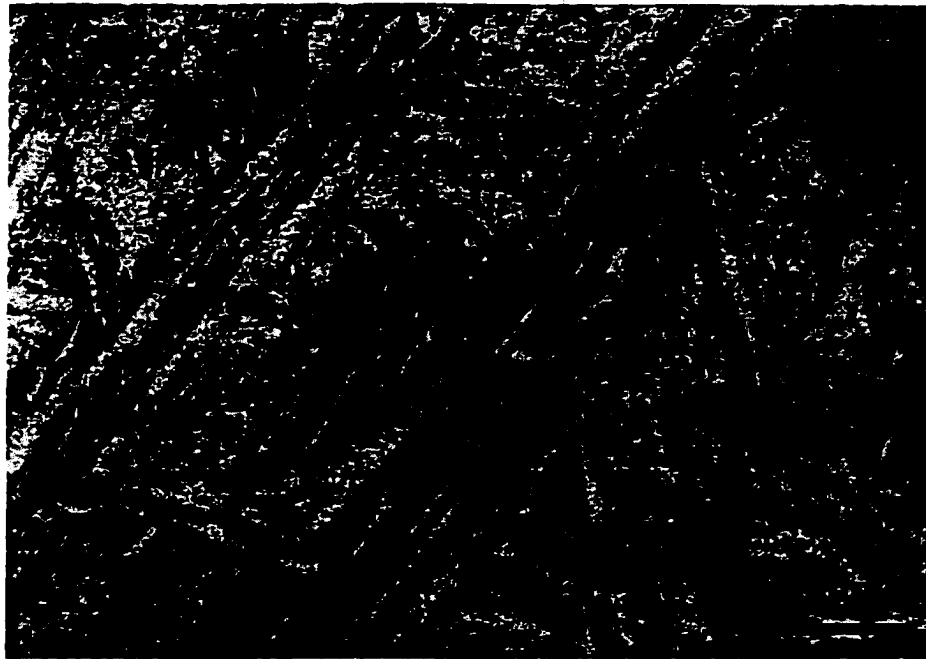


(b)

Figure 4.18(a&b). Examples of typical fusion zone microstructures with a 5% N₂ addition to the shielding gas for a travel speed of 0.847 cm/sec.

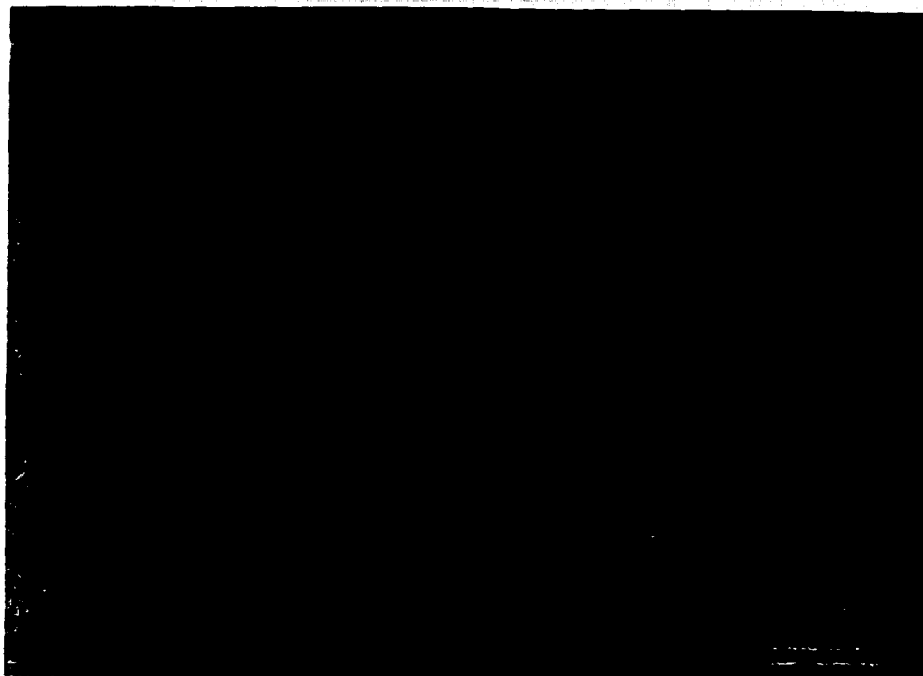


(a)



(b)

Figure 4.19. Examples of typical fusion zone microstructures with a 10% N₂ addition to the shielding gas at a travel speed of 0.847 cm/sec.

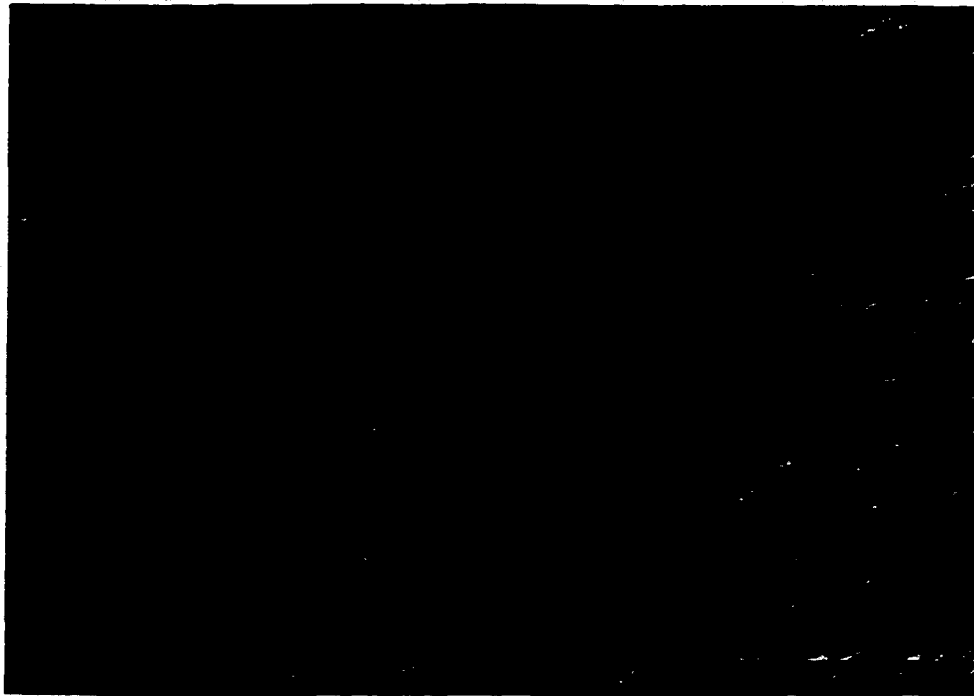


(a)



(b)

Figure 4.20(a&b). Examples of typical fusion zone microstructures with a 15% N₂ addition to the shielding gas and a travel speed of 0.847 cm/sec.



(a)



(b)

Figure 4.21(a&b). Examples of typical fusion zone microstructures with a 20% N₂ addition to the shielding gas and a travel speed of 0.847 cm/sec.

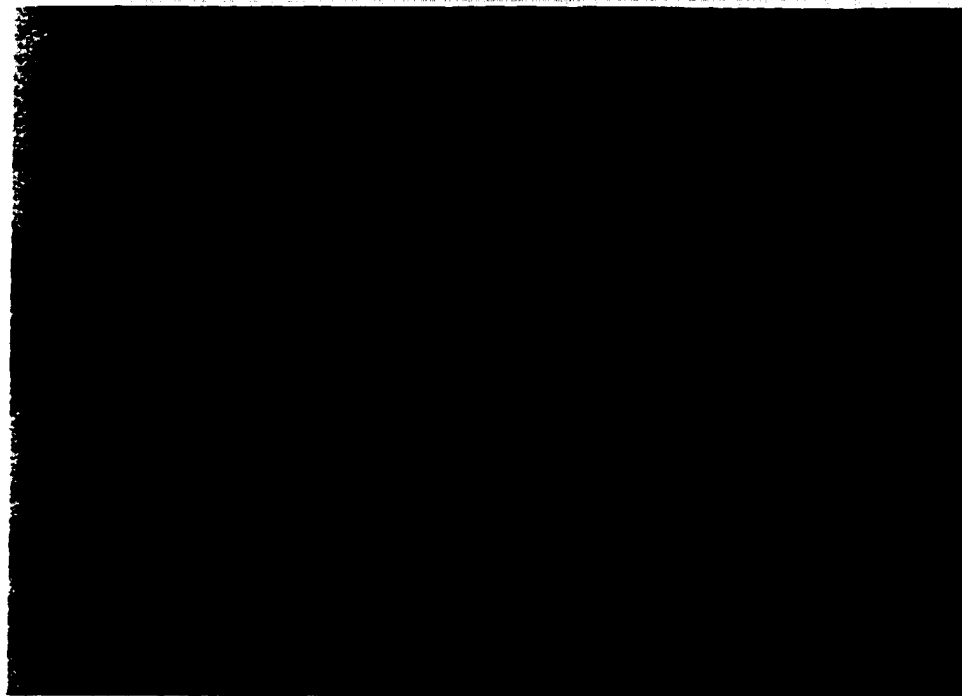


Figure 4.22. Examples of typical fusion zone microstructures with a 5% N₂ addition to the shielding gas at a travel speed of 0.423 cm/sec.

rapid travel speed. On the other hand, a closer examination of the microstructures in Figures 4.23(a&b) shows several significant differences. First, the various structures observed in the microstructures at a more rapid travel speed are not present and are replaced by needle like precipitates in the fusion zone. Unlike precipitates observed at a higher travel speed, these larger precipitates are not aligned and are surrounded by a more darkly etched region than the ferrite regions shown in Figure 4.22. These needle-like precipitates are assumed to be iron nitride phases. Such phases have been previously observed within the weld pool,²⁵ and are believed to be Fe_4N .

Higher nitrogen partial pressures in the shielding gas at this travel speed also produce these needle-like precipitates. Figures 4.24(a&b) show several prominent microstructural characteristics in the fusion zone with a 10% N_2 addition. These precipitates, especially in Figure 4.24(a), are present throughout but are dominant in the more darkly etched regions. On the other hand, the weld metal directly adjacent to the nitrides is much lighter in color, as though the surrounding material is stripped of nitrogen by the precipitate. The same conditions are also observed with even higher additions of nitrogen to the shielding gas in Figures 4.25(a&b) and 4.26(a&b) for 15% N_2 and 20% N_2 additions, respectively. Each condition produces the same needle-like precipitates as those observed at lower nitrogen concentration, and no significant changes in the appearance of the fusion zone are observed in either case.

Based on these results, it is apparent that the presence of nitrogen in the shielding gas affects the weld metal microstructure. The prevalent microstructure in the fusion zone, though, is further dependent on the choice of welding parameters, which, in turn, determine the cooling rates for the solidifying weld metal. For example, at the more rapid travel speed, the fusion zone contains microstructures usually associated with rapid cooling rates. On the other hand, as the travel speed is decreased, these microstructures disappear from the fusion zone and are replaced by needle-like precipitates. Therefore, even though nearly equivalent nitrogen concentrations are measured for each welding speed, the nitrogen exists in the fusion zone in a number of different forms.



(a)

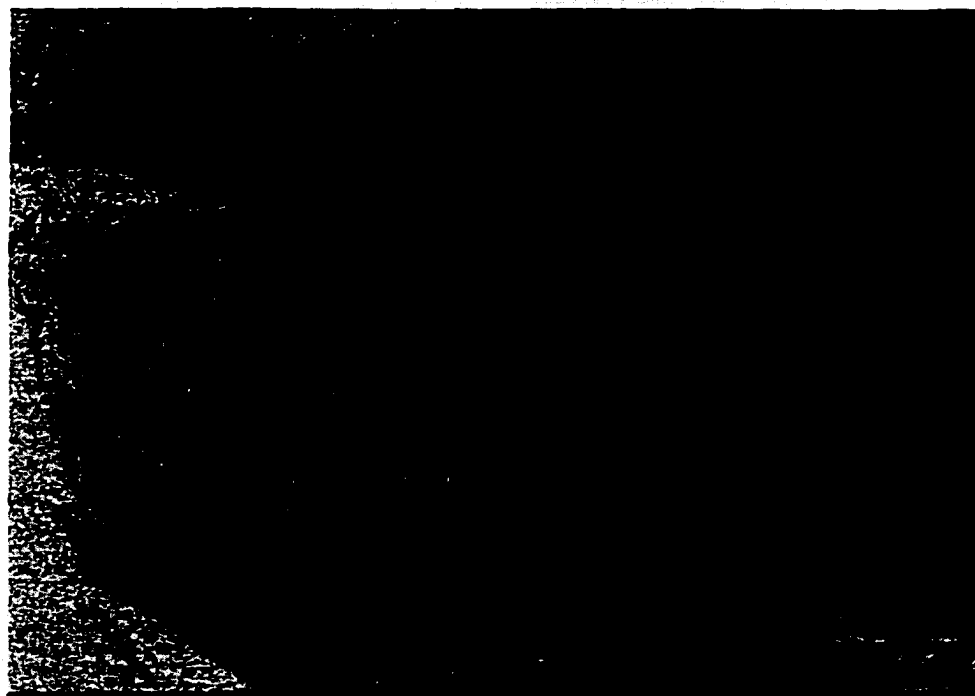


(b)

Figure 4.23(a&b). Examples of typical fusion zone microstructures with a 5% N₂ addition to the shielding gas at a travel speed of 0.423 cm/sec.

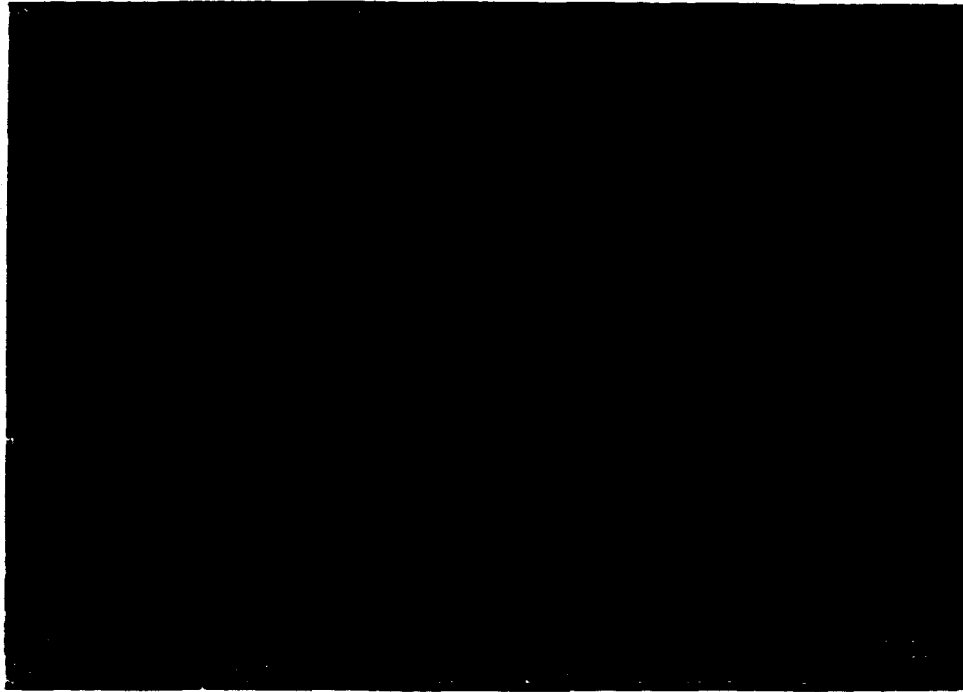


(a)

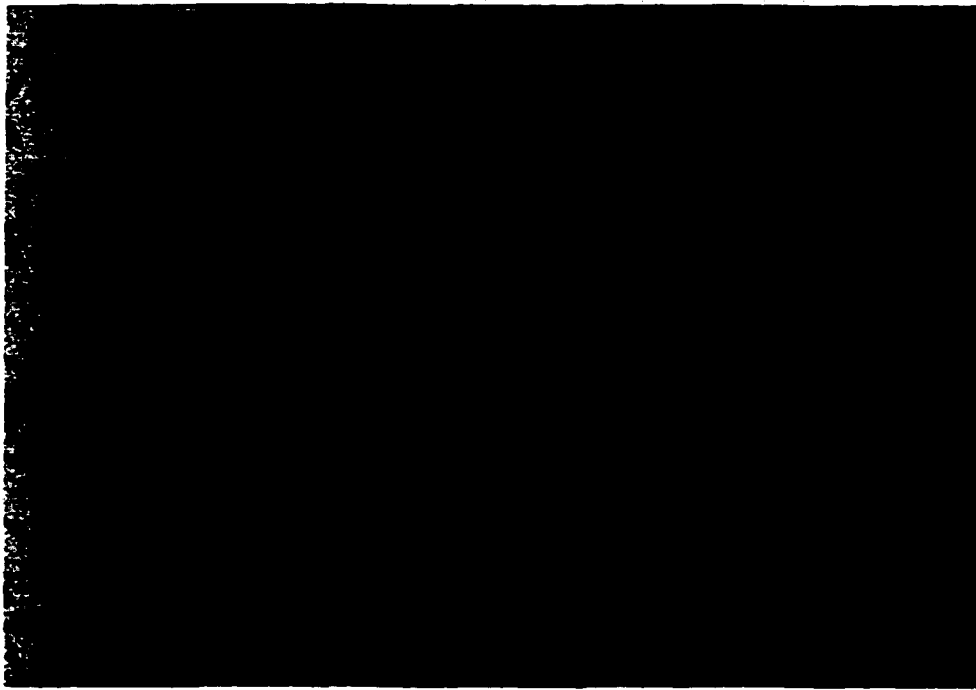


(b)

Figure 4.24(a&b). Examples of typical fusion zone microstructures with a 10% N₂ addition to the shielding gas at a travel speed of 0.423 cm/sec.

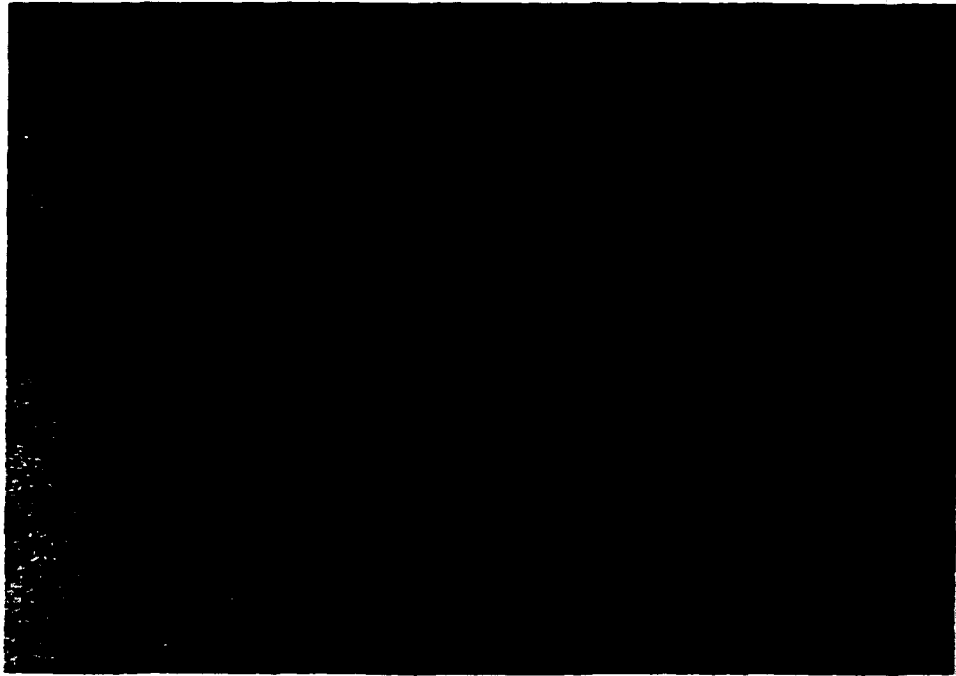


(a)

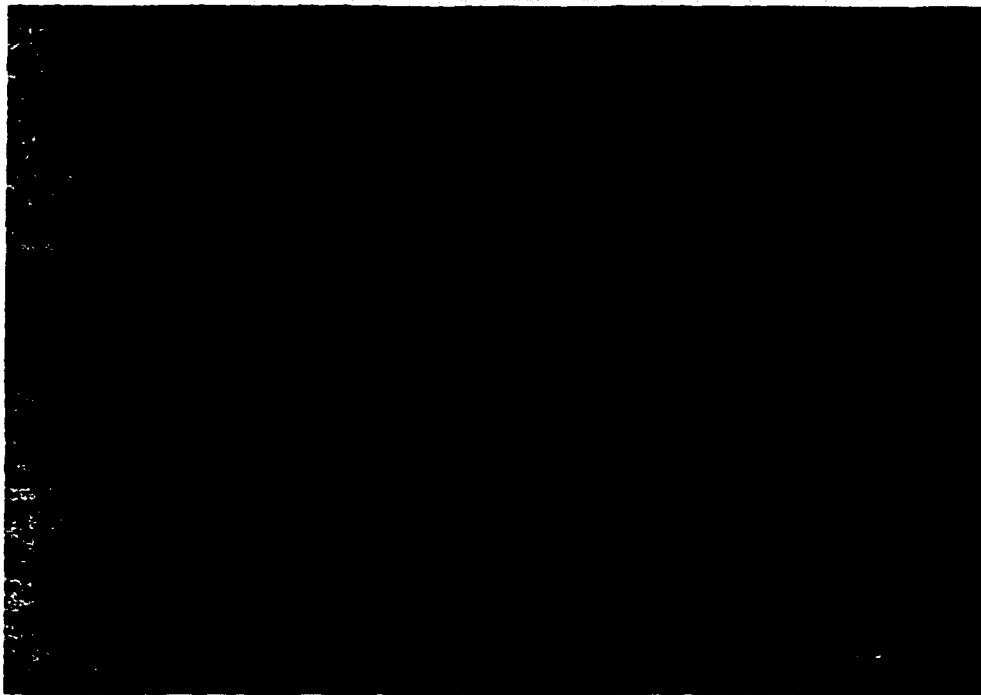


(b)

Figure 4.25(a&b). Examples of typical fusion zone microstructures with a 15% N₂ addition to the shielding gas at a travel speed of 0.423 cm/sec.



(a)



(b)

Figure 4.26(a&b). Examples of typical fusion zone microstructures with a 20% N₂ addition to the shielding gas and a travel speed of 0.423 cm/sec.

4.3.5 Microhardness Distribution Across the Weld Pool

Changes in the weld metal microstructure observed at different locations in the weld metal may be an indication of changes in the nitrogen concentration in the weld metal. It is difficult to measure nitrogen at individual locations in the weld metal, given the small size of the weld pools studied here and the difficulty in detecting nitrogen at low levels using conventional techniques. A simple measure of the distribution of nitrogen in the weld metal can be made by analyzing changes in the Vickers' Hardness Number (VHN) across the weld pool width and depth. Even though the microhardness measurements may not give accurate values for the nitrogen concentration at a specific location, changes in the microhardness value give an indication of changes in the amount of nitrogen present across the weld pool.

Microhardness measurements have been made at 0.25 mm intervals across the width and depth of the weld pool, including the base metal, the columnar grain regions, which may be representative of a heat-affected zone, and the fusion zone, using a load of 200 grams on the indenter. A summary of the average microhardness measurements for each welding condition is shown in Tables 4.9 and 4.10 across the width and depth of the weldment, respectively. The effects of changes in the welding parameters with only a pure Ar shielding gas on the resulting microhardness values across both the width and depth of the weldment are shown in Figures 4.27 and 4.28, respectively. Little to no variation in the microhardness values across either the depth or width of the weldments is observed for each set of welding parameters. A slight increase in microhardness is observed in the columnar grains and fusion zone, but, on average, it is rather small. Even with a decrease in the travel speed, there is little difference in the behavior or magnitude of the VHN values measured in any of the weldment regions.

When nitrogen is added to the shielding gas, there is a significant increase in the VHN values in the fusion zone. The relationships between nitrogen additions to the shielding gas at a travel speed of 0.847 cm/sec and the resulting microhardness measurements across the width and depth of the fusion zone are shown in Figures 4.29(a&b) and 4.30(a&b) for nitrogen additions of 5 and 10%, respectively. In each case, there is a significant increase in the VHN values across the columnar grain regions into the fusion

Table 4.9. Summary of Vickers' hardness measurements across the width of the weldment for each welding condition. Load is 200 gm. for all conditions.

<u>Welding Conditions</u>	<u>Nitrogen Concentration in Weld Pool (ppm)</u>	<u>Base Metal Hardness (VHN)</u>	<u>Columnar Grains (VHN)</u>	<u>Minimum Fusion Zone Hardness (VHN)</u>	<u>Maximum Fusion Zone Hardness (VHN)</u>	<u>Average Fusion Zone Hardness (VHN)</u>
<i>0.847 cm/sec</i>						
Pure Ar	20	111	98	105	141	123
Ar - 5% N ₂	382.25	99	108	107	279	213
Ar - 10% N ₂	508	102	118	137	275	197
Ar - 15% N ₂	495	97	98	101	283	211
Ar - 20% N ₂	600	91	95	119	235	206
<i>0.423 cm/sec</i>						
Pure Ar	20	105	114	108	136	125
Ar - 5% N ₂	480.5	86	87	115	183	155
Ar - 10% N ₂	615	85	88.44	99	179	155
Ar - 15% N ₂	716	87	89	128	189	151
Ar - 20% N ₂	558.5	88	88	79.8	172	144

Table 4.10. Summary of Vickers' hardness measurements across the depth of the weldment for each welding condition. Load is 200 gm. for all conditions.

<u>Welding Conditions</u>	<u>Nitrogen Concentration in Weld Pool (ppm)</u>	<u>Base Metal Hardness (VHN)</u>	<u>Columnar Grains (VHN)</u>	<u>Minimum Fusion Zone Hardness (VHN)</u>	<u>Maximum Fusion Zone Hardness (VHN)</u>	<u>Average Fusion Zone Hardness (VHN)</u>
<i>0.847 cm/sec</i>						
Pure Ar	20	94	102	112	121	116
Ar - 5% N ₂	382.25	114	115	212	253	220
Ar - 10% N ₂	508	110	115	220	255	242
Ar - 15% N ₂	495	108	114	218	265	247
Ar - 20% N ₂	600	96	90	153	220	202
<i>0.423 cm/sec</i>						
Pure Ar	20	109	122	114	145	130
Ar - 5% N ₂	480.5	92	93	105	190	150
Ar - 10% N ₂	615	82	93	124	179	155
Ar - 15% N ₂	716	92	101	143	178	166
Ar - 20% N ₂	558.5	86	90	102	161	139

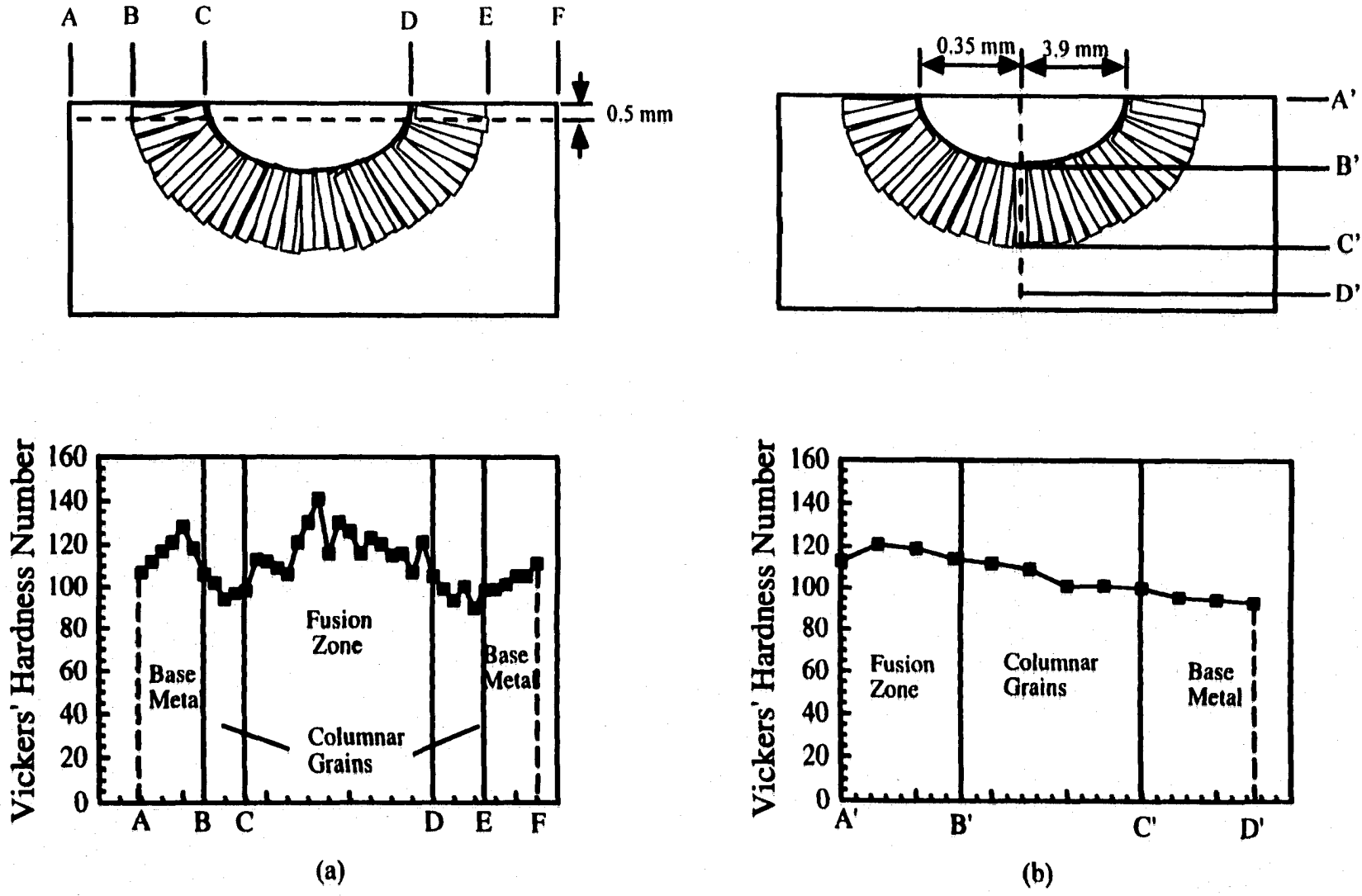


Figure 4.27(a&b). Microhardness measurements taken across both the (a) width and (b) depth of the weldment for pure Ar shielding gas for a travel speed of 0.847 cm/sec.

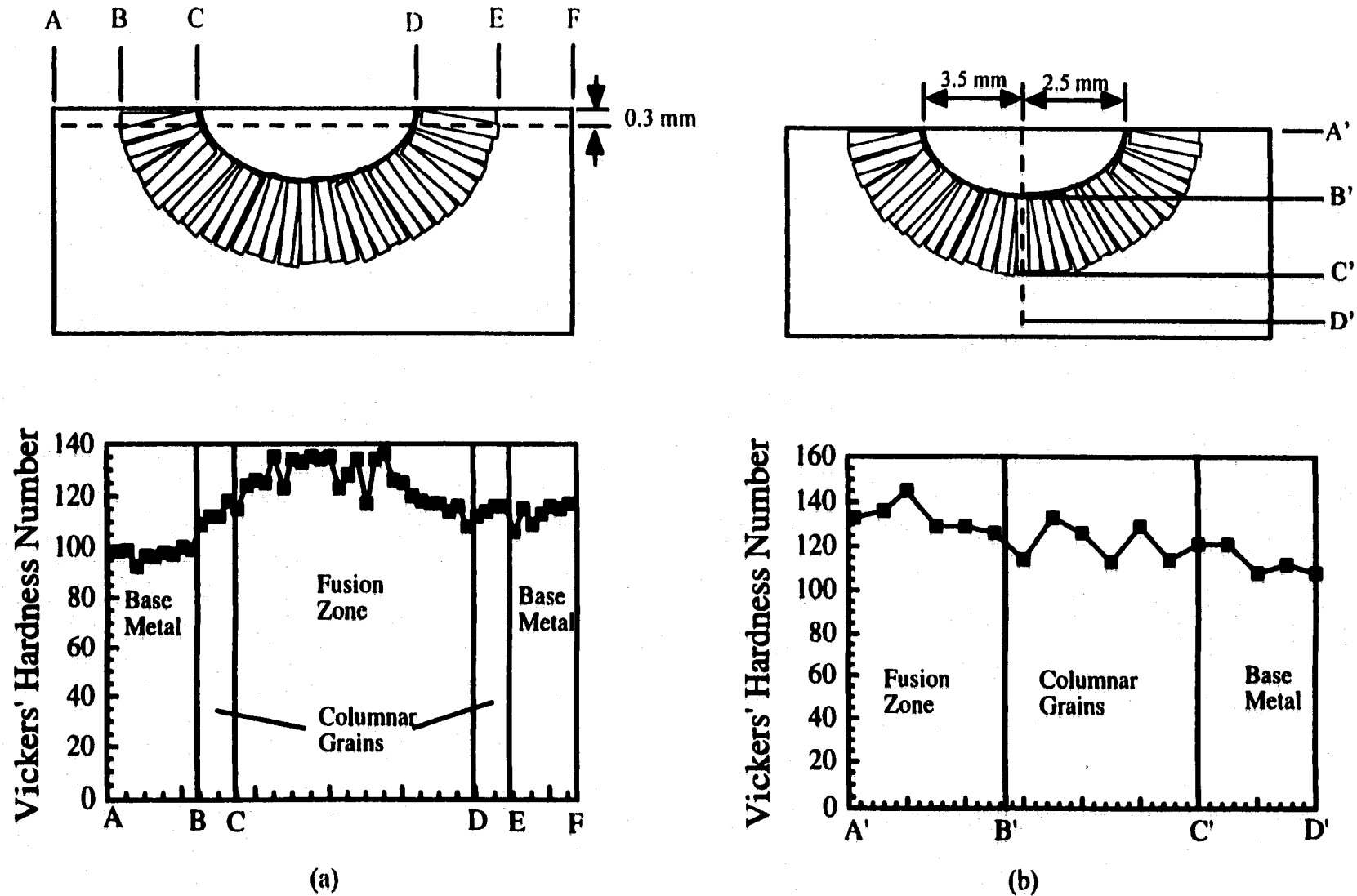


Figure 4.28(a&b). Microhardness measurements taken across both the (a) width and (b) depth of the weldment for a pure Ar shielding gas for a travel speed of 0.423 cm/sec.

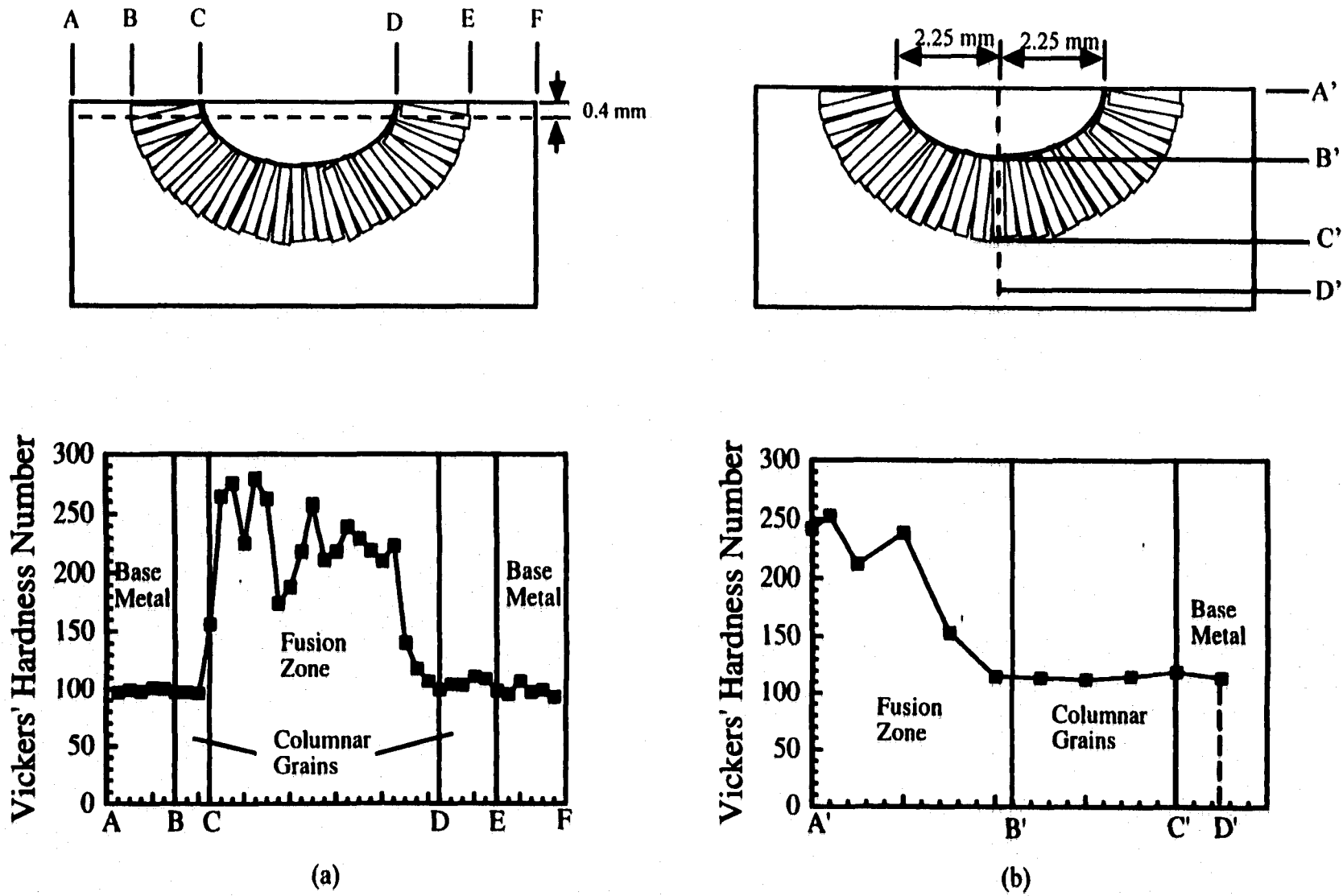


Figure 4.29(a&b). Microhardness measurements taken across both the (a) width and (b) depth of the weldment for a 5% N₂ addition to the shielding gas for a travel speed of 0.847 cm/sec.

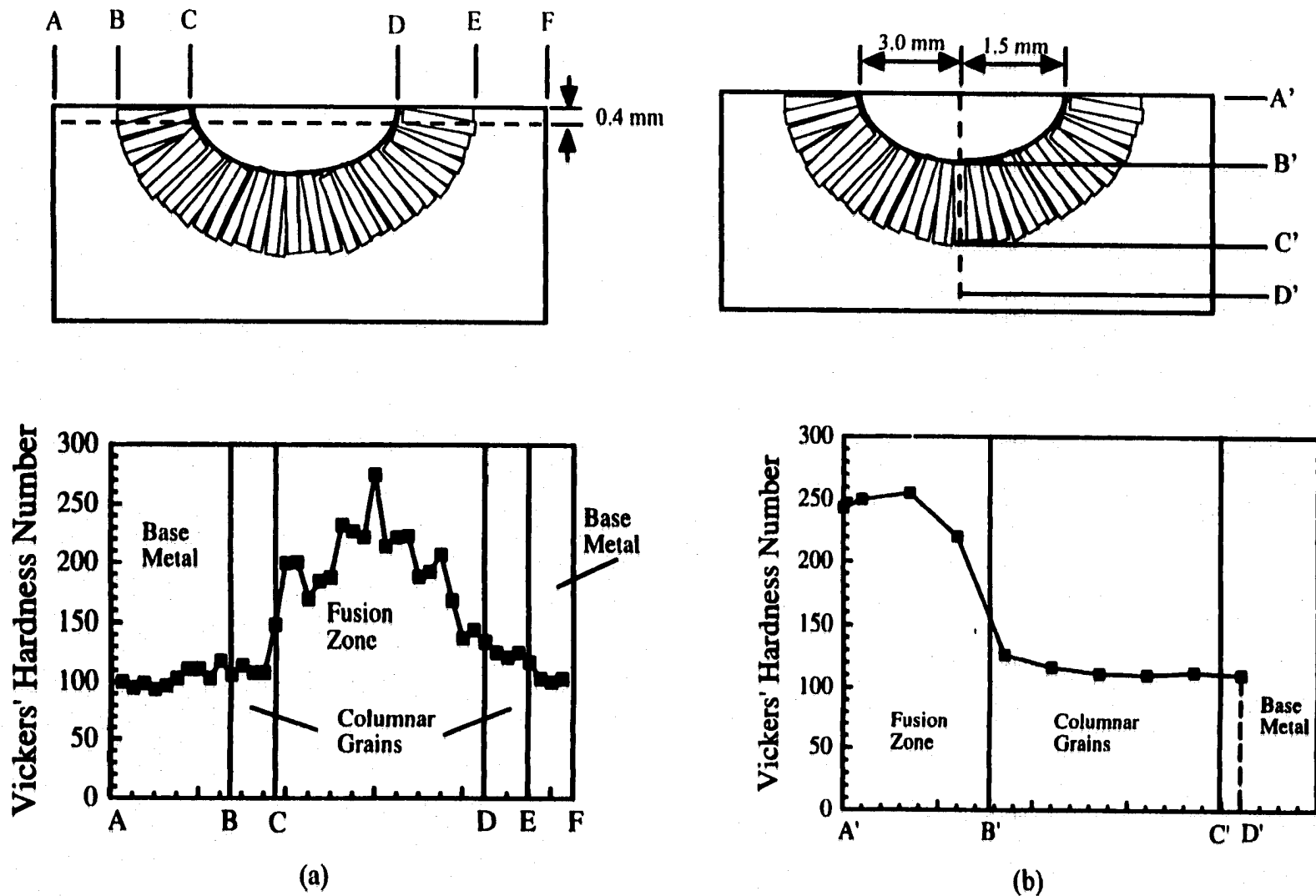


Figure 4.30(a&b). Microhardness measurements taken across both the (a) width and (b) depth of the weldment for a 10% N₂ addition to the shielding gas for a travel speed of 0.847 cm/sec.

zone. Across the width of fusion zone, though, there are significant variations in the observed microhardness values. No such variations are observed along the depth of the fusion zone, where there is a general decrease in microhardness values as the depth is increased, pointing to a drop in the nitrogen content in the weld metal at greater depths. Although higher additions of nitrogen are made to the shielding gas, there are no significant effects on the microhardness values measured in the fusion zone.

There is a significant change in the magnitude of the microhardness values across the width and depth of the weld pool with a decrease in the travel speed. Figures 4.31(a&b) and 4.32(a&b) show the microhardness measurements across both the width and depth of the weld pool with nitrogen additions of 5 and 10%, respectively, at a travel speed of 0.423 cm/sec. In particular, there is a decrease in the magnitudes of the measured microhardness values across the width and depth of the fusion zone, as compared to those measured at a more rapid travel speed. On the other hand, the general trends, signified by an increase in the microhardness in the fusion zone, remain the same.

A comparison between the VHN values observed under different welding conditions with the addition of nitrogen to the shielding gas has been made. Figures 4.33 and 4.34 show both the average and maximum microhardness values, respectively, for each welding condition as a function of the nitrogen addition to the shielding gas. There is little to no difference between the average and maximum microhardness values across both the width and depth of the weld pool for each welding condition. The general trends do not significantly change with the location of the measurements. For example, there is no change whether they are taken across the width or depth of the fusion zone. In all cases, the microhardness generally increases with the addition of nitrogen to the shielding gas but remains generally constant with further nitrogen additions.

4.3.6 X-Ray Analysis of Weld Metal

There are rather significant changes in the fusion zone microstructure with the addition of nitrogen to the shielding gas and changes in the welding speed. The identification of these various species has been attempted using x-ray diffraction techniques. A two circle diffractometer and a Mo-K α x-ray source have been used here. The potential ap

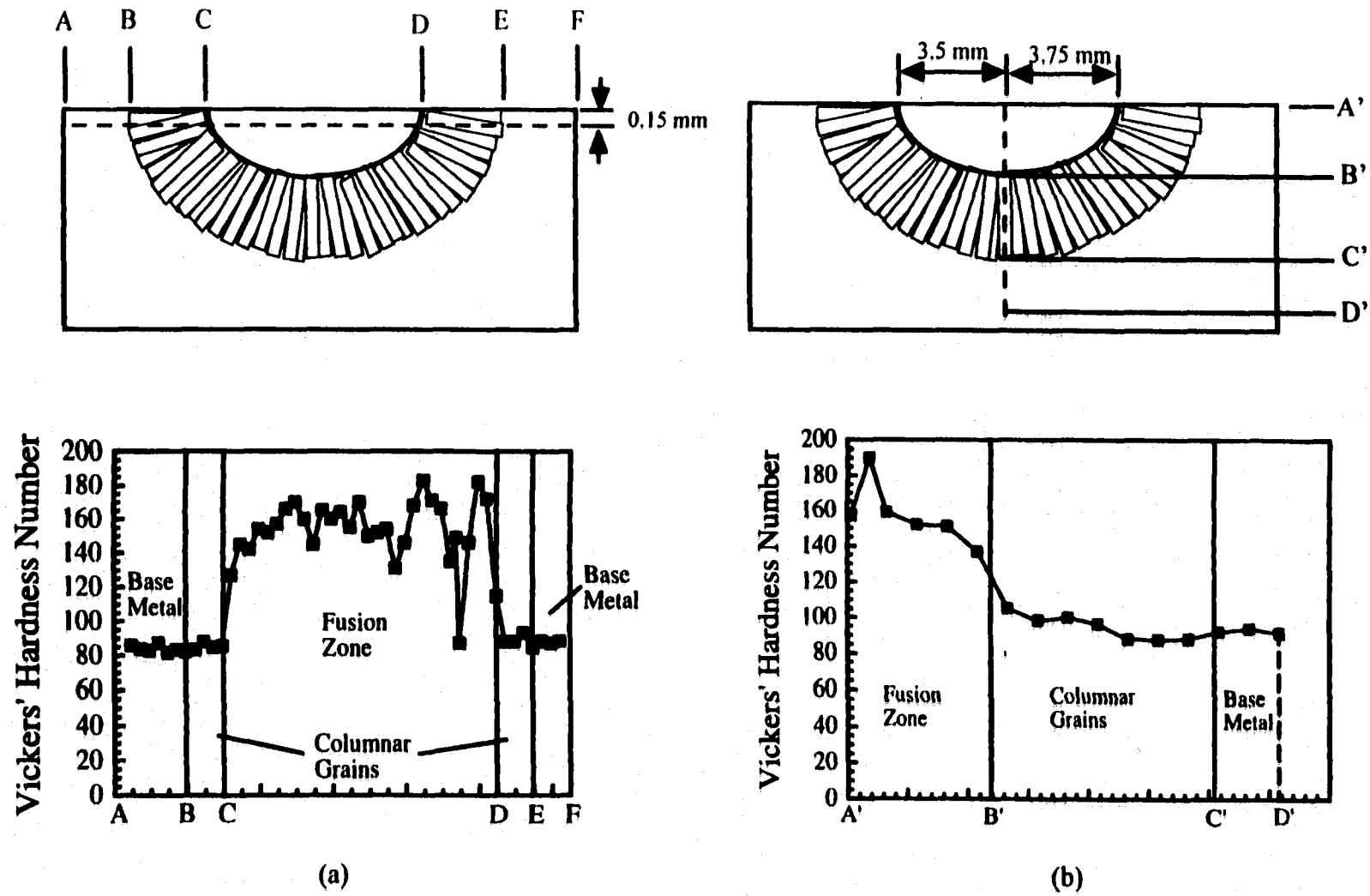


Figure 4.31(a&b). Microhardness measurements taken across both the (a) width and (b) depth of the weldment for a 5% N₂ addition to the shielding gas for a travel speed of 0.423 cm/sec.

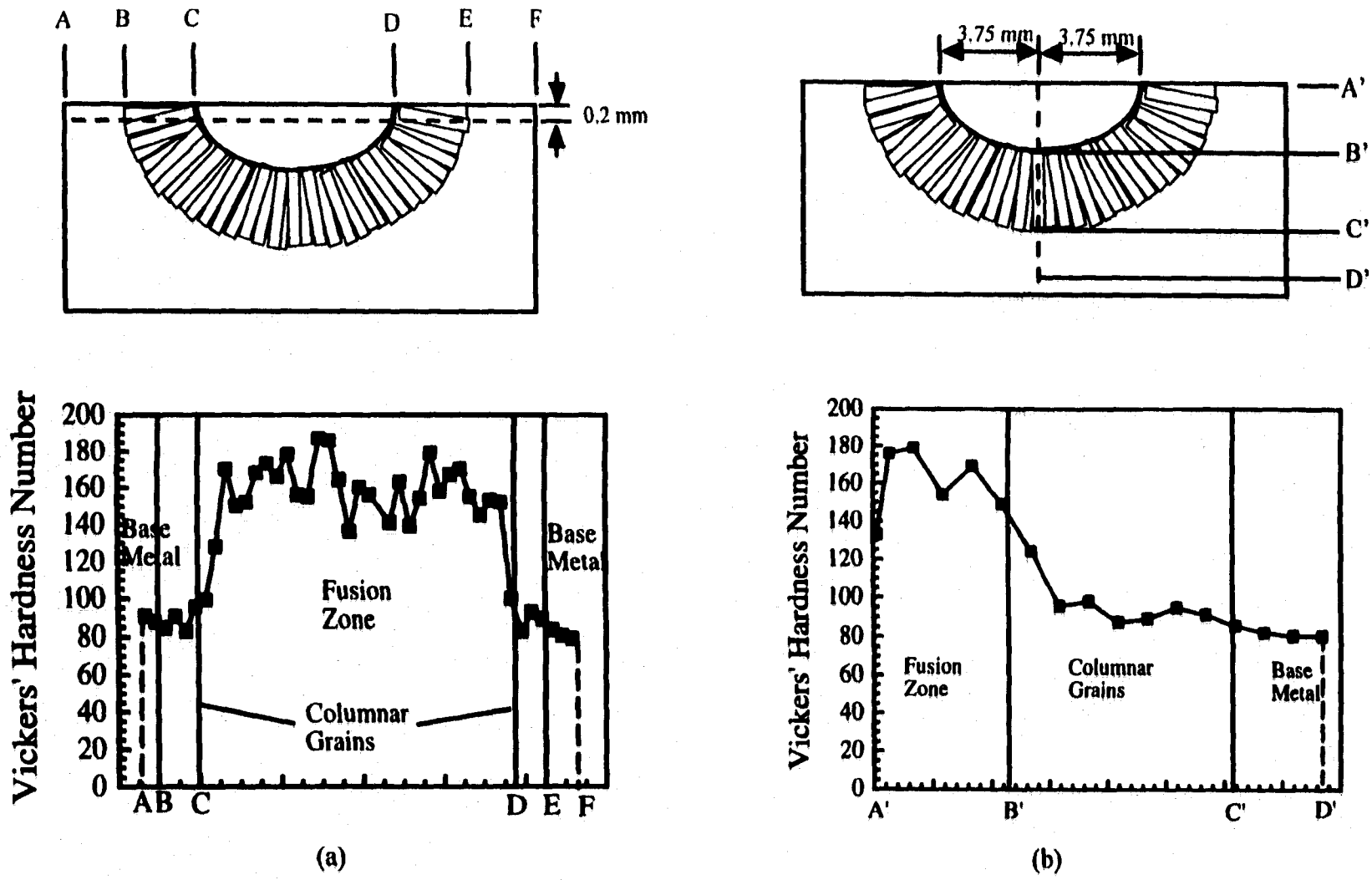
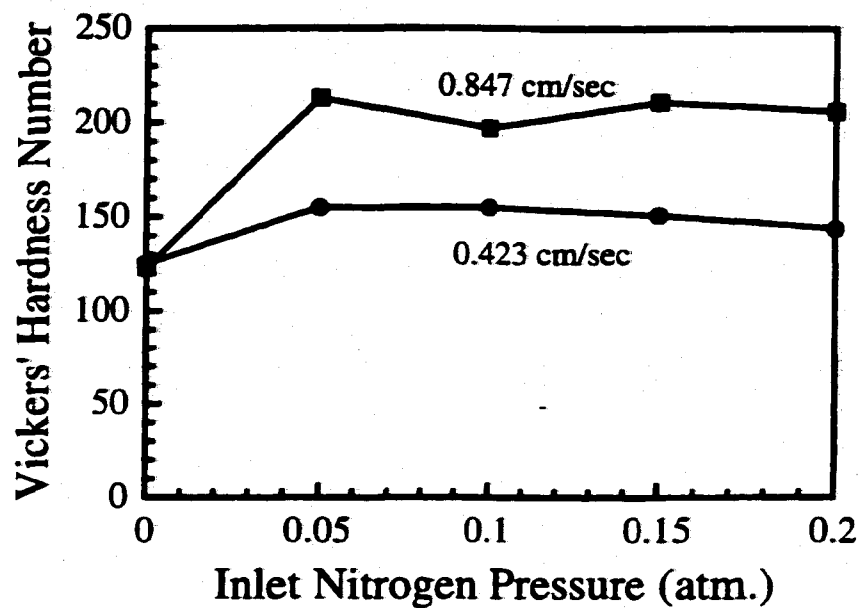
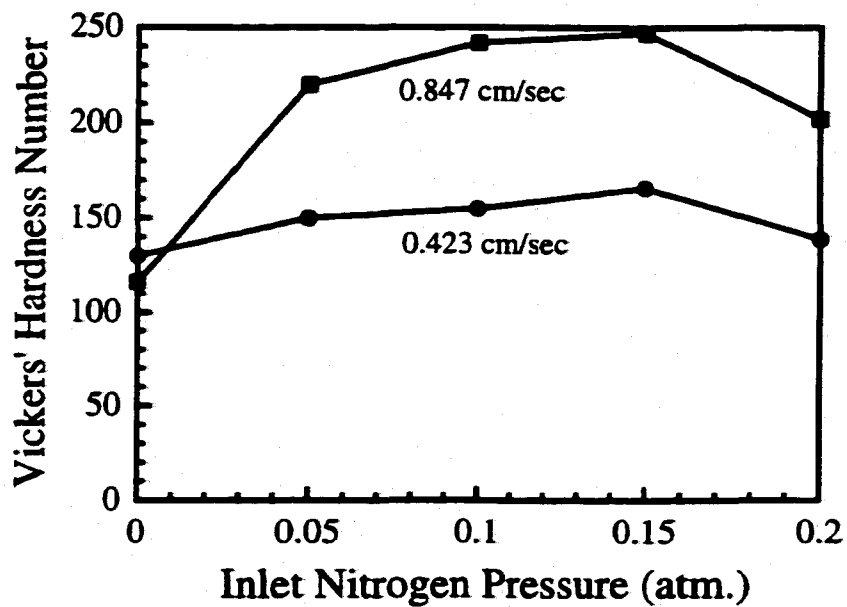


Figure 4.32(a&b). Microhardness measurements taken across both the (a) width and (b) depth of the weldment for a 10% N₂ addition to the shielding gas for a travel speed of 0.423 cm/sec.

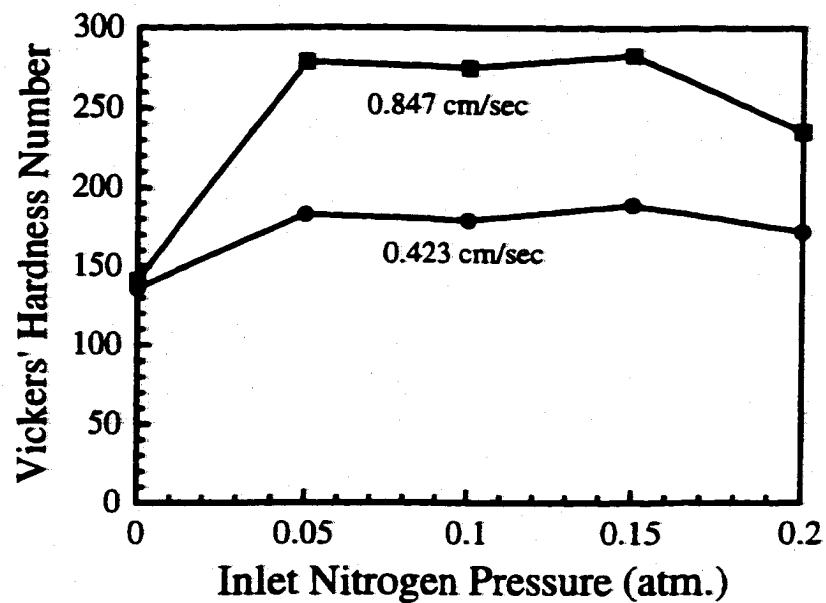


(a)

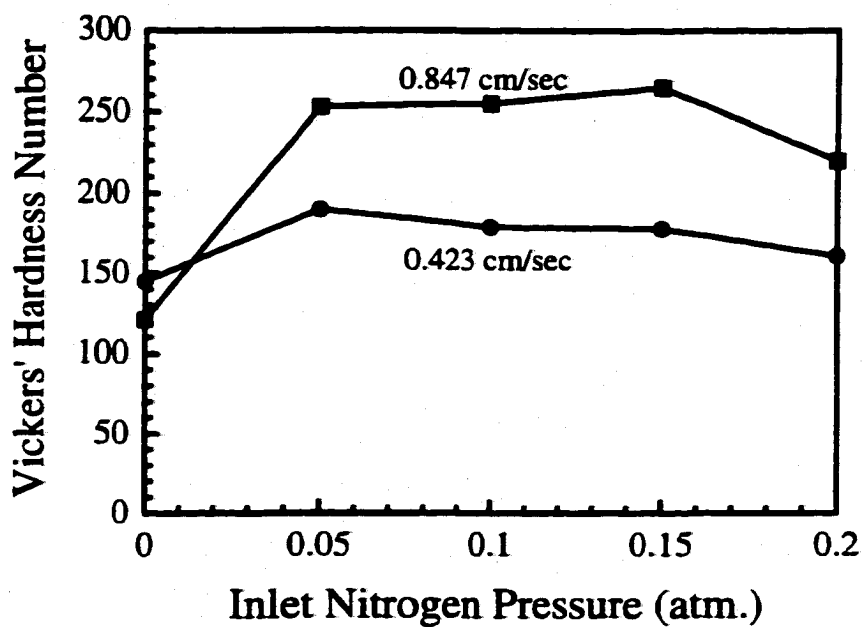


(b)

Figure 4.33(a&b). Comparison between average microhardness measurements for each welding condition across the (a) width and (b) depth of the weldment.



(a)



(b)

Figure 4.34(a&b). Comparison between maximum microhardness measurements for each welding condition across the (a) width and (b) depth of the weldment.

plied to the x-ray tube was 50 KV, and a current of 10 mA was maintained. Each sample has been analyzed along the top of section (d), as shown in Figure 4.2. The top surface is chosen to allow for only the weld metal, and not a significant amount of base metal, to be analyzed. X-ray scans have been made at a scanning speed of 1° per minute for 2θ values ranging from 15 to 56°.

Since x-ray analysis of each sample is made only along the top surface, the question of the location of the phases identified within the sample becomes important. Most metal samples strongly absorb x-rays, thereby reducing the intensity of the incident beam to nearly zero in a very short distance below the metal surface. Therefore, the diffracted beams originate chiefly in a thin surface layer. The effective depth of x-ray penetration and thus the depth of the specimen in which the phases identified exist are not precisely known because the intensity of the incident beam decreases exponentially with distance below the surface.

The integrated intensity diffracted by an infinitesimally thin layer at a depth, x , below the surface is defined by the following relation:

$$dI_D = \frac{I_0 ab}{\sin \alpha} \exp\left[-\mu x \left(\frac{1}{\sin \alpha} + \frac{1}{\sin \beta}\right)\right] dx \quad (4.10)$$

where I_D is the diffracted intensity, I_0 is the incident intensity, α and β are angles further defined, μ is the absorption coefficient, x is the depth below the surface of the sample, a is the volume fraction of the specimen containing particles having the correct orientation for reflection of the incident beam, and b is the fraction of the incident energy which is diffracted by the unit volume. Even though the above relationship applies to an infinitesimally thin layer at a given depth, the application of this same methodology to a sample of infinite thickness still only applies to a sample of a few thousandths of an inch for most metals.²⁶

There may be a number of species present in the fusion zone. In particular, each sample has been analyzed for the presence of retained austenite, martensite, and various iron nitride phases in the weld pool. A summary of the lattice parameters for these species²⁷⁻³¹ is shown in Table 4.11. In addition to the nitrogen-based phases, lattice

Table 4.11. Summary of lattice parameters for prominent phases in the iron-nitrogen system.

Phase	Structure	<i>a</i> (Å)	<i>b</i> (Å)	<i>c</i> (Å)	Reference
Fe - N-martensite (α')	Tetragonal	$2.865 - 0.0019 X_N$	----	$2.868 + 0.024 X_N$	30
α - Fe	B-Cubic	2.8664	----	----	31
N - austenite (γ)	Cubic	$3.564 + 0.0077 X_N$	----	----	31
Fe - C martensite (α')	Tetragonal	$2.866 - 0.0026 X_C$	----	$2.866 + 0.0246 X_C$	30
Fe - C austenite (γ)	Cubic	$3.555 + 0.0092 X_C$	----	----	30
Fe ₄ N (γ')	Cubic	3.795	----	----	29
Fe ₈ N or Fe ₁₆ N ₂ (α'')	Tetragonal	5.72	----	6.29	27 33
Fe ₂ N (ξ)	Orthorhombic	5.523	4.830	4.425	29
Fe ₃ N (ϵ)	Hexagonal	2.701		4.370	28

parameters for martensite and austenite phases in the Fe-C system are included in order to compare the characteristics with those same phases observed in the Fe-N system. When comparing the lattice parameters for these phases in each materials system, the lattice parameters are nearly identical, and, therefore, the phases are very similar.

The corresponding 2θ value for each reported d-spacing value has been calculated using Bragg's Law for a Mo-K α x-ray radiation source. Bragg's Law is shown in the following relationship:²⁶

$$n\lambda = 2d \sin\theta \quad (4.11)$$

where n is an integer, which is assumed to be unity, λ is the wavelength of the characteristic radiation in Å, d is the characteristic interplanar spacing in Å, and θ is the angle between the radiation source and the diffracting atom locations. A summary of the d spacing values and the 2θ values for the phases of interest is shown in Appendix C. These phases include ferrite (α -Fe) and austenite (γ -Fe), along with several iron nitride phases (Fe_4N , Fe_3N , Fe_2N , and Fe_8N).

Each weld sample has been analyzed, and the observed peaks and their corresponding phase identifications are summarized in Appendix C. As expected, only ferrite (α -Fe) peaks are observed in the x-ray analysis of the base metal. On the other hand, when the base metal is welded in a pure Ar shielding gas, additional peaks are present in the spectra. One of the effects caused by the welding of the base metal is the appearance of additional peaks very close to the primary ferrite peaks. These additional peaks are attributed to the presence of martensite in the weld metal. The appearance of these additional peaks is more prevalent at the more rapid travel speed, at which the weld metal undergoes more significant thermal cycles. On the whole, though, these peaks are not dominant, and, given their rather low intensities, it can be concluded that there is actually very little martensite present in these weld pools.

Of primary interest here, though, is the effect of nitrogen additions to the shielding gas on the phases present in the weld metal. Unlike the spectra observed with a pure Ar shielding gas, these spectra each contain a rather large number of additional peaks, in-

cluding Fe_4N , Fe_2N , Fe_8N , and Fe_3N . The appearance and intensity of these peaks in the x-ray spectra depend on the amount of nitrogen added to the shielding gas. For example, at a 5% N_2 addition, Fe_4N , and Fe_2N peaks are present in the spectra. As the nitrogen addition to the shielding gas is increased, a number of additional nitride peaks appear. When the nitrogen addition to the shielding gas reaches 20%, a rather large number of these nitride peaks are present in the diffraction pattern.

In addition to the nitride phases, martensite and austenite phases are also identified. Martensite peaks are also present at the lower nitrogen additions to the shielding gas studied here, but these peaks tend to disappear as the nitrogen addition to the shielding gas is increased. These peaks seem to be replaced by those associated with Fe_8N , which is recognized as an intermediate phase formed during the martensitic transformation. At the highest nitrogen additions studied here, an austenite ($\gamma\text{-Fe}$) peak also appears. This final observation is consistent with previous observations³⁰⁻³² in which the amount of retained austenite present in a sample increases with an increasing amount of nitrogen in solution.

Similar to the conditions observed at a travel speed of 0.847 cm/sec, several iron nitride phases are present in the spectra for a welding speed of 0.423 cm/sec. For example, Fe_8N , Fe_3N , Fe_2N , and Fe_4N are present at nitrogen additions to the shielding gas as low as 5%. Of these various nitrides, Fe_2N and Fe_4N dominate. As the nitrogen addition to the shielding gas is increased, though, the number of peaks and the peak intensity are both reduced. In general, though, nitride species are present in greater abundance at this welding speed as compared to the more rapid travel speed. There is also evidence for the presence of martensite in the weld metal at this nitrogen addition. Martensite present at low nitrogen additions is also reduced, and it is replaced by the appearance of Fe_8N . An austenite ($\gamma\text{-Fe}$) peak is even observed with a 20% N_2 addition to the shielding gas.

There are a number of similarities between the characteristics of the x-ray spectra shown for both welding speeds. As nitrogen is added to the shielding gas for both welding conditions, the effect on the peak intensity, especially at large nitrogen additions, i.e. approaching 20% N_2 , is pronounced. All peaks observed across the spectra decrease in intensity and many disappear. This is also true for the ferrite peaks, even though the

amount of ferrite present in the samples should not decrease by such a significant amount. In many cases, the same peaks are not present in the spectra for different nitrogen additions at a single travel speed.

In general, this x-ray analysis has aided in further understanding the microstructures observed in the weld metal. In particular, the presence of nitride phases and several non-equilibrium phases, such as martensite and retained austenite, has been confirmed. The intensities of the nitride peaks are rather small in each case and can be attributed to the nature of the nitride phases in the weld pool. These nitrides are a dispersed phase, and, when compared with the bulk volume of the sample being analyzed, actually do not take up much volume. In addition, the location of the nitride phases is not entirely uniform, so the detection of these phases is also determined, in part, by the location on the weld pool exposed to the x-ray beam. On the other hand, little can be determined concerning the identity of the individual precipitates and phases present in the weld metal. A more localized analysis, such as that possible through a transmission electron microscopy study, is needed to attain this more specific knowledge.

4.3.7 Effect of Microstructure on Nitrogen Solubility

Two distinct microstructures have been observed in each of these welding conditions. At the more rapid travel speed, the microstructure is complex and contains a number of non-equilibrium structures. As the travel speed is reduced, rather large needle-like precipitates appear in the fusion zone along with rather significant amounts of porosity. These changes in the fusion zone microstructure are expected to have an effect on the nitrogen solubility in the weld metal, but there is little change in the magnitude of the nitrogen concentration in each sample.

Typically, the nitrogen solubility in iron is determined by Sieverts' Law calculations, which have been discussed in previous sections. Once nitrogen is absorbed in iron, though, it may exist in a variety of forms in equilibrium with the iron phase, as shown in the Fe-N equilibrium phase diagram in Figure 2.1. It is similar in many respects to the Fe-C system. For example, there are several stable iron-nitride phases present in the lower temperature range, and since a eutectoid reaction is present, the presence of a pear-

litic phase is expected. Non-equilibrium phases are also observed in the Fe-N system.³³⁻
³⁷ Little work, though, has been performed on Fe-N martensite when compared with that done on the Fe-C martensitic phase. Martensite in the Fe-N system has been observed to exist between nitrogen concentration of 0 to 2.7 wt.% [N]. Alloys containing up to 0.7 wt.% [N] have been observed to be fully martensitic when quenched. As the nitrogen concentration is further increased, the alloys contain progressively more retained austenite. At 2.34 wt.% N, the specimen becomes completely austenitic after being quenched to 293 K.

At a slower travel speed, needle-like precipitates are observed in the fusion zone. These precipitates are assumed to be Fe₄N, which is a stable nitride species present in the iron-nitrogen phase diagram at approximately 5.77 wt.% [N]. Previous researchers have also observed similar iron nitride phases, which they also identified as Fe₄N, in iron weld metal exposed to a nitrogen-containing shielding gas.²⁵ Fe_xN phases have nitrogen concentrations ranging from 5.77 to greater than 11.0 wt.% [N], as shown in Table 2.1 and the available thermodynamic data is included in Table 4.12. As shown in this table, no available thermodynamic data for the formation of Fe₃N could be located. This phase is typically observed on iron surfaces and is formed by the interaction between ammonia (NH₃) gas and solid iron.³⁹ These common iron nitrides, such as Fe₄N and Fe₈N, though, form only during cooling or exposure to nitrogen containing gases at temperatures in the vicinity of 673 to 773 K. Neither iron nitride phase is stable at elevated temperatures or at lower nitrogen partial pressures. For example, Fe₄N is not stable at elevated temperatures until P_{N₂} reaches 100 to 10000 atm. and becomes stable at lower temperatures and nitrogen partial pressures between 10 to 100 atm.^{8,40-42}

When these nitride phases are present in the weld pool, there is a change in the nitrogen solubility from that calculated using Sieverts' Law. The temperature dependence for the solubility of nitrogen in α-Fe with the presence of nitrides is defined by the following two relationships when considering the presence of Fe₄N and Fe₈N, respectively:²⁷

$$\ln[\underline{N}(\text{wt.}\%)]_{\text{Fe}_4\text{N}} = -\frac{1814}{T} + 1.09 \quad (4.12)$$

Table 4.12. Summary of values of free energies of formation at 298 K for iron nitride phases.

Nitride Phase	ΔH_f° (cal/mol)	ΔG_f° (cal/mol)	S° (cal/K-mol)	C_p° (cal/K-mol)	References
Fe ₂ N	-900	2600	24.2	16.8	38
Fe ₃ N	---	---	---	---	---
Fe ₄ N	-2550	890	37.3	29.3	38
Fe ₈ N	-2700	2100	---	---	27

$$\ln[\underline{\text{N}}(\text{wt.}\%)]_{\text{Fe}_8\text{N}} = -\frac{2160}{T} + 2.51 \quad (4.13)$$

Figure 4.35 shows the nitrogen solubility in α -Fe with the presence of these nitrides.²⁷ The nitrogen solubility with the presence of secondary nitride phases far exceeds Sieverts' Law calculations. In fact, the presence of these nitrides allows nitrogen concentrations well in excess of 1000 ppm to exist in the iron sample. Therefore, much like the presence of martensite or retained austenite, the presence of these nitride phases in the weld metal affects the nitrogen solubility in the solid phase. More nitrogen can reside in the solid than dictated by Sieverts' Law calculations.

In addition to these various microstructural features in the fusion zone, the presence of porosity is also an important consideration. Porosity formation in the weld metal is based on the nitrogen solubility in both liquid and solid iron. Nitrogen solubility is much greater in liquid iron than in solid iron. In the Fe-N system, the thermodynamic solubility limit is determined by the nitrogen solubility in liquid iron, which is approximately 450 ppm at 1873 K and 1 atm. N_2 .^{5,7} If the concentration of nitrogen in solution in the weld metal exceeds this limit, nitrogen gas is desorbed from the liquid metal, either as diatomic or monatomic nitrogen and porosity is formed in the weld metal. This evolution of nitrogen is supported by the formation of blowholes and pores in the weld metal. The weld metal nitrogen concentration is thus primarily controlled by the evolution of nitrogen during the cooling of the weld metal.

There is a connection between the microstructure of the weld metal, the presence of porosity, and the measured nitrogen concentration in the fusion zone. The microstructures present in the weld metal and the absence or presence of porosity are measures of the final measured nitrogen concentration. Thermodynamic limits for the maximum concentration of nitrogen in liquid iron are established by the formation of nitride compounds or by the nucleation of gas bubbles. With the presence of second phases in the weld metal, the nitrogen solubility changes from that calculated using the Sieverts' Law basis for nitrogen saturation.

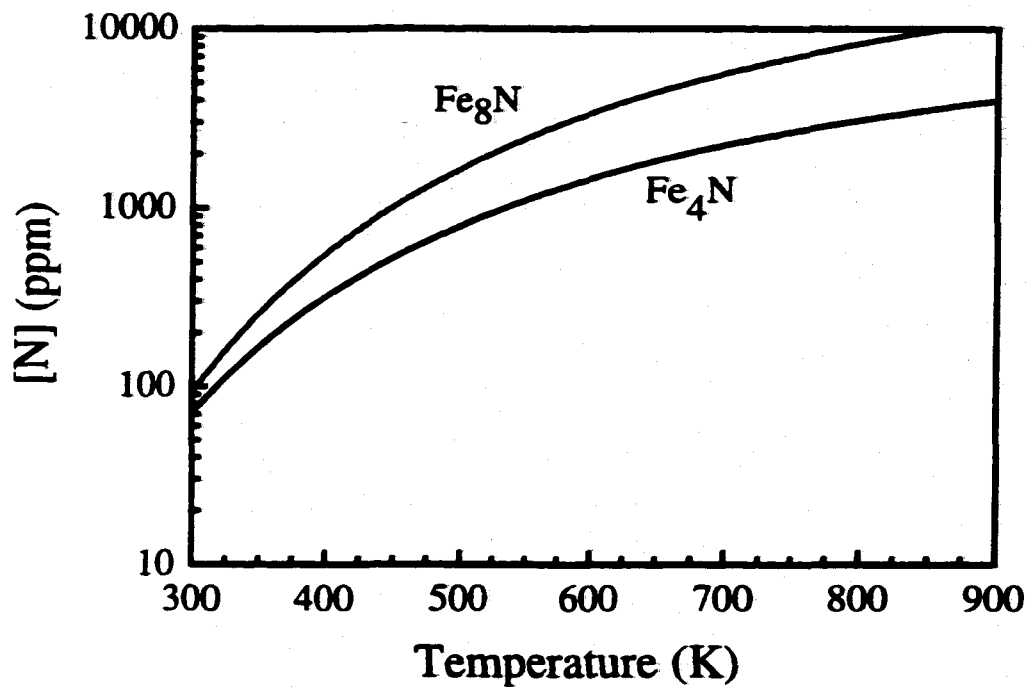


Figure 4.35. Change in the nitrogen solubility with the presence of nitride phases in α -Fe.²⁷

4.4 OVERVIEW

Other GTA welding experiments similar to those discussed here have been reported by Kuwana and Kokawa,² who also performed GTA welding experiments on pure iron with an Ar-N₂ shielding gas. The base metal chemistry and a summary of their experimental parameters are shown in Table 4.13. In their welding experiments, these authors used a higher power input and slower travel speed than any used here. Nevertheless, their results are very similar to those observed in these experiments. Figure 4.36 shows a summary of the GTA welding experiments performed here along with results from Kuwana and Kokawa.² There is a generally small increase in the nitrogen concentrations observed in the weld metal with further nitrogen additions to the shielding gas. These nitrogen concentrations, though, are similar in magnitude, regardless of the choice of welding speed or input power.

Even though similar nitrogen concentrations are observed in each weld sample, the weld metal displays significantly different characteristics. These weld metal characteristics are dependent on the choice of welding parameters. For example, changes in travel speed produce significantly different microstructures, ranging from those containing various non-equilibrium microstructures to others containing needle-like precipitates. Variations in these microstructural characteristics also alter the nitrogen solubility in the solid iron. The appearance of the weld metal microstructure is also not uniform, with different locations in the weld pool displaying different microstructures. Since the formation of iron nitrides and these other microstructural features are solid state processes, they do not influence the dissolution of nitrogen into the iron weld metal and appears to be not particularly important to this study. On the other hand, the nitrogen concentration in the fusion zone is dependent on all these reactions.

In addition to the various weld metal microstructures, the appearance of porosity in the weld line also occurs with changes in the welding parameters. Blowholes and porosity present in the weld metal are voids created by gas trapped in the weld metal and have been directly related to gas absorption in the weld metal. The presence or absence of porosity in the weld metal also seems to be connected to the choice of welding parameters. As observed in these experiments, significant porosity appears in the weld line at a

Table 4.13. Experimental Welding Parameters in Kuwana and Kokawa study.²

<u>Welding Parameters</u>	
Arc Current (A)	50 – 300
Arc Voltage (V)	13 – 31
Travel Speed (mm/sec)	0.83 – 5.0
Electrode Diameter (mm)	3.2 (W - 2% Th)
Total Pressure	0 – 1.0 atm.
Shielding Gas Compositions*	N ₂ Gas System
	N ₂ – Ar (Gas Mixture)
	N ₂ – He (Gas Mixture)
	N ₂ – H ₂ (Gas Mixture)
Base Metal Chemistry (wt.%)	99.8974 Fe 0.004 C
	0.006 Mn 0.003 P
	0.005 S 0.007 Si
	0.003 Al 0.04 Cr
	0.018 Ni 0.0026 [N]
	0.0090 [O] 0.005 Mo

* Nitrogen partial pressure varies between 0 and 1 atm.

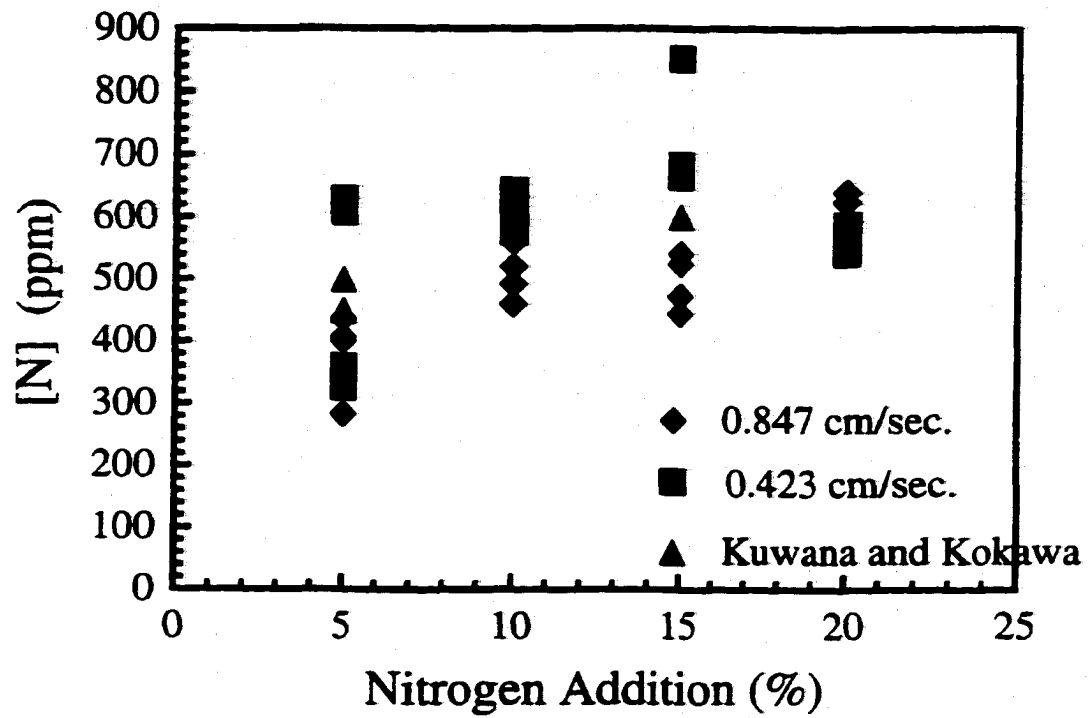


Figure 4.36. Summary of experimental nitrogen concentrations observed during the GTA welding of pure iron.

slower travel speed and with higher nitrogen additions to the shielding gas. On the other hand, no porosity is present at a more rapid travel speed with these same nitrogen additions to the shielding gas. In both cases, though, a similar nitrogen concentration is observed in the weld metal.

Therefore, a connection between the choice of welding parameters, the measured nitrogen concentration in the weld metal, the resulting microstructure, and the formation of porosity appears to exist. The nitrogen concentration in the weld pool is dependent on the absorption and desorption of nitrogen from the liquid and solid portions of the weldment and the solidification and solid state phase transformations occurring in the weld metal. Weld metal cooling rates are thus primary driving forces behind the final properties of the weldment. Since only the travel speed has been altered in these experiments, the weld metal cooling rates have been altered.

Nevertheless, the final nitrogen concentrations are all very similar in magnitude, thus leading to the conclusion that the nitrogen present in the weld metal is determined at the time of solidification of the weld pool. Therefore, the nitrogen concentrations are dependent on the supply of monatomic nitrogen from the plasma phase above the weld pool, the absorption of this monatomic nitrogen on the weld pool surface, and the transport of nitrogen throughout the weld pool interior. These factors are not easily determined experimentally but are more effectively calculated using mathematical modeling techniques. A greater knowledge of the heat transfer and fluid flow in the weld pool during welding operations is thus necessary in order to determine both the cooling cycles experienced by the weld metal and the fluid flow properties dictating nitrogen transport in the weld pool.

REFERENCES

- ¹ C.J. Allum, "Nitrogen Absorption from Welding Arcs", *Bulletin of Welding Research Council*, 369, Dec. 1991-2, 68-84.
- ² T. Kuwana and H. Kokawa, "The Nitrogen Absorption of Iron Weld Metal during Gas Tungsten Arc Welding", *Trans. Jap. Weld. Soc.*, 1986, 17(1), 20-26.
- ³ M. Uda and S. Ohno, "Spattering Phenomenon for Iron-Nitrogen System during Arc Melting", *Trans. Nat. Res. Inst. Metals*, 1978, 20(6), 358-365.
- ⁴ T. Kuwana, H. Kokawa, and N. Muramatsu, "Effects of Chromium and Nickel on Nitrogen Absorption of Arc-Melted Iron", *Trans. Jap. Weld. Soc.*, 1989, 20(1), 10-16.
- ⁵ S.A. Gedeon and T.W. Eagar, "Thermochemical Analysis of Hydrogen Absorption in Welding", *Weld. J.*, 1990, 69, 264s-271s.
- ⁶ K. Mundra and T. DebRoy, "A General Model for Partitioning of Gases between a Metal and Its Plasma Environment", *Metall. and Mater. Trans. B*, 1995, 26B, 149-157.
- ⁷ T.A. Palmer and T. DebRoy, "Physical Modeling of Nitrogen Partition between the Weld Metal and Its Plasma Environment", *Weld J.*, 1996, 75(7), 197s-207s.
- ⁸ W. T. Landford, Jr., N.L. Samways, R.F. Craven, and H.E. McGannon, The Making, Shaping, and Treating of Steel, 10th Edition, (Association of Iron and Steel Engineers, Pittsburgh, PA), 1985, pp. 404-406.
- ⁹ N.S. Corney and E.T. Turkdogan, "The Effect of Alloying Elements on the Solubility of Nitrogen in Iron", *J. Iron Steel Inst.*, 1955, 180, 344-348.
- ¹⁰ E.T. Turkdogan, "Physical Chemistry of Oxygen Steelmaking. Thermochemistry and Thermodynamics", in BOF Steelmaking. Volume 2: Theory, ed. By R.D. Pehlke, W.F. Porter, R.F. Urban, and J.M. Gaines, (Iron and Steel Society of AIME, New York), 1975, pp. 1-190.
- ¹¹ R.D. Pehlke and J.F. Elliott, "Solubility of Nitrogen in Liquid Iron Alloys. 1. Thermodynamics", *Trans. AIME*, 1960, 218, 1088-1101.
- ¹² R.D. Pehlke and J.F. Elliott, "Solubility of Nitrogen in Liquid Iron Alloys II. Kinetics", *Trans. Met. Soc. AIME*, 1963, 227, 844-855.
- ¹³ K.N. Kapranov and G.G. Utlinskii, "Porosity in Welding Copper in Nitrogen Plasma", *Welding Int.*, 1991, 5(9), 735-737.

- ¹⁴ S. Ohno and M. Uda, "Effects of Hydrogen and Nitrogen on Blowhole Formation in Pure Nickel at Arc Welding and Non-Arc Melting", *Trans. Nat. Res. Inst. Metals*, 1981, 23(4), 243-248.
- ¹⁵ R.A. Woods, "Porosity and Hydrogen Absorption in Aluminum Welds", *Weld. J.*, 1974, 53(3), 97s-108s.
- ¹⁶ R.P. Martukanitz and P.R. Michnuk, "Sources of Porosity in Gas Metal Arc Welding of Aluminum", *Aluminium*, 1982, 58(5), 276-279.
- ¹⁷ J. Littleton, J. Lammas, and M.F. Jordan, "Nitrogen Porosity in Gas Shielded Arc Welding of Copper", *Weld J.*, 1974, 53(12), 561s-565s.
- ¹⁸ T. Kuwana, H. Kokawa, and A. Honda, "Effects of Nitrogen and Titanium on Porosity and Microstructure in Ar-N₂ Gas Metal Arc Welded Copper", *Trans. Jap. Weld. Soc.*, 1987, 18(2), 159-166.
- ¹⁹ V.N. Lipodaev, *et al.*, "Porosity of Joints in the Welding of High-Alloy Austenitic Nitrogen-Bearing Steels", *Avt. Svarka*, 1975, No. 8, 12-15.
- ²⁰ J.E. Ramirez, B. Han, and S. Liu, "Effect of Welding Variables and Solidification Substructure on Weld Metal Porosity", *Metall. and Mater. Trans. A*, 1994, 25A, 2285-2294.
- ²¹ R. Halmshaw, Industrial Radiology: Theory and Practice, 2nd ed., (Chapman & Hall, London), 1995.
- ²² "Standard Guide for Radiographic Testing", ASTM Designation: E 94 - 93, 1993, 1-11.
- ²³ "Standard Test Method for Radiographic Examination of Weldments", ASTM Designation: E 1032 - 95, 1995, 455-459.
- ²⁴ "Standard Reference Radiographs for Steel Fusion Welds", ASTM Designation: E 390 - 95, 1995, 138-141.
- ²⁵ S. Kou, Welding Metallurgy, John Wiley and Sons, New York, 1987.
- ²⁶ B.D. Cullity, Elements of X-Ray Diffraction, (Addison-Wesley Publishing Company, Inc., Reading, MA), 1956.
- ²⁷ J.D. Fast and M.B. Verriyp, "Solubility of Nitrogen in Alpha-Iron", *J. Iron Steel. Inst.*, 1955, 180, 337-343.

- ²⁸ K.H. Jack, "The Iron-Nitrogen System: The Crystal Structures of ϵ -Phase Iron Nitrides", *Acta Cryst.*, 1952, 5, 404-411.
- ²⁹ K.H. Jack, "Binary and Ternary Interstitial Alloys I. The Iron Nitrogen System: The Structures of Fe_4N and Fe_2N ", *Proc. Roy Soc. A*, 1948, 195, 34-41.
- ³⁰ T. Bell and W.S. Owen, "The Thermodynamics of the Martensite Transformation in Iron-Carbon and Iron-Nitrogen", *Trans. Met. Soc. AIME*, 1967, 239, 1940-1949.
- ³¹ L.G. Berry, ed., Powder Diffraction Files, (Joint Committee on Powder Diffraction Standards, Swarthmore, PA), 1974.
- ³² K.H. Jack, "The Iron-Nitrogen System: The Preparation and the Crystal Structures of Nitrogen-Austenite (γ) and Nitrogen-Martensite (α')", *Proc. Roy. Soc. A*, 1951, 208, 200-215.
- ³³ K.H. Jack, "The Occurrence and the Crystal Structure of α'' -Iron Nitride; A New Type of Interstitial Alloy Formed During the Tempering of Nitrogen-Martensite", *Proc. Roy. Soc. A*, 1951, 208, 216-224.
- ³⁴ T. Bell and W.S. Owen, "Martensite in Iron-Nitrogen Alloys", *J. Iron Steel Inst.*, 1967, 205, 428-434.
- ³⁵ T. Bell, "Martensite Transformation Start Temperature in Iron-Nitrogen Alloys", *J. Iron Steel Inst.*, 1968, 206, 1017-1021.
- ³⁶ T. Bell and D. Brough, "The Tempering of Iron-Nitrogen Massive Martensite", *Metal Sci.*, 1970, 4, 171-177.
- ³⁷ M.G.A. Biswas and I. Codd, "An Electron Transmission Study of Iron-Nitrogen Martensite", *J. Iron Steel Inst.*, 1968, 206, 494-497.
- ³⁸ F.D. Rossini, D.D. Wagman, W.H. Evans, S. Levine, and I. Jaffe, Selected Values of Chemical Thermodynamic Properties, (National Bureau of Standards, Washington, DC), 1952.
- ³⁹ Y. Inokuti, N. Nishida, and N. Ohashi, "Formation of Fe_3N , Fe_4N , and Fe_{16}N_2 on the Surface of Iron", *Met. Trans. A*, 6A(4), 773-784.
- ⁴⁰ J.W. Mellor, A Comprehensive Treatise on Inorganic and Theoretical Chemistry, Volume VIII, Supplement I, Nitrogen (Part I), (Longmans), 1967, pp. 214-233.

⁴¹ L.J. Dijkstra, "Precipitation Phenomena in the Solid Solutions of Nitrogen and Carbon in Alpha Iron below the Eutectoid Temperature", *Metals Transactions*, 1949, 185, 252-260.

⁴² H.A. Wriedt, "Thermodynamics of Gamma Prime Iron Nitride ("Fe₄N") at 500°C", *Trans. Met. Soc AIME*, 1969, 245, 43-46.

Chapter 5

MATHEMATICAL MODELING OF NITROGEN DISSOLUTION IN GTA WELDING

5.1 BACKGROUND

Heat transfer and fluid flow processes contribute significantly to the development of weld metal properties.^{1,2} Mathematical modeling has been used to understand the magnitude and effects of the fluid flow and heat transfer in the weld pool.^{3,4} Through these calculations, convection is considered the dominant driving force for liquid flow in the weld pool during arc welding and is driven in varying degrees by the surface tension gradient at the weld pool surface, otherwise known as the Marangoni force, the buoyancy force, and electromagnetic forces. Mathematical modeling has also been used to understand complex physical phenomena related to welding.⁵⁻¹⁰ Several of these phenomena include the prediction of microstructures in C-Mn steels,^{5,6} the growth and dissolution of oxide inclusions during the submerged metal arc (SMA) welding of low alloy steels,⁷ the role of sulfur in affecting weld pool size and shape during the laser spot welding of tool steels,^{8,9} and the vaporization of volatile alloying elements in stainless steels during laser welding.¹⁰

The dissolution of nitrogen from the plasma phase above the weld pool into the liquid metal at the weld pool surface is another of these complex physical processes. It is typically characterized by a competition between the absorption of monatomic nitrogen at the weld pool surface and the desorption of diatomic nitrogen gas from the solidified weld metal outside the arc column.¹¹⁻¹⁴ The dominant role of monatomic nitrogen in the nitrogen absorption reaction has long been recognized,¹⁵⁻¹⁸ and several models have been developed.^{15,16} These models provide a qualitative basis for understanding the principal role of the plasma phase in this reaction. Since fluid flow and heat transfer processes significantly impact on the properties of the weld metal surface and interior, there should be a similar effect on the nitrogen dissolution reaction.

A mathematical model to calculate the nitrogen concentration in the weld pool has been developed. This model is based on the absorption of monatomic nitrogen from the plasma phase onto the weld pool surface and its subsequent transport into the weld pool interior. The amount of monatomic nitrogen present in the plasma phase above the weld pool is calculated using the methodology described in Chapter 3. Once this monatomic nitrogen partial pressure is known, the amount of nitrogen absorbed on the metal surface can be calculated using the surface temperatures determined by the heat transfer and fluid flow models. Nitrogen absorbed on the weld pool surface is then transported to the weld pool interior by the vigorous fluid flows present within the weld pool provide a significant convective component to the transport of nitrogen. The validity of this model has also been tested by comparing the modeling results with previously discussed experimental results from a series of (GTA) welding experiments.

5.2 MATHEMATICAL FORMULATION

5.2.1 Governing Equations

The governing equations for spot welding conditions, or conditions defined by a stationary heat source, have been defined elsewhere.¹⁹⁻²¹ During typical arc welding operations, though, the heat source moves at a constant velocity. Therefore, modifications must be made to the governing equations to account for this movement of the heat source, primarily in the coordinate system used to solve these equations. Previous researchers have formulated these governing equations in a fixed coordinate system (x,y,z), such as in a Lagrangian solution scheme.^{22,23} However, the welding problem becomes unsteady, and the solution of the equations of conservation of mass, momentum, and energy requires a large number of grids to accurately represent the moving heat source and the spatial variation of the heat flux. A small time step is also necessary to ensure accuracy and stability of the solution, making computation time very large and the solution procedure rather burdensome.

On the other hand, these problems can be avoided if the coordinate system is attached to the heat source and moves with it, such as in an Eulerian solution scheme. In this system, which is schematically shown in Figure 5.1, the heat source and the molten metal

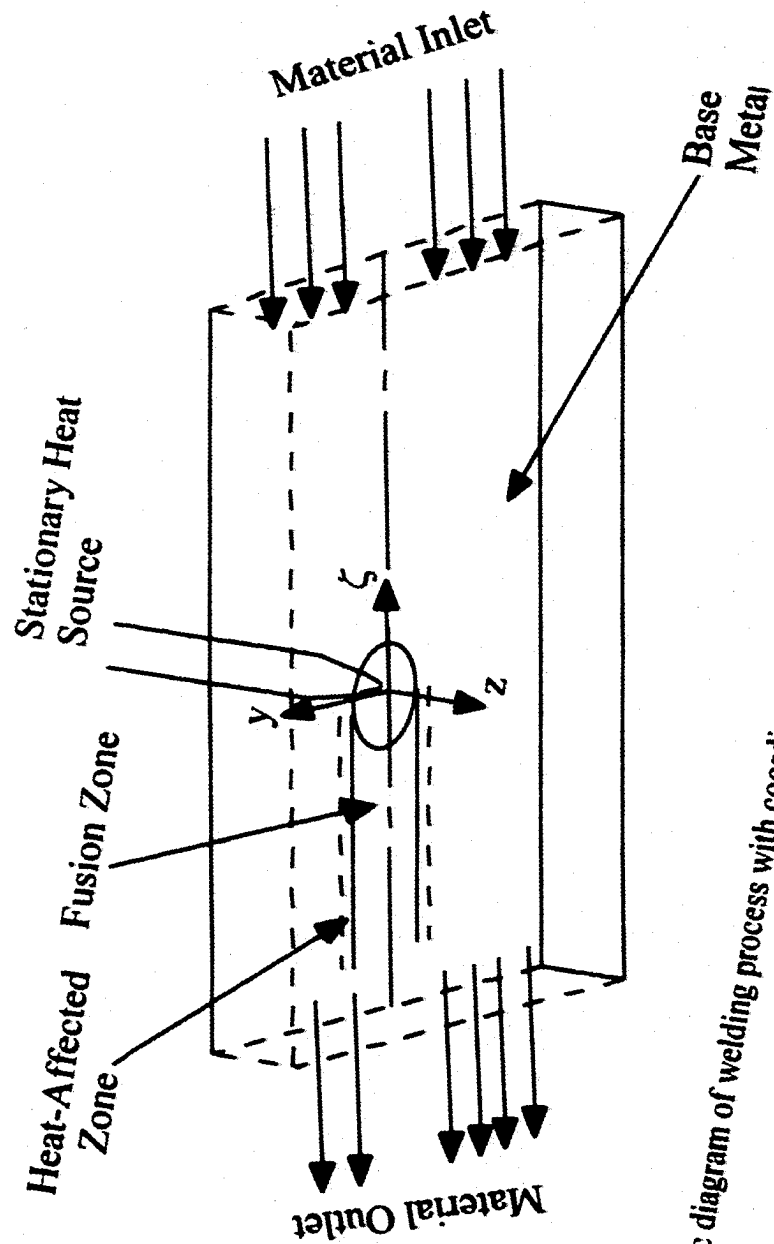


Figure 5.1. Schematic diagram of welding process with coordinate system attached to the heat source.

under it are fixed in space, and the material enters and leaves the computational domain at the welding velocity.^{24,25} The governing equations for the conservation of mass, momentum, energy, and the nitrogen concentration in the weld pool are formulated for a coordinate system (ζ, y, z, t) attached to the moving heat source.²⁶ Under these conditions, the problem becomes steady state in a short period of time after the start of welding, thus making the solution much easier by decreasing computation time and the number of grids required significantly.

5.2.1.1 Momentum Equation in Moving Coordinate System (ζ, y, z)

Given the moving heat source and the coordinate system used here, there are several velocity components to be taken into account. Specifically, there is both a convective velocity and the velocity of the moving heat source. In order to treat the convective velocity as the primary unknown in the governing equations, the net velocity (V') is defined with respect to the frame attached to the heat source and is expressed in the following relationship:

$$V' = V + U \quad (5.1)$$

where the V is the convective velocity term and U is the welding velocity. Using Equation (5.1), the steady state versions of the modified governing equations can be derived with V as the primary unknown velocity. Based on this formulation, the final forms of the equations are shown below. The continuity equation is shown in Equation (5.2):

$$\nabla \cdot (\rho V) = 0 \quad (5.2)$$

where ρ is the density.

The general momentum equation is shown in the following equation:

$$\frac{\partial}{\partial t} (\rho V) + \nabla \cdot (\rho V V) = -\nabla P + \mu \nabla \cdot (\nabla V) + S + S_{e-p} - \nabla \cdot (\rho U V) \quad (5.3)$$

where t is the time, μ is the viscosity, P is the effective pressure, S is the source term, which takes into account both the buoyancy (F_b) and electromagnetic forces (F_e), S_{e-p} is the source term which modifies the momentum equation in the mushy zone, and U , V , and V' are velocity components described above..

Each component of the source term present in Equation (5.3) is defined individually. First, the buoyancy force, F_b , is the natural convection effect and is defined in the following equation:

$$F_b = \rho g \beta (T - T_{ref}) \quad (5.4)$$

where ρ is the density, g is the acceleration due to gravity, β is the thermal expansion coefficient, and T_{ref} is an arbitrarily defined temperature. The force due to Marangoni convection is introduced in the form of boundary conditions for the u and v momentum equations and is discussed in a subsequent section.

Since an electric arc is used as the power source, electromagnetically driven flow is caused by the interaction between the divergent current path in the weld pool and the magnetic field. The interaction between the divergent current path in the weld pool and the magnetic field it creates gives rise to electromagnetically driven flow in the pool.^{2,27} The electromagnetic force, F_e , is given by the following relationship:

$$F_e = J \times B \quad (5.5)$$

where J is the current density vector and B is the magnetic flux vector. The electromagnetic field in the workpiece is defined by the steady-state version of Maxwell's equations using the MHD approximation.^{2,26-27} The definitions for J and B are defined below:

$$J = \sigma_e E \quad (5.6)$$

$$\mathbf{B} = \mu_m \mathbf{H} \quad (5.7)$$

where σ_e is the electrical conductivity, \mathbf{E} is the electric field vector, \mathbf{H} is the magnetic field vector, and μ_m is the magnetic permeability. Since the heat source is considered axisymmetric, the electromagnetic force is incorporated as part of the source term, S , defined in the governing equation for the conservation of momentum.

5.2.1.2 Energy Equation

When solving for the conservation of energy during the arc welding process, the total enthalpy is considered rather than the temperature in order to account for phase changes in the material. The total enthalpy of the material, H , is shown in the following relationship:

$$H = h + \Delta H \quad (5.8)$$

$$h = \int C_p dT \quad (5.9)$$

where h is the sensible heat, C_p is the specific heat, and ΔH is the latent heat content. Both the total and sensible enthalpy are assumed to vary linearly with the temperature. Figure 5.2 shows the calculated linear relationship between the temperature and the enthalpy. In this figure, T_s is the solidus temperature and T_l is the liquidus temperature. The latent heat content, $\Delta H = F(T)$, is assumed to vary linearly with temperature.^{26,28}

$$F(T) = L \quad T > T_l \quad (5.10)$$

$$F(T) = L \left(\frac{T - T_s}{T_l - T_s} \right) \quad T_s \leq T \leq T_l \quad (5.11)$$

$$F(T) = 0 \quad T < T_s \quad (5.12)$$

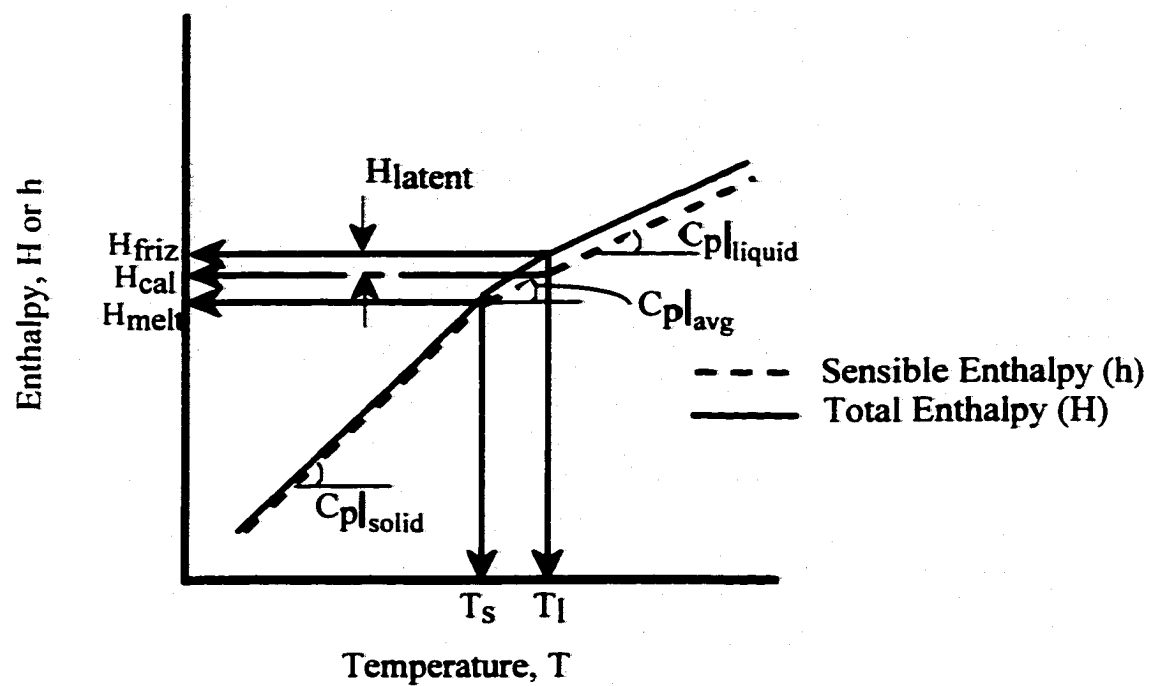


Figure 5.2. Summary of enthalpy-temperature relationship used in the calculations for heat transfer and fluid flow.

Based on this relationship for the total enthalpy, the conservation of energy equation is thus given by the following relationship:

$$\begin{aligned} \frac{\partial}{\partial t}(\rho h) + \nabla \cdot (\rho V h) = \nabla \cdot \left(\frac{k}{C_p} \nabla h \right) - \nabla \cdot (\rho V \Delta H) - \nabla \cdot (\rho U \Delta H) \\ - \nabla \cdot (\rho U h) - \frac{\partial}{\partial t}(\rho \Delta H) + S \end{aligned} \quad (5.13)$$

where k is the thermal conductivity and S is the source term. The source term accounts for the latent heat of melting and the convective transport of latent heat in the two-phase region or mushy zone and is further defined by the following relationship:

$$S = -[\nabla \cdot (\rho V \Delta H) + \nabla \cdot (\rho U \Delta H)] \quad (5.14)$$

where the last term in this equation, $\nabla \cdot (\rho U \Delta H)$, represents the latent heat exchange due to the phase change occurring at the pool boundaries due to the movement of the heat source. Since pure iron is being considered here, there is no two-phase region or mushy zone present mushy. The fraction liquid to be considered is either zero or one, and the liquidus and solidus temperatures are the same.

5.2.1.3 Conservation of Nitrogen Equations

Nitrogen is introduced into the weldment through the absorption of monatomic nitrogen from the plasma phase present into the weld pool surface. It is then transported to the weld pool interior through both convective and diffusive processes and can potentially diffuse into the base metal. The conservation of the nitrogen concentration in the weld metal is defined by the following relation:²¹

$$\frac{\partial}{\partial t}(\rho C) + \nabla \cdot (\rho V C) = \nabla \cdot (\rho D \nabla C) - \nabla \cdot (\rho U C) \quad (5.15)$$

where C is the nitrogen concentration and D is the nitrogen diffusion coefficient in iron.

The diffusion coefficient for nitrogen diffusion in both the solid (α , γ , and δ) and liquid iron phases is defined in the following relationship.

$$D = D_0 e^{\left(\frac{E_0}{RT}\right)} \quad (5.16)$$

where D_0 is the diffusivity of nitrogen (cm^2/sec), E_0 is the activation energy for diffusion (cal/mol), R is the ideal gas constant (1.987 cal/mol-K), and T is the temperature (K). The diffusion coefficient depends primarily on temperature, and the values for D_0 and E_0 , shown in Table 5.1, vary for each iron phase.³⁰⁻³⁴

Several studies have been performed on the diffusion of iron in solid iron phases. From these studies, empirical relationships describing the diffusion behavior in the solid iron phase have been developed. For example, the following empirical relationship describes the diffusion coefficient for nitrogen in bcc iron.³⁰

$$\ln D = -0.861 \left(\frac{10^4}{T} \right) - 16.763 \quad (5.17)$$

where D is the diffusion coefficient (cm^2/sec) and T is the temperature (K).

Nitrogen diffusion occurs within the liquid weld pool, across the interface between the weld pool and the solid base metal, and throughout the solid base metal. There is a significant difference in the nitrogen diffusion behavior in liquid and solid iron phases. Diffusion coefficients for nitrogen in solid iron are many orders of magnitude less than that for nitrogen in liquid iron, which is typically assumed to be constant and not dependent on temperature.^{33,34} As the temperature is further decreased, the nitrogen diffusion coefficient in solid iron significantly decreases. In this model, nitrogen diffusion within the base metal over the time frame of welding is assumed to be negligible, except between the liquid iron and the base metal adjacent to the weld pool, which is primarily composed of δ -Fe. Therefore, the nitrogen diffusion coefficient is not

Table 5.1. Summary of nitrogen diffusion constants in α , γ , δ , and liquid iron phases.³³⁻³⁴

Iron Phase	Temperature Range (K)	D (cm²/sec)	D₀ (cm²/sec)	E (kcal/mol)	Reference
α	273 - 1184	---	7.80×10^{-3}	18.9	33
γ	1185 - 1662	---	0.91	40.26	33
δ	1663 - 1810	---	7.80×10^{-3}	18.9	33
Liquid	> 1811	0.00011	---	---	33,34

allowed to go any lower than a value of $2.666 \times 10^{-5} \text{ cm}^2/\text{sec}$, which is the equivalent of the nitrogen diffusion coefficient in $\delta\text{-Fe}$ at the $\delta - \gamma$ transition.

5.2.1.4 Effects of Turbulence in the Weld Pool

The equations described above are based on the assumption of laminar flow in the weld pool. On the other hand, presence of turbulence in the fluid flow within the weld pool can provide a significant enhancement to the mass transport properties. For example, the role of turbulence in enhancing the heat transfer in the weld pool has been examined by previous researchers.³⁵ Elements of the K- ϵ model for the calculation of turbulent fluid flow and heat transfer in the weld pool are also included in this model to calculate the turbulent fluid flow and heat transfer. The effects of turbulence on the fluid flow and heat transfer in the weld pool have been included in this model through the use of effective viscosity and thermal conductivity values. The effective viscosity and thermal conductivity are expressed in the following relations.

$$\mu_{\text{eff}} = \mu_t + \mu \quad (5.18)$$

$$k_{\text{eff}} = k_t + k \quad (5.19)$$

where μ_{eff} and k_{eff} are the effective viscosity and thermal conductivity, respectively, μ_t and k_t are the turbulence values, and μ and k are the molecular values.

$$\mu_t = \frac{C_\eta \rho K^2}{\epsilon} \quad (5.20)$$

where C_η is an empirical constant, K is the turbulent kinetic energy, and ϵ is the dissipation rate of turbulent kinetic energy. In this case, the value for turbulent viscosity is defined by the application of an enhancement factor to the value for the molecular viscosity (μ).

The turbulent thermal conductivity is related to the turbulent viscosity by the turbulent Prandtl number, Pr_t .

$$Pr_t = \frac{C_p \mu_t}{k_t} = 0.9 \quad (5.21)$$

To simulate turbulent conditions in the weld pool, the value of the Prandtl number is set equal to 0.9. Based on this relationship, the value for the turbulent thermal conductivity is determined. Table 5.2 includes these turbulent values along with the other thermophysical properties used in these calculations.

Similarly, the effect of turbulence in the weld pool on the transport of nitrogen in the weld pool is also considered. Turbulence in the weld pool is considered here to further enhance the mixing and transport of nitrogen in the weld pool. Previous studies have shown that the enhancement caused by turbulence can be taken into account by applying an enhancement factor to the thermophysical properties. A similar concept has not been applied to mass transport in the weld pool. Therefore, an enhancement factor has been applied to the diffusion coefficient of nitrogen in liquid iron.

5.2.2 Solution Procedure

A control-volume-based computational method developed elsewhere²⁶ has been used here to solve the governing equations defined above. In the solution scheme, these governing equations are represented in a finite difference form and solved iteratively on a line-by-line basis utilizing a Tri-Diagonal Matrix Algorithm (TDMA). The Semi-Implicit Method for Pressure-Linked Equations (SIMPLE) algorithm has been employed for the discretization of the equations. COMPACT-3D, available from Innovative Research, Inc., has been used to solve these governing equations. It is a general-purpose program for the calculation of fluid flow, heat and mass transfer, chemical reaction, turbulence, and related processes in three-dimensional situations. In order to solve for each of these different flow conditions, the program utilizes the solution of a general equation, which is shown below:³⁶

$$\frac{\partial}{\partial t}(\rho\phi) + \frac{\partial}{\partial x_i}(\rho u_i \phi) = \frac{\partial}{\partial x_i} \left(\Gamma \frac{\partial \phi}{\partial x_i} \right) + S \quad (5.22)$$

where ρ is the density, ϕ is the dependent variable to be solved, Γ is considered the diffusion coefficient, and S is the source term. The general equation contains basically four terms: the unsteady term, the convection term, the diffusion term, and the source term. The dependent variable can stand for a variety of physical quantities, and the choice of ϕ gives appropriate meaning to both Γ and S . In order to solve specific situations, such as heat transfer and fluid flow in the weld pool, a separate adaptation scheme has been developed.

In the development of the governing equations tailored for this adaptation, the value of Γ can be defined for conservation of momentum, energy, and nitrogen concentration, respectively, using the following equations:

$$\Gamma = \nu \quad \text{for transport of momentum} \quad (5.23)$$

$$\Gamma = \frac{K}{C_p} \quad \text{for transport of heat} \quad (5.24)$$

$$\Gamma = \rho D \quad \text{for transport of nitrogen concentration} \quad (5.25)$$

where ν is the viscosity of the liquid metal, K is the thermal conductivity, C_p is the specific heat, ρ is the density, and D is the diffusivity.

In the solution procedure, the solution of the governing equations for momentum and energy are decoupled from the solution of the equation of conservation of nitrogen concentration. During arc welding, the weld pool geometry reaches steady-state conditions in a very short time after the start of welding. This condition allows the transient terms from the governing equations to be removed and the steady state versions of the governing equations for conservation of mass, momentum, and energy to be solved. Without

any time dependence for the solution of the temperature and velocity in the weld pool, a great deal of computational effort is saved. On the other hand, the nitrogen concentration calculations are time dependent. Therefore, the fully transient, three-dimensional form of the governing equation for the conservation of nitrogen concentration is solved separately from the steady state temperature and velocity fields. The residual nitrogen concentration in each weld line is determined by summing the mass of nitrogen across the weld pool cross section at the point in time at which the weld line is solidified.

In order to solve for these specific conditions, the thermophysical properties for pure iron are placed in the adaptation routine to be solved by COMPACT 3-D. Table 5.2 lists the thermophysical properties used in these calculations.^{34,37-39} The values shown in this table have been taken from a number of standard references for pure liquid and solid iron phases and form the basis for the ensuing calculations.

5.2.3 Grid Generation

The grid system used in this model is based on the equations given below, which are described in one dimension but can be applied in all three dimensions. Figure 5.3 shows a schematic diagram of the components of the grid system used here. Locations for the solution of scalar quantities, defined by ϕ in the Equation (5.18), and the velocity components are specifically defined in the figure. These velocity components are solved at the center of each control volume, defined by the locations of the solution of the scalar quantities at each corner.

The equations below, in which $XU(I)$ is the location of the u-velocity component in the x direction, describe the grid system shown in Figure 5.3 in one dimension.³⁶

$$XU(I) = XL \left(\frac{I-2}{L-2} \right)^n \quad \text{if } n > 0 \quad (5.26)$$

$$XU(I) = XL \left(1 - \left(1 - \frac{I-2}{L-2} \right)^{-n} \right) \quad \text{if } n \leq 0 \quad (5.27)$$

Table 5.2. Summary of the thermophysical properties used in the calculations described here.^{33,37-39}

Material Property	Value	References
Density of Liquid Metal (gm/cm ³)	7.20	33
Liquidus Temperature (K)	1811	33
Solidus Temperature (K)	1811	33
Viscosity of Liquid (gm/cm-sec)	0.06	37
Thermal Conductivity of Solid Iron (cal/cm-sec-K)	-0.05	37
Thermal Conductivity of Liquid Iron (cal/cm-sec-K)	0.2	37
Specific Heat of Solid Iron (cal/gm-K)	0.168	33
Specific Heat of Liquid Iron (cal/gm-K)	0.193	37
Enthalpy of Solid Iron at Melting Point (cal/gm)	250.76	38
Enthalpy of Liquid Iron at Melting Point (cal/gm)	314.76	38
Temperature Coefficient of Surface Tension (dynes/cm-K)	-0.43	39
Coefficient of Thermal Expansion (1/K)	1×10^{-5}	37

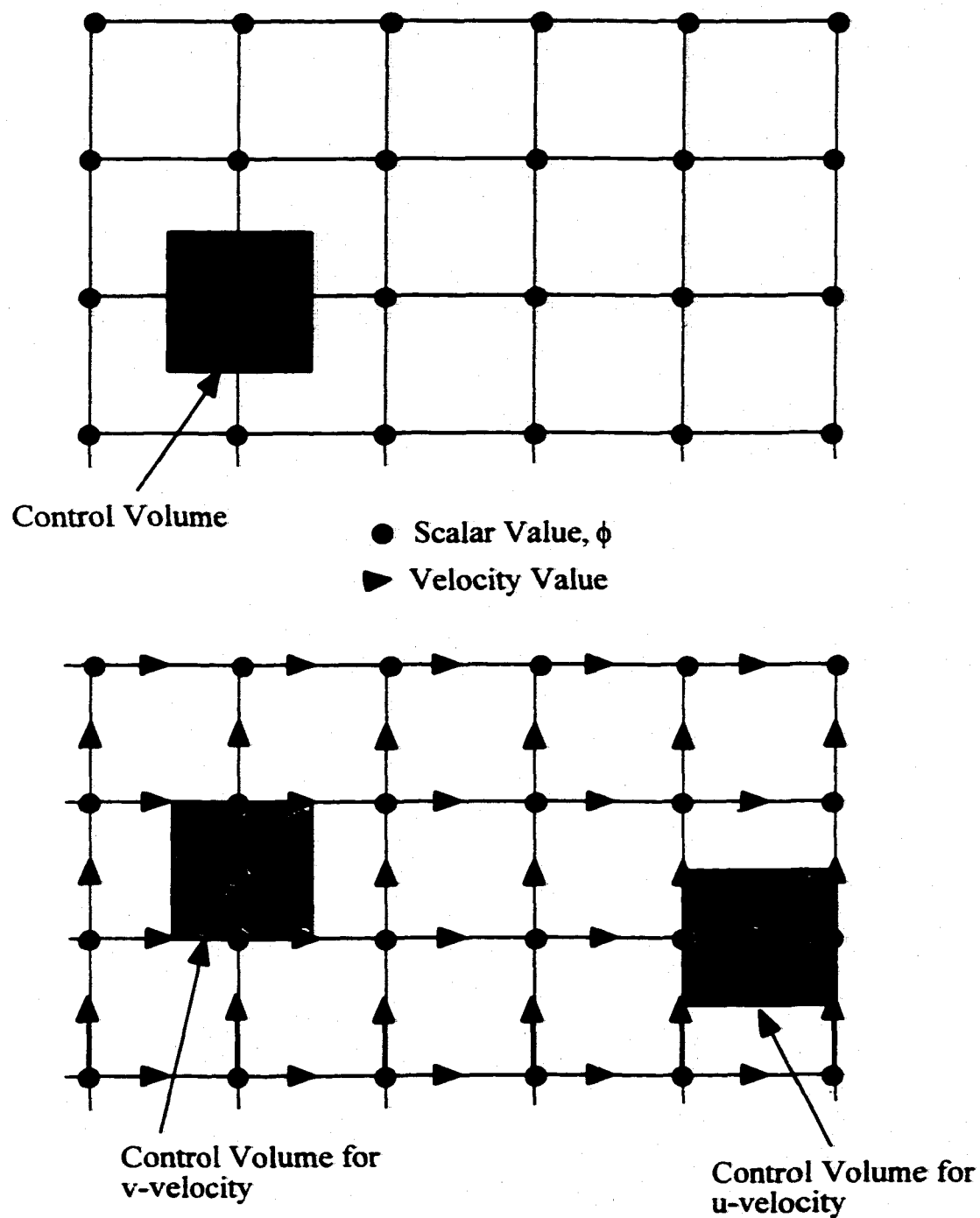


Figure 5.3. Schematic diagram of grid scheme used in these calculations.

where XL is the domain length in the x direction, $L1$ is the number of grid points, $(L1-2)$ is the number of control volumes, and n is an exponent.

A non-uniform grid has been used in this calculation scheme to account for the large temperature gradients commonly present in welding operations. When the exponent, n , is positive, the grid is finer near the left boundary and progressively coarser toward the right boundary, where it is nearly uniform. For a negative exponent, n , the opposite is the case. The same methodology applies in both the y and z directions in the Cartesian coordinate system used here. This grid system has dimensions of 96 grids in the x direction, 25 grids in the y direction, and 26 grids in the z direction. Using this grid system, the enthalpies, velocities, and the nitrogen concentration are solved. Since such a large number of grids are used here and are of inconsistent uniformity, the grid system is divided into zones, 16 in the x direction along the direction of scanning, 6 in the y direction, and 6 in the z direction. This grid system allows for finer grids to be used in the region under the heat source and to become coarser in other regions.

5.2.4 Boundary Conditions

Boundary conditions for the solution of the equations of conservation of mass, momentum, energy, and nitrogen concentration are defined primarily along the plane of symmetry and the top surface. Since the steady state temperature and velocity fields in the weld pool are solved prior to the time dependent nitrogen concentrations, different sets of boundary conditions are thus required for each solution set. The boundary conditions for the solution of the equations for the conservation of mass, momentum, and energy are shown in Figure 5.4. In this figure, the $y = 0$ plane represents a plane of symmetry which runs longitudinally along the center of the weld line. This choice of geometry allows these equations to be solved for only half the workpiece, thus saving significant computational time and effort.

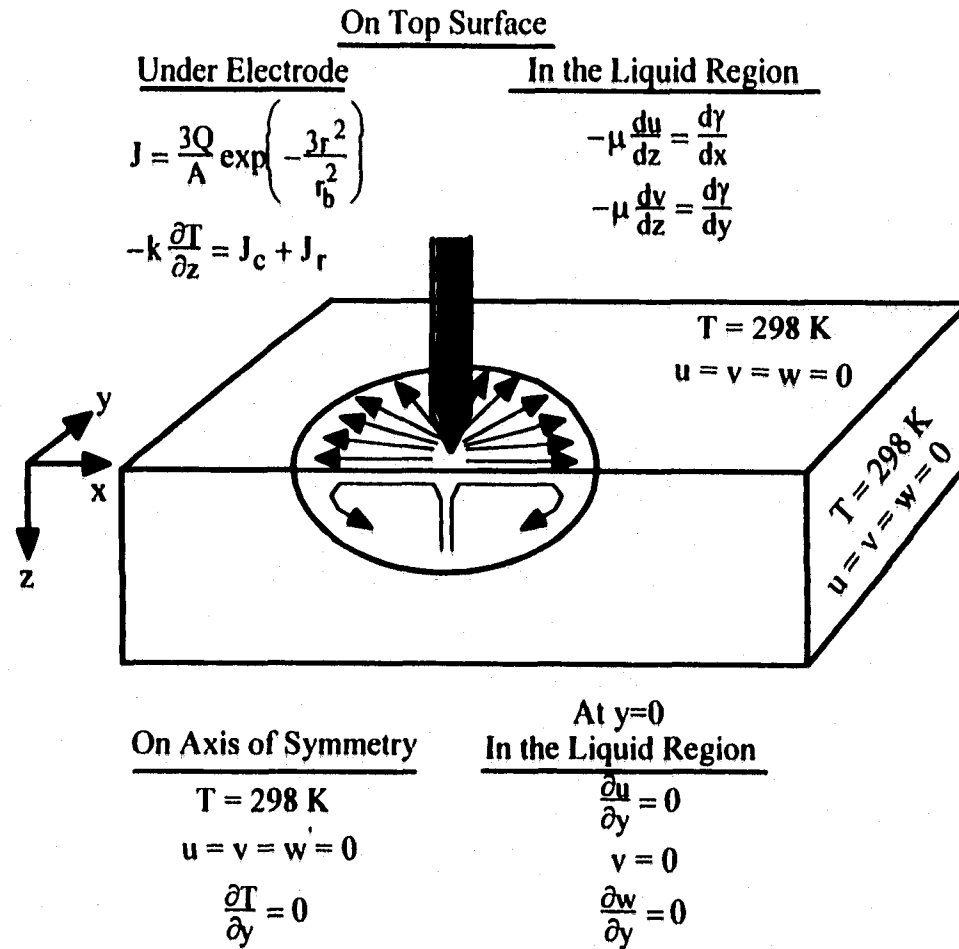


Figure 5.4. Summary of boundary conditions used in the mathematical model for solution of heat transfer and fluid flow in the weldment.

5.2.4.1 Momentum Equations

The initial and boundary conditions for the entire geometry are shown in Figure 5.4. In the solid portion of the weldment, all velocities, u , v , and w are set equal to zero, and the initial temperature is set at 298 K. In the liquid region of the weldment, the boundary conditions are further refined, especially at the top surface and along the axis of symmetry. The weld pool surface defined by this top surface is first considered to be flat, and the flow of liquid out of the face is not permitted. Boundary conditions along the plane of symmetry are defined by a zero flux of the u and w components of velocity, shown in Equations (5.24) and (5.25), as well as a v component of velocity set equal to zero.

$$\frac{\partial u}{\partial y} = 0 \quad (5.28)$$

$$\frac{\partial w}{\partial y} = 0 \quad (5.29)$$

Fluid flow in the weld pool is primarily driven by the surface tension on the weld pool surface, which is characterized by large temperature gradients. A shear stress, also known as a Marangoni stress, is produced as a result of this temperature variation on the weld pool surface,^{1,2} and is defined by an effective tangential stress, τ , in the following relationship:

$$\tau = \left(\frac{d\gamma}{dT} \right) \nabla T \quad (5.30)$$

where γ is the surface tension, $\left(\frac{d\gamma}{dT} \right)$ is the temperature coefficient of surface tension, and ∇T is the temperature gradient.

Similar conditions are assumed at the top surface, ($z = 0$). Specifically, the flux of the u and v velocity components are defined in the following relationships:

$$-\mu \frac{du}{dz} = \frac{d\gamma}{dx} \quad (5.31)$$

$$-\mu \frac{dv}{dz} = \frac{d\gamma}{dy} \quad (5.32)$$

where μ is the viscosity and γ is the surface tension of the liquid iron. The z-component of velocity, w , at this location is also defined to be zero.

5.2.4.2 Energy Equation

In the gas tungsten arc (GTA) welding process, energy is supplied by the electrode and transferred to the weld metal over a rather short distance. Boundary conditions for the solution of the equation of conservation of energy are shown along with those for the conservation of momentum in Figure 5.4. In this figure, heat transfer from the arc to the weld metal is assumed to be Gaussian in nature. The energy flux from the arc to the weld metal is prescribed on the top surface by the following relationship:

$$J_h(\zeta, y, z)_{z=0} = \frac{3Q\eta}{\pi r_b^2} e^{-\left[\frac{3(\zeta^2 + y^2)}{r_b^2} \right]} \quad (5.33)$$

where Q is the power input, which is the product of current and voltage, η is the process efficiency or the percentage of energy absorbed during GTA welding, r_b is the arc radius, and ζ and y are the distances in the welding and the width direction, respectively, from the origin of the arc in the coordinate system attached to the heat source.

Knowledge of the process efficiency is an important consideration in the calculation of heat transfer and fluid flow in the weld pool. During arc welding, there is an imperfect transfer of energy from the electrode to the weld pool surface. Previous studies have investigated the efficiency of various welding processes using calorimetry.⁴⁰ In general,

the maximum efficiency of the GTA welding process has been measured to be approximately 80%. In this case, near optimal conditions are assumed, and the process efficiency is set at a value of 75%.

As discussed in a previous section, the equation for the conservation of energy is solved in terms of enthalpy rather than temperature. When discussing the boundary conditions for the solution of the energy equation, though, it is much easier to use temperature rather than enthalpy. During the solution, these temperatures can be easily converted to enthalpies. On the sample surfaces, the temperature is initially set at 298 K, and is maintained at this level at the surfaces far from the heat source. Heat transfer in the liquid metal portion of the weldment on the top surface is defined by the following relationship:

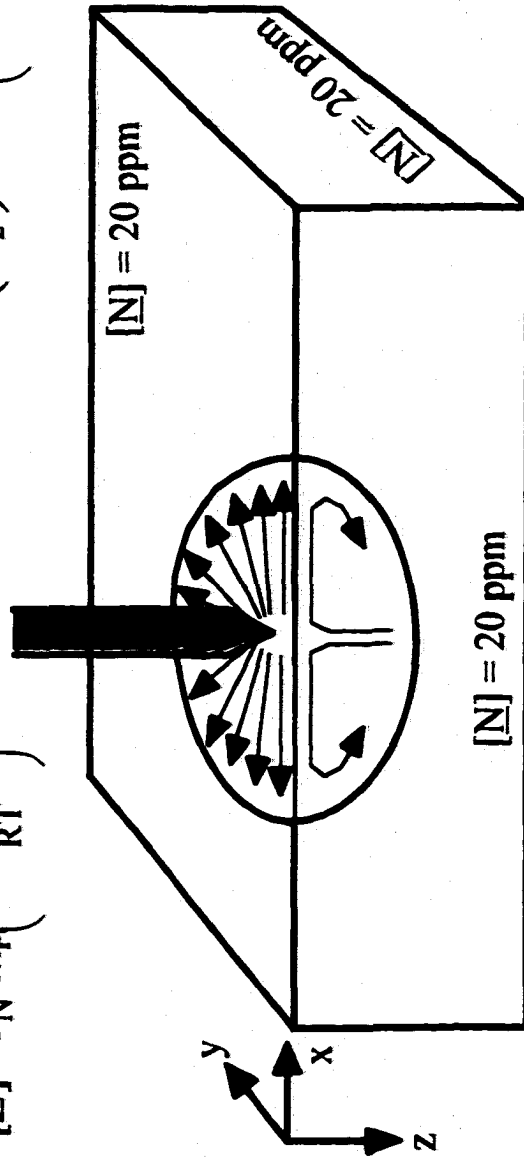
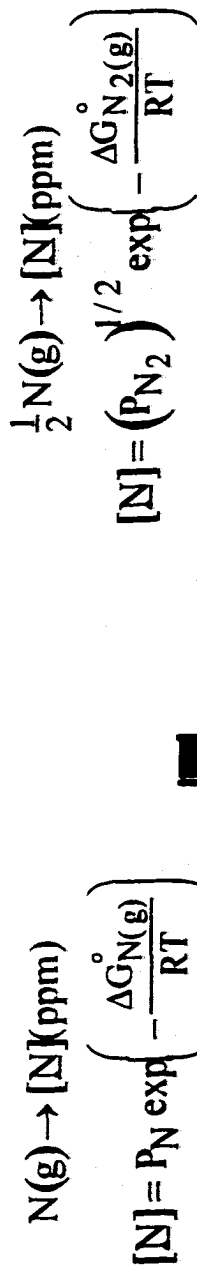
$$-k \frac{\partial T}{\partial z} = J_c + J_r \quad (5.34)$$

where k is the thermal conductivity, J_c is the conductive heat loss, and J_r is the radiative heat loss. On the axis of symmetry, the temperature gradient is set to zero, as shown in the following relationship.

$$\frac{dT}{dy} = 0 \quad (5.35)$$

5.2.4.3 Conservation of Nitrogen Concentration

Initial and boundary conditions used in the solution of the equation of the conservation of nitrogen concentration are summarized in Figure 5.5. An initial nitrogen concentration of 20 ppm, which is the initial nitrogen concentration in the base metal used in the experiments, is assumed on each face and throughout the weldment. Nitrogen is introduced into the weldment only at the top surface and, specifically, in the liquid weld metal underneath the heat source. In this location, the resulting nitrogen concentration in the liquid metal is based on the absorption of monatomic nitrogen at the calculated surface



On Plane of Symmetry ($y=0$ plane)

$$\frac{dc}{dy} = 0$$

Figure 5.5. Summary of boundary conditions used in the mathematical model for solution of nitrogen concentration distribution in the weldment.

temperatures. The relationships shown below define both the prevalent reaction and the relation used to solve for the nitrogen concentration in the weld pool at this location.



$$[\text{N}] = P_{\text{N}} \exp\left(-\frac{\Delta G_{\text{N(g)}}^{\circ}}{RT}\right) \quad (5.37)$$

where $[\text{N}]$ is the nitrogen concentration, P_{N} (atm.) is the monatomic nitrogen partial pressure, $\Delta G_{\text{N(g)}}^{\circ}$ (cal/mol) is the free energy relationship for the reaction in Equation (5.36), T (K) is the temperature, and R is the ideal gas constant (1.987 cal/mol-K).⁴¹⁻⁴⁵ Table 5.3 lists the free energy relationships for the nitrogen absorption reactions. The monatomic nitrogen partial pressure used here is defined by the electron temperature distribution above the weld pool and calculated using the methodology presented in Chapter 3.

In the region outside the arc column, diatomic nitrogen species are the dominant players in the nitrogen absorption reaction and the nitrogen dissociation reaction is minimal. Therefore, the following relations define both the reaction for the absorption of diatomic nitrogen on the solid iron surface and the relation used to calculate the nitrogen concentration here:



$$[\text{N}] = (P_{\text{N}_2})^{1/2} \exp\left(-\frac{\Delta G_{\text{N}_2(\text{g})}^{\circ}}{RT}\right) \quad (5.39)$$

where P_{N_2} is the diatomic nitrogen partial pressure (atm), $\Delta G_{\text{N}_2(\text{g})}^{\circ}$ (cal/mol) is the free energy relationship for the reaction in (5.38), which is shown in Table 5.3. In this region, the diatomic nitrogen partial pressure outside the arc column is determined using the re-

Table 5.3. Summary of free energies used in nitrogen absorption reactions. ^{17,41-43,45}

Reaction	Phase	Free Energy (cal/mol)	Temperature Range (K)	Reference
$\frac{1}{2} \text{N}_2(\text{g}) \rightarrow \text{N}(\text{g})$	Gas	$86596.0 - 15.659 T$	273 - 1811	42
$\text{N}(\text{g}) \rightarrow \underline{\text{N}}(\text{wt.}\%)$	Liquid	$-85736.0 + 21.405 T$	>1811	41,42,45
$\text{N}(\text{g}) \rightarrow \underline{\text{N}}(\text{wt.}\%)$	Solid - δ	$-83476.4 + 17.689 T$	1663 - 1810	42,43
$\text{N}(\text{g}) \rightarrow \underline{\text{N}}(\text{wt.}\%)$	Solid - γ	$-84536.0 + 24.599 T$	1185 - 1662	42,45
$\text{N}(\text{g}) \rightarrow \underline{\text{N}}(\text{wt.}\%)$	Solid - α	$-83476.4 + 17.689 T$	273 - 1184	42,43
$\frac{1}{2} \text{N}_2(\text{g}) \rightarrow \underline{\text{N}}(\text{wt.}\%)$	Liquid	$860.0 + 5.71 T$	>1811	42,45
$\frac{1}{2} \text{N}_2(\text{g}) \rightarrow \underline{\text{N}}(\text{wt.}\%)$	Solid - δ	$3119.6 + 2.03 T$	1663 - 1810	42,43
$\frac{1}{2} \text{N}_2(\text{g}) \rightarrow \underline{\text{N}}(\text{wt.}\%)$	Solid - γ	$-2060 + 8.94 T$	1185 - 1662	17,42
$\frac{1}{2} \text{N}_2(\text{g}) \rightarrow \underline{\text{N}}(\text{wt.}\%)$	Solid - α	$3119.6 + 2.03 T$	273 - 1184	42,43

lation for the thermal dissociation of the diatomic nitrogen. Both the dissociation reaction and the relation used to solve for the diatomic nitrogen partial pressure are defined below:



$$P_{\text{N}_2} = \left(\frac{P_{\text{N}}}{\exp\left(\frac{\Delta G^\circ}{RT}\right)} \right)^2 \quad (5.41)$$

where ΔG° is the free energy for the nitrogen dissociation reaction shown in Equation (5.35) and is further defined in Table 5.3.

Nitrogen concentrations calculated on the weld pool surface are not allowed to exceed a given saturation level.¹⁶⁻¹⁸ This value is defined by Sieverts' Law for the surface temperature and a nitrogen partial pressure of 1 atm. For example, the saturation level of nitrogen in liquid iron at a temperature of 1600°C and a total pressure of 1 atm is approximately 450 ppm. The absorbed nitrogen is then transported to the weld pool interior by convective and diffusive processes. Along the plane of symmetry, the nitrogen concentration gradient (dc/dy) is zero. Nitrogen concentrations at locations away from the sample surface and the weld pool are prescribed to be equal to the initial nitrogen concentration of the base metal ($[\text{N}] = 20 \text{ ppm}$).

5.3 RESULTS OF MODELING CALCULATIONS

5.3.1 Temperature and Velocity Calculations

The GTA welding of pure iron samples has been studied for the welding parameters summarized in Table 5.4. In this study, the effect of a change in the travel speed has been primarily studied. Table 5.4 also summarizes the key output data for each welding condition, ranging from the calculated weld pool dimensions to the peak temperature and the maximum fluid flow velocities. These values are based on the calculation of the steady-state temperature and velocity fields in the weld pool, and they display several key

Table 5.4. Summary of welding parameters and output data from these calculations.

	Condition #1	Condition #2
Arc Current (A)	150	150
Arc Voltage (V)	25	25
Travel Speed (cm/sec)	0.846	0.423
Process Efficiency (η)	80	80
Heat Input Rate (cal/sec)	285.5	285.5
Heat Output Rate (cal/sec)	-281.1	-285.5
Ratio (Heat In/Heat Out)	-0.9845	-0.9998
Peak Temperature (K)	2377	2551
Maximum Velocities (cm/sec)		
u_{MAX}	6.38	10.59
v_{MAX}	8.25	12.26
w_{MAX}	1.05	1.66
Weld Pool Depth (cm)	0.07742	0.1212
Weld Pool Width (cm)	0.7345	1.0223
Number of Grids	62400	62400

differences with changes in the welding parameters. For example, a decrease in the travel speed produces a weld pool both deeper and wider and containing higher temperatures and velocity fields than those observed at the more rapid travel speed.

Many of these values, though, cannot be verified by the accompanying experiments. On the other hand, the experimental weld pool width and depth can be easily compared with calculated results, as shown in Table 5.5. An aspect ratio, defined as the width to depth ratio, is computed for each condition and provides a measure of the general weld pool shape in each condition. In each case, the calculated weld pool dimensions generally correspond with those measured in the experimental pools. A comparison of the calculated and experimental aspect ratios show the weld pools to be similarly shaped, even though the calculated weld pools tend to be wider. An examination of the calculated weld pool cross sections provides an explanation.

Results of the steady state calculations for heat transfer and fluid flow in the weld pool are shown in three dimensions in Figures 5.6 and 5.7. Only half the weld pool, cut along the axis of symmetry, is shown in each figure. It is much easier to understand how the temperature and velocity fields determine the shape and size of the weld pool by analyzing these figures. Weld pool cross sections, showing both the calculated temperature and velocity fields for each set of welding parameters, are compared with the experimental cross sections in Figures 5.8(a&b) for each welding condition. In each case, the calculated temperature and velocity fields display similar characteristics, even though the values vary in magnitude, and are comparable with the respective experimental cross section. These temperature and velocity fields form the basis for calculating the resulting nitrogen concentrations in the weld pool and will be applied to the following calculations.

5.3.2 Electron Temperature and Monatomic Nitrogen Partial Pressure Calculations

As explained in previous chapters, nitrogen absorption during arc welding is characterized by a series of complex interactions between the plasma phase and the weld metal. For example, the nitrogen concentration on the weld pool surface is based, in part, on the amount of monatomic nitrogen present above the weld pool. Monatomic nitrogen is the

Table 5.5. Comparison between modeled and experimental weld pool dimensions.

	Width (cm)		Depth (cm)		$\frac{\text{Width}}{\text{Depth}}$	
	Experimental	Calculated	Experimental	Calculated	Experimental	Calculated
Condition #1	0.55	0.65	0.09	0.08	6.11	8.12
Condition #2	0.7	1.02	0.13	0.12	5.38	8.5

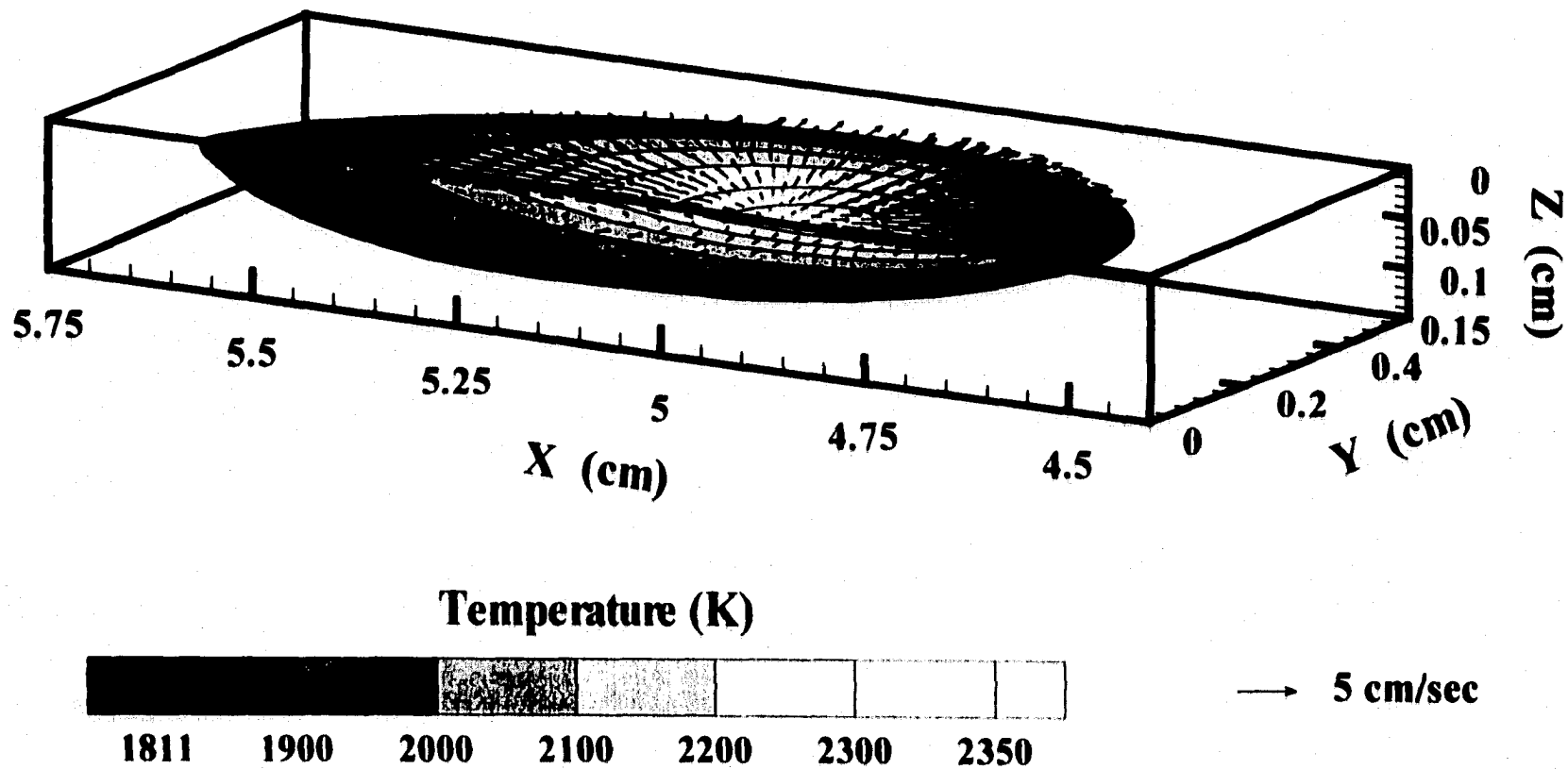


Figure 5.6. Three-dimensional diagram showing modeling results for both temperature and fluid flow fields in the weld pool for a travel speed of 0.847 cm/sec.

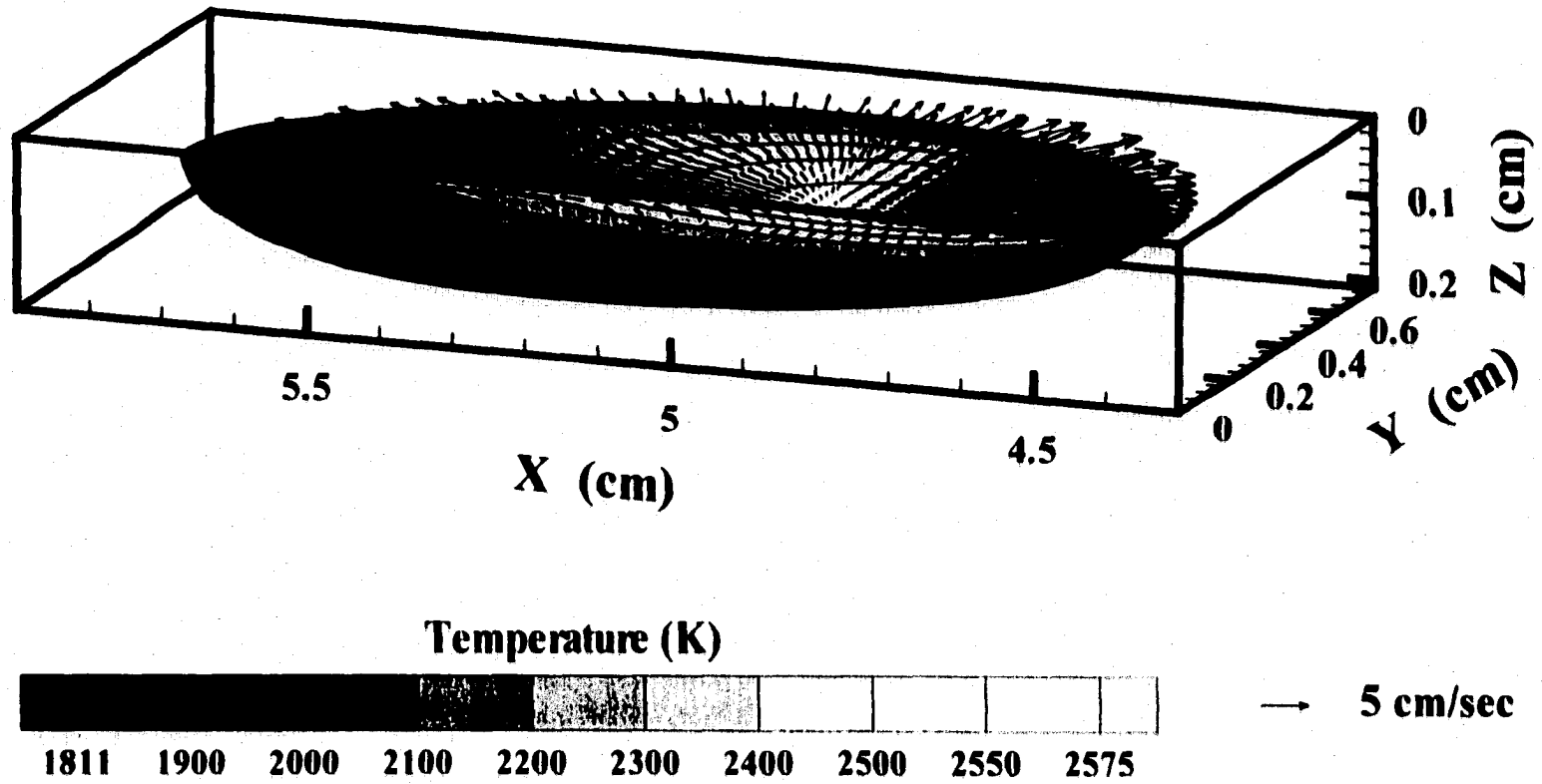
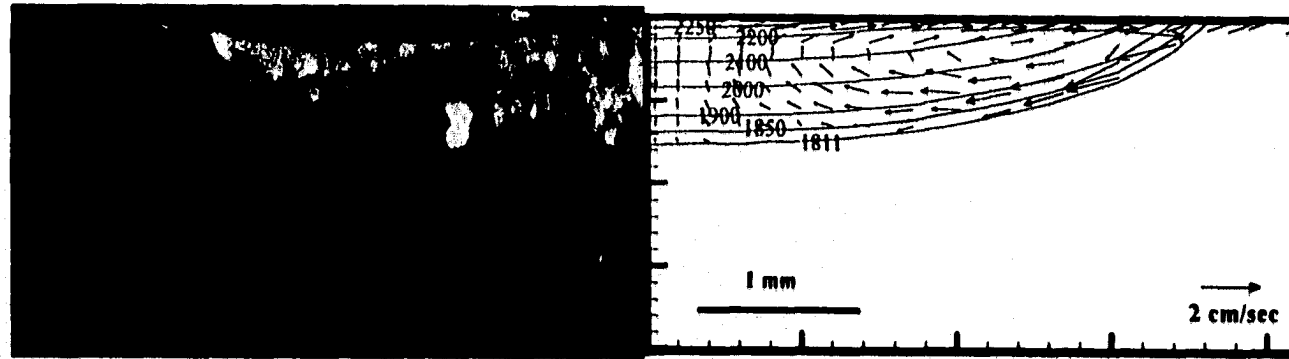
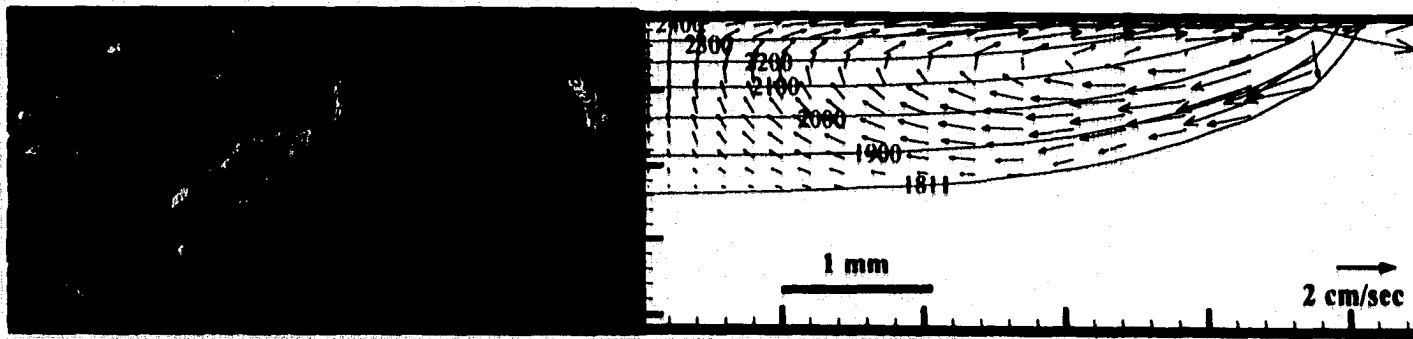


Figure 5.7. Three-dimensional diagram showing modeling results for both temperature and fluid flow fields in the weld pool for a travel speed of 0.423 cm/sec.



(a)



(b)

Figure 5.8(a&b). Comparison of calculated temperature and velocity fields along the cross section of the weld line with the corresponding experimental weld pool cross sections for a travel speed of (a) 0.847 cm/sec and (b) 0.423 cm/sec.

dominant species in the nitrogen dissolution reaction during arc welding^{11,14,16-18} and originates from the plasma phase in the arc column above the weld pool surface. The partial pressure of monatomic nitrogen above the weld pool is determined by the electron temperature distribution in this region. Therefore, the relationship between the electron temperature, the monatomic nitrogen partial pressure, and the nitrogen concentration on the sample surface is investigated here.

Previous researchers have both measured and calculated the electron temperatures present in the plasma phase at various locations in the arc column.⁴⁶⁻⁵² Temperatures in the plasma phase tend to range from approximately 3000 to 20000 K across the arc column, with higher temperatures near the electrode and lower temperatures near the weld pool surface. As the weld pool surface is approached, though, the characteristics of the plasma phase in the arc column significantly change, and a dark space, as shown in Figure 5.9(a), is observed directly adjacent to the weld pool surface. Whereas the plasma phase present in the arc column is assumed to be in local thermodynamic equilibrium (LTE), there are substantial deviations from LTE and significant temperature gradients across this dark space. Given these conditions and that the actual size of this boundary layer is unknown, straightforward approximations for this region are difficult.

Since the electrode acts as the cathode and the weld pool as the anode in the GTA welding arc, the dark space can be equated to an anode boundary region. This region has been previously modeled⁵³ and divided into different regions, as shown in Figure 5.9(b). The size of this entire layer, L , is assumed to be slightly larger than both the electron mean free path, λ_e , and the Debye length, λ_D , which is a measure of the sheath distance caused by the charge cloud surrounding the anode. In most cases, these distances equate to lengths on the order of tens to hundreds of microns. Such a small distance makes it is very difficult to measure or accurately calculate the electron temperature or the ensuing monatomic nitrogen partial pressure directly above the weld pool surface.

Temperatures within this boundary layer are expected to be significantly less than those found in the arc column and approach those on the weld pool surface. Monatomic nitrogen partial pressures have been calculated in a temperature range typical of that assumed to exist in this region and are shown in Figure 5.10 for several Ar-N₂ gas mixtures.

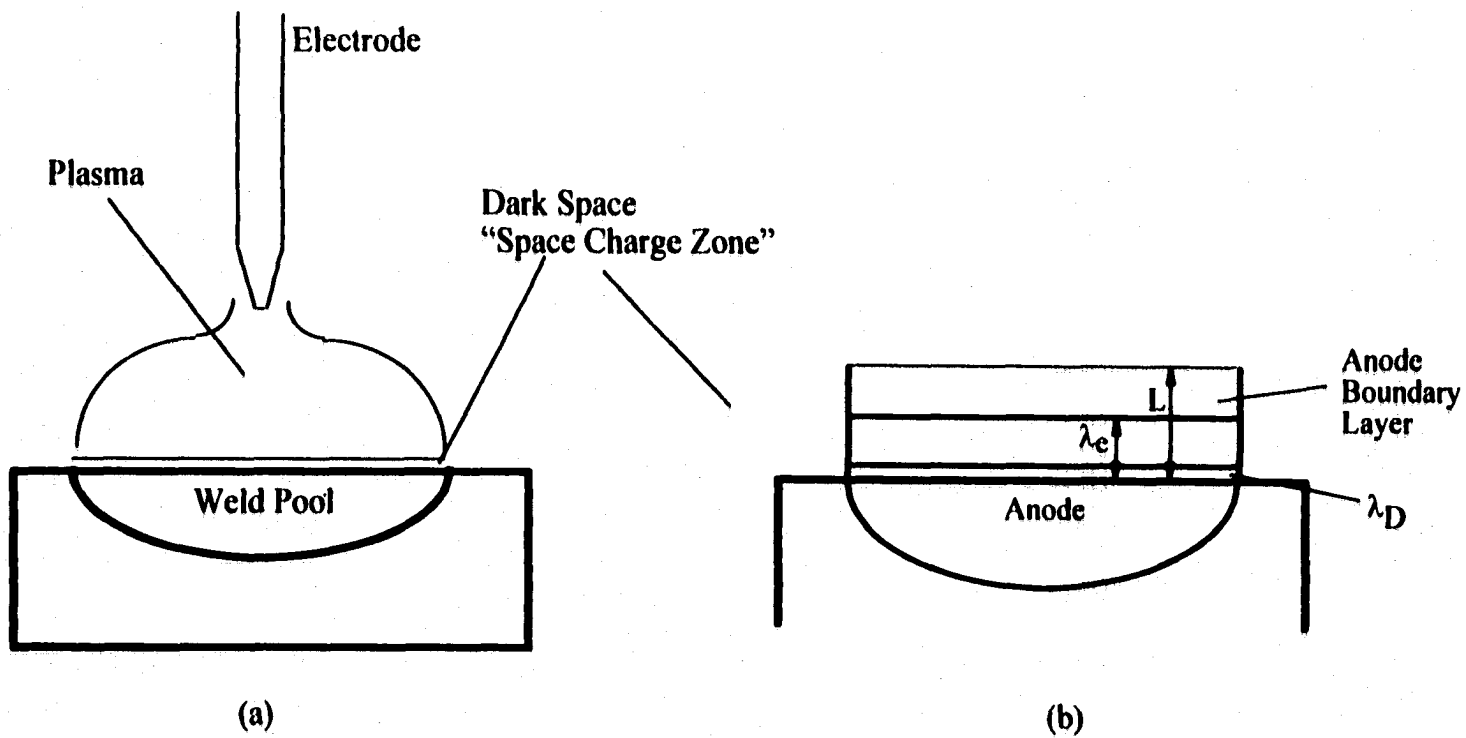


Figure 5.9(a&b). Schematic diagram showing the structure of the dark region between the equilibrium plasma phase in the arc column and the weld pool surface.⁵³

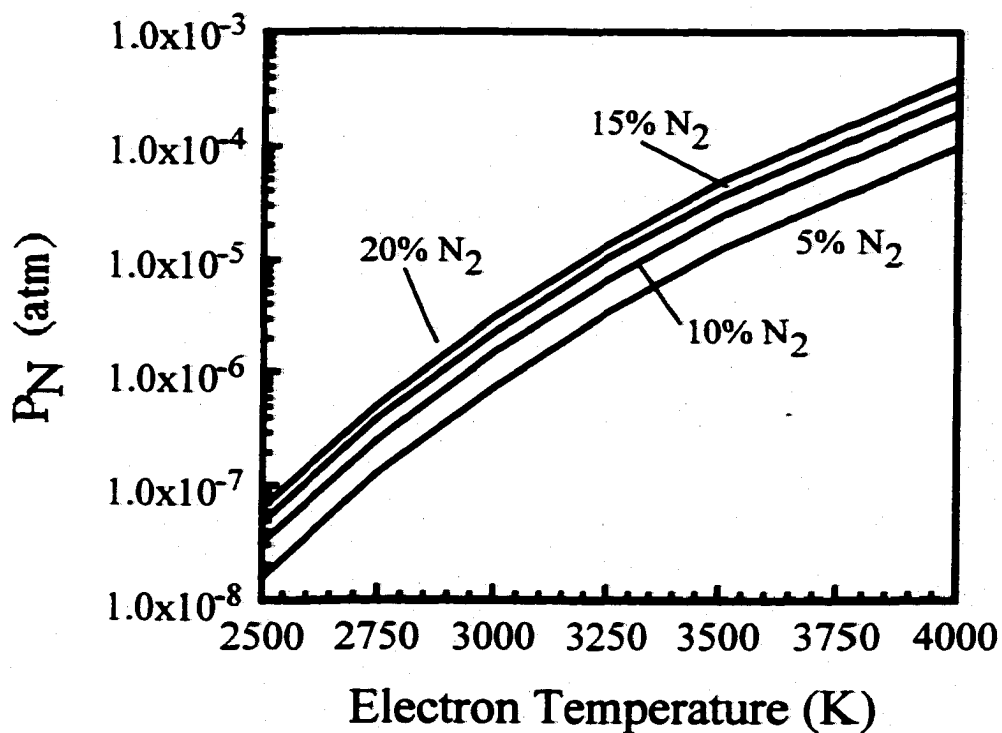


Figure 5.10. Graph showing dramatic changes in monatomic nitrogen partial pressures with rather small changes in the electron temperature. The electron temperature range shown in this figure matches those temperatures similar to those found in the anode boundary layer.

Even though only a narrow temperature range is shown here, monatomic nitrogen partial pressures vary by up to five orders of magnitude. Therefore, even a small variation in the temperature directly above the weld pool can significantly affect the amount of monatomic nitrogen available to take part in the nitrogen dissolution reaction. This significant variation in the monatomic nitrogen partial pressure makes the calculation of the nitrogen concentration on the weld pool surface even more difficult.

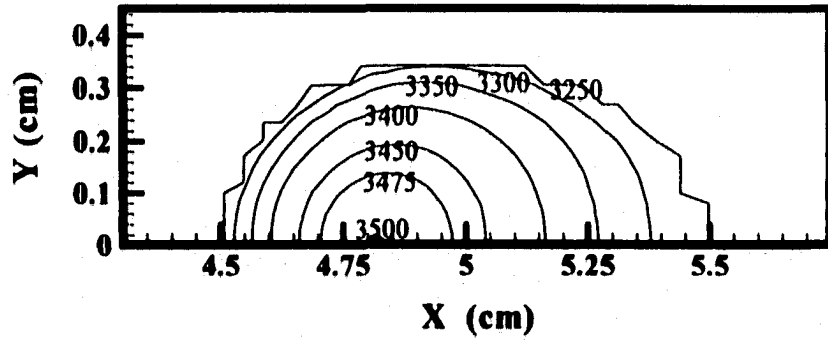
A steep monatomic nitrogen partial pressure dependence and a lack of knowledge of the electron temperature adjacent to the weld pool surface further complicate the understanding of the nitrogen dissolution reaction. Since the location of the plasma phase and the electron temperatures adjacent to the weld pool surface play important roles, the plasma phase is assumed to cover the entire weld pool surface and changes with the size of the weld pool. The electron temperatures vary across the weld pool surface with a maximum electron temperature directly under the heat source and a minimum value at the solid-liquid interface. Outside the arc column and the liquid metal region, the electron temperature above the base metal is equal to the surface temperature.

Since the difference between the maximum and minimum electron temperatures across the weld pool surface are not known, variations of 250°C and 500°C are assumed to exist. Several sets of minimum and maximum electron temperatures, ranging from 4000 to 2500 K, are shown in Table 5.6 with their accompanying monatomic nitrogen partial pressures. The electron temperature is assumed to vary linearly as a function of the weld pool surface temperature between the maximum electron temperature at the weld pool center and the minimum electron temperature at the liquid-solid interface. The resulting electron temperature distributions for each set of welding parameters are shown in Figure 5.11(a-d) and 5.12(a-d), respectively, for several electron temperature distributions.

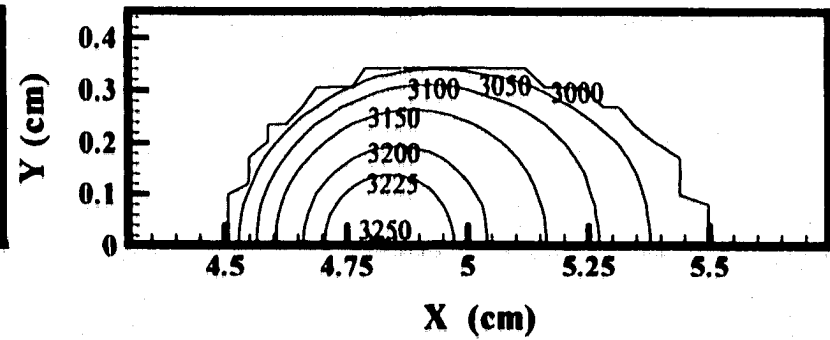
These electron temperature distributions are thus used as the basis for calculating the monatomic nitrogen partial pressures above the weld pool surface. Monatomic nitrogen partial pressures distributions are similar to those for the electron temperatures over the weld pool. For example, a maximum monatomic nitrogen partial pressure is assumed to exist directly under the heat source, and a minimum value exists at the solid-liquid inter-

Table 5.6. Summary of electron temperature and monatomic nitrogen partial pressure (P_N) distributions.

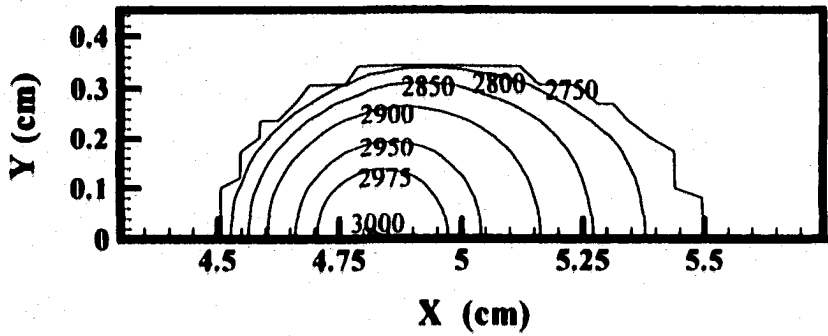
Electron Temperatures		5% N₂		10% N₂		15% N₂		20% N₂	
Maximum	Minimum	P_N Max (atm.)	P_N Min (atm.)	P_N Max (atm.)	P_N Min (atm.)	P_N Max (atm.)	P_N Min (atm.)	P_N Max (atm.)	P_N Min (atm.)
250 K Difference									
3500 K	3250 K	1.209×10^{-5}	3.364×10^{-6}	2.417×10^{-5}	6.728×10^{-6}	3.626×10^{-5}	1.009×10^{-5}	4.834×10^{-5}	1.346×10^{-5}
3250 K	3000 K	3.364×10^{-6}	7.576×10^{-7}	6.728×10^{-6}	1.516×10^{-6}	1.009×10^{-5}	2.274×10^{-6}	1.346×10^{-5}	3.032×10^{-6}
3000 K	2750 K	7.576×10^{-7}	1.305×10^{-7}	1.516×10^{-6}	2.611×10^{-7}	2.274×10^{-6}	3.916×10^{-7}	3.032×10^{-6}	5.222×10^{-7}
2750 K	2500 K	1.305×10^{-7}	1.586×10^{-8}	2.611×10^{-7}	3.172×10^{-8}	3.916×10^{-7}	4.757×10^{-8}	5.222×10^{-7}	6.343×10^{-8}
500 K Difference									
4000 K	3500 K	9.692×10^{-5}	1.209×10^{-5}	1.938×10^{-4}	2.417×10^{-5}	2.907×10^{-4}	3.626×10^{-5}	3.877×10^{-4}	4.834×10^{-5}
3500 K	3000 K	1.209×10^{-5}	7.576×10^{-7}	2.417×10^{-5}	1.516×10^{-6}	3.626×10^{-5}	2.274×10^{-6}	4.834×10^{-5}	3.032×10^{-6}
3250 K	2750 K	3.364×10^{-6}	1.305×10^{-7}	6.728×10^{-6}	2.611×10^{-7}	1.009×10^{-5}	3.916×10^{-7}	1.346×10^{-5}	5.222×10^{-7}
3000 K	2500 K	7.576×10^{-7}	1.586×10^{-8}	1.516×10^{-6}	3.172×10^{-8}	2.274×10^{-6}	4.757×10^{-8}	3.032×10^{-6}	6.343×10^{-8}



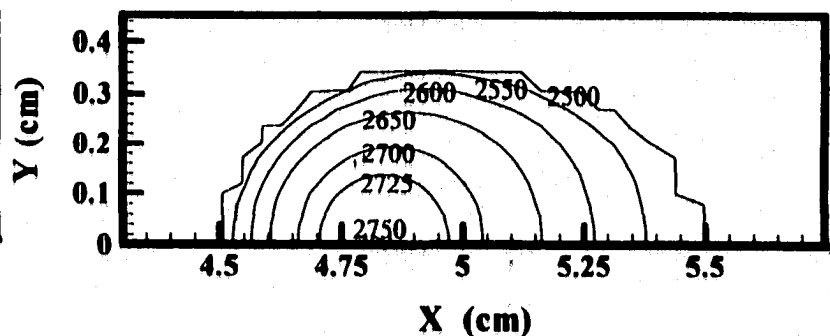
(a)



(b)

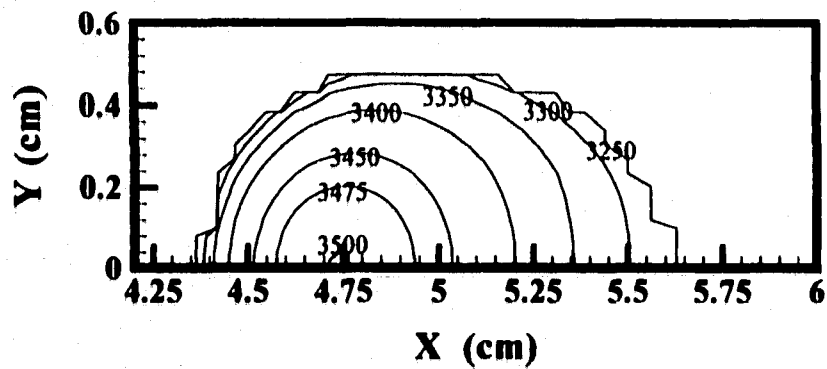


(c)

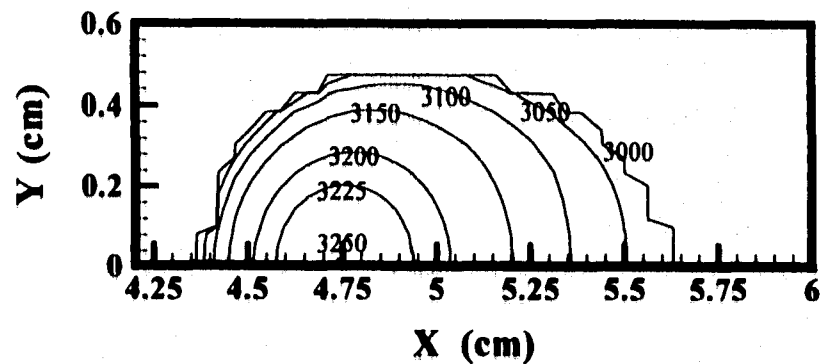


(d)

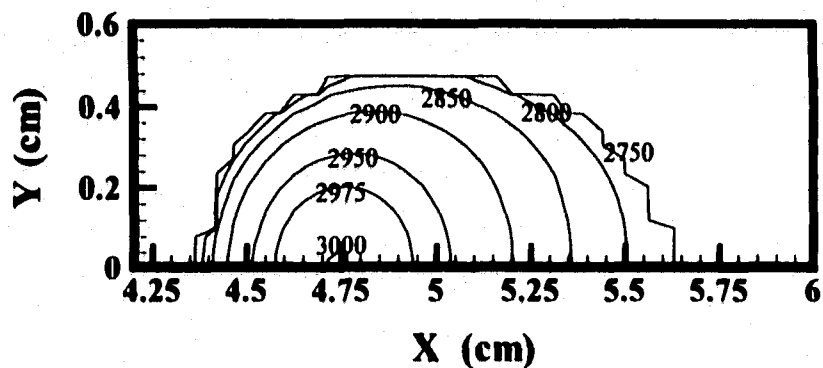
Figure 5.11(a-d). Electron temperature distributions for differences in electron temperature of 250 K between the center of the heat source and the edge of the weld pool for maximum electron temperatures of (a)3500 K, (b) 3250 K, (c) 3000 K, and (d) 2750 K for a travel speed of 0.847 cm/sec. All temperatures are in degrees Kelvin.



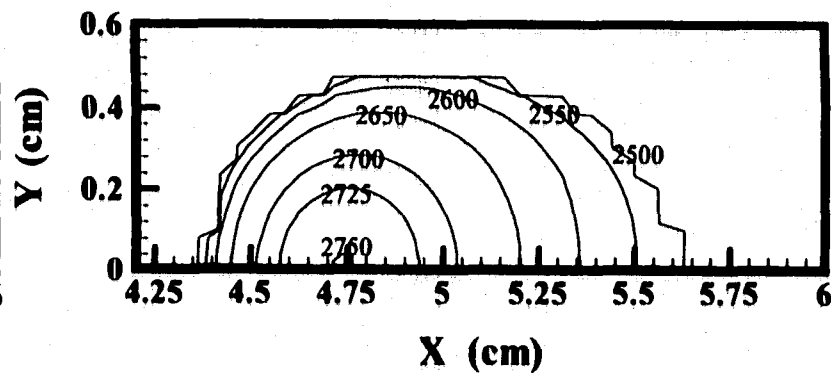
(a)



(b)



(c)



(d)

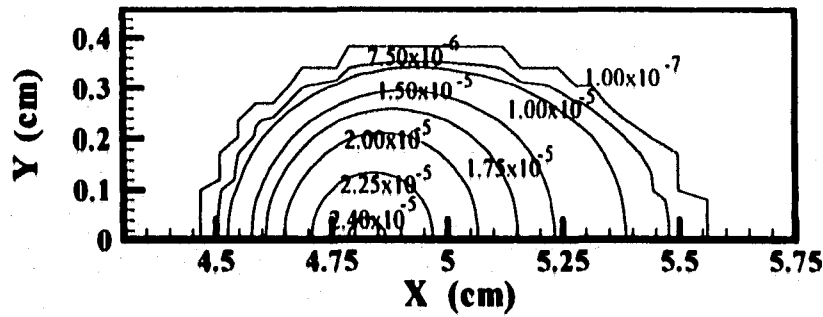
Figure 5.12(a-d). Electron temperature distributions for differences in electron temperature of 250 K between the center of the heat source and the edge of the weld pool for maximum electron temperatures of (a) 3500 K, (b) 3250 K, (c) 3000 K, and (d) 2750 K for a travel speed of 0.423 cm/sec. All temperatures are in degrees Kelvin.

face. In general, the monatomic nitrogen partial pressures, shown in Table 5.6, vary by a factor of between 5 and 10. Outside the arc column, the monatomic nitrogen partial pressure is determined by the nitrogen dissociation reaction in Equation (5.40) and the free energy data shown in Table 5.3 at the sample temperature.

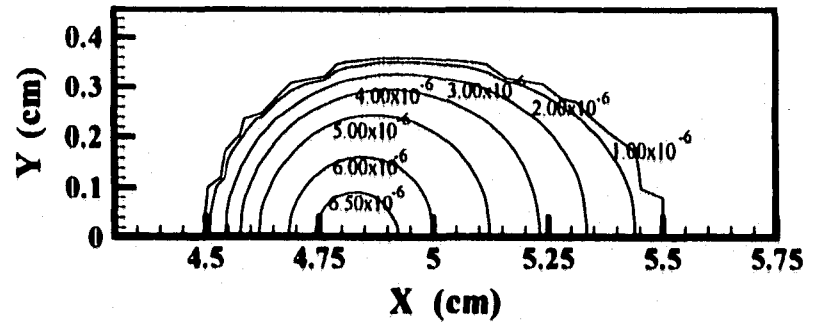
Between its maximum value at the weld pool center and its minimum value at the liquid-solid interface, the monatomic nitrogen partial pressure varies linearly as a function of the electron temperature. Examples of these monatomic nitrogen partial pressure distributions across the weld pool surface are plotted in Figures 5.13(a-d) to 5.16(a-d) for each set of welding parameters, respectively. Figures 5.13(a-d) and Figures 5.14(a-d) show monatomic nitrogen partial pressure distributions for several electron temperature distributions at each travel speed. As the electron temperatures above the weld pool are increased, the monatomic nitrogen partial pressures increase. In each case, there is little to no difference between these partial pressure distributions and those observed at the more rapid travel speed.

The effect of changes in the amount of nitrogen added to the shielding gas on the monatomic nitrogen partial pressure distribution is shown in Figures 5.15(a-d) and 5.16(a-d) for each set of welding parameters. As more nitrogen is added to the shielding gas, the monatomic nitrogen partial pressures above the weld pool surface increase. With small nitrogen additions to the shielding gas, the monatomic nitrogen partial pressure displays a rather steep variation across the weld pool surface. At higher nitrogen additions, though, the monatomic nitrogen partial pressure distribution becomes less steep, and the monatomic nitrogen partial pressures are greater in magnitude.

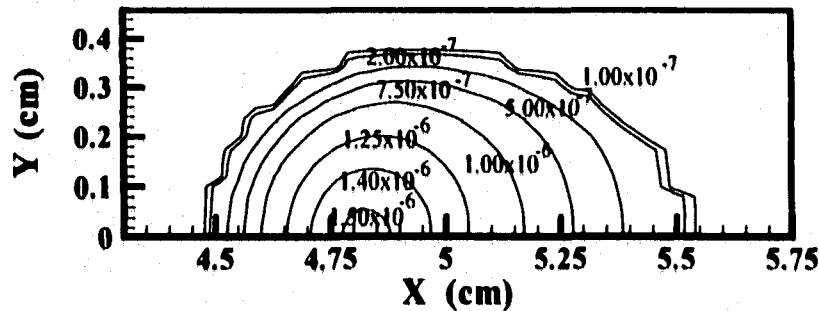
At these electron temperatures, the monatomic nitrogen partial pressures across the liquid metal surface are several orders of magnitude larger than the monatomic nitrogen partial pressure at atmospheric pressure and a temperature of 1873 K. Previous researchers have also noted the enhanced levels of monatomic nitrogen above the weld pool and the role they play in enhancing the nitrogen concentration in the weld pool. In this case, these monatomic nitrogen partial pressures form the basis for the calculation of the nitrogen concentration on both the weld pool surface and throughout its interior.



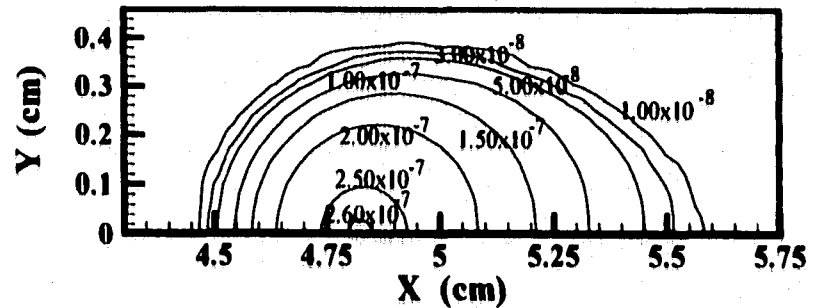
(a)



(b)

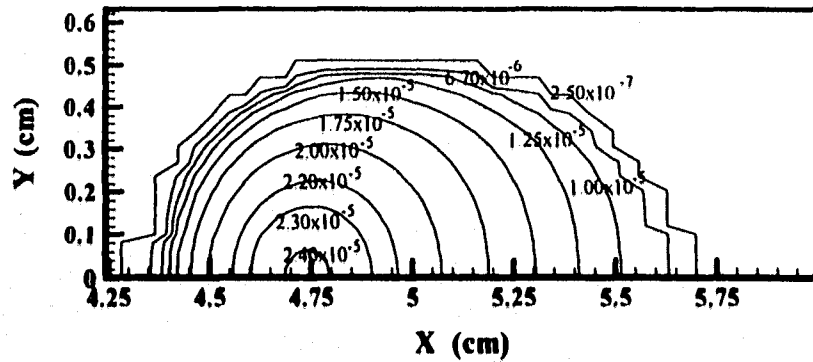


(c)

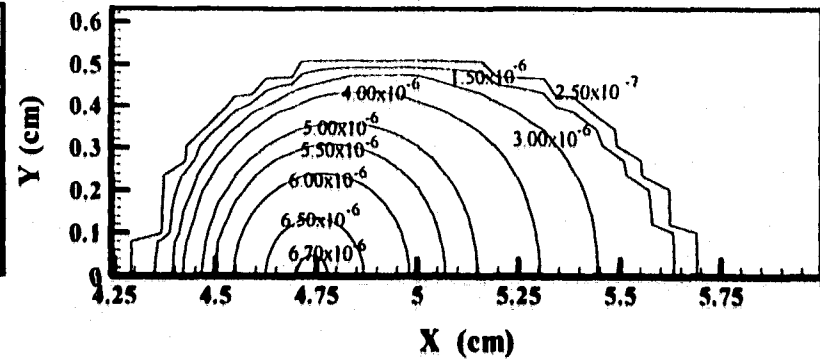


(d)

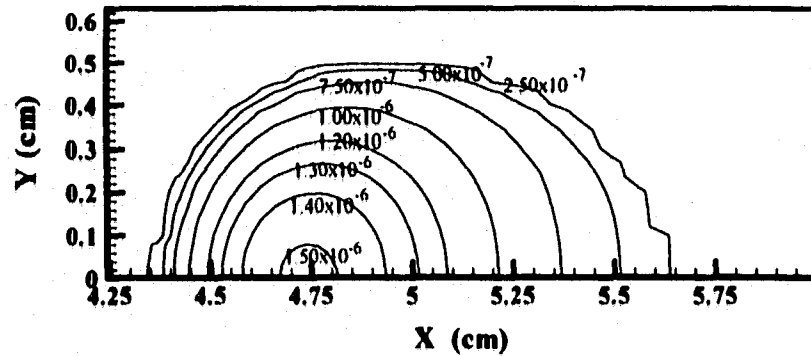
Figure 5.13(a-d). Monatomic nitrogen partial pressure (atm.) distribution calculations based on the electron temperature distributions used above with a difference of 250°C between the center of the heat source and the edge of the weld pool for maximum electron temperatures of (a) 3500 K, (b) 3250 K, (c) 3000 K, and (d) 2750 K for a travel speed of 0.847 cm/sec with a 10% N₂ addition to the shielding gas.



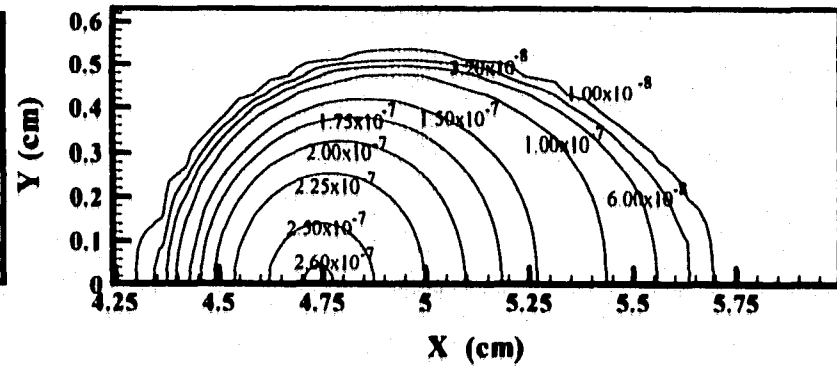
(a)



(b)

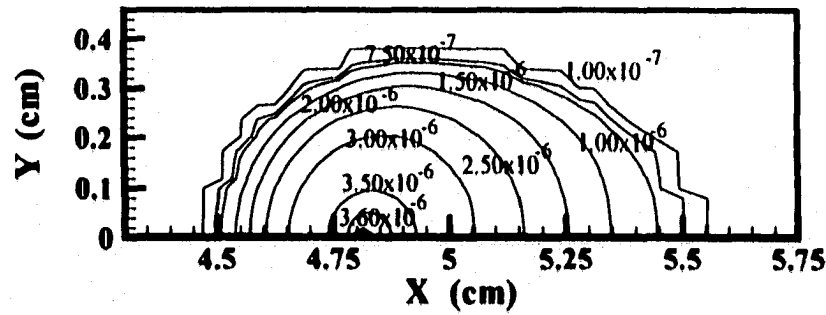


(c)

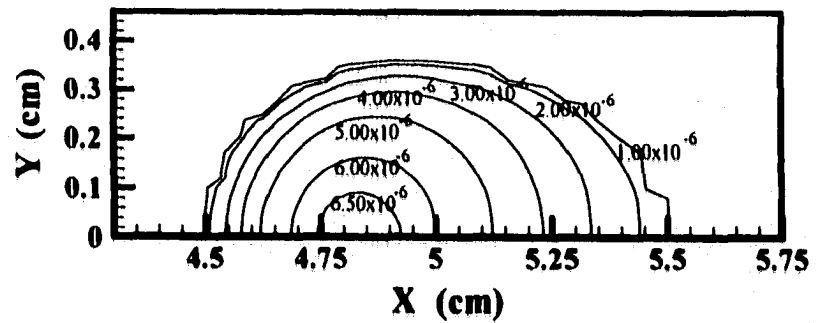


(d)

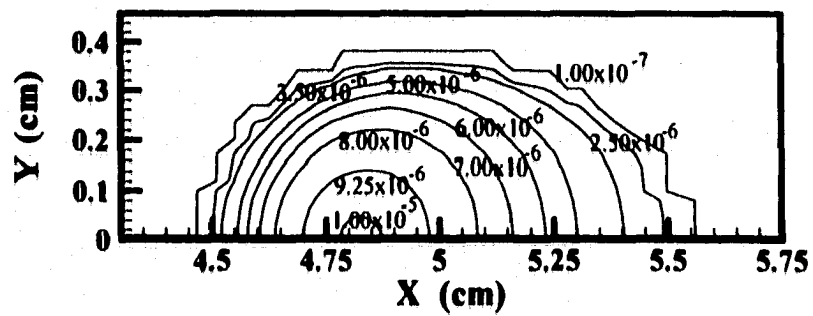
Figure 5.14(a-d). Monatomic nitrogen partial pressure (atm.) distribution calculations based on the electron temperature distributions used above with a difference of 250°C between the center of the heat source and the edge of the weld pool for maximum electron temperatures of (a) 3500 K, (b) 3250 K, (c) 3000 K, and (d) 2750 K for a travel speed of 0.423 cm/sec with a 10% N₂ addition to the shielding gas.



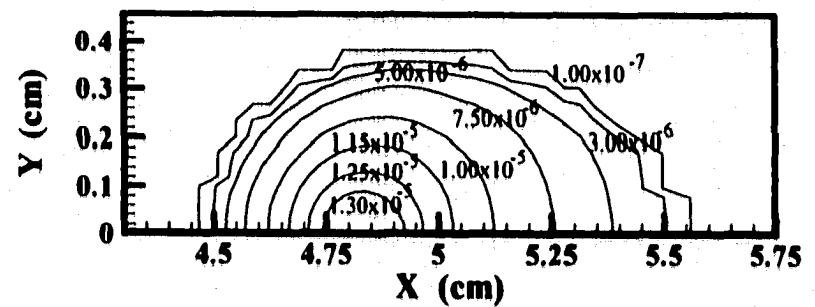
(a)



(b)

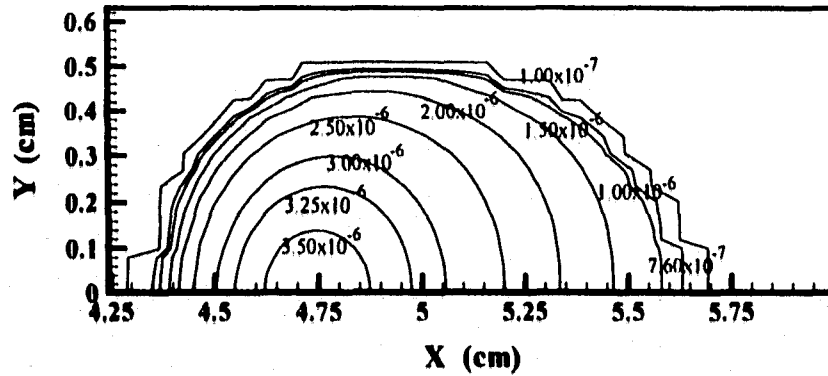


(c)

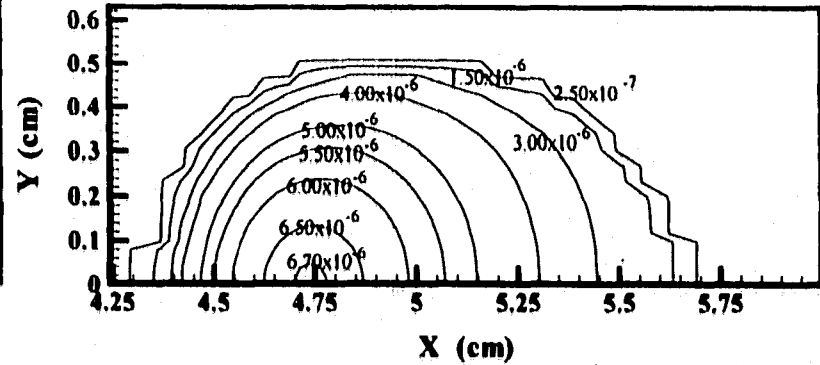


(d)

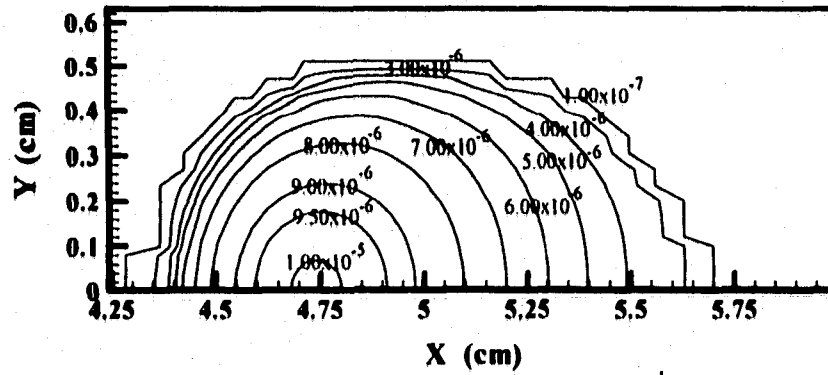
Figure 5.15(a-d). Monatomic nitrogen partial pressure (atm.) distribution calculations for an electron temperature distribution between 3250 and 3000 K for nitrogen additions to the shielding gas of (a) 5%, (b) 10%, (c) 15%, and (d) 20% for a travel speed of 0.847 cm/sec.



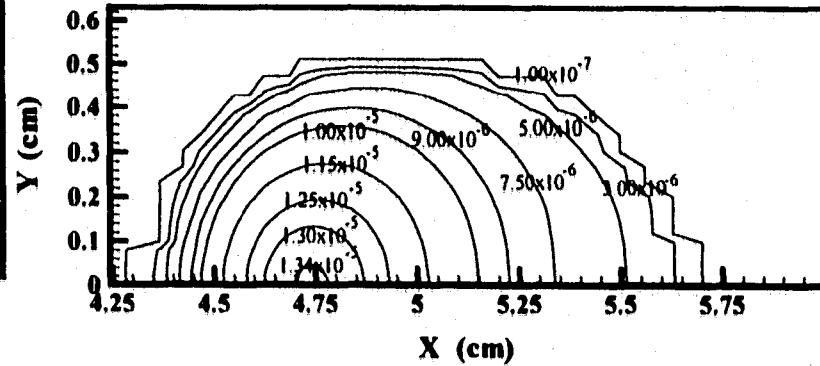
(a)



(b)



(c)



(d)

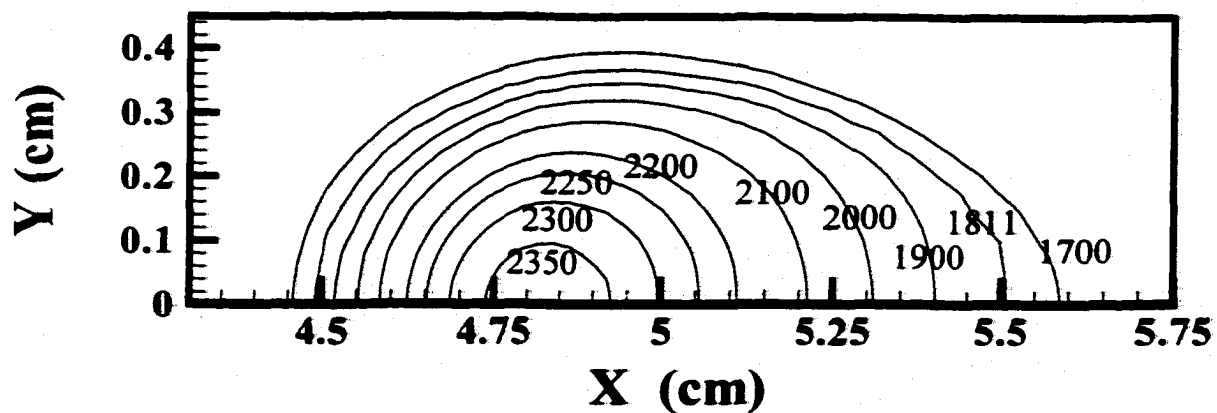
Figure 5.16(a-d). Monatomic nitrogen partial pressure (atm.) distribution calculations for an electron temperature distribution between 3250 and 3000 K for nitrogen additions to the shielding gas of (a) 5%, (b) 10%, (c) 15%, and (d) 20% for a travel speed of 0.423 cm/sec.

5.3.3 Nitrogen Surface Concentrations

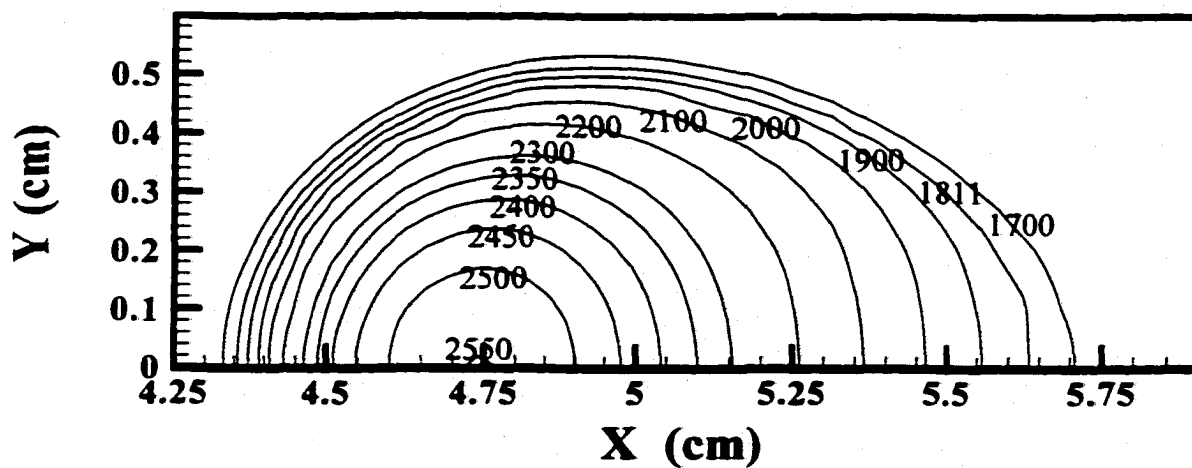
Nitrogen concentrations on the weld pool surface are calculated by combining the monatomic nitrogen partial pressures with the temperature distribution on the weld pool surface. The temperature distributions on the weld pool surface for the welding parameters examined here have been calculated in a previous section and as shown in Figures 5.17(a&b). Peak temperatures vary between 2377 K at a travel speed of 0.847 cm/sec and 2551 K at a travel speed of 0.423 cm/sec. Even though the magnitudes of the temperatures across the weld pool surface and the weld pool dimensions are different, there is little difference in the general shape of the temperature distribution.

The thermal histories experienced by the weld pool can then be calculated. Figures 5.18(a&b) show the computed thermal profiles along the weld centerline for each welding condition. A summary of important variables, such as the cooling rate and the time the weld pool remains liquid, is included in Table 5.7. According to these calculations, the weld pool remains molten one second at the more rapid travel speed and for nearly three seconds at the less rapid travel speed.

Nitrogen concentrations on the weld pool surface have thus been calculated based on both the monatomic nitrogen partial pressure and the calculated surface temperatures for each travel speed. Figures 5.19(a-d) and 5.20(a-d) show the calculated nitrogen concentration distributions on the weld pool surface for several electron temperature gradients at each travel speed. The calculated nitrogen concentrations on the weld pool surface have similar appearances, even with changes in the electron temperature distribution, at a constant travel speed. For example, an electron temperature distribution between 3250 and 3000 K at a travel speed of 0.847 cm/sec, as shown in Figure 5.19(b), produces nitrogen concentrations, which are a minimum at the weld pool center and increase to the nitrogen saturation levels at the weld pool periphery. As the electron temperature is increased, a greater area of the weld pool surface reaches the nitrogen saturation levels. When the travel speed is decreased, as shown in Figures 5.20(a-d), a similar behavior is observed in the nitrogen concentration distribution. On the other hand, a smaller proportion of the weld pool surface reaches nitrogen saturation for the electron temperature distributions analyzed.

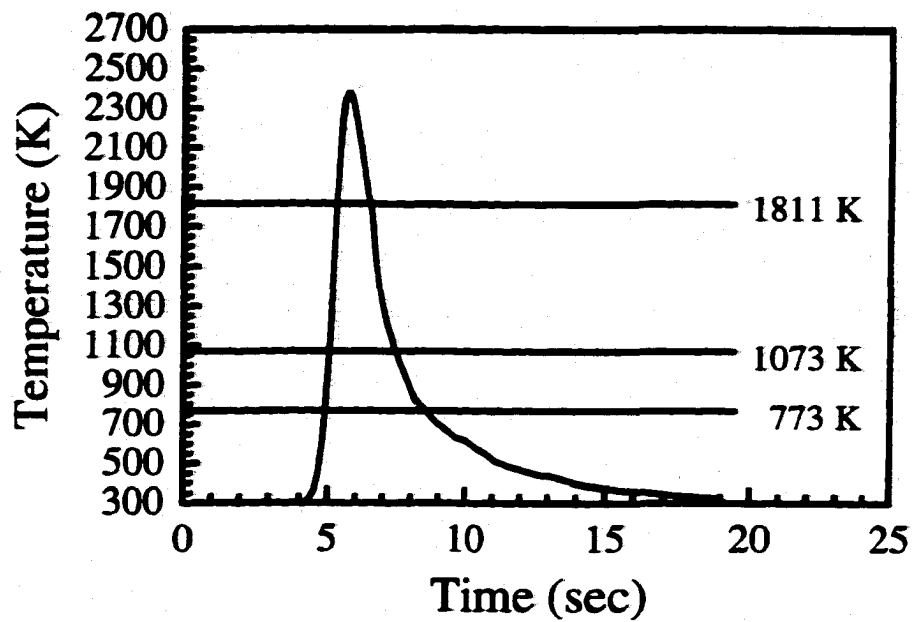


(a)

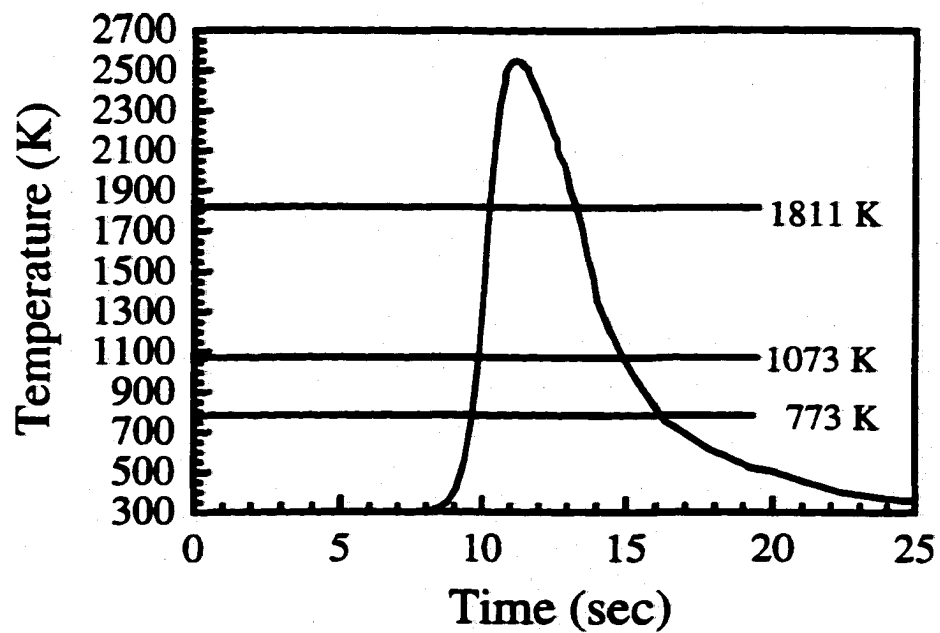


(b)

Figure 5.17(a&b). Temperature profiles on the weld pool surface for a travel speed of (a) 0.847 cm/sec and (b) 0.423 cm/sec. All temperatures are in degrees Kelvin.



(a)

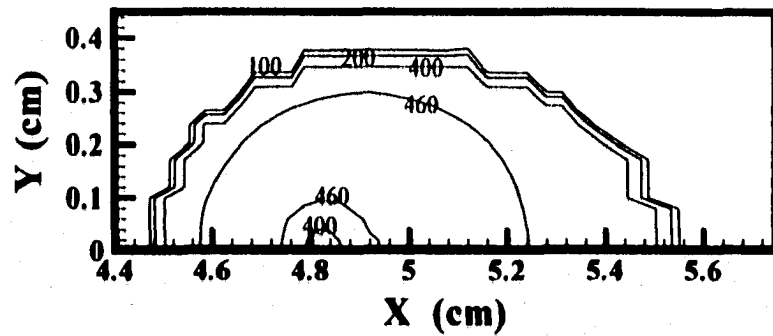


(b)

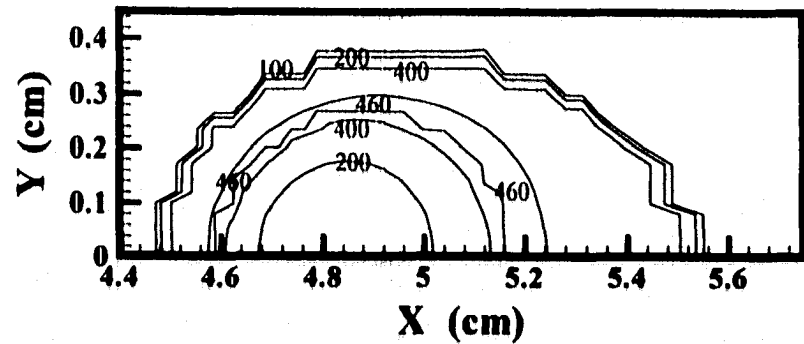
Figure 5.18(a&b). Calculated thermal cycle on the weld pool surface at the weld centerline for a travel speed of (a) 0.847 cm/sec and (b) 0.423 cm/sec.

Table 5.7. Summary of calculated cooling rates based on the thermal cycles from each set of welding parameters.

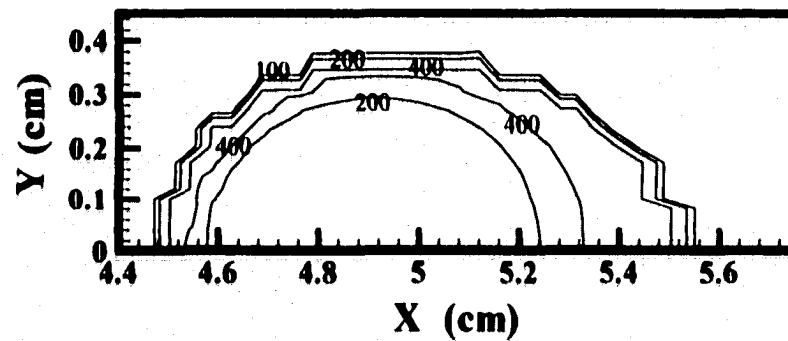
	Condition #1	Condition #2
Maximum Temperature in Weld Pool (K)	2377	2551
Time Weld Metal is Liquid (sec)	1.12	2.99
Cooling Rate in Liquid Metal Region (K/sec)	725.60	352.40
Time for Thermal Cycle to pass between 1073 to 773 K (sec)	0.65	1.40
Cooling Rate in 1073 to 773 K Region (K/sec)	416.70	200.00



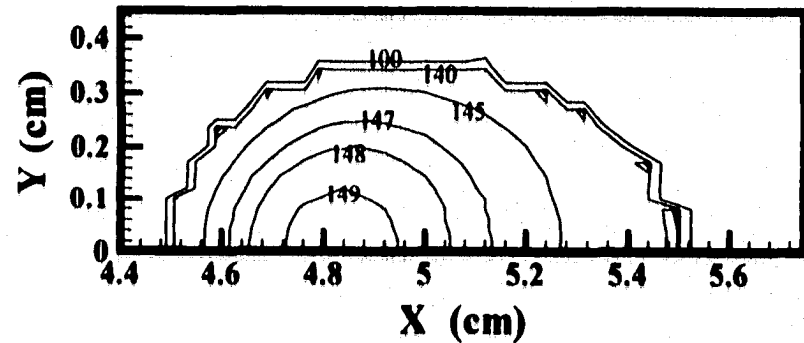
(a)



(b)

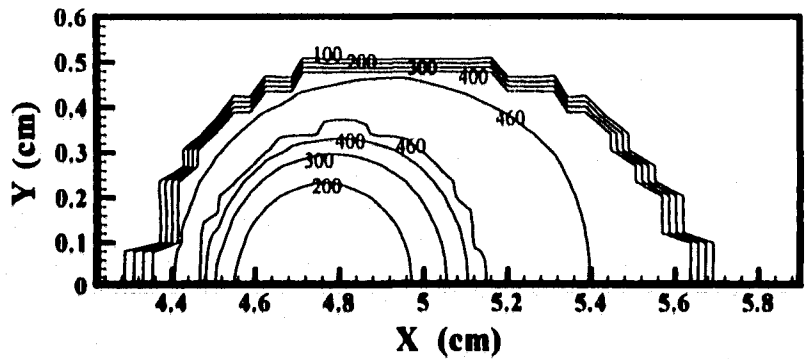


(c)

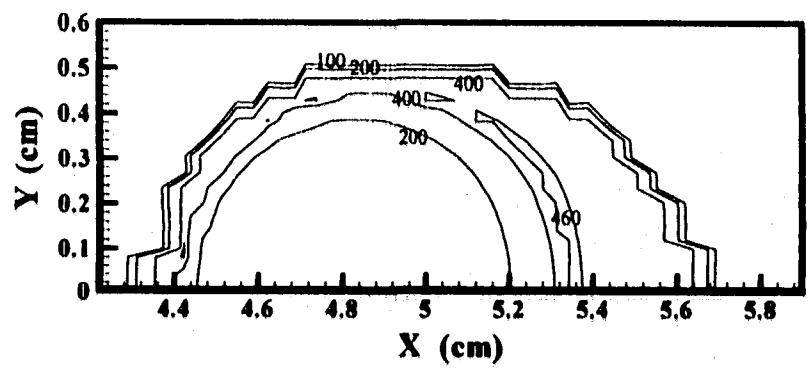


(d)

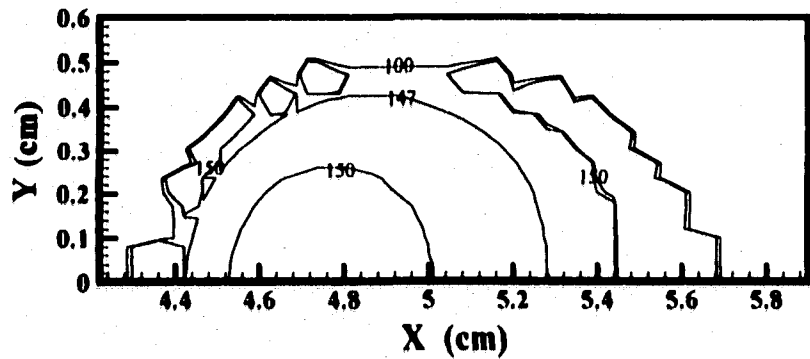
Figure 5.19(a-d). Nitrogen concentration (ppm) distributions calculated based on the monatomic nitrogen partial pressure and electron temperature distributions across the weld pool surface with a difference of 250°C between the center of the heat source and the edge of the weld pool for maximum electron temperatures of (a) 3500 K, (b) 3250 K, (c) 3000 K, and (d) 2750 K for a travel speed of 0.847 cm/sec with a 10% N_2 addition to the shielding gas.



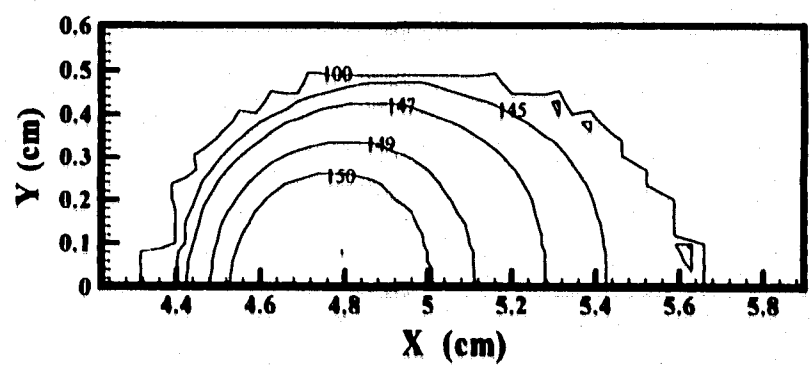
(a)



(b)



(c)



(d)

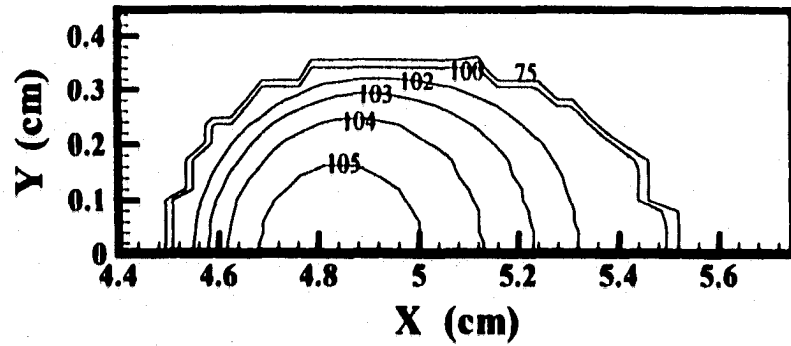
Figure 5.20(a-d). Nitrogen concentration (ppm) distributions calculated based on the monatomic nitrogen partial pressure and electron temperature distributions across the weld pool surface with a difference of 250°C between the center of the heat source and the edge of the weld pool for maximum electron temperatures of (a)3500 K, (b) 3250 K, (c) 3000 K, and (d) 2750 K for a travel speed of 0.423 cm/sec with a 10% N₂ addition to the shielding gas.

Nitrogen concentration distributions on the weld pool surface change at lower electron temperatures. Figure 5.21(a-d) and 5.22(a-d) show the nitrogen surface concentration distributions for each welding condition, respectively, for several nitrogen additions to the shielding gas with electron temperatures between 2500 and 2750 K. At no nitrogen addition do the nitrogen concentrations on the weld pool surface reach the nitrogen saturation levels, but the nitrogen concentrations increase as more nitrogen is added to the shielding gas. At these electron temperatures, the monatomic nitrogen partial pressures are much lower, resulting in lower nitrogen concentrations on the weld pool surface. Once nitrogen additions to the shielding gas reach 20%, monatomic nitrogen partial pressures become significant enough to produce nitrogen concentrations on the weld pool surface which approach the nitrogen saturation values.

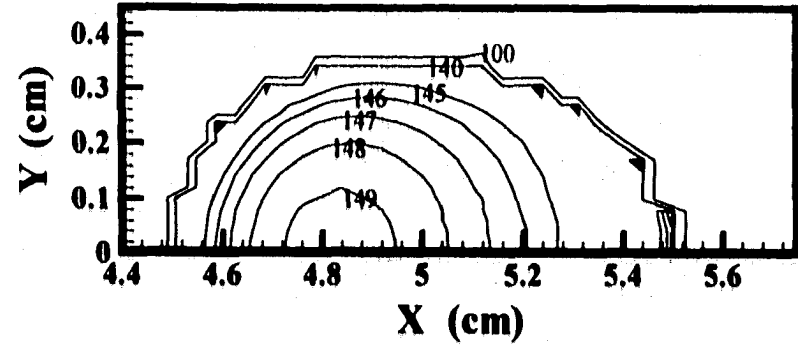
In each case, the nitrogen concentrations tend to follow the monatomic nitrogen solubility behavior described in previous sections. This solubility behavior is primarily defined by a significant decrease in the nitrogen solubility with an increase in temperature. For example, the weld pool center, with the highest surface temperatures, displays the lowest nitrogen concentrations, and the weld pool periphery, which has the lowest surface temperatures, displays the highest nitrogen concentrations. These nitrogen concentrations have little dependence on the monatomic nitrogen partial pressures considered here, since the lowest nitrogen concentrations are observed in regions with the highest monatomic nitrogen partial pressures.

5.3.4 Nitrogen Transport Mechanism

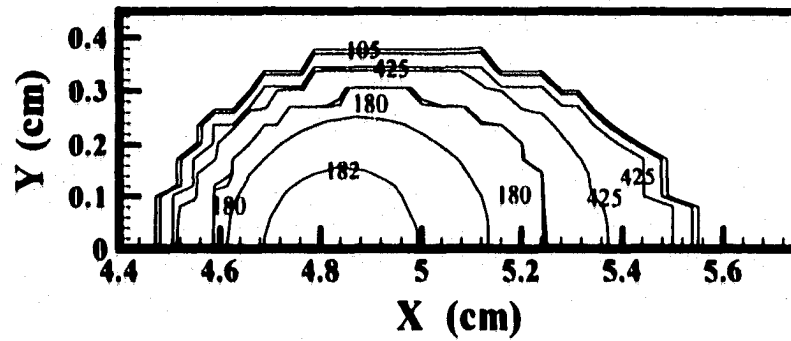
These nitrogen concentration distributions on the weld pool surface act as a source of nitrogen to the interior of the fusion zone and play a preeminent role in determining the resulting nitrogen concentration. Nitrogen absorbed at the weld pool surface is transported to the weld pool interior by either diffusion or convection driven processes. The dominant transport process can be determined in qualitative terms using a dimensionless number. The Peclet number for mass transfer^{1,2} has been previously used to determine this dominant transport process and gives meaning to the role of convection as compared



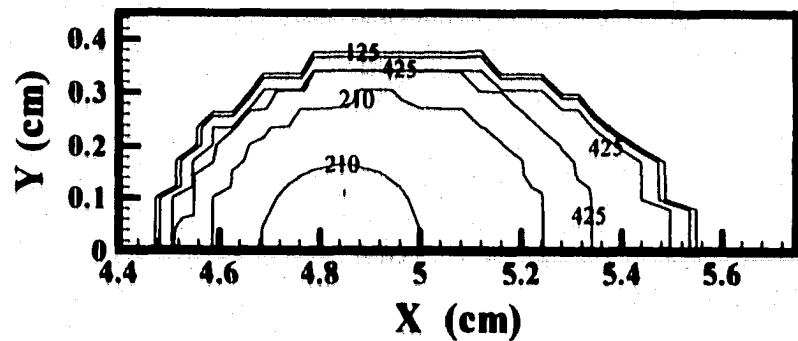
(a)



(b)

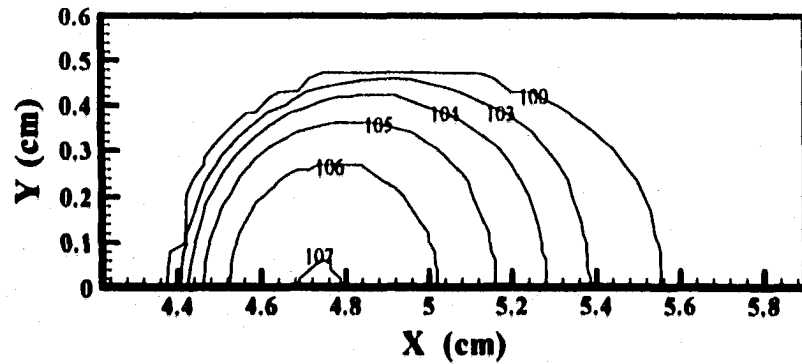


(c)

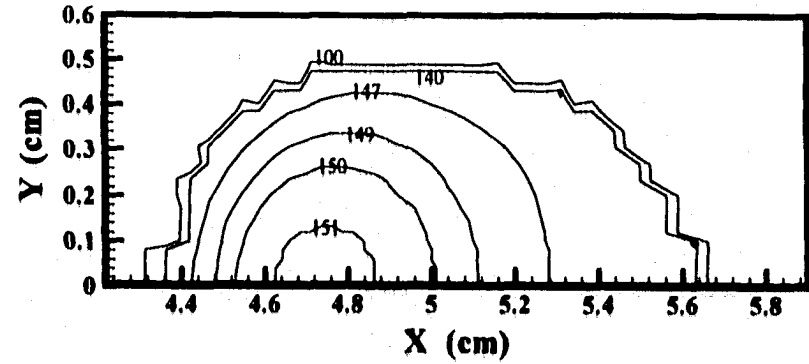


(d)

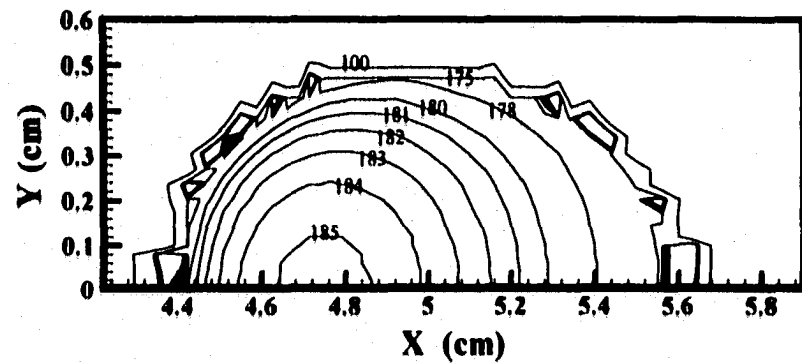
Figure 5.21(a-d). Nitrogen concentration (ppm) distributions calculated based on an electron temperature distribution between 2750 and 2500 K above the weld pool surface and nitrogen additions of (a) 5% N₂, (b) 10% N₂, (c) 15% N₂, and (d) 20% N₂ to the shielding gas at a travel speed of 0.847 cm/sec.



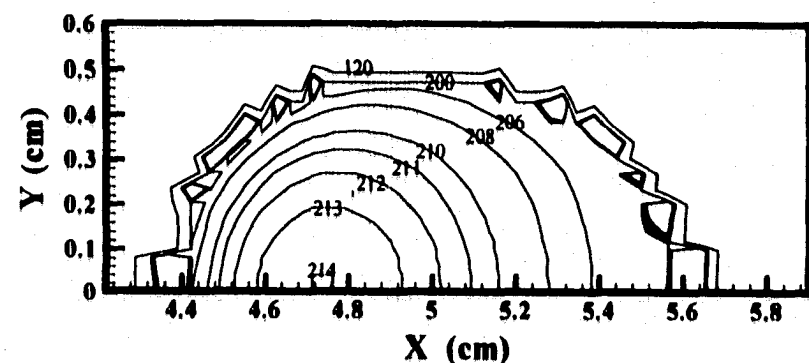
(a)



(b)



(c)



(d)

Figure 5.22(a-d). Nitrogen concentration (ppm) distributions calculated based on an electron temperature distribution between 2750 and 2500 K above the weld pool surface and nitrogen additions of (a) 5% N₂, (b) 10% N₂, (c) 15% N₂, and (d) 20% N₂ to the shielding gas at a travel speed of 0.423 cm/sec.

to diffusion in transporting nitrogen throughout the weld pool. It is defined in the following relationship.

$$Pe_m = \frac{V_{max} L}{D} \quad (5.42)$$

where V_{max} is the maximum fluid flow velocity in the weld pool (cm), L is the depth of the weld pool (cm), and D is the diffusivity of nitrogen in the liquid iron ($0.00011 \text{ cm}^2/\text{sec}$) in the weld pool.^{33,34} If the calculated Peclet number is significantly less than one, diffusion is the dominant transport mechanism. At values much greater than one, convection becomes the dominant transport mechanism. A summary of the Peclet number calculations for each welding condition is shown in Table 5.8. For both welding conditions, the Peclet number is very large ($\gg 1$), indicating that the Peclet number calculations, the dominant transport mechanism in the weld pool is considered to be convection.

5.3.5 Nitrogen Concentration Distribution in the Weld Pool Interior

5.3.5.1 Role of Electron Temperature Distribution

These calculated nitrogen concentrations on the weld pool surface are now combined with the calculated temperature and fluid flow fields to calculate the nitrogen concentration distribution in the weld pool. Knowledge of the fluid flow is important, since prior to weld metal solidification, nitrogen is transported through the weld pool interior by liquid flow, which, in turn, determines the final nitrogen concentration distribution. The calculation of the nitrogen concentrations in the weld pool is performed in a transient, three-dimensional manner. Examples of the results of these calculations are shown in Figures 5.23 and 5.24, respectively, for each travel speed. In each figure, the transient nitrogen concentrations are superimposed on the steady state weld pool shape. An indication of how the nitrogen concentration varies in the weld pool, up to solidification, is thus given. These calculations, therefore, provide the basis for the following discussion.

The time dependent nature of the nitrogen concentration distribution in the weld pool has been further examined by determining the effects of changes in the electron tempera-

Table 5.8. Summary of Peclet number calculations for each welding set of welding parameters.

	Condition #1	Condition #2
Maximum Velocity (cm/sec)		
u_{max}	6.38	10.59
v_{max}	8.25	12.26
w_{max}	1.05	1.66
Depth of Weld Pool (cm)	0.08	0.12
Width of Weld Pool (cm)	0.73	1.02
Diffusivity (cm²/sec)	0.00011	0.00011
Peclet Number	5806	13508

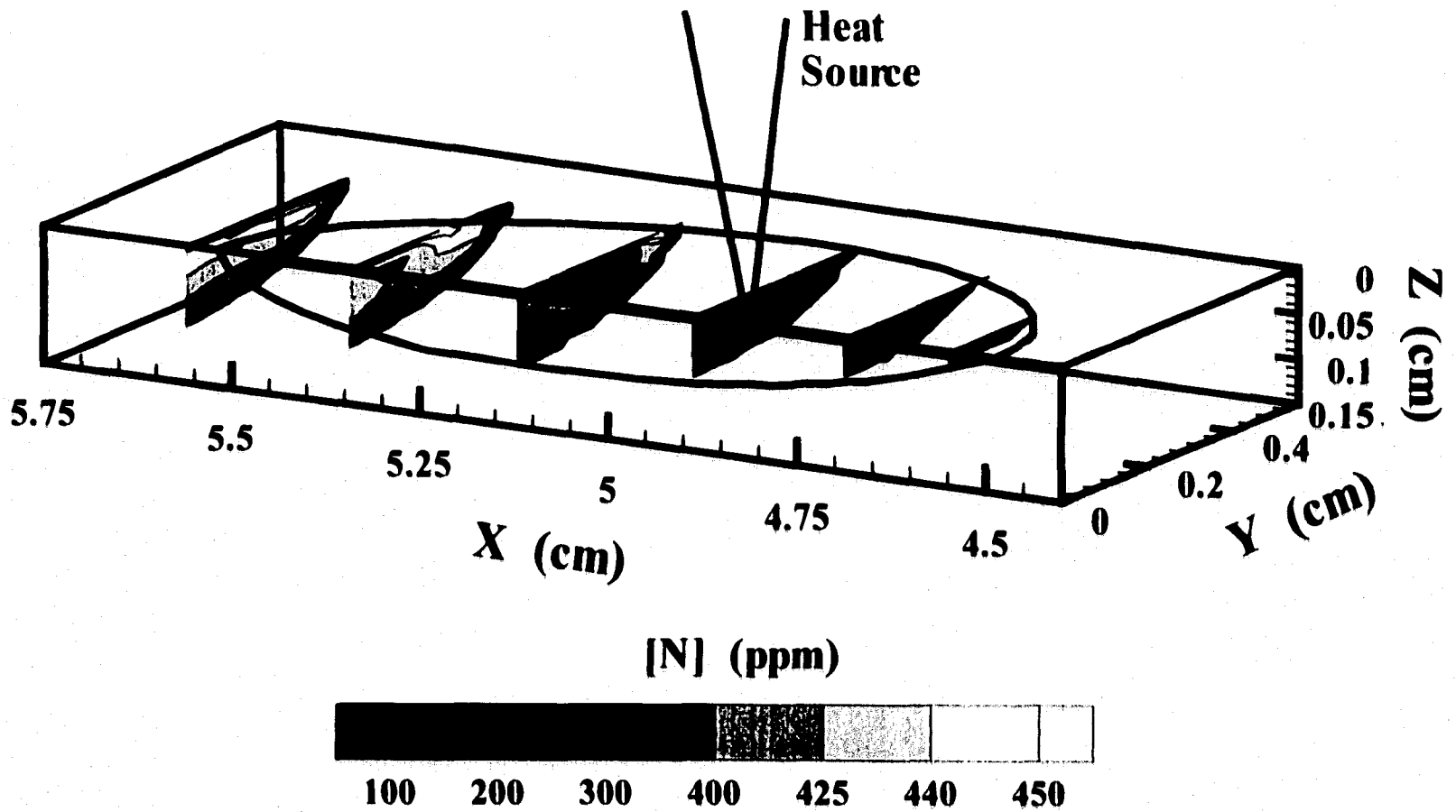


Figure 5.23. Three dimensional plot of nitrogen concentrations in the weld pool at several times for a travel speed of 0.847 cm/sec. Electron temperatures between 3250 and 3000 K for a 10% N₂ addition to the shielding gas are assumed.

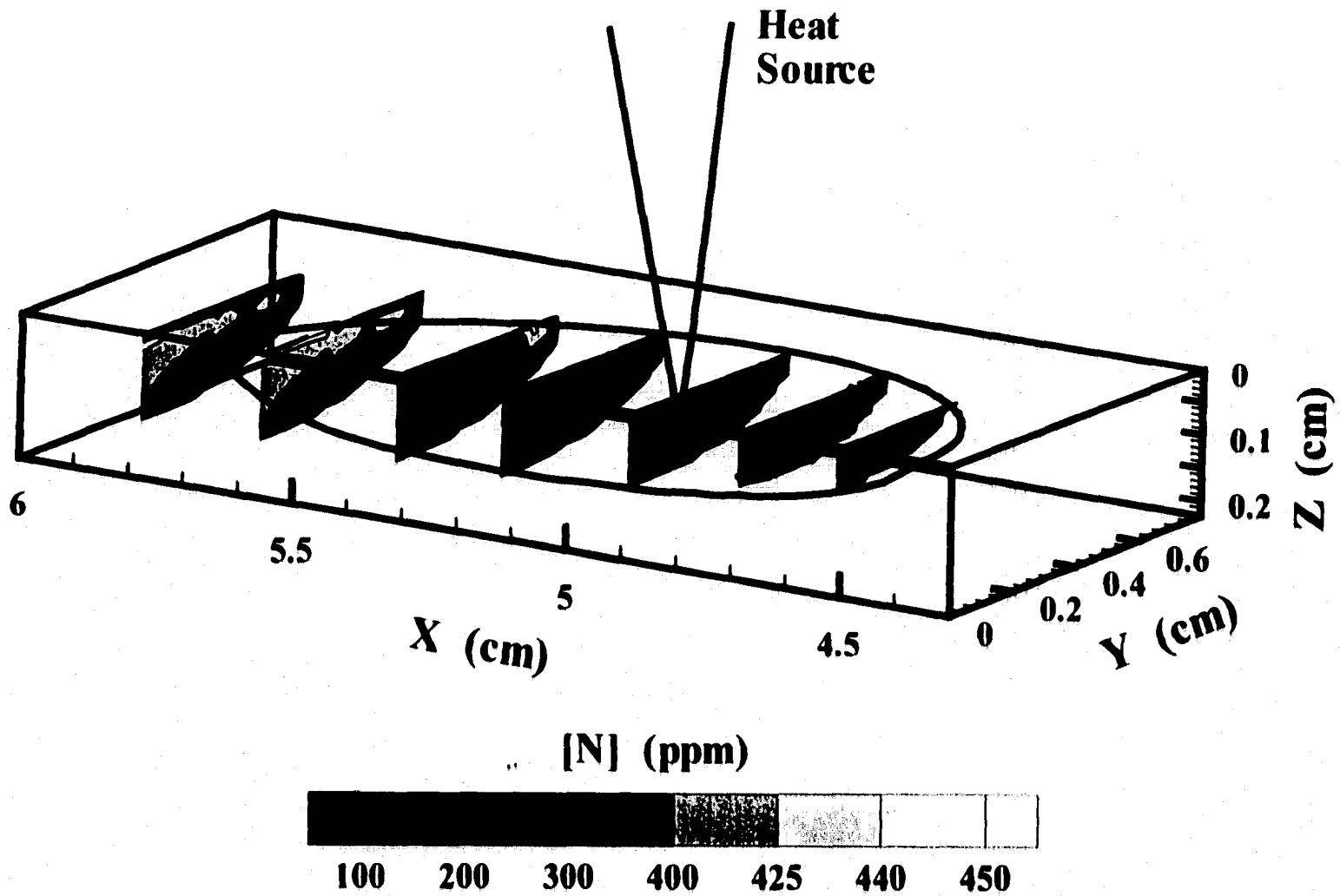
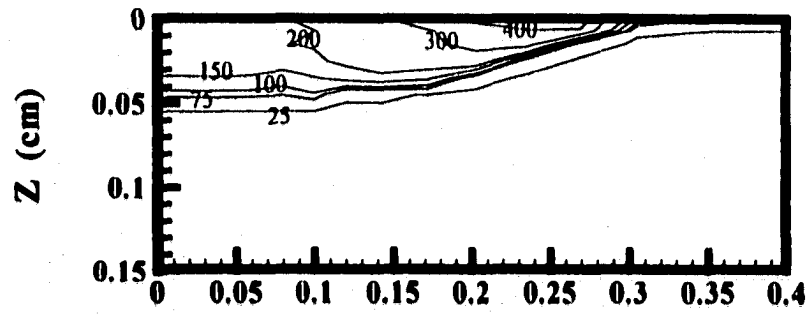


Figure 5.24. Three dimensional plot of nitrogen concentrations in the weld pool at several times for a travel speed of 0.423 cm/sec. Electron temperatures between 3250 and 3000 K for a 10% N₂ addition to the shielding gas are assumed.

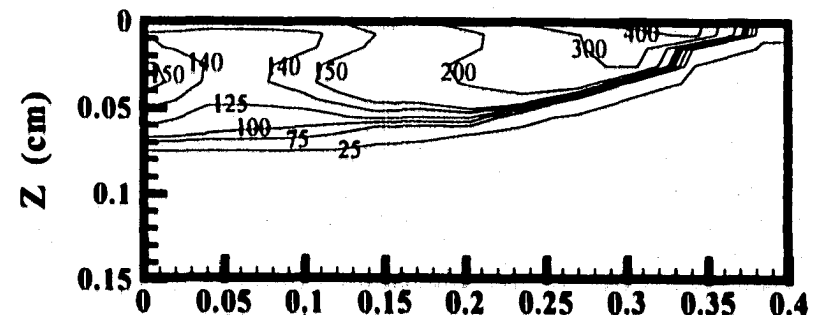
tures above the weld pool and the nitrogen additions to the shielding gas. Figures 5.25(a-d) to 5.28(a-d) show the evolution of the nitrogen concentration distribution in the weld pool at several points in time leading up to weld pool solidification. Nitrogen pick-up in the weld pool is rapid, and the evolution of the nitrogen concentration distribution is affected by the fluid flow patterns in the weld pool up to the time of weld pool solidification. A change in the electron temperatures above the weld pool significantly affects the nitrogen concentration distribution in the weld pool. At electron temperatures between 3250 and 3000 K, nitrogen concentrations in the weld pool interior vary spatially across the weld pool width and depth at the time of solidification. On the other hand, electron temperatures between 2750 and 2500 K produce rather homogeneous nitrogen concentrations, due to the low monatomic nitrogen partial pressures present above the weld pool.

In general, the nitrogen concentration distributions closely follow the calculated fluid flow fields in the weld pool. Areas of highest nitrogen concentration correspond to regions where the liquid metal has been transported from the weld pool surface. On the other hand, areas with lower nitrogen concentrations correspond to those where the continuous supply of material to the weld pool surface is low, such as in the lower corners of the weld pool away from the centerline. As time increases, the nitrogen concentrations further increase both in the center of the weld pool and at the outer edges. Upon solidification, the nitrogen is trapped in place, given the rapid thermal cycles experienced by the solidified weld metal and the rather slow diffusion speed of nitrogen in solid iron. By the time the weld pool solidifies, the nitrogen concentrations are highest in the weld pool center and decrease as the liquid-metal interface is approached.

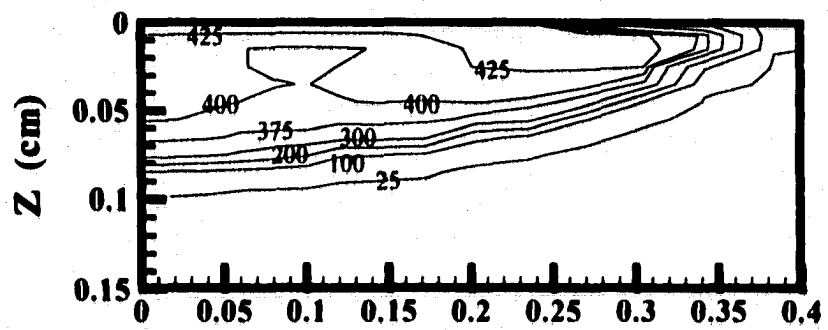
The effects of several electron temperature distributions on the nitrogen concentration distributions at the time of solidification are shown in Figures 5.29(a-d) and 5.30(a-d), respectively, for each travel speed with a constant nitrogen addition to the shielding gas. In each case, the nitrogen concentrations vary spatially across both the width and depth of the weld pool, but decrease in magnitude with decreasing electron temperatures. At the lowest electron temperatures, between 2750 and 2500 K, the nitrogen concentrations in the weld pool are nearly homogenous.



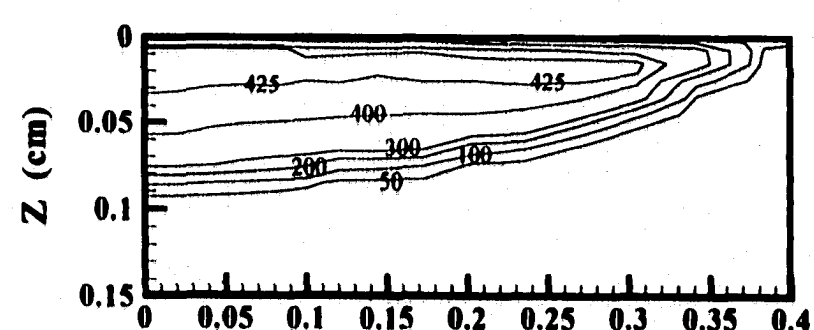
(a)



(b)

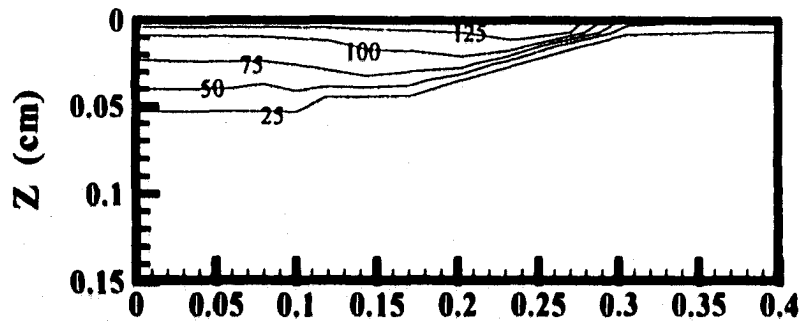


(c)

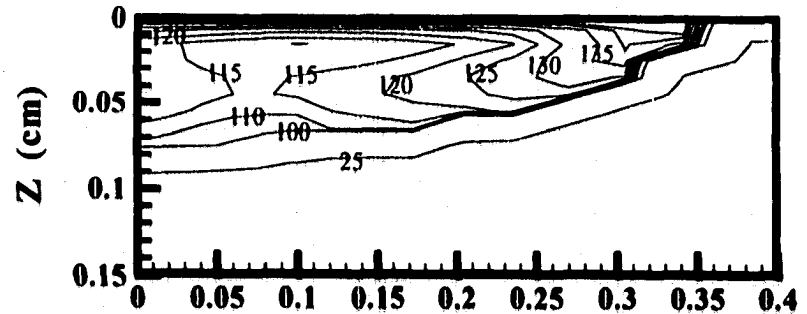


(d)

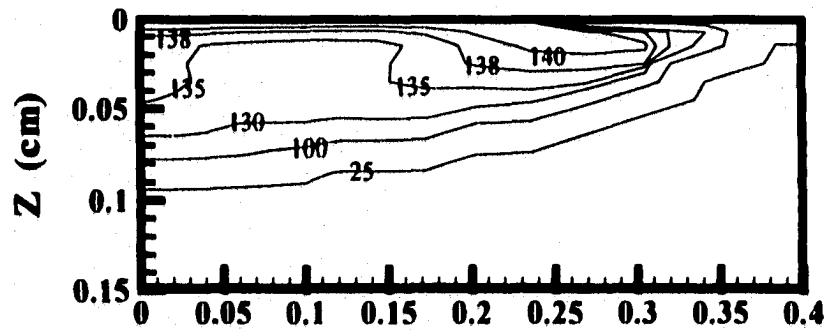
Figure 5.25(a-d). Nitrogen concentration distribution in the weld pool over a range of times for electron temperatures assumed to range from 3250 to 3000 K for a travel speed of 0.847 cm/sec with a 10% N₂ addition to the shielding gas. (a) 0 sec., (b) 0.25 sec., (c) 0.50 sec., (d) 1.0 sec.



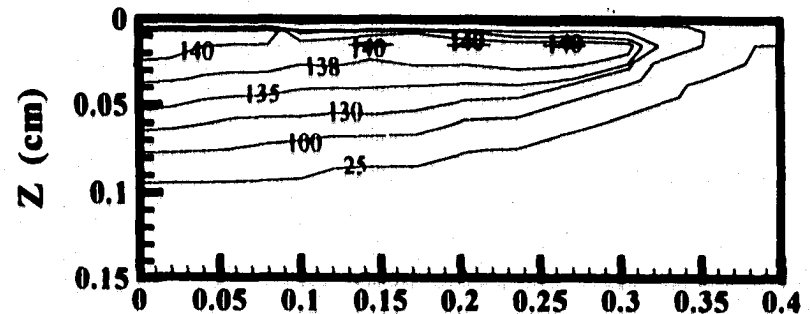
(a)



(b)



(c)



(d)

Figure 5.26(a-d). Nitrogen concentration distribution in the weld pool over a range of times for electron temperatures assumed to range from 2750 to 2500 K for a travel speed of 0.847 cm/sec with a 10% N₂ addition to the shielding gas. (a) 0 sec., (b) 0.25 sec., (c) 0.50 sec., (d) 1.0 sec.

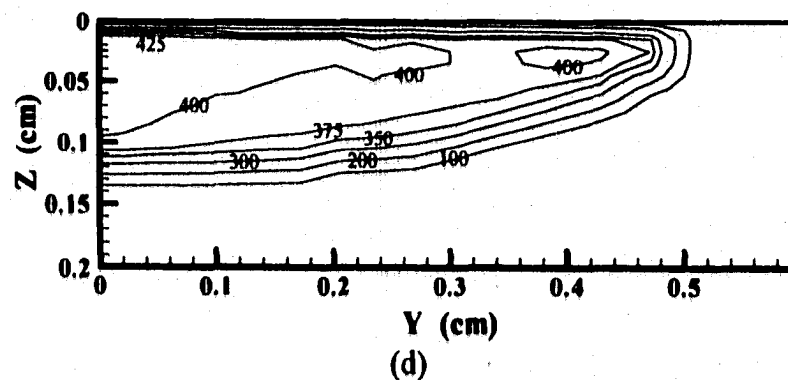
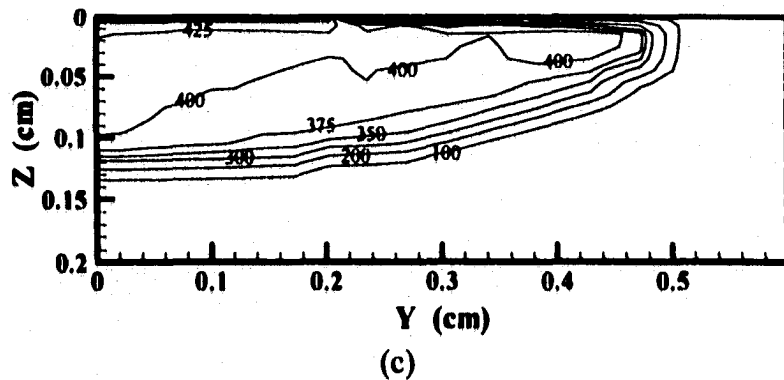
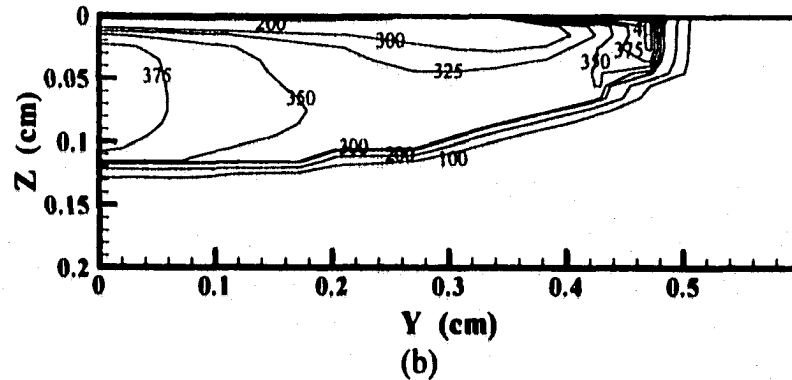
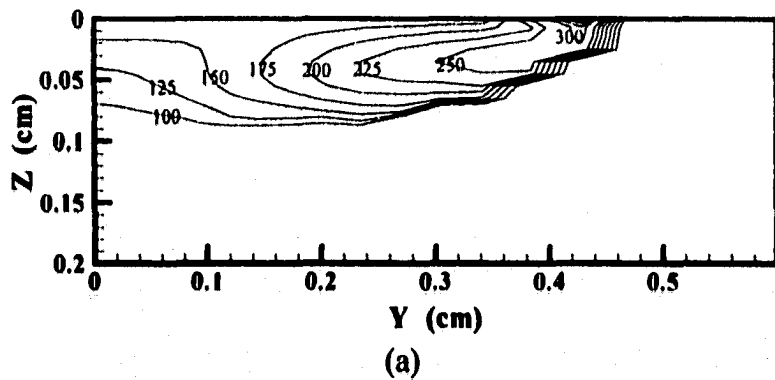
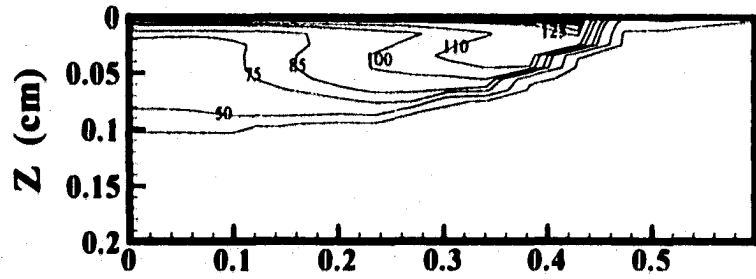
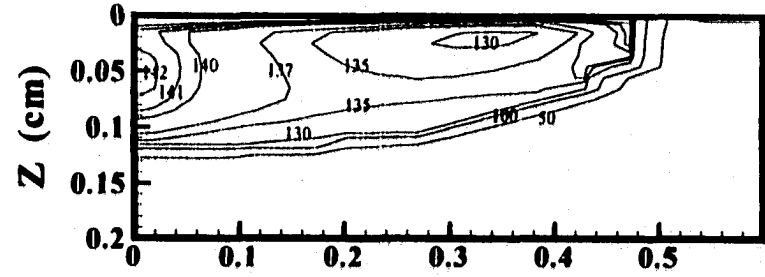


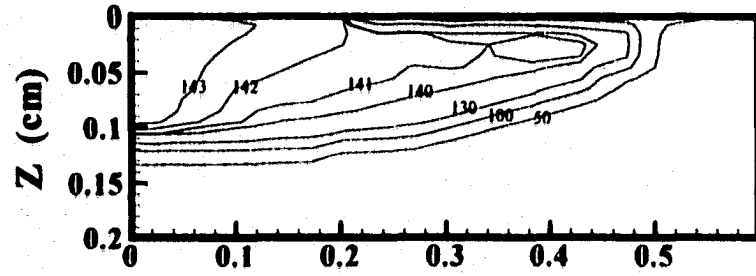
Figure 5.27(a-d). Nitrogen concentration distribution in the weld pool over a range of times for electron temperatures assumed to range from 3250 to 3000 K for a travel speed of 0.423 cm/sec with a 10% N₂ addition to the shielding gas. (a) 0 sec., (b) 1.0 sec., (c) 2.0 sec., (d) 3.0 sec.



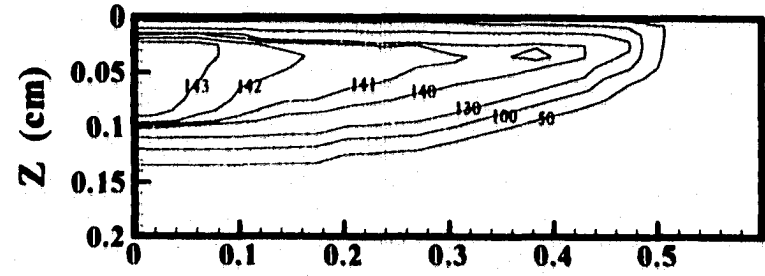
(a)



(b)



(c)



(d)

Figure 5.28(a-d). Nitrogen concentration distribution in the weld pool over a range of times for electron temperatures assumed to range from 2750 to 2500 K for a travel speed of 0.423 cm/sec with a 10% N₂ addition to the shielding gas. (a) 0 sec., (b) 1.0 sec., (c) 2.0 sec., (d) 3.0 sec.

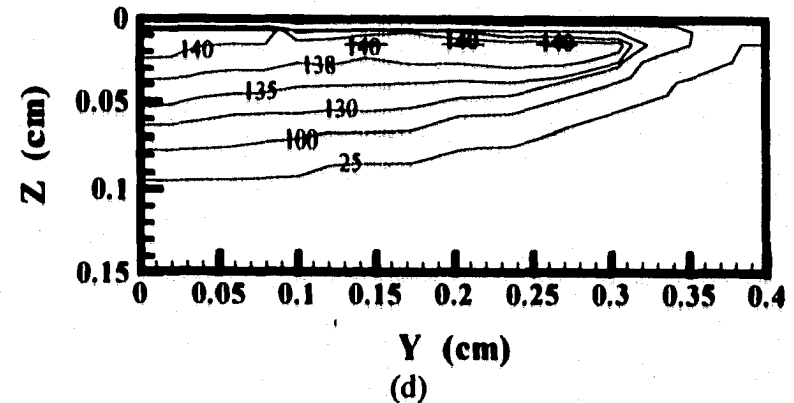
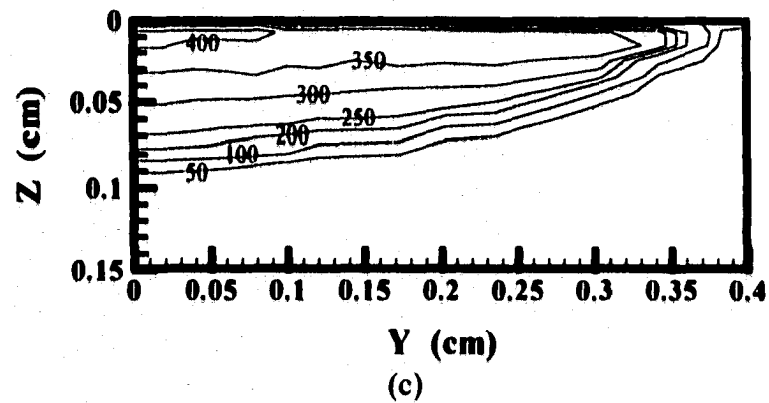
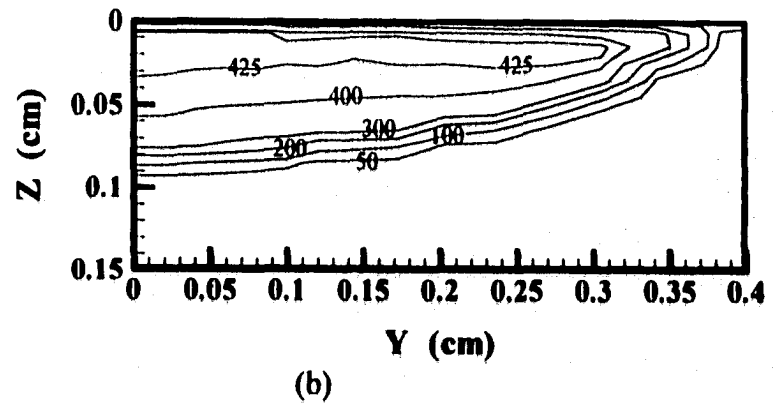
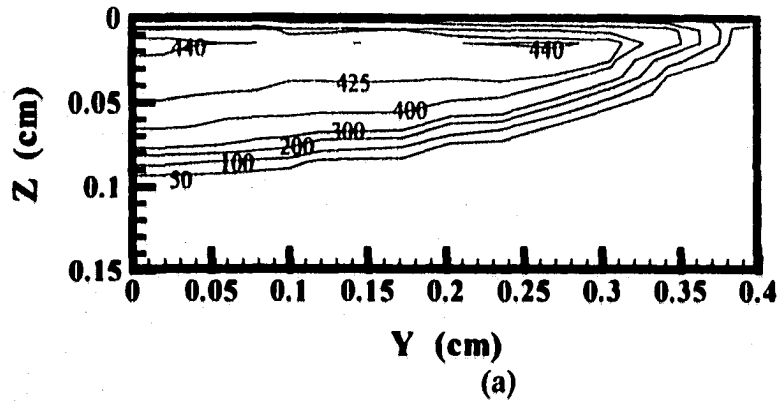


Figure 5.29(a-d). Nitrogen concentration distributions in the weld pool for electron temperature distributions across the weld pool ranging between (a) 3500 and 3250 K, (b) 3250 and 3000 K, (c) 3000 and 2750 K, and (d) 2750 and 2500 K, with a 10% N_2 addition to the shielding gas.

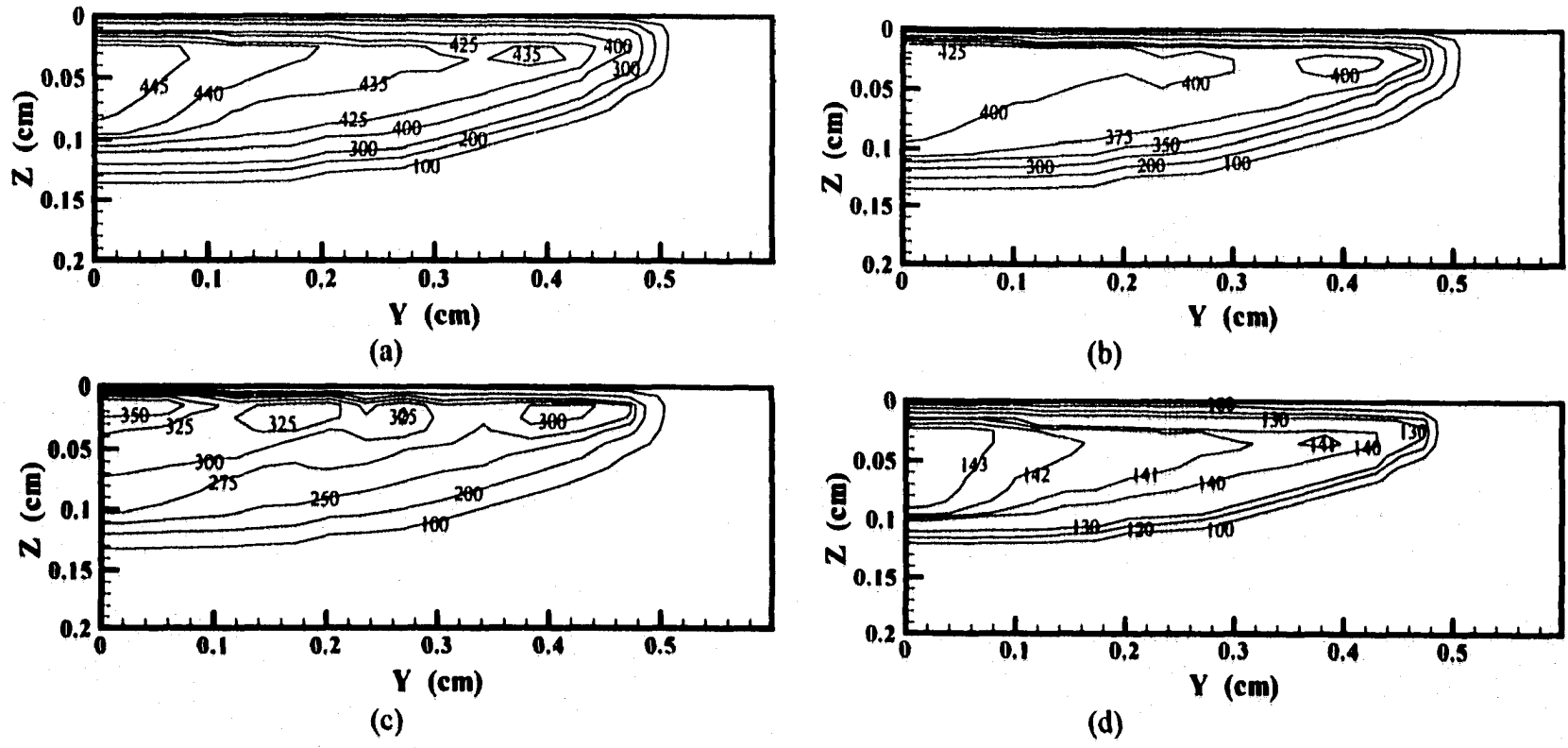


Figure 5.30(a-d). Nitrogen concentration distributions in the weld pool for electron temperature distributions across the weld pool ranging between (a) 3500 and 3250 K, (b) 3250 and 3000 K, (c) 3000 and 2750 K, and (d) 2750 and 2500 K, with a 10% N₂ addition to the shielding gas and a travel speed of 0.423 cm/sec.

Figures 5.31(a-d) and 5.32(a-d) show the effects of changes in the nitrogen addition to the shielding gas at electron temperatures between 2750 and 2500 K at each travel speed. With increasing nitrogen additions to the shielding gas, both the monatomic nitrogen partial pressure above the weld pool and the nitrogen concentrations in the weld pool increase. These increased nitrogen concentrations correspond to increases in the nitrogen concentrations on the weld pool surface. Therefore, a relationship between the monatomic nitrogen partial pressure above the weld pool, the nitrogen concentration on the weld pool surface, and the nitrogen concentration in the weld pool interior can be assumed.

The overall nitrogen concentration in the weld pool is calculated by the integration of the nitrogen concentration across the weld pool cross section at a point in time after which the liquid metal in the weld pool has solidified. Table 5.9 and Figures 5.33 and 5.34 compare the experimental and calculated nitrogen concentrations in the fusion zone for each travel speed with several electron temperature distributions and nitrogen additions to the shielding gas. In general, these calculated nitrogen concentrations are far in excess of Sieverts' Law calculations and increase with both increasing electron temperatures and nitrogen additions to the shielding gas. At higher electron temperatures, though, the calculated nitrogen concentrations do not increase with increasing nitrogen additions to the shielding gas, as shown in each figure for electron temperatures between 3250 and 3000 K.

These differences in the calculated nitrogen concentrations depend on the nitrogen surface concentrations. At high electron temperatures, the nitrogen surface concentrations reach saturation. Low electron temperatures, on the other hand, produce nitrogen concentrations on the weld pool surface far below nitrogen saturation levels. The weld pool can therefore accept more nitrogen, which in this case is supplied by increases in the nitrogen addition to the shielding gas. At both travel speeds, though, the calculated nitrogen concentrations in the weld pool consistently fall below the experimental results.

This disparity between the experimental and modeled results can be explained, in part, by the assumptions in the model concerning the nitrogen desorption reaction. In these calculations, the nitrogen desorption reaction is assumed to occur at the nitrogen

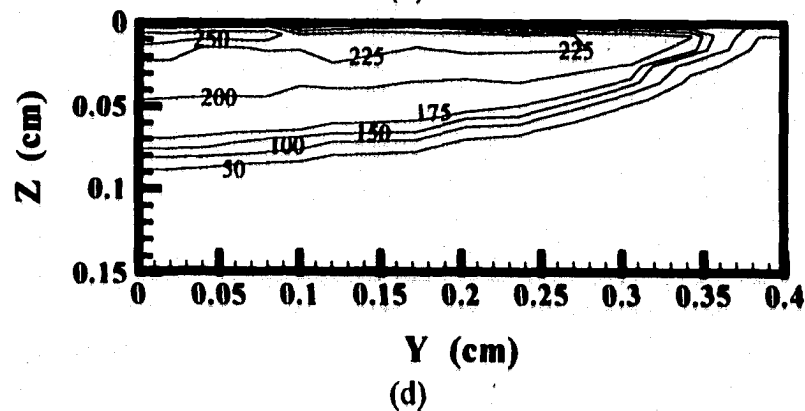
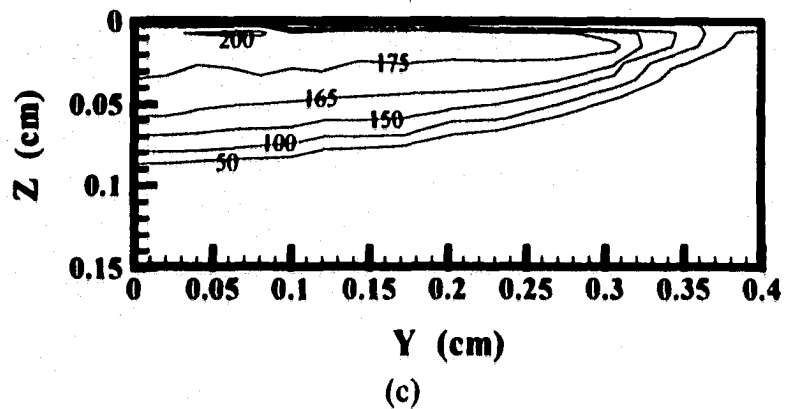
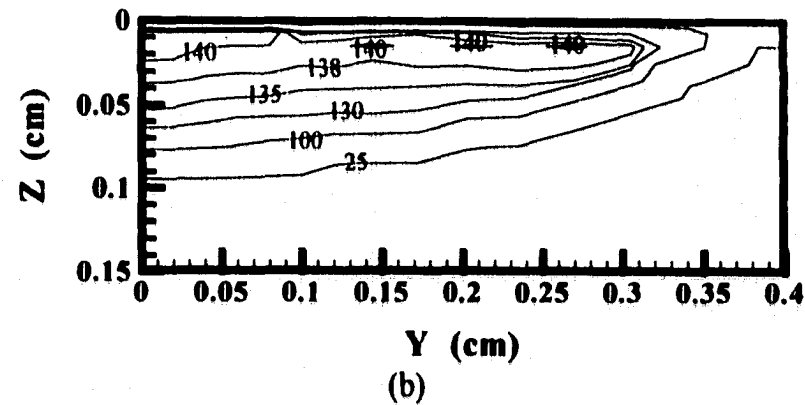
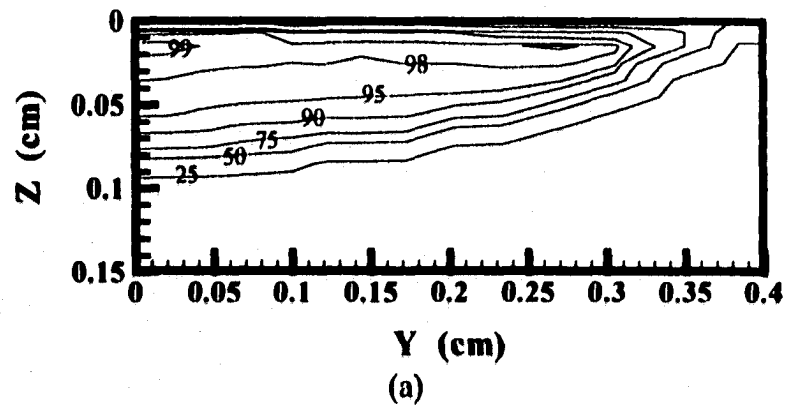


Figure 5.31(a-d). Nitrogen concentration distributions in the weld pool for an electron temperature distribution across the weld pool surface between 2750 and 2500 K for (a) 5% N_2 , (b) 10% N_2 , (c) 15% N_2 , and (d) 20% N_2 additions to the shielding gas for a travel speed of 0.847 cm/sec.

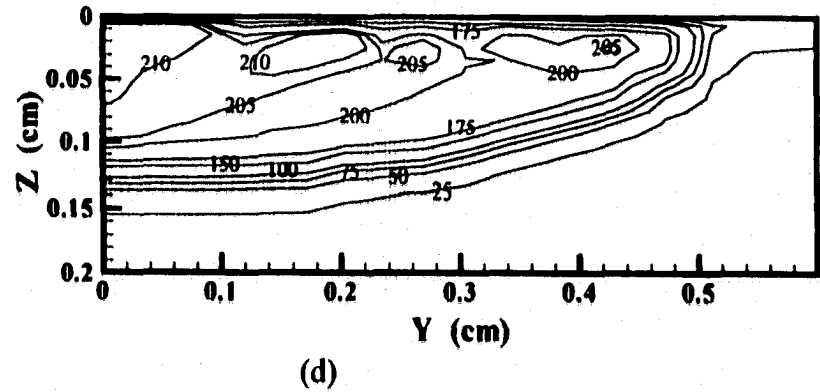
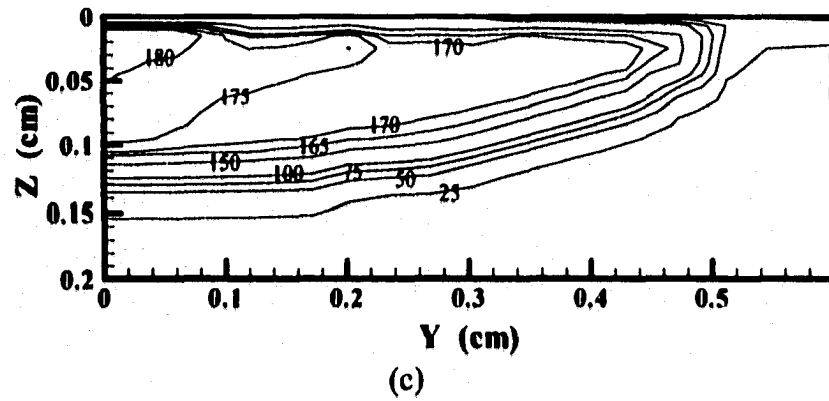
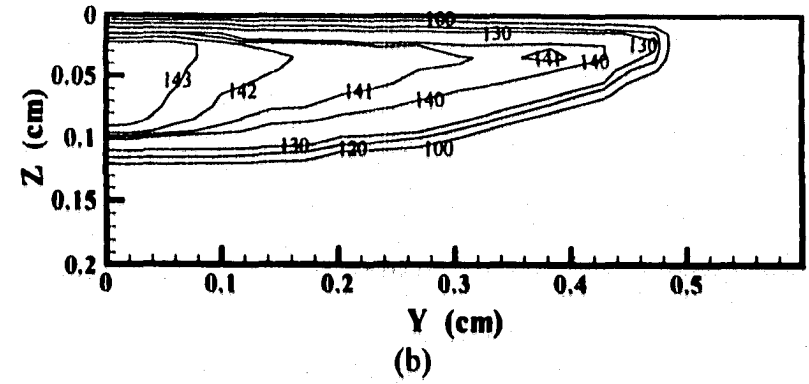
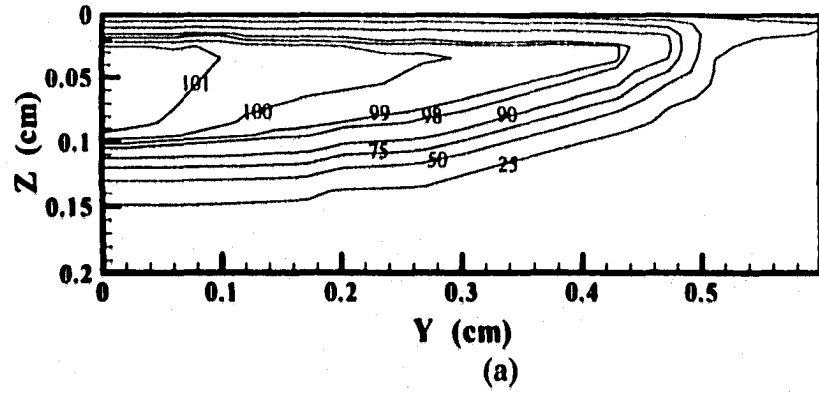


Figure 5.32(a-d). Nitrogen concentration distributions in the weld pool for an electron temperature distribution across the weld pool surface between 2750 and 2500 K for (a) 5% N_2 , (b) 10% N_2 , (c) 15% N_2 , and (d) 20% N_2 additions to the shielding gas for a travel speed of 0.423 cm/sec.

Table 5.9. Comparison between experimental and computed nitrogen concentrations in the fusion zone. Calculations are performed with several electron temperature distributions above the weld pool and an enhancement factor of 20.

Nitrogen Addition to the Shielding Gas	Experimental Nitrogen Concentrations	Calculated Nitrogen Concentration (ppm)			
		3500 – 3250 K	3250 – 3000 K	3000 – 2750 K	2750 – 2500 K
Condition #1					
5% N ₂	382.5	368.6	339.6	214.0	87.1
10% N ₂	508	372.1	360.5	289.4	122.1
15% N ₂	495	372.8	368.1	319.8	154.1
20% N ₂	600	373.4	371.4	337.3	185.5
Condition #2					
5% N ₂	480.5	386.5	341.8	207.3	93.8
10% N ₂	615	399.5	371.6	288.5	132.3
15% N ₂	716	324.1	385.4	404.1	165.2
20% N ₂	558.5	346.2	393.0	406.3	196.6

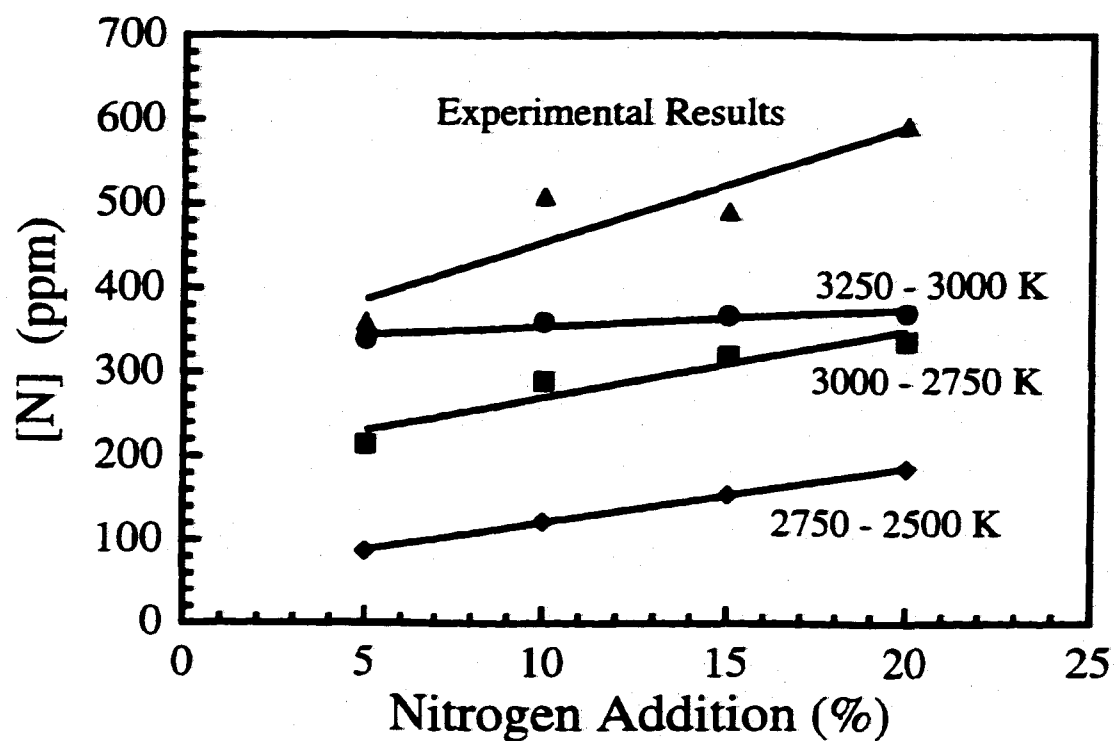


Figure 5.33. Comparison between experimental and modeled nitrogen concentrations in the weld pool for both high and low assumed electron temperatures above the weld pool for a travel speed of 0.847 cm/sec.

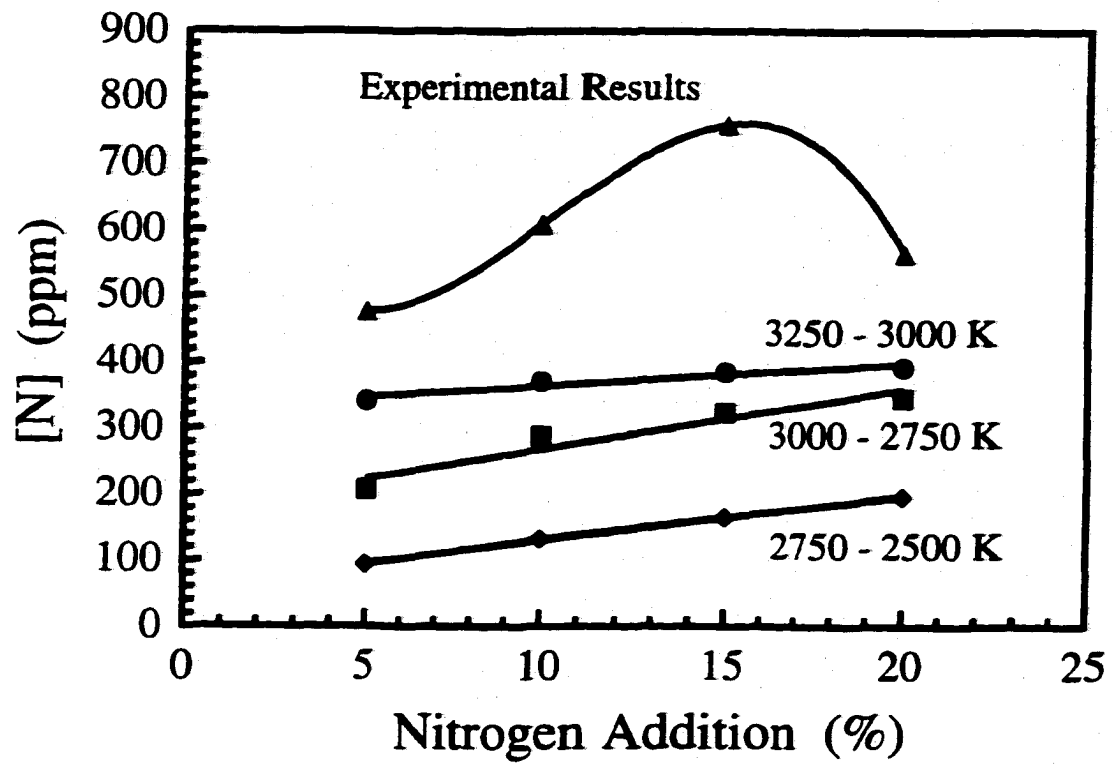


Figure 5.34. Comparison between experimental and modeled nitrogen concentrations in the weld pool for both high and low assumed electron temperatures above the weld pool for a travel speed of 0.423 cm/sec.

concentration on the weld pool surface equivalent to the values calculated by Sieverts' Law at the surface temperature and a nitrogen partial pressure of 1 atm. On the other hand, the nitrogen desorption reaction requires a degree of nitrogen supersaturation in the liquid metal in order to occur. The effect of several levels of nitrogen supersaturation in the weld metal on the resulting nitrogen concentration in the weld metal is examined.

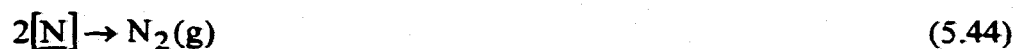
5.3.5.2 Level of Nitrogen Supersaturation in the Weld Pool

The reaction mechanism for the removal of carbon in solution in the liquid iron is shown in Equation (5.43).



It has been noted^{54,55} that during the decarburization of iron melts, carbon concentrations can be up to 15 times higher than those predicted by equilibrium calculations. The removal of carbon from the melt through the evolution of CO(g) from liquid iron has been found to be dependent upon the availability of nucleation sites for bubble formation within the melt. As the number of heterogeneous nucleation sites increases, the level of carbon supersaturation in the melt decreases.

When this example is applied to the question of the amount of nitrogen present in the weld pool, it is found that the desorption of the dissolved nitrogen plays an important role in determining the nitrogen concentrations in the weld pool. Desorption of nitrogen can also be assumed to occur via bubble formation in the weld pool and is governed by the following chemical reaction:



In order for these nitrogen bubbles to nucleate, the liquid iron must be supersaturated with nitrogen. This level of supersaturation is not well defined. It depends in part on the number of heterogeneous nucleation sites for nitrogen bubbles to form. Given the char-

acteristics of the weld pool, there is no shortage of such sites. For example, bubbles can nucleate on the weld pool surface or at locations along the liquid-solid interface.

The presence of nitrogen supersaturation has been considered in the existing model for an electron temperature distribution between 3250 and 3000 K. Figures 5.35(a-d) and 5.36(a-d) show the calculated nitrogen concentrations on the weld pool surface for several nitrogen supersaturation levels and each set of welding parameters. As the nitrogen supersaturation level is increased, the nitrogen concentrations on the weld pool surface, in turn, increase. No change in the nitrogen concentration distribution on the weld pool surface is observed with increases in the nitrogen addition to the shielding gas.

The resulting nitrogen concentration distributions across the weld pool cross sections have also been calculated. Figures 5.37(a-d) and 5.38(a-d) show these calculated nitrogen concentration distributions for a nitrogen addition to the shielding gas of 10% and an electron temperature distribution between 3250 and 3000 K and each set of welding parameters. There is little difference between the general shape of the nitrogen concentration distribution for each welding condition as the level of nitrogen supersaturation in the melt is increased. On the other hand, the nitrogen concentration levels observed in the weld pool interior significantly increase with an increase in the level of nitrogen supersaturation.

The nitrogen concentration in the weld pool is determined from these calculated nitrogen concentration distributions. Table 5.10 lists the calculated nitrogen concentrations and the nitrogen concentrations calculated at a nitrogen partial pressure of 1 atm. and a temperature of 1873 K for the levels of nitrogen supersaturation discussed in the previous two figures. For each nitrogen addition to the shielding gas, the nitrogen concentration in the weld pool increases with an increasing level of nitrogen supersaturation. No change in the nitrogen concentration, though, is observed with an increase in the nitrogen addition to the shielding gas.

These calculated values compare favorably with the experimental results, as shown in Figures 5.39 and 5.40. In these figures, the experimental results are compared with the calculated nitrogen concentrations for several levels of nitrogen supersaturation in the weld metal for each set of welding parameters, respectively. Unlike previous compari-

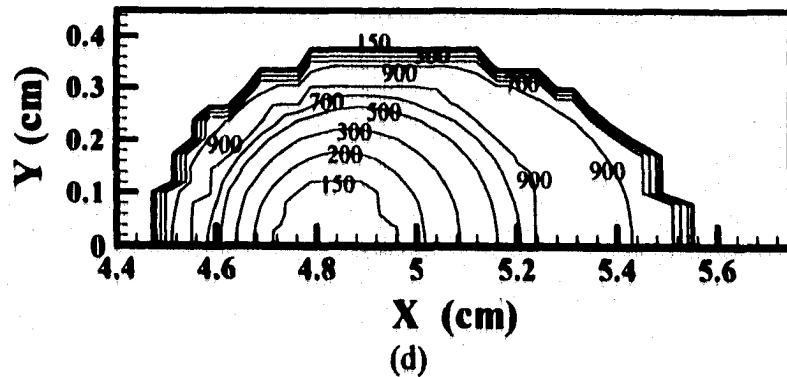
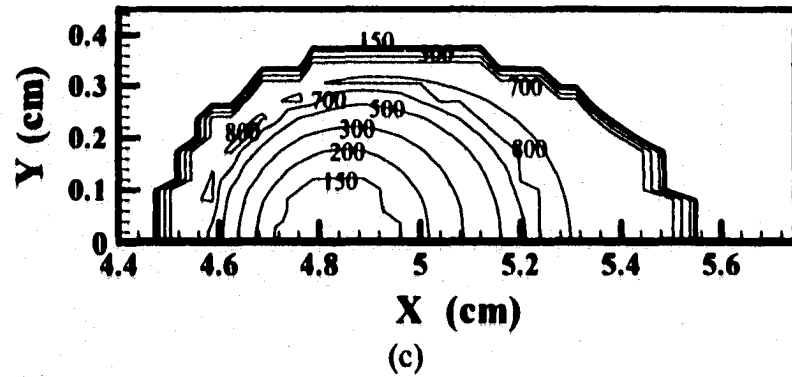
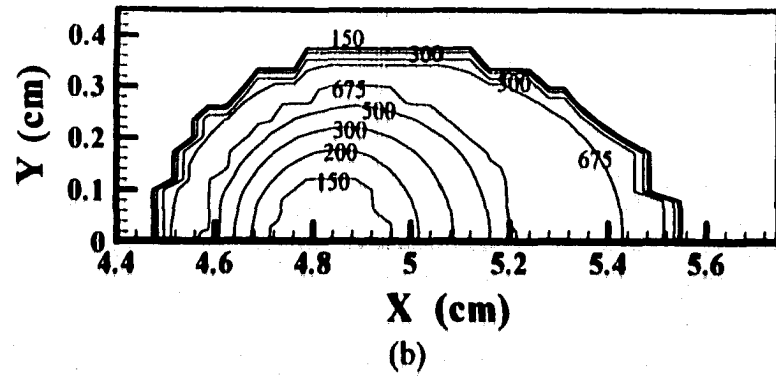
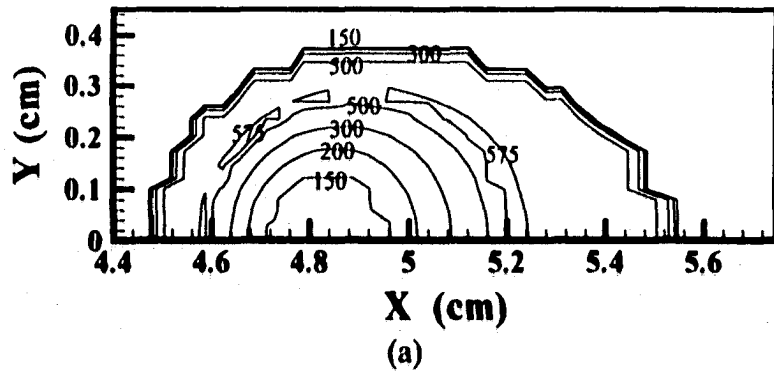
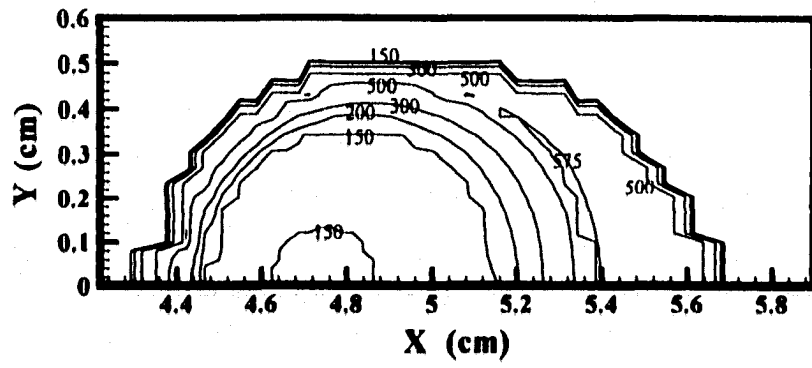
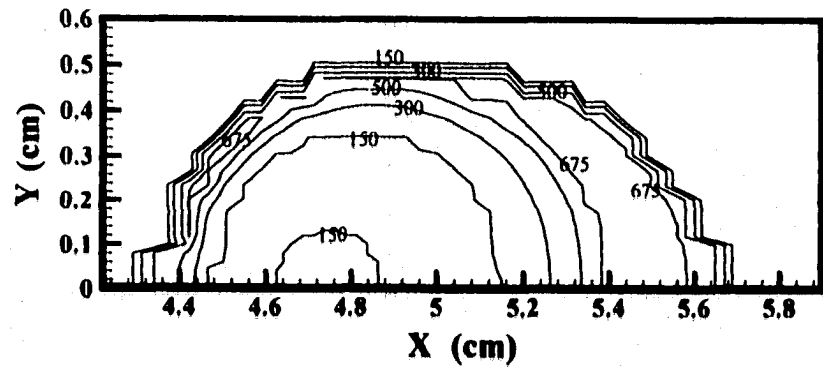


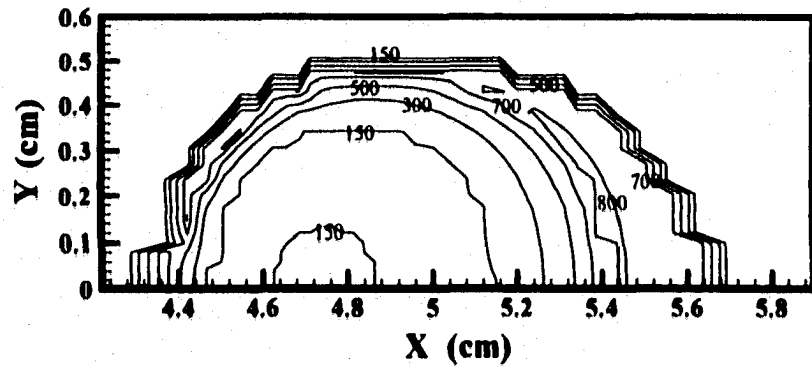
Figure 5.35(a-d). Calculated nitrogen concentrations on the weld pool surface (expressed in ppm) at a travel speed of 0.847 cm/sec and a 10% N₂ addition to the shielding gas at an electron temperature distribution between 3250 and 3000 K for enhancements in the nitrogen supersaturation of (a) 1.25, (b) 1.50, (c) 1.75, (d) 2.00.



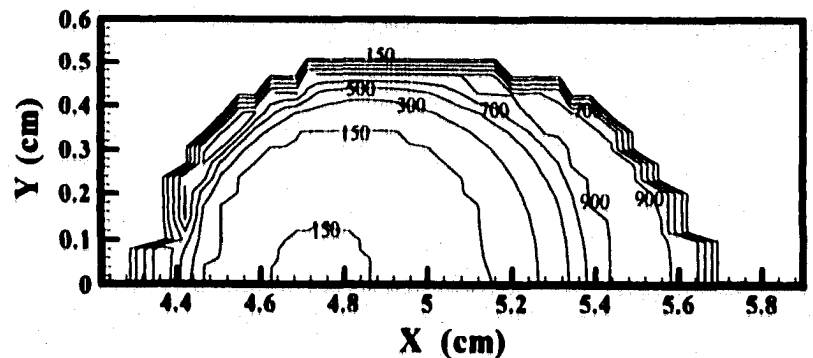
(a)



(b)

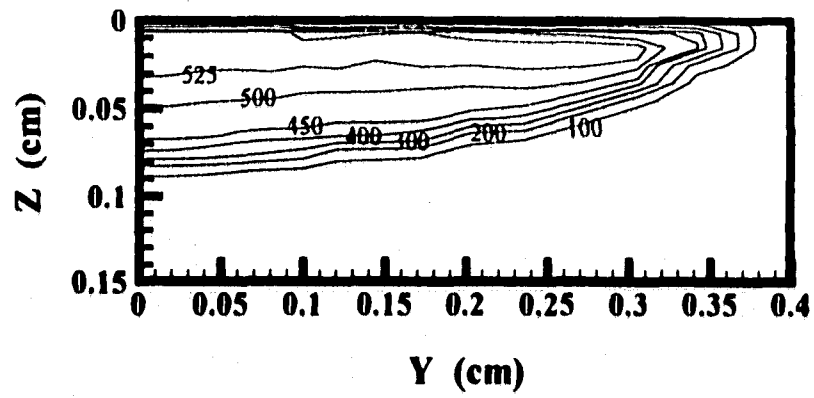


(c)

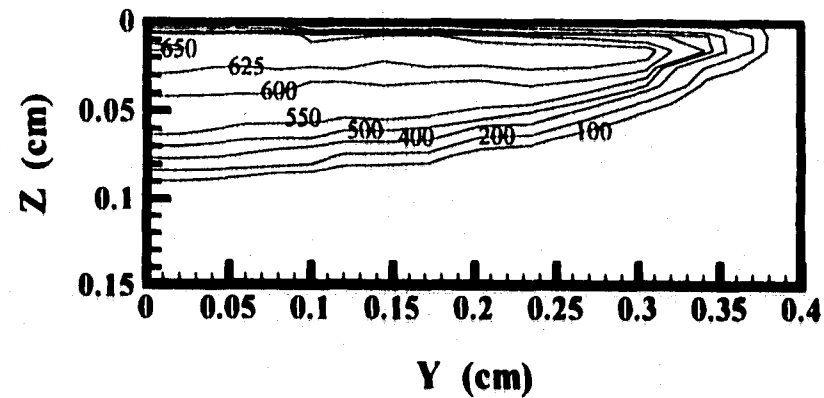


(d)

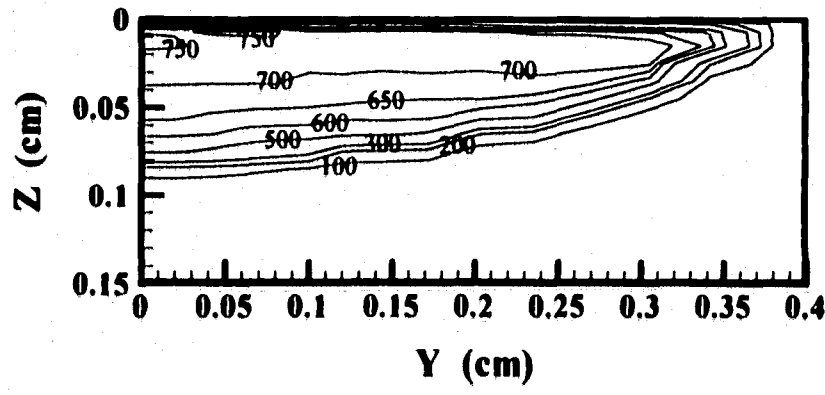
Figure 5.36(a-d). Calculated nitrogen concentrations on the weld pool surface (expressed in ppm) at a travel speed of 0.423 cm/sec and a 10% N₂ addition to the shielding gas at an electron temperature distribution between 3250 and 3000 K for enhancements in the nitrogen supersaturation of (a) 1.25, (b) 1.50, (c) 1.75, (d) 2.00.



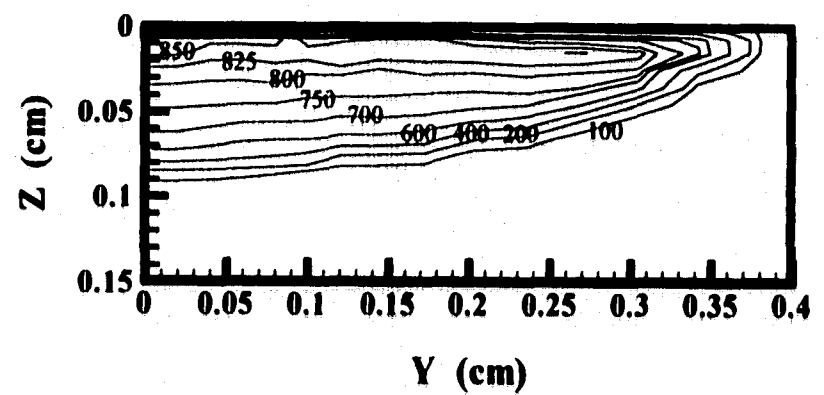
(a)



(b)



(c)



(d)

Figure 5.37(a-d). Calculated nitrogen concentration distributions in the weld pool interior (expressed in ppm) at a travel speed of 0.847 cm/sec and a 10% N₂ addition to the shielding gas for enhancements in the level of nitrogen supersaturation of (a) 1.25, (b) 1.50, (c) 1.75, and (d) 2.00.

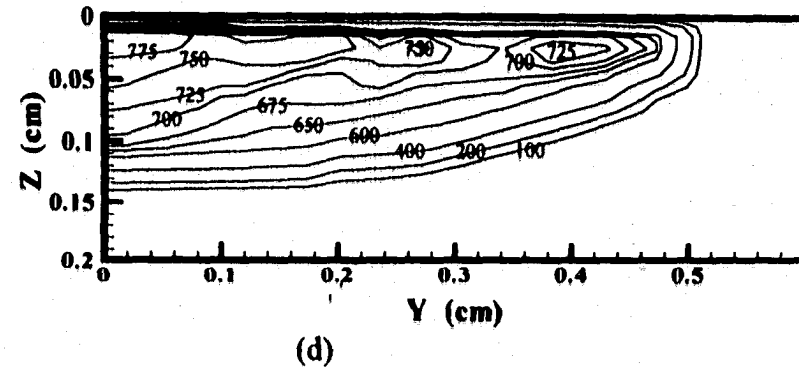
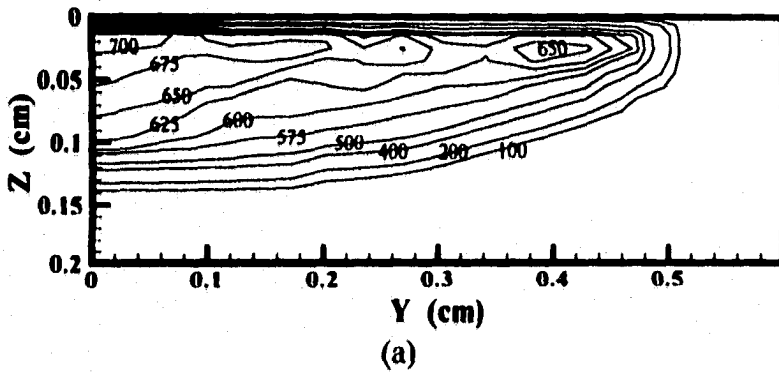
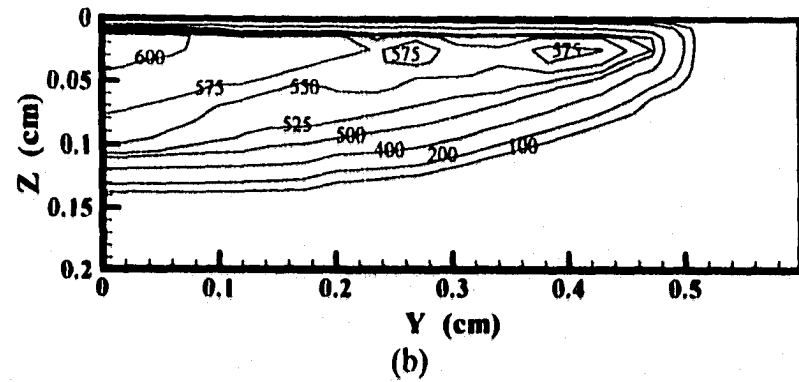
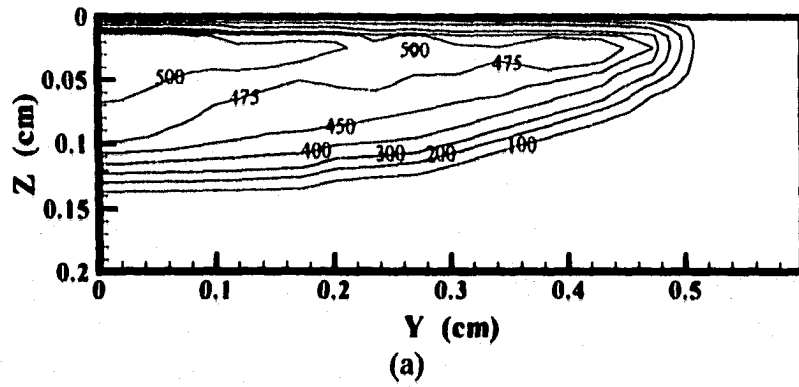


Figure 5.38(a-d). Calculated nitrogen concentration distributions in the weld pool interior (expressed in ppm) at a travel speed of 0.423 cm/sec and a 10% N_2 addition to the shielding gas for enhancements in the level of nitrogen supersaturation of (a) 1.25, (b) 1.50, (c) 1.75, and (d) 2.00.

Table 5.10. Summary of calculated nitrogen concentrations for several levels of nitrogen supersaturation with an electron temperature distribution between 3250 and 3000 K.

Enhancement Factor	[N] (ppm) (T=1873 K)	Nitrogen Addition			
		5% N ₂	10% N ₂	15% N ₂	20% N ₂
<i>Welding Condition #1</i>					
1.00	448	339.6	360.5	368.1	371.4.8
1.25	560	410.2	442.1	454.3	459.9
1.50	672	475.7	520.5	538.3	547.0
1.75	784	536.2	595.6	620.5	632.2
2.00	896	593.1	669.0	700.2	716.1
<i>Welding Condition #2</i>					
1.00	448	341.8	371.6	385.4	393.0
1.25	560	409.5	451.2	471.3	482.2
1.50	672	471.2	527.4	553.8	569.4
1.75	784	528.1	600.8	634.1	654.0
2.00	896	582.5	671.0	711.7	736.1

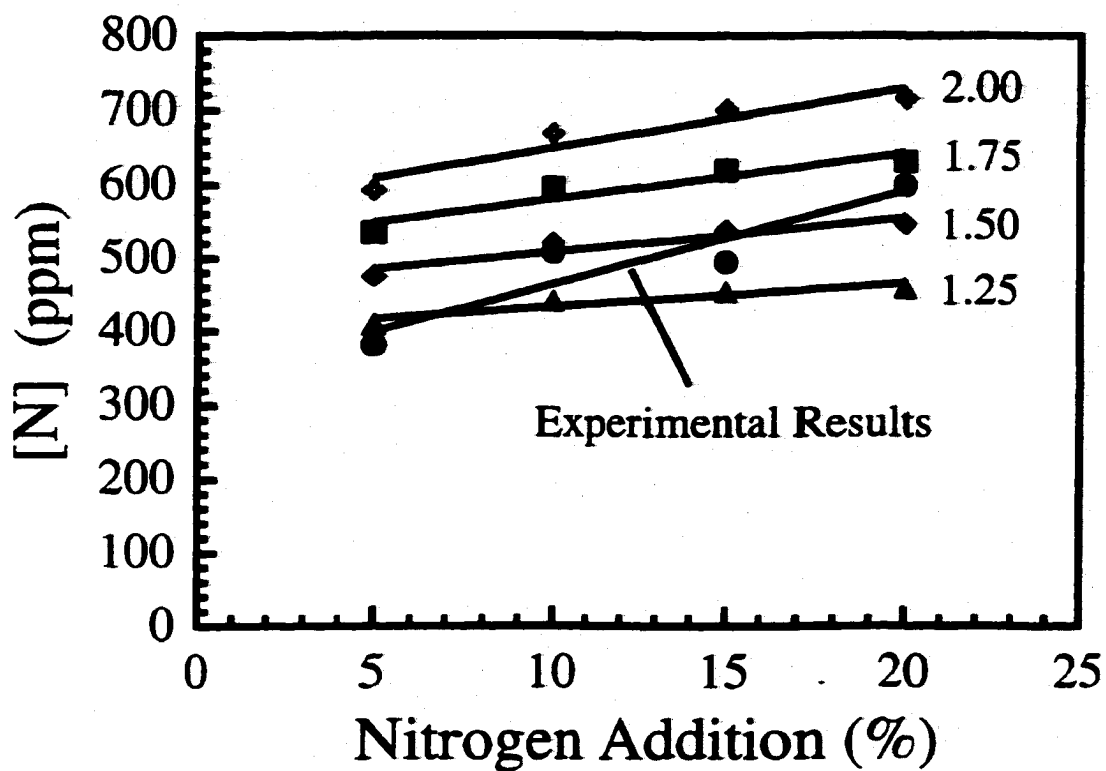


Figure 5.39. Comparison between experimental and calculated nitrogen concentrations over a range of nitrogen additions to the shielding gas for several levels of nitrogen supersaturation for a travel speed of 0.847 cm/sec and an electron temperature range between 2750 and 3000 K.

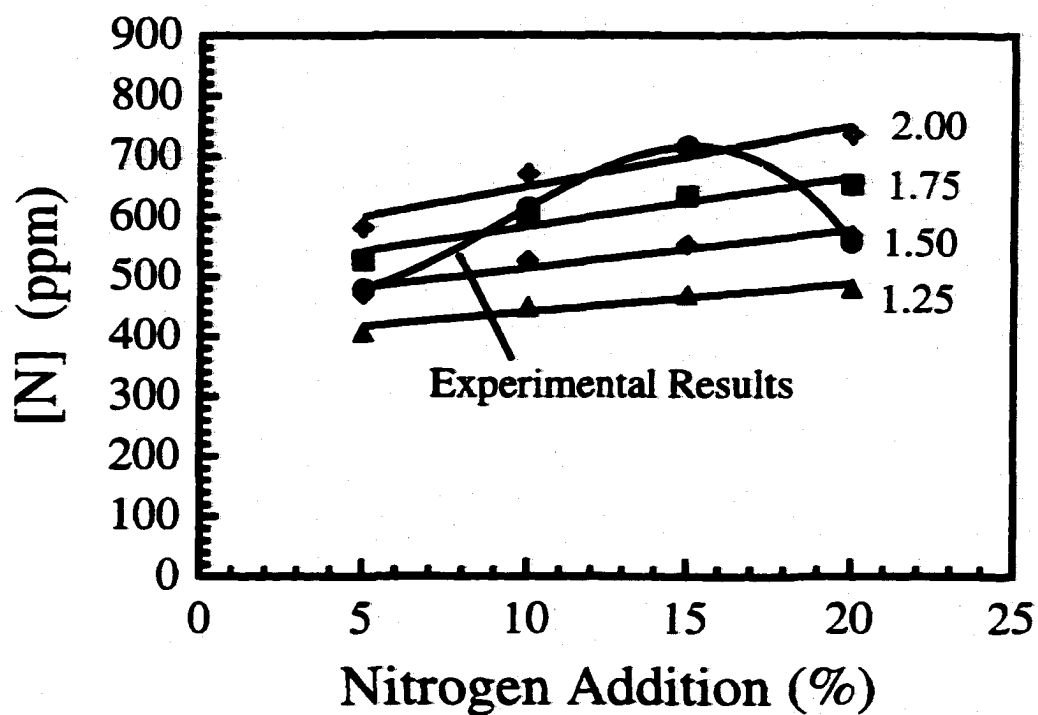


Figure 5.40. Comparison between experimental and calculated nitrogen concentrations over a range of nitrogen additions to the shielding gas for several levels of nitrogen supersaturation for a travel speed of 0.847 cm/sec and an electron temperature range between 3000 and 3250 K.

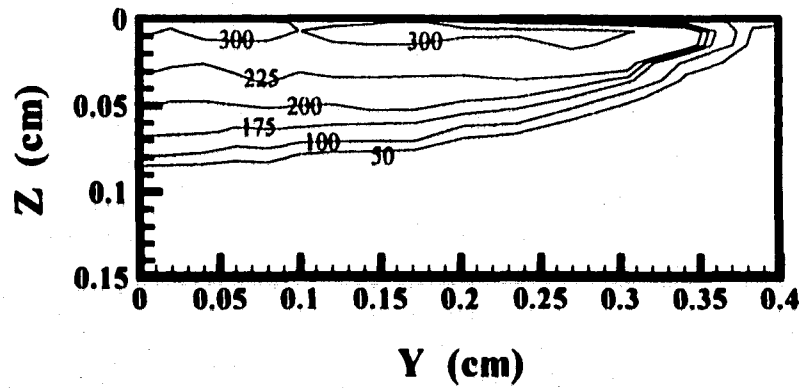
sons without a level of nitrogen supersaturation applied to the calculated results, these modeled results fall in the same range of values as those observed experimentally. In most cases, enhancements between 50 and 75% produce nitrogen concentrations on the same level as those observed experimentally, regardless of the welding parameters. Additionally, the nitrogen concentration increases with higher additions of nitrogen to the shielding gas for both travel speeds analyzed here, thus following the same general trends as the experimental results.

5.3.5.3 Effect Of Changes In The Level of Turbulence in the Weld Pool

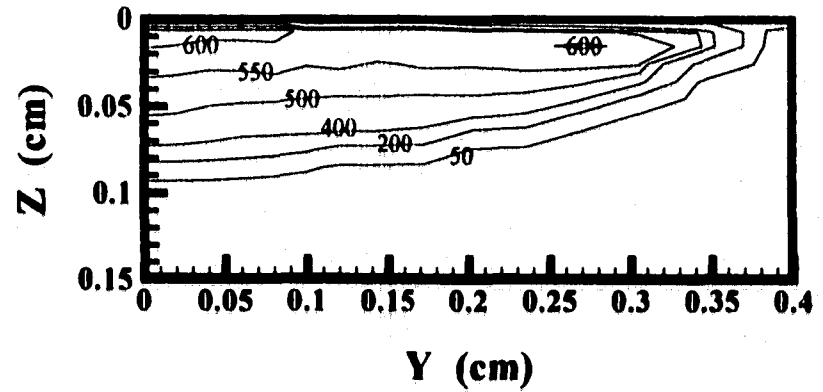
In the calculations discussed in the previous sections, the presence of turbulence in the weld pool has been assumed. Little is known, though, about the quantitative role of turbulence in the weld pool on the resulting nitrogen concentration distribution. One way to take into account this agitated or turbulent fluid flow is to enhance the diffusion coefficient. This concept is based on previous work which took into account the role of convection in the weld pool and its effect on heat transfer by enhancing the thermal conductivity value.³⁵ Changes in the diffusion coefficient may shed further light on the level of turbulence in the weld pool and its effect on the resulting nitrogen concentration.

Calculations have been made with several mass transport enhancement factors for each travel speed, nitrogen supersaturation levels between 50 and 75%, and electron temperatures between 3250 and 3000 K. Figures 5.41(a-d) and 5.42(a-d) show the final calculated nitrogen concentration distributions in the weld pool at each travel speed for several mass transport enhancement factors with electron temperatures between 3250 and 3000 K and a nitrogen supersaturation of 50%. With increases in the enhancement factor, nitrogen concentrations increase throughout the weld pool, and especially along the weld centerline. Changes in the welding parameters and the nitrogen supersaturation levels do not produce any significant changes in the general nitrogen concentration distribution in the weld pool under these conditions.

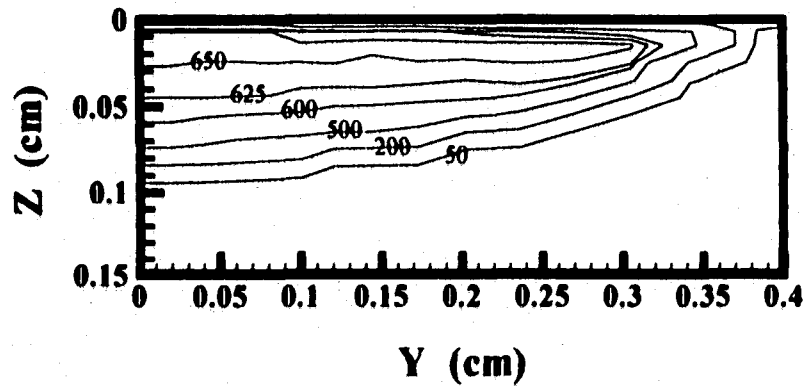
The calculated residual nitrogen concentrations for several diffusion coefficients with electron temperatures between 3250 and 3000 K are listed in Tables 5.11 and 5.12 for each travel speed and nitrogen supersaturations of 50 and 75%. Figures 5.43 and 5.44



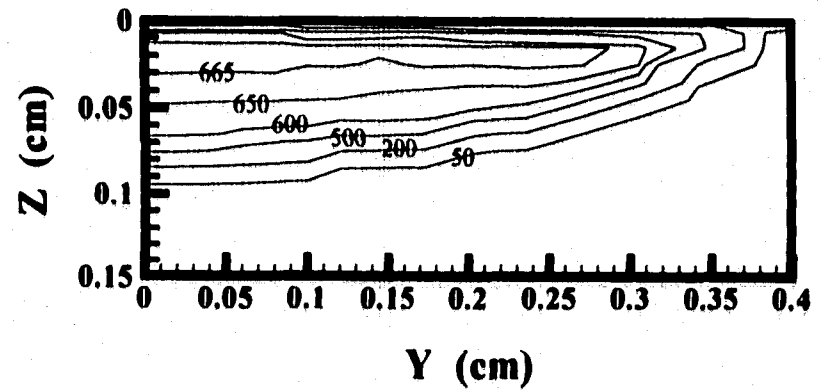
(a)



(b)

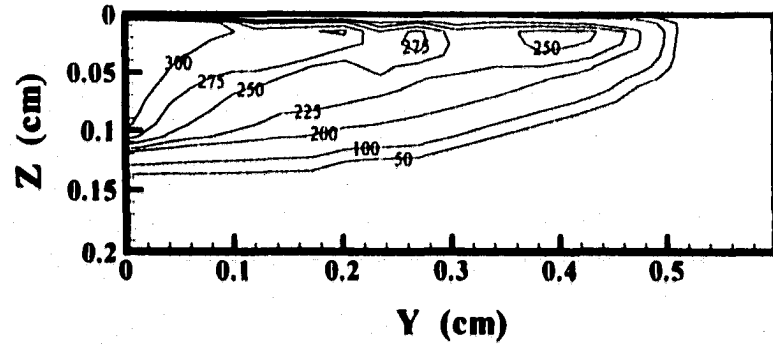


(c)

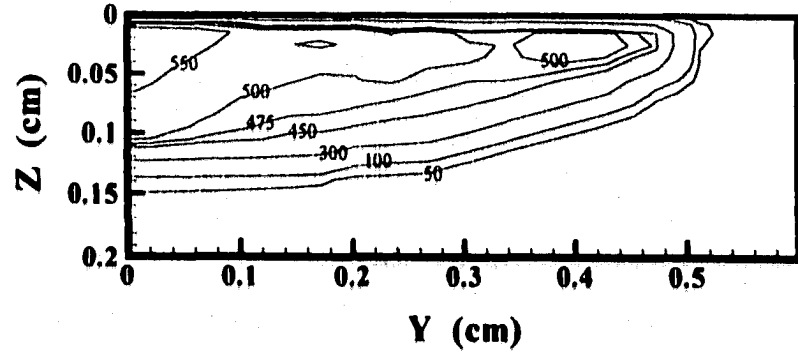


(d)

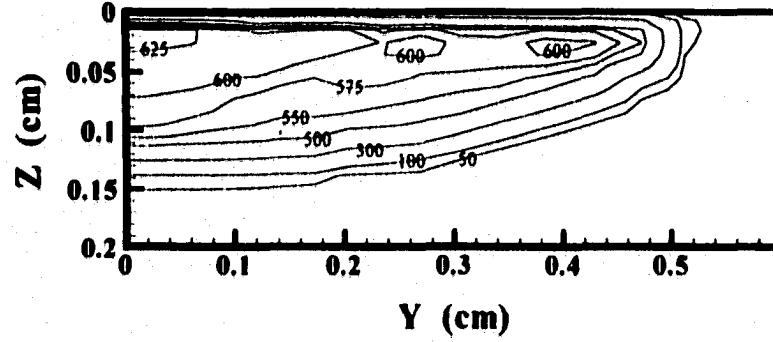
Figure 5.41(a-d). Summary of final nitrogen concentration distributions for several mass transport enhancement factors for a travel speed of 0.847 cm/sec and a 10% N₂ addition to the shielding gas for electron temperatures ranging from 3250 to 3000 K. (a) 1, (b) 10, (c) 30 and (d) 50. A nitrogen supersaturation level of 50% is assumed.



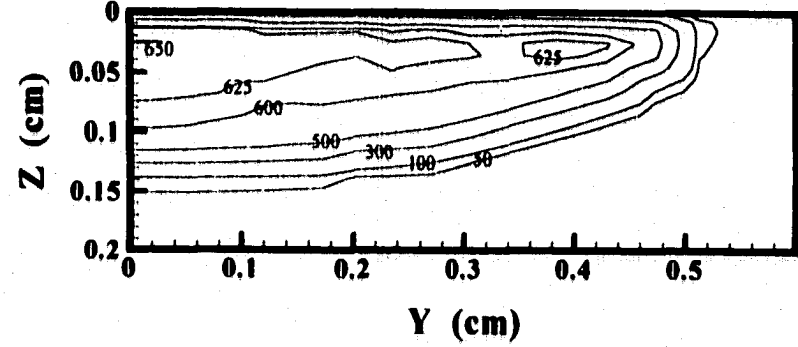
(a)



(b)



(c)



(d)

Figure 5.42(a-d). Summary of final nitrogen concentration distributions for several mass transport enhancement factors for a travel speed of 0.423 cm/sec and a 10% N₂ addition to the shielding gas for electron temperatures ranging from 3250 to 3000 K. (a) 1, (b) 10, (c) 30, and (d) 50. A nitrogen supersaturation level of 50% is assumed.

Table 5.11. Summary of mass transport enhancement factors used in the calculation of the nitrogen concentration distribution in the weld metal for an electron temperature distribution ranging from 3250 to 3000 K and a nitrogen supersaturation of 50%.

Enhancement Factor	D_N (cm ² /sec)	Final Nitrogen Concentration (ppm)			
		5% N ₂	10% N ₂	15% N ₂	20% N ₂
<i>Condition #1</i>					
1	1.100×10^{-4}	174.2	204.4	220.9	231.4
5	5.500×10^{-4}	342.6	387.2	407.3	418.2
10	1.100×10^{-3}	414.5	461.6	481.7	492.1
20	2.200×10^{-3}	475.7	520.5	538.3	547.0
30	3.300×10^{-3}	504.2	545.1	560.3	567.4
40	4.400×10^{-3}	520.5	555.8	571.1	577.1
50	5.500×10^{-3}	530.9	565.8	577.3	582.4
<i>Condition #2</i>					
1	1.10×10^{-4}	216.0	264.5	294.0	313.9
5	5.50×10^{-4}	371.3	435.1	469.4	490.6
10	1.10×10^{-3}	424.7	487.3	518.9	538.0
20	2.20×10^{-3}	471.2	527.4	553.8	569.4
30	3.30×10^{-3}	497.9	548.2	570.4	583.2
40	4.40×10^{-3}	517.1	562.1	581.0	591.5
50	5.50×10^{-3}	531.5	572.2	588.3	597.0

Table 5.12. Summary of mass transport enhancement factors used in the calculation of the nitrogen concentration distribution in the weld metal for an electron temperature distribution ranging from 3250 to 3000 K and a nitrogen supersaturation of 75%.

Enhancement Factor	D_N (cm ² /sec)	Final Nitrogen Concentration (ppm)			
		5% N ₂	10% N ₂	15% N ₂	20% N ₂
<i>Condition #1</i>					
1	1.100×10^{-4}	191.0	227.6	248.4	261.1
5	5.500×10^{-4}	381.7	438.8	465.9	480.0
10	1.100×10^{-3}	464.4	525.6	553.3	566.9
20	2.200×10^{-3}	536.2	595.6	620.5	632.2
30	3.300×10^{-3}	570.4	625.6	647.3	657.1
40	4.400×10^{-3}	590.4	641.8	660.9	669.1
50	5.500×10^{-3}	603.4	651.6	668.7	675.8
<i>Condition #2</i>					
1	1.10×10^{-4}	234.5	292.3	326.6	350.9
5	5.50×10^{-4}	410.0	489.8	531.1	558.1
10	1.10×10^{-3}	472.3	551.8	590.6	615.0
20	2.20×10^{-3}	528.1	600.8	634.1	654.0
30	3.30×10^{-3}	561.0	626.9	655.6	671.9
40	4.40×10^{-3}	584.8	644.8	669.5	683.1
50	5.50×10^{-3}	602.9	657.8	679.3	690.7

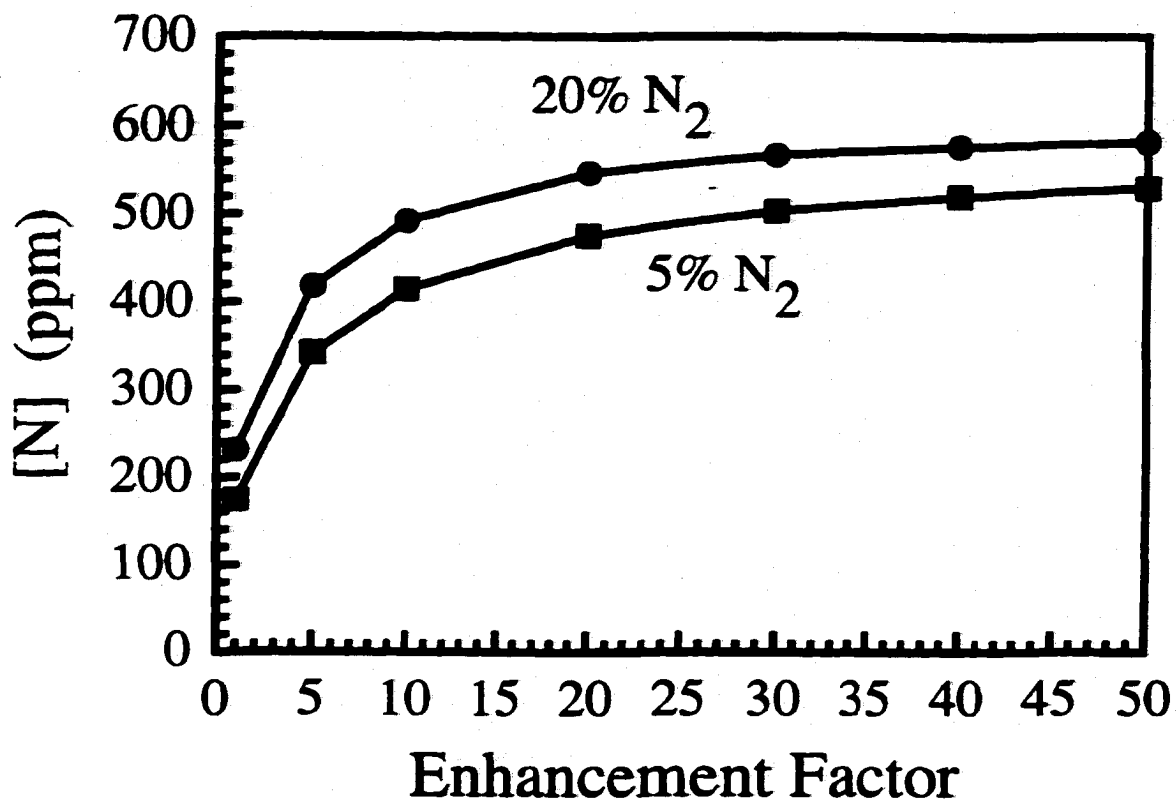


Figure 5.43. Summary of calculated nitrogen concentrations for a number of enhancement factors for a travel speed of 0.847 cm/sec and 5% and 20% N₂ additions to the shielding gas and an electron temperature distribution above the weld pool ranging from 3250 to 3000 K and a 50% nitrogen supersaturation level.

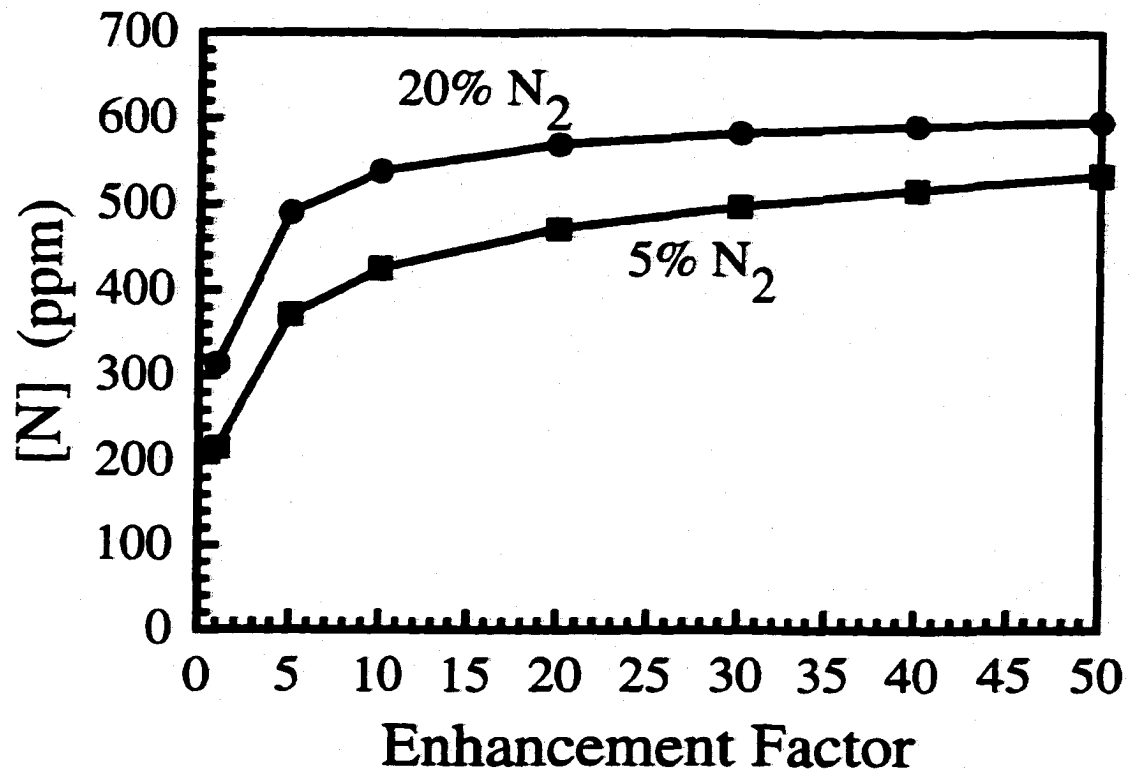


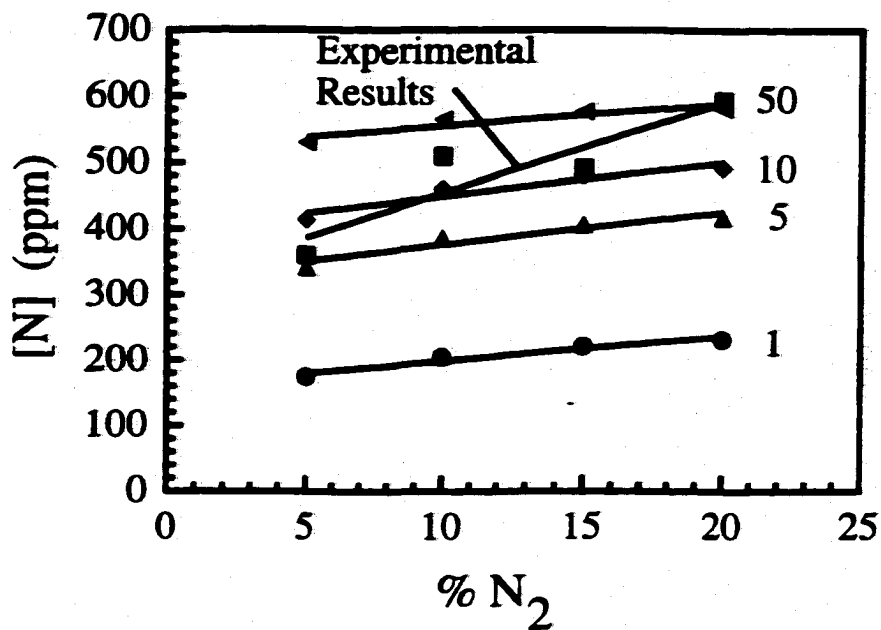
Figure 5.44. Summary of calculated nitrogen concentrations for a number of enhancement factors for a travel speed of 0.423 cm/sec and 5% and 20% N₂ additions to the shielding gas and an electron temperature distribution above the weld pool ranging from 3250 to 3000 K and a 50% nitrogen supersaturation level.

summarize the calculated nitrogen concentrations in the weld pool as a function of the enhancement factor for 5% and 20%N₂ additions to the shielding gas for each travel speed and a nitrogen supersaturation of 50%. At each travel speed and level of nitrogen supersaturation, the effect of increasing the nitrogen diffusion coefficient on the residual nitrogen concentration is the same. The addition of more nitrogen to the shielding gas has little effect on the calculated nitrogen concentrations over the range of diffusion coefficients. On the other hand, the calculated nitrogen concentrations significantly change with higher diffusion coefficients and a constant nitrogen addition to the shielding gas.

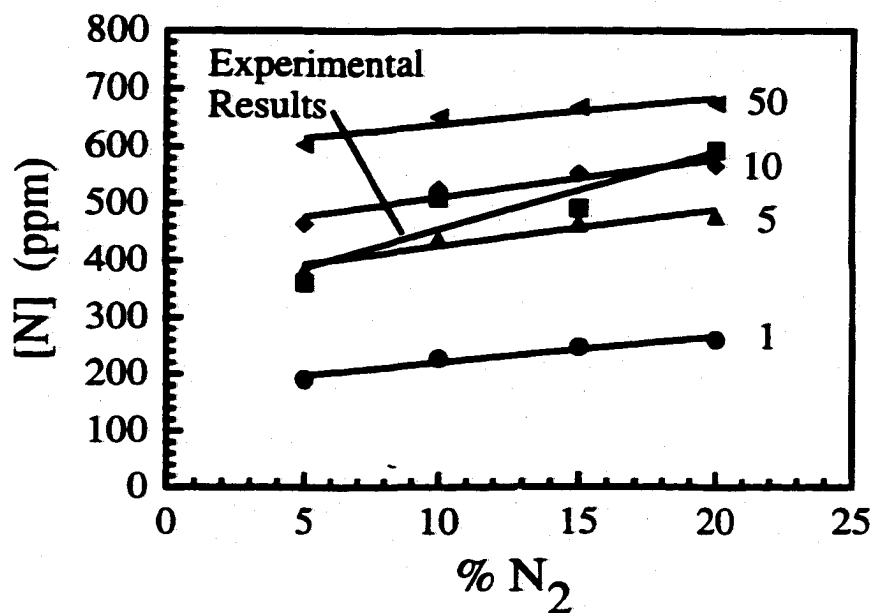
A comparison between the calculated and experimental nitrogen concentrations has also been made at each travel speed and nitrogen supersaturation level in Figures 5.45(a&b) and 5.46(a&b). In each case, changes in the nitrogen diffusion coefficient affect the resulting residual nitrogen concentration. For example, the nitrogen concentrations with no enhancement in the nitrogen diffusion coefficient are significantly lower than the experimental results. When the nitrogen diffusion coefficient is enhanced, the calculated residual nitrogen concentrations fall in the range of the experimental results. At enhancements of 10 and above, though, the nitrogen concentrations do not vary as significantly and there is little difference in the resulting nitrogen concentrations. Taken as a whole, turbulence is an important component in the calculation of the nitrogen concentration, but the choice of the level of enhancement in the diffusion coefficient appears insignificant, as long as the value is 10 or above.

5.4 OVERVIEW

Nitrogen concentrations in iron and steel weldments exposed to nitrogen-containing shielding gases during GTA welding are far in excess of Sieverts' Law calculations. Any significant understanding of nitrogen dissolution is hindered by the interaction of a nitrogen-containing plasma phase with a vigorously circulating weld pool. A model to calculate the nitrogen concentration in the weld metal during the GTA welding of iron has been developed here. This model is based, in part, on the calculation of the turbulent, steady-state velocity and temperature fields in the weld pool, which are determined by the solution of the equations of conservation of mass, momentum, and energy in three-

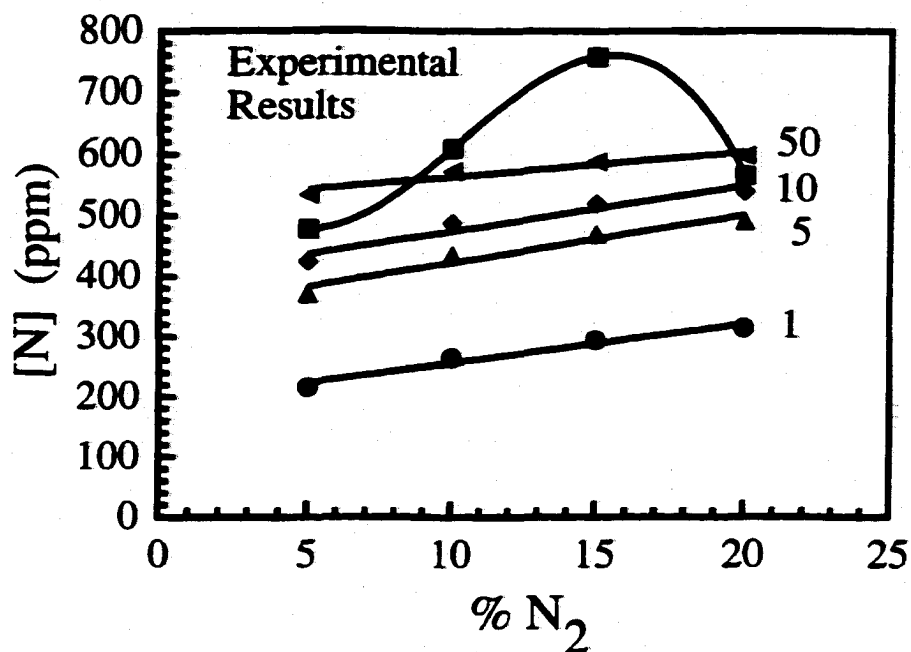


(a)

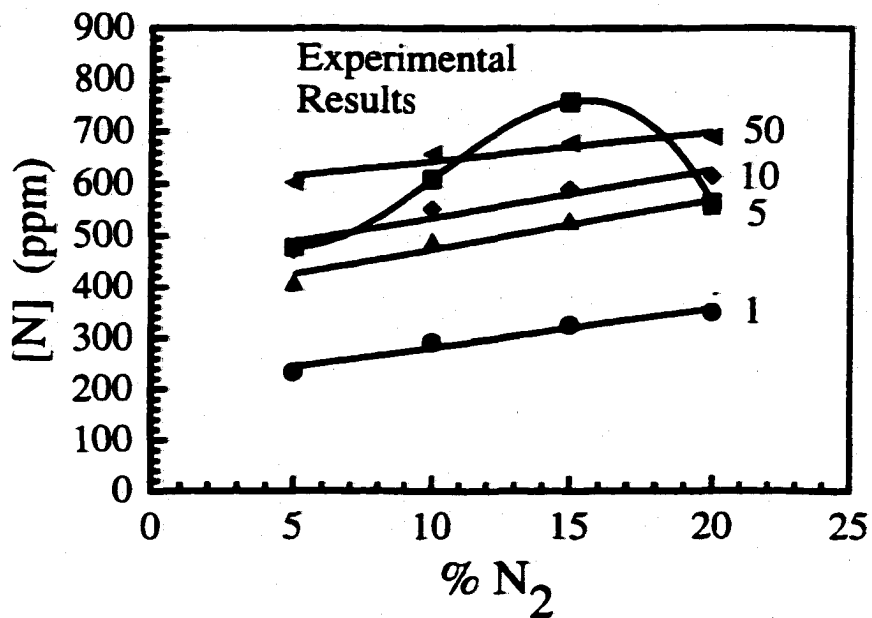


(b)

Figure 5.45(a&b). Comparison between experimental nitrogen concentrations and modeled results for several mass transport enhancement factors at electron temperatures between 3250 and 3000 K for a travel speed of 0.847 cm/sec and nitrogen supersaturation levels of (a) 50% and (b) 75% greater than the nitrogen equilibrium concentration.



(a)



(b)

Figure 5.46(a&b). Comparison between experimental nitrogen concentrations and modeled results for several mass transport enhancement factors at electron temperatures between 3250 and 3000 K for a travel speed of 0.423 cm/sec and nitrogen supersaturation levels of (a) 50% and (b) 75% greater than the nitrogen equilibrium concentration.

dimensions. Based on these results, nitrogen concentrations in the weld pool can then be calculated in a transient manner. The evolution of nitrogen concentration in the weld pool as a function of time can be then determined, and the residual nitrogen concentration in the weld pool is based on the nitrogen concentration distribution in the weld metal at the time of solidification.

The calculation of the nitrogen concentrations in the weld pool are based on the combination of calculations involving the plasma phase above the weld pool, the interface between the weld pool surface and the plasma phase, and the weldment interior. Monatomic nitrogen partial pressures are calculated as a function of the electron temperatures in the plasma phase using the calculation methodology discussed in Chapter 3. Characteristics of the plasma phase, such as the electron temperature distribution, control the monatomic nitrogen partial pressure above the weld pool. The temperature distribution in the plasma phase directly adjacent to the weld pool surface, though, is not well understood. Independent experiments have established the existence of electron temperatures between 2500 and 4000 K above the weld pool surface. These electron temperatures dictate the supply of monatomic nitrogen to the weld pool surface, and, in turn, control, along with the weld pool surface temperatures, the nitrogen concentrations on the weld pool surface.

Nitrogen concentrations on the weld pool surface are calculated as a function of both the monatomic nitrogen partial pressure and the weld pool surface temperatures. Once absorbed at the weld pool surface, nitrogen is then transported to the weldment interior predominantly by convection processes. The presence of turbulence, which is taken into account by increasing the nitrogen diffusion coefficient, further enhances the transport of nitrogen. Nitrogen desorption, which occurs via bubble formation at the liquid metal surface, is characterized by a supersaturation of nitrogen in the weld metal and is also considered in this model.

To test the validity of this model, the modeling results have been compared with the results of several autogeneous GTA welding experiments performed in pure iron. The general shape and size of the experimental and modeled weld pools are similar. Both the modeling and experimental results produce nitrogen concentrations between 2.7 and 4.7

times higher than Sieverts' Law calculations for a temperature of 2000 K and nitrogen partial pressures between 0.05 and 0.20 atm. When the modeling and experimental results are compared, both results are equivalent in magnitude for a given set of welding parameters and follow similar trends with changes in the nitrogen addition to the shielding gas and the travel speed.

The modeling calculations also display several features, which contribute to these results. Electron temperatures in the plasma phase adjacent to the weld pool in a range around 3000 K are found to produce levels of monatomic nitrogen sufficient to produce nitrogen concentrations in the weld pool equivalent to the experimental results. Levels of nitrogen supersaturation, which are between 50 and 75% higher than the equilibrium nitrogen concentration, are required to produce the nitrogen concentrations equivalent to the experimental results. In each of these calculations, the incorporation of turbulence in the calculations is important to the final results, but changes in the level of turbulence have little effect.

REFERENCES

- ¹ S.A. David and T. DebRoy, "Current Issues and Problems in Welding Science", *Science*, 1992, 257, 497-502.
- ² T. DebRoy and S.A. David, "Physical Processes in Fusion Welding", *Reviews of Modern Physics*, 1995, 67(1), 85-112.
- ³ S. Kou and Y.H. Wang, "Computer Simulation of Convection in Moving Arc Weld Pools", *Met. Trans. A*, 1986, 17A, 2271-2277.
- ⁴ C. Chan, J. Mazumder, and M.M. Chen, "A Two-Dimensional Transient Model for Convection in Laser Melted Pool", *Metall. Trans. A*, 1984, 15A, 2175-2184.
- ⁵ K. Mundra, T. DebRoy, S.S. Babu, and S.A. David, "Weld Metal Microstructure Calculations from Fundamentals of Transport Phenomena in the Arc Welding of Low-Alloy Steels", *Weld. J.*, 1997, 76(4), 163-s – 171-s.
- ⁶ Z. Yang and T. DebRoy, "Weld Metal Microstructure Prediction from Fundamentals of Transport Phenomena and Phase Transformation Theory", *Sci. Tech. Weld. Joining*, 1997, 2(2), 53-58.
- ⁷ T. Hong, W. Pitscheneder, and T. DebRoy, "Quantitative Modelling of Motion, Temperature Gradients, and Growth of Inclusions in Weld Pool", *Sci. Tech. Weld. Joining*, 1998, 3(1), 33-41.
- ⁸ W. Pitscheneder, T. DebRoy, K. Mundra, and R. Ebner, "Role of Sulfur and Processing Variables on the Temporal Evolution of Weld Pool Geometry during Multikilowatt Laser Beam Welding of Steels", *Weld. J.*, 1996, 75(3), 71-s – 80-s.
- ⁹ W. Pitscheneder, M. Gruböck, K. Mundra, T. DebRoy, and R. Ebner, "Numerical and Experimental Investigations of Conduction-Mode Laser Weld Pools", in Mathematical Modelling of Weld Phenomena 3, ed. by H. Cerjak, London, The Institute of Materials, 1997, 41-63.
- ¹⁰ K. Mundra and T. DebRoy, "Calculation of Weld Metal Composition Change in High-Power Conduction Mode Carbon Dioxide Laser-Welded Stainless Steel", *Met. Trans. B*, 1993, 24B, 145-155.
- ¹¹ M. Uda and S. Ohno, "Effect of Surface Active Elements on Nitrogen Content of Iron under Arc Melting", *Trans. Nat. Res. Inst. Met.*, 1973, 15(1), 20-28.
- ¹² M. Uda and T. Wada, "Solubility of Nitrogen in Arc-Melted and Levitation Melted Iron and Iron Alloys", *Trans. Nat. Res. Inst. Metals*, 10(2), 1968, 21-33.

- ¹³ G. den Ouden, "The Role of Nitrogen in Electric Arc Welding", *Philips Weld. Reporter*, 13(1), 1977, 1-6.
- ¹⁴ G. den Ouden and O. Griebeling, "Nitrogen Absorption During Arc Welding", *International Trends in Welding Science and Technology*, eds. S. A. David and J. M. Vitek, (ASM International, Materials Park, OH), 1990, pp. 431-435.
- ¹⁵ S.A. Gedeon and T.W. Eagar, "Thermochemical Analysis of Hydrogen Absorption in Welding", *Weld. J.*, 1990, 69(7), 264-s – 271-s.
- ¹⁶ K. Mundra and T. DebRoy, "A General Model for Partitioning of Gases between a Metal and Its Plasma Environment", *Metall. and Mater. Trans. B*, 1995, 26B, 149-157.
- ¹⁷ T.A. Palmer and T. DebRoy, "Physical Modeling of Nitrogen Partition between the Weld Metal and Its Plasma Environment", *Weld J.*, 1996, 75(7), 197s-207s.
- ¹⁸ T.A. Palmer, K. Mundra, and T. DebRoy, "Nitrogen Dissolution in the Weld Metal - Current Status and Research Opportunities", in *Mathematical Modelling of Weld Phenomena 3*, ed. by H. Cerjak, (The Institute of Materials, London, 1997), pp. 3-40.
- ¹⁹ S. Kou and D.K. Sun, "Fluid Flow and Weld Penetration in Stationary Arc Welds", *Metall. Trans. A*, 1985, 16A, 203-213.
- ²⁰ T. Zacharia, S.A. David, J.M. Vitek, and T. DebRoy, "Weld Pool Development During GTA and Laser Beam Welding of Type 304 Stainless Steel, Part I: Theoretical Analysis", *Weld. J.*, 1989, 68(12), 499-509.
- ²¹ A. Paul and T. DebRoy, "Free Surface Flow and Heat Transfer in Conduction Mode Laser Welding", *Metall. Trans. B*, 1988, 19B, 851-858.
- ²² T. Zacharia, S.A. David, J.M. Vitek, and T. DebRoy, "Modeling of Interfacial Phenomena in Welding", *Metall. Trans. B*, 1990, 21B, 600-603.
- ²³ C. Chan, J. Mazumder, and M.M. Chen, "A Two-Dimensional Transient Model for Convection in Laser Melted Pool", *Metall. Trans. A*, 1984, 15A, 2175-2184.
- ²⁴ S. Kou and Y.H. Wang, "Three-Dimensional Convection in Laser Melted Pools", *Met. Trans. A*, 1986, 17A, 2265-2270.
- ²⁵ C. Prakash, M. Sammonds, and A.K. Singhal, "A Fixed Grid Numerical Methodology for Phase Change Problems Involving a Heat Source", *Int. J. Heat Mass Transfer*, 1987, 30(12), 2690-2694.

- ²⁶ K. Mundra, T. DebRoy, and K.M. Kelkar, "Numerical Prediction of Fluid Flow and Heat Transfer in Welding with a Moving Heat Source", *Num. Heat Trans. A*, 1996, 29, 115-129.
- ²⁷ S. Kou, Welding Metallurgy, (John Wiley & Sons, New York), 1987, 309-401.
- ²⁸ V.R. Voller and C. Prakash, "A Fixed Grid Numerical Modelling Methodology for Convection-Diffusion Mushy Region Phase Change Problems", *Int. J. Heat Mass Transfer*, 1987, 30(8), 1709-1719.
- ²⁹ K. Mundra, J.M. Blackburn, and T. DebRoy, "Absorption and Transport of Hydrogen during Gas-Metal Arc Welding of a Low Alloy Steel", *Sci. Tech. Weld. Joining*, 1997, 2(4), 174-184
- ³⁰ M.L. Wasz and R.B. McLellan, "Nitrogen Diffusion in BCC Iron", *Scripta Met. et Mat.*, 1993, 28, 1461-1463.
- ³¹ P. Grieveson and E.T. Turkdogan, "Kinetics of Reaction of Gaseous Nitrogen with Iron Part II: Kinetics of Nitrogen Solution in Alpha and Delta Iron", *Trans. Met. Soc. AIME*, 1964, 230, 1604-1609.
- ³² K. Schwerdtfeger, "Diffusion of Oxygen and Nitrogen in Liquid Iron", *Trans. Met. Soc. AIME*, 1967, 239, 134-138.
- ³³ W.T. Lankford, N.L. Samways, R.F. Craven, and H.E. McGannon, ed., The Making, Shaping, and Treating of Steel, 10th ed., United States Steel Corporation, 1985.
- ³⁴ E.T. Turkdogan, in BOF Steelmaking, ed. by R.D. Pehlke *et al.*, (Iron and Steel Soc. AIME, New York), 1975, 1-190.
- ³⁵ M.H. Davies, "Numerical Modelling of Weld Pool Convection in Gas Metal Arc Welding", Ph.D. Thesis, The University of Adelaide, South Australia, 1995.
- ³⁶ Reference Manual for COMPACT-3D Version 3.1, Innovative Research, 1993.
- ³⁷ E.A. Brandes, ed., Smithells Metals Reference Book, 6th ed., (Butterworths, London), 1983.
- ³⁸ M.W. Chase, Jr., C.A. Davies, J.R. Downey, Jr., D.J. Frurip, R.A. McDonald, and A.N. Syverud, JANAF Thermochemical Tables, 3rd Ed., (American Chemical Society and American Institute for Physics, Washington, DC), 1985.
- ³⁹ P. Sahoo and T. DebRoy, "Interfacial Tension Between Low Pressure Argon Plasma and Molten Copper and Iron", *Metall. Trans. B*, 1987, 18, 597-601.

- ⁴⁰ W.H. Giedt, L.N. Tallerico, and P.W. Fuerschbach, "GTA Welding Efficiency: Calorimetric and Temperature Field Measurements", *Weld. J.*, 1989, 68(1), 28-s - 32-s.
- ⁴¹ H.E. McGannon, ed., The Making, Shaping and Treating of Steel, 9th edition, United States Steel Corporation, 1971, 330-331.
- ⁴² F. Elliott and M. Gleiser, Thermochemistry for Steelmaking I, Addison-Wesley Publishing Co., Reading, MA, 1963, 75.
- ⁴³ J.D. Fast and M.B. Verriyp, "Solubility of Nitrogen in Alpha-Iron", *J. Iron Steel. Inst.*, 1955, 180, 337-343.
- ⁴⁴ R.B. McLellan and K. Alex, "The Thermodynamics of Nitrogen Austenite", *Sripta Met.*, 1970, 4, 967-970.
- ⁴⁵ R.D. Pehlke and J.F. Elliott, "Solubility of Nitrogen in Liquid Iron Alloys. 1. Thermodynamics", *Trans. AIME*, 1960, 218, 1088-1101.
- ⁴⁶ R.T.C. Choo, J. Szekely, and R.C. Westhoff, "On the Calculation of the Free Surface Temperature of Gas-Tungsten-Arc Weld Pools from First Principles: Part I. Modeling the Welding Arc", *Met. Trans. B*, 23B, 1992, 357-369.
- ⁴⁷ J.F. Key, J.W. Chan, and M.E. McIlwain, "Process Variable Influence on Arc Temperature Distribution", *Weld. J.*, 62(7), 1983, 179s-184s.
- ⁴⁸ A.E.F. Gick, M.B.C. Quigley, and P.H. Richards, "The Use of Electrostatic Probes to Measure the Temperature Profiles of Welding Arcs", *J. Phys. D: Appl. Phys.*, 6, 1973, 1941-1949.
- ⁴⁹ J. Wendelstorf, I. Decker, H. Wohlfahrt, and G. Simon, "TIG and Plasma Arc Modeling: A Survey", in Mathematical Modelling of Weld Phenomena 3, ed. by H. Cerjak, (The Institute of Materials, London, 1997), pp. 848-897.
- ⁵⁰ G.N. Haddad and A.J.D. Farmer, "Temperature Measurements in Gas Tungsten Arcs", *Weld. J.*, 1985, 64(12), 399s-342s.
- ⁵¹ A.J.D. Farmer and G.N. Haddad, "Temperature Determinations in a Free-Burning Arc: I. Experimental Techniques and Results in Argon", *J. Phys. D: Appl. Phys.*, 1984, 17, 1189-1196.
- ⁵² M.B.C. Quigley, P.H. Richards, D.T. Swift-Hook, and A.E.F. Gick, "Heat Flow to the Workpiece from a TIG Welding Arc", *J. Phys. D: Appl. Phys.*, 1973, 6, 2250-2258.

⁵³ H.A. Dinulescu and E. Pfender, "Analysis of the Anode Boundary Layer of High Intensity Arcs", *J. Appl. Phys.*, 1980, 51(6), 3149-3157.

⁵⁴ C. Bodsworth, Physical Chemistry of Iron and Steel Manufacture, (Longmans, London), 1963.

⁵⁵ R.G. Ward, An Introduction to the Physical Chemistry of Iron & Steel Making, (Edward Arnold Publishers, London), 1962.

Chapter 6

SUMMARY AND CONCLUSIONS

6.1 CURRENT STATE OF THE ART

Weld metal nitrogen concentrations above those predicted by Sieverts' Law are commonly observed during the arc welding of iron and steel. A comprehensive review of the previous work in this area has been compiled here and includes a number of explanations for this behavior. Among these, the absorption of monatomic nitrogen from the plasma phase, which resides above the liquid metal surface, is recognized as the predominant mechanism for the introduction of nitrogen into the liquid metal. Monatomic nitrogen species are produced in the plasma phase in greater numbers than those observed in the absence of a plasma phase. The final nitrogen concentration is then determined by the simultaneous absorption of monatomic nitrogen on the weld pool surface and the desorption of nitrogen from the weldment. Desorption can occur both when the weld metal has solidified and at the liquid metal surface.

Overall, the previous work has been rather qualitative in nature and has concentrated solely on the interaction between the nitrogen-containing plasma phase and the liquid iron. No existing model predicts the nitrogen concentration from only knowledge of the welding parameters, such as the arc current, arc voltage, and nitrogen partial pressure in the shielding gas. For example, the two temperature model does not provide an *a priori* means for predicting the nitrogen concentration in the weld pool and is dependent on the choice of the dissociation temperature. In addition, these models do not account for the complexity of the welding process, including the interaction between the plasma phase and the molten metal, the transport of nitrogen in the weld metal considering the vigorous fluid flow within the weld pool.

Even though the nitrogen dissolution reaction is very complex, it is affected by events taking place in three regions: the plasma phase, the plasma-metal interface, and the liquid weld pool. This study has coupled existing knowledge of each of these regions in the

form of transport phenomena, plasma physics, and thermodynamic calculations into a model, which produces realistic nitrogen concentrations in the weld metal. The compilation of this work represents the first comprehensive effort to calculate the nitrogen concentration in iron during GTA welding as a function of only the known welding variables. The following sections present the primary aspects of the model and summarize the conclusions of this study.

6.1.1 Nitrogen in the Plasma Phase

The nature and concentration of various nitrogen-bearing species in the welding arc during GTA welding operations have been determined here. These values are based on detailed calculations of the partition functions for each nitrogen-bearing species. It is necessary to calculate these values from fundamentals since the plasma phase temperatures are significantly higher than those in metals processing operations, for which the current thermodynamic database is catered. Number density calculations show that neutral monatomic and diatomic species dominate near the surface of the weld pool in GTA welding arcs. On the other hand, ionic and atomic species dominate away from the weld pool surface.

The monatomic nitrogen partial pressures in the plasma are formed at temperatures higher than weld pool surface temperatures. These higher electron temperatures produce monatomic nitrogen partial pressures high enough to cause dramatic increases in the amount of nitrogen absorbed in the weld metal. For example, at plasma temperatures higher than 5000 K, the iron weld pool surface reaches nitrogen saturation at all temperatures. This level of nitrogen saturation is defined as the nitrogen concentration. Therefore, the temperature difference between the plasma and the weld metal surface plays a significant role in the enhanced nitrogen dissolution process.

Along with the calculation of the various nitrogen species densities in the plasma phase, the electron density in the plasma phase is calculated. Knowledge of the electron density is necessary for the determination of transport properties in the plasma phase. The calculations performed here show significant differences in the electron density between an argon and a helium plasma for electron temperatures below approximately

15000 K. This difference in electron density decreases progressively as the electron temperature increases. Additions of oxygen and nitrogen to pure argon have little effect on the electron density over the range of temperatures. On the other hand, when oxygen and nitrogen are added to pure helium, significant increases in the electron density are observed at temperatures below approximately 15000 K.

Additions of oxygen into a nitrogen-containing plasma, like the addition of air into the welding arc, affect the species density distribution of nitrogen species in the welding arc. With the addition of oxygen, the production of intermediate nitrogen-oxygen species, such as NO, has been assumed here. Calculations show a significant increase in the monatomic nitrogen number density with the addition of oxygen to the shielding gas than without this oxygen addition. These calculations therefore provide a conclusive scientific basis to explain the experimentally observed enhancement in nitrogen concentrations with the addition of oxygen to the arc.

Emission spectroscopic studies of glow discharge plasmas containing the same gas compositions as those in the above calculations have also been performed. These studies provide evidence for the existence of NO species in the plasma phase at low temperatures and the important role of dissociation of diatomic species as the temperature is increased. As a whole, these emission spectroscopic studies reinforce the trends in species densities calculated here.

6.1.2 Nitrogen in the Weld Metal

A model to calculate the nitrogen concentration in the weld metal during the GTA welding of iron has been developed here. This model is based, in part, on the calculation of the turbulent, steady-state velocity and temperature fields in the weld pool, which are determined by the solution of the equations of conservation of mass, momentum, and energy in three-dimensions. Based on these results, nitrogen concentrations in the weld pool can then be calculated in a transient manner. The evolution of nitrogen concentration in the weld pool as a function of time can be then determined, and the residual nitrogen concentration in the weld pool is based on the nitrogen concentration distribution in the weld metal at the time of solidification.

The calculation of the nitrogen concentrations in the weld pool are based on the combination of calculations involving the plasma phase above the weld pool, the interface between the weld pool surface and the plasma phase, and the weldment interior. Monatomic nitrogen partial pressures are calculated as a function of the electron temperatures in the plasma phase using the calculation methodology discussed in Chapter 3. Nitrogen concentrations on the weld pool surface are calculated as a function of both the monatomic nitrogen partial pressure and the weld pool surface temperatures. Once absorbed at the weld pool surface, nitrogen is then transported to the weldment interior predominantly by convection processes. The presence of turbulence, which is taken into account by increasing the nitrogen diffusion coefficient, further enhances the transport of nitrogen. Nitrogen desorption, which occurs via bubble formation at the liquid metal surface, is characterized by a supersaturation of nitrogen in the weld metal and is also considered in this model.

To test the validity of this model, several autogeneous GTA welding experiments in pure iron have been performed at two travel speeds with a number of nitrogen additions to the argon shielding gas. Nitrogen concentrations have also been measured at several locations along each weld line and compared with the modeling results. The general shape and size of the experimental and modeled weld pools are similar. Both the modeling and experimental results produce nitrogen concentrations between 2.7 and 4.7 times higher than Sieverts' Law calculations for a temperature of 2000 K and nitrogen partial pressures between 0.05 and 0.20 atm. When the modeling and experimental results are compared, both results are equivalent in magnitude for a given set of welding parameters and follow similar trends with changes in the nitrogen addition to the shielding gas and the travel speed.

The modeling calculations also display several features, which contribute to these results. Electron temperatures in the plasma phase adjacent to the weld pool in a range around 3000 K are found to produce levels of monatomic nitrogen sufficient to produce nitrogen concentrations in the weld pool equivalent to the experimental results. Levels of nitrogen supersaturation, which are between 50 and 75% higher than the equilibrium nitrogen concentration, are required to produce the nitrogen concentrations equivalent to

the experimental results. In each of these calculations, the incorporation of turbulence in the calculations is important to the final results, but changes in the level of turbulence have little effect.

6.2 FUTURE WORK

The work performed here represents a significant advancement in the understanding of nitrogen dissolution during the arc welding of iron and steels. It provides a capability not previously available and sheds light on the complex reactions occurring in the weld pool during nitrogen dissolution. This work, though, focuses on a rather narrow topic in the realm of arc welding processes and on only a single materials system. On the other hand, it provides a firm basis for examining a number of related reactions occurring during GTA and other welding processes for a range of materials systems. Several specific areas for further research are discussed below.

Number density calculations performed here shed a great deal of light on the amount of each species present to take part in the nitrogen dissolution reaction. However, the calculations are based on a number of assumptions concerning the electron temperatures in the plasma phase. The effect of changes in the welding parameters on the electron temperature distribution in the arc column, especially in the region adjacent to the weld pool surface, needs to be better understood. A better understanding of the electron temperature distribution, using either modeling or experimental techniques, would provide a more accurate knowledge of the monatomic nitrogen partial pressure available to participate in the nitrogen absorption reaction.

A connection between the nitrogen concentration, the microstructure, and the formation of porosity has been suggested here. Both the microstructural evolution and the formation of porosity are of significant interest in welding research, yet are not well understood in the iron-nitrogen system. Much of the knowledge gained through this study can be applied to develop new models specifically addressing either of these topics. The development of such models would represent significant advancements in the understanding of welding processes.

In this work, the GTA welding process has been chosen because of its relative simplicity in the realm of gas dissolution reactions. For example, only a single pathway for gas dissolution is present during the GTA process. GMA welding is a much more complex process with multiple pathways for gas dissolution, ranging from the plasma-weld pool interface to the molten electrode in contact with the plasma phase to the drop as it is transferred to the liquid metal. Previous studies have shown that the nitrogen concentrations are significantly higher during GMA welding than during GTA welding. The effects of these additional pathways on the amount of nitrogen present in the weld metal are not well understood and must be known in order to develop a more general quantitative understanding of nitrogen dissolution in these arc welding processes.

Appendix A

CALCULATION OF PARTITION FUNCTIONS

A.1 PARTION FUNCTIONS OF ATOMIC SPECIES

When calculating the species densities in a plasma phase, the values of the partition functions for the individual species must first be determined.^{1,2} The partition function of a given species is the sum of the partition functions associated with each independent energy mode. In the case of a monatomic gas, the partition function for each monatomic species can be defined as follows:

$$Z_i = \sum g e^{-E_i/kT} \quad (\text{A.1})$$

where k is the Boltzmann constant, T is the absolute temperature, and g is the degree of degeneration or statistical weight of the energy level, E_i .

The degree of degeneration of an atom, is defined as the number of different solutions for independent wave functions which correspond to a given energy level. The degree of degeneration in an atom is expressed in quantum mechanical terms as the value $2l+1$, where l is the quantum number representing the angular momentum component of that energy level.³ Values for the various constants unique to the atomic species to be analyzed are available in standard reference sources.⁴ Table A1 shows the values and units required for each of these constants in the solution of this relation and other important relations to follow. In addition, Tables A2 through A6 show the constants for the atomic energy levels used in the calculation of the partition functions for the respective atomic and ionic species for nitrogen and oxygen.

A.2 PARTION FUNCTIONS OF MOLECULAR SPECIES

The calculation of the partition function for a molecule is much more complicated than that for an atom because of its more complicated structure with a greater number of energy levels. These various energy levels interact in ways not seen for the case of an

Table A.1. Summary of important constants.

Constant	Definition	Value	
m_e	Rest mass of an electron	9.11×10^{-31} kg	
k	Boltzmann's Constant	1.38×10^{-23} J/K	8.62×10^{-5} eV/K
		0.695 cm ⁻¹	
h	Planck's Constant	6.63×10^{-34} J-sec	4.14×10^{-15} eV-sec
c	Speed of Light	3.0×10^{10} cm/sec	

Table A.2. Summary of Electronic energy levels⁴ for nitrogen atoms (N).

Energy Level Designation	J	Energy (cm ⁻¹)	Degeneracy (g)
2p ³ 4S ⁰	1½	0	4
2p ³ 2D ⁰	2½	19224.464	6
	1½	19233.177	4
2p ³ 2P ⁰	1½	28838.92	2
	½	28839.306	4

Table A.3. Summary of Electronic energy levels⁴ for singly charged monatomic nitrogen ions (N^+).

Energy Level Designation	J	Energy (cm^{-1})	Degeneracy (g)
$2p^2\ ^3P$	0	0	1
	1	48.7	3
	2	130.8	5
$2P^2\ ^1D$	2	15316.2	5
$2p^2\ ^1S$	0	32688.8	1
$2p^3\ ^3S^0$	2	46784.6	5

Table A.4. Summary of Electronic energy levels⁴ for oxygen atoms (O).

Energy Level Designation	J	Energy (cm ⁻¹)	Degeneracy (g)
2p ⁺ ³ P	2	0	5
	1	158.265	3
	0	226.977	1
2p ⁺ ¹ D	2	15867.862	5
2p ⁺ ¹ S	0	33792.583	1

Table A.5. Summary of Electronic energy levels⁴ for singly charged monatomic oxygen ions (O^+).

Energy Level Designation	J	Energy (cm⁻¹)	Degeneracy (g)
$2p^3\ ^4S^0$	$1\frac{1}{2}$	0	4
$2p^3\ ^2D^0$	$2\frac{1}{2}$	26808	6
	$1\frac{1}{2}$	26830.5	4
$2p^3\ ^2P^0$	$1\frac{1}{2}$	40466.9	4
	$\frac{1}{2}$	40468.4	2

Table A.6. Summary of Electronic energy levels⁴ for doubly charged monatomic oxygen ions (O^{++}).

Energy Level Designation	J	Energy (cm⁻¹)	Degeneracy (g)
$2p^2\ ^3P$	0	0	1
	1	113.4	3
	2	306.8	5
$2p^2\ ^1D$	2	20271	5
$2p^2\ ^1S$	0	43183.5	1

atom. In general, the internal modes of energy storage in a molecule are electronic, vibrational, and rotational. The degree of degeneration for a given energy level in a molecule is also affected by this large number of energy levels and the interaction between them. Therefore, the degree of degeneration for a molecule is defined in terms of specific energy levels. Molecular states designated ${}^n\Sigma$ have degeneracy, $g_e = n$ and all other molecular states (${}^n\pi, {}^n\Delta, {}^n\Phi$, etc.) have degeneracy, $g_e = 2n$.^{1,2}

The internal partition function for molecular species is the product of the partition functions relating to the different energy modes characteristic of the molecule and is defined by the following relationship.

$$Z_i = Z_{el}Z_vZ_rZ_c \quad (\text{A.2})$$

where Z_{el} is the electronic partition function, Z_v is the vibrational partition function, which refers to a harmonic oscillation of the molecule with a frequency corresponding to the distance $\omega_e - 2x_e\omega_e$ between the two lowest vibrational levels, Z_r is the rotational partition function, which refers to a rigid rotator with a moment of inertia corresponding to that of the zero-point vibration, and Z_c is a correction factor taking into account anharmonicity, centrifugal forces, and interaction between vibration and rotation. The spectroscopically determined constants for each molecular species are available in standard reference books on molecular spectra. These constants are presented⁵⁷ in Tables A7 through A10 for nitrogen and oxygen species.

The electronic partition function for the molecular species, Z_{el} , is defined in the following relationship:

$$Z_{el} = g \exp\left(-A_0 \frac{hc}{kT}\right) \quad (\text{A.3})$$

where g is the degeneracy, A_0 is the energy level in cm^{-1} , h is Planck's constant, c is the speed of light, and T is the electron temperature.

Table A.7. Summary of spectroscopically determined values⁵ used in calculation of partition functions for nitrogen molecule, N₂.

	X(¹ Σ _g ⁺)	A(³ Σ _u ⁺)	B(³ Π _g)	a(¹ Π _u)
A ₀ , (cm ⁻¹)	0	49774	59328	68957
ω _e , (cm ⁻¹)	2359.61	1460.4	1732.84	1692.3
x _e ω _e , (cm ⁻¹)	14.445	13.93	14.44	13.32
B _e , (cm ⁻¹)	2.007	1.440	1.643	1.642
α, (cm ⁻¹)	0.018	0.013	0.018	0.021
D, (cm ⁻¹)	5.77x10 ⁻⁶			

Table A.8. Summary of spectroscopically determined values⁵ used in calculation of partition functions for nitrogen molecular ion, N_2^+ .

	$X(^2\Sigma_g^+)$	$A(^2\Pi_{ui})$	$B(^2\Sigma_u^+)$	$a(^4\Sigma_u^+)$	$D(^2\Pi_{gi})$
$A_0, (cm^{-1})$	0	9166.9	25461.4	25467	52318.2
$\omega_e, (cm^{-1})$	2207	1903.7	2419.84	2398	907.7
$x_e \omega_e, (cm^{-1})$	16.10	15.02	23.18	14	11.91
$B_e, (cm^{-1})$	1.93176	1.7444	2.04756	2.071	1.113
$\alpha, (cm^{-1})$	0.01881	0.0188	0.024	0.014	0.02
$D, (cm^{-1})$	6.10×10^{-6}	5.6×10^{-6}	6.17×10^{-6}		5×10^{-6}

Table A.9. Summary of spectroscopically determined values⁵ used in calculation of partition functions for oxygen molecule, O₂.

	X(³ Σ _g ⁻)	a(¹ Δ _g)	b(¹ Σ _g ⁺)	c(¹ Σ _u ⁻)	A'(³ Δ _u)
A ₀ , (cm ⁻¹)	0	7918.1	13195.1	33057.3	34690
ω _e , (cm ⁻¹)	1580.19	1483.5	1432.77	794.29	850
x _e ω _e , (cm ⁻¹)	11.38	12.9	14.0	12.736	20
B _e , (cm ⁻¹)	1.44563	1.4264	1.40037	0.915	0.96
α, (cm ⁻¹)	0.0159	0.0171	0.0182	0.0139	0.026
D, (cm ⁻¹)	4.84x10 ⁻⁶	4.86x10 ⁻⁶	5.35x10 ⁻⁶	7.40x10 ⁻⁶	5.55x10 ⁻⁶

Table A.10. Summary of spectroscopically determined values⁵ used in calculation of partition functions for oxygen molecular ion, O_2^+ .

	$X(^2\Pi_g)$	$a(^4\Pi_{ui})$	$A(^2\Pi_u)$	$b(^4\Sigma_g^-)$
A_{o_2} (cm^{-1})	0	32964	40669.3	49552
ω_e (cm^{-1})	1904.77	1035.69	898.25	1196.7
$x_e \omega_e$ (cm^{-1})	16.25	10.39	13.57	17.09
B_e (cm^{-1})	1.6913	1.1046	1.0617	1.28729
α (cm^{-1})	0.01976	0.01575	0.01936	0.02206
D (cm^{-1})	5.32×10^{-6}	4.88×10^{-6}	5.94×10^{-6}	5.81×10^{-6}

The vibrational partition function for the molecular species, Z_v , is defined by the relationship in Equation (A.4).

$$Z_v = (1 - e^{-u})^{-1} \quad (\text{A.4})$$

where the variable u is defined in the following relationship:

$$u = \frac{hc(\omega_e - 2x_e\omega_e)}{kT} \quad (\text{A.5})$$

The rotational partition function, Z_r , is defined below:

$$\ln Z_r = -\ln 2\sigma + \frac{\sigma}{3} \quad (\text{A.6})$$

where the variable σ is defined in the following relationship:

$$\sigma = \frac{hc(B_e - \frac{\alpha}{2})}{kT} \quad (\text{A.7})$$

where B_e is a constant which accounts for the interaction between vibration and rotation. The final correctional partition function, Z_c , accounts for the interaction between various components of the molecular energy levels and is defined in the following relationship.

$$\begin{aligned} \ln Z_c = & \frac{1}{u} (2\gamma + 6\gamma^{1/2}x^{1/2} + 2x) + (3\gamma - 3\gamma^{1/2}x^{1/2} - 2x) \\ & + \frac{u}{6} (-3\gamma + 3\gamma^{1/2}x^{1/2} + 5x) - \frac{u^2}{6}x + \frac{u^3}{120}(\gamma - \gamma^{1/2}x^{1/2}) + x \end{aligned} \quad (\text{A.8})$$

where γ and x are defined in Equations (A.9) and (A.10).

$$\gamma = \frac{B_e}{\omega_e} \quad (\text{A.9})$$

$$x = \frac{x_e \omega_e}{\omega_e} \quad (\text{A.10})$$

The calculation of internal partition functions, Z_i , for both atomic and molecular species is necessary for the solution of the Saha-Eggert relation for the ionization reactions and for the solution of the equilibrium constants for the dissociation reactions of nitrogen and oxygen. Figures A1 through A3 display the calculated partition functions for inert gases and diatomic and monatomic nitrogen and oxygen species as a function of temperature.

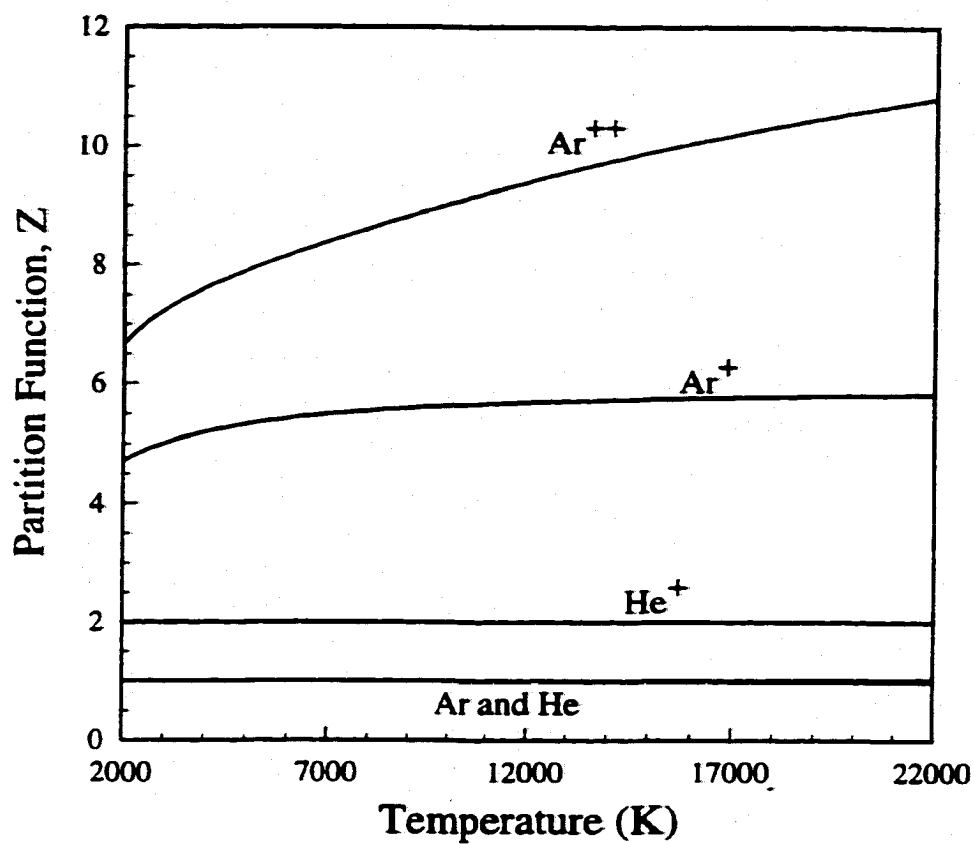


Figure A.1. Plot of computed partition functions as a function of temperature for argon and helium species in the plasma phase.

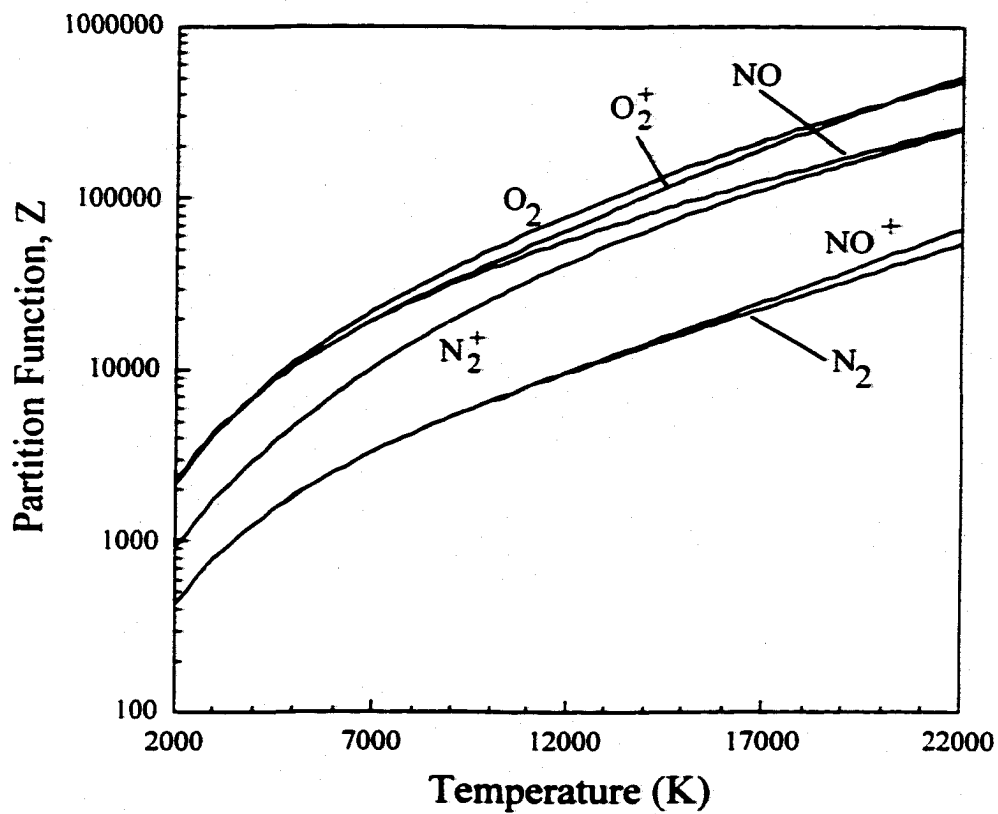


Figure A2. Plot of computed partition functions as a function of temperature for molecular oxygen and nitrogen species in the plasma phase.

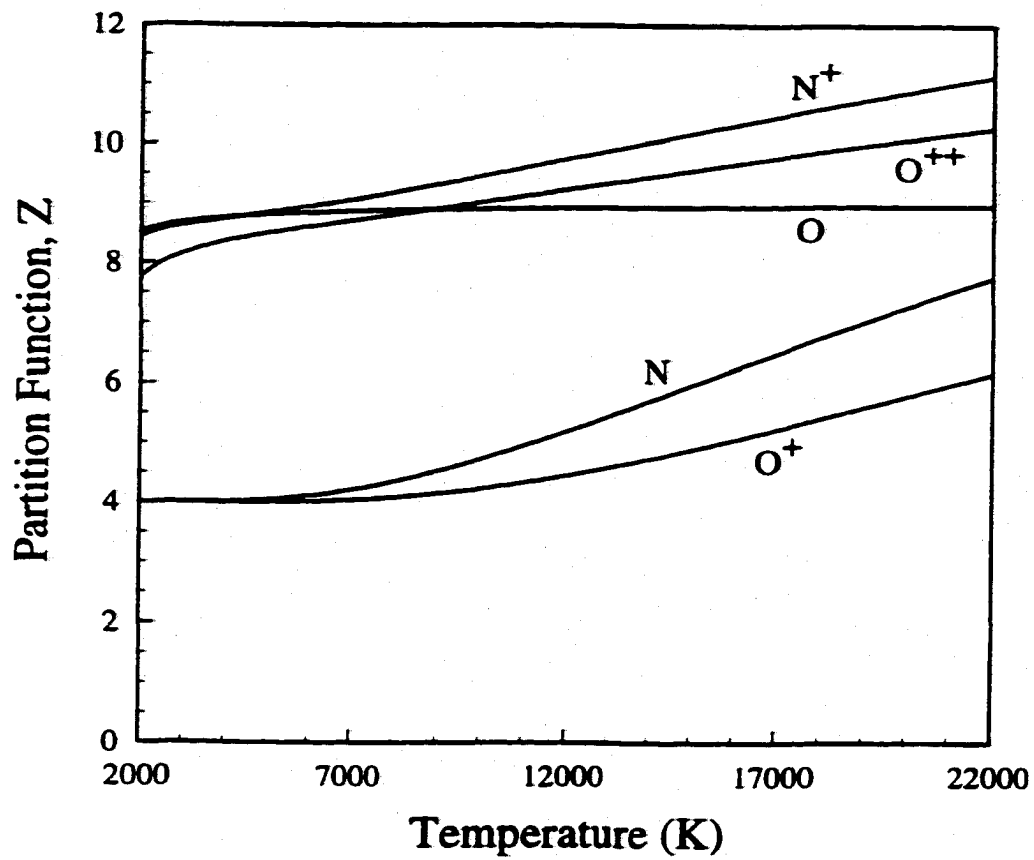


Figure A3. Plot of computed partition functions as a function of temperature for atomic oxygen and nitrogen species in the plasma phase.

REFERENCES

- ¹ K.S. Drellishak, D.P. Aeschliman, and A.B. Cambel, "Partition Functions and Thermodynamic Properties of Nitrogen and Oxygen Plasmas", *Phys. of Fluids*, 1965, 8(9), 1590-1600.
- ² K.S. Drellishak, C.F. Knopp, and A.B. Cambel, "Partition Functions and Thermodynamic Properties of Argon Plasma", *Phys. of Fluids*, 1963, 6(9), 1280-1288.
- ³ J. Avery: 'The Quantum Theory of Atoms, Molecules, and Photons', 77-79; 1972, New York, McGraw Hill.
- ⁴ C.E. Moore, Atomic Energy Levels, NSRDS-NBS 35, Vols. 1-3: (National Bureau of Standards, Washington, DC, 1971).
- ⁵ G. Herzberg, Molecular Spectra and Molecular Structure, Vol. IV: Constant of Diatomic Molecules, (Van Nostrand, New York, 1979)

Appendix B

THERMODYNAMIC BASIS FOR DISSOCIATION REACTION CALCULATIONS

The degree of dissociation of a diatomic gas can be computed with knowledge of the free energy of both the molecular and atomic species. These values are calculated from available spectroscopically determined data, which appear in the form of the partition functions. The Helmholtz free energy of one mole of an ideal gas is shown in the following relationship.¹

$$f - u_0 = -kT \ln \left[\frac{ev}{N_A h^3} (2\pi mkT)^{3/2} Z_i \right]^{N_A} \quad (\text{B.1})$$

where f is the Helmholtz free energy of one mole of an ideal gas, u_0 is the free energy at absolute zero, e is the base of the natural logarithms (2.71828), v is the volume containing the gas, m is the mass of a single molecule, and Z_i is the internal partition function of the species being analyzed.

The molar free enthalpy, $g - u_0$, can thus be rewritten in the following forms:¹

$$g - u_0 = f - u_0 + pv = f - u_0 + RT \quad (\text{B.2})$$

$$-\frac{g - u_0}{T} = \frac{5}{2} R \ln T + \frac{3}{2} R \ln M - R \ln p + R \ln \frac{2^{3/2} \pi^{3/2} e k^{5/2}}{h^3 N_A^{3/2}} - R + R \ln Z_i \quad (\text{B.3})$$

where $R = kN_A$ is the gas constant, M is the molecular weight, and p is the pressure. Using the relation in Equation (B.3), the molar free enthalpy for each species, i.e. the atomic

and molecular nitrogen and oxygen, can be calculated and substituted in the following equations to determine the equilibrium constant.

Since the dissociation reaction defines the conversion of one mole of ideal gaseous N_2 at a pressure of 1 atm. to two moles of ideal gaseous N at the same pressure, the Gibbs free energy can be defined as follows:¹

$$\Delta G^\circ = 2g^\circ(N) - g^\circ(N_2) \quad (B.4)$$

where g° represents the molar free energies of the ideal gases at the standard pressure. By substituting the relationships for the Gibbs free energy shown above into the definition of the reaction constant and taking into account the statistical mechanical definitions for the dissociation reaction, the following general relation can be defined.¹

$$\log K = \frac{g^\circ(N_2) - u_0^\circ(N_2)}{RT} - 2 \frac{g^\circ(N) - u_0^\circ(N)}{RT} - \frac{\Delta U_0^\circ}{RT} \quad (B.5)$$

where ΔU_0° is the dissociation energy at absolute zero deduced from spectroscopic data. Values for each free energy term in Equation (B.5), $g^\circ(i) - u_0^\circ(i)$, are determined in Equation (B.3), while the dissociation energy, ΔU_0° , for nitrogen, oxygen, and other diatomic molecules, is an available constant. For example, nitrogen has a dissociation energy of 9.764 eV, and Table B.1 summarizes both the ionization and dissociation energies for both nitrogen and oxygen and other species of interest. Figure B.1 also shows the calculated equilibrium constants for the dissociation of N_2 , O_2 , and NO as a function of temperature. Once the equilibrium constant is determined, it can be substituted into Equation (3.6) for nitrogen and Equation (3.12) for oxygen, and relations for the dissociation reactions thus developed.

Table B.1. Summary of ionization and dissociation energies for several species of interest.

Species in Arc	Dissociation Energy (eV)	Ionization Energy (eV)
Ar (g)	----	15.755
He (g)	----	24.580
N ₂ (g)	9.759	15.581
N	----	14.54
O ₂ (g)	5.115	12.071
O	----	13.614
O ⁺	----	35.146
NO (g)	6.496	9.264

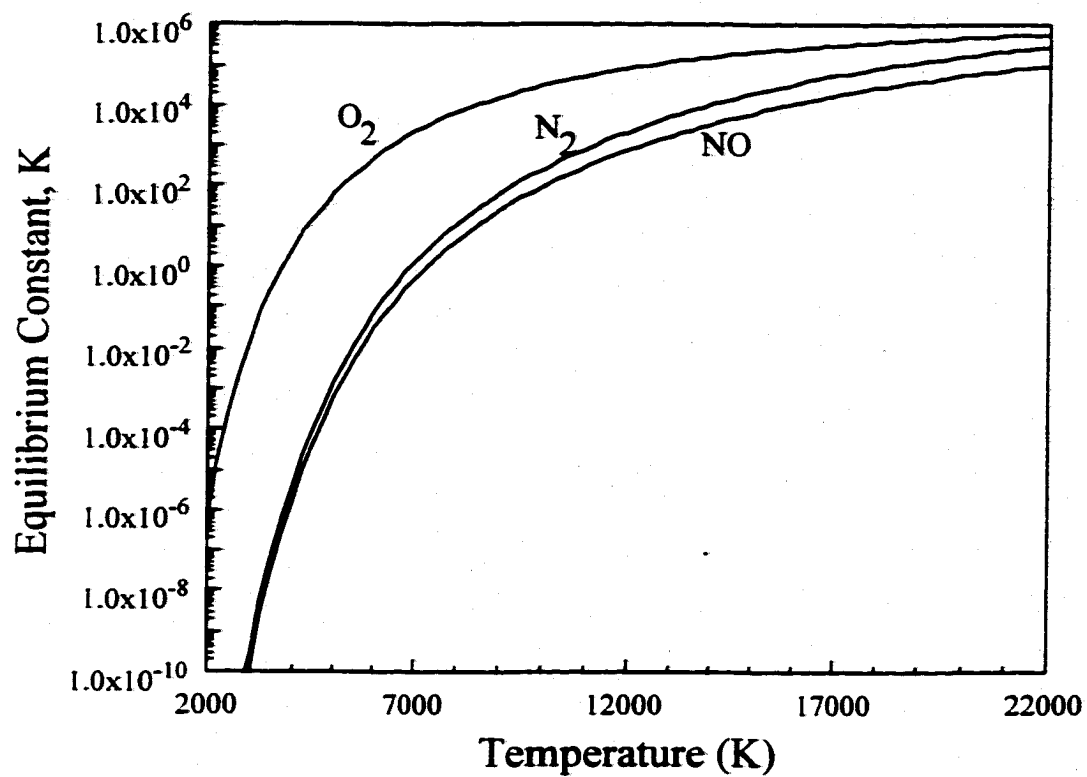


Figure B.1. Comparison of the computed equilibrium constants for the dissociation of N_2 , O_2 , and NO expressed by reactions (3.5), (3.12), and (3.28) plotted as a function of temperature.

REFERENCES

- ¹ J.D. Fast, "The Dissociation of Nitrogen in the Welding Arc", *Philips Res. Rep.*, 1947, 2, 382-398.

APPENDIX C

SUMMARY OF X-RAY ANALYSIS OF WELD SAMPLES

Table C.1. Summary of d-spacing and 2θ values for ferrite(α -Fe) in the iron system.¹

d_{hkl} (Å)	hkl	$2\text{Mo K}\alpha 1$ $\lambda = 0.7093 \text{ Å}$
2.027	110	20.16
1.433	200	28.66
1.170	211	35.29
1.013	220	40.97
0.906	310	46.07
0.826	222	50.76

Table C.2. Summary of d-spacing and 2θ values for nitrogen austenite (γ -Fe) in the iron-nitrogen system.²

d_{hkl} (Å)	hkl	$2 \text{ Mo } K_{\alpha 1}$ $\lambda = 0.7093 \text{ Å}$
2.058	111	19.85
1.782	200	22.96
1.260	220	32.70
1.075	311	38.54
1.029	222	40.33
0.891	400	46.91
0.818	331	51.41
0.797	420	52.85
0.727	422	58.36
0.686	333	62.27

Table C.3. Summary of d-spacing and 2θ values for nitrogen martensite (α' -Fe) in the iron-nitrogen system.²

d_{hkl} (Å)	hkl	2 Mo Kα $\lambda = 0.7093$ Å
2.026	110	20.17
1.433	200	28.67
1.170	112	35.28
1.013	220	40.97
0.766	321	55.18
0.611	332	70.98
0.478	442	95.92
0.390	552	130.90

Table C.4. Summary of d-spacing and 2θ values for nitrogen Fe_4N .³

d_{hkl} (Å)	hkl	2 Mo $K_{\alpha 1}$ $\lambda = 0.7093$ Å
3.790	100	10.74
2.684	110	15.19
2.191	111	18.63
1.897	200	21.55
1.697	210	24.13
1.549	211	26.47
1.342	220	30.65
1.265	300	32.56
1.200	310	34.38
1.144	311	36.12
1.095	222	37.80
1.053	320	39.37
1.014	321	40.95
0.949	400	43.89

Table C.5. Summary of d-spacing and 2θ values for nitrogen Fe_8N_4

d_{hkl} (Å)	hkl	<u>2 Mo Kα</u> <u>$\lambda = 0.7093$ Å</u>
4.232	101	9.62
4.045	110	10.06
3.145	002	12.95
2.860	200	14.25
2.483	112	16.43
2.116	202	19.30
2.022	220	20.20
1.538	321	26.66
1.239	332	33.26
0.963	442	43.24
0.783	552	53.84
0.659	662	65.11

Table C.6. Summary of d-spacing and 2θ values for nitrogen Fe_2N .⁵

d_{hkl} (Å)	hkl	$2 \text{ Mo K}\alpha 1$ $\lambda = 0.7093 \text{ Å}$
3.45	101	11.80
2.804	111	14.53
2.404	210	16.97
2.207	002	18.50
2.11	211	19.35
1.97	121	20.74
1.697	301	24.13
1.626	212	25.20
1.60	311	25.61
1.457	131	28.18
1.422	103	28.89
1.385	400	29.68
1.365	113	30.12
1.255	213	32.83
1.206	040	34.21
1.197	420	34.47
1.166	041	35.42
1.104	004	37.48
1.065	332	38.90
1.055	422	39.29
1.003	214	41.42
0.9299	423	44.84
0.9103	530	45.86
0.9074		46.02
0.9026		46.28

Table C.7. Summary of d-spacing and 2θ values for nitrogen Fe_3N .²

d_{hkl} (Å)	hkl	$2 \text{ Mo K}\alpha 1$ $\lambda = 0.7093 \text{ Å}$
2.38	100	17.14
2.19	002	18.64
2.09	101	19.54
1.61	102	25.45
1.37		30.01
1.24	103	33.24
1.16	200	35.61
1.14	112	36.25
1.10	004	37.62
1.04	202	39.88
0.92		45.35
0.88	210	47.54
0.86	211	48.71
0.82	212	51.26
0.76	213	55.64

Table C.8. Summary of peaks observed in the base metal.

<u>2θ</u> <u>(degrees)</u>	<u>Intensity</u> <u>(A.U.)</u>	<u>Phase</u> <u>I.D.</u>
20.16	100	α -Fe
28.66	76	α -Fe
35.29	100	α -Fe
40.97	33	α -Fe
46.07	37	α -Fe
50.76	5	α -Fe

Table C.9. Summary of peaks observed with pure Ar additions to the shielding gas for all welding conditions.

Welding Speed = 0.847 cm/sec			Welding Speed = 0.423 cm/sec		
<u>2θ</u> <u>(degrees)</u>	<u>Intensity</u> <u>(A.U.)</u>	<u>Phase</u> <u>I.D.</u>	<u>2θ</u> <u>(degrees)</u>	<u>Intensity</u> <u>(A.U.)</u>	<u>Phase</u> <u>I.D.</u>
20.16	100	α-Fe	20.16	100	α-Fe
28.66	43	α-Fe	28.66	26	α-Fe
35.28	59	α'-Fe	28.67	29	α'-Fe
35.29	80	α-Fe	35.29	86	α-Fe
40.97	30	α-Fe	40.97	20	α-Fe
46.07	31	α-Fe	46.07	21	α-Fe
50.76	4	α-Fe	50.76	6	α-Fe
55.18	33	α'-Fe	55.18	29	α'-Fe

Table C.10. Summary of peaks observed for several N₂ additions to the shielding gas for a welding speed of 0.847 cm/sec and a 5% N₂ addition to the shielding gas.

2θ (degrees)	Intensity (A.U.)	Phase I.D.
18.63	7	Fe ₄ N
19.35	30	Fe ₂ N
20.16	100	α - Fe
28.66	29	α - Fe
28.67	19	α' - Fe
28.89	18	Fe ₂ N
35.28	67	α' - Fe
35.29	70	α - Fe
35.42	39	Fe ₂ N
40.97	11	α - Fe
46.07	17	α - Fe
50.76	6	α - Fe
55.18	17	α' - Fe

Table C.11. Summary of peaks observed for several N₂ additions to the shielding gas for a welding speed of 0.847 cm/sec and a 10% N₂ addition to the shielding gas.

2θ (degrees)	Intensity (A.U.)	Phase I.D.
19.35	11	Fe ₂ N
20.10	81	α'-Fe
20.16	81	α -Fe
20.17	81	α'-Fe
20.20	65	Fe ₈ N
28.89	20	Fe ₂ N
35.28	49	α'-Fe
35.29	52	α -Fe
35.61	20	Fe ₃ N
40.95	21	Fe ₄ N
40.97	18	α -Fe
40.97	19	α' - Fe
46.02	23	Fe ₂ N
46.07	25	α -Fe
46.28	13	Fe ₂ N
50.76	5	α -Fe
55.18	20	α' - Fe
55.64	6	Fe ₃ N

Table C.12. Summary of peaks observed for several N₂ additions to the shielding gas for a welding speed of 0.847 cm/sec and a 15% N₂ addition to the shielding gas.

2θ (degrees)	Intensity (A.U.)	Phase I.D.
19.35	25	Fe ₂ N
19.85	58	γ-Fe
20.16	80	α-Fe
20.20	51	Fe ₈ N
21.55	6	Fe ₄ N
28.66	21	α-Fe
30.65	6	Fe ₄ N
35.29	48	α-Fe
35.42	27	Fe ₂ N
35.61	24	Fe ₃ N
37.80	5	Fe ₄ N
40.97	17	α - Fe
46.07	17	α - Fe
46.28	9	Fe ₂ N
55.18	20	α'-Fe
55.64	11	Fe ₃ N

Table C.13. Summary of peaks observed for several N₂ additions to the shielding gas for a welding speed of 0.847 cm/sec and a 20% N₂ addition to the shielding gas.

2θ (degrees)	Intensity (A.U.)	Phase I.D.
18.64	6	Fe ₃ N
19.35	31	Fe ₂ N
19.54	31	Fe ₃ N
20.16	27	α-Fe
22.96	7	γ-Fe
28.66	10	α-Fe
30.65	6	Fe ₄ N
35.29	21	α-Fe
35.61	10	Fe ₃ N
37.80	8	Fe ₄ N
40.95	8	Fe ₄ N
46.07	11	α Fe
55.18	11	α'-Fe
55.64	6	Fe ₃ N

Table C.14. Summary of peaks observed for several N₂ additions to the shielding gas for a welding speed of 0.423 cm/sec and a 5% N₂ addition to the shielding gas.

2θ (degrees)	Intensity (A.U.)	Phase I.D.
16.43	13	Fe ₃ N
20.16	100	α-Fe
25.45	4	Fe ₃ N
28.66	19	α - Fe
28.67	19	α'-Fe
28.89	11	Fe ₂ N
33.26	3	Fe ₃ N
35.29	59	α-Fe
35.42	33	Fe ₂ N
40.95	19	Fe ₄ N
40.97	11	α-Fe
46.07	28	α-Fe
46.28	14	Fe ₂ N
50.76	4	α-Fe
55.18	22	α'-Fe
55.64	10	Fe ₃ N

Table C.15. Summary of peaks observed for several N₂ additions to the shielding gas for a welding speed of 0.423 cm/sec and a 10% N₂ addition to the shielding gas.

2θ (degrees)	Intensity (A.U.)	Phase I.D.
16.43	12	Fe ₃ N
18.50	16	Fe ₂ N
19.54	17	Fe ₃ N
20.16	100	α-Fe
21.55	6	Fe ₄ N
25.45	4	Fe ₃ N
28.66	28	α-Fe
35.29	77	α-Fe
35.42	39	Fe ₂ N
37.62	6	Fe ₃ N
40.97	13	α-Fe
46.02	25	Fe ₂ N
50.76	6	α-Fe
55.64	11	Fe ₃ N

Table C.16. Summary of peaks observed for several N₂ additions to the shielding gas for a welding speed of 0.423 cm/sec and a 15% N₂ addition to the shielding gas.

2θ (degrees)	Intensity (A.U.)	Phase I.D.
16.43	6	Fe ₃ N
20.16	56	α-Fe
28.66	10	α-Fe
35.29	35	α-Fe
40.95	9	Fe ₄ N
46.07	14	α-Fe
46.28	8	Fe ₂ N
50.76	3	α-Fe
55.18	11	α'-Fe
55.64	6	Fe ₃ N

Table C.17. Summary of peaks observed for several N₂ additions to the shielding gas for a welding speed of 0.423 cm/sec and a 20% N₂ addition to the shielding gas.

2θ (degrees)	Intensity (A.U.)	Phase I.D.
16.43	12	Fe ₈ N
19.85	26	γ-Fe
20.16	29	α-Fe
20.20	14	Fe ₈ N
20.74	11	Fe ₂ N
35.29	22	α-Fe
35.61	8	Fe ₃ N
40.95	7	Fe ₄ N
46.07	16	α-Fe
46.28	8	Fe ₂ N
55.18	13	α'-Fe
55.64	5	Fe ₃ N

REFERENCES

- ¹ L.G. Berry, ed., Powder Diffraction Files, (Joint Committee on Powder Diffraction Standards, Swarthmore, PA), 1974.
- ² K.H. Jack, "The Iron-Nitrogen System: The Crystal Structures of ϵ -Phase Iron Nitrides", *Acta Cryst.*, 1952, 5, 404-411.
- ³ B.D. Cullity, Elements of X-Ray Diffraction, (Addison-Wesley Publishing Company, Inc., Reading, MA), 1956.
- ⁴ K.H. Jack, "The Occurrence and the Crystal Structure of α'' -Iron Nitride; A New Type of Interstitial Alloy Formed During the Tempering of Nitrogen-Martensite", *Proc. Roy. Soc. A*, 1951, 208, 216-224.
- ⁵ K.H. Jack, "Binary and Ternary Interstitial Alloys I. The Iron Nitrogen System: The Structures of Fe_4N and Fe_2N ", *Proc. Roy. Soc. A*, 1948, 195, 34-41.

VITA

Todd A. Palmer holds B.S. and M.S. degrees in Metals Science and Engineering, and a Ph.D. degree in Materials Science and Engineering, all from the Pennsylvania State University. In addition to his academic pursuits, Dr. Palmer has served as a field artillery officer in the U.S. Army Reserve and Pennsylvania Army National Guard. He has served in a number of battery level assignments and is a Commandant's List graduate of the U.S. Army Field Artillery Officer Basic Course at Fort Sill, OK.

He is the author of several publications, and has received numerous awards. These awards include the 1999 ASM Graduate Student Paper Competition, the 1997 American Council of IIW winning entry for the Granjon International Graduate Student Paper Competition, and an American Welding Society Graduate Research Fellowship, which he held from 1995 to 1998.

He is a member of ASM International, TMS, and the American Welding Society, and has served on the organizing committee for the Golden Anniversary McFarland Award Symposium, 'Metals Into The 21st Century', at Penn State University in April 1998.